Preeti Joshi
Shakti S. Gupta
Anoop Kumar Shukla
Sachin Singh Gautam   *Editors*

Advances in Engineering Design

Select Proceedings of FLAME 2020

🌰 Springer

Lecture Notes in Mechanical Engineering

Series Editors

Francisco Cavas-Martínez, Departamento de Estructuras, Universidad Politécnica de Cartagena, Cartagena, Murcia, Spain

Fakher Chaari, National School of Engineers, University of Sfax, Sfax, Tunisia

Francesco Gherardini, Dipartimento di Ingegneria, Università di Modena e Reggio Emilia, Modena, Italy

Mohamed Haddar, National School of Engineers of Sfax (ENIS), Sfax, Tunisia

Vitalii Ivanov, Department of Manufacturing Engineering Machine and Tools, Sumy State University, Sumy, Ukraine

Young W. Kwon, Department of Manufacturing Engineering and Aerospace Engineering, Graduate School of Engineering and Applied Science, Monterey, CA, USA

Justyna Trojanowska, Poznan University of Technology, Poznan, Poland

Preeti Joshi · Shakti S. Gupta ·
Anoop Kumar Shukla · Sachin Singh Gautam
Editors

Advances in Engineering Design

Select Proceedings of FLAME 2020

Editors
Preeti Joshi
Department of Mechanical Engineering
Amity School of Engineering
and Technology
Noida, Uttar Pradesh, India

Anoop Kumar Shukla
Department of Mechanical Engineering
Amity School of Engineering
and Technology
Noida, Uttar Pradesh, India

Shakti S. Gupta
Department of Mechanical Engineering
Indian Institute of Technology Kanpur
Kanpur, Uttar Pradesh, India

Sachin Singh Gautam
Department of Mechanical Engineering
Indian Institute of Technology Guwahati
Guwahati, Assam, India

Preface

This book presents a pool of research articles on different aspects of engineering design from the 2nd International Conference on Future Learning Aspects for Mechanical Engineering (FLAME), which was organized by Amity University, Uttar Pradesh, Noida, India, from August 5 to 7, 2020.

The conference aims to provide a platform for academician, scientist, and researcher across the globe to share their scientific ideas and vision in the areas of thermal, design, industrial, production, and interdisciplinary areas of mechanical engineering. The FLAME-2020 conference played a key role to set up a bridge between academician and industry.

Due to COVID-19 outbreak around the world, the meetings and gatherings were banned, besides strict immigration policy. Based on most authors appeal and health consideration, after careful discussion, the conference committee changed this event to online conference.

The conference presented almost 600 participants to interchange scientific ideas. During the three-day conference, the researchers from academics and industry offered the most recent cutting-edge findings, went through several scientific brainstorming sessions, and exchanged ideas on practical socioeconomic topics. This conference also provided opportunity to establish a network for joint collaboration between academician and industry. Major emphasis was focused on the recent developments and innovations in various fields of Mechanical engineering through plenary lectures. The book covers mechanical design areas such as computational mechanics, finite element modeling, computer-aided designing, tribology, fracture mechanics, and vibration. The book brings together different aspects of engineering design and will be useful for researchers and professionals working in this field.

The editors would like to acknowledge all the participants who have contributed to this volume. We also deeply express our gratitude to the generous support provided by, Amity University, Noida. The editors also thank the publishers and every staff of the department and institute who have directly or indirectly assisted to accomplish this goal. Finally, the editors would also like to express gratitude to the

Respected Founder President Amity University, Dr. Ashok K. Chauhan, for providing all kinds of supports and blessings.

In spite of sincere care, there might be typos and always a space for improvement. The editors would appreciate any suggestions from the reader for further improvements of this book.

Noida, India   Preeti Joshi
Kanpur, India   Shakti S. Gupta
Noida, India   Anoop Kumar Shukla
Guwahati, India   Sachin Singh Gautam
September 2020

About This Book

Innovation, technology, material, resources, and various other factors have important role in the design of a component. The book presents various chapters incorporating mechanical design in the form of computer-aided designing, finite element modeling, computational mechanics, vibration and fracture mechanics. Experimental, computational, and analytical aspects in the field of design are discussed in various chapters in this book. The book brings together different aspects of engineering design and will be useful for researchers and professionals working in this field.

The FLAME 2020 was held at Amity University, Noida, India, in August 2020. Numerous scientists, researchers and industry experts presented the future aspects of process/product design. This conference provided a forum for research scholars, scientists, undergraduate, postgraduate, and industry experts to discuss latest challenge and future need in the area of design and development of green product.

Contents

About the Editors

Dr. Preeti Joshi completed her PhD from Indian Institute of Technology, Roorkee, India. She did her Master of Technology also from Indian Institute of Technology, Roorkee, India. Currently, she is working as an Assistant Professor in Amity University Noida. Her research interest involves finite element modelling, carbon nanotubes, nano composites, modelling and simulation. Dr. Joshi is having 6 years of working experience in teaching various UG and PG courses in mechanical engineering. She has published various research articles in refereed international journals and conferences.

Dr. Shakti S. Gupta is Associate Professor at the Indian Institute of Technology, Kanpur, India. He did his Masters from Indian Institute of Science, Bangalore, and his PhD from Virginia Tech, USA. His research interest includes linear and non-linear structural mechanics, mechanics of nanomaterials and their characterization, and engineering mechanics. He is a recipient of several awards such as DRDO's Silicon Medal for National Science Day oration, and the Daniel Fredrick Scholarship for excellent performance in the graduate program in the Department of Engineering Science and Mechanics, Virginia Tech.

Dr. Anoop Kumar Shukla is presently working as Assistant Professor in the Department of Mechanical Engineering Amity University Noida. He did B.Tech from Institute of Engineering & Rural Technology, Allahabad, and M.Tech from Harcourt Butler Technological Institute, Kanpur. He received Ph.D. degree in 2017 from Dr. APJ Abdul Kalam Technical University, Lucknow. He has more than 8 years of teaching and research experience. His area of research is energy conversion and thermal management, combined power cycles, biofuels, gas turbine cooling, and advanced thermodynamics. He has published more than twenty research papers in peer-reviewed international journals and conferences. He has published two book chapters in Methanol and the Alternate Fuel Economy and Industrial Applications of Green Solvents: Volume II.

Dr. Sachin Singh Gautam is currently an Assistant professor in the Department of Mechanical Engineering, IIT Guwahati. He carried out his post-doctoral research at AICES, RWTH Aachen University, Germany. He finished his PhD and M.Tech. in the area of high velocity impact problems from IIT Kanpur. Dr. Gautam has undertaken projects from SERB, DST and VSSC, ISRO. He has recently received funding to enhance the functionalities of ISRO's structural analysis software tool FEASTSMT. Also, his students have been working on research projects in joint collaboration with Siemens R&D, Gurgaon and Cummins R&D Pune. He has guided two PhD students, and further supervising eight students. He has guided 19 M.Tech. students. His research group has received three best paper awards, and a best poster award. Two of his masters students have been awarded DAAD fellowship for carrying out their master's thesis project work in German universities. He is also the recipient of best teacher award. He has published around 15 book chapters, 22 journal papers, and 50 national/international; conference publications. His current area of research is in computational contact mechanics, isogeometric analysis, GPU computing, and application of machine learning in computational mechanics.

Size-Dependent Natural Frequency Variation Analysis of Single-Layer Graphene Sheet

Harshad Patel, Saumil Desai⃝, **and Mitesh B. Panchal**⃝

Abstract In this technical paper, the single-layer graphene sheet (SLGS) of zigzag atomic structure is introduced and natural frequency variation analysis of graphene sheet has been performed. The properties of graphene sheet are affected by different anomalies and changes of parameters such as effect of varying length & width considering cantilever and bridge boundary conditions. This paper comprised of two predominant approaches; analytical and finite element method. The analytical approach has been executed considering classical plate theory for transverse vibration of SLGS as plate and ANSYS software has been employed for verifying results were obtained, using an analytical approach. Moreover, after substantiating consequential results from both approaches; comparison of natural frequency variation has been performed to validate the analytical approach. In the presented analysis the zigzag configurations (10,0), (14,0), and (18,0) of SLGS with bridged and cantilevered configurations are analyzed against variation in the length of SLGS. The obtained results were observed that as the length of SLGS increases, its natural frequencies decreases. And, the natural frequency of SLGS of the same size is found higher for bridged configuration as compared cantilevered configuration. The performed analysis is found to be useful for the development of Graphene-based ultrahigh-frequency sensor systems.

Keywords Single layer graphene sheet · Natural frequency · Finite element analysis

H. Patel
Central Institute of Plastics Engineering and Technology, Ahmedabad, Gujarat, India
e-mail: patel.harshad0585@gmail.com

S. Desai · M. B. Panchal (✉)
Nirma University, Ahmedabad, Gujarat, India
e-mail: mitesh.panchal@nirmauni.ac.in

S. Desai
e-mail: saumil.desai@nirmauni.ac.in

1 Introduction

Single-layer graphene sheet proffered astounding properties in the area of electronics, bio-medical, electrical, mechanical, and all these are directed to find multitudinous application [1–3]. Graphene has extraordinary properties in terms of application compared to other material like phosphorene nanoribbons [4]. In the recent material innovation, graphene has immerged as the strongest material in the field of material engineering as it possesses interesting and extraordinary properties [5, 6]. It is thin too and lightweight with tremendous electrical, optical, and thermal properties which made it versatile material in the application of various fields, such as electronics, aviation, sensors, solar panels, etc. [7–9]. Graphene has being become interesting material due to its profound properties like thermal conductivity as 5000 W/mK [10], explored surface area as 2630 m^2/g [11], mobility of electron at room temperature as 250,000 cm^2/Vs [12], and reasonable electrical conductivity. Graphene has carbon arrangement in a single layer with honeycomb structure which is said hexagons [13].

There have been done many researches on single-layer graphene sheet from 1970 to date which included a study of transverse vibration of graphene [14], torsional vibration, dynamic analysis on graphene [15] sheet. Further research was extended with different boundary conditions and with or without masses attached to graphene sheets to cultivate comprehension of behaviors of graphene sheets against various conditions [16]. There are many researches were completed too regarding various boundary conditions like clamped-pinned-free without mass boundary condition, clamped-pinned with masses boundary condition [17], and a combination of two. One predominant aspect of graphene is observed that to date; there has been very less research completed on configuration modification and effect of variation of configuration on natural frequency and other parameters [18, 19].

2 Modeling Approach

2.1 Analytical Approach

In this study, single phase of the modeling approach is adopted for graphene sheets without defect and zigzag atomic arrangement configuration is employed. It is assumed that graphene is a kind of rectangular plate and so that classical thin plate theory said Kirchoff theory can be applied to it, as graphene has single layer atom arrangement [20]. All the assumptions are taken as same as used in classical plate theory, and finally equilibrium approach has been applied to the rectangular plate. There are various solution methods that are available for getting the equation of motion of rectangular plate but one predominant method is the equilibrium approach to obtain the equation of motion. Here, displacement of graphene is considered in transverse direction, and solution is obtained by recalling Blevin's solution for natural frequency [21, 22]. Considering the equilibrium approach in 'Z' direction,

Table 1 Properties of graphene

Sr. No.	Property	Value
1	Poisons ratio υ	0.456
2	Density ρ	1161 kg/m^3
3	Young's modulus E	1 TPa $= 10^{12}$ Pa

Table 2 Dimensions of graphene

Sr. No.	Dimensions	Value
1	Length of graphene sheet, a	10 A $= 10^{-9}$ m
2	Width, b	21.315 A $= 2.1315 \times 10^{-9}$ m
3	Thickness	0.17 nm $= 1.7 \times 10^{-10}$ m

the equation of motion can be obtained as, [22] (Tables 1 and 2).

$$D\left(\frac{\partial^4 w}{\partial^4 x} + 2\frac{\partial^4 w}{\partial^2 x \times \partial^2 y} + \frac{\partial^4 w}{\partial^4 y}\right) + \rho h \frac{\partial^2 w}{\partial t^2} = 0 \tag{1}$$

Solution of the above equation of motion (free vibration) is expressed as below:

$$
\begin{aligned}
W(x, y) =\ & A1\ \sin\alpha x \sin\beta y +\ A2\ \sin\alpha x \cos\beta y +\ A3\ \cos\alpha x \sin\beta y +\ A4\ \cos\alpha x \cos\beta y \\
& +\ A5\ \sinh\theta x \sinh\emptyset y +\ A6\ \sinh\theta x \cosh\emptyset y +\ A7\ \cosh\theta x \sinh\emptyset y \\
& +\ A8\ \cosh\theta x \cosh\emptyset y
\end{aligned}
$$

where, $\lambda2 = \alpha2 + \beta2 = \theta2 + \emptyset2$.

Blevins had formulated a solution for the various boundary conditions for the above equation so recalling the solution of Blevins for finding natural frequency of plate is expressed as, [21, 22].

$$\omega_{ij} = \sqrt{\left\{\frac{\pi^4 D}{\alpha^4 h\rho}\right\}\left\{G_x^4 + G_y^4\left(\frac{a}{b}\right)^4 + 2\left(\frac{a}{b}\right)^4\left[\vartheta\, H_x H_y + (1-\vartheta)J_x J_y\right]\right\}} \tag{2}$$

where D Flexural Density $= \frac{Eh^3}{12(1-\vartheta^2)}$, $G_x, H_x, J_x, G_y, H_y, J_y =$ constants depending on BCs.

For bridged boundary condition (FFCC),

ω_{11} as : $G_x = 1.506$, $H_x = 1.248$, $J_x = 1.248$, $G_y = 0$, $H_y = 0$, $J_y = 0$
ω_{12} as : $G_x = 2.5$, $H_x = 4.658$, $J_x = 4.658$, $G_y = 0$, $H_y = 0$, $J_y = 0$.

Sample calculation of (5,5) armchair configuration of rapheme is formulated as:

Fig. 1 Continuum solid model of single-layer graphene sheet along with boundary conditions
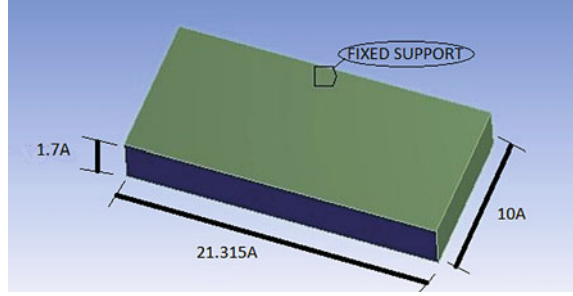
$$\text{Flexural rigidity } (D) = \frac{Eh^3}{12(1-\vartheta^2)} = \frac{10^{12} \times \left(3.45 \times 10^{-10}\right)^3}{12\left(1-0.456^2\right)} = 4.3203 \times 10^{-18} \text{ N.m}$$

$$\omega_{11} = \sqrt{\left\{\frac{\pi^4 \times 4.3203 \times 10^{-18}}{\left(10^{-9}\right)^4 \times 1161 \times 1.7 \times 10 - 10}\right\} \left\{ \begin{array}{l} 1.506^4 + 0^4 \left(\frac{10^{-9}}{2.1315 \times 10^{-9}}\right)^4 + 2\left(\frac{10^{-9}}{2.1315 \times 10^{-9}}\right)^4 \\ \times [0.456 \times 1.248 \times 0 + (1-0.456)1.248 \times 0] \end{array}\right\}}$$

$$= 6.62 \times 10^{12} \text{ Hz}$$

$$\omega_{12} = \sqrt{\left\{\frac{\pi^4 \times 4.3203 \times 10^{-18}}{\left(10^{-9}\right)^4 \times 1161 \times 1.7 \times 10 - 10}\right\} \left\{ \begin{array}{l} 2.5^4 + 0^4 \left(\frac{10^{-9}}{2.1315 \times 10^{-9}}\right)^4 + 2\left(\frac{10^{-9}}{2.1315 \times 10^{-9}}\right)^4 \\ \times [0.456 \times 4.658 \times 0 + (1-0.456)1.248 \times 0] \end{array}\right\}}$$

$$= 6.73 \times 10^{12} \text{Hz}$$

So from the above calculation similar procedure can be adopted for cantilever boundary condition (FFFC) and results can be compared.

2.2 Finite Element Analysis

Simulation of continuum approach of rapheme sheet for frequency analysis of (10,0), (14,0), and (18,0) zigzag configuration with various lengths have been carried out in ANSYS workbench shown in Fig. 1. Dimensions of configuration were taken 10 nm × 21.315 Å with a width of 170 pm which became the diameter of carbon atom. But CAD software is enabled to generate this size of object and so that in ANSYS modeler, input dimensions were set as 0.001×0.0021315 μm and thus 2D rectangular rapheme sheet was extruded by 0.00017 μm.

2.3 Finite Element Analysis (Space Frame Approach)

In the previous calculation, graphene sheet is considered as a continuous plate for getting analytical solution of natural frequency but in the actual scenario, it is a single layer carbon sheet possesses a hexagonal lattice structure [23, 24].

We can validate the continuum approach by executing simulation in ANSYS APDL. For creating a space frame model in ANSYS APDL, coordinates of carbon atoms are generated in software and for that, each coordinate works as a key point in the active plane of ANSYS APDL. After getting all key points in ANSYS APDL, they were connected by line for obtaining lattice structure.

3 Result and Discussion

Three approaches to analyzing graphene sheet have given reasonable results with minor differences in the natural frequency in separate boundary conditions. Total three simulations of zigzag configurations graphene sheets were executed as an analytical solution, in Ansys Workbench and as a space frame approach in ANSYS APDL. Moreover, length of the graphene sheet has been set as 23.391, 47.995, 72.603, 97.213, 121.822 A for all approaches which are shown in Tables 3 and 4 for two different boundary conditions as, bridged boundary condition and cantilever boundary condition. Using Nano Modeler software, coordinates of space frame model have been generated using different lengths of graphene sheet and regarding that length, width of graphene sheet has been set by software. After creating successfully three configurations of zigzag atomic arrangement, all coordinates were exported in ANSYS APDL to generate the require size of graphene sheet and which is shown in Fig. 2. In bridged boundary conditions, two edges of graphene sheet are

Table 3 Comparison of natural frequency (bridge boundary condition)

Configuration (Zigzag)	Width (m)	Length (m)	Analytical (Hz)	FEA (Hz)	FEA (SFA)
(10,0)	9E-10	2.3391E-09	1.93E + 12	1.71E + 12	1.86E + 12
		4.7995E-09	4.93E + 11	4.40E + 11	4.89E + 11
		7.2603E-09	2.16E + 11	1.94E + 11	2.05E + 11
		9.7213E-09	1.20E + 11	1.08E + 11	1.14E + 11
		1.21822E-08	7.65E + 10	6.91E + 10	7.28E + 10
(14,0)	1E-09	2.3391E-09	1.92E + 12	1.80E + 12	2.00E + 12
		4.7995E-09	4.90E + 11	4.52E + 11	5.10E + 11
		7.2603E-09	2.26E + 11	2.00E + 11	2.15E + 11
		9.7213E-09	1.36E + 11	1.12E + 11	1.45E + 11
		1.21822E-08	8.00E + 10	7.01E + 10	7.20E + 10
(18,0)	2E-09	2.3391E-09	1.99E + 12	1.74E + 12	1.60E + 12
		4.7995E-09	4.95E + 11	4.52E + 11	4.20E + 11
		7.2603E-09	2.13E + 11	1.99E + 11	2.10E + 11
		9.7213E-09	1.25E + 11	1.11E + 11	1.50E + 11
		1.21822E-08	7.96E + 10	7.03E + 10	7.24E + 10

Table 4 Comparison of natural frequency (cantilever boundary condition)

Configuration (Zigzag)	Width (m)	Length (m)	Analytical (Hz)	FEA (Hz)	FEA (SFA)
(10,0)	9E-10	2.3391E-09	3.26E + 11	2.97E + 11	2.90E + 11
		4.7995E-09	7.75E + 10	7.01E + 10	7.60E + 10
		7.2603E-09	3.39E + 10	3.05E + 10	3.19E + 10
		9.7213E-09	1.89E + 10	1.70E + 10	1.80E + 10
		1.2182E-08	1.20E + 10	1.08E + 10	1.14E + 10
(14,0)	1E-09	2.3391E-09	3.26E + 11	3.01E + 11	3.15E + 11
		4.7995E-09	7.75E + 10	7.09E + 10	7.78E + 10
		7.2603E-09	3.39E + 10	3.08E + 10	3.25E + 10
		9.7213E-09	1.89E + 10	1.71E + 10	1.90E + 10
		1.2182E-08	1.20E + 10	1.09E + 10	1.14E + 10
(18,0)	2E-09	2.3391E-09	3.30E + 11	3.05E + 11	3.30E + 11
		4.7995E-09	7.78E + 10	7.16E + 10	7.90E + 10
		7.2603E-09	3.36E + 10	3.18E + 10	3.39E + 10
		9.7213E-09	1.80E + 10	1.77E + 10	2.05E + 10
		1.2182E-08	1.29E + 10	1.15E + 10	2.30E + 10

Fig. 2 Space frame model of zigzag (10,0) modeled using FEM package ANSYS
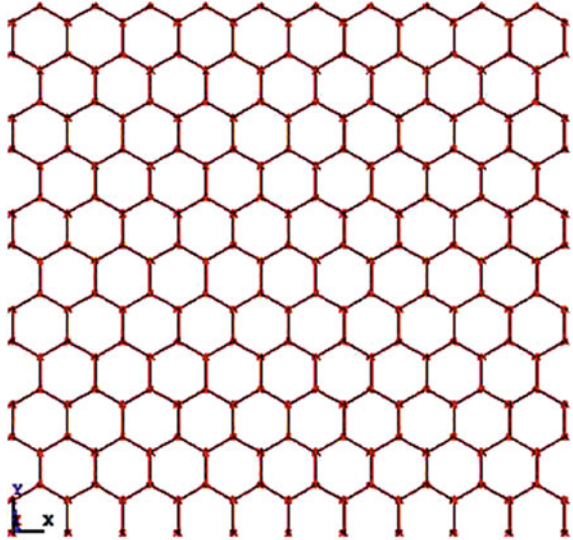
fixed and two edges are set free to deform whereas in cantilever condition, one edge is fixed and three edges are allowed to deform.

As we know that natural frequency is affected by mass of the material and stiffness of the material, increment in length of the graphene sheet added the mass of carbon atoms in the sheet. This added mass resulted in change in natural frequency as per Fig. 3 and in Fig. 3, we can see that added mass decreases natural frequency of graphene sheet. In the bridged boundary condition, (18,0) configuration shows lower frequency at small length of sheet, whereas (14,0) shows higher frequency but ultimately as length of sheet increased, natural frequency matches to same value as in all configuration.
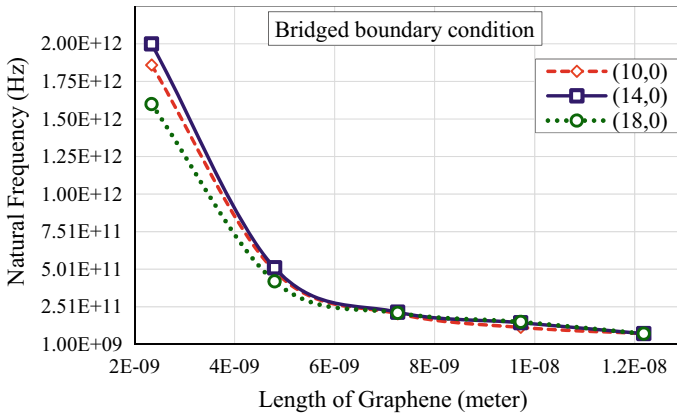
Fig. 3 Variation of natural frequency with respect to length of SLGS in Zigzag atomic structures, for bridged boundary conditions
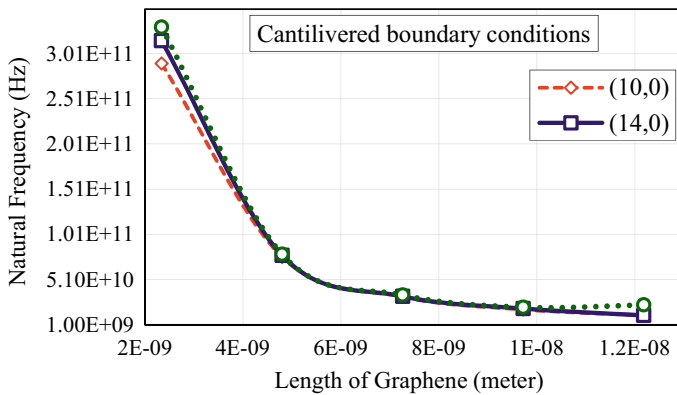
Fig. 4 Variation of natural frequency with respect to length of SLGS in Zigzag atomic structures, for cantilevered boundary conditions

In cantilever boundary condition, Fig. 4 shows changes in natural frequency phenomenon completely due to free edges from three sides. As in this case results obtained in space frame approaches similar to boundary conditions but little higher natural frequency is shown due to motion allow from three sides. Less mass of carbon atoms shows higher frequency in (18,0) configuration whereas (10,0) shows lower natural frequency in the same approach for less mass of graphene sheet.

4   Conclusion

In the study of natural frequency of single-layer graphene sheet with different length phenomenon considering different configuration (10,0), (14,0), (18,0); it is observed that there is a little variation between analytical, FEA, and SFA approaches as ranges from 1 to 6%. In bridge boundary conditions, small size of SLGS resulted in higher natural frequency around 2.0E12 Hz as shown in (14,0) configuration whereas increment in length of SLGS, decreases natural frequency. On the contrary, in cantilever boundary condition, shortest length of SLGS gave very low-frequency compare to bridge boundary condition while considering any atomic structure. Increasing length of graphene sheet resulted in increment in width too but key sight of result can be seen from the Fig. 5 that after certain length of graphene sheet, minor variation is observed in natural frequency as stability can be achieved due to addition of mass does not affect too much. But one predominant data was observed regarding two boundary conditions that there is a huge variation in natural frequency for short
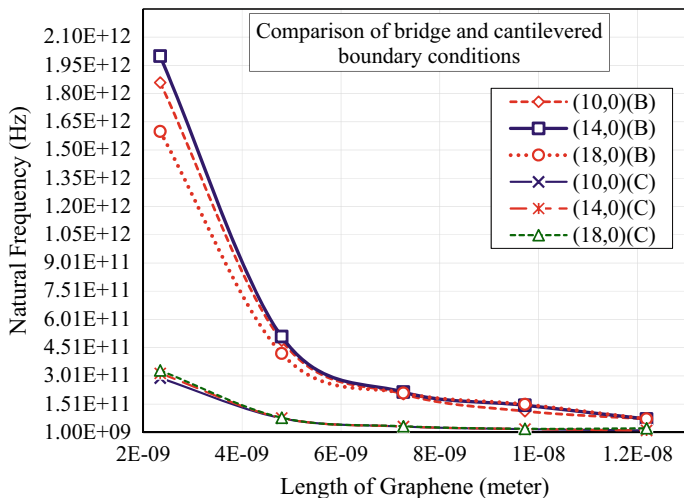
Fig. 5 Variation of natural frequency against length of SLGS, comparison between bridged [(10,0)(B), (14,0)(B), (18,0)(B)] & cantilevered [(10,0)(C), (14,0)(C), (18,0)(C)] boundary conditions

length of graphene sheet so it is suggested that for some application where too much variation is not required, then length of graphene sheet can be kept higher for avoiding variation in frequency.

References

1. Peng X-F, Chen K-Q (2015) Comparison on thermal transport properties of graphene and phosphorene nanoribbons. Sci Rep 5(1):16215
2. Chowdhury R, Adhikari S, Scarpa F, Friswell MI (2011) J Phys D Appl Phys 44(20), 20540:1–11
3. Scarpa F, Adhikari S (2008) J Phys D Appl Phys 41(8):085306:1–5
4. Duplock EJ, Scheffler M, Lindan PJD (2004) Hallmark of perfect graphene. Phys Rev Lett 92(22):225502
5. Gupta SS, Batra RC (2010) J Comput Theor Nanosci 7(10):2151–2164
6. Timoshenko S (1940) Theory of plates and shells. McGraw-Hill Inc., London
7. Papageorgio DG, Kinloch IA, Young RJ (2015) Graphene/elastomer nanocomposites. Carbon 95:460–484
8. Raju APA, Lewis A, Derby B, Young RJ, Kinloch IA, Zan R et al (2014) Wide-area strain sensors based upon graphene-polymer composite coatings probed by Raman spectroscopy. Adv Func Mater 24(19):2865–2874
9. Eda G, Chhowalla M (2010) Chemically derived graphene oxide: towards large area thin film electronics and optoelectronics. Adv Mater 22(22):2392–2415
10. Balandin AA, Ghosh S, Bao W, Calizon I, Teweldebrhan D, Miao F et al (2008) Superior thermal conductivity og single-layer graphene. Nano Lett 8(3):902–907
11. Zhu Y, Murali S, Cai W, Li X, Suk JW, Potts JR et al (2010) Graphene and graphene oxide: synthesis, properties, and application. Adv Mater 22(35):3906–3924
12. Novoselov K, Geim AK, Morozov S, Jiang D, Katsnelson M, Grigorieva I et al (2005) Two-dimensional gas of massless Dirac fermions in graphene. Nature 438(7065):197–200
13. Wang Q, Varadan VK Vibration of carbon nanotubes studied using nonlocal continuum mechanics. Smart Mater Struct
14. Jena S, Chakraverty S (2019) Dynamic analysis of single-layered graphene nano-ribbons (SLGNRs) with variable cross-section resting on elastic foundation. Curved Layered Struct 6:132–145. https://doi.org/10.1515/cls-2019-0011
15. Ren WJ, Shen ZB, Tang GJ (2016), Vibration analysis of a single-layered graphene sheet-based mass sensor using the Galerkin strip distributed transfer function method
16. Ansari R, Arash B, Rouhi H (2011) Vibration characteristics of embedded multi-layered graphene sheets with different boundary conditions via nonlocal elasticity. Compos Struct 93:2419–2429
17. Laura PAA, Pombo JL, Susemihl EA (1974) A note on the vibration of a clamped free beam with a mass at the free end. J Sound Vib 37:161–168
18. Natsuki T (2015) Theoretical analysis of vibration frequency of graphene sheets used as nanomechanical mass sensor. Electronics 4:723–738. https://doi.org/10.3390/electronics4040723
19. Samaei AT, Aliha MRM, Mirsayar MM (2015) Frequency analysis of a graphene sheet embedded in an elastic medium with consideration of small scale. Mater Phys Mech 22:125–135
20. Shen Z-B, Tang H-L, Li D-K, Tang G-J (2012) Vibration of single-layered graphene sheet-based nanomechanical sensor via nonlocal Kirchhoff plate theory. Comput Mater Sci 61:200–205
21. Blevins R (2001) Formula for natural frequency and mode shape. Krieger, Hellerup, Denmark
22. Belvins RD (1984) Formulas for natural frequency and mode shape. R.E. Krieger
23. Rakesh Prabhu T, Roy T (2010) Finite element modeling of multiwalled carbon nanotube. National Institute of Technology Rourkela

24. Zenkour A (2016) Vibration analysis of a single-layered graphene sheet embedded in visco-Pasternak's medium using nonlocal elasticity theory. J Vibroeng 18. https://doi.org/10.21595/jve.2016.16585

Design and Fabrication of Portable Tensometer for Natural Fibers

Roney Peter and B. P. Sharma

Abstract Present research proposed to develop a portable and handy tensometer to investigate the tensile strength as well as plot stress–strain variations of natural fibers onsite of plants when connected to a laptop. This research is focused on the portability and easy handling with respect to cost and weight of such device which can be taken at the place directly for identification and recognition of suitable fibers available in nature. In the present research work, a portable and handy tensometer is proposed to develop with different sensing and mechanical elements. Initial investigation can be done at the location of plants by removing a part of fiber and gripping with this portable tensometer. After design and fabrication, a spring was used as a load sensing element and the spring stiffness was found out to be 782.75 N/m; few samples of dhak fibers were investigated, and the tensile force recorded was 14.24605. Results were compared with computerized universal testing machine, and the device developed was found to be 72.97%.

Keywords Tensometer · Tensile strength · Natural fibers · Spring stiffness

1 Introduction

An earlier name for a tensile testing machine was tensometer. Nowadays, universal testing machine (UTM) additionally referred to as a universal tester, materials checking machine or materials test frame, is employed to check the tensile strength and compressive strength of materials. The "universal" a part of the name reflects that it will perform several customary tensile and compression tests on materials, components and structures of all kind of materials. But, these apparatus are mainly used in industries, are very expensive, high maintenance and also require skilled labor. This goes totally out of the economical boundaries if we need to check the

R. Peter (✉) · B. P. Sharma
Amity University, Noida, Uttar Pradesh, India
e-mail: ronpeter44@gmail.com

B. P. Sharma
e-mail: bpsharma@amity.edu

properties of naturally occurring fibers, so to test natural fibers in their natural conditions with all the constraints such as portability, economic feasibility, ease of use, availability and low power consumption. Natural or synthetic fibers are used for reinforcements in polymers to enhance its several mechanical properties. But, for investigating tensile behavior of these individual fibers, highly sophisticated and costly machines such as computerized universal testing machine and tensometers are available in the market. Now, due to mobility constraints and cost of those equipment, it is very difficult to investigate and find out suitable natural fibers available in different part of forming or non-forming places. The overview of the work is to create a tensile strength testing apparatus. The main components of the device are linear actuation mechanism, specimen clamping mechanism and a load sensing element with microcontroller unit using economically feasible materials which are easily available or machine which is economical, easy to use and portable so that it can be used onsite for tests in schools and colleges for experiments on behavior of different naturally occurring fibers, their properties due to the their place of occurrence and natural factors and hence to investigate their future applications. The device developed in the present proposal will be the first working prototype, the results will be compared with computerized universal testing machine and errors will be calculated. Further, developments will be made to reduce the errors significantly, to make the device more accurate.

2   Literature Review

Lim and Kim [1] talk about a study in which a small and handy tensile testing machine was developed to make students performs tensile tests during class using a small tensile testing element. The tensile testing device consists of a stepper motor, a load cell, a load cell amplification module, a data acquisition system and frame. The detected load signal is sent to the data acquisition system. The DAQ system with the help of LabVIEW software receives the signals from the load cell and displacement sensing device [1]. But the current proposal consists of a simple lead screw mechanism which does not require any electrical input but can be operated manually with desired rate of movement and instead of a load cell, this device consists of a tension spring to calculate the load applied, and the only electrical component used in this device is a TOF distance sensor which does not require any power supply module as a stepper motor does.

Velmurugan et al. [2] explained about the study of palmyra fiber reinforced with epoxy composites with the help of FEA along with various fiber volume distributions, and these results were compared with an experimental result. The tensile property of Palmyra fiber composite material can be obtained using tensometer. The result is obtained from Ansys software as per the composite analytical proceedings. Compare the experimental and analytical values, and this comparison helps in determining tensile strength of any natural fiber [2]. But the current proposal talks about a device which can be used to determine the tensile strength of a natural fibers onsite by just

clamping specimens to the device and a laptop or a mobile device. This device does not use any heavy end software for analysis but gives the results according to the tensile load applied to break the fiber.

Ferguson [3] explored about the strength of threads, string and yarn made of different and then study the properties of the fibers from which these are made, an experimental setup is used to measure the breaking strength [3]. This creates a comparison reference for the students so that they can use this reference to for application in daily use. In part II, the amount of static electricity held by these fabrics in both wet and dry condition also provides data about fabric [3]. But the current proposal talks about a device which can be used to determine the tensile strength of a natural fibers onsite by just clamping specimens to the device and a laptop or a mobile device. This does not involve any comparison of fibers with another fiber.

Kranjec et al. [4] explained about a microcontroller, namely Raspberry Pi 3B+, which can be used as a device for controlling the variables during tensile testing for research in materials. A list of materials required for the same was made to connect all the necessary equipment and the whole hardware setup with a connection board which was put in a small enclosure to make it portable and test were compared with commercially available Instron 8802 device; the comparison was sufficiently accurate for research purposes [4]. But the current proposal consists of an Arduino as a microcontroller which is five to six times cheaper and easy to work with. It is about a portable device with all the mechanical and electrical components, not only a control system for a tensile testing machine but also which can measure the tensile strength of natural fibers onsite without any complex control system.

Talib et al. [5] in 2019 described how the use of toy-bricks such as LEGO parts (Mindstorms EV3 and Technics) as building blocks for a small tensile testing equipment for the characterization of natural fibers with a load cell of capacity 2 kg and was programmed with open-source programming language. An oil palm fiber was tested, and damages due to the deformation were noticed [5]. But the current proposal is about a portable tensile strength testing device made of aluminum extrusion profiles and plexi glass which makes is durable and strong; it has the load cell capacity of about 40 kgs which provides the device with versatility, plus the device has its own electrical enclosure which makes it portable, and hence, testing can be done onsite. The proposed device will also give precise reading of tensile strength of the fibers which are being tested.

McGillicudy [6] explored information about the endangered whale species that is The North Atlantic Right Whale. They studied the entanglement of these whales in ropes are deadly for them; therefore, whale safe rope (WSR) was developed this rope will cause a localized point of stress, and hence, the rope will break off theoretically at point of impact. This study involves design and development of an apparatus to test and evaluate the characteristics of WSR or similar ropes foe which image processing and data accusation techniques were used in the device. The results and test methodology were robust which would allow future researchers to understand the behavior of the ropes in marine industries [6]. But the current proposal is about a portable tensile strength testing device for natural fibers not ropes and onsite investigation

can be made with help of this device the proposed device can give precise data about the tensile strength; as soon as the specimen clamped in the device breaks, this will provide knowledge about the future application of the fiber in various fields.

Based on the literature reviewed, it has been concluded that none of the author has reported about any device used for investigation of tensile strength of natural fiber that is low in cost and can be taken onsite for investigation and neither single one of them have mentioned about the ease of use and setup of any kind of portable device. Therefore, present research is focused on design and fabrication of such portable, handy and easy to use tensile strength testing machine. This tensometer can be taken at the place directly for identification and recognition of suitable fibers available in nature. Initial investigation can be done at the location of plants by removing a part of fiber and gripping with this portable tensometer.

3 Experimental Investigation

3.1 Design and Fabrication

Design of the device was made in consideration that the fibers investigated are natural fiber; therefore, the maximum force to which the tension spring was chosen is maximum 50 N of force. The test frame of the device is made of plywood attached together with nails and wood glue shown in Fig. 1. For attaching the specimen, metal hooks were used. The actuation mechanism used in the device is a lead screw linear actuation mechanism. There are two ends where the specimens will be attached, one is with the spring and the other will be the locknut part of the lead screw mechanism. The stationary part consists of a time of flight distance sensor that will measure the spring displacement.
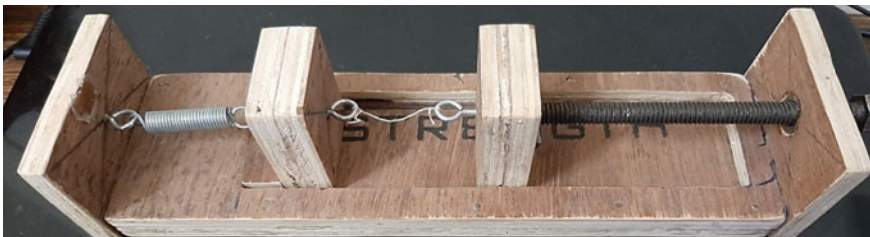
Fig. 1 Actual model of device

Table 1 Stiffness of spring

Mass applied (kg)	Force = m × 9.8 (N/m)	Displacement of spring (m)	Stiffness (k) = f/x
0.5	4.9	0.0075	777
1.0	9.8	0.0125	784
1.5	14.7	0.0187	786
2.0	19.6	0.025	784

Mean = (777 + 784 + 786 + 784)/4, spring stiffness = 782.75 N/m

3.2 Testing

As the device is using a tension spring to measure the value of load, spring stiffness is to be determined by a formula to calculate load applied. So, for finding out the spring stiffness a spring balance with the same spring is used (mentioned in Table 1).

Diameter of the fiber is calculated using a wire gauge or a micrometer which comes to be 0.19 mm or 0.00019 m. Thread is attached to the hooks provided in the sliding blocks (shown in Fig. 2). Arduino is connected to the computer and open Arduino IDE.

- Program is executed, and serial monitor is opened where the readings from the distance sensor will be displayed shown in Fig. 3.
- Bolt is slowly rotated to create tension on the thread attached to the hooks, as the tension increases the spring starts to elongate.
- A point will come where the thread will break, maximum value of the distance travelled by the spring through the calculation is given below.

The initial and final readings of the spring displacement are known, so by subtracting, this gives the displacement of the spring or the change in the length

Fig. 2 Device during testing
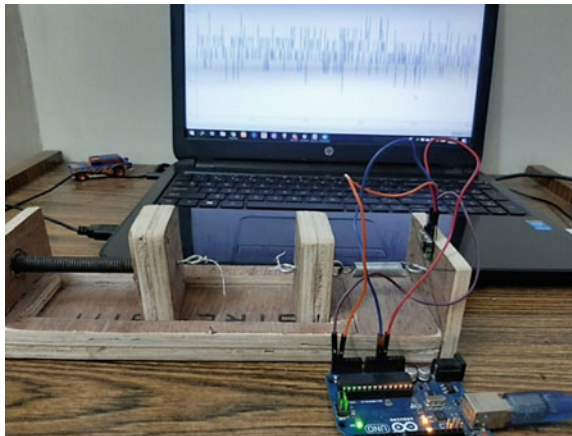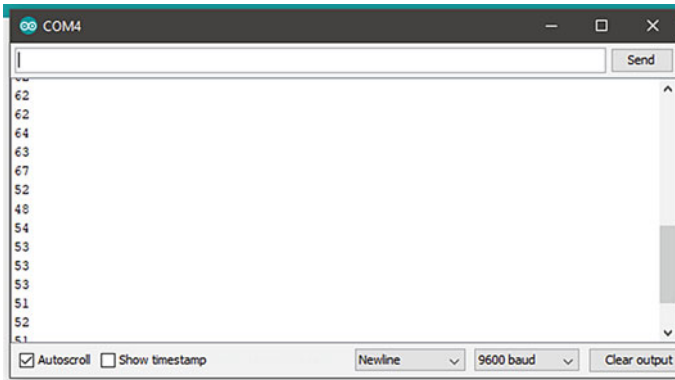
Fig. 3 Readings from the serial monitor

Table 2 Displacement of spring calculation

Initial readings before breaking (mm)	Final readings after breaking (mm)
61	79
59	76
61	79
59	77
60	80
Mean = 60 mm	Mean = 78.2 mm

of the spring shown in Table 2 (i.e.,): $78.2 - 60 = 18.2$ mm or we can say $x = 0.0182$ m, from the formula $F = kx$.

Calculating F we get, $F = 782.75 \times 0.0182$ ($F = 14.246$ N).

4 Result and Discussion

The results from the developed device (Shown in Figs. 4 and 5) were compared with laboratory tested results from a computerized universal testing machine, where the average tensile force was recorded as **19.525 N** and the developed device measured the value to be 14.246 N; therefore, percentage error $= 27.03\%$.

5 Conclusions

- A portable and handy tensile strength testing device was designed and fabricated.
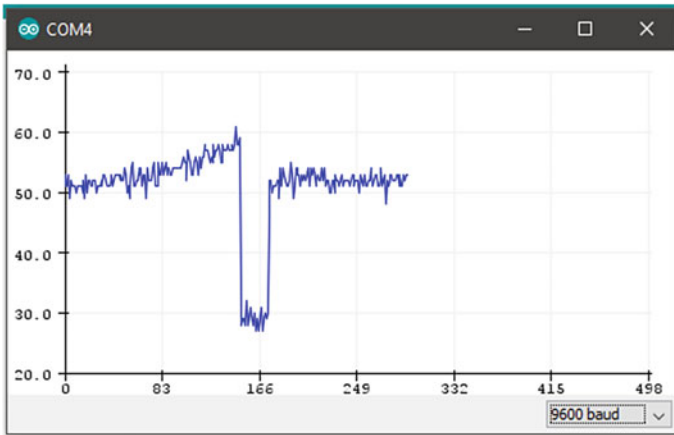
Fig. 4 Graph between time and deflection, from Arduino IDE

Fig. 5 Test specimen after breaking of the fiber

- The device was fabricated using easily available and cheap materials, and therefore, the device fabricated is very economic.
- A tension spring was used in the device, and its stiffness was calculated and was found to be 782.75 N/m.
- The device was tested using "Dhak" fibers, and the result was found to be 14.246 N.
- The test results were compared with previously tested laboratory results of the same fibers, and 27.03% error was calculated.
- It was concluded that a device is made that is able to test tensile strength of natural fiber with very close proximity, with an accuracy of 72.97%, can be taken onsite for investigation, easy to use, and is relatively very economical.

References

1. Lim W, Kim H-K (2013) Design and development of a miniaturized tensile testing machine. Semantic scholar, Seoul National University of Science and Technology, Seoul, Republic of Korea

2. Velmurugan G, Vadivel D, Arravind R, Vengatesan SP, Mathiazhagan A, Mohamed Rijuvan R (2012) Tensile test analysis of natural fiber reinforced composite. Int J Mech Ind Eng (IJMIE) 2(4). ISSN: 2231-6477
3. Ferguson L (2009) Properties of fibers and fabrics materials education
4. Kranjec M, Korinšek J, Ambrož M, Kunc R (2020) Control system for a tensile-testing device using low-cost hardware and open-source software. Strojniski Vestnik J Mech Eng 66(3):155–163
5. Talib AT, Mohammed MAP, Baharuddin AS, Mokhtar MN, Wakisaka M (2019) Mecahnical characterization of lingocellulisic fibres using toy bricks tensile tester. J Mech Behav Biomed Mater 97:58–64
6. McGillicudy G (2005) Characterization of weak rope through the design and construction of a portable tensile testing machine. University of New Hampshire

Increasing Power Train Efficiency Using Regenerative Clutch System

Bilal Nazeer, Madhusudan Grover, Vishnu Datta, and Rohit Sharma

Abstract The present paper relates to regenerative clutch in light motor vehicles. This arrangement of power trains is an alternative to the conventional clutch system which is being used in light motor vehicles. In the current powertrains, there are a lot of losses incurred during the transmission of power from the engine to the wheels. This happens due to the slippage between the friction plates of the clutch. The regenerative clutch system is a developed version of the current powertrains. This invention consists of a developed clutch system which could convert the slippage into electrical energy which could be stored in the battery and can be used for auxiliaries and even for acceleration of the vehicle. During half clutching in traffic jams, the clutch pedal is partially pressed to get the required power to the wheels. The remaining power which is being generated by the engine gets converted into heat and frictional loss and results in wear and tear of the clutch plates. But while using the regenerative clutch system, this lost energy can be saved and can be stored in the form of electrical energy.

Keywords Automobile vehicles · Automobile industry · Hybrid vehicles · Regeneration · Clutch system · Powertrain

1 Introduction

Powertrains which are being currently used in vehicles are good for open roads but have a major drawback which reduces their efficiency and practicality in city traffic. This is because powertrains use friction clutches to engage and disengage the power coming from the engine to the gearbox. In congestive city traffic, the engine of our cars produces more power (even at low RPMs) than we actually require, resulting in a recurrent use of the clutch pedal while driving. The clutch pedal is not fully released in traffic jams. This condition is known as Half Clutching. Half Clutching allows the driver to utilize a fraction of power generated by the engine to move the car,

B. Nazeer · M. Grover · V. Datta · R. Sharma (✉)
Department of Mechanical Engineering, Amity School of Engineering and Technology, Amity University Uttar Pradesh, Noida, India
e-mail: r25sharma@gmail.com

while the additional power of the engine is dissipated as heat due to friction between the friction clutch plates. Hence, this results in poor fuel economy in traffic. That is where the regenerative Clutch System comes into play. It can send the required amount of power on wheels and store the additional power generated by the engine as electricity and use it again. Also, it can do it with up to 97% efficiency and eliminate all the major losses associated with the clutch mechanism and do it without any friction or hydraulic coupling. It is feasible in existing power trains. This clutch system will not only be able to engage or disengage the engine but will also be able to send the required amount of power to the wheel (can be controlled by clutch pedal) and convert and store the additional power as electricity. It will channelize the power coming from the engine to either the wheels or to the power storage and will conserve the energy in half clutching conditions.

2 Losses in Friction Clutches

2.1 Friction Clutch

A clutch is a mechanical device that engages and disengages power transmission especially from driving shaft to drive shaft. In the simplest application, clutches connect and disconnect two rotating shafts (drive shafts or line shafts). In these devices, one shaft is typically attached to an engine or other power unit (the driving member) while the other shaft (the driven member) provides output power for work.

The purpose of friction clutches is to connect a moving member to another that is moving at a different speed or stationary, often to synchronize the speeds, and/or to transmit power. Usually, as little slippage (difference in speeds) as possible between the two members is desired.

2.2 Limitations of Friction Clutches

1. Due to friction between the two plates, a lot of energy is lost in the form of heat due to friction. This heat loss is unavoidable.
2. Due to excessive use, friction plates get worn out and need to be replaced frequently.
3. As there is more number of mechanical parts, wear and chances of failure are more.
4. While driving in heavy city traffic, clutch pedal is partially pressed due to which slippage occurs. This slippage is then converted into heat energy which can decrease the total power available at the output shaft. Hence this decreases the overall efficiency of the engine which affects the fuel economy [1].

2.3 Experimental Data of Losses in Friction Clutches

We did a test on a car to find out how much power is actually getting wasted while driving in traffic jams.

Vehicle Specifications:

Vehicle—Renault Duster.

Engine Capacity—1598 cc or 1.6 L.

Power—109 Ps @ 5700 Rpm.

Torque—150 Nm @ 3800 Rpm.

Transmission—5 Speed Manual.

We used OBD-II (On-Board Diagnostics) device to read how much power engine is producing and the amount of power actually going to wheels at different clutch positions, vehicle speed, and many other parameters which were given to us by the real-time readings of the ECU (Fig. 1). The results are shown in Table 1.

The amount of heat loss generated at different clutch positions (derived from ECU readings in Fig. 1) is as shown in Table 2.

The curve shown in Fig. 2, denoting the losses due to the friction clutch was however later calculated using other obtained data.

- Losses (denoted by blue curve)—Power lost (Watts) due to the slippage of friction clutch during the half-clutching.

Fig. 1 Power and torque characteristics of the test car (as provided by the car manufacturer)
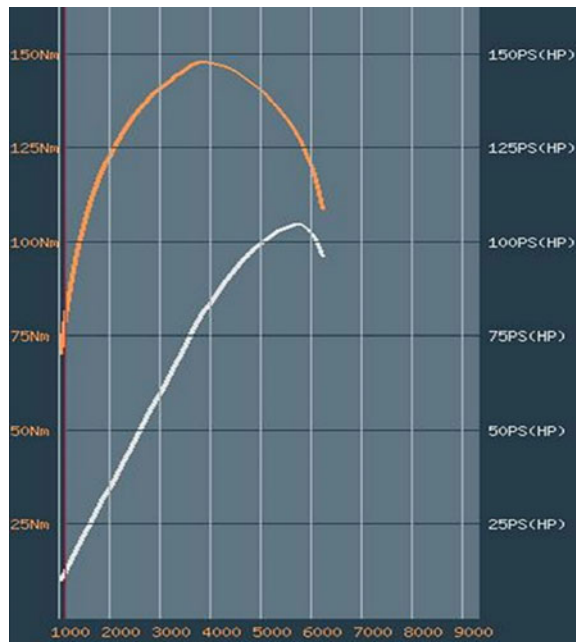
Table 1 Indicates the OBD II readings as obtained from the ECU of the test car

Clutch %	Torque (Nm)	RPM	Speed (kmph)	Average (kmpl)	Load (%)	Power (W)
0	0	846	0	0	65.9	0
25	110	852	3	1.5	71.4	2055
50	610	966	5	1.6	63.5	1915
75	580	1013	6	2.5	63.5	2160
100	870	1018	10	3.1	71.0	5420

Table 2 Heat loss generated during different clutch positions

Clutch %	Losses (W)	Power from engine (W)	Power on wheel (W)	Speed (m/h)
0	0	3816	0	0
25	2073	4123	2055	3000
50	3072	4081	1915	5000
75	2818	4884	2160	6000
100	0	5573	5420	10,000
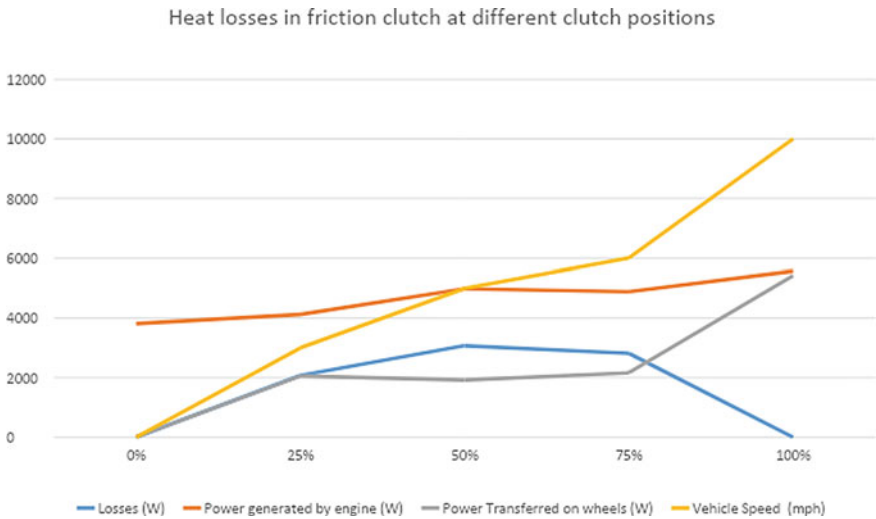
Fig. 2 The various parameters obtained through vehicle ECU using an OBD II adapter

- Power generated by engine (denoted by orange curve)—Total power generated by engine at the different clutch position. The accelerator paddle was not pressed at any point during the test yet the engine powered varied throughout the test as at different clutch positions the power required to accelerate the car was different hence ECU adjusted the engine power generation accordingly.

- Power transferred on wheels (Grey)—Total power transferred to wheel after the clutch slippage. It can be seen that during the half clutching period this value was much lower than the power generated by engine. This was due to the power dissipated as heat energy during the slippage.
- Vehicle Speed (denoted by yellow curve)—Speed of vehicle in m/h at different clutch positions.

2.4 Solution to the Problem

As discussed in the sections above, conventional friction clutches, used in majority of the powertrain in automobiles, incur a lot of losses. These losses were both economical and physical. Hence, the need of the hour was to have a change in the conventional powertrains to minimize the losses.

Therefore, after a lot of research and innovation, a new system, named Regenerative Clutch System, was introduced. The new innovation is capable of regenerating electricity, which was earlier dissipated as heat and frictional energy and saving in in a battery which can be further used for powering the auxiliaries or even during acceleration of the vehicle.

3 Proposed Regenerative Clutch System

3.1 Working of Regenerative Clutch System

In this system, the conventional friction clutch is being replaced by a Regenerative Clutch between gearbox and engine. When the vehicle is in traffic, the driver uses the half clutching to move the vehicle. Half clutching enables the driver to send the required power to drive the vehicle to the wheels. In friction clutches, the additional power is converted to heat energy which is dissipated. But in the case of Regenerative Clutch, the relative motion between the input and output shafts will generate electricity which can be stored in a battery. This electrical energy can be further used in auxiliaries or assist the engine at the time of acceleration [2]. When the clutch pedal is fully released, the output shaft of the engine and the input shaft of the gearbox are mechanically coupled by the regenerative clutch. The amount of mechanical power to be transmitted to wheels can be controlled using microcontrollers and additional engine power will be converted to electricity.

Hence the proposed clutch system can transfer the required power from engine to wheel and convert additional power from the engine to electricity without using any kind of friction or hydraulic coupling.

The CAD model is also created, showing the front view, side view, and isometric view shown in Fig. 3.
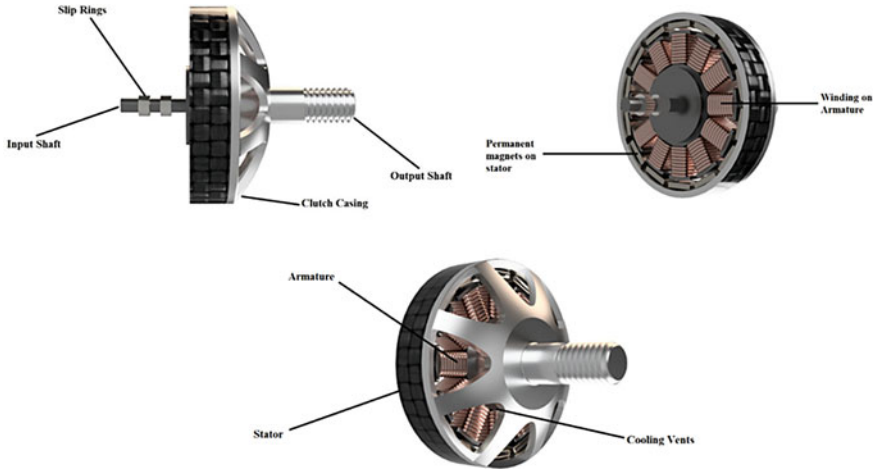
Fig. 3 Side view, front view, and isometric view of regenerative clutch system

4 Results

For result estimation, the efficiency of dynamo is assumed to be 95%. The estimation shows the amount of energy the can be conserved if a regenerative clutch system is used instead of conventional friction clutch (Table 3).

Figure 4 plots the estimated results that can be obtained if a regenerative clutch system is used instead of a friction clutch. For result estimations, the efficiency of dynamo was assumed to be 95% and other losses in power train were neglected.

- Losses—The losses can be drastically minimized if the heat energy lost during the slippage can be converted to electricity.
- Power Regenerated—This curve plots the amount of power that can be conserved at different clutch positions by replacing the friction clutches with regenerative clutch system.
- Power generated by engine—This curve remains unchanged even after the regenerative clutch system is employed.

Table 3 The energy conservation by regenerative clutch system

Clutch %	Power from engine (W)	Power on wheel (W)	Regenerated power (W)	Losses (W)	Speed (m/h)
0	3816	0	0	0	0
25	4123	2055	1969	103.65	3000
50	4981	1915	2918	153.6	5000
75	4884	2160	2677	140.9	6000
100	5573	5420	0	0	10,000
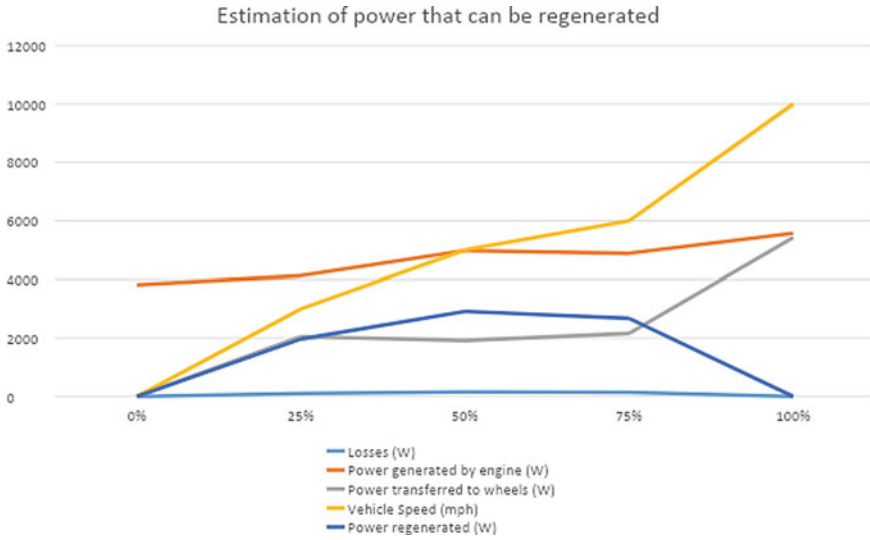
Fig. 4 The energy conserved by regenerative clutch system (the Navy Blue line shows the regenerated energy whereas the Light Blue line shows the losses)

- Power transferred to wheel—This curve remains unchanged even after the regenerative clutch system is employed.
- Vehicle Speed—This curve remains unchanged even after the regenerative clutch system is employed.

5 Conclusion

Conventional friction clutches, used in the powertrains of a majority of vehicles, had a lot of limitations. They incurred a lot of losses which included heat loss, wear, and tear, etc. Hence they couldn't be termed as ideal powertrains. Hence, a new and efficient powertrain was needed to replace the conventional one which would be better in terms of efficiency and performance. Therefore, the Regenerative Clutch System was introduced. This invention consists of a developed clutch system that could convert the slippage into electrical energy which could be stored in the battery and can be used for auxiliaries and even for acceleration of the vehicle. During half clutching in traffic jams, the clutch pedal is partially pressed to get the required power to the wheels. The remaining power which is being generated by the engine gets converted into heat and frictional loss and results in wear and tear of the clutch plates. But while using the regenerative clutch system, this lost energy can be saved and can be stored in the form of electrical energy. This innovation can be replaced by conventional clutch systems in cars and can be save a lot of fuel and can be economically efficient in the near future.

References

1. Newcomb TP, Merritt HE (1962) Effect of spline friction on the torque capacity and interface temperatures reached during a multi-disc clutch engagement. J Mech Eng Sci 4(4)
2. Reed Jr et al (2001) Method of converting an existing vehicle powertrain to a hybrid powertrain system. United States Patent US 6332257 B1

Design of Shock-Free Conical Nozzles

Shubham Maurya, A. Shaji, V. Mahesh, C. K. Krishnadasan, and G. Levin

Abstract Conventional conical nozzles consist of a circular-arc throat profile with tangentially attached conical section. This configuration leads to formation of a weak shock as reported in several earlier works. This article presents a method that eliminates the weak shock by incorporating slight modifications in the throat profile. The modified throat profile is analysed using method of characteristics (MOC) and validated by inviscid computational fluid dynamics (CFD) simulation.

Keywords Conical nozzle · Oblique shock · Method of characteristics · Computational fluid dynamics

1 Introduction

Conventional conical nozzles have a circular-arc throat section along with tangentially attached conical divergent section. As reported in the literature [1–4], there is formation of weak oblique shocks originating from the region just downstream of the junction of circular-arc and conical divergent section and coalescing near the axis of symmetry. Darwell and Badham [1], Migdal and Kosson [2] have analytically predicted the formation of weak oblique shocks using MOC and Back and Cuffel [3] have experimentally verified the same.

The weak oblique shock formation is due to the fact that at the junction of circular-arc and conical section the conical section acts as an obstruction to the flow which has been expanded by the circular arc [1–4]. The solution to this problem as outlined in various earlier works entails incorporation of a MOC determined transition contour between circular-arc and conical section [1, 2, 5]. This transition contour has an inflexion point.

In the present work, the oblique shocks are eliminated by introducing a *buffer* profile after circular arc. The conical divergent section is attached tangentially to this *buffer* profile. Contrary to transition contour, the *buffer* profile has no inflexion point.

S. Maurya (✉) · A. Shaji · V. Mahesh · C. K. Krishnadasan · G. Levin
Solid Propulsion and Research Entity, Vikram Sarabhai Space Centre (ISRO), Trivandrum 695022, India
e-mail: shubham.maurya3@gmail.com

The novelty of this study is hence the elimination of inflexion points in the design of shock-free conical nozzles.

2   Mathematical Formulation

For steady, supersonic, inviscid, irrotational and axisymmetric flow, MOC equations are given as [6]:

$$\frac{\sqrt{M^2 - 1}}{1 + \frac{\gamma-1}{2}M^2} \frac{\mathrm{d}M}{M} + \mathrm{d}\theta - \frac{\tan\theta}{\sqrt{M^2 - 1} + \tan\theta} \frac{\mathrm{d}x}{r} = 0 \tag{1}$$

$$\frac{\mathrm{d}r}{\mathrm{d}x} = \tan(\theta - \mu) \tag{2}$$

$$\frac{\sqrt{M^2 - 1}}{1 + \frac{\gamma-1}{2}M^2} \frac{\mathrm{d}M}{M} - \mathrm{d}\theta - \frac{\tan\theta}{\sqrt{M^2 - 1}\tan\theta + 1} \frac{\mathrm{d}r}{r} = 0 \tag{3}$$

$$\frac{\mathrm{d}r}{\mathrm{d}x} = \tan(\theta + \mu) \tag{4}$$

where x and r are axial and radial coordinates, respectively, M is Mach number and θ is flow inclination angle (see Fig. 1). The Eqs. (1) and (2) hold along right running characteristic (C-), whereas Eqs. (3) and (4) hold along left running characteristic (C+). The above four equations are solved numerically for calculating the flow field
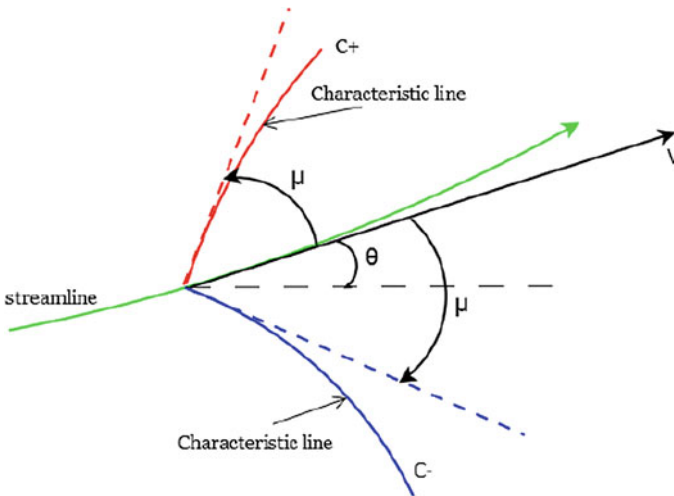
Fig. 1 Left (C+) and right (C-) running characteristic lines

parameters M and θ at locations given by coordinates x and r. The methodology for solving these equations is adopted from Ref. [6].

3   Methodology

As mentioned earlier, the conventional conical nozzles consist of a circular-arc throat section and a tangentially attached conical section (see Fig. 2). The nozzle wall angle variation along the length of nozzle (nozzle throat lies at $x = 0$) is shown in Fig. 3 (orange line). The junction of circular arc and cone can be identified from the figure as to be the point after which wall angle remains constant. It can be observed that the wall angle variation through this point is not smooth.

In the proposed shock-free nozzle design, the wall angle variation is smoothened out (see Fig. 3, blue line), resulting in a *buffer* profile as shown in Fig. 2. For the case considered, the cone half angle is chosen to be 21°. The shock-free and conventional conical nozzle geometries (with cone half angle = 21°) are plotted in Fig. 2. The *buffer* profile (blue colour, Fig. 2) increases the wall angle gradually to 21° (see Fig. 3) so that flow field computation using MOC can be worked out successfully without leading to merging of characteristics (see Fig. 4). The conical section is then attached tangentially to this *buffer* profile. The MOC computations are initiated after determining an initial-value line [7] and specifying the nozzle contour.
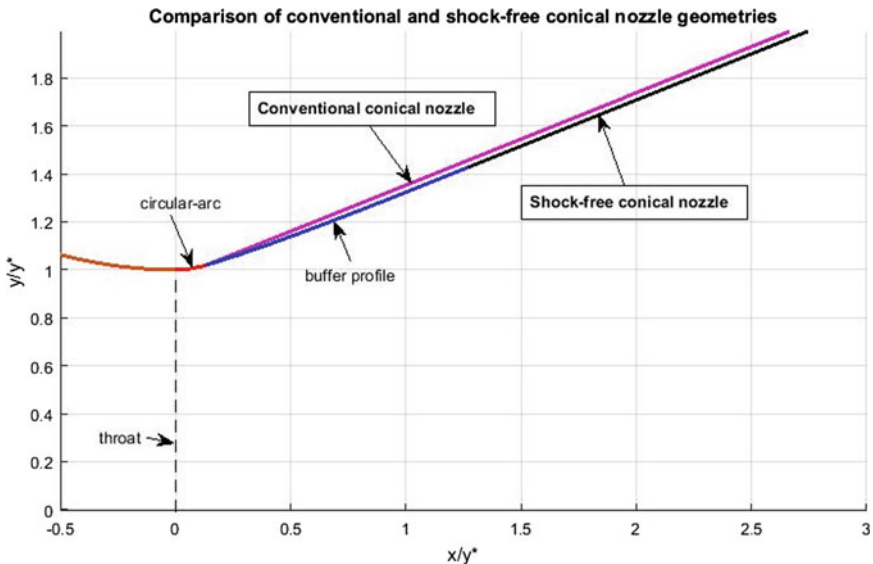
Fig. 2 Comparison of conventional and shock-free conical nozzle geometries (*Note*: y* is throat radius, and axial and radial dimensions are normalized with respect to y*)
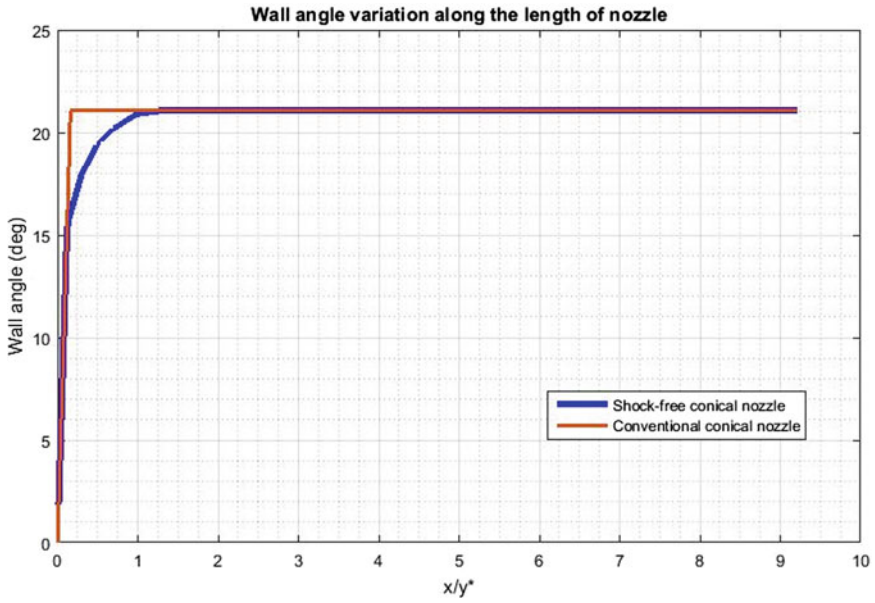
Fig. 3 Plot of wall angle variation along nozzle length for conventional and shock-free configurations
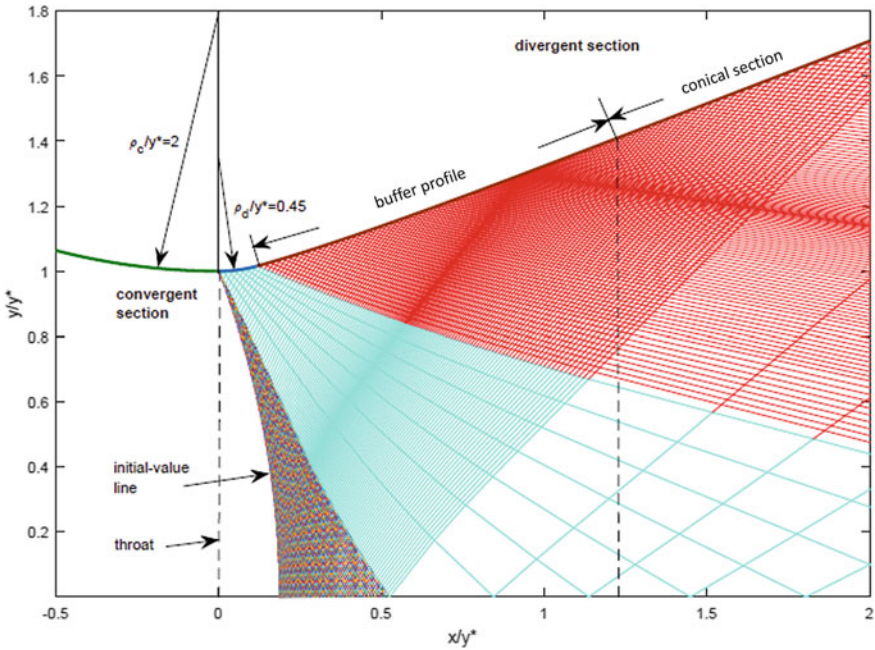
Fig. 4 Characteristic mesh inside shock-free nozzle

The selection of *buffer* profile involves trial and error as quite often the characteristics merge (indicating formation of weak oblique shock) making it impossible for the computation of rest of the flow field. Hence, the *buffer* profile is chosen in such a way that there is no coalescence or merging of characteristics so that MOC computations can be continued successfully.

4   Results and Discussion

The Mach number distribution along nozzle axis as computed using MOC is plotted in Fig. 5. It is seen that there are minor jumps in Mach number at few locations, which is arising because right running characteristics are coming closer to each other near the axis. The shock-free conical nozzle is validated using inviscid CFD simulation, and the Mach number distribution along nozzle axis is also shown in Fig. 5. The grid independency for CFD simulation was established with 18,200, 72,800 and 291,200 numbers of quadrilateral cells. The boundary conditions at nozzle inlet are specified by stagnation pressure and stagnation temperature such that the throat is
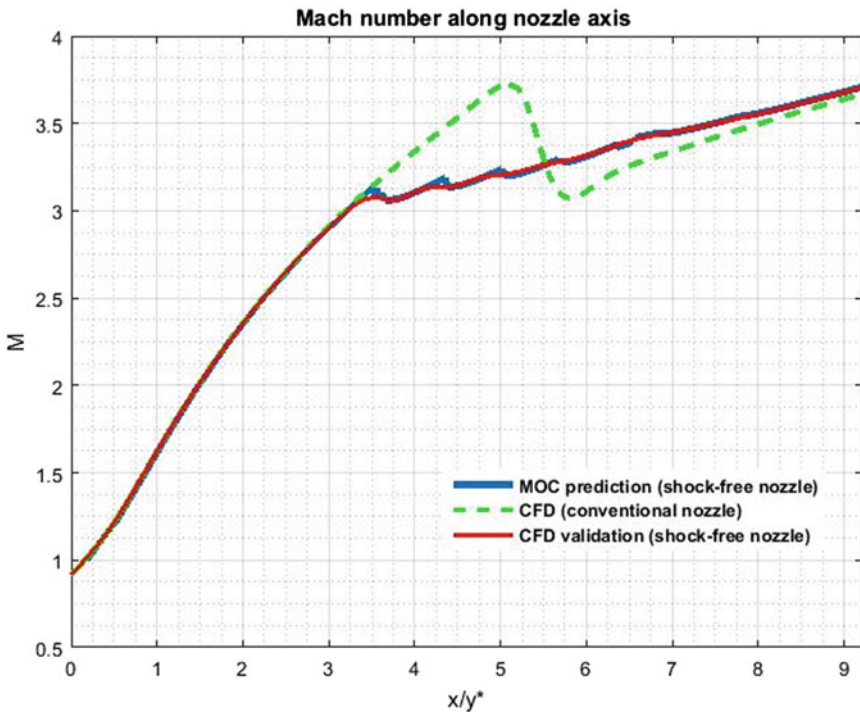
Fig. 5 Mach number variation along nozzle axis for shock-free and conventional conical nozzle configurations

choked whereas nozzle exit uses supersonic outflow boundary condition, nozzle wall is treated as adiabatic with free slip boundary condition, and nozzle axis is taken as axisymmetric. The governing equations are Euler equations, and viscosity effects are neglected. The CFD simulation was done with air exhibiting ideal gas properties and ratio of specific heats taken as 1.23 so as to validate the MOC computed flow field (since, $\gamma = 1.23$ in MOC Eqs. (1) and (3)).

Furthermore, the conventional and shock-free configurations are examined by inviscid CFD simulation. The elimination of shock in shock-free conical nozzle is confirmed through the Mach number plot along the axis of nozzle, where unlike conventional nozzle, there is no rise and fall in Mach number as observed in Fig. 5.

The Mach number palette for both conventional and shock-free conical nozzles is shown in Fig. 6, and the absence of weak oblique shock in shock-free conical nozzle is again verified.
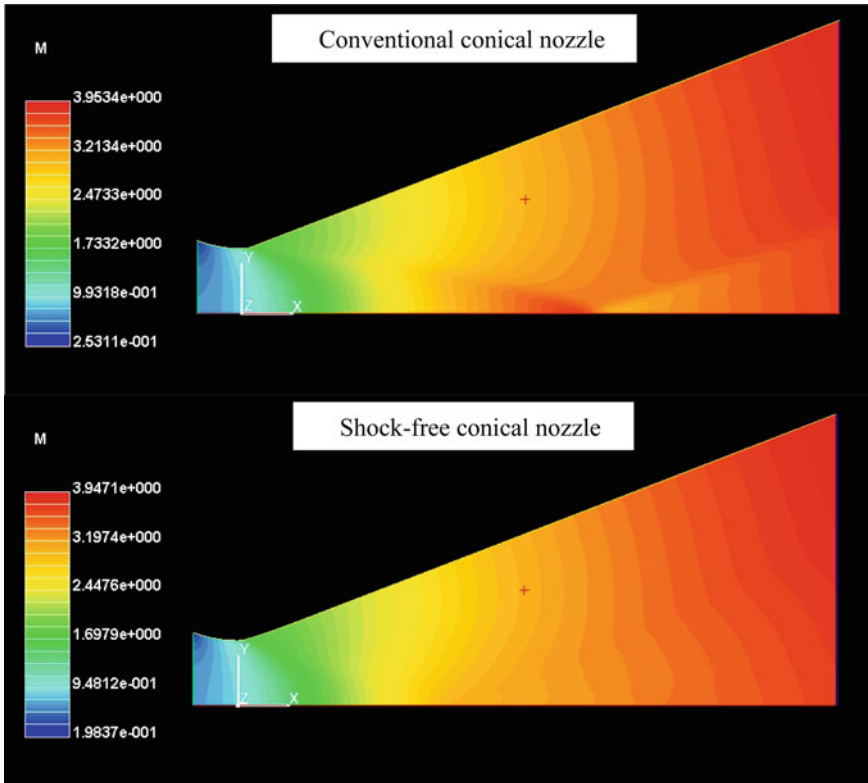
Fig. 6 Mach number palette for conventional and shock-free conical nozzle configurations. *Note* the presence/absence of a weak oblique shock in the conventional/shock-free configuration

5 Conclusions

A shock-free conical nozzle of 21° cone half angle was designed, and inside flow field was computed by MOC and validated using inviscid CFD simulation. The weak oblique shock elimination was also confirmed by inviscid CFD simulation. A major feature in this nozzle is that there is no inflexion point unlike the ones discussed in earlier works.

Further scope of this study would be to extend the shock-free conical nozzle design for other values of cone half angle. Moreover, the smoothing procedure of wall angle, i.e. selection of *buffer* profile, can be further refined so that trial and error can be avoided.

References

1. Darwell HM, Badham H (1963) Shock formation in conical nozzles. AIAA J 1(8):1932–1934
2. Migdal D, Kosson R (1965) Shock predictions in conical nozzles. AIAA J 3(8):1554–1556
3. Back LH, Cuffel RF (1966) Detection of oblique shocks in a conical nozzle with a circular-arc throat. AIAA J 4(12):2219–2221
4. Cuppoletti D, Gutmark E, Hafsteinsson H, Eriksson L-E (2014) The role of nozzle contour on supersonic jet thrust and acoustics. AIAA J 52(11):2594–2614
5. Callis LB (1966) An analysis of supersonic flow phenomena in conical nozzles by a method of characteristics. NASA TN D-3550
6. Argrow BM, Emanuel G (1988) Comparison of minimum length nozzles. J Fluids Eng 110:283–288
7. Sauer R (1947) General characteristics of the flow through nozzles at near critical speeds. NACA TM No. 1147

Transition of Stratified-Wavy Flow to Intermittent Flow Pattern: Nonlinear Analysis of Pressure Fluctuations

Sunny Saini, Jignesh Thaker, and Jyotirmay Banerjee

Abstract Gas–liquid two-phase flow is commonly observed in petroleum and chemical industries. Stratified flow pattern is simpler form of gas–liquid two-phase flow in which higher density fluid flows under the lower density fluid with non-disturbed interface. Small alteration of flow rate, chemical and physical properties of phases and pipe orientation or geometry lead to transition from stratified to wavy and then intermittent flow. Intermittent flow is associated with sudden pressure surge, erosion-corrosion and fatigue stress in the pipeline. This causes pipe failure at bend, T- and I-sections. Such failures lead to hazards and economic losses for the industries. It is required to develop a realistic approach for predicting the transition of such patterns in order to avoid intermittent flow inside pipe. In current study, transition from stratified to wavy and then intermittent flow patterns has been identified experimentally using recurrence network analysis of recorded pressure fluctuations for different flow conditions. The recorded time series of instantaneous pressure fluctuations have been analyzed using traditional recurrence quantification and recurrence network analysis. The two coefficients, recurrence rate and entropy, have been used for differentiating the dynamics between these two-phase flow patterns.

Keywords Stratified flow · Intermittent flow · Flow transition · Recurrence analysis

S. Saini (✉) · J. Banerjee
Sardar Vallabhbhai National Institute of Technology, Surat, Gujarat, India
e-mail: jaish0220@gmail.com

J. Banerjee
e-mail: jbnaer@gmail.com

J. Thaker
Adani Institute of Infrastructure Engineering, Ahmedabad, Gujarat, India
e-mail: jpthaker85@gmail.com

1 Introduction

Gas–liquid two-phase flow in horizontal pipe exhibits several flow patterns due to the effect of gravity on the different density phases and compressible nature of gas phase. A small instability at the interface of stratified flow (type of separated flow pattern in which both the phases are separated from each other by a non-disturbed interface) due to change in flow rate and properties of fluids leads to intermittent flow pattern. Since the last five decades, several cases of pipe failures or ruptures are reported due to presence of intermittent flow inside the piping system [1–3]. Intermittent flow is characterized by intermittent appearance of liquid pocket separated by large elongated gas bubbles moving on top of the liquid layer or liquid film. Intermittent flow pattern includes plug and slug flow, and it is categorized based on the presence of bubble or aeration in liquid slug/plug.

Several researchers have identified formation of slug flow from wavy-stratified flow based on their experimental research [4–6]. Kordyban and Ranov [4] have identified the transition of wavy-stratified flow to slug flow and reported sudden pressure surging in the flow due to high aeration at slug front. Later, few researchers [7–9] reported erosion-corrosion phenomenon in the pipe associated with the presence of slug flow or mostly due to aeration inside the liquid slug. Such erosion and flow accelerated corrosion (FAC) lead to rupturing of pipe inner wall and finally cause pipe failure [10]. Hence, it is required to correctly predict the formation of intermittent flow in gas–liquid transportation pipeline for preventing the economic loss and catastrophic failures in the industries.

In the present article, flow visualization is carried out at different values of Re_{SL} and Re_{SG} to obtain the transition of flow patterns. However, industrial pipelines are generally opaque where flow cannot be visualized. Thus, to obtain the change in flow dynamics in opaque pipes with transition of flow patterns, simultaneously, pressure signals are recorded with flow visualization. However, due to low pressure difference and nominal change in pressure signal in stratified and wavy-stratified flow, pressure signal alone does not provide adequate information for the same species of these separated forms of two-phase flow patterns. Moreover, fast Fourier transform (FFT) and power spectral density (PSD) function represent the frequency of the flow but failed to obtain the flow dynamics when flow transition takes place. With this aim, attempt has been made to predict the transition of flow patterns and internal flow dynamics in opaque pipe using nonlinear dynamical analysis tool (also called recurrence analysis) which is useful for further investigate the recorded time series pressure signals meticulously. Recurrence analysis is representation of the multi-dimensional reconstructed phase space trajectory in two-dimensional form where both axes are time axis and show dynamical behavior of the nonlinear dynamical signal. Recurrence analysis is carried out in two parts: qualitative analysis (recurrence plot which shows change in dynamical behavior) and quantitative analysis (recurrence quantification which quantified the dynamical change in the recurrence plot). Recurrence quantification is reported here based on two parameters: recurrence rate and entropy.

2　Experimental Details

Experiments are carried out on two-phase air–water flow test rig described by Thaker and Banerjee [1]. Flow patterns are visualized on a 25 ± 0.15 mm diameter and 14 m long transparent pipe. Photron FASTCAM high-speed camera is used to capture the images at different Re_{SL} and Re_{SG}. Simultaneously, at different flow rates, the time series pressure signals are measured using WIKA pen-type pressure transducer as shown in Fig. 1. The range of the pressure transmitter is 0–0.4 bar with the sensing of pressure fluctuation in milliseconds at an accuracy of 0.25%. The measured time series pressure signals are used to develop the recurrence plot using Marwan's equation [10]:

$$R_{i,j}^{m,\varepsilon_i} = \Theta\big(\varepsilon_i - \big||x_i - x_j|\big|\big), x_i \in \mathbb{R} i, j = 1, \ldots, N \ldots \ldots \ldots \tag{1}$$

where $R_{i,j}^{m,\varepsilon_i}$ is the recurrence matrix, Θ is Heaviside function, N is the window size or range of the recurrence plot, $\| \|$ is the norm parameter, ε_i is the threshold distance, and x_i, x_j are the distances between the two points. The recurrence analysis is required to quantify the signals and distinguish between two-different flow patterns even when their recurrence plots may look similar. Five parameters for analysis were proposed by Webber and Zbilut [11] on the basis of diagonal line structure, and three parameters were proposed by Marwan [10] on the basis of vertical line structure. In the present work, recurrence rate and entropy are used to identify the flow pattern transition. Recurrence rate (RR, also represented as %REC) is the number of recurring points out of the total number of data points of pressure signal. Recurring points are the points which fall within the threshold distance or radius parameter.

Fig. 1 Pressure transmitter

Fig. 2 Phase space
trajectory for slug flow
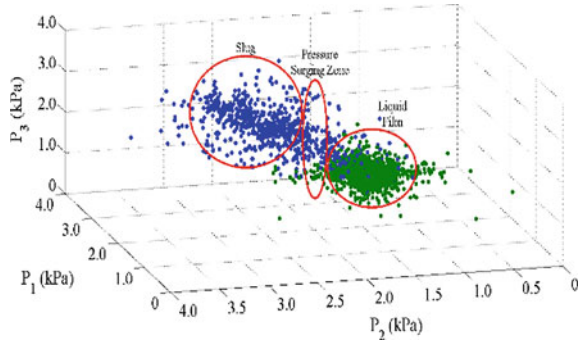
$$\%\mathrm{REC} = \frac{1}{N^2 - N} \sum_{i \neq j = 1}^{N} R_{i,j}^{m, \varepsilon_i} \ldots \ldots \ldots \tag{2}$$

The Shannon entropy (ENT) parameter shows the complexity of the system which represents the dynamic change of the system possesses.

$$\mathrm{ENT} = - \sum_{l = d_{min}}^{N} p(l) ln p(l) \ldots \ldots \ldots \tag{3}$$

where

$$p(l) = \frac{H_D(l)}{\sum_{l=d_{\min}}^{N} H_D(l)}, \ H_D(l) = \sum_{i=j=1}^{N} \left(1 - R_{i-1}, R_{j-1}\right)$$

$$\times \left(1 - R_{i+l}, R_{j+l}\right) \prod_{k=0}^{l-1} R_{i+k}, R_{j+k} \ldots \tag{4}$$

$H_D(l)$, is histogram of diagonal lines in recurrence matrix.

The complexity is represented through phase space trajectory shown in Fig. 2. The complexity of the flow is dependent on the magnitude and the variation of frequency of pressure signal as shown in Fig. 2.

3   Results and Discussions

3.1   Analysis of Recurrence Plot for Flow Transition

In the present section, flow visualization and recorded pressure signals are reported for a fixed $\mathrm{Re_{SG}}$ (=1500) and by increasing $\mathrm{Re_{SL}}$ from 1350 to 3650. At low $\mathrm{Re_{SL}}$

(=1350), stratified flow is obtained which transits into wavy flow pattern with increase in Re_{SL} to1800. Such increment in Re_{SL} leads to increase in hydraulic gradient and form a wavy interface. Simultaneously, liquid film holdup also increases, and path of gas flow over the wave crest reduces significantly which leads to K–H instability [5]. Hence, slug flow is developed in the pipe which is shown in Fig. 5. The detailed analysis of the transition from stratified flow to slug flow is elucidated in the following paragraphs.

As shown in Fig. 3a, at low Re_{SL} (=1350) stratified flow pattern is obtained in which, gas flows over the liquid film with non-disturbed interface (smooth or non-wavy interface) due to low density of gas and buoyancy effect. Less shearing action has been observed at the gas–liquid interface due to lower values of Re_{SG} (=1500) and Re_{SL} (=1350). Moreover, interfacial instability is not found so significant in the liquid region. This is mainly due to the flow condition falling under the range of laminar region for both the phases and also less influence by the gas flow over the liquid surface. Thus, stratified flow induces less pressure influence on the pipe wall. Hence, pressure of the flow is not large enough, whereas some pressure fluctuation is observed as shown in Fig. 3b. This leads to increase in the standard deviation of the flow and also increase the threshold distance for the wavy flow pattern. These data points recur within specified threshold distance which is having low values for the stratified flow condition. Hence, homogeneous type of recurrence plot is obtained for the stratified flow pattern as shown in Fig. 3c. Homogeneous type structure of the recurrence plot signifies that stratified flow pattern is less dynamic, i.e., with space and time change in flow is less (smooth interface of stratified flow resembles the less variation in the flow).

With increase in Re_{SL} (=1800), keeping fixed Re_{SG} (=1500), hydraulic gradient or liquid holdup of the liquid increases (Fig. 4a). Hence, according to wave theory [12], waves are developed at the gas–liquid interface. As the wave flow over the liquid film, it induces pressure variation and increases the pressure fluctuation as shown in Fig. 4b. This leads to increase in the standard deviation of the flow and also increase the threshold distance for the wavy flow pattern. Hence, as shown in Fig. 4c, high density, dispersed type of recurrence plot is obtained.

With further increase in Re_{SL}, slug flow developed in the pipe which causes sudden surge in pressure of the flow as shown in Fig. 5b. In addition, liquid holdup and wave amplitude are also increased further. Due to high gas velocity and narrow passage of wave crest, suction at the wave crest (since the pipe is closed conduit) induces and leads to high amplitude of wave which is called K–H wave [6]. Hence, due to pressure difference between the wave crest (low pressure or suction develops due to high velocity of gas flow over the crest) and trough (gas flow strike the trough region and separates over the wave crest which develops eddies at the wave trough and leads to high pressure), the wave elevates and blocks the gas flow path (in Fig. 5a). This results in development of slug flow pattern inside the piping system. In slug flow, when slug passes through the pressure point, sudden pressure surging is observed. This results in longer distance between the data points for slug and liquid film which does not recur within the threshold distance. This phenomenon leads to white strips/lines between two successive slugs/liquid films (shown in Fig. 5c).

Fig. 3 Stratified flow: **a** At
$Re_{SL} = 1350$ and $Re_{SG} = 1500$, **b** pressure signal and
c recurrence plot
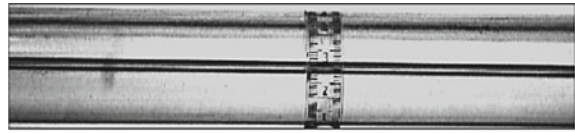
(a)
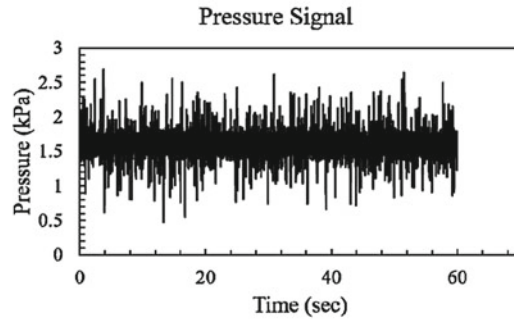
(b)
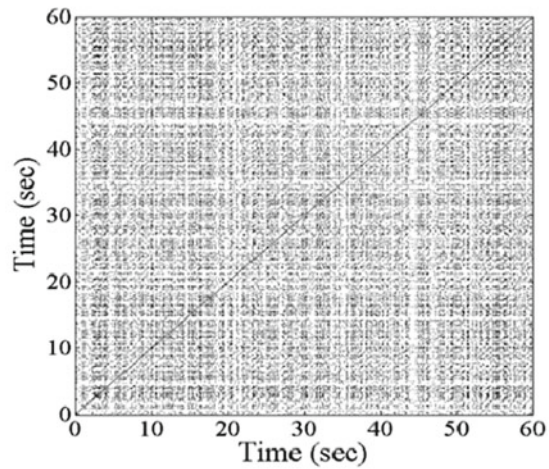
(c)

The obtained recurrence structure is a checkerboard structure which signifies that
flow pattern transition takes place from wavy-stratified to intermittent flow pattern.
The large rectangular shape (Fig. 5c) represents the liquid film which is at low
amplitude pressure and almost recurs by threshold distance for long duration due to
low frequency. The small rectangles represent (Fig. 5c) the slug which is observed
for small time interval and signifies the high velocity of slug.

Fig. 4 Wavy flow: **a** At
$Re_{SL} = 1800$ and $Re_{SG} = 1500$, **b** pressure signal and
c recurrence plot
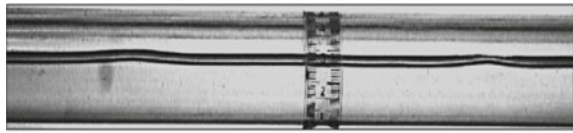
(a)
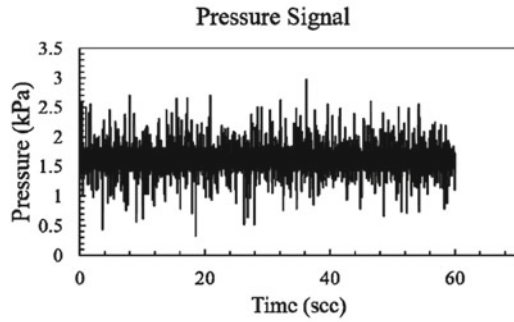
(b)
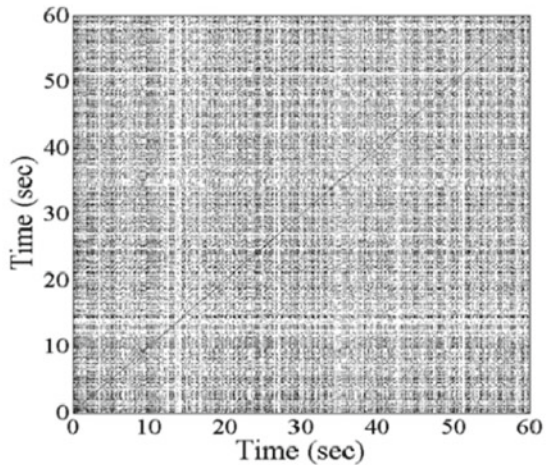
(c)

With further increase in Re_{SL} (=3650), development of slug rate increases which results in increment in slug frequency (shown in Fig. 6a). Such increment in slug frequency can be observed from the pressure signals plotted in Fig. 6b when compared to pressure signal at $Re_{SL} = 2750$ plotted in Fig. 5b in terms of observing the number of high-pressure spikes from both the figures. From the recurrence plot shown in Fig. 6c, it has been observed that slug and liquid film represents the less and high dense rectangles, respectively. While comparing the recurrence plots of Figs. 5c and

Fig. 5 Slug flow: **a** At Re_SL = 2750 and Re_SG = 1500, **b** pressure signal and **c** recurrence plot

(a)
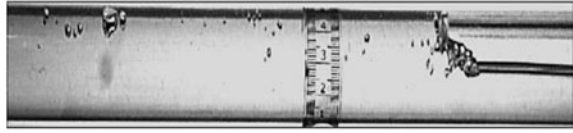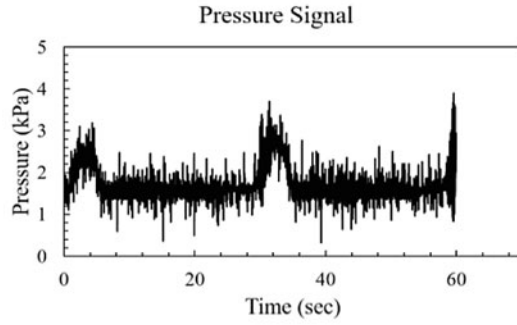
Pressure Signal

(b)
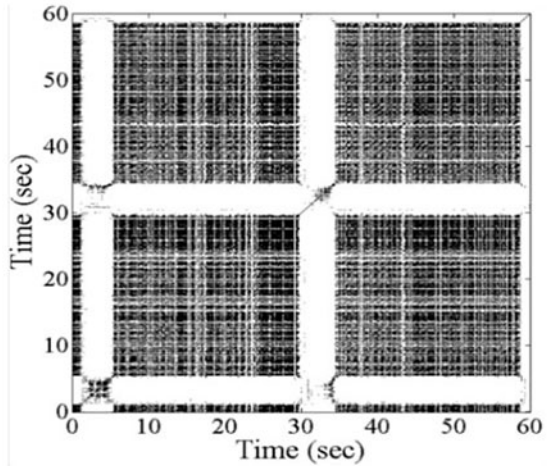
(c)

6c, more numbers of rectangular shapes are observed in Fig. 6c which signifies the number of slugs per unit time (means slug frequency) increases gradually.

Fig. 6 Slug flow: **a** At Re$_{SL}$ = 3650 and Re$_{SG}$ = 1500, **b** pressure signal and **c** recurrence plot
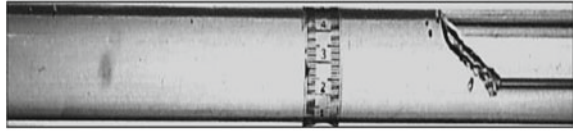
(a)
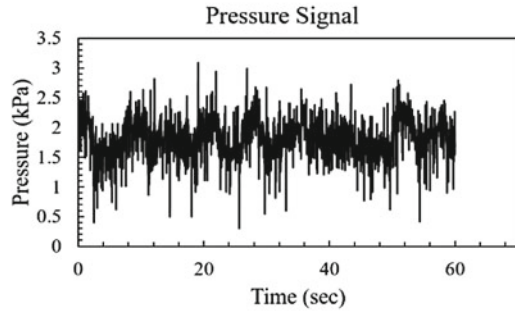
(b)
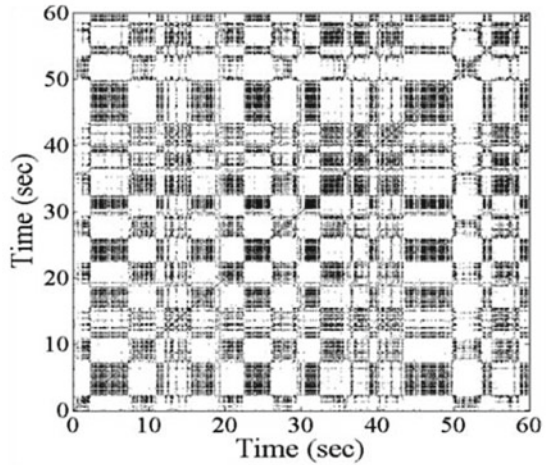
(c)

3.2 Recurrence Quantification Analysis of Transition of Flow Pattern

Recurrence plot represents the dynamics of flow pattern. However, some flow patterns cannot be distinguished only based on recurrence plot. For example, less aerated and high aerated slug flow shows rectangular shape of liquid film and slug. Also, pseudo-slug demonstrates similar type of recurrence plot. Hence, there is a requirement to quantify the recurrence plot for distinguishing the flow sub-regimes.

At $Re_{SL} = 1350$ and $Re_{SG} = 1500$, stratified two-phase flow is associated with accountable pressure compared to single-phase flow and also associated with fluctuation in pressure. This results in increase in standard deviation and threshold distance value. In addition, for stratified flow, less data points recur within threshold distance. Thus, recurrence rate is not higher for stratified flow (shown in Fig. 7). Also, if the threshold distance is less, small diagonal lines are developed by less number of recurring points. Simultaneously, a less number of diagonal lines are developed at the time of interval, i.e., within the range of threshold distance, and less segment of phase space trajectory at time 'i' passes through another segment of phase space trajectory at 'j' and recurs. Hence, the less number of diagonal lines is distributed in recurrence plot which leads to low value of entropy for the stratified flow (shown in Fig. 8).

With increase in Re_{SL} (=1800), for a fixed Re_{SG} (=1500), waves are developed at the interface which induces pressure and pressure fluctuation. However, compared to stratified flow, pressure in wavy flow does not increase significantly, but pressure fluctuation increases higher. This results in small increment in threshold distance. Thus, due to increase in pressure fluctuation, a less number of data points fall inside the specified threshold distance, and this results in small increment in recurrence

Fig. 7 Influence of Re_{SL} on recurrence rate of the flow and observed flow pattern transition
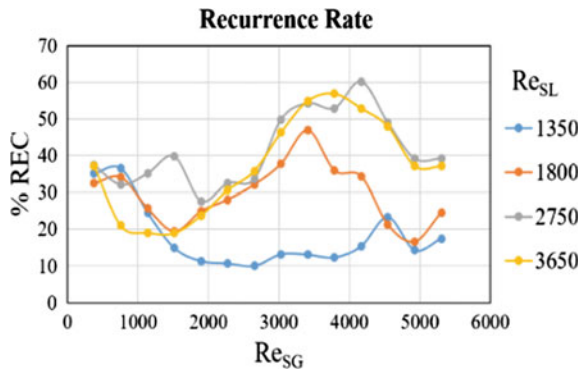
Fig. 8 Influence of Re_{SL} on entropy of the flow and observed flow pattern transition
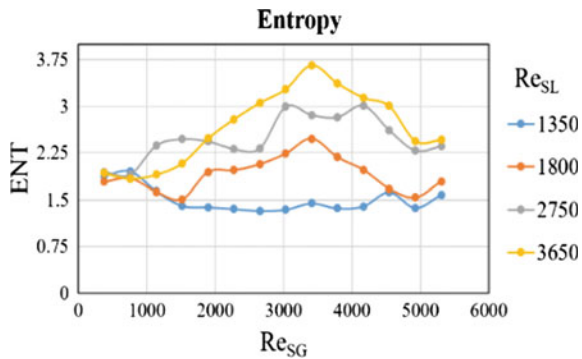
rate (shown in Fig. 7). Also, if the distance between the recurrence points is large, distribution of diagonal line is not higher, and this leads to small increment in entropy for the wavy flow pattern (shown in Fig. 8). With further increase in Re_{SL} (=2750), wavy-stratified flow transits into slug flow, and sudden pressure surging is recorded. When the slug flows through the pipe, large pressure variations or surging have been observed from high amplitude (slug) to low amplitude (liquid film). This leads to high threshold distance which results in high recurrence rate or recurrence density (in Fig. 7). Also, slug or liquid film phase space trajectory segments pass through each other. Hence, the number of diagonal lines and probability for distribution of diagonal lines significantly increase. This leads to increase in entropy for slug flow pattern (Fig. 8). With further increase in Re_{SL} (=3650), liquid holdup is further increased which leads to frequency of the slug. Hence, such increment in frequency causes sudden pressure variation from liquid film to slug and vice versa associated with less increment in threshold distance. Hence, a number of data points fall outside of the threshold distance which results in decrement of recurrence rate for slug flow (shown in Fig. 7). Due to rapid change in state of flow from liquid slug to liquid film, the diagonal lines are not developed well which causes decrement in the entropy of the slug flow pattern (shown in Fig. 8). It is also depicted that with increase in Re_{SG} frequency of the slug decreases and pressure drop between slug and liquid film increases which results in increment in the recurrence rate and entropy (shown in Figs. 7 and 8). Thus, from the recurrence quantification analysis, it is observed that with increase in Re_{SL}, frequency of the slug increases due to increase in liquid holdup, whereas pressure drop for slug flow does not increase significantly. On the other hand, with increase in Re_{SG}, pressure drop between slug and liquid film increases which leads to increase in plug/slug velocity in the pipe.

4   Conclusion

The following conclusions are derived from the present work:

- At low Re_{SL} (1350) and Re_{SG} (1500), stratified flow is obtained and shows a homogeneous type of recurrence plot. Low value of recurrence rate and entropy is obtained for stratified flow.
- With increase in Re_{SL} (1800), waves are obtained at the interface and recurrence plot structure changes to dispersed type structure. Also, threshold distance increases which leads to increment in the recurrence rate and entropy of the flow. This distinguishes wavy flow from the stratified flow.
- With further increase in Re_{SL} (2750), keeping fixed Re_{SG} (1500), checkerboard-like structure of recurrence plot is obtained in which white strip/line represents the surging of sudden pressure. Hence, with increase in pressure, recurrence rate and entropy increase sharply. The sudden change in recurrence parameter demarcates the flow pattern transition to slug flow.

References

1. Ossai CI, Boswell B, Davies IJ (2015) Pipeline failures in corrosive environments—a conceptual analysis of trends and effects. Eng Fail Anal 53:36–58
2. Khaksarfard R, Paraschivoiu M, Zhu Z, Tajallipour N, Teevens PJ (2013) CFD based analysis of multiphase flows in bends of large diameter pipelines. In CORROSION 2013. NACE International
3. Biomorgi J, Hernández S, Marín J, Rodriguez E, Lara M, Viloria A (2012) Internal corrosion studies in hydrocarbons production pipelines located at Venezuelan Northeastern. Chem Eng Res Des 90(9):1159–1167
4. Kordyban ES, Ranov T (1970) Mechanism of slug formation in horizontal two-phase flow. J Basic Eng 92(4):857–864
5. Barnea D, Taitel Y (1993) Kelvin-Helmholtz stability criteria for stratified flow: viscous versus non-viscous (inviscid) approaches. Int J Multiph Flow 19(4):639–649
6. Andritsos N, Hanratty T (1987) Interfacial instabilities for horizontal gas-liquid flows in pipelines. Int J Multiph Flow 13(5):583–603
7. Sun J-Y, Jepson WP (1992) Slug flow characteristics and their effect on corrosion rates in horizontal oil and gas pipelines. In: SPE annual technical conference and exhibition. Society of Petroleum Engineers
8. Ahmed WH, Bello MM, El Nakla M, Al Sarkhi A, Badr HM (2014) Experimental investigation of flow accelerated corrosion under two-phase flow conditions. Nucl Eng Des 267:34–43
9. Thaker J, Banerjee J (2016) Influence of intermittent flow sub-patterns on erosion-corrosion in horizontal pipe. J Petrol Sci Eng 145:298–320
10. Marwan N, Romano MC, Thiel M, Kurths J (2007) Recurrence plots for the analysis of complex systems. Phys Rep 438(56):237–329
11. Webber CL, Zbilut JP (2005) Recurrence quantification analysis of non-linear dynamical system. In: Riley MA & Van Orden GC (eds) Tutorials in contemporary nonlinear methods for the behavioral sciences, Chapter 2, pp 26–94
12. Jeffreys H (1925) On the formation of water waves by wind. Proc R Soc Lond A 107(742):189–206

Study, Modeling, and Analysis of Lightweight Chassis

Salman Khan and V. P. Singh

Abstract Nowadays, electric vehicles are being introduced to minimize environmental pollution, and however, there are several issues with the smooth implementation of electric vehicles as an alternative for conventional fuel run vehicles. The major issue with electric vehicles is the short distance of travel due to various reasons. Major factors are the weight of the vehicle which adversely affects its performance. The chassis is the backbone of vehicle which carries the effective load and withstands the shock and vibrations. Thus, weight reduction of chassis while maintaining the strength is the area of concern. In the present work, an attempt is made to study and analyze the presently used chassis for the different materials.

Keywords Chassis · Lightweight · Electric vehicle · Carbon fiber

1 Introduction

In the recent years, the pollution is a major problem for the whole world. One of the main sources of pollution is the greenhouse gas (GHGs) emission from petrol, diesel, and gas vehicles. In 2009, the transportation sector produced 25% GHGs of total GHGs produced by energy-related sectors [1]. To minimize the pollution, many automobile manufacturers are going for the launch of electric vehicles that provide green and revolutionary solution in place of conventional fuel run vehicles [2]. The major problem of electric vehicle is short range of traveling distance in one go which is approximately around 100 km [3]. Distance of traveling depends upon the weight of the vehicle. The total weight of the vehicle includes battery weight, chassis weight, control unit weight, steering system weight, and weight of other components. Weight of passengers is an additional weight which is not considered for analysis. A study shows that energy efficiency' can be increased from 5 to 8% by reducing 10% of

S. Khan · V. P. Singh (✉)
Mechanical Engineering Department, Harcourt Butler Technical University, Kanpur, India
e-mail: vpsingh@hbtu.ac.in

S. Khan
e-mail: mdsalmankhan195@gmail.com

vehicle weight [4]. The chassis is the main part of the vehicle that supports battery weight and other component's weight that are installed on the chassis [5, 6]. Weight of chassis is about 30–40% of total vehicle weight, so the chassis is designed for weight reduction. In the present work, different types of chassis are being studied by considering different materials and their analysis parameters.

2 Literature Review

Georgios et al. [7] performed their work on the one-seated prototype electric vehicle "Louis" chassis, their main target to study chassis deformation. Torsisius et al. [8] did their work on stress analysis of ladder-type crossover electric car chassis structure using FEM. They analyzed two types of chassis, solid plate beam chassis and perforated plate beam chassis.

Ahmad et al. [9] had designed and studied monocoque chassis design. In this chassis design, an attempt was made to develop an electric vehicle chassis that have lightweight and able to provide high specific strength and high specific stiffness and easy to manufacture. Rane et al. [10] did their work for redesign of the forklift chassis using optimization techniques. Author focused their work on the optimum material distribution to get an idea of the load flow path based on which new design with higher strength-to-weight ratio as compared with original design could be obtained. Marco et al. [11] focused their study on finite element analysis used for weight reduction. Applications were presented and discussed with the aim of showing their potential. A focus was given to weight reduction in automotive chassis design applications. The author provided a quick overview on structural optimization methods. Author explained how topology and topometry optimizations were more suitable for an early development stage, whose outcome could be further refined through size and shape optimizations. Prabhakaran et al. [12] perform structural analysis for weight reduction. Basic calculations based on the bending theory and values of stress and deflection were obtained. Stress and deflections were obtained by finite element analysis. Designs are modified by sensitive analysis for weight reduction. Comparison of the results showed that out of three cases third case resulted in about 6.7% of weight reduction. Luccarelli et al. [13] studied the car architecture of optimized positioning of electric components. They compared the traditional and electric vehicle based on wheel size as a key reference to measure the wheel proportion.

3 Material and Its Specification

The selection of material is the first and most crucial factor for chassis design. Most important criteria of material selection are lightweight, economic effectiveness, safety, recyclability, and life cycle consideration [10]. The carbon fiber chassis proposed in the present work is mainly because it is lighter, stiffer, stronger, fatigue

resistant, corrosion resistant, energy damping, thermal expansion, and manufacturing flexibility [14]. For chassis to be stiff and light in weight, it should be made from material with high ratio of elastic modulus E over density ρ. The monocoque chassis uses plates, so for plates elastic modulus and density ratio $\sqrt[3]{E}/\rho$ are used as stiffness indicator and $\sigma^{1/2}/\rho$ are used as strength indicator [15] (Table 1).

For the design of monocoque chassis, carbon fiber-reinforced epoxy is used that provides good design freedom. Using this material stiffer, stronger, and easy to manufacture chassis with approximate reduction of 40–60% of weight can be achieved [14] (Tables 2 and 3).

The prototype electric vehicle "Louis" is designed by TUC Eco racing team, and in this chassis aluminum 6061–T4 is used (Table 4).

Ladder type of beam is of two types: one is solid plate beam and another is perforated plate beam, and material used for ladder-type beam is alloy steel (Table 5).

Table 1 Material specific stiffness and specific strength [15]

Material	High strength, low alloy steel	Aluminum(6061-T6)	Magnesium (AZ91-T6)	Glass fiber composite (E-glass fiber polyester)	Carbon fiber composite (T300-epoxy)	Carbon fiber composite (M40-epoxy)
Specific stiffness ($\sqrt[3]{E}/\rho$)	1	2.03–2.06	2.61–2.65	2.41–2.51	4.42–4.52	5.34–5.59
Specific strength ($\sigma^{1/2}/\rho$)	1.26–1.23	2.51–2.54	2.84–3.06	4.88–11.8	9.21–11.8	6.00–8.63

Table 2 Unidirectional CFRE property [16]

Properties	Value (GPa)
Elastic modulus E_x	380.100
Elastic modulus E_y	28.269
Elastic modulus E_z	28.269
Poisson's ratio ν_{xy}	0.336
Poisson's ratio ν_{yz}	0.025
Poisson's ratio ν_{xz}	0.336
Poisson's ratio ν_{xz}	4.213
Shear modulus G_{xy}	13.790
Shear modulus G_{yz}	4.213
Shear modulus G_{xz}	2539.400
Tensile strength σ_x 2539	8.251
Compressive strength σ_{compx}	4.722

Table 3 Multiply laminates property [16]

Properties	Value (GPa)
Elastic modulus E	160.206
Shear modulus G	54.580
Tensile strength σc	971.400
Poisson's ratio ν	0.468

Table 4 Aluminum 6061–T4 property [8, 17]

Properties	Value
Density	2.7 g/cm^3
Elastic modulus	69 GPA
Poisson's ratio	0.33

Table 5 Alloy steel property [18]

Properties	Value
Density	7.7 g/cm^3
Poisson's ratio	0.28
Elastic modulus	210 GPa

4 Study of Previously Designed Space Frame Type and Monocoque Chassis

The performance of vehicle is better with equal distribution of load on front and rear axle and having low center of gravity [19]. The space frame-type chassis is made from the tube. These types of chassis have less space to install mechanical and electrical equipment [6]. However, these types of chassis have more weight, thus another monocoque-type chassis is designed that has lightweight and provides manufacturing flexibility [9, 18]. Manufacturing of space-type chassis is complex and has the risk due to many tube cutting and welding together [19]. The space-type chassis is designed on the principle that the tube is being loaded on their strongest direction [20].

The static model analysis of "Louis" model is set to calculate the von Mises stresses and deformations. The 2016 model chassis (shown in Figs. 1 and 2) has stresses lower than the material yield strength. Its weight (7 kg) is 34% lesser than the 2014 model [5] (Figs. 3 and 4). For designing, chassis stiffness-to-weight ratio is an important parameter and the stiffness weight ratio is the square of natural frequency [7].

$$\text{Natural frequency } (\omega) = \sqrt{\frac{K}{M}}$$

Fig. 1 Louis model 2016 [7]

Fig. 2 Louis model 2014 [7]

Fig. 3 Perforated plate chassis [8]
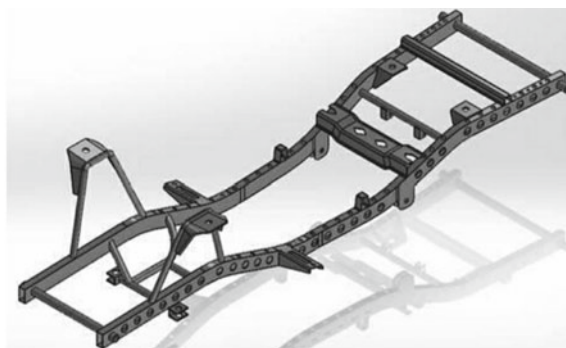
Fig. 4 Solid plate chassis [8]
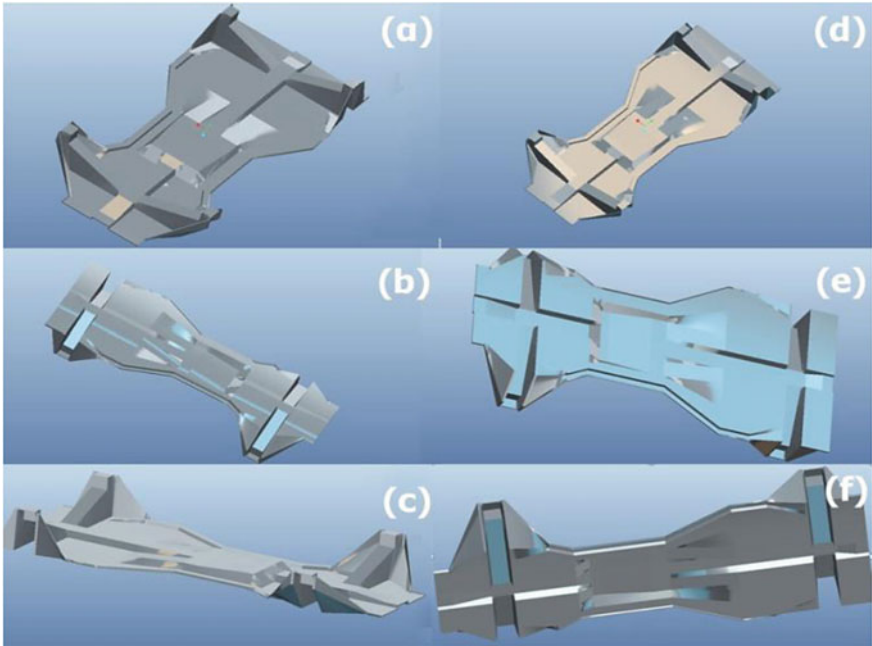
Fig. 5 Monocoque chassis [21]

where ω is the natural frequency, *K* is the stiffness of the chassis, and *M* is the mass of the chassis.

Ladder beam chassis is of two types: solid plate chassis and perforated plate chassis. The purpose of making perforated beam chassis is to reduce the weight. Weight of perforated plate chassis is 22.5% lesser than the solid plate chassis, thus perforated plate-type chassis is recommended for electric vehicle [6, 22].

In the monocoque chassis, strength is provided by entire panel instead of tubes. These types of chassis are easy to form complex shape. The manufacturing and assembly are easy and more accurate. For mass production, its repeatability is high and easy for manufacturing in robotized factory (shown in Fig. 5) [21].

5   Finite Element Stress Analysis

The linear static stress analysis is performed and von Mises stress and deformation are being calculated. Louis model chassis has von Mises stress as 56.63 MPa shown in Fig. 6, that is made of aluminum has yield strength as 255 MPa thus it is safe [7].

The maximum stress of perforated plate chassis is 25% higher than the solid plate chassis and maximum deflection of perforated plate chassis is 20% higher than the solid plate chassis as shown in Fig. 7. Safety factor of perforated plate chassis is 20%

Fig. 6 Stress analysis and deformation of Louis 2016 model [7]
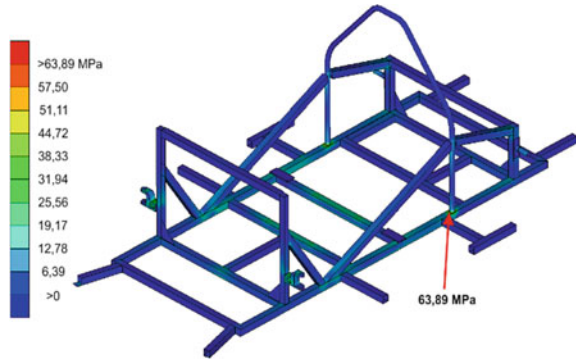
Fig. 7 Deflection analysis of Louis 2016 model [7]
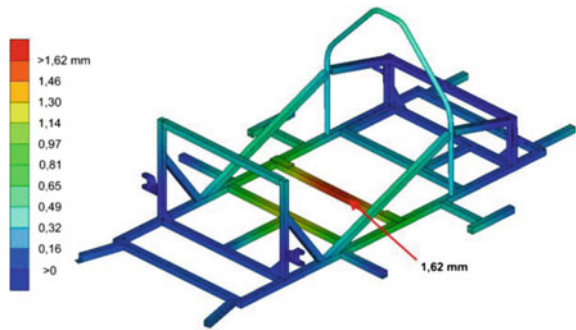
lower shown in Fig. 8, than the solid plate chassis shown in Fig. 9 [8]. Safety factor is the critical parameter so perforated plate-type chassis is more suitable than solid plate-type chassis for electric vehicles.

The monocoque chassis is extremely light 5.38 kg than the Louis 2016 model have weight 7 kg. The maximum stress in monocoque chassis is found to be 917.20 MPa and deformation of 21.38 mm shown in Fig. 10b [22].

6 Conclusions

Design of lightweight chassis with better stiffness-to-weight ratio is required for electric vehicle. The monocoque-type chassis has better stiffness-to-weight ratio than space frame-type chassis. CFRE monocoque chassis provides better flexibility in manufacturing and provides more space to install mechanical and electrical components. The specific stiffness and specific strength indicate that the carbon fiber composite (M40-epoxy) is more suitable for making monocoque chassis.
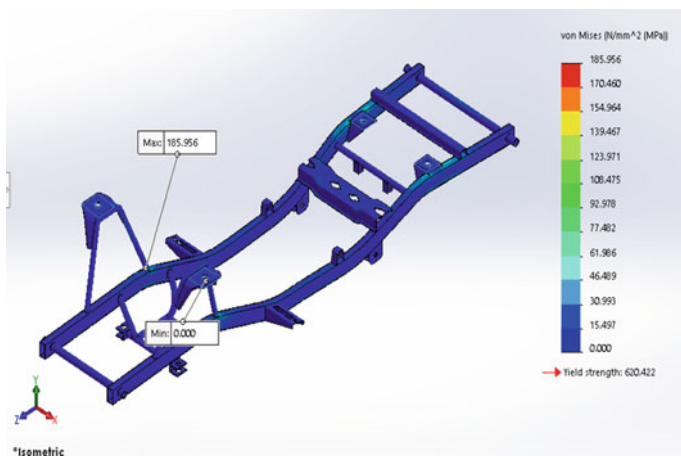
Fig. 8 Stress analysis of perforated plate chassis [8]
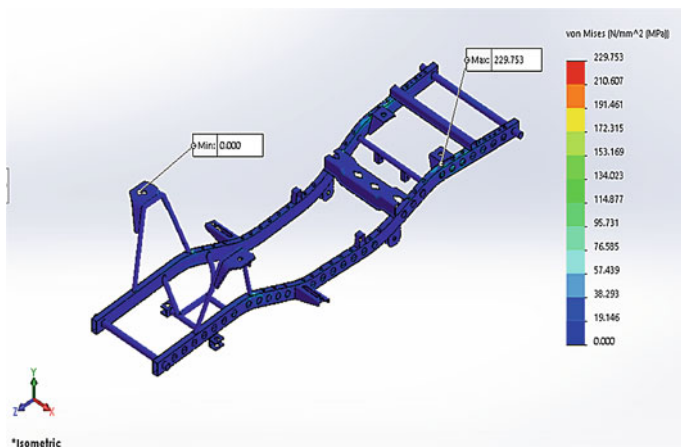
Fig. 9 Stress analysis of solid plate chassis [8]
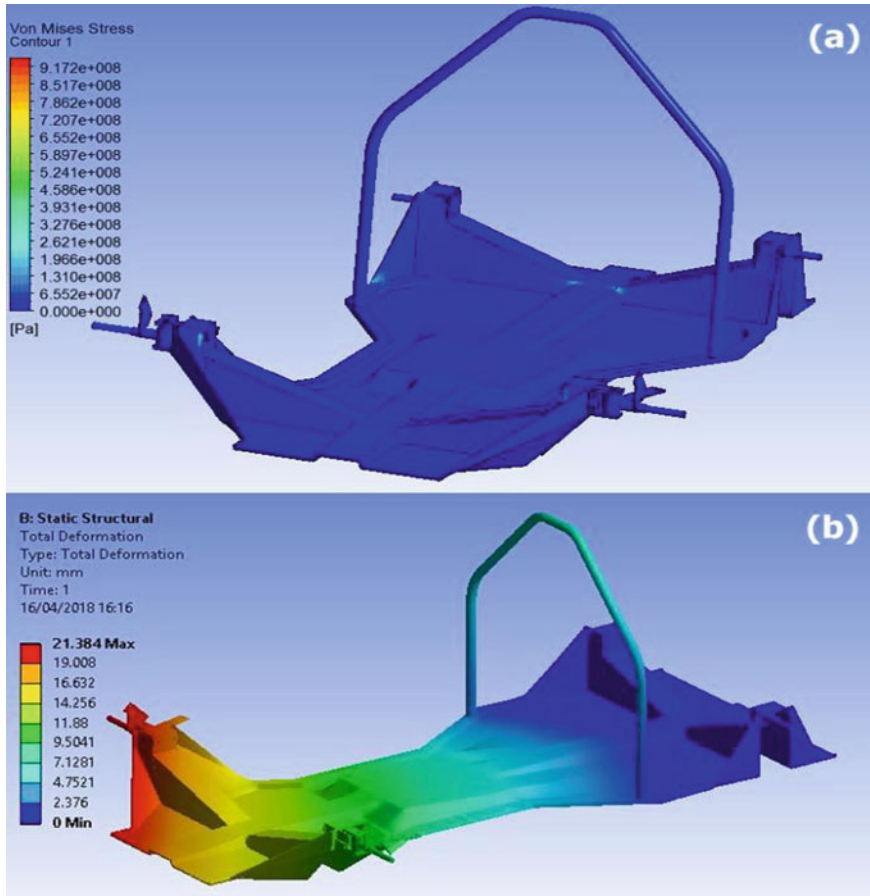
Fig. 10 Stress analysis of monocoque chassis [21]

References

1. Un-Noor F, Padmanaban S, Mihet-Popa L, Mollah MN, Hossain E (2017) A comprehensive study of key electric vehicle components, technologies, challenges, impacts, and future direction of development. Energies 10:1217
2. Mahmoudi C, Flah A, Sbita L (2014) An overview of electric vehicle concept and power management
3. Guzani A et al (2016) Electric vehicle design, modeling and optimization. AFM EDP Sci 17:405
4. bin Ab Razak MS, bin Hashim MH, Ngatiman NA (2017) Design of electric vehicle racing car chassis using topology optimization method. MATEC Web Conf 97:01117
5. Jamadar MAL, Mhetre VS, Patil RR, Arwade MM (2019) Basic design of electric vehicle. Int Res J Eng Technol (IRJET) 6(3)
6. Tsirogiannis EC, Stavroulakis GE, Makridis SS (2019) Electric car chassis for shell Eco Marathon competition: Design, model and finite element analysis. World Electr Veh J 10:8

7. Koumartzakis G, Spanoudakis P, Tsourveloudis NC (2017) Design and development of a prototype electric vehicle's chassis. In: 7th BETA CAE international conference
8. Taufik A, Rashid N, Maz lan, Al Faruq MS, Zahir M (2014) Electric car chassis design and analysis by using CATIAV5R19. IOSR J Mech Civ Eng (IOSR-JMCE) 11(4):56–59. e-ISSN: 2278-1684, p-ISSN: 2320-334X, Version III
9. Taufik AZ et al (2014) Electric car chassis design and analysis by using CATIAV5R19. IOSR J Mech Civ Eng (IOSR-JMCE) 11(4):56–59. e-ISSN: 2278-1684, p-ISSN: 2320-334X, Version III
10. Rane HS, Reddy PS (2013) Finite element analysis and optimization of an Forklift chassis. In: Voltas material handling, altair technology conference, vol 1, pp 1–6
11. Cavazuuti M, Splendi L (2011) Structural optimization of automotive chassis: theory, setup, design. In: Structural and multidisciplinary optimization. pp 1–3
12. Prabakaran S, Gunasekar K Structural analysis of chassis frame and modification for weight reduction. Int J Eng Sci Res Technol 3(5):595–600. ISSN: 2277-9655
13. Luccarelli M, Tobias Matt D, Russo Spena P Purpose design for electric car. In: Chair of automotive technology. Department of Mechanical Engineering T U Munich
14. Duleba B, Greskovic F (2013) Simulation of loading the polymer/carbon fiber composites and prediction of safety factors. Int J Eng Innov Technol (IJEIT) 2(8):134–140
15. Tempelman E (2014) Light weight materials, light weight design. In: Fundamentals of materials and design. pp 247–258
16. Tsirogiannis EC, Stavroulakis GE, Makridis S Design and modelling methodologies of an efficient and lightweight carbon-fiber reinforced epoxy monocoque chassis, suitable for an electric car. Mater Sci Eng Adv Res 2(1)
17. Dynamic Analysis and Shape Optimization of Electric Car Chassis (2017) Dynamic analysis and shape optimization of electric vehicle chassis. Int J Aerosp Mech Eng 4(4)
18. Material Property Data. Available online: https://www.matweb.com
19. Wagtendonk WJ (1996) Principles of helicopter flight. Aviation Supplies and Academics Inc., Newcastle, WA, USA
20. Tsirogiannis EC, Siasos GI, Stavroulakis GE, Makridis SS (2018) Lightweight design and welding manufacturing of a Hydrogen fuel cell powered car's chassis. World Electr Veh J Challenges 9:25
21. Gritt PS (2002) An introduction to brake systems. In: SAE Brake Colloquium. DaimlerChrysler, pp 1–52
22. Tsirogiannis EC, Stavroulakis GE, Makridis SS (2019) Optimised ultrafast lightweight design and finite element modelling of a CFRP monocoque electric car chassis. Int J Electr Hybrid Veh 11(3)

Finite Element Analysis of Soft Body Armour Using Shear Thickening Fluid

Anshuman Sharma, Tanishq Uppal, Virendra Singh, Preeti Joshi, and R. K. Tyagi

Abstract The heavyweight, reduced mobility, and less flexibility of Conventional body armour's have led to the user becoming easily exhausted. In this work, study and modelling of armours which are lighter in weight, offer greater flexibility and impact resistance than its Conventional archetype has been done. Finite Element methods have been thoroughly employed to better perform the simulation, which encapsulates the analysis of both, the projectile (bullet) and the Impact (Body armour). Models are developed for neat Kevlar layers and Kevlar with Shear Thickening Fluid (STF) impregnated between the layers. The effect of shear thickening has been represented and is simulated as friction between the different Kevlar layers. Analysis of energy absorption for neat Kevlar and STF introduced Kevlar is performed and a comparative study specifying the Depth of indentation for both the models has been done, thereby giving results in terms of greater energy absorption capability or resistance of STF infused Kevlar.

Keywords Finite element analysis · Shear thickening fluid · Kevlar · Body armour · Impact resistance · Abaqus · Kevlar composite · Neat kevlar composite

1 Introduction

From time immemorial, the use of body armour has been to protect one's life, be it on the battlefield or elsewhere. History cites a record of the Oldest body armour from Sumer civilization, present in what is now known as 'The South of Iraq'.With the passage of time and the advancement and innovation of the human-made weapons, body armours became more Technologically advanced and durable [1, 2]. Historically, armour was only used by the Military personnel, but its usage gradually began to spread to ordinary people for self-defence. High-tech weapons, in today's world, have become easily accessible to commoners, private security guards and militants [3]. This extensive use of weapons has made it very important to design body armors

A. Sharma (✉) · T. Uppal · V. Singh · P. Joshi · R. K. Tyagi
Mechanical Engineering Department, Amity University Noida, Noida, India
e-mail: ansh060898@gmail.com

better than the previous ones. Therefore, the need for a significant improvement in the performance to weight ratio and performance to thickness ratio of the body Armor became consequential. So, to improve upon the previous shortcomings, Shear thickening fluid-based armors came into play.

STF-based body armor is made of kevlar soaked in STF (shear-thickening fluid) [4]. Kevlar was developed in 1965 by Stephanie Kwolaek at DuPont and was introduced in 1971 in the market [5]. Kevlar is a material with high strength and stiffness. Kevlar, when woven and layered into a fabric [6], proves to be at least five times stronger in terms of tensile strength in comparison to steel, and at the same time being lightweight and flexible. Kevlar can withstand maximum temperatures of 450 °C without getting any deformation and lowest temperature of −196 °C kevlar is chemical resistant as well as its thermal expansion (coefficient) is negative in value [7, 8].

In order to check the viability of the armor, depth of penetration into the armor by the bullet is taken as its main characteristic [9, 10]. The standard of the depth of penetration into the armor varies from country to country. According to the present European standard, it allows 25 mm of back-face signature in armor, whereas the US armor standard allows for 44 mm back-face signature [11]. In this analysis, European standards have been adopted. The software used in the designing and simulation of the improved body armor is Abaqus, a type of Computer Aided Designing software, having its application in Finite Element Analysis and Computer-Aided Engineering.

2   Modelling and Simulation

The aim of this study is to analyse the performance of STF infused body armor under ballistic testing with an intention to replace the previously used ceramic and steel body armors. So, to improve the flexibility, layers of kevlar were used and made lighter using STF impregnate kevlar.

A sandwich composition of kevlar and STF was made in Abaqus. The structure of the composite was $100 \times 100 \times 5$ mm in shape [12]. Bullet of the given characteristic (Table 1) was made of lead. The thickness of the sheet increased 5 mm after every simulation in which the bullet passes the composition. The sample was named model-a, model-b and so on. Listed below is the chart that contains the properties of the bullet that was made in simulation. Bullet is fired from a distance of 5 ± 0.5 m. Table 2 shows modelling parameters for neat kevlar and STF Kevlar [13].

Table 1 Characteristic of bullet used

Ammunition	Bullet weight/gram	Bullet diameter (mm)	Velocity (m/s)	Energy (kJ)
9 × 9 115 grs full metal jacket (FMJ)	115	10	200	519.507

Table 2 Modelling parameter for Neat and STF kevlar

Parameter	Neat kevlar	STF kevlar
Type	Neat	STF
E_{11}	84.62 GPa	84.62 GPa
E_{22}, E_{33}	1.34 GPa	1.34 GPa
G_{12}, G_{23}, G_{12}	24.4 GPa	24.4 GPa
Failure strain	0	0
Failure stress	3.9 GPa	3.9 GPa
Shell thickness	0.11	0.11
Integration points	2	2
Dynamic coefficient of friction	0.2 (yarn-to-yarn) 0.18 (projectile-to-fabric)	1.62 (yarn-to-yarn) 0.9 (projectile-to-fabric)
Exponential decay coefficient	1.23	1.23

In order to create the model, first we need to select the "create part" option in the software. A part of 100×100 mm was created with a thickness of 5 mm. This part will be the first layer of kevlar fabric.

After creating the part, the properties of Kevlar were assigned to it, as shown in Figs. 1 and 2. The properties included were as follows:

Mass density	Young's modulus	Poisson's ratio
1.44	70	0
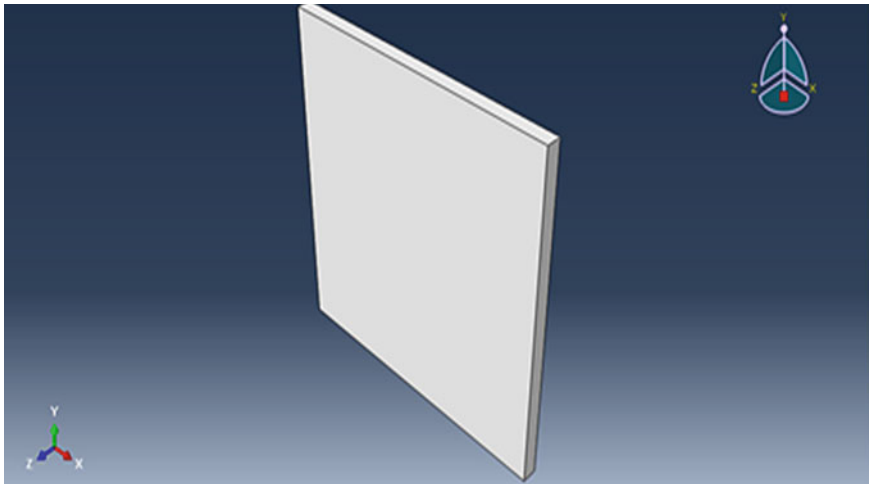
Fig. 1 Structure of the layer for the composite
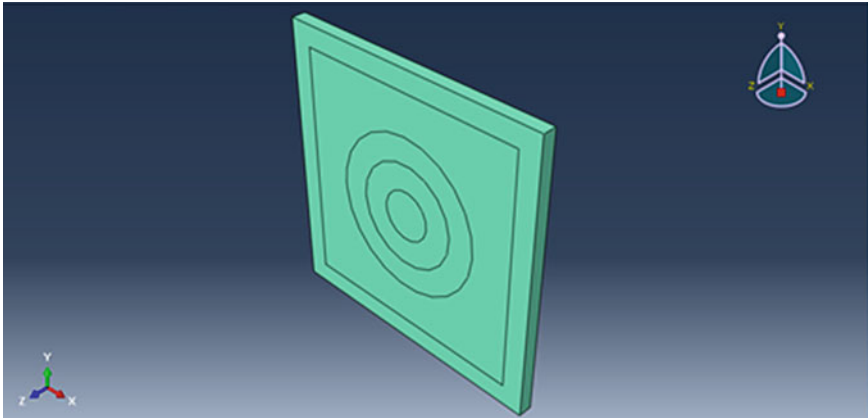
Fig. 2 Kevlar layer after introducing the properties

After creating this layer, we then moved on to creating another part, and that will be the impactor. For this, again the "create part" option was selected, with the type being "discrete rigid" and the base feature was given as "shell" with "revolution type". This was done so that when the part is created and revolved around the axis 360°, it comes out like a bullet (solid impactor). The length of this part was 30 mm and the thickness was given as 10 mm. After assigning these dimensions, the part was revolved to 360° around the axis, and doing so yielded the part as shown in the Fig. 3.
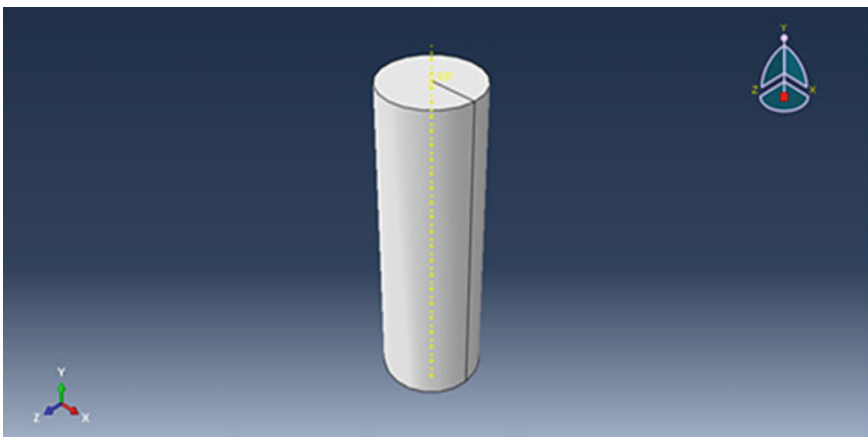
Fig. 3 Impactor
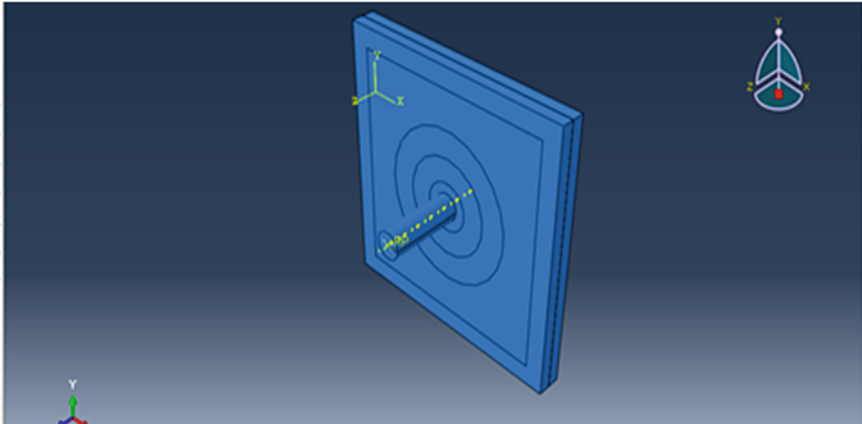
Fig. 4 Parts are assembled, and the layers are joined

After getting this, we assigned a reference point to this part, as it will be useful in the assembly of the parts. We then moved on to the assembly part. Part 1 (i.e., the kevlar layer) was selected twice so as to get composite/sandwich structure (i.e., two layers joined together). As of now, the application of Shear Thickening Fluid (STF) was not done, as we first did the impact testing on the composite without STF and then with application of STF (layered between the two layers of Kevlar), so as to compare. After the assembly of all the parts, the reference point of the impactor was aligned with the center of the layers, so as to give it a path for the projectile as shown in Fig. 4.

The next step was the interaction. For this, the "create interaction property" option was selected, and the type assigned was "contact". Then in the contact property options, drop down the "mechanical" section, and select "normal behaviour." The next step was creating boundary conditions. For this, we have to open the "Load" module, and in that, select the "create boundary condition" option as shown in Fig. 5. The category selected was "Mechanical" and the type of selected step was taken as "symmetry". After this, the velocity of the impactor was assigned as 200 m/s. This was done by selecting the option "edit predefined field", and in that, the distribution was set as "uniform" and the velocity was put as 200.

The next step was that of meshing. The mesh module was selected, and then part 2 (impactor) was selected. The process that follows is also known as seeding. Now, the "global seeds" option was selected, and the same was done for part 1 (Kevlar Layers). The result was as follows in Figs. 6 and 7.

Now came the final part, and that was the "job" module, where the simulation is done. In this part, the software analyzes the impact on the composite and it is after that, that we conclude the results of the computer analysis.
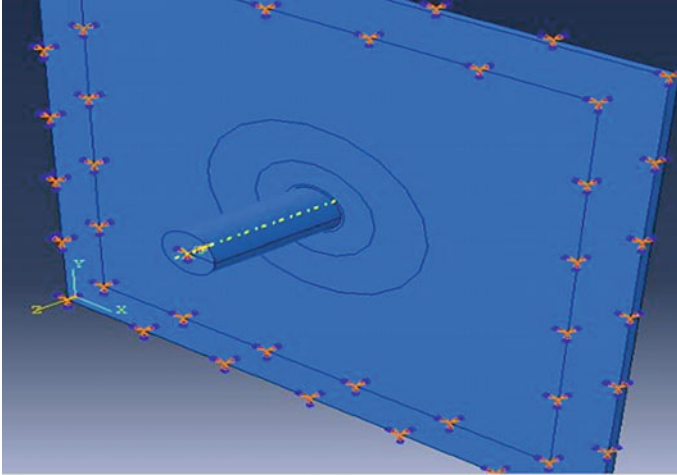
Fig. 5 Boundary conditions created, and velocity assigned
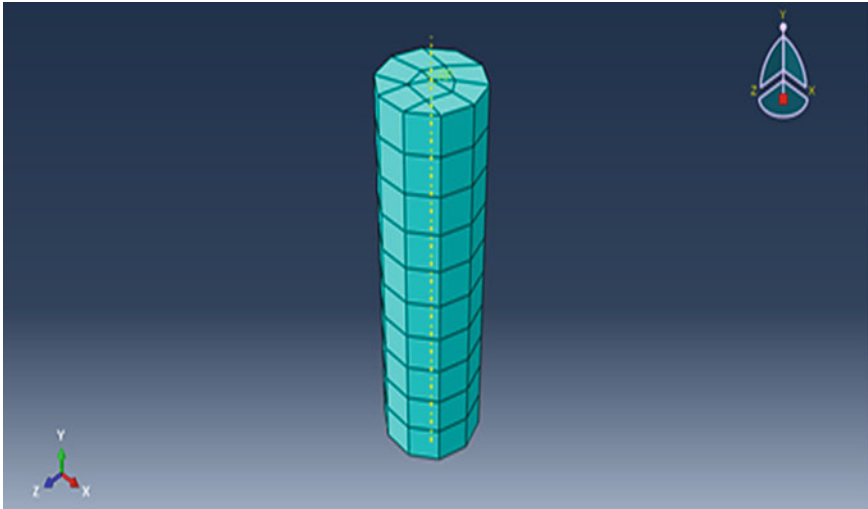
Fig. 6 Impactor after seeding

3 Result and Discussion

3.1 Neat Kevlar Composite

The series of images Figs. 8, 9 and 10, that follow show that when STF was not applied, the impactor penetrated the kevlar layers completely.
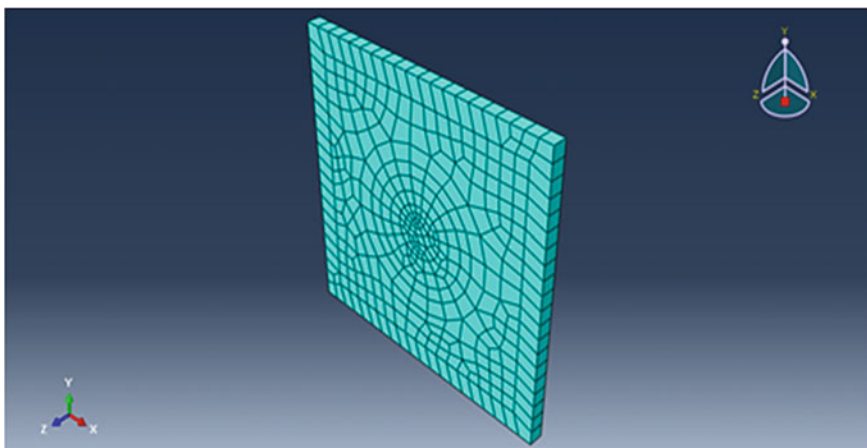
Fig. 7 Kevlar layers after seeding (meshing)
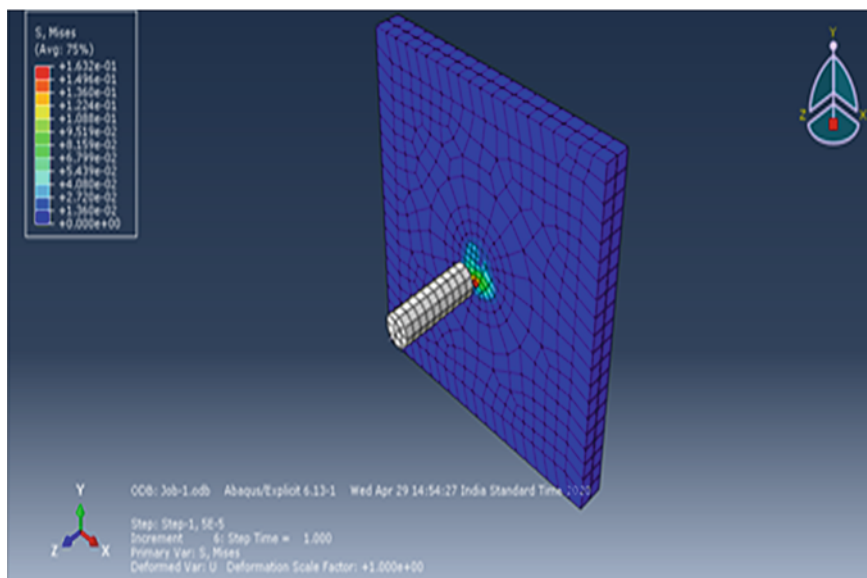
Fig. 8 Impactor and the kevlar layers (composite), impact ready

3.2 STF Impregnated Kevlar Composite

Now, let us see the behaviour of the composite when STF has applied and the impactor impacts in Fig. 11a and b. The application of STF is represented by the addition of "coefficient of friction" in the interaction module. Coefficient of friction = 1.62.
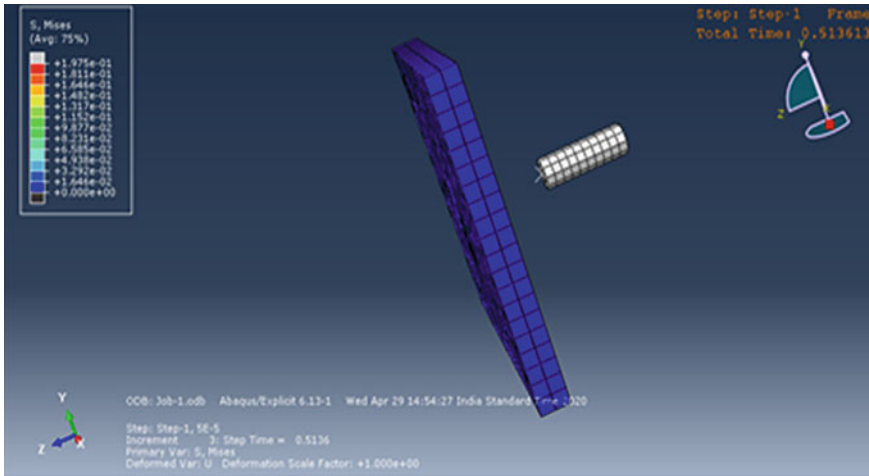
Fig. 9 Projectile of the impactor, about to strike
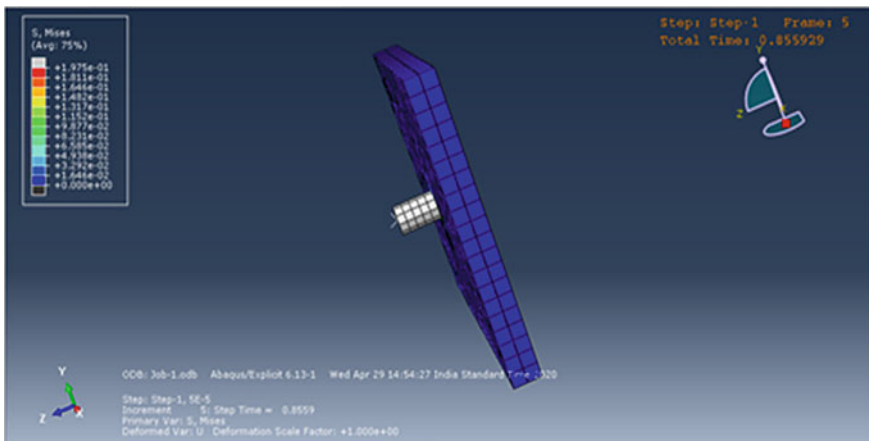
Fig. 10 The impactor penetrates the neat kevlar composite

The above-shown images show that when STF was applied, the impactor could not penetrate the composite. Hence, we can say, that the software analysis concluded that when Kevlar Fabric layers are impregnated with Shear Thickening Fluid, it absorbs a great amount of energy and is significantly stab-proof.

After performing the analysis with the application of STF, it was seen that the impactor was not able to penetrate the composite, hence the indentation was negligible. To represent the application of STF, in the interaction module, the coefficient of friction (1.62) was added, and due to this, the energy absorption of the composite was increased significantly, so much so that the amount of penetration came out

(a)   (b)
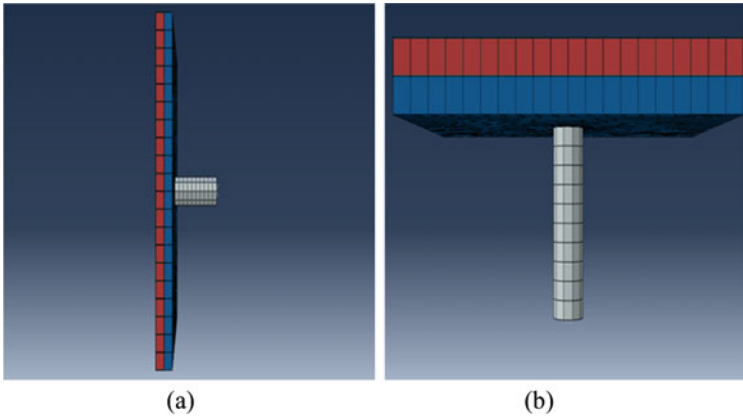
Fig. 11 **a, b** Two different views of the model showing no penetration of the impactor

to be of a much lesser value. Hence, the software analysis displayed that when a neat kevlar composite was infused with Shear Thickening Fluid, it absorbed a great amount of energy, claiming it to be significantly stab-proof.

4 Conclusion

A brief understanding of body armours with the application STF impregnated kevlar fabrics was done and its advantage over conventional body armours was studied. Our objective was, modelling of a Shear Thickening Fluid (STF) based body armour using finite element analysis, and the software used for that was Abaqus. As shown in this report, we designed the composite and simulated the impact resistance. The methodology adopted, in order to get a comparative result, was the designing of two sets of composites in which one had the application of STF between the kevlar layers and the other didn't. As a result, the composite in which the Kevlar layers were impregnated with STF showed significant resistance towards the impact as compared to that shown by the neat kevlar composite. Energy absorption in both types was also compared, and it was concluded that when Kevlar fabrics (layers) were impregnated with Shear Thickening Fluid, it yielded a high resistance, stab-proof body armour, and because of its chemical composition, properties and lightweight, its usage will be significantly convenient and easy as compared to that of conventional body armours.

5 Future Scope

Conventional body armors, as were studied about, witness numerous problems and inconvenience which must not be faced by the wearers during a warhead, hostile engagement, or any sort of emergency situation, as it hinders the performance, effectiveness with which the task ought to be completed, agility, etc., and in worst case scenario it may cause unwanted casualty. The body armor that we aim to fabricate and design deals with these problems and many others, not just securing the objectives of the personnel/wearers/soldiers but also nullifies the hindrances faced by them in this process. This project of ours establishes the use of Shear Thickening Fluid in already existing body armors, to improve the resistance against impact, hence developing and infusing fabric with STF is also our top priority.

References

1. Gabriel RA, Metz KS (1991) From Sumer to Rome: the military capabilities of ancient armies. ABC-CLIO
2. Gabriel RA (2007). The ancient world. Greenwood Publishing Group. ISBN: 978-0-313-33348-4
3. Pyke AJ, Costello JT, Stewart IB (2015) Heat strain evaluation of overt and covert body armour in a hot and humid environment. Appl Ergon 47:11–15. https://doi.org/10.1016/j.apergo.2014.08.016. ISSN: 1872-9126. PMID: 25479969
4. Hazell PJ (2015) Armour: materials, theory, and design. Boca Raton, FL. ISBN: 9781482238303. OCLC: 913513740
5. Johnson T (2015) . Military.com. Retrieved 5 March 2015
6. Mera H, Takata T (2000) High-performance fibers. Ullmann's Encycl Ind Chem. https://doi.org/10.1002/14356007.a13_001. ISBN: 978-3527306732
7. How Kevlar® works: a simple introduction. Explainthatstuff.com (2009-12-07). Retrieved on 2012-05-26
8. KEVLAR Technical Guide. dupont.com. Retrieved on 2012-05-26
9. Kim CG, Kim IJ, Lim G, Yoon BI (2010) The ballistic impact characteristics of woven fabrics impregnated with a colloidal suspension and flattened rolls. Adv Sci Tech 71:74–79
10. Wilhelm M, Bir C (2008) Injuries to law enforcement officers: the backface signature injury. Forensic Sci Int 174(1):6–11. https://doi.org/10.1016/j.forsciint.2007.02.028. ISSN: 0379-0738
11. Chhabra RP, Richardson JF (1999) Non-Newtonian flow in the process industries. Butterworth-Heinemann, Woburn, MA
12. Moon JB, Son GS, Park YR, Kim CG (2011) The effect of the number of fabric on CFRP-fabric hybrid composite impact shield performance. In: 18th international conference on composite materials. Jeju, Korea
13. Park Y, Kim Y, Baluch AH, Kim CG (2015) Numerical simulation and empirical comparison of the high velocity impact of STF impregnated Kevlar fabric using friction effects

A Low-Cost Novel Design for Knee Orthosis

Himanshu Verma, Abid Ali Khan [ID], and Siddharth Bhardwaj [ID]

Abstract In the present study, a torsional spring-based passive knee brace design has been proposed to work as a shock absorber and reduce the load transmitted through the knee joint. The design consisted of thigh and shank support, which forms a hinge joint in the sagittal plane to support the knee extension using a double torsional spring. The brace was modelled considering the anthropometry data of 90th percentile Indian male population. The proposed design was developed in NX 12.0, and later, a finite element analysis (FEA) was carried out in ANSYS Workbench 16.0 to study model deformation. The designed knee brace was found to provide approximately 50% rebound of the load transmitted through the knee joint of a person weighing 80 kg. Further possible modifications in the design were discussed in order to improve the workability of the proposed model.

Keywords Spring-loaded exoskeleton · Double torsional spring · PLA material

1 Introduction

Knee joint problems such as cartilage tears, strained ligaments, osteoarthritis, particularly in elderly population, are rising day by day due to excess loading of the knee joint [1, 2]. Reducing the load transferred from the knee is a non-pharmacological solution that has been found to relieve patients with knee joint pain. Knee braces have shown success and a prior management strategy before going for a surgery to relieve pain in such patients [3].

A knee brace is an ergonomically designed structure or a device that works mechanically or electrically, providing support to the knee joints [3] and eventually

H. Verma (✉) · A. A. Khan · S. Bhardwaj
Department of Mechanical Engineering, Aligarh Muslim University, Aligarh, Uttar Pradesh, India
e-mail: hv33822@gmail.com

A. A. Khan
e-mail: abid.khan.me@amu.ac.in

S. Bhardwaj
e-mail: siddharth.bhardwaj@live.com

reducing knee joint loading during flexion/extension [4]. Both passive and active actuation have been sought in the past for delivering the knee support assistance. Active powered knee braces include electronic actuators involving electric motors or pneumatics. These actuators are driven by biomechanical or bioelectrical sensorial inputs generated during body movements [5].

Although the actively actuated knee provides a routed method of delivering the therapy and movements, the design, however, tends to be bulky and requires a power source for the operation. Prophylactic knee braces, generally used by the athletes/sportsperson, have the mechanically passively way to provide support. These knee brace gives support to the knee and prevents the chances of medial collateral ligament (MCL) injuries of the knee [6].

Functional knee braces are advised to be worn by the patients having anterior cruciate ligament (ACL) surgeries and for those having a recent injury in their knee [7]. These bracing are also good for the rotation following the ACL tear [8]. Unloader/Off-loader knee braces are especially for osteoarthritis patients. These bracing changes the line of the force which previously transmitted through the knee joint [9, 10].

In a recent study, it was found that the knee osteoarthritis patients using the unloader knee brace have significant improvement in their pain while walking and stair climbing. These patients also reported an overall improvement in quality of life with the use of braces [11]. These braces reduce the load from the medial compartment of the knee which is more likely to be affected in osteoarthritis. But the problem with these designs is that the straps provided behind the thigh and shank do not provide full support and also the re-bounce force is fixed and forms the bottleneck of the design.

The objective of the present study was to design a low-cost mechanical knee brace for assisting knee extension movement, which could be helpful in activities such as sit to stand transfer. In the proposed design, full support for the thigh and shank was provided and the re-bounce force (assisting force) can be changed by simply changing the number of springs depending upon the patient needs.

2 Methodology

The study comprises of development of knee brace for assisting the knee extension during sit to stand postural transfer. Final design was reached after refining two design iterations based upon the human physical interface and mechanical design challenges. Later, finite element analysis (FEA) was conducted on the final design to study the stress distribution and deformation while usage.
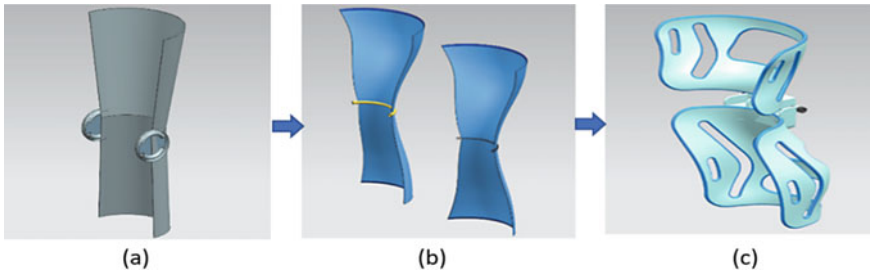
Fig. 1 Design iterations

2.1 Design Iterations

For designing the knee brace, it was decided to create a thigh and shank support to avoid the stresses at the region of contact.

In the first model, circular wound spring placed at the epicondyle of the knee was considered (Fig. 1a). As an initial model, the design did not consider the human body curves and the re-bounce mechanism.

The second model considered the use of coiled spring behind the knee. In the model, the design was based on the 90th percentile anthropometric data of Indian population [12] (Fig. 1b). However, a good physical interaction of the brace was still not achieved, since the spring may contact the user skin during sitting posture.

To address these issues, a third design was sought, where the torsional springs were used (Fig. 1c). The shank and thigh component material were also removed to reduce the weight of the brace.

2.2 Torsional Spring Design

Considering the area available for the attaching the springs and the re-bounce required, double torsional springs were chosen [13]. The spring rate was computed based upon the 50% re-bounce force for 80 kg person. Due to the space constraints available for the implantation of spring in the knee brace, an iterative scheme was considered (as shown in Fig. 2) to evaluate the optimal spring design parameters for achieving the required re-bounce. Optimal parameter involved in the designing of a double torsional spring was leg distance, mean diameter, wire diameter, number of turns.

The iterative scheme starts by selecting the material and wire diameter. Taking deflection of 90°, torque was calculated, and the mandrel size was chosen. Assuming the leg length and mean diameter of the spring, active number of coils were calculated by taking the number of turns in each coil as 4. After that, the mean diameter under deflection with tolerance, spring rate and the developed stress were calculated. If the calculated stress was less than the yield stress of the material, the design was reported

Fig. 2 Iteration scheme for
calculating the requisite
spring specifications

Start

Material selection

Selection of wire diameter

Deflection

Calculation of torque

Seletion of mandrel size

Assume leg distance and mean diameter

Number of active turns

Check mean diameter under deflection with tolerance — Less

More

Calculation of spring rate

Calculation of bending stress

Comparing calculated stress with material yield stress — More

Less

Finalize spring

safe; otherwise, the iteration was repeated again by assuming a different leg length
and mean diameter. The optimal spring parameters found from the iterative scheme to
be used in the design of the knee orthosis were found to be as follows: wire diameter
= 1 mm; leg length = 20 mm; mean diameter = 7 mm; outer and inner diameter =
8 and 6 mm; number of turns = 4 (each coil); spring rate = 114.86 Ncm/revolution.

2.3 Finite Element Analysis

For the finite element analysis (FEA) of the proposed design, static structural module
in the ANSYS Workbench version 16.0 (Ansys Inc., USA) was used.

Material selection. There are several materials available for designing springs like music wire, oil-tempered chrome silicon, etc. After comparing the different material on the basis of strength and usage, stainless steel 302 (ASTM A313) [14] was selected as the spring material. It was decided to produce the thigh and shank support structure by 3D printing; for this, PLA and ABS material was considered, and after the comparison between both the materials (Table 1), PLA was decided to be used. For the FEA, the material were assumed to be homogeneous and isotropic.

Mesh geometry. Tetrahedron mesh with a size of 0.001 mm was selected for the spring, while tetrahedron mesh of size 0.01 mm was chosen for the thigh and shank support structures. A lower mesh size for the spring was reasonable as the wire diameter chosen for spring was only 1 mm. Perfect nodes were ensured with the taken mesh size.

Boundary conditions. For the analysis, it was assumed that the deflection in the coiled portion was negligible. So, a fixed support was provided at the spring coil (Fig. 3a), while a force of 33.34 N (the value was obtained for 80 kg person assisted by a spring re-bounce force of 50% via three springs) was applied to the spring legs (Fig. 3b and 3c). For the analysis of the supporting structures (shank and thigh), a uniformly distributed load of 100 N was applied on the spring supported area. Brace supports in contact with the human body was given fixed constrain in the analysis.

Table 1 Mechanical properties of PLA and ABS material [15]

Property	ABS	PLA
Tensile strength (MPa)	44.81	57.8
Tensile modulus (GPa)	2.21	3.3
Flexural strength (MPa)	75.84	55.3
Flexural modulus (GPa)	2.28	2.3
Melting point (°C)	205	175
Density (g/cm^3)	1.04	1.23–1.25
Elongation at break (%)	20	3.8
Rockwell hardness	R105–R110	R70–R90
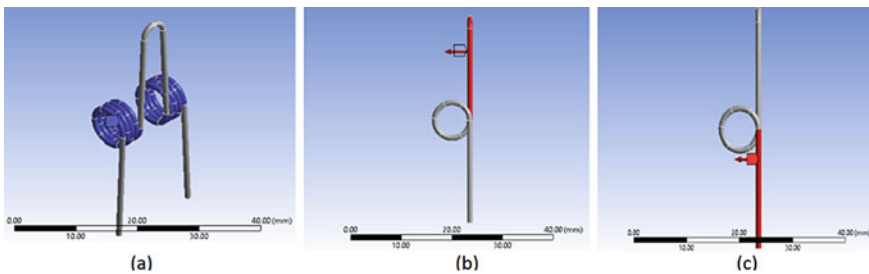
Fig. 3 Spring boundary conditions for FEA

3 Results and Discussion

Figure 4 shows the static structural analysis result for the total deformation (elastic) in the spring. The maximum deformation was reported to be 1.95 mm at the joined end of the spring (U-shaped region). The coiled region showed no deflection as fixed constrains were provided in this region (as shown in Fig. 3a).

Figure 5a and b shows the total deformation in the thigh and shank support respectively. The maximum deformation of 7.64×10^{-4} mm was found in the thigh support, while the shank support suffered maximum deformation of 6.08×10^{-4} mm. The maximum deformation was reported at the sharp corners of thigh and shank support. As the fixed support was given to the structure which directly comes in contact with the person's body, thus the deformation in this section was found to be 0 mm.

In order to further reduce the deformation in the support structures (thigh and shank support), a 4 mm thick aluminium plate was inserted into the slots that were designed in the spring mounting position with the hypothesis that this may improve the stress distribution owing to improved bearing surface area. The FEA deflection

Fig. 4 Total deformation in the spring
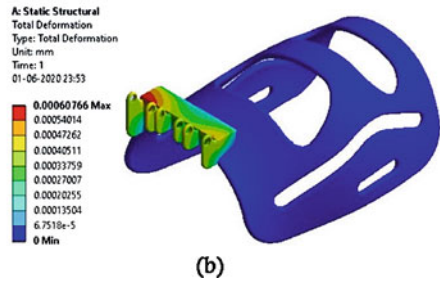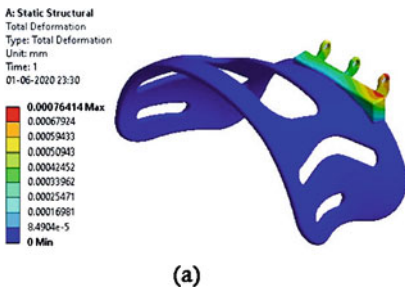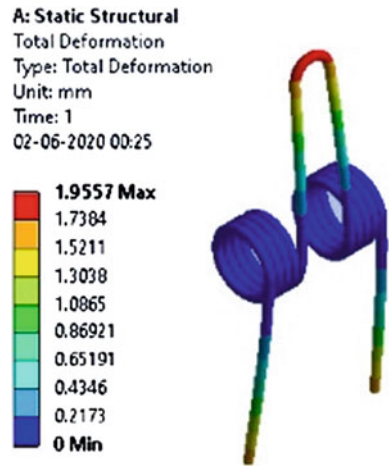
Fig. 5 FEA result for **a** thigh support and **b** shank support
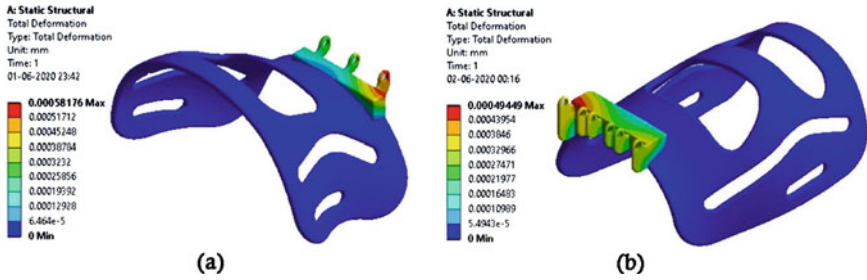
Fig. 6 FEA result for slotted design for **a** thigh support and **b** shank support

results for the slotted design are shown in Fig. 6a and b for thigh and shank support, respectively. As evident from the analysis, an overall reduction of 23.8 and 18.6% was obtained for the thigh and shank support, respectively. The maximum deformation, however, occurred at the same location where the maximum deformation was developed in un-slotted design (Fig. 5). As the deformation in the thigh and shank support is quite low, further modification in the spring specification is possible to achieve the particular task.

Compared to the unloader/off loader knee braces [9, 10], the proposed design has full thigh and shank support which is essential for improving the user comfort while wearing. Also, with the manifestation of the additive manufacturing (such as fused deposition modelling (FDM)), the strength of the support can be improved by changing the infill parameters in 3D printing. The discussed design for the knee brace is modular and can be adapted to the users of varying anthropometry and size. Also, the re-bounce can be easily adapted by changing the spring stiffness, in the current design; however, the stiffness was chosen to provide a re-bounce of 50%. This is advantageous compared to the unloader knee brace, where the stiffness is fixed.

4 Conclusion and Future Scope

The study investigated spring-based mechanical design for knee brace. Optimal spring rate was found to be 114.86 Ncm/revolution to give a 50% rebound affect during knee extension. The FEA study conducted on the designed knee showed a maximum deflection of 5.8×10^{-4} mm, which was under safer limit of operation. The proposed design of knee brace can be easily adapted to the required re-bounce by changing the number of springs. The methodology adopted in designing the knee brace can be used for developing modular braces through additive manufacturing such as fused deposition modelling, etc. The developed brace can be used in the applications ranging from occupational use to frail assistance.

References

1. Karas V, Calkins TE, Bryan AJ, Culvern C, Nam D, Berger RA, Rosenberg AG, Della Valle CJ (2019) Total knee arthroplasty in patients less than 50 years of age: results at a mean of 13 years. J Arthroplasty 34:2392–2397. https://doi.org/10.1016/j.arth.2019.05.018

2. Salve H, Gupta V, Palanivel C, Yadav K, Singh B (2010) Prevalence of knee osteoarthritis amongst perimenopausal women in an urban resettlement colony in South Delhi. Indian J Public Health 54:155–157. https://doi.org/10.4103/0019-557X.75739

3. Chen B, Zi B, Wang Z, Qin L, Liao WH (2019) Knee exoskeletons for gait rehabilitation and human performance augmentation: a state-of-the-art. Mech Mach Theory 134:499–511. https://doi.org/10.1016/j.mechmachtheory.2019.01.016

4. Priore LB, Lack S, Garcia C, Azevedo FM, de Oliveira Silva D (2020) Two weeks of wearing a knee brace compared with minimal intervention on Kinesiophobia at 2 and 6 weeks in people with Patellofemoral pain: a randomized controlled trial. Arch Phys Med Rehabil 101:613–623. https://doi.org/10.1016/j.apmr.2019.10.190

5. Askari H, Asadi E, Saadatnia Z, Khajepour A, Khamesee MB, Zu J (2018) A flexible tube-based triboelectric–electromagnetic sensor for knee rehabilitation assessment. Sens Actuators, A 279:694–704. https://doi.org/10.1016/j.sna.2018.05.016

6. Sinclair JK, Vincent H, Richards JD (2017) Effects of prophylactic knee bracing on knee joint kinetics and kinematics during netball specific movements. Phys Ther Sport 23:93–98. https://doi.org/10.1016/j.ptsp.2016.08.005

7. Théoret D, Lamontagne M (2006) Study on three-dimensional kinematics and electromyography of ACL deficient knee participants wearing a functional knee brace during running. Knee Surg Sports Traumatol Arthrosc 14:555–563. https://doi.org/10.1007/s00167-006-0072-3

8. DeVita P, Torry M, Glover KL, Speroni DL (1996) A functional knee brace alters joint torque and power patterns during walking and running. J Biomech 29:583–588. https://doi.org/10.1016/0021-9290(95)00115-8

9. Briggs KK, Matheny LM, Steadman JR (2012) Improvement in quality of life with use of an unloader knee brace in active patients with OA: a prospective cohort study. J Knee Surg 25:417–421. https://doi.org/10.1055/s-0032-1313748

10. Ebert JR, Hambly K, Joss B, Ackland TR, Donnelly CJ (2014) Does an unloader brace reduce knee loading in normally aligned knees? Clin Orthop Relat Res 472:915–922. https://doi.org/10.1007/s11999-013-3297-8

11. Lazaro RM, Dec KL (2019) Knee orthoses for sports-related issues. In: Atlas of orthoses and assistive devices. Elsevier, pp 259–267. https://doi.org/10.1016/B978-0-323-48323-0.00025-1

12. Chakrabarti D, National Institute of Design (1997) Indian anthropometric dimensions for ergonomic design practice. National Institute of Design

13. Zhang B, Li C, Wang T, Wang Z, Ma H (2019) Design and experimental study of zero-compensation steering gear load simulator with double torsion springs. Measurement 148:1–9. https://doi.org/10.1016/j.measurement.2019.106930

14. Weiguo HOU, Weifang Z, Xiao LIU, Zongren W, Meili D (2011) Failure analysis of aviation torsional springs. Chin J Aeronaut 24:527–532. https://doi.org/10.1016/S1000-9361(11)60061-7

15. Farbman D, McCoy C (2016) Materials testing of 3D printed ABS and PLA samples to guide mechanical design. In: ASME 2016 11th international manufacturing science and engineering conference, MSEC 2016. Blacksburg, Virginia, USA, pp 1–12. https://doi.org/10.1115/MSEC2016-8668

Weight Optimization and Force Analysis of an ATV Roll Cage

Ashutosh Kumar, Shubham Agarwal, Mrinal Deep, Umang Tyagi, Gaganpreet Kaur, and Navendra Singh

Abstract A roll cage is a rigid frame structure which provides adequate safety to the driver in static and dynamic condition. Designing and fabricating a roll cage of an ATV with weight optimization without sacrificing driver safety is a challenging task. Optimizing weight of the roll cage by maintaining strength to weight ratio is very important to enhance the performance of the vehicle. The primary objective of this paper is to reduce the weight of the roll cage and performing simulations of the roll cage on various forces like front impact force, side-impact force, rear impact force, rollover force, torsional rigidity and remote force in a dynamic condition of an ATV. The software used for designing the roll cage is solid works. We have also calculated the forces on which the roll cage is simulated by considering the dynamic force which will be acting on the vehicle in real-time condition.

Keywords Roll cage · Impact force · Weight optimization · Strength to weight ratio

1 Introduction

The frame of a roll cage is designed to install all the other subsystems of the vehicle i.e. suspension, steering, transmission etc. on the frame of the roll cage. The major function of the roll cage is to protect the driver from the impact forces that will be encountered by the vehicle during running. The front bracing of the roll cage provides strength to the roll cage from the front and the rear bracing provide strength at the rear of the roll cage, so, therefore, combining both the bracing will increase the overall strength of roll cage. The designing stage comprised of finding the constraints and

A. Kumar (✉) · S. Agarwal · M. Deep · U. Tyagi · G. Kaur · N. Singh
Department of Mechanical Engineering, ABES Engineering College, Ghaziabad, India
e-mail: ashutoshkumar0026@gmail.com

S. Agarwal
e-mail: shubhamhtc612@gmail.com

M. Deep
e-mail: mrinal.deep98@gmail.com

analysis of forces, strain–stress results, deformation results, we also considered the ease of manufacturability while designing the same.

2 Literature Review

Mohanty [1] has researched the different cross-sections of material that can be used to design the lighter roll cage with high strength. He also performed impact testing of the roll cage at various impacts such as front-impact test, side-impact test and torsional test. Kinetic energy theorem was used to calculate the forces at the time of impact on the roll cage.

Mahajan [2] performed dynamic analysis of roll cage the designing of the roll cage was done on the solid work designing software and the dynamic analysis of same was performed by using the hyper mesh software. In the dynamic analysis, different crash test were analysed so as to ensure the safety of driver.

Selmer [3] analysed the pre-existing ATV to determine the flaws and then design the new chassis that is improved as compared to the previous design. The overall suspension alignment points were also changed to optimize the roll cage at an advanced level. Stress and deflection analysis were performed on the design similar to the final design and changes were made accordingly.

Raj [4] designed the roll cage in accordance with the SAE BAJA rulebook. The roll cage is designed in such a way that it is market-ready. Three-Dimensional protection is provided to the driver which is very crucial in determining the overall shape of the vehicle. It includes all possible crash conditions and those conditions are analysed in static conditions.

Jain [5] performed modelling and finite element analysis of ATV roll cage. During the designing phase of roll cage, his few objectives were driver safety, ease of manufacturing, lightweight of vehicle, ergonomics. The paper shows static analysis of roll cage of ATV by performing simulations in ANSYS 16.0 & CAD modelling done in CREO 4.O. to obtain optimum FOS (factor of safety) in the worst condition under specific rules proposed by Society of Automotive Engineers (SAE) Which ensures that the roll cage will be safe in all conditions.

3 Design Analysis

The design was built while focusing on weight optimization without compromising driver safety. We have used pipes of various cross-section and thickness to reduce weight and increase the bending strength of the roll cage. The members of roll cage are classified into two categories, primary members and secondary members. Each category of members serves a different purpose. Primary members are used for providing the main shape and support to the vehicle. The secondary members are

Fig. 1 Basic roll cage
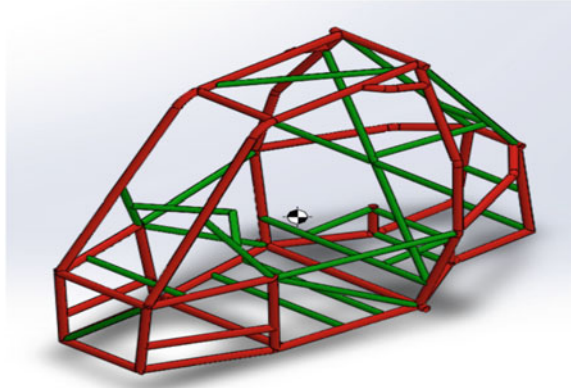
used for providing triangularization to the primary members and they also provide additional points on the roll cage frame to mount other subsystems.

The figure shown in Fig. 1 separates the primary members from the secondary members. here the red color depicts the primary members and the green color depicts the secondary members of the rollcage.

For making the roll cage lightweight by maintaining strength to weight ratio, we compared bending strength (Sb) and bending stiffness (Kb) of different cross-sections and thicknesses. Table 1 shows the comparison of bending strength and bending stiffness.

4 Force Analysis and Simulations

Safety of vehicle and driver are the major concerns while designing an ATV roll cage. It is the basic requirement that designed roll cage withstands the forces that come forces that it will encounter while running and also those which might be experienced during a crash of the vehicle. Physical testing of the frame is quite costly and time-consuming. Simulations are performed and design modifications are done based on the results. In Ansys we can define our own material and perform analysis of the same frame by using different materials. The properties of the materials are shown in Table 3. The crosssection of pipe for primary, secondary 1 and secondary 2 is shown in Table 2. We have used this software to make certain the safety of the driver and make changes were based on failed results if any. To perform the analysis of our roll cage effectively, we calculated the forces it will encounter during the impact of major forces such as front impact and rollover. The testing of the roll cage was performed under five scenarios in which different forces were applied in different methods so as to find the strength of the roll cage during a collision. The simulations which were performed included Front Impact, Torsional, Rollover, Side Impact and Rear Impact. Each simulation presented a different scenario that the frame might

Table 1 Bending strength and bending stiffness of different materials

S. No.	Cross section (mm)	Moment of inertia	AISI 1020		AISI 1018		AISI 1022		AISI 4130		4340	
			Sb	Kb	Sb	Kb	Sb	Kb	Sb	Kb	Sb	Kb
1	25.4	1.35E + 04	3.77E + 05	2.69E + 09	3.93E + 05	2.76E + 09	4.25E + 05	2.69E + 09	4.88E + 05	2.69E + 09	2.03E + 05	2.84E + 09
2	31.7	1.72E + 04	3.17E + 05	3.45E + 09	4.02E + 05	3.54E + 09	4.35E + 05	3.45E + 09	5.00E + 05	3.45E + 09	5.11E + 05	3.64E + 09
3	31.7	1.86E + 04	4.10E + 05	3.72E + 09	4.33E + 05	3.817E + 09	4.69E + 05	3.72E + 09	5.39E + 05	3.72E + 09	5.51E + 05	3.92E + 09
4	38.1	3.06E + 04	5.62E + 05	6.12E + 09	5.90E + 05	6.275E + 09	6.42E + 05	6.12E + 09	7.39E + 05	6.12E + 09	7.55E + 05	6.27E + 09

Table 2 Pipe cross-sections

Members	Cross-section (mm)	Thickness (mm)
Primary	31.75	1.6
Secondary 1	25.4	1
Secondary 2	25.4	2

Table 3 Material comparison on the basis of mechanical properties

Specifications	Choosen material (AISI 4130)	Recommended material (AISI 1018)
Density (g/cc)	7.85	7.87
Yield strength (MPa)	460	370
Tensile strength (MPa)	560	440
Elongation (%)	21.50	15
Poisson's ratio	0.29	0.29
Bending moment	500 Nm	

experience during accidents and the forces were calculated to the analyse the roll cage at each scenario.

5 Impact Analysis Calculations

5.1 Front Impact Calculations

Front impact analysis is done by considering some specifications such as the force of vehicle with driver is taken to be 220 kg and velocity of vehicle is taken as 50 kmph or 13.88 mps and impact time is taken to be 0.2 s. Figures 2, 3 and 4 shows the stresses generated and the deformation analysed and the factor of safety in the frontal impact.

For performing the analysis, we fixed all the rear mounting tab as constraints and the force is applied on the front mounting tab opposite to the direction of motion of the vehicle, restricting the deformation along the axis of motion of the vehicle.

The force is calculated by using impulse momentum formula which is given as:

$$F \times t = m \times v \quad (1)$$

where F = force, m = mass of vehicle = 220 kg, t = impact time = 0.2 s, v = velocity of vehicle = 13.88 mps.

Fig. 2 Stress generated in front impact
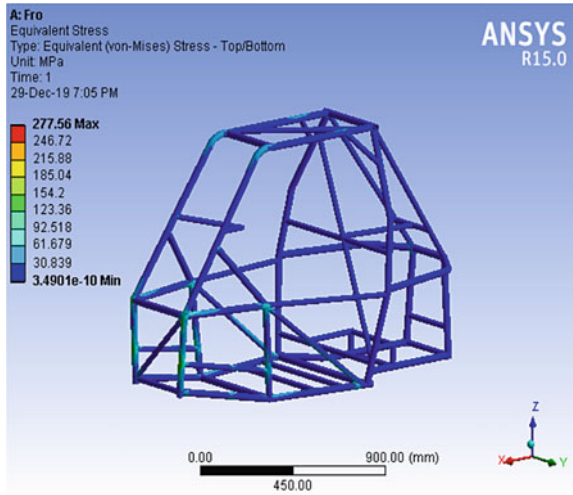
Fig. 3 Deformation generated in front impact
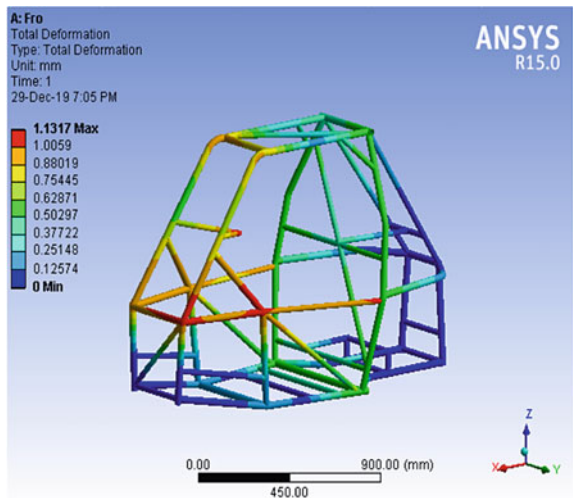
$$F = (m \times v)/t(2) = (220 \times 13.88)/0.2 = 15268 \text{ N}$$

Fig. 4 Factor of safety in
front impact
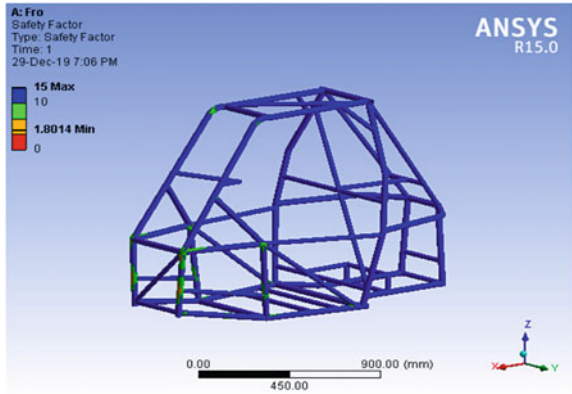
5.2 Rear Impact Calculations

For rear impact analysis, the vehicle is hit form the rear side due to which the rear part
of the vehicle bears the impact force. Figures 5, 6 and 7 shows the stresses generated
and the deformation analysed and the factor of safety in the rear impact.

For analysis, all the front mounting tab are fixed and the force is applied on the
rear mounting tab opposite to the direction of motion of the vehicle, restricting the
deformation along the axis of motion of the vehicle.

For impact force, we use impulse momentum theorem:

$$F \times t = m \times v = (m \times v)/t = (220 \times 13.88)/0.2 = 15268 \text{ N}$$

Fig. 5 Stress generated in
rear impact
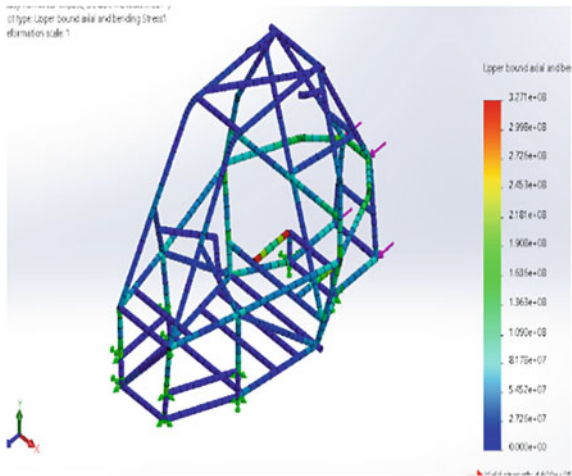
Fig. 6 Deformation
generated in rear impact
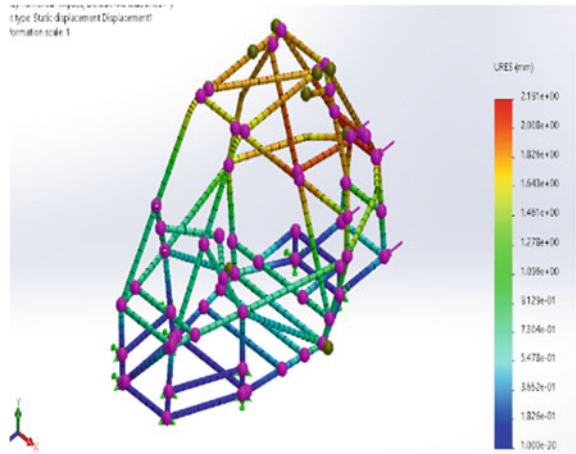
Fig. 7 Factor of safety in
rear impact
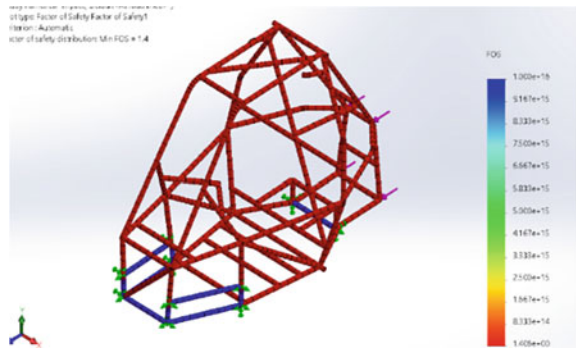
5.3 Side Impact Analysis

For side impact analysis, when the vehicle is running at a particular speed and hit by
another vehicle sideways, then the impact time will be 0.4 s as, during side impact,
the impact will be perpendicular to the wheel base of the vehicle. This will result in
an increase in impact time by 0.2 s. The variation of stresses generated, deformation
produced, and factor of safety is shown in Figs. 8, 9 and 10.

For simulation, the knuckle points on one side of the vehicle are taken as
constraints and force is applied on outermost points where the impact will occur
on the roll cage.

$$F \times t = m \times v = (220 \times 13.88)/0.4 = 7634 \text{ N}$$

Fig. 8 Stress generated in side impact
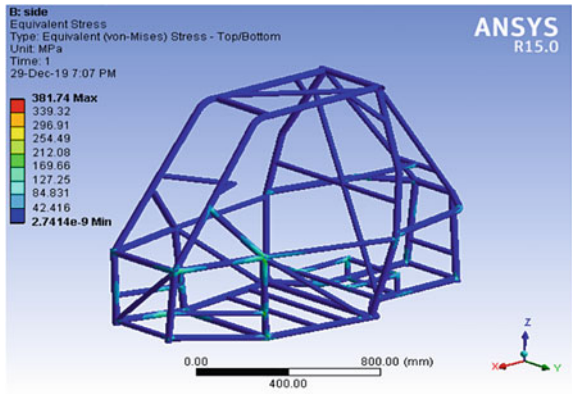
Fig. 9 Deformation generated in side impact
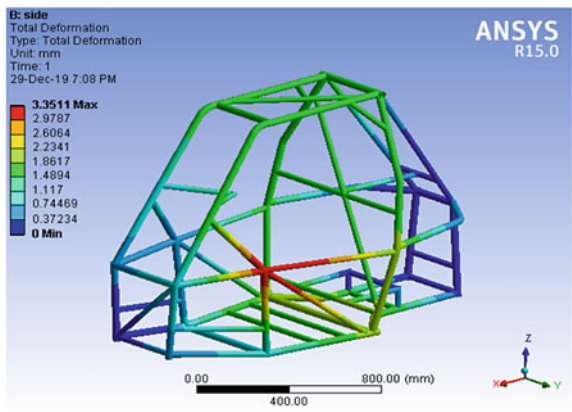
Fig. 10 Factor of safety in side impact
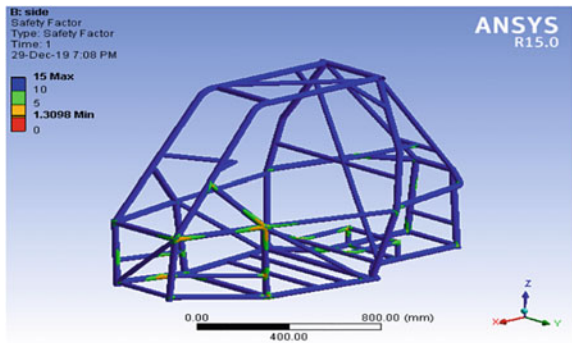
5.4 Torsional Analysis

During lateral load transfer, the biggest and adverse effect of torsional deflection can be easily observed on ATVs. So, to avoid torsional failure in roll cage, a twist was allowed which will help in distribution of some amount of weight transfer between front and rear tyres which in result deviates these values from there designed values shown in Figs. 11 and 12. This results in a decrease in chances of occurrence of torsional failure of an ATV. The analysis of factor of safety is shown in Fig. 13.

For calculating force for torsional impact, we simulated our roll cage on different G-forces of 2, 2.5, 3 and 3.5G and considering the severity of torsional impact, we considered a force of 3.5G for torsional analysis. For impact, front and rear knuckle points are considered as constraints alternatively and force is being applied on the roll cage.

$$F = 3.5G$$

Fig. 11 Stress generated in torsion
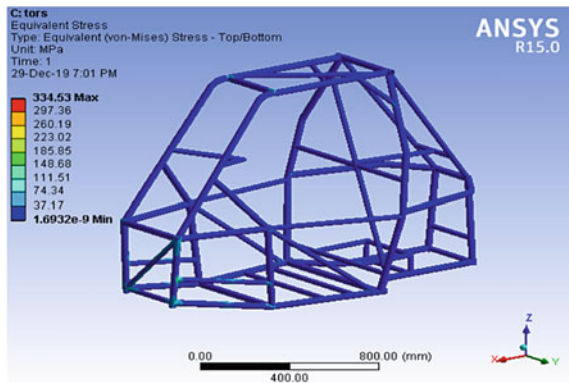
Fig. 12 Deformation generated in torsion
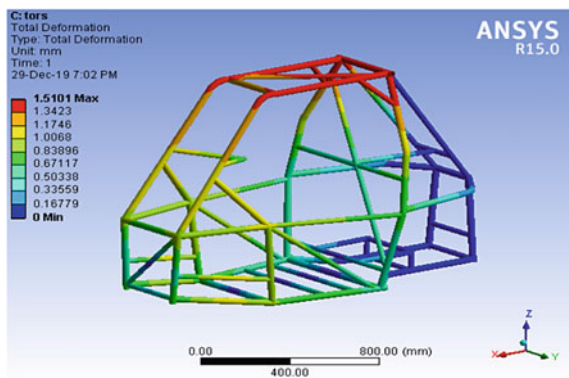
Fig. 13 Factor of safety in torsion
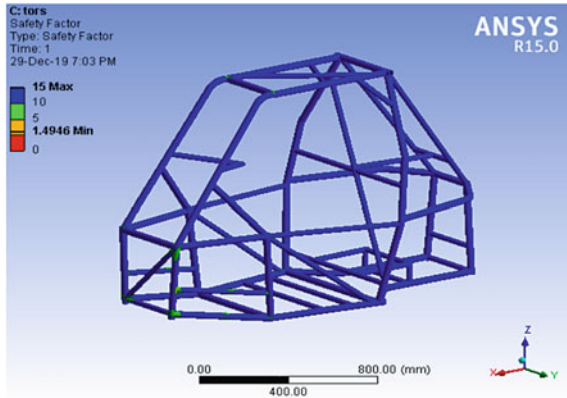
$$F = 3.5 \times 220 \times 9.81 = 7553.7 \text{ N}$$

5.5 Rollover Analysis

Rollover analysis is done to determine the possibility of the driver is able to come out of the vehicle after impact. In roll over analysis, vehicle observes a force while rolling due to which impact is observed on the upper side of the vehicle. this will damage the roll cage from top side which can reduce the area from which the driver comes out of the vehicle. Plot of stress variation, deformation variation and factor of safety is shown in Figs. 14, 15 and 16 for rollover analysis.

For roll over analysis, simulations on various G-forces like 2, 3, 4G is done and based on the results a force of 4G is considered for analysis. All the knuckle points

Fig. 14 Stress generated in rollover
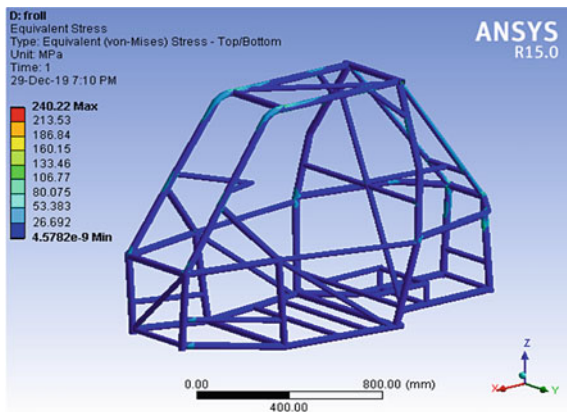
Fig. 15 Deformation
generated in rollover
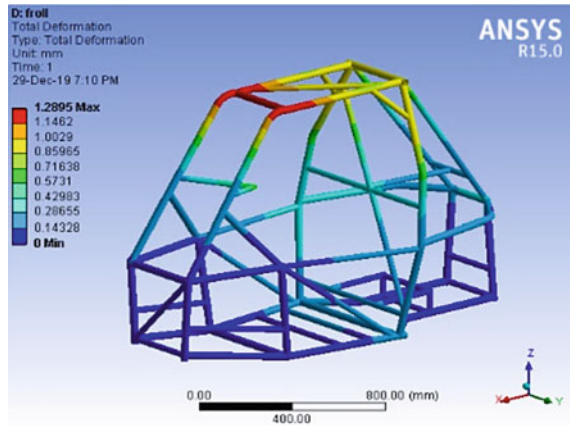
Fig. 16 Factor of safety in
rollover
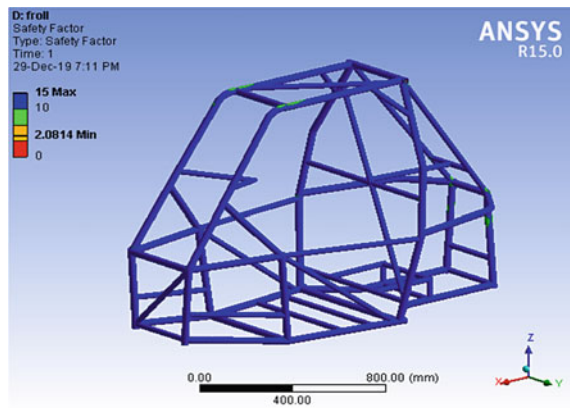
are fixed and force is applied on the upper side of the vehicle i.e. on front FAB of
the vehicle.

$$F = 4G$$

$$F = 4 \times 220 \times 9.81 = 8632.8 \text{ N}$$

Table 4 shows the values of factor of safety for front, rear, side, torsional and
rollover analysis.

Table 4 Values of factor of safety for various analysis

S. No.	Impact analysis	Force (G)	Stress (mpa)	Deformation (mm)	FOS
1	Front	7	277.5	1.13	1.8
2	Rear	7	223	1.56	2.06
3	Side	3.5	334.7	3.35	1.4
4	Torsional	3.5	334.5	1.51	1.4
5	Rollover	4	240.2	1.28	2.08

6 Conclusion

The results which we achieved after simulation of roll cage on various scenarios which the vehicle might face at dynamic state clearly shows that the vehicle will remain safe at the time of impact as the minimum factor of safety that we achieved was 1.4 that was during torsional analysis of roll cage, which is standard for designing an ATV roll cage. using pipes of different cross-sections helped us to increase the overall strength of the roll cage while reducing the weight at the same time.

References

1. Y. Mahajan (2017) Design and dynamic analysis of roll cage for the off-road vehicle. IJSART 3(6)
2. Mohanty AK, Jambhulkar A (2018) Design and development of roll cage: IRJET 5(3)
3. Raina D, Gupta RD (2015) Design and development for roll cage of all-terrain vehicle. IJTRE 2(7)
4. Boyd DK, Killen CD, Parkinson MB Manikin design: a case study of formula sae design competition. The Pennsylvania State University, University Park, Pennsylvania, USA
5. Raj H (2017) Design and analysis of the roll cage of an ATV. IJERT 6(9)

Structural Analysis of Single and Multiple Cracked Column with Buckling Using Fem

Prem Narayan Vishwakarma and Ajay Sharma

Abstract Engineering structures are having structural defects such as cracks due to long-term services, vibrations and material non-uniformity. Cracks in structural members cause to local changes in their stiffness, and consequently, their static and dynamic behaviour is changed. Analytical and numerical have been developed during the years. In this present work, the buckling of column with single and multiple non-propagating edge cracks is studied by use of the finite element method (ANSYS12) and transfer matrix method. The column is modelled as an assembly of sub-segments connected by mass less rotational springs whose flexibilities depend on the local flexibilities introduced by the cracks. Further, results are compared by ANSYS12 and transfer matrix method.

Keywords Cracked beam · Buckling · Finite element method · Transfer matrix

1 Introduction

As the jib crane is used for material handling purpose in most of the manufacturing industries. Jib crane having a hanging arm which acts as a cantilever beam thus it is subjected to axial compressive load and moment; also, it is subjected to the vibrations caused by various heavy machinery it is entrapped by cracks which further turn into failure. The cracks may develop from the long-term service, impact applied cyclic loads, aerodynamic loads, shrinkage, etc. Therefore, it is very essential to analysis the behaviour of buckling, stability of column, vibration analysis, crack failure [1–5]. A jib crane comprises of a derrick bolstered on a level bar that is cantilever from a vertical section, the flat bar turns about the vertical hub framed by the segment to give an even range to the crane [4]. The beam also serves as the track for the hoist trolley to provide radial travel along the length of the beam (Fig. 1). Standard capacities of a jib crane range up to about 5000 kg and can rotate 180–360°. The mechanical properties of structural steel are mentioned in Table 1.

P. N. Vishwakarma (✉) · A. Sharma
Mechanical Engineering Department, Amity School of Engineering and Technology, Amity University, Noida, India
e-mail: pnvishwakarma@amity.edu

Fig. 1 Jib crane model
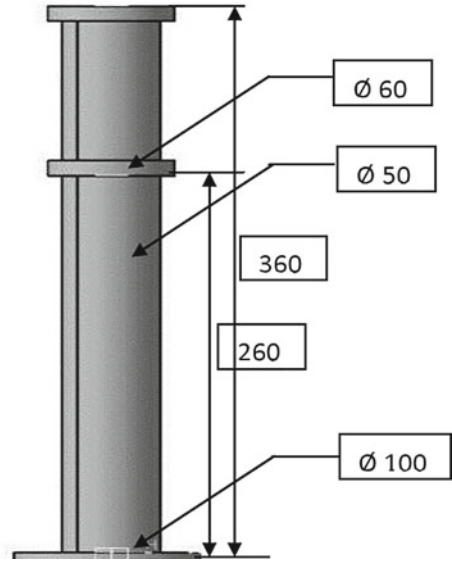
Table 1 Mechanical properties

Mechanical properties	Description
Material	Structural steel
Young's modulus	2×10^{11} N/m^2
Poisson's ratio	0.26
Density	7860 kg/m^3
Yield strength	2.5×10^8 N/m^2
I_{xx}	0.003 kgm^2
I_{yy}	0.078 kgm^2
Property of material	Isotropic

2 Modelling Software

CATIA is used to create model of column [6–8]. Solid model of column is shown in Fig. 2.

2.1 Analysis Software

The ANSYS 12.0 is used for structural analysis of column [9–11]. Material data selected for pre-process is structural steel. Input parameters for ANSYS are given in Table 2.
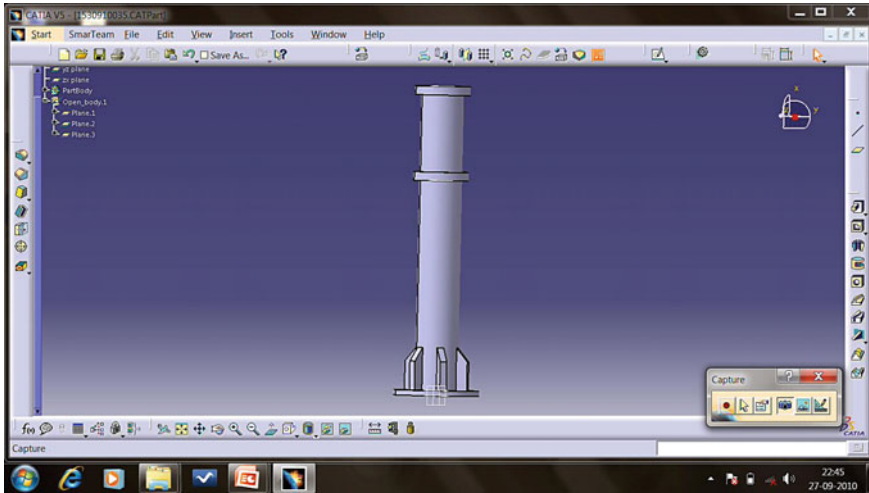
Fig. 2 Solid model of column

Table 2 Input parameters for ANSYS 12

Constraints	Constraints values
I_{xx}	0.003 kgm^2
I_{yy}	0.078 kgm^2
I_{zz}	0.078 kgm^2
Density	7860 kg/m^3
Poisson's ratio	0.266
Young's modulus	2×10^{11} N/m^2
Property of material	Isotropic

2.2 Beam Element

SOLID45 is utilized for the 3D displaying of strong structures [12, 13]. The component is characterized by eight hubs having three degrees of opportunity at every hub: interpretations in the nodal *x*, *y* and *z* headings as shown in Fig. 3. The element has plasticity, creep, swelling, stress stiffening and large deflection. The degrees of freedoms for solid45 beam element are UX, UY and UZ.

2.3 Mesh Model and Boundary Conditions

Mapped mesh model generated using tetrahedron 4 nodes as shown in Fig. 4. Total number of nodes are 8138, and total number of elements are 4278.
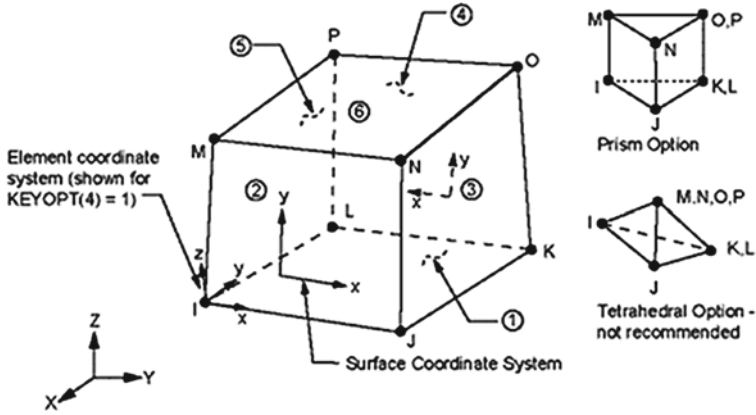
Fig. 3 Geometry of solid45 element

Fig. 4 Mesh model of jib
crane column
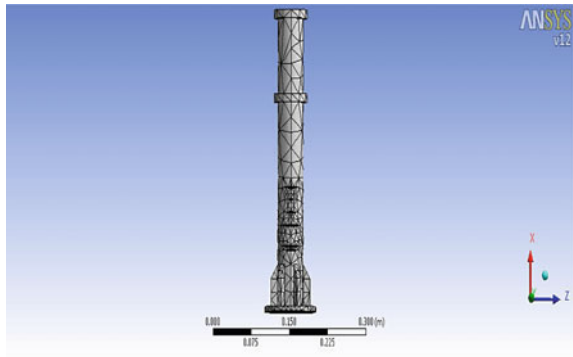
Boundary conditions taken as shown in Fig. 5 with 'A'—Zero displacement
provided in 'X' Direction 'B'—Zero displacement provided in 'Y' Direction 'C'—
Zero displacement provided in 'Z' Direction 'D'—Force applied of 1764 N. Static
structural analysis of column without crack is shown in Fig. 6.

Fig. 5 Boundary conditions
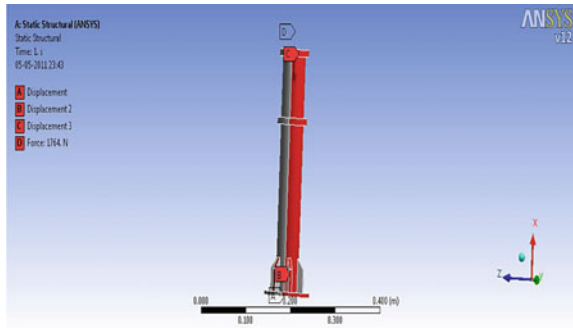
Fig. 6 Static structural analysis of column without crack
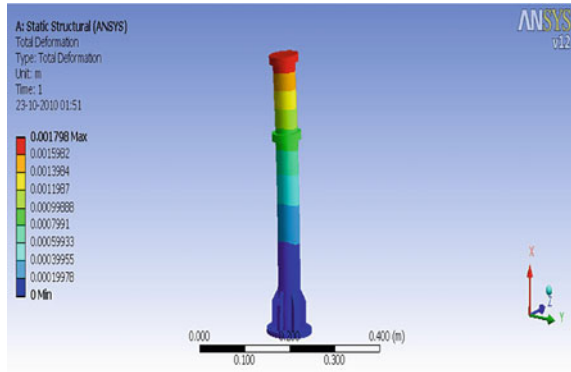
3 Static Structural Analysis of Column with Single Crack

Consider crack in column of jib crane as depth 13 mm, width 6.5 mm, thickness 2 mm, position 212 mm (from top) as shown in Fig. 7. The analysis results for column with single crack are shown in Figs. 8, 9 and 10.

Load multiplier for single cracked column is given in Table 3. Load multiplier factor is computed 658.68, and thus, the critical load for buckling is calculated as:

Critical load = Load multiplier × Force applied.

Critical load = 684.37 × 1764.

Fig. 7 Column with single crack (Line diagram)
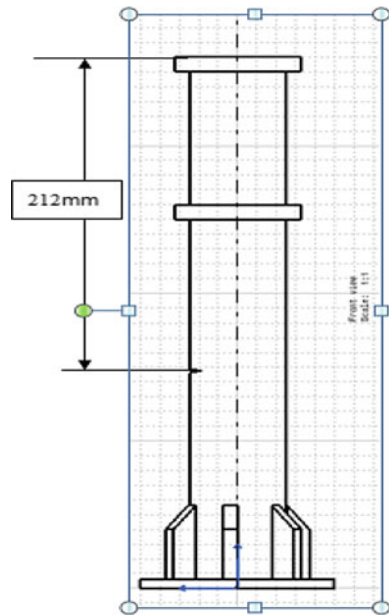
Fig. 8 Column with single
crack (Structural analysis)
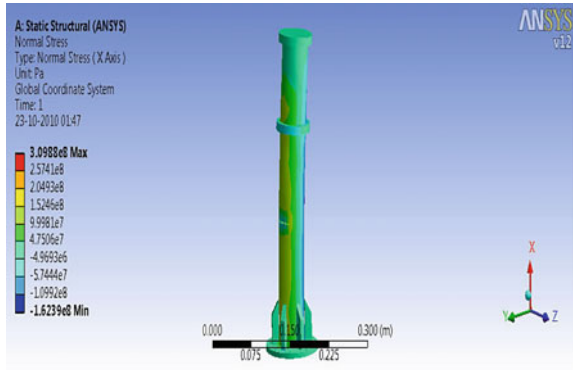
Fig. 9 Maximum stress
zone
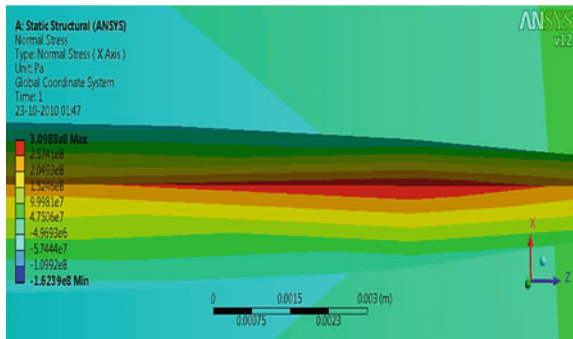
Fig. 10 Buckling analysis
of column with one crack
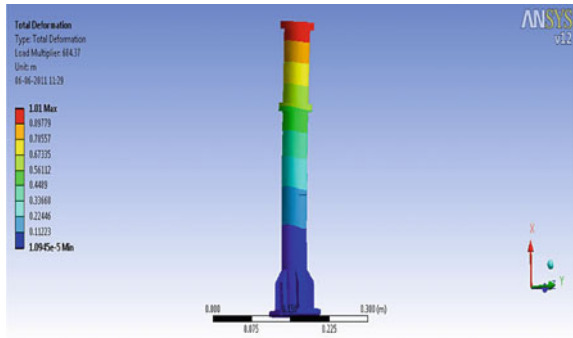
Critical load for a single crack column = 1207.22 k.

Table 3 Load multiplier data for single crack

Mode	Load multiplier
1	684.37
2	6015.6
3	15,111
4	26,902
5	39,051
6	51,329

3.1 Static Structural Analysis of Column with Multiple Crack

Consider multiple cracks in column (Fig. 11) with their locations as depth 13 mm, width 6.5 mm, thickness 2 mm, position 1st crack 212 mm (from top end), position 2nd crack 227 mm (from top end), position 3rd crack 257 mm (from top end). Analysis results for column with multiple crack are shown in Figs. 12 and 13.

Fig. 11 Model of jib crane column with multiple cracks
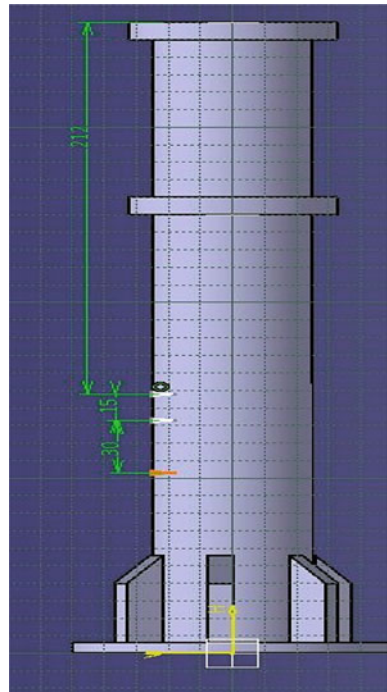
Fig. 12 Static structural
analysis of column with
multiple cracks
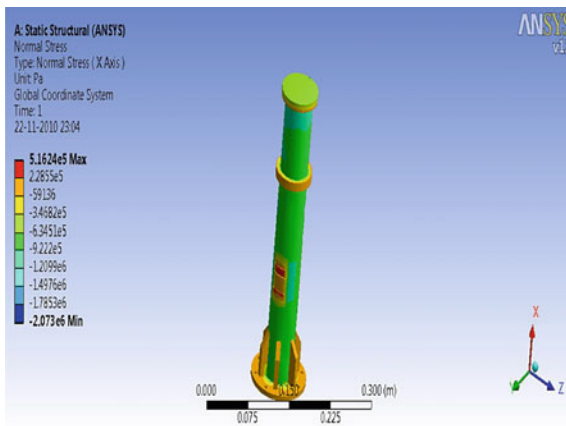
Fig. 13 Buckling analysis of
column with multiple cracks
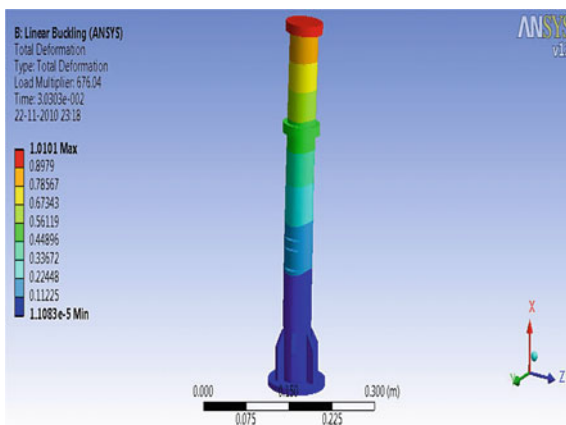
Table 4 Load multiplier data
for multiple crack

Nodes	Load multiplier
1	676.04
2	6045.4
3	14,860
4	26,435
5	38,834
6	50,360

4 Buckling Load Calculation for Multiple Cracks

Load multiplier factor is calculated as 676.04 as shown in Table 4, and thus, the critical load can be calculated as:

Critical load = Load multiplier × Force applied.

Critical load = 676.04 × 1764.

Critical load for a multi-cracked column = 1192 kN.

4.1 Transfer Matrix Method

In the numerical model, the split areas are commonly spoken to as massless rotational springs. Additionally, local adaptability coefficients of these springs are elements of the profundities of splits and the distance across of the cross-segment of the segment (Fig. 14).

The differential equation for buckling of the first segment can be written as:

$$\frac{d^4 y_1}{dx^4} + \frac{k^2 d^2 y_1}{dx^2} = 0$$

Solution of above differential equation is: $y_1(x) = A_1 + A_2 x + A_3 \sin(kx) + A_4 \cos(kx)$.

Where $k^2 = P/EI$, and P is the axial compressive force.

The generalized solution for above equation is given by:
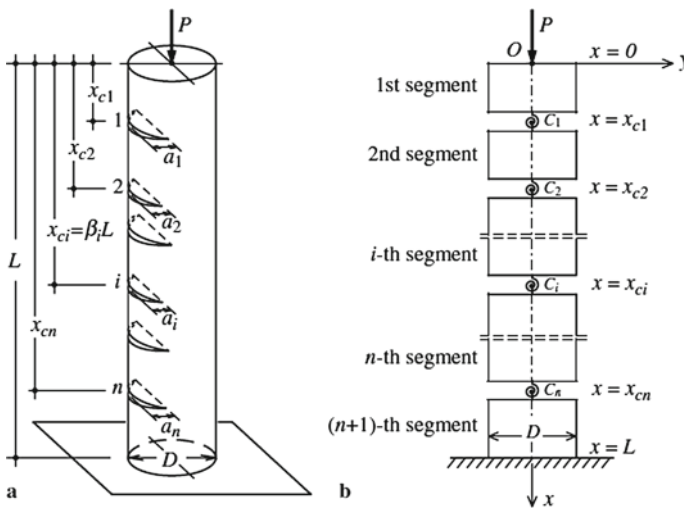
Fig. 14 Segments in transfer matrix method

$$T_1 = [B(x_{c1})][B(0)]^{-1}$$

where $[T_1]$ is called 'the transfer matrix'.
  and

$$[B(x)] = \begin{bmatrix} 1 & x & \sin(kx) & \cos(kx) \\ 0 & 1 & k\cos(kx) & -k\sin(kx) \\ 0 & 0 & p\sin(kx) & p\cos(kx) \\ 0 & -p & 0 & 0 \end{bmatrix}$$

After applying boundary condition (one end fixed and other end is free) in above equation will reduce to:

$$\begin{bmatrix} 0 \\ 0 \end{bmatrix} = \begin{bmatrix} T11 & T12 \\ T21 & T22 \end{bmatrix} \begin{bmatrix} y1(0) \\ \theta1(0) \end{bmatrix}$$

5 Results and Discussion

5.1 Buckling Load for Single Column Using Transfer Matrix Method

The generalized equation for single crack column:

$$\cos(kL) - EICik \sin(\beta kL) \cos[(1 - \beta)kL] = 0$$

$$k2 = P/EI$$

where $\beta = xCi/L$, and Ci is flexibility of cracked column.
  For jib crane column.
  $L = 360$ mm.
  $D = 50$ mm.
  $\beta = 0.58$.
  Ci $= 0.26$.
  $k = 0.00170$.
  Thus after substitution of values of L, β, Ci and k in above equations, critical buckling load for single cracked jib crane column (Pcr) is calculated as 1740 kN.

Table 5 Comparison of buckling load for single and multiple crack

Single crack			Multiple crack		
Buckling load (transfer matrix method) kN	Buckling load (ANSYS12) kN	Error percentage	Buckling load (transfer matrix method) kN	Buckling load (ANSYS12) kN	Error percentage
1740	1207.22	30%	1345.81	1192	11%

5.2 Buckling Load for Multiple Column Using Transfer Matrix Method

The generalized equation for multiple cracks is:

$$\cos(kL) - EIC_ik \Sigma \sin(\beta_ikL)\cos[(1 - \beta_i)kL]$$
$$+ (EI)2k2\{C_1C_2\sin(\beta_1kL)\sin[(\beta_2 - \beta_1)kL]\cos[(1 - \beta_2)kL]\}$$
$$+ C_2C_3\sin(\beta_2kL)\sin[(\beta_3 - \beta_2)kL]\cos[(1 - \beta_3)kL] = 0$$

For jib crane column with multiple cracks.
$L = 360$ mm, $i = 1 \dots 3$.
$D = 50$ mm.
$\beta_1 = 0.58$,
$\beta_2 = 0.63$,
$\beta_3 = 0.71$,
$C_i = 0. 26$,
$k = 0.0001497$.
$k2 = P/EI$.

Thus after substitution of values of L, β_1, β_2, β_3, C and k in above equation, critical buckling load for single cracked jib crane column (Pcr) is calculated as 1345.81 kN.

Thus, the buckling load values obtained by ANSYS and transfer method are compared and provided in Table 5.

6 Conclusion

It considered that a changing position of cracks causes more reduction in critical buckling load than in case of multiple cracks. It shows the variation of the critical load to the buckling load depending upon the dimension crack depth a/D for the dimension crack location of x/L. If the location of the crack changes nearer to fixed end where the buckling moment is maximum results in a greater reduction in the critical buckling load and is therefore more critical in the stability behaviour of the column.

From transfer matrix method, the critical buckling load of multiple cracked column is 22% lower in comparison with single cracked column. From ANSYS12, the critical buckling load of multiple cracked column is 13% lower in comparison with single cracked column.

References

1. Chandra Kishen JM, Kumar A (2004) Finite element analysis for fracture behaviour of cracked beam columns. Finite Elem Anal Des 40:1773–1789
2. Gurel MA (2007) Buckling of slender prismatic circular columns weakened by multiple edge cracks. Acta Mech 188:1–19
3. Chan SL, Su GP (2002) Stability analysis and parametric study of pre-stressed stayed columns. Eng Struct 24:115–124
4. Springer WT, Rezniek A The prediction of the natural frequencies shifts for a cantilever L-section beam due to the presence of a crack. In: 12th international modal analysis conference, vol 994. pp 889–897
5. Stubbs N (1990) Global non-destructive damage evaluation in solids. Int Modal Anal Conf 5:67–79
6. Sharma SK, Sharma RC (2018) Simulation of quarter-car model with magnetorheological dampers for ride quality improvement. Int J Veh Struct Syst 10(3):169–173
7. Sharma SK, Chaturvedi S (2016) Jerk analysis in rail vehicle dynamics. Perspect Sci 8:648–650
8. Sharma SK, Kumar A (2018) Multibody analysis of longitudinal train dynamics on the passenger ride performance due to brake application. In: Proceedings of the institution of mechanical engineers part K: journal of multi-body dynamics
9. Pinabasi S, Okay F, Akpinar E, Erdogan H Stability analysis of two segment stepped columns with different end conditions and internal axial loads. Math Prob Eng 2013. Article Id: 858906
10. Sharma RC, Palli S, Koona R (2017) Stress and vibrational analysis of an Indian railway RCF bogie. Int J Veh Struct Syst 9(5):296–302
11. Palli S, Koona R, Sharma SK, Sharma RC (2018) A review on dynamic analysis of rail vehicle coach. Int J Veh Struct Syst 10(3):204–211
12. Sharma RC, Sharma SK (2018) Sensitivity analysis of three-wheel vehicle's suspension parameters influencing ride behavior. Noise Vib Worldwide 49(7–8):272–280
13. Sharma SK, Saini U, Kumar A (2019) Semi-active control to reduce lateral vibration of passenger rail vehicle by using disturbance rejection and continuous state damper controller. J Vib Eng Technol 7(2)

Selection of Investment Portfolio Using Multi-criteria Decision Model (MCDM) and Integer Programming Model

Fiseha M. Guangul, Gezae Mebrahtu, and Subhash Chandra

Abstract This paper is an attempt to select few vital investment projects among a number of feasible projects using MCDM and linear integer programming in the face of limited financial resources. The tangible and intangible considerations are taken care of using analytical hierarchy process (AHP) and simple multi-attribute rating technique (SMART) to establish relative position weights (RPW) for all the projects. These RPW's are used as coefficients of the objective function for the optimization model that eventually ensures strategic alignment of projects with organizational goal to enhance competeveness and economic value. The current research is pertinent to the applied research area that seeks solution for investment decisions. The criteria and sub-criteria are identified beforehand to evaluate individual project using MCDM (AHP). AHP is applied for the projects qualified in the evaluation process to get relative position weights (RPW). The objective function will make use of relative position weight (RPW) as coefficients of decision variables in optimizing the solution. The model of multiple investments involving dependency, resource sharing, growing opportunities, constraints, etc., is formulated. The integer programming model in conjunction with multi-criteria decision model (MCDM) is being used for evaluation and selection of optimal portfolio.

Keywords Relative position weight (RPW) · Project portfolio (PP) · Analytical hierarchy process (AHP) · Multi-criteria decision model (MCDM)

F. M. Guangul
Department of Mechanical Engineering, Middle East College, Seeb, Oman
e-mail: fiseham2002@yahoo.com

G. Mebrahtu · S. Chandra (✉)
Department of Manufacturing Technology, FTVETI, Addis Ababa, Ethiopia
e-mail: suchandra404@gmail.com

G. Mebrahtu
e-mail: gezaemebrahtu@gmail.com

101

1 Introduction

A portfolio is a mixed investment strategy that aims at maximization of returns and minimizes risks [1]. It is a cumbersome task if not impossible before companies to decide the worth of investment in particular industries for the expected returns under the prevailing risks. Such state of affairs pose dire dearth of wrongful decisions and its reverberation thereof. The simple procedures used by organizations may not serve well as many assumptions will make the formulations far from real problem. The solution near optimal is difficult to obtain without the aid of structured mathematical formulation which is capable of including many parameters that affects the outcome [2].

A sizeable number of new projects are included in due course of time in the portfolio that can yield optimal worth to the company with limited resources. The information relating to new projects, ongoing investments, constraints, interdependence between projects, quantifiable and subjective benefits, and risks have to be integrated to arrive at optimum portfolio of projects. The wrong decisions in selecting the project have negative consequences, the first is that the resources available in unsuitable projects are consumed, and the second is that the organization loses benefits that could benefit from using resources in suitable projects [3].

Hence, improved integrated technique is explored that assists in finding the optimal project portfolio. AHP model is constructed to evaluate projects and RPW are assigned to articulate company's overall objective function.

There exists a number of portfolio selection models; however, many of them may not live up to expectations to accommodate all the constraints. Thus, it may result into non-optimal and non-ideal solution. Quantification of intangible factors is not adequately addressed or dropped while model formulation by the researches [4]. The analytical hierarchy process (AHP) along with simple multi-attribute rating technique (SMART) is used to find the constants of the maximization objective function. Integrated approach enables to minimize the shortcomings arising of the methods when used independently. Both the qualitative and quantitative parameters using systematic methodology are used in evaluating the weighted score of individual investment project [5]. Meyer-cooumta presents the model which includes both the factors intangible as well as tangible.

The most vital goals of project portfolio [4, 6, 7] are:

(i)   Maximization of portfolio's value: Select projects that can yield more return.
(ii) Optimal mix of projects: List of mix of feasible projects, like between long term projects, short terms; high risk, lower risk; and in terms of markets, technologies, product categories, etc., is included to be evaluated collectively to achieve maximum business value.
(iii) Strategy driven portfolio. The projects are in line with strategy and strategic priorities.
(iv) Right number of projects: There should be only manageable number of projects.

2　Development of Project Portfolio Selection Model

An optimization model is developed using integer programming, subject to constraints and objective function that takes care of economic and societal needs of the enterprise. A comprehensive model that can address maximum real-life parameters has been attempted. The model presents wider perspective of handling issues of varied nature pertinent to organization. The standard tools find it difficult to consider all of them in a single problem. There is no universal method that assure effective process while considering factors both internal and external to the company [8, 9].

Six steps of PPM process are given below:

1. **Strategic Planning**: Projects must be in line with organization objectives [10].
2. **Opportunity Identification**: It aims at converting threats into opportunity and developing far sightedness from one and all for top down or bottom up decision making [4].
3. **Individual Project Evaluation**: In this step, three distinct phases are included.
   Pre-filtering: Some projects are filtered during the evaluation and feasibility test [11].
   Investment evaluation: The basic scoring, economic, and decision analysis are the common tools used to evaluate the new investment. The purpose of evaluation is to choose technically, commercially, and financially viable projects.
   Screening: Screening is to examine the projects thoroughly and rigorously as compared to pre-filtering stage.
4. **Portfolio Selection**: Model identifies best combinations of projects (new and ongoing) that meets the objective of the company optimally [12, 13]. The model developed has the following features.

   (i)　　Realistic: The realistic data of resources are used.
   (ii)　 Capable: The versatility and ability to take most factors.
   (iii)　 Transparent: Decisions and assumptions are thoroughly deliberated before arriving the consensus to prevent edict opinion
   (iv)　 Extensive: It must include the information in breadth and depth.
   (v)　　Flexible: Model must be accommodative to accept changes in some parameters.
   (vi)　 Cost-effective: The data must be collected from reports and other authentic published sources to keep data analysis cost low.
   (vii)　 Consistent: The model should provide similar results in case of identical projects.
   (viii) Iterative: Model can start with a simple data and change the variable to see correlation with end result and gradually add more complex items.
   (ix)　 Maximize the utility: Selection of portfolio that maximizes the aggregate of strategic objective of the company.
   (x)　　Check for on-going investments: The key drivers for on-going investments that can alter utility substantially should be available.

(xi)   Hierarchical objectives: Organizational breakdown structure is explicitly prepared to aid evaluation of hierarchical objectives

(xii) Easily automated: It is about data preparation, storage and retrieval, and data handing for fast solution.

5. **Portfolio Adjustment**: It is the final review by experts, and changes are accepted and verified with set objectives [14].

6. **Portfolio Monitoring**: Once the investments are selected, the progress of the projects has to be monitored as extrinsic factors that may influence the outcome of the projects [15].

3   Criteria Identification and Evaluation of Relative Position Weight

3.1   *Evaluation of Criteria*

Vital six criteria consist of nineteen sub-criteria that are identified and evaluated using AHP and weighed on the basis of the same [2]. The selection of project will depend upon the evaluation criteria and the accuracy of experts' opinion. The project selection is driven by the monetary return in case of private companies and social welfare, and environmental issues are driving forces in case of public enterprises [16]. The potential criteria and their sub-criteria are briefly explained in Table 1 for the purpose of ease of understanding and evaluation [2, 17–19].

3.2   *Prioritizing the Criteria and Scoring Projects*

The AHP has been used by many authors for getting the relative scores of attributes using the pair-wise comparison. The AHP model has to be developed first, then the next step is to find the relative weights of each criterion. The relative position weights of the projects are determined for each sub-criteria and then transformed into a coefficient for objective function by combining the relative values through the scoring method.

But AHP has its own limitations. Some of them are: (i) Expert must have thorough understanding of problem formulation. (ii) Matrix operations are performed, and it may take considerable time if done manually. (iii) AHP cannot be used for more than ten factors to get reliable relative weights [20, 21].

SMART is a simple method used to aid managerial decision processes. SMART can handle any number of criteria to find the relative weights [22] which is not possible in case of AHP. Both tangible and intangible criteria and sub-criteria are identified and expressed in hierarchical structure. The relative rankings of each criterion in the pair-wise metrics based on their contribution toward stated objectives are calculated

Table 1 List of criteria and sub-criteria with description [17]

No.	Criteria and sub-criteria	Description for evaluation
1	Technical evaluation [TEV]	
1.1	Production system [PRS]	Technology that is appropriate to local context
1.2	Scale of operation [SCO]	The cost of production depends upon volume and variety
1.3	Input material [INM]	The more the ease of availability of material, the better it is
1.4	Technical proficiency [TEP]	The more the technical know-how, the greater the score
2	Commercial criteria [COC]	
2.1	Demand of product [DOP]	The rank is proportional to demand
2.2	Market place of the product [MPP]	If supply chain and logistics is low, the better it is
3	Socio-economic evaluation [SEE]	
3.1	Foreign exchange [FOE]	If the foreign exchange generated is high, then it is ranked high
3.2	GDP contribution [GDP]	The greater it can contribute, the greater the rank
3.3	Public welfare [PUW]	The higher the social welfare, the greater the rank
3.4	Impact on environment [IOE]	The higher the environmental protection, the greater the rank
4	Monetary criteria [MOC]	
4.1	Project outlay [PRO]	The less the outlay of project, the priority weight is high
4.2	Working capital [WOC]	The lower the working capital, the greater the rank
4.3	Means of initial finance [MFI]	The availability of initial finance options, the higher the rank
5	Investment assessment [INC]	
5.1	Net present value [NPV]	The more positive the cash flow over project life, the greater the rank
5.2	Internal rate of return [IRR]	Higher the prospects of IRR, higher is the priority rank
5.3	Financial gain [FIG]	The greater the profitability index, the greater the priority weight
5.4	Payback period [PBP]	The shorter the PBP, the better it is
6	Institutional appraisal [IAP]	
6.1	Managerial skillfulness [MAS]	The better the managerial stewardship, the more preferred it is
6.2	Availability of skilled manpower [ASM]	The ease of availability of skilled manpower
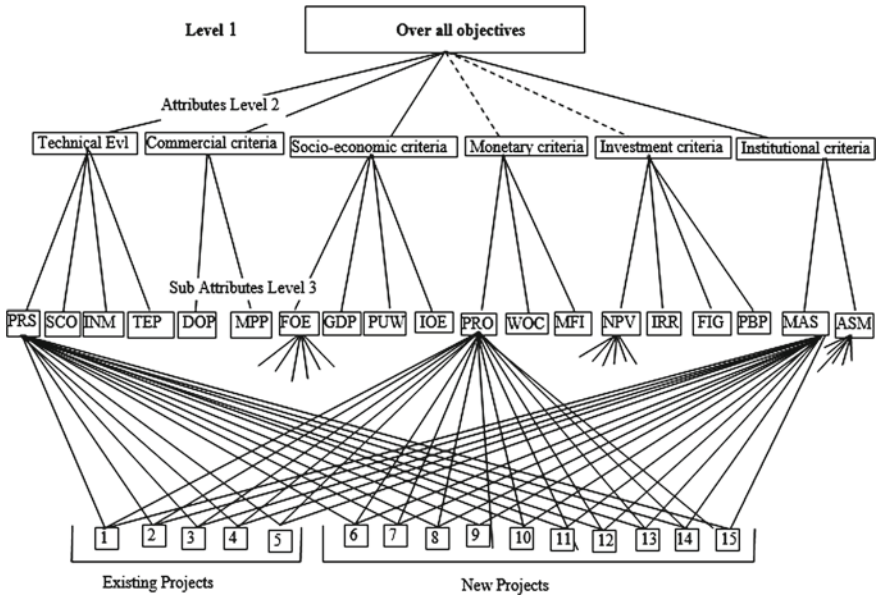
Fig. 1 AHP frame that indicates overall objectives, criteria, and screened projects

using AHP. Finally, how each criterion has their impact on each project is done to rank projects w.r.t each other [23]. These weights are used as a coefficient of the objective function developed. The schematic of AHP model with the overall objective of the company, criteria, sub-criteria, and the potential projects as alternatives is shown in Fig. 1. The appraisal team will evaluate the generated portfolios on the basis of objective function value, subjected to certain constraints [22, 24].

3.3 Formulation of Integer Programming Model for the Evaluation of Projects

Selection of a number of projects from a large number of feasible projects is a highly complex problem. Balance has to be attained among potentially conflicting tangible and intangible criteria, such as risk, and socio-economic requirements, contingent projects, and mutually exclusiveness. Resources are considered as a constraint during optimization stage for portfolio.

The options relating 'select or not select', inter relations, interdependence, etc., can be modeled to binary problem to solve the optimization problem.

4 Formulation of Linear Programming Model

i. Binary variable: The decision variables are defined by

$$X_i = \begin{cases} 1 & \text{if project } i \text{ is selected} \\ 0 & \text{if project } i \text{ is not selected} \end{cases} \quad \text{for } i = 1 \text{ to } n$$

ii. Objective function: The objective function is given by

$$\text{Max } Z = \sum_{i=1}^{n} a_i X_i \tag{1}$$

where Z is the value of objective function to be maximized. And a_i is the relative weight of project i

iii. Resources constraint: Resource constraints must be duly taken care of to address the scarce resources. The resources can be budget, input materials, manpower, etc. When many projects compete for the same resource, the model will have projects whose sum of demand for certain resources will not exceed the availability of resources.

The resource constraint can be written as:

$$\sum_{i=1}^{n} a_{ij} X_i \leq C_j \tag{2}$$

where a_{ij} is the quantity of resource j required for project X_i and C_j is the available amount of resource j.

iv. Obligatory projects: There are projects that are bound to be in the portfolio [17, 22, 23]. The constraint for such projects is given by:

$$X_i = 1, \quad \text{for } i \in S_m \tag{3}$$

where S_m is the set of obligatory projects.

v. Project interrelationship: Once the interrelationships between projects are known, then constraints are developed.

(i) Mutual exclusiveness: Projects are mutually exclusive if only one project is included for the formation of the portfolio

$$\sum_{i \in s_n} X_i \leq 1 \tag{2}$$

where S_n represents a set of mutually exclusive projects.

(ii) Contingent projects: The following constraint relationship for the decision variables X_j and X_k ensures that project k will be considered if project j is included in the portfolio. The relation is given by

$$X_j \leq X_k \tag{3}$$

One project may also be contingent on two or more projects. If project k is contingent on projects h and j, then project k is selected if projects h and j are included in the list. The constraint is given by

$$X_h + X_j \leq 2X_k \tag{4}$$

(iii) One of the two or both: No less than one project should be selected. The following relationship for the two projects j and k is given by

$$X_j + X_k \geq 1 \tag{5}$$

(iv) Both or neither: Either both or none will be included in the portfolio. The following relationship is used to model constraint.

$$X_j = X_k \tag{6}$$

(v) Bound on the number of projects: The maximum number of projects should not exceed a specified limit 'n' from 'm' possible candidates.

$$\sum_{j=1}^{m} X_j \leq n \tag{7}$$

The other constraints may be developed as per the problem at hand.

5 Model Testing

The model is tested for case situation with data that are collected from the Corporate Office. Some information may be different from reality as corporate may not reveal all of them. The procedure has been discussed for solving problems for actual data or estimated data [17].

5.1 Portfolio Analysis

(i) Assessment of Criteria and Sub-criteria: The priority weights of the criteria, sub-criteria, using AHP for different demand instances are obtained. The objective function and constraints in different scenarios are formulated. The same is solved using 0–1 integer programming to derive optimal portfolio. The priority weights at each level 2 and level 3 are given below in Table 2 [17]

Table 2 Summary of criteria, sub-criteria and the overall priority value

Main criteria (MC)		Sub-criteria (SC)		Overall value (B * D) = K_j
Identification (A)	Priority value (B)	Identification (C)	Priority value sub-criteria (D)	
Technical evaluation (TEV)	0.13	[PRS]	0.24	0.031
		[SCO]	0.16	0.021
		[INM]	0.48	0.062
		[TEP]	0.12	0.016
Commercial criteria (COC)	0.196	[DOP]	0.667	0.131
		[MPP]	0.333	0.065
Socio-economic evaluation (SEE)	0.261	[FOE]	0.231	0.06
		[GDP]	0.154	0.04
		[PUW]	0.462	0.121
		[IOE]	0.154	0.04
Monetary criteria (MOC)	0.087	[PRO]	0.545	0.047
		[WOC]	0.182	0.016
		[MFI]	0.273	0.024
Investment criteria (INC)	0.261	[NPV]	0.316	0.082
		[IRR]	0.316	0.082
		[FIG]	0.211	0.055
		[PBP]	0.158	0.041
Institutional appraisal (IC)	0.065	[MAS]	0.333	0.022
		[ASM]	0.667	0.043

(ii) Calculation of normalized relative weights of coefficient: Three instances of the demand of the project 10 (X_{10}) are considered.

Instance 1: Volume of sales of project X_{10} is high
Instance 2: Volume of sales of project X_{10} is medium
Instance 3: Volume of sales of project X_{10} is low

The list of ongoing projects of the endowment are given in Table 3. The names of the projects are not real.

The projects details and constraints

(1) The amount of investment for the first year is Birr 500 million
(2) Project X_1, X_2, X_3, X_4, and X_5 are mandatory projects, because the projects are ongoing.
(3) Either of the projects X_8 or X_{14} must be included in the portfolio.
4) At least one of the projects X_{10} and $X13$ must be included in the portfolio.

The calculation of the coefficients of the objective function (a_i) is given below.

Table 3 List of feasible projects on-going and new projects [17]

SN	Budget (in million Birr)	Name of the project
1	28	Forestry and wild life development (X_1)
2	35	Molded plastic product (X_2)
3	25	Beekeeping and honey processing (X_3)
4	40	Textile technology (X_4)
5	50	Livestock farming (X_5)
6	30	Cardboard project (X_6)
7	30	Red meat export house project (X_7)
8	50	Floriculture project (X_8)
9	20	Agro products (X_9)
10	120	Starch project (X_{10})
11	70	Packaging bag project (X_{11})
12	100	X_{12}
13	100	X_{13}
14	70	X_{14}
15	70	X_{15}

$$a_i = \left[\frac{\sum_{j=1}^{m} K_j X_{ji}}{\sum_{i=1}^{n} \cdot \sum_{j=1}^{m} K_j X_{ji}} \right] * 1000$$

Where a_i is the coefficient of X_i in the objective function

$\sum_{j=1}^{m} K_j X_{ji}$ is weighted value of project i, where K_j is the weight of sub-criteria j calculated using AHP. X_{ji} is the score of project i awarded out of hundred for sub-criteria j.

The value of a_i for different demand scenario is given in Tables 4 and 5.

The value of objective function as obtained by Eq. 1 is given in Table 6.

HSV stands for high sales volume, MSV for medium sales volume, and LSV for low sales volume.

6 Results and Discussions

The model developed is powerful tool to support the management decisions in selection of projects to be combined in portfolio. The blending of tangible and intangible factors in solving project portfolio is more realistic. Under high sales volume of

Table 4 Calculation of project weight against the sub-criteria using SMART in high demand scenario [17]

Sub-criteria		Project's SMART score														
Description	Weight (K_j)	X_{j1}	X_{j2}	X_{j3}	X_{j4}	X_{j5}	X_{j6}	X_{j7}	X_{j8}	X_{j9}	X_{j10}	X_{j11}	X_{j12}	X_{j13}	X_{j14}	X_{j15}
PRS	0.031	80	60	70	60	80	60	70	70	70	84	60	80	80	70	60
SCO	0.021	70	80	70	80	70	70	70	70	90	100	90	70	70	80	90
INM	0.062	90	70	90	60	90	90	90	80	60	100	80	90	90	80	60
TEP	0.016	100	70	80	60	80	70	80	60	40	98	70	90	90	60	50
DOP	0.131	80	90	90	100	70	90	60	100	90	98	80	90	90	70	100
MPP	0.065	90	80	90	100	70	90	60	100	80	100	80	80	80	90	100
FOE	0.06	30	30	70	80	60	40	80	100	30	100	30	60	60	80	40
GDP	0.04	70	70	70	70	70	70	70	70	70	98	70	70	70	70	70
PUW	0.121	100	60	80	60	80	60	100	70	60	84	60	90	90	70	60
IOE	0.04	100	0	70	0	40	20	40	0	100	56	20	100	100	40	0
PRO	0.047	90	90	90	90	70	90	90	70	90	0	60	30	30	50	50
WOC	0.016	90	90	90	90	70	90	90	70	90	0	60	30	30	50	50
MFI	0.024	90	90	90	90	70	90	90	70	90	0	60	30	30	50	50
NPV	0.082	0	90	60	100	60	100	70	100	0	100	90	70	70	80	100
IRR	0.082	0	90	60	100	60	100	70	100	0	100	90	70	70	80	100
FIG	0.055	0	90	60	100	60	100	70	100	0	100	90	70	70	80	100
PBP	0.041	0	100	70	100	90	70	90	70	70	98	90	60	50	70	100
MAS	0.022	100	60	80	60	80	60	80	70	50	84	50	90	90	70	50
ASM	0.043	100	70	80	70	80	70	80	60	20	84	60	90	90	70	50
$\sum_{j=1}^{m} K_j X_{ji}$		62.49	73.82	76.66	80.84	70.33	77.86	75.61	81.41	53.9	85.51	70.47	75.5	75.09	71.75	73.93

(continued)

Table 4 (continued)

Sub-criteria		Project's SMART score														
Description	Weight (K_j)	X_{j1}	X_{j2}	X_{j3}	X_{j4}	X_{j5}	X_{j6}	X_{j7}	X_{j8}	X_{j9}	X_{j10}	X_{j11}	X_{j12}	X_{j13}	X_{j14}	X_{j15}
a_i		57	67	69	73	64	70	68	74	49	77	64	68	68	65	67

Table 5 Values of a_i for projects in different demand scenarios

Project		X_1	X_2	X_3	X_4	X_5	X_6	X_7	X_8	X_9	X_{10}	X_{11}	X_{12}	X_{13}	X_{14}	X_{15}
a_i values	High demand	57	67	69	73	64	70	68	74	49	77	64	68	68	65	67
	Medium demand	58	68	71	74	65	72	70	75	50	61	65	70	69	69	68
	Low demand	59	70	72	76	66	74	71	77	51	37	67	71	71	68	70

project X_{10}, the investment portfolio comprises project X_1, X_2, X_3, X_4, X_5, X_6, X_7, X_8, X_9, X_{10}, and X_{15}. In case of low or medium demand of project X_{10}, the investment portfolio selects projects X_1, X_2, X_3, X_4, X_5, X_6, X_7, X_8, X_9, and X_{13}. The project X_8 is getting selected from mutually exclusive projects X_8 and X_{14}. At least one project from projects X_{10} and X_{15} must be included. The model is generic and can be used by corporate office to make best of it for its worthiness. In high demand scenario, projects 6, 7, 8, 9, 10, and 15th projects are selected where 15 projects are existing projects.

The suitability of the model is validated through the composition of portfolio that is evaluated by the management. The concept of PP can be used in government budget allocation to ensure proper utilization of scarce public fund in different sectors. Firms that invest in short-term/long-term issues, high risk/low risk issues, tax free investment can also model the portfolio and select the investments that will yield the maximum return. The data analyzed are from one of the endowments of Ethiopian industries. The results are similar to the decisions made.

7 Conclusions and Recommendations

The critical factors that are used to optimize the project portfolio include economic, social, and environmental concern, available resources and related constraints, the relationship between projects in the portfolio, strategic alignment of projects and organization, and the benefit of portfolio performance. Anticipating future opportunities is also important rather only managing the ongoing endeavors for the success of business. There are corporate houses and governments that invest in different industries/sectors for economic development which can take advantage of such models for maximum intended return. It is a justifiable to introduce the project portfolio management (PPM) approach in the corporate offices for the optimized solution of investments with respect to quantitative and qualitative criteria. A good portfolio management process can help business in addressing the future opportunities. It is necessary to develop mathematical models to select projects for portfolio with the most objective alignment toward the final goal of the organization. The significant amount of quantitative data and other available MCDM tool will aid in taking better decision making, validating the results and getting preferred optimized solution.

Table 6 An optimal solution of 0–1 linear integer programming

Projects		X_1	X_2	X_3	X_4	X_5	X_6	X_7	X_8	X_9	X_{10}	X_{11}	X_{12}	X_{13}	X_{14}	X_{15}	Objective function value
Different demand scenarios for project X_{10} product	HSV	1	1	1	1	1	1	1	1	1	1	0	0	0	0	1	735
	MSV	1	1	1	1	1	1	1	1	1	0	0	0	1	0	1	740
	LSV	1	1	1	1	1	1	1	1	1	0	0	0	1	0	1	740

Recommendations: The application of scientific method for optimal allocation of fund has to be embraced in both private or governmental organizations that undertake investments in different sectors. The problem has to be formulated for a specific company based on the company's requirement, objectives, and its policy. The company must have well authentic and structured data to evaluate feasible projects that must qualify to join the portfolio. The mathematical model used is a tool to ensemble the available data and to give an optimize solution based on the given inputs to the model.

References

1. Levy H, Sarnat M (1994) Capital investment and financial decisions (5th edn). Pretice Hall International (UK) Ltd
2. Bierman H, Smidt S (1994) The capital budgeting decision, economic analysis of investment project (7th edn). Machmillan Publishing Company
3. Baqeria K, Emran M, Mahsa MG (2019) Multi objective project portfolio selection. J Project Manag 4:249–256
4. Cooper RG, Edgett SJ (2006) Portfolio management for new products, Working Paper No. 11. The Product Development Institute
5. Lopes YG, De Almeida AT (2013) A multicriteria decision model for selecting a portfolio of oil and gas exploration projects. Pesquisa Operacional 33(3):417–441
6. Pieter Meyer-COO-UMTA, Value and Importance of Portfolio Management in Organizations www.pmisa.org.za/PMISA%20PfM%20Value%20Proposition%20Final%201%2001.pdf—Internet; UMT Consulting (2006)
7. De Klerk SW (2005) Validating the core problem of project portfolio management in the multi-project environment, Master's Thesis, University of Pretoria
8. Knutson J (2001) Project management for business professionals: a comprehensive guide. Wiley
9. Business Engine: Embracing the complete value of project portfolio management, Business Engine Corporation (2004)
10. Geoghan T, Snow B (2001) Introduction to the project portfolio management process. www.semizone.com/productfile/44/stan2444/overview_notes.pdf—Internet; Stanford Advanced Project Management
11. Norrie JL (2006) Improving results of project portfolio management in the public sector using balanced strategic scoring model, Doctoral Thesis, RMIT University
12. Dye LD, Pennypacker JS (2000) Project portfolio management and managing multiple projects: two sides of the same coin. In: Proceedings of the project management institute annual seminars and symposium
13. Linstrom L (2004) A portfolio approach to capital project management, Master's Thesis, Faculty of Engineering, Built Environment and Information Technology, University of Pretoria
14. Dickinson MW (1999) Technology portfolio management: optimizing independent projects over multiple time periods, Masters Thesis, Massachusetts Institute of Technology
15. Martikainen J (2002) Portfolio management of strategic investments in metal products industry, Master's Thesis, Helsinki University of Technology
16. Heiskanen J (2005) Project evaluation methods for R&D portfolio management, TAMPEREEN YLIOPISTO Taloustieteidenlaitos
17. Fiseha M (2008) Project portfolio management (ppm) approach for project selection. Master's Thesis, School of Graduate Studies, A.A.U. Technology Faculty, Mechanical Engineering Department, Industrial Engineering

18. Palcic I, Lalic B (2009) Analytical hierarchy process as a tool for selecting and evaluating projects. Int J Simul Model 8(1):16–26
19. Masoud RG, Farimah MR, Maryam G (2020) Portfolio selection: a fuzzy-ANP approach, Financial Innovation
20. Ghasemzadeh F, Archer N, Iyogum P (1999) A zero-one model for project portfolio selection and scheduling. J Oper Res Soc 50(7):745–755
21. Saaty TL (1990) Decision making for leaders, the analytical hierarchy process for decision for complex world. PWS Publications
22. Enterprise Solution Competency Center (2007) Performance measurement. http://www.army.mil/escc/pfm/port_m.htm
23. Chandra S, Kodali R, Kumar A (2000) An improved multi-goal fuzzy heuristic for facility layout problems (FLPS). Industr Eng J XXIX(11) Official journal of the Indian institution of industrial engineering
24. Pieter Meyer-COO-UMTA (2006) Value and importance of portfolio management in organizations www.pmisa.org.za/PMISA%20PfM%20Value%20Proposition%20Final%201%2001.pdf—Internet; UMT Consulting

Vibro-acoustic Analysis of Simple Vehicle Cabin Using Finite Element Method

Mitesh B. Panchal , **Prasad Yeole, and Reena Trivedi**

Abstract The reduction in interior noise is an important concern in noise, vibration, and harshness (NVH) for different reasons. Noise and vibration of the passenger cabin are the signature points to the overall impression of the vehicle quality. Very high noise and vibration at the driver's ear position make noise and vibration a key issue. Long exposure to high noise levels are major factors of risk to worker health and safety. Thus, it is very important to study the noise generated inside the cabin. Experimental method is carried out, but it is very expensive and time consuming. This article is based on the development of predictive finite element acoustic structural analysis to study the vibro-acoustic behavior of the excavator cabin. The displacement response of cabin under the external force excitation is analyzed between 0 and 300 Hz. The displacement response is mapped to acoustic cavity surface by the normal surface interaction. The distribution of internal acoustic field is calculated, and sound pressure level response is obtained at the driver's ear. The methodology has been established for acoustic analysis of cabin, and sound pressure level has been reduced by 20 dB.

Keywords Automotive interior noise · Fluid structural interaction · Sound pressure level

1 Introduction

At the present time, customer believes that comfort in the vehicle is nearly as important as mechanical performance. NVH is of rising concern to car manufacturers, and therefore, engineers have to exploit efficient and quitter designs in a moderately short

M. B. Panchal · R. Trivedi (✉)
Nirma University, Ahmedabad, Gujrat 382481, India
e-mail: reena.trivedi@nirmauni.ac.in

P. Yeole
Larsen & Toubro, Vadodara, Gujrat, India

time [1]. CAE processes are being used significantly as part of this 'time compression'. This enables analyst to quantitatively study the effect of various design iterations, rather than building several prototypes in the design process. Vehicle manufacturer are instituting new practices, which permits the engineering group to develop novel cars that combine excellent mechanical abilities with a high level of comfort [2]. It is very important for automobile companies to design automobiles with low power train and road noise in the passenger compartment. Noise is generated from the various mechanical components like tires, engine, transmission, and exhaust system. This is transmitted through the body of the car to passenger compartment. Frequency response analysis is used to find the sound pressure level (SPL) at the driver's and passenger ear locations at different driving speeds and engine speeds [3].

The passengers' compartment noise can be reduced by optimizing the size of structural components such as suspension bushing and dampers, powertrain mounts, exhaust system hangers, and body mount. It can also be minimized by deploying sound-absorbing materials to the metallic structures of the automobiles [4]. Various sound-absorbing materials are positioned in the passenger compartment such as dash panel trim, floor carpet, headliner, side trim, and rear trim. In addition, the structural design itself can be altered to change vibration load paths to reduce the noise level. These design decisions are usually made by trial and error. Vibro-acoustics is an influential aspect of the vehicle NVH performance [5]. Structure borne noise dominates mainly in low and mid frequency range (around 500 Hz). In automobile design and development, it is crucial to predict structure borne noise before prototype is presented [6]. The vibro-acoustic analysis is carried out by most widely used approach is FEM [7]. Dmmak et al. studied the numerical analysis of vibro-acoustic problem in presence of uncertainty [8]. Ebert et al. discussed opportunities and limits on vibro-acoustic design of vehicle structures using energy flow-based numerical simulation [9].

2   Problem Definition and Flowchart

The cases under investigation consist of simplified vehicle cabin for earth moving equipment. The basic intension is to reduce the noise level and increase the comfort in driver's cabin. The operators are relatively large impacted by interior sound field of excavator. Due to this the operator's ear easily leads to the operator fatigue. Hence, interior sound analysis of cabin is very important. Vibro-acoustic analysis is carried out for this simulation as major source of noise is vibration. Analysis is carried out for low frequency range (0–300 Hz). After simulation results, root cause for noise inside the cabin is studied. Flowchart for performing the acoustic simulation is shown in Fig. 1.
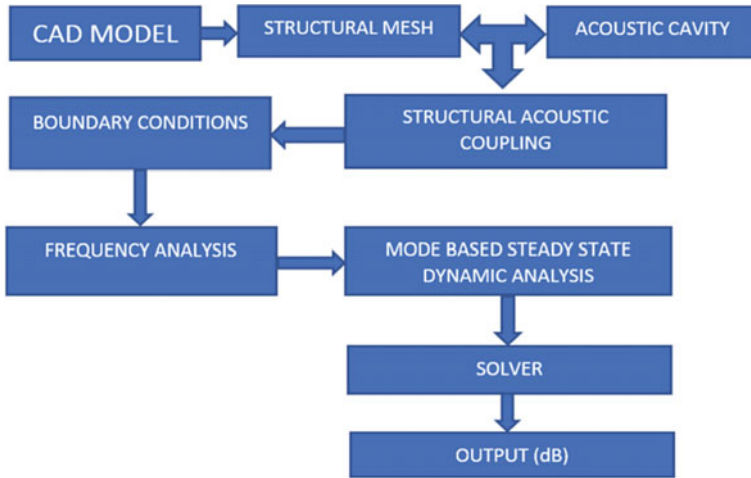
Fig. 1 Flowchart for performing the acoustic simulation

3　Methodology

To develop the methodology, it is necessary to develop sample model. The sample model of cabin is shown in Figs. 2 and 3. The model is created with the help of Hyper mesh software. The model consists of Quad, Hexa, Penta, and Tetra elements. Quad elements are used for modeling the structure mesh. Hexa and Penta elements are used to model the seat and. Tetra elements are used to model the acoustic fluid (air). The material used for construction of structure is steel. Closed shell foam is used for modeling the seat. The air is present inside the cabin. The analysis software used is ABAQUS. The meshed model is generated Hyper mesh. Material properties,

Fig. 2 Structural mesh
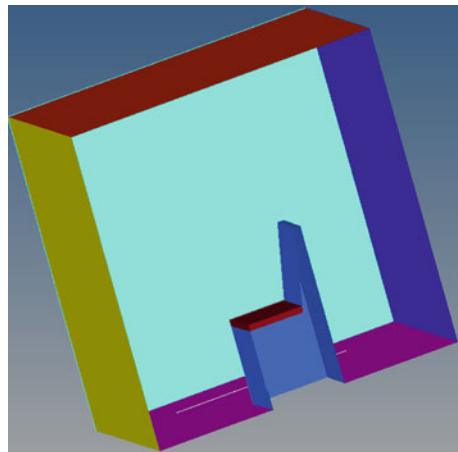
Fig. 3 Structural mesh with fluid filled inside
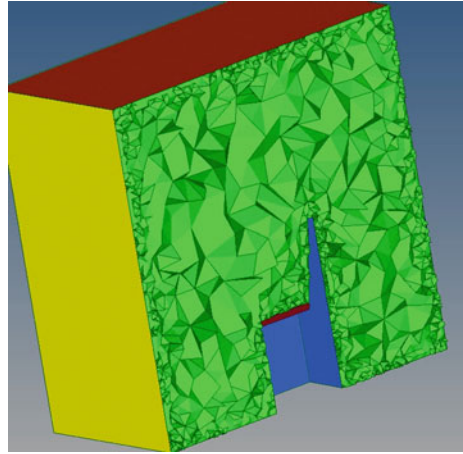
loading, and boundary conditions are also applied in Hyper mesh by using ABAQUS user profile. ABAQUS linear perturbation step is used for solving the model, and ABAQUS Viewer is used to view the results.

The size of element for air cavity is taken as (1/6) th of the wavelength for the maximum frequency of interest. Structural damping is taken as 3%. Maximum frequency of interest is 300 Hz. The maximum element length is calculated considering the wavenumber and wavelength. For FEA, it is necessary to maintain at least six elements per wavelength. Wavelength calculation,

$$\lambda = \frac{c}{f}$$

where $c = 344$ m/s and $f = 300$ Hz, $= 1.1467$ m.

There has to be at least six elements per wavelength,

$$\text{maxwave length} = \frac{\lambda}{\text{no.of elements}}$$

In this meshing, maximum element size and minimum element size are set as 115 and 191, respectively. Gradual meshing parameter is used. The fluid medium surface is selected as the slave that constrains the values at each fluid node as an average of the values at nearby master surface nodes. The point-wise fluid solid condition,

$$\frac{1}{\varrho_f} \frac{\partial p}{\partial x} \cdot \overline{n} + \ddot{u} \cdot \overline{n} = 0$$

is imposed at the slave nodes, resulting in displacement degree of freedom added to the fluid slave surface. Master surfaces constrain the slave surfaces by displacement degree of freedom and others are eliminated. Slave pressures are not constrained

Table 1 Properties of structural materials

Material	Density (T/mm³)	Young's modulus (MPa)	Poisson's ratio
Steel	7.85e-09	2.0e05	0.3
Glass	1.14e-09	1500	0.38
Closed shell foam	2.7e-09	110	0.3

Table 2 Properties of acoustic material

Material	Density (T/mm³)	Bulk modulus (MPa)
Air medium	1.2 e-12	0.142

directly. Acceleration as a base motion is assigned to the mountings. The pressure response is computed at driver ear location. The acoustic pressure is requested at the driver ear node set. Material properties for structural and acoustic materials are given in Tables 1 and 2, respectively.

4   Results and Discussions

The sound pressure level at driver ear node for baseline design is shown in Fig. 4

From Fig. 4, it is clear that maximum SPL is found at 6.455 Hz. It shows that maximum acceleration also occurs at 6.455 Hz (Fig. 5).

It is observed that the most significant contributions to the engine firing frequency SPL given by the roof and the side panels of the cabin model. Based on the results,

Fig. 4 SPL Versus frequency
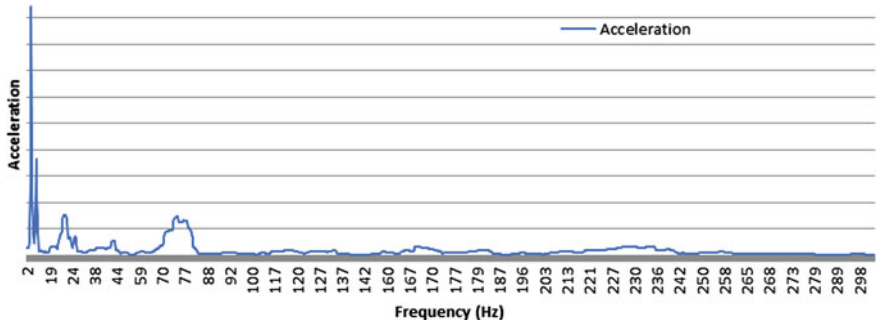
Fig. 5 Acceleration Versus Frequency
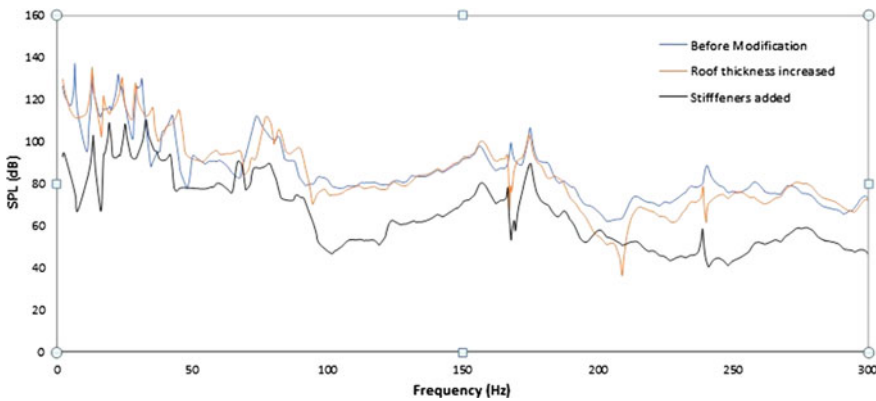
Fig. 6 Comparison of SPL for design modifications

the following changes were designed and implemented. The thickness of roof metal panel was stiffened. Stiffeners are added on the side panels of the cabin to increase the stiffness of the panels. Figure 6 shows the comparison of the all the design alternatives before and after modification of the design.

The drastic peaks reductions in all frequency range were observed referring to the side panels where vibration energy content was complex.

5   Conclusions

The finite element method is used to predict the sound level inside the cabin. In this study vibration of panels has been studied and effect of thickness on roof is also studied. The methodology for acoustic simulation of cabin is set. Sound pressure level can be reduced by shifting resonance frequency and changing stiffness of the

structure. Some important conclusions drawn from the above discussions are as follows:

- The root cause of the noise level inside the cabin is also predicted by the structural response of the cabin.
- Increasing the panel thickness could not decreased SPL in all conditions and it depends on frequency and position of specific point.
- With design modification in final results, overall reduction of 20 dB in sound pressure level is achieved.

References

1. Yenerer H, Stan AC, Sendur P, Basdogan I (2014) Vibro-acoustic analysis of a heavy duty truck cabin. Dyn Vib Contr Energy Fluids Eng Micro Nano Manuf 2:V002T07A025
2. Demirkan O, Basdogan I, Ozguven HN, Caliskan M (2014) Prediction of vibro-acoustic response of enclosed spaces by using structural modification techniques. In: Proceedings of ISMA2010, pp 4293–4306
3. Desai DA (2014) Simulation of vibro-acoustic performance of an automotive door hinge. World Congr Eng Comput Sci II:22–24
4. Wang Y, Zhang J, Liu X, Le V (2012) Interior acoustic field analysis of hydraulic excavator' s cabin based on BEM. Appl Mech Mater 141:323–327
5. Marzbanrad J, Beyg MA (2012) Vehicle cabin noise simulation due to high frequencies stimulation. Int J Automot Eng 2(2):117–123
6. Kirkegaard PH, Dickow KA, Anderson L, Sjostrom A (2012) Accuracy of dynamic and acoustic analysis of lightweight panel structures: a comparison of ABAQUS and ANSYS. In: Eleventh international conference on computational structures technology, paper 195
7. Dassault Systems Simulia Corporation., Providence, RI, USA: ABAQUS analysis user's manual, Version 6.14
8. Dammak K, Koubaa S, El Hami A, Walha L, Haddar M (2019) Numerical modelling of vibro-acoustic problem in presence of uncertainty: application to a vehicle cabin. Appl Acoust 144:113–123
9. Johannes E, Torsten S, Clarissa S, Joachim B, Tobias M (2009) Opportunities and limitations on vibro-acoustic design of vehicle structures by means of energy flow-based numerical simulation. In: International conference on noise and vibration engineering, Belgium, pp 4127–4142

Thermo-mechanical Analysis of Functionally Graded Material for Cylindrical Shell Subjected to Internal Pressure for Varying Volume Gradation

Vyom Shah, Darshita Shah, and Dhaval Shah

Abstract Functionally Graded Material (FGM) is a distinctive type of material in which properties vary steadily and smoothly across any direction which gives overall high performance in terms of mechanical and thermal aspects. Functionally graded material (FGM) application has a wide scope in modern tools and technology, which includes aerospace, pressure vessel of a nuclear reactor, High end cutting tools, etc. The main prominence of this paper is to present the structural mechanical and thermal analysis of cylindrical shells made up of ceramic and Aluminum used for fabrication of pressure vessels and reactors in heavy engineering applications. The FGM cylindrical is subjected to different boundary conditions and internal pressure. The material properties of FGM are pondered over the thickness utilizing power-law using MATLAB programming. The novel methodology for finite element analysis is applied for different volume gradations using MACROS in ANSYS APDL. The analysis outcomes for functionally graded materials are matched with a composite sandwich cylinder for the same boundary conditions. It was discovered that Von-Mises stress created in FGM is 22.23% less in comparison with sandwich structure, the stress in x, y, and z-direction is 22.23, 23.97, and 37.92% less and deflection is 18.11% less compared to sandwich cylindrical shell of aluminum and ceramic.

1 Introduction

The demand for special-purpose material has been increased with the advancement in technology which can fulfills and withstand rigorous thermo-mechanical load and meets product requirement. The conventional use of metals and alloy has its limitation whereas, in composites material, properties change suddenly which leads to

V. Shah · D. Shah (✉) · D. Shah
Mechanical Engineering Department, Institute of Technology, Nirma University, Ahmedabad, India
e-mail: darshita.shah@nirmauni.ac.in

the problem of delamination and stress concentration between interfaces. Functionally graded materials (FGMs) added much popularity as properties vary smoothly and continuously across the direction as well as property can be tailored according to the desired purpose. The FGM has an extra edge over conventional materials from automobiles to aviation and other industries due to its advantages over metals and composites. The cylindrical shells from FGM can be fabricated using powder metallurgy, laser cladding, and sintering process. Many researchers worked on the analysis of functionally graded material. Sarathchandra et al. [1] analyzed a functionally graded cylindrical shell made up of tungsten carbide and structural steel. Lin et al. [2] found the application of functionally graded material in civil structure to harvest solar energy more efficiently. Paulion et al. [3] explained an overview of functionally graded materials and their manufacturing processes like vapor decomposition technique, powder methodology, and solid freeform fabrication (SFF) method. The various mechanics model like a self-consistent model, Mori-Tanaka model, Tamura-Tomota-Ozawa (TTO) and Hashin-Shtrikman method for analytical analysis of functionally graded materials was also explained. Mohammad et al. [4] found the effect of parameters on asymmetric deformation for FG pressure vessels under thermo-mechanical loading conditions using numerical methods. Parida and Jena [5] described the overview of modeling, designing, and various manufacturing techniques used in the current stage of industrial application for FGM. Sondhi et al. [6] performed linear elastic analysis for variable thickness clamped rotating FGM disks of different profiles and found that disks of the variable profile have a significant reduction of stress compared to uniform profile. Bhandari and Purohit [7] analyzed the tailoring property of a functionally graded plate under transverse loading conditions. Shahzamanian et al. [8] found the application of functionally graded material for disc brake where heat is generated due to contact friction between brake pad and disc, Coulomb friction is taken as a source of heat. Bayat et al. [9] performed a thermo-mechanical analysis of a non-uniform functionally graded disc under a steady temperature field and observed, a disc with a concave thickness profile is the lightest and the one with a uniform profile is the heaviest in weight. Cooley [10] developed a patch to retrofit a cracked aircraft wash structure and reduce thermal-induced cracking. Wasim et al. [11] analyzed a rectangular plate made up of functionally graded material with the help of ANSYS parametric design language (APDL) in which material properties vary according to an exponential law. Ramu et al. [12] presented a modal analysis of functionally graded material plates to find its natural frequencies and different mode shapes and compared it with a plate of a homogeneous material. Hedia [13] used functionally graded material in dental implants and observed that the optimal material for the dental implant was functionally graded material of hydroxyapatite and titanium. Belhocine [14] analyzed a solid disc subjected to a thermal load for various material gradations during design and compared the result for the best optimum material.

In this research paper, a proper and user-friendly analysis methodology is defined for a cylindrical shell made of functionally graded materials. Conventionally various laws are directly used to calculate material properties of FGM after which an analysis is performed. The varying material properties across the thickness are calculated

according to power law using MATLAB programming. The steady-state thermal and static structural analysis is performed using ANSYS APDL for functionally graded material made up of aluminum and ceramic. The analysis results are compared with a sandwich cylinder of aluminum and ceramic. MACROS is defined for steady-state thermal and static structural analysis of cylindrical shells.

2 Methodology

2.1 Mathematical Modelling of FGM

There are many theories available to define the material properties of FGM through or across any direction. Theoretical laws, for example, exponential law, power law, vogit models, Mori Tanaka law, and so forth are accessible. The cylindrical shell is split into numerous layers of extremely thin thickness and presume that every layer will have a homogeneous property. The property of each layer is governed by one of the theoretical models. The exponential law and power law gives the best outcome in terms of calculating material property. Exponential law is utilized in analytical analysis while power law gives the best result for practical and simulations.

Materials property like density (ρ), modulus of elasticity (E), the coefficient of heat conduction (K), and coefficient of thermal expansion (α), etc. are defined by power-law using Eq. (1) for FGMs.

$$P(z) = (P_t - P_b)\left(\frac{z}{h} - 0.5\right)^N + P_b \tag{1}$$

where, $P_{(z)}$ = Property of material, P_t = Top plane material, P_b = Bottom plane material, N = Volume gradient, Z = Height at which material property is defined and h = Distance from neutral axis.

2.2 Variation of Modulus of Elasticity (E) and Thermal Conductivity (K)

Functionally graded material (FGM) because of its distinctive nature material properties vary steadily across any given direction and so it is required to define to code a program that can calculate material property at any point across the thickness. The MATLAB software is utilized for programming to decide material properties according to the power law. Program is prepared in user-friendly aspect in which the user has to input some governing parameters such as thickness, number of layers and for that volume gradation material properties are required to define, it will split

the material into predefined layers and property of each layer will be allocated at the center of that layer.

Figure 1 shows the FGM cylinder divided into n number of layers. Modulus of elasticity (E) and thermal conductivity (K) of functionally graded material with a thickness of 1 mm and 10 division is defined for different volume gradation (n). Figure 2 shows a variation of modulus of elasticity for $0.1 \leq n \leq 10$ and Fig. 3 shows a variation of thermal conductivity for $0.1 \leq n \leq 10$.

Fig. 1 FGM cylinder with ceramic at inner diameter and aluminium at an outer diameter
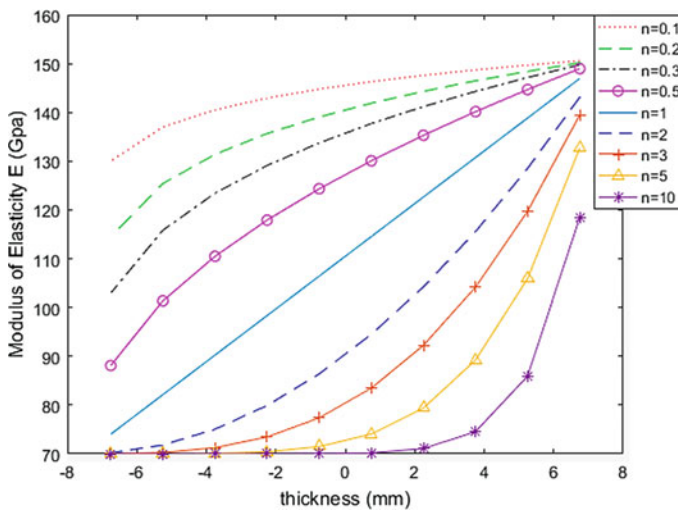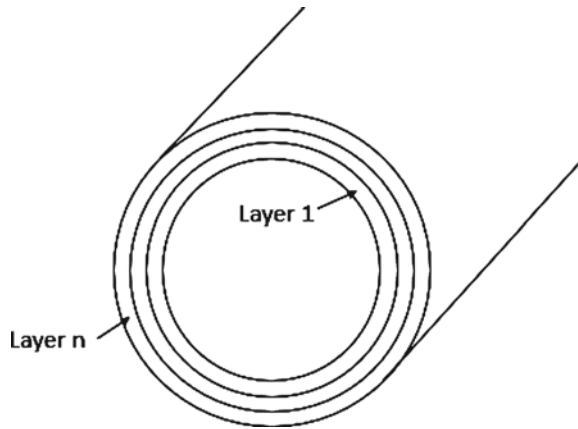
Fig. 2 Variation of modulus of elasticity for different volume gradation across thickness
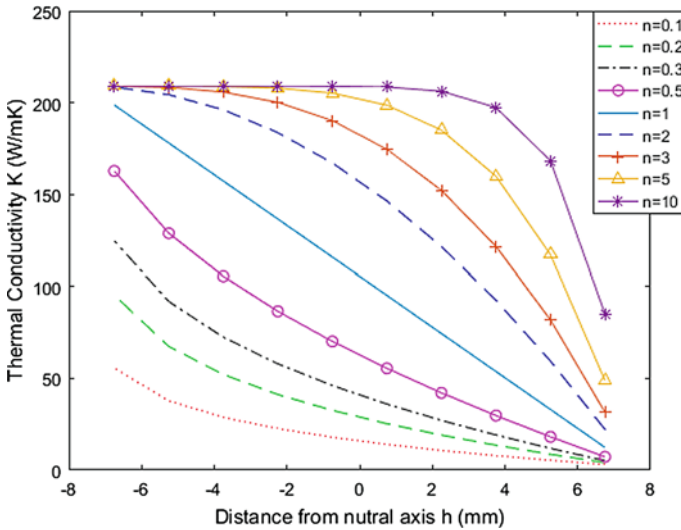
Fig. 3 Variation of thermal conductivity for different volume gradation across thickness

3 Finite Element Analysis

Finite element analysis of functionally graded cylindrical shells is performed. The first step is to model a functionally graded cylinder followed by meshing and applying boundary conditions.

3.1 Modeling of FGM Cylinder

A rectangular cylindrical shell of 1500 mm length, 1500 mm diameter, and thickness of 15 mm is considered for analysis purposes. The cylindrical shell is modeled in ANSYS using ACP tool system as shown in Fig. 4. The cylindrical shell is divided into 10 layers of equal thickness with aluminium at outer diameter and ceramic at the inner diameter. The meshing is generated using SHELL 181 element shown in Fig. 5. The static structural and steady-state thermal analysis is performed after applying proper boundary conditions.

3.2 Analysis Procedure

The cylinder is fixed at one edge and uniform pressure of 1.2 MPa is applied to at internal surface. After that proper boundary condition and loading condition analysis

Fig. 4 Layering of
functionally graded cylinder
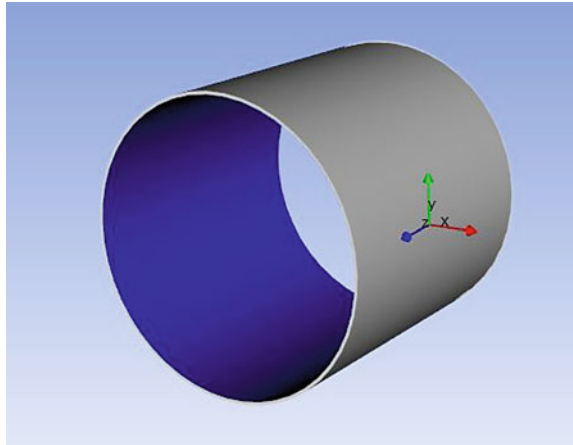
Fig. 5 Meshing of FGMs
cylinder
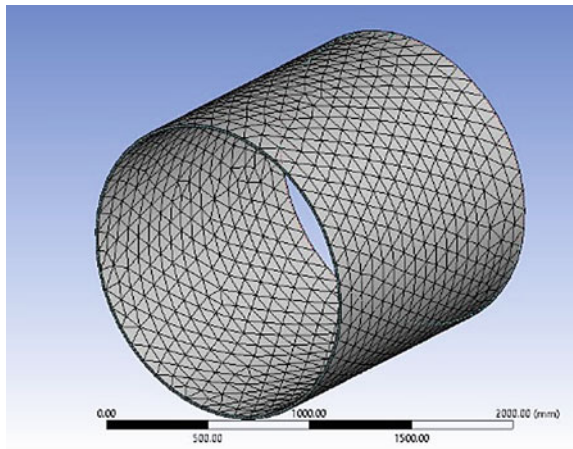
are performed. Various material properties are defined in Table 1. Flow chart approach
of methodology for the analysis of functionally graded material is illustrated in Fig. 6.

Table 1 Material properties of aluminium and ceramic

Material properties	Aluminium (6061-T6)	Ceramic (partially stabilized zirconia)
Modulus of elasticity (E) [MPa]	70×10^3	151×10^3
Density (ρ) [Kg/m^3]	2700	5700
Coefficient of thermal expansion (α) [°C^{-1}]	23×10^{-6}	10×10^{-6}
Thermal conductivity (K) [W/mK]	209	2
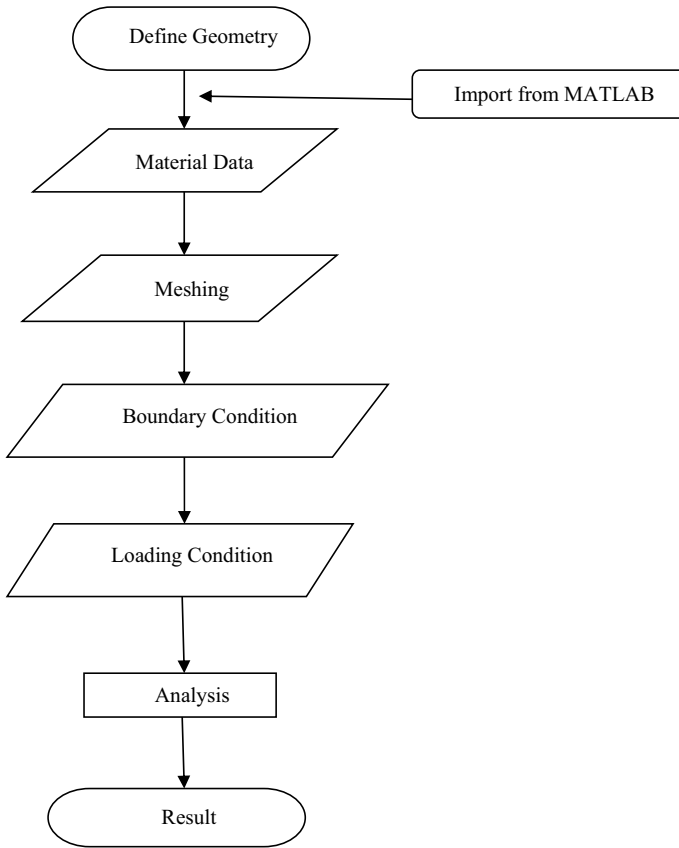
Fig. 6 Flow chart for methodology of analysis of functionally graded material

Figure 7 shows Von-Mises stress generated in cylinder for $n = 0.2$, Fig. 8 shows stress in deflection for $n = 0.2$, Fig. 9 shows stress in x-direction for $n = 0.2$ and Fig. 10 shows thermal flux for $n = 0.2$. Similarly analysis of cylindrical shell for different volume gradient ($n = 0.1, 0.2, 0.3, 0.5, 1, 2, 3, 5$ and 10) and for sandwich cylinder is performed.

4   Result and Discussion

4.1   Effect of Stresses with Respect to Volume Gradation

As volume gradation 'n' tends to move from 0.1 to 10, the percentage of constituents of aluminium in functionally graded cylindrical shells increases. Von-Mises stress

Fig. 7 Von-Mises for n = 0.2
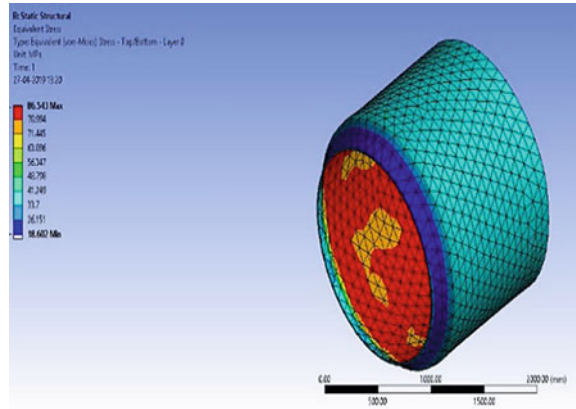
Fig. 8 Deflection for n=0.2
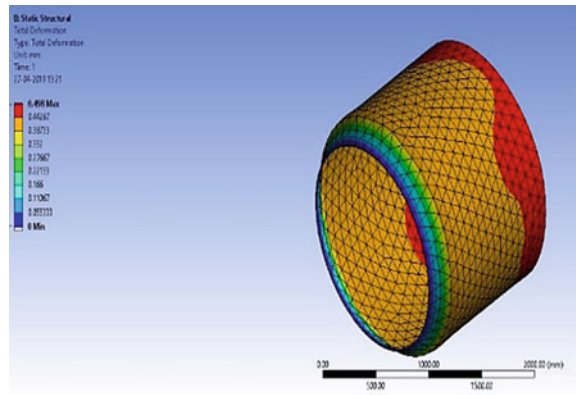
Fig. 9 Stress in X-direction for n = 0.2
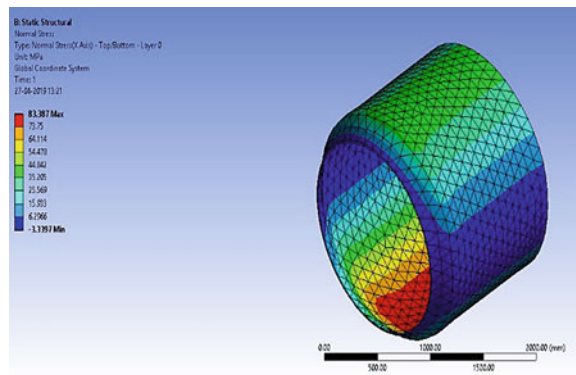
Fig. 10 Thermal Flux for n = 0.2
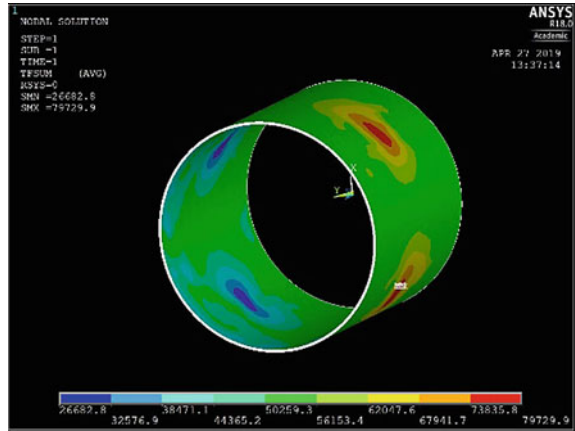
generated is minimum for the functionally graded shell for $n = 0.1$, which is 22.23% less than stress generated in aluminium/ceramic sandwich cylinder. Stress in X, Y, and Z direction for $n = 0.1$ in the functionally graded shell is 22.23, 23.97, and 37.92% less than that of stress generated in the sandwich shell. Figure 11 illustrates the comparison of various stress generated for different volume gradations and aluminium/ceramic sandwich cylinder. Various stresses generated in the shell for $n = 0.1$ are less it is because constituent of ceramic is dominant over aluminium so overall modulus of elasticity is more compared to $n = 10$.

Fig. 11 The comparison of various stress generated for different volume gradation and for aluminium/ceramic cylindrical shell
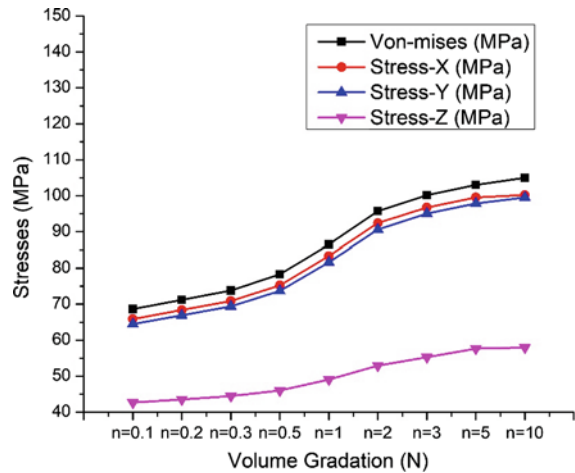
Fig. 12 Variation of thermal flux and deflection for various volume gradation
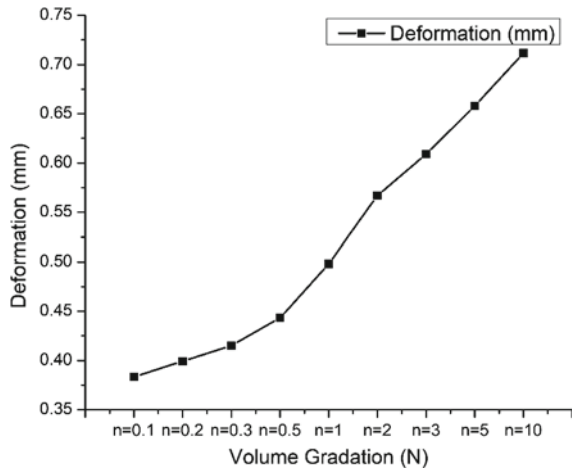
4.2 Effect of Deflection with Respect to Volume Gradation

Functionally graded cylindrical shell has minimum deflection for $n = 0.1$ which is 33% lower compared to deflection generated in a sandwich cylindrical shell. Thermal flux increases as volume gradation increases from 0.1 to 10. The constituent of aluminium for $n = 10$ is more compare to $n = 0.1$ which results in increasing thermal conductivity and thus thermal flux increases. Figure 12 illustrates the graphical representation of the variation of deflection and thermal flux.

4.3 Variation of Temperature for Different Volume Gradation

As volume gradation, 'n' tends to move from 0.1 to 10 temperature at the outer surface of the cylinder also increases. Figure 13 illustrate the variation of temperature at the outer surface of the cylinder for different volume gradation.

5 Conclusions

Functionally graded material has better thermal and mechanical performance than composites and alloys. The steady-state thermal and static structural analysis has been performed based on a novel methodology for FGM cylindrical shells.

- The von-Mises stress developed in FGM is 22.23% less than compared to the sandwich structure.

- Stress in *x, y,* and *z*-direction is 22.23, 23.97, and 37.92% less and deflection is 18.11% less than the sandwich structure of ceramic and aluminum.
- Thermal gradation across the thickness also increases as volume gradation increases. As volume gradation increases from 0.1 to 10 density of aluminum particles in FGM increases, so for better thermal performance, it is desired to have more density of ceramic. Material properties vary linearly when $n = 1$ which also gives better mechanical and thermal performance than the sandwich cylinder.

The different thermal and mechanical properties gradually change in the case of functionally graded materials. This FGM has a wide scope in modern tools and technology, which includes aerospace, pressure vessel of a nuclear reactor, high end cutting tools, etc. The thermo-mechanical analysis can be performed for different components for varying volume gradation.

References

1. Sarathchandra DT, Kanmani Subbu S, Venkaiah N (2018) Modeling and analysis of functionally graded cylindrical shell. Mater Today 5:8587–8595
2. Lin Q, Chen F, Yin H (2017) Experimental and theoretical investigation of the thermo-mechanical. Eng Struct 138:17–26
3. Paulino GH, Jin Z, Dodds RH, Sahu SK, Badgayan ND, RamaSreekanth PS (2017) Failure of functionally graded materials
4. Mohammad K, Fu K, Tang Y (2019) Multi-directional functionally graded material for enhancing durability of shell structure. Int J Press Vessel Pip
5. Parida S, Jena P (2019) An overview: different manufacturing technique used for fabrication of functionally graded material. Mater Today Proc 18:2942–2950
6. Sondhi L, Thawait A, Sanyal S, Bhowmick S (2019) Stress and deformation analysis of variable thickness clamped rotating disk of functionally graded orthotropic material. Mater Today: Proc 18:4431–4440

7. Bhandari M, Purohit K (2014) Static response of functionally graded material plate under transverse load for varying aspect ratio. Int J Metals
8. Shahzamanian M, Sahari B, Bayat M, Mustapha F, Ismarrubie ZN (2010) Finite element analysis of thermoelastic contact problem in functionally. Compos Struct 92:1591–1602
9. Bayat M, Saleem M, Sahari BB, Hamouda AMS, Mahdi E (2009) Mechanical and thermal stresses in a functionally graded rotating. Int J Press Vessels Pip 86:357–372
10. Cooley WG (2005) Application of functionally graded materials in aircraft. Ohio, Air Force Institute of Technology
11. Wasim, M. K., Helal, D. Y. Shi, Analysis Of Functionally Graded Rectangular Plate by ANSYS, Key Engineering Materials, 572, 505–508 (2013)
12. Ramu I, Mohanty SC (2014) Modal analysis of functionally graded material plates using finite element. Proced Mater Sci 6:460–467
13. Hedia HS, Mahmoud N (2004) Design optimization of functionally graded. Bio-Med Mater Eng 14:133–143
14. Belhocine A, Bouchetara M (2012) Thermal analysis of a solid brake disc. Appl Therm Eng 32:59–67

Development of Tractor Seat Suspension System for Improving the Ride Comfort

Deep Shukla, Saurabh Modi, and Reena Trivedi (iD)

Abstract In the present study, the vibration of the driver's seat of agricultural tractors is investigated. Considering three different weight of operators and only seat suspension system of the tractor, simulation is carried out. The suspension system is to be developed for improving the ride comfort for the tractor operator. The damper is designed for the suspension system of the seat for increasing the ride comfort. After setting up the model in finite element analysis simulation, joints were given. The bump profile was created and exported in simulation software for calculating the time of tractor to run over the bump. The time calculated is used in giving the bump-like motion to the seat. Three different weights are considered, a spring preload needs to be adjusted according to the weight. A methodology is developed to reduce the acceleration of the seat when it travels over the bump. It is observed during the simulation that the bottoming was observed when the seat travels over the bump. An iterative method is carried out for designing the damper for different weight of operators. A damper is designed for reducing the acceleration and dynamic force of the operator seat.

1 Introduction

Agricultural tractors have contributed a great amount of efficiency in agriculture operations making them easy and many times eliminating the human labour. But on the other hand, tractor operators are exposed to many harmful situations which influence many negative health effects on tractor drivers [1]. The seat dynamics decide the postures and create a specific pattern for a longer period in that same position. The seat is one of the components affecting the driver's health and causing discomfort. The exposure levels can be controlled statically and dynamically. The static conditions include foam and support provided by the seat, type and geometry of the cushion, posture and orientation of the operator and location from the controller options, amount of time spent and occupant anthropometry.

D. Shukla · S. Modi · R. Trivedi (✉)
Nirma University, Ahmedabad, Gujarat 382481, India
e-mail: reena.trivedi@nirmauni.ac.in

Secondly, considering the dynamic conditions, the influence comes from the terrain-like agricultural field (working conditions) and tractor system (engine) [2, 3]. The high level of vibrations that arise from the terrain or engine is transferred from cabin floor to tractor operator's seat and to whole body of operator.

Vibrations experienced by the operator are in vulnerable range of 0.5–5 Hz. The frequency generated by the uneven roads and agricultural terrain is low about 5–7 Hz and the frequency generated by the engine system is high. It easy to overcome the frequency of high range rather than the frequency of low range-like uneven road and agricultural terrain [5–7].

Low frequency vibrations with high amplitude must be controlled for keeping the health of the operator safe and maintain the comfort level. This is the main reason that the tractor operators are subjected to low back pain and many other health issues [8]. For maintaining the comfort level and keeping the operator's health out of harmful effects, some techniques are developed by the engineers and researchers, namely passive system, semi-active system and active system.

Passive system: It consists of mechanical equipment like spring, damper or rubber pads for isolating the acceleration developed from the working conditions.

Semi-active system: It consists of springs, rubber pads and consists of special type of damper, like magneto-rheological damper.

Active system: This system is used to reduce the vibration with help of vibration sensors, electric circuits, hydraulic components, electric motors, etc.

2 Literature Review

Farming is a physically tough occupation and farmworkers work at potential risk of musculoskeletal disorders such as osteoarthritis (OA) of the hip and knee, low back pain (LBP), neck and upper limb complaints and hand-arm vibration syndrome (HAVS). Farmers more often have knee OA and LBP than workers in occupations with fewer physical demands. Tractor drivers (as shown in Fig. 1) seem to have more LBP [2]. In many occupations, workers are exposed to oscillatory motions (vibration). Vibration of powered hand-held tools and workpieces (hand transmitted vibration) and the vibration of seats and floor supporting the body (whole body vibration) can cause discomfort, interference with activities, injury and disease. For hand transmitted vibration, the daily exposure limit value standardized to an eight hours reference period shall be 5 m/s^2 r.m.s. The daily exposure action value standardized to an eight hours reference period shall be 2.5 m/s^2 r.m.s. For whole body vibration, the daily exposure limit value standardized to an eight hours reference period shall be 1.15 m/s^2 r.m.s. [1].

Fig. 1 Position of driver on
tractor seat [4]
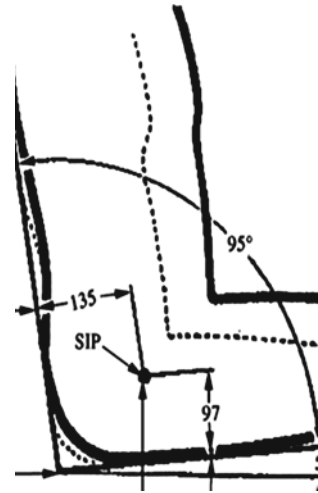
3   Objectives

The design of tractors used in developing countries is not comfortable for the tractor
operators. Due to economic reasons of the tractor operators, the tractor manufacturers
do not install in-built suspension system to match the comfort level of the tractor
operators. To increase the comfort level of the tractor operators, a suspension system
is developed or modified. Three operators of different weight were considered mainly
45, 68 and 100 kg. Separate 3 kg of seat is also considered.

- To design the damper which provides the suitable comfort to the tractor operator
  with iterative method of simulation.
- To reduce the vibration and jerks when tractor crosses the bump.
- To reduce the dynamic displacement of the seat.

4   Methodology

The following methodology is followed in order to design the seat.

4.1   Model Setup

Softwares used for the project are Altair HyperMesh and MSC ADAMS. CAD model
provided was imported in Altair HyperMesh and then was imported to MSC ADAMS.
The joints were given to the model. After removing the redundancies, model was
simulated. The operator (driver) was not modelled, but a point mass (lumped mass)
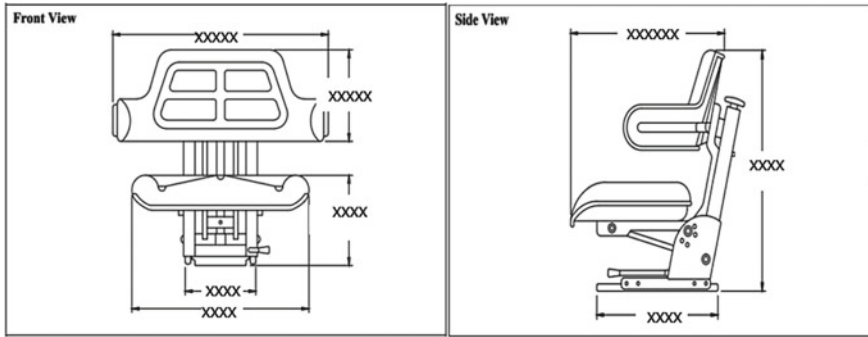
Fig. 2 Schematic diagram of seat [3]

was introduced of the same weight as operator. The schematic diagram of the seat suspension system is shown in Fig. 2.

4.2 Creating Bump Profile

The bump profile was created according to the standards provided. The height of bump is 55 mm, length of 345 mm and radius of 243.82 mm were created (Fig. 3).

Creating bump profile, an extra road (straight line) was also created of 175 mm to ensure the correct motion, when driver sits on the seat and then it travels over bump.

After the whole bump profile was created as shown in Fig. 4, an object on the profile was given translation motion. The motion was optimized and verified, and the time to run over the bump was estimated.

This time data was used as an input parameter to create a bump-like motion on the seat as given in Table 1. Data was used as a spline curve while giving motion
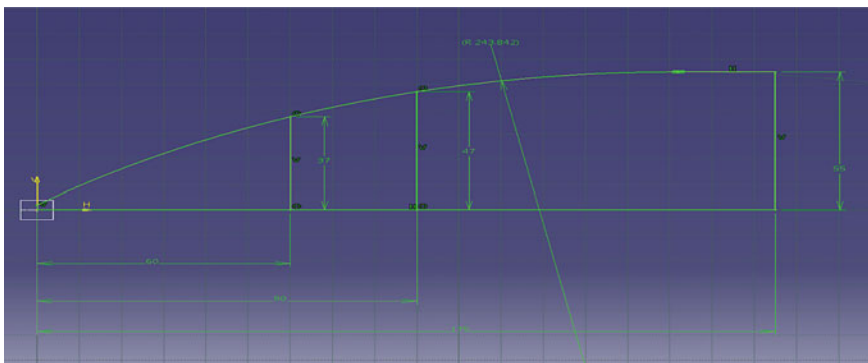
Fig. 3 Dimensions of bump profile
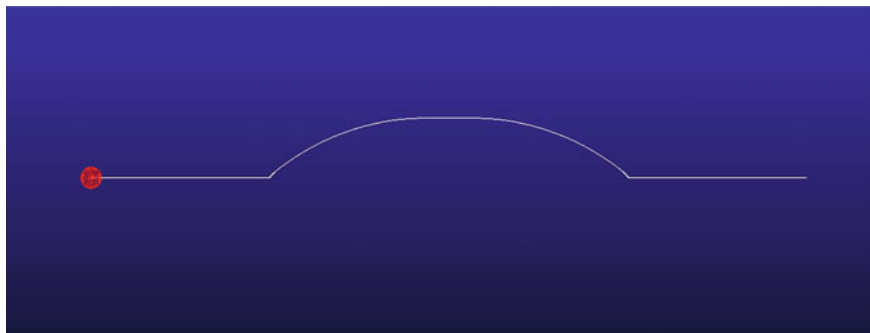
Fig. 4 Bump profile created in software

Table 1 Details of bump

Object run over	Time taken (s)
Only road	0.063
Only bump	0.13606
Total bump and road	0.26206

to the seat. Vehicle speed is not considered in MBD because only seat is considered and not whole vehicle.

4.3 Details of Spring

The model was provided with the spring details as mentioned in Table 2.

Table 2 Details of spring

Wire diameter	6 mm
Coil diameter	20 mm
Active coils	17
Stiffness	95.7 N/mm
Free length	167 mm
Installed length	167.8 mm
Preload	371.1 N
Initial tension	295.1 N

4.4 Adjusting Spring Preload

In developing countries, the suspension system for seat is provided only with springs used to attenuate the vibration. The suspension system with only springs is provided with the adjustable spring tensioner as shown in Fig. 5. By rotating the adjustable knob, the preload in the spring can be adjusted according to the weight of the operator (Fig. 6). The limit of the spring tensioner knob is from 45 to 100 kg.

Location of the adjustable knob for different operators. The weight of seat is added with weight of each operator, while simulating the model. After implementing the above steps, simulations were carried out to reduce the seat acceleration and dynamic displacement by introducing the damper.
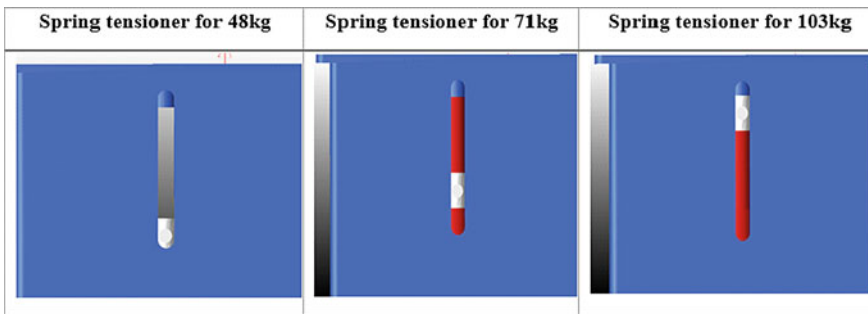
Fig. 5 Adjustable Spring preload

Fig. 6 Location of knob with respect to different weights in ADAMS

5 Results and Discussion

Based on the iterations carried out in the software, the following results were obtained as shown in Fig. 7. First, the simulations were carried out for 45 kg of operator and 3 kg of seat. As the damper was to be designed with iterative method, initially, the value of damper was kept zero and then gradually it was increased until the optimum value was obtained. Similarly, the same value of damping co-efficient was obtained for 68 and 100 kg weights of operators. The properties of spring were kept constant while simulating the different weight of operators. The optimum results obtained are,

It was observed that for every three operators, as the damping co-efficient was increased, the acceleration was decreased. Higher negative acceleration is observed in 100 kg weight of operator. It was observed during the simulation that the bottoming effect was taking place due to the colliding of the sliding pin within the slot as shown in Fig. 8. Because of the colliding of the pin, the jerks and bottoming effects are observed and are magnified in the seat suspension system which can be harmful to

For 45kg Damping coefficient – 1.5Ns/m Max acceleration – 1.25E4mm/s² Min acceleration – 1.2E4 mm/s²	
For 68kg Damping coefficient – 1.75 Ns/m Max acceleration – 1.9E4 mm/s² Min acceleration – 1.2E4 mm/s²	
For 100kg Damping coefficient – 1.95 Ns/m Max acceleration – 0.8965E4 mm/s² Min acceleration – 6.48E4 mm/s²	
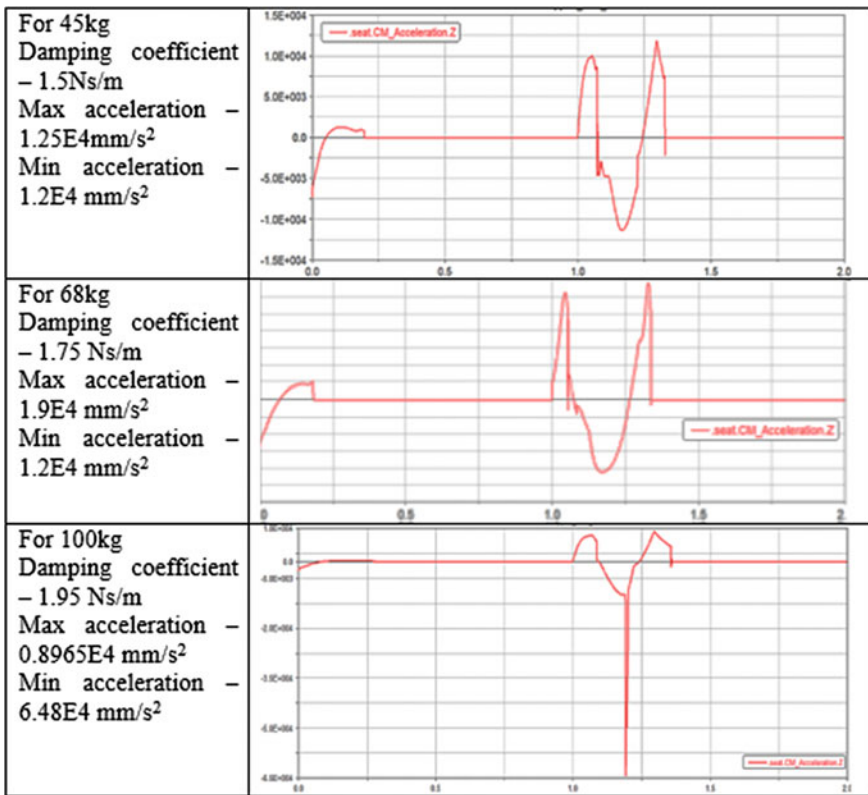
Fig. 7 Damping co-efficient and acceleration for different weight of operator
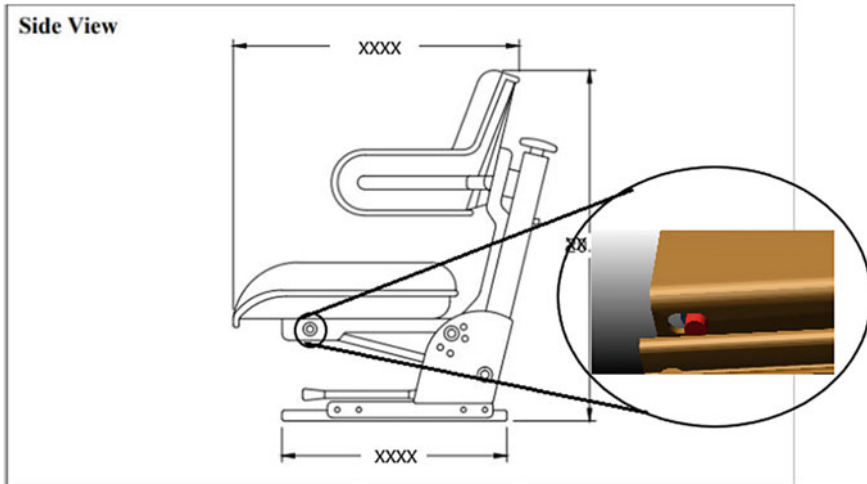
Fig. 8 Location of pin and slot in seat suspension system

the operator's health. The solution of this bottoming problem is still under further study.

6   Conclusion

In this paper, the design of tractor seat suspension system for improving the ride comfort is performed successfully. Three different test cases based on different weight of driver are performed. Acceleration for different weight of driver is studied for different co-efficient of damping and the suspension system has been improved to bring the human comfort.

References

1. Griffin MJ (2004) Minimum health and safety requirements for workers exposed to hand-transmitted vibration and whole-body vibration in the European Union. Occup Environ Med 61(5):387–397
2. Walker-Bone K, Palme KT (2002) Musculoskeletal disorders in farmers and farm workers (2002). Occup Med (Lond). 52(8):441–450
3. Mandapuram S, Rakheja S, Boileau P-E et al (2015) Energy absorption of seated body exposed to single and three-axis whole body vibration. J Low Freq Noise Vib Active Control 34:21–38
4. Mehta CR, Tewari VK (2000) Seating discomfort for tractor operators—a critical review. Int J Industr Ergon 25:661–674
5. Bovenzi M, Betta A (1994) Low-back disorders in agricultural tractor drivers exposed to whole-body vibration and postural stress. Appl Ergon 25(231):241

6. Fairley TE (1995) Predicting the discomfort caused by tractor vibration. Ergon 38:2091–2106
7. Scarlett AJ, Price JS, Stayner RM (2007) Whole-body vibration: evaluation of emission and exposure levels arising from agricultural tractors. J Terra Mech 44:65–73
8. Kumar A, Mahajan P, Mohan D, Varghese M Tractor vibration severity and driver health: a study from rural India. J Agric Engng Res https://doi.org/10.1006/jaer.2001.0755

Modelling and Real-Time Simulation for Hot Coil Marking

Nirav Thakkar and Shruti Bhatt

Abstract In manufacturing industry, final product marking is very important task for identification. There are various marking technologies available in industry like laser marking and robotic marking system with various end effectors according to relevant application. In steel industries, coils are made from hot rolling process and during manufacturing temperature of coils are very high. Presently, in steel industry for coil identification, they are using robotic marking machine with dot matrix and nozzle system. Using this system they are marking information of coil like width, thickness, manufacturing date, etc. In robotic marking, machine has monopoly in marking industry, but at the same time, high capital investment and maintenance cost are involved. In steel industry during down time phase, operators need to mark manually on hot coil which is very tiresome and unsafe job. So the overall objective of project is to configure new hot coil marking machine with less complex parts and cost compared to robotic marking machine. To achieve above objective, we adopted modified nozzle system technology and three-axis movement for marking. In this modified system, we used disc template, solenoid valve, stepper motor and pump for nozzle marking. The design has been modified using Creo Parametric 3.0 to control three-axis motion of stepper motor, opening and closing of solenoid valve and rotation of disc template, and simulation has been developed using MATLAB software. This simulation will show running time of our marking machine and also the graphs of three axes. Final working prototype has been developed with above reference. This modified hot coil marking system will substitute present marking machine with less cost and maintenance. It will be helpful.

Keywords Steel coil marking · Nozzle system · Modelling and control simulation

N. Thakkar · S. Bhatt (✉)
Department of Mechanical Engineering, Nirma University, Ahmedabad, India
e-mail: shruti.mehta@nirmauni.ac.in

1 Introduction

1.1 Background

In compact strip production (CSP) mill, hot coil is made by rolling process. Slab is cut to the pre-decided length and this hot slab is directly fed to the tunnel furnace (of length 185–260 m). In tunnel furnace slab, temperature is equalized across the cross-section. Temperature of slab at entry of tunnel furnace is about 950 °C and it is heated to a temp of about 1050 °C (Fig. 1). Hot slab from tunnel furnace is passed through high pressure descaler and then directly to mill for making hot-rolled coil. CSP Mill is equipped with automatic gauge control (AGC), hydraulic loopers for F1-F4, differential tension looper for F5, continuously variable crown, work roll bending and shifting to get good quality of strip profile and flatness. After F6, strip passes through automatically controlled laminar cooling for getting good mechanical properties. This strip is coiled and transported to coil yard by pallet type conveyor. The thin slab comes out of the caster goes to the straightening unit, thereby goes to the pendulum shear where it is cut according to the required length moving towards the tunnel furnace where a uniform temp is maintained throughout the slab, then it goes to mill area through entry roller table. A hydraulic shear is provided before the descaler for the need of any emergency cutting, then moving towards descaler to remove the oxide layer, then goes to the finishing mill (F1-F7) through entry side guides, and a profile gauge is provided before F1. The thickness of the coil is reduced as per the requirement and pass schedule calculations in further stands. A complete contour and profile of the strip are found by the gauge at the end of F7, and the run out roller table at the end of mill stands is used to transfer the roll strip from mill to the coiler, and at the same time, the strip is cooled through laminar cooling to get the required metallurgical properties. The entry side guide at the end of the run out roller table guides the strip laterally and through the pinch roll unit the strip head is guided
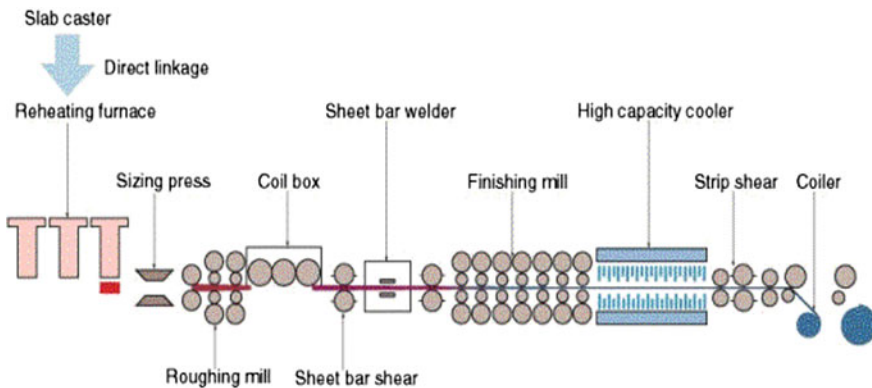
Fig. 1 Schematic diagram of the hot-rolled plates in the CSP process [1]

to the down coiler on to the mandrel where the wrapper rolls help in maintaining the gap adjustment. Then, the coil is withdrawn from the coiler and moved to the coil yard [1].

1.2 Process Objective

The objective of this process is to design and simulate hot coil marking machine for steel plant which will mark date, weight, grade, width and thickness on hot-rolled coil. To achieve above objective, conceptual methodology has been formed considering the following aspect (1) design mechanism which will provide the motion to nozzle for letter printing on coil, (2) nozzle selection and providing proper flow of ink with predefined position for date, grade marking, etc. [2]. Mechanism of marking machine includes design and selection of various parts which provides three-axis motion and one disc template in which characters and letters are embossed to mark on coil and to achieve proper flow angle stepper motor, solenoid valve, pump, etc., are selected and fitted with disc template to execute marking on coil. In further step, to simulate the entire process to control disc rotation with stepper motor, pump flow, nozzle angle and solenoid valve opening and closing to get accurate marking control programme has been developed which will interfaced conceptual model [3].

2 Process Methodology

2.1 Component Modelling and Selection

To modelled mechanism of hot coil marking machines following points are considered in this section, (1) volume of paint to mark one letter, (2) nozzle spray angle requirement according to specification of letter size, (3) pump flow rate of ink with given pressure range, (4) total torque calculation to select stepper motor to impart motion to assembly [4]. Now as shown in Table 1 to analyses volume of paint required for one letter marking and per minute consumption of ink following criteria has been specified and calculated.

To consider nozzle requirement, according to specified height and width the diagonal of one letter will be 82.5 mm. So we have to choose a nozzle that covers one

Table 1 One letter marking specification

S. No.	Height (mm)	Width (mm)	Thickness of ink (μ)	Area (mm^2)	Volume (mm^3)	Consumption of paint
One letter	66	50	400	5384.560	2153.82	2.154×10^{-3} litre per 0.5 s

letter of 82.5 mm diameter circle. As shown in Fig. 2, the following key aspect has been considered for the selection of nozzle with ink spray angle. The spray angle is the opening angle which the nozzle jet of droplets forms at the moment when it leaves the nozzle orifice, and it is one of the fundamental parameters for the choice of a given nozzle. In fact, the amplitude of the spray angle determines in connection with the distance between the nozzle orifice and the target to be covered, and the spray coverage and the density of liquid sprayed with respect to the cover area. It is important to note that, because of several factors like gravity forces and aerodynamic drag, the spray angle value cannot be maintained, but in a limited distance, normally up to 300 mm from the orifice. For air-assisted atomizers, it is improper to use the term spray angle, since no precise value can be measured but considering our marking requirement according to Eq. (1) to calculate theoretical spray coverage (TSC), where (1) ASC = actual spray coverage, (2) TSC = theoretical spray coverage, (3) ASA = actual spray angle, (4) TSA = theoretical spray angle is θ (5) L = spray distances.

$$TSC = 2L \tan (\theta/2) \tag{1}$$

So here from nozzle catalogue, we have selected a convergence nozzle with the following specification (1) spray angle of 90°, (2) theoretical spray coverage is 100 mm and (3) distance from nozzle orifice is 50 mm. Now, to control flow, rate per minute pump has been selected according to the following specification from catalogue as mention in Table 2. Pump power has been calculated by considering specific gravity of ink is 1.4 and efficiency of pump at 1 lpm is 60%.

Now to impart the motion through lead screw on overall assembly to mark three rows with date, grade, etc., on hot coil following characteristics has been considered
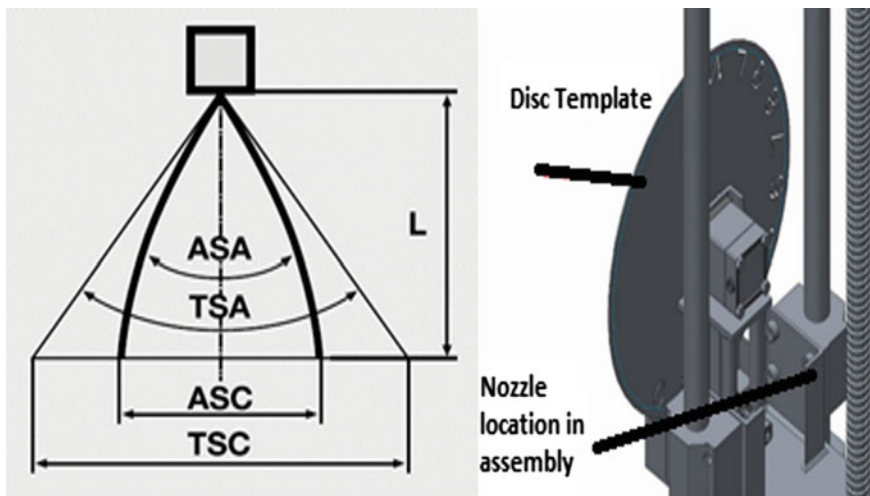
Fig. 2 Spray angle and nozzle mounting

Table 2 Pump selection criteria according to nozzle specification

S. No.	Pump pressure range	Standard nozzle pressure	Flow rate from nozzle	Flow rate from pump	Pump power
1	0–69 bar	5 bar	0.4698 lpm	1.050 lpm	0.568 KW

as shown in Table 3 and shown in Fig. 3. Now after modelling all the components in assembly, the next most important function of assembly is to mark required data in sequence on coil so the simulation of all components has been covered in subsequent topic.

Table 3 Lead screw and stepper motor specification

S. No.	Overall weight of assembly	Material	Nominal screw	Lead	Root diameter	Efficiency	Torque (lead screw nut)	Motor torque
1	60 kg	SS303	12.7 mm	5 mm	9.27 mm	62%	0.755 N-m	2.3 N-m with 1.8° step angle
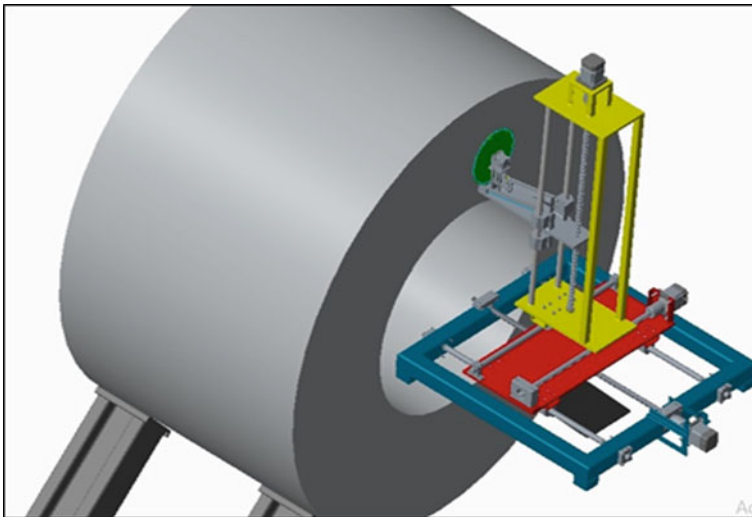
Fig. 3 Final assembly for hot coil marking machine

3 Process Simulation

3.1 Determination of Dimensions and Generation of Data

Now as shown in Fig. 4, the marking range of coil is mention with all reference dimension. First row of coil marking is referred to month and year (e.g. 09-2014), second row of coil marking is refer to width and thickness of coil (e.g. 1200 2–20 mm) and third row of coil marking is refer to grade and weight of coil (e.g. 18–25 ton). To define home position the centre of the first letter should be the centre of nozzle convergence point. So from Fig. 3, we can get the relative position for Y and Z-axis [4]. The X-axis is relative to the width of the coil and the relative home position required in the X-axis will vary accordingly. The nozzle convergence point should be 50 mm away for the required size of letter. The relative travel for the centre of the first letter from the home position is 269.258 mm. After deduction of 50 mm, it will be 219.258 mm, so from this, we get to know the relative travel required for x, y and z which is

$$X = 500 - (\text{Width of the coil}/2) + 219.258 \tag{2}$$

$$Y = (\text{Outer diameter} - 1600 + 241.239) \tag{3}$$

Now, in the next step, we need to give inputs such as all the letters which we need to mark on coil, outer diameter of coil and thickness of the coil to the GUI generated in MATLAB [5, 6]. Now, to generate simulation, we need to define velocity of
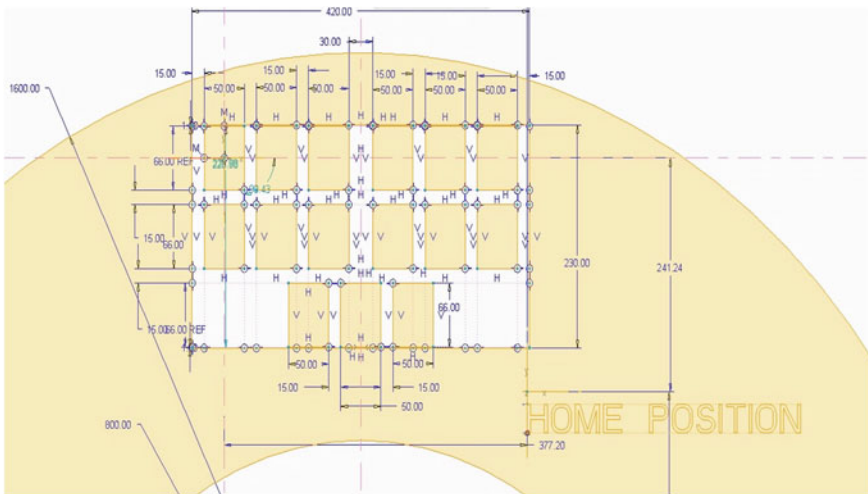
Fig. 4 Dimension of marking range
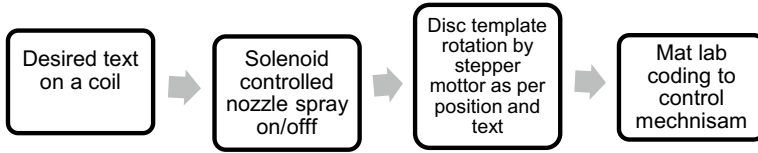
Fig. 5 Process simulation to mark on hot coil
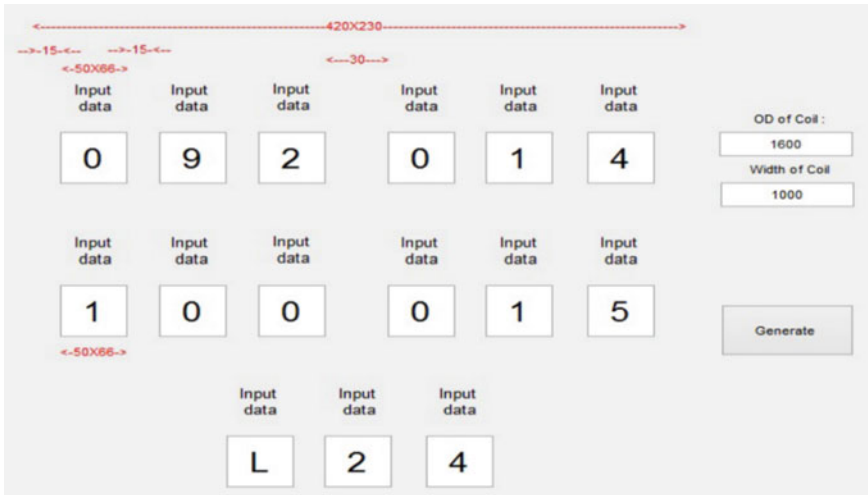
Fig. 6 GUI input data for coil marking row wise

motor relative to time and after the execution of these data result the maximum time required for the full simulation is 115 s which is divided into the intervals of 0.01 s to represent the motion with accurate results. Figures 5 and 6 show the generated graphs for desired position of the nozzle convergence point, opening time for solenoid valve and angular position of disc template (Fig. 7). To simulate all the marking positions accurately, according to the varying requirements and varying inputs, there are 5 motors used for representation of the motion 3 velocity motors for x, y, z-axis motion of the nozzle and one positional motor for disc template and one positional motor for solenoid actuation (Fig. 8).

4 Conclusion

This new conceptual model has less complex parts and easy to maintain through marking process. In this concept, all the selected parts design is considered with all aspects of coils dimension to mark identification code row wise. The movement
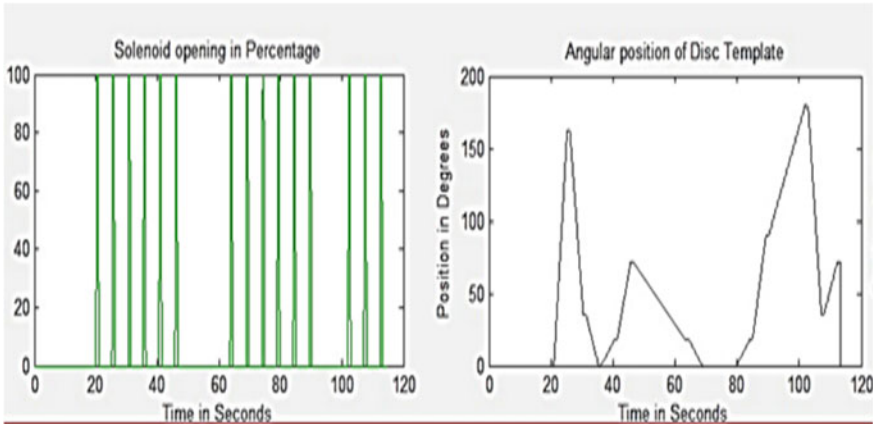
Fig. 7 Position of two motors according to time
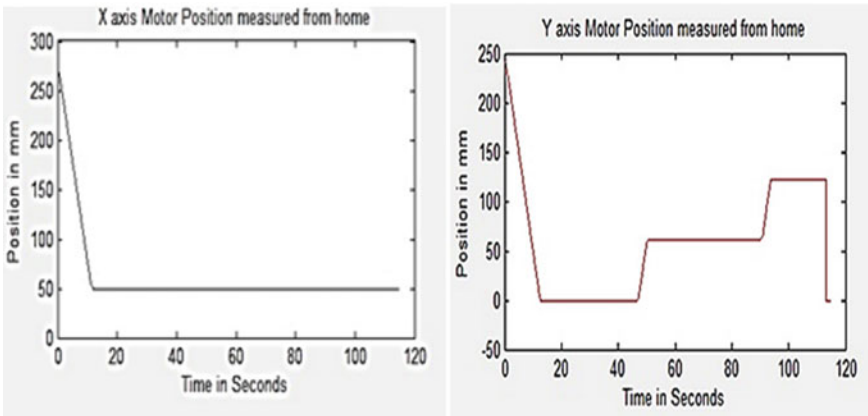
Fig. 8 Solenoid opening and angular position of disc template to mark letter according to position

accuracy of all the motors has been checked through simulation to mark exact identi-
fication data row wise and even total time duration also notified to mark each data on
coil can be calculated as 115 s through simulation. Even ink flow rate through nozzle
has been checked and on which area spray coverage should be there has also been
calculated according to coil specification. Overall, this conceptual design and simu-
lation will be helpful to mark on hot coil for small industry where robotic marking is
quiet costly, heavy maintenance aspect and considering worker's safety during down
time of this complex and costly machine.

References

1. Roberts WL (1983) Hot rolling of steel. CRC Press
2. Park, S Lee J (2006) Development of real-time character recognition system for the steel-iron plant. In: International conference on hybrid information technology
3. Altintas A (2009) A graphical user interface for programming stepper motor used at different kinds of applications. Mathem Comput Appl 14(2):139–146
4. Liu D (2010) Simulation and character recognition for plate marking machine. In: 2nd international conference on signal processing systems
5. Liu D (2010) Marking process analyse in plate marking machine. In: Proceedings of the ninth international conference on machine learning and cybernetics, Qingdao, 11–14 July 2010
6. Kiss I, Wessely E, Maslan E, Hrabcak M (2012) Contribution to the reliability and security of identification of hot coils in the production process. In: Annals of DM for 2012 and proceedings of the 23rd international DAAAM symposium, vol 23(1)

Performance Evaluation of Vortex Generator for Drag Reduction in Automobiles

Akhila Rupesh, Maddireddy Greeshma, and Sabiha Parveen

Abstract The world is facing a serious challenge of global warming. The scientist estimates 1.5 °C rise in global temperature till 2025 due to the pollution in various sectors. The automobiles, the key component of the world's growth, account nearly 45–75% of the total pollution and have a major scope of transformation. This problem can be solved by using alternative/renewable fuels or using the aerodynamic principles. In this article, 'vortex generators,' an application of aerodynamic solutions is studied using computational method for drag reduction. Vortex generator is a very tiny and cost-effective instrument has shown its applications in the airplane performance and the Formula 1 front wing. Vortex generators reduce the air resistance of the car by delaying the flow separation at the rear of the car. It uses the momentum transfer principle to delay the flow separation. It enables the boundary layer to overcome the skin resistance. The vortex generators are available in various shapes, among them six major types are tested in this study. An Audi A4 model is used for the testing purposes and modeled in the SOLIDWORKS software. The A4 is a 5 seater Sedan and has a length of 4726 mm, width of 1842 mm and a wheelbase of 2820 mm. The three types of vortex generators are applied on the model and tested in the computational fluid dynamics model using ANSYS workbench module. The computational results are compared with the original car at various speed and the iterations of the heights. The results are compared in terms of drag, lift, velocity distribution, pressure distribution and streamline visualization. The vortex generator improves the aerodynamic performance of the car with the 10% of the drag reduction. This will improve the fuel efficiency of the sedan automobiles and reduction in the CO_2 emission without adding any significant cost in manufacturing.

A. Rupesh (✉)
Mangalore Institute of Technology and Engineering, Moodbidri, Karnataka, India
e-mail: akhilarupesh56@gmail.com

M. Greeshma
Lovely Professional University, Punjab, India
e-mail: greeshmareddy23@gmail.com

S. Parveen
Manav Rachna International Institute of Research and Studies, Faridabad, India
e-mail: sabihaparveen1711@gmail.com

1   Introduction

The invention of the engine and the evolution of the automobiles are termed as the
greatest revolutions in the history of mankind. It enables fast transportations and
brought the world closer to each other. The automobiles are the greatest contributor
of today's economic activity and prosperity of the world. Automobiles have played
a key role in improving the standards of human lifestyle.

The coin has two sides. The automobiles also come with the major drawback of
hazardous pollution due to tailpipe emission. In India, the automobiles contribute
nearly to 45–75% of the overall air pollution [1]. The world remains ignorant about
the dangerous effect of the tailpipe emission, but at the end of the twentieth century,
it starts to show its adverse effects. The major developed cities facing smoke problem
affecting the visibility and human health of the citizen. The world remains eye
opening after the discovery of 'ozone layer depletion.'

Global warming is putting questions on the existence of the island countries and
health of citizens. The scientist believes the unpredictable behavior of nature and
severe droughts in many parts of the world and just a trailer and picture will be
awful if proper and stricter actions are not taken. This brings global lawmaker to the
table and to develop policies like 'Paris Accord'. These problems concern with an
automobile can be solved by hybrid and electric car, low emission alternating fuels
and aerodynamic solutions.

This paper deals with the aerodynamic solution for the reduction of the emissions.

2   Methodology

The methodology is based on the study of 'vortex generators,' their various types
and its effectiveness in the drag reduction. This is achieved by delaying the flow
separations at the rear of the sedan automobile. The flow separation is delayed by
tripping or the energizing the boundary layer developed around the profile of the
automobile. The delay in the flow separation helps to reduce the low-pressure area
which develops at the rear end [2, 3]. The low-pressure area is the major reason
for the drag generation. The vortex generators energize the boundary layer at the
possible position of the flow separation by momentum transfer phenomenon [4].
This phenomenon makes boundary layer capable of overcoming the surface friction
and hence delays the flow separations.

The vortex generators are very smart and cost-effective aerodynamic tool which
helps to reduce the drag of the automobile and also helps to increase the downforce
without adding any drag [5]. The aviation sector and the pinnacle of automobile

research 'Formula 1' also using the application of vortex generators for the same outputs. The vortex generator allows efficient use of engine power and thus it is a beneficial solution to the instability in the Middle East and fuel prices are rising. The use of vortex generator is also beneficial for solar/electric cars as it allows the efficient use of battery energy and helps to improve the range without increasing the battery capacity.

2.1 Phenomenon of Flow Separation

When air comes in contact with the sedan car, it develops a boundary layer across the contour of the car. The air in contact with car experienced surface resistance which makes the velocity of air zero known as stagnation point. The air flow follows the contour of the car but experiences the difficulty to remains in contact with the car. This is because the increase in the surface resistance and the pressure at the rear of the car where geometry changes suddenly [6]. This results in flow separation at the rear of the car. The flow separation causes vortices at the rear of the car which develops a low-pressure area. This low-pressure area is largest constitute of a drag force and needs to minimize to reduce the drag by delaying flow separation [7, 8]. The vortex generators, a tiny device helps to delay the flow separations by creating turbulence at the surface level. This causes a phenomenon called 'momentum transfer' which adds up extra energy in the surface layer and helps to overcome the surface resistance, and thus delay the flow separation. This principle of delaying flow separation can be also seen on the potholes on the golf ball.

To check the effectiveness of vortex generator for the aerodynamic benefits like reduction in drag and increase in downforce, an Audi A4 model is selected. The modeling of the vehicle is done in the SOLIDWORKS software as shown in Fig. 1.

To find the dimension of the vortex generator initially, the Reynolds number for the vehicle at 30 m/s is calculated. Reynolds number, $\text{Re} = v \times \frac{L}{\mu} = 9502358$ where, V = velocity of the car = 30 m/s; L = length at point of separation = 3.5 m and μ = kinematic viscosity = 1.511×10^{-5}. This followed by calculating height of
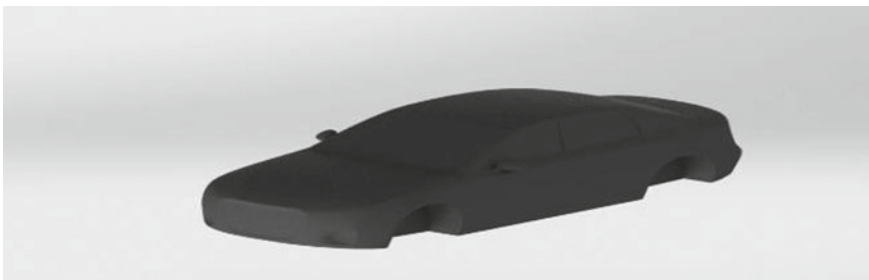
Fig. 1 Modeled car in SOLIDWORKS

Fig. 2 Designing parameter
of vortex generator
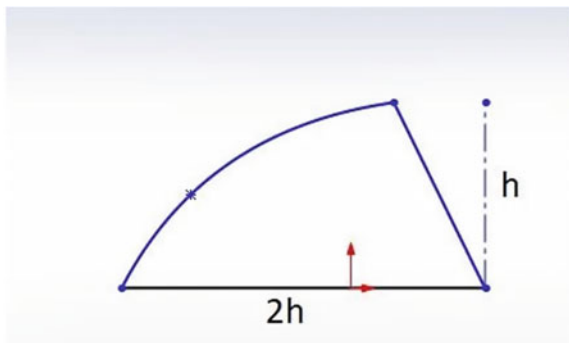
the boundary layer in the Y-axis. BL Thickness $= 5 \times \frac{L}{\sqrt{Re}} = 6$ mm [8]. By the
principle of VG, height of VG = height of boundary layer [4], the 6 mm is selected
as a reference height for the iterations (Fig. 2).

There are basically three types of the vortex generators studied in this paper.
Among them, bump-shaped VG is selected for the initial iterations. The bump-
shaped VG is then tested at a various height ranging from 2 to 30 mm using ANSYS
FLUENT model, and the values of drag and downforce are then compared with the
original model. The vortex generators are placed at the rear side of the car, where
flow is prone to separated due to sudden geometry change [4]. The position of the
flow separations is observed with computational streamline results (Fig. 3). The result
indicates the zone for height ranging 2–6 mm is favorable for the drag reduction. The
remaining VGs are then tested for this height variation. The results of all the vortex
generators are then tabulated and compared themselves for the drag and downforce
values. The best performing VG among all is further compared with the original car
at the various speed of 10, 20, 30, 35 m/s as shown in Table 1. The results are also
displaced with the help of pressure distribution, velocity distribution and streamlines

Fig. 3 Positioning of vortex
generator
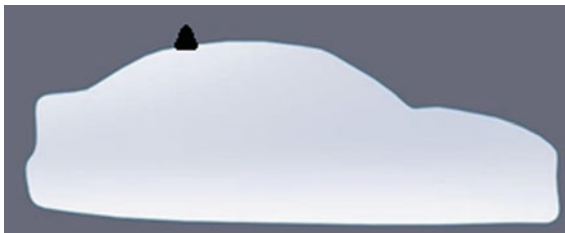
Table 1 Drag and lift of car without VG

Velocity	10 m/s	20 m/s	30 m/s	35 m/s
Drag (N)	17.3029	66.046	144.732	189.83
Lift	-8.17	−38.844	−95.04	−132.108

visualization. The results will be validated in terms of streamline flow, pressure and velocity distribution. The study of point of separation will be carried out using a streamline visualization technique.

3   Result and Discussion

The computational results of the car without application of the vortex generator are shown as follows:

The flow separates rapidly at the rear end with the increase in the speed as it is unable to follow the contour with increases in the speed. This leads to the more low-pressure area and thus the drag (Fig. 4).

3.1   Bump-Shaped VG

The computational results of the car with bump-shaped VG (Fig. 5) at 30 m/s are shown in Fig. 6.

From Table 2, it is clear that the optimum usage of VG's height from 2 mm to 6 m, if it further increase the vortex generator produces the self-drag due to momentum transfer phenomenon where VG helps to overcome the surface friction with added
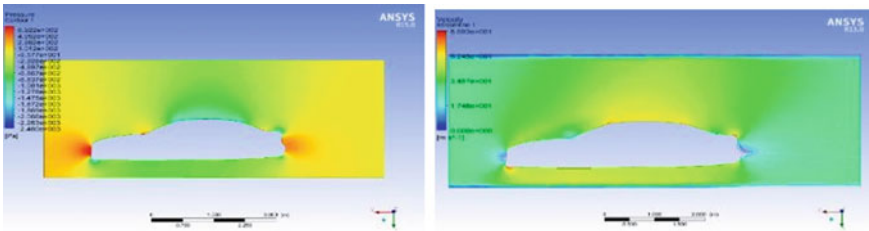
Fig. 4   Pressure and velocity distribution without VG at 30 m/s

Fig. 5   Bump-shaped VG
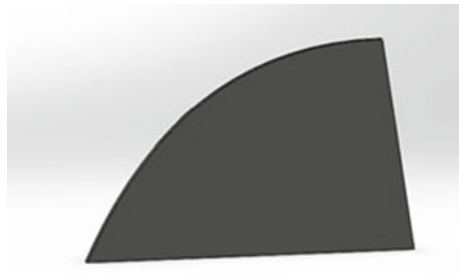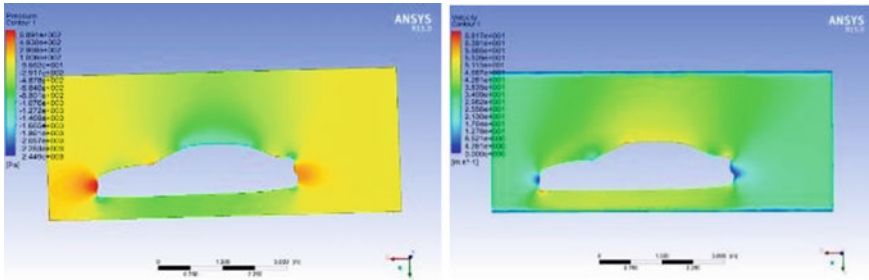
Fig. 6 Velocity and pressure distribution with bump VG of 6 mm height at 30 m/s

Table 2 Lift and drag of car with bump VG at 30 m/s

Height	2 mm	4 mm	6 mm
Drag(N)	139.303	142.83	142.83
Lift(N)	−95.32	−94.318	−112.118

velocity. The effect gets diminishes with height as the vortex generator produces self-drag.

3.2 Delta-Shaped VG

The computational results of the car with delta-shaped VG (Fig. 7) at 30 m/s are shown as follows:

Fig. 7 Delta-shaped VG
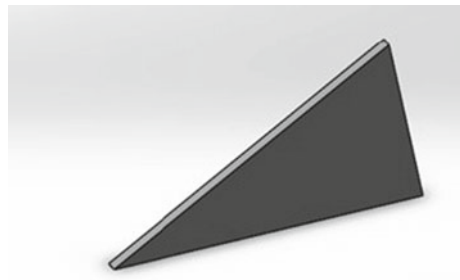
Table 3 Lift and drag of car with delta VG at 30 m/s

Height	2 mm	4 mm	6 mm
Drag(N)	144.054	150.271	152.495
Lift(N)	−69.451	−71.84	−73.15
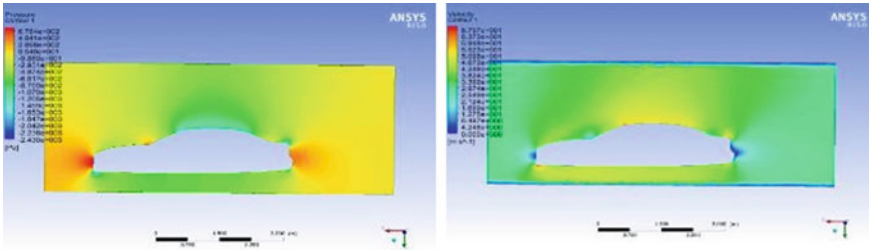
Fig. 8 Velocity and pressure distribution with delta VG of 6 mm height at 30 m/s

Table 3 shows the drag and lift values at 30 m/s, and Fig. 8 shows the velocity and pressure distribution with delta VG of 6 mm height at 30 m/s

3.3 Triangle-Shaped VG

The computational results of the car with triangle-shaped VG (Fig. 9) at 30 m/s are shown as follows:

The triangular-shaped VG shows the superior performance. The low-pressure area is decreased considerably due to delay in the effective flow separation. This is can be seen from the velocity distribution in Fig. 10 where a large rise in the velocity occurs at the upper contour of the car. The 6 mm height VG shows around 10% reduction in the drag without the expense the downforce performance. The triangular VG's vortices form at the separation point and are not harming the drag performance. Table 4 shows the lift and drag of car with triangle VG at 30 m/s.

Figure 11 shows the comparison between drag produced when bump, delta and triangle VG are evaluated at 30 m/s.

Fig. 9 Triangle-shaped VG
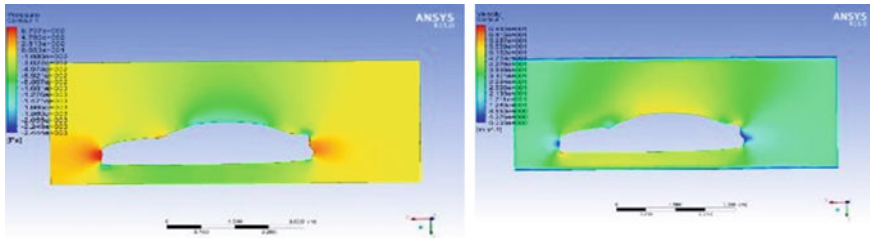
Fig. 10 Velocity and pressure distribution with triangle VG of 6 mm height at 30 m/s

Table 4 Lift and drag of car with triangle VG at 30 m/s

Height	2 mm	4 mm	6 mm
Drag(N)	142.78	138.013	130.92
Lift(N)	−101.35	−72.9205	−97.7816
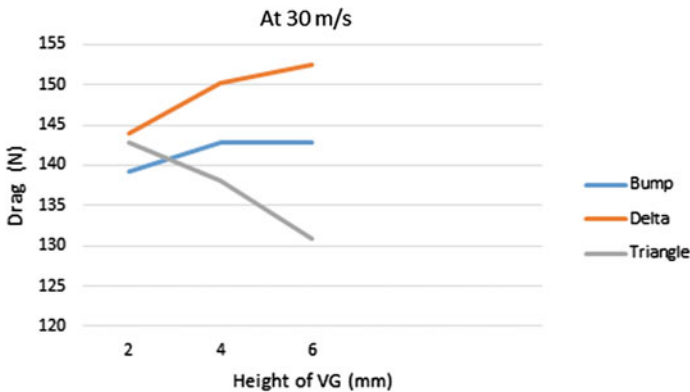
Fig. 11 Comparison between different types of VG at 30 m/s

After comparing the results obtained in Tables 2, 3 and 4 with original values in Table 1, it is very evident that the triangular-shaped VG shows the superior performance among the above VG. The low-pressure area is decreased considerably due to delayed in the effective flow separation. This can be seen from velocity distribution figure where large raise in velocity occurs at the upper contour of the car. It is evident that the triangular vortex generator with 6 mm of height shows excellent performance in terms of drag and downforce. Hence, these parameters of rectangular vortex generator are tested at a different speed and compared with the original results as in Table 5.

From the Table 5, the application of triangle-shaped vortex generator helps to reduce the drag force up to 10% without hampering downforce performance.

Table 5 Drag comparison with and without applications of vortex generators

Spec.	Without vg (10 m/s)	Triangle (10 m/s)	Without vg (20 m/s)	Triangle (20 m/s)	Without vg (30 m/s)	Triangle (30 m/s)	Without vg' (35 m/s)
Drag(N)	17.3029	15.646	66.046	61.561	144.732	130.92	175.183
Lift(N)	−8.17	−8.65	−38.844	−40.533	−95.04	−97.786	−132.108

4 Conclusion

As vertex generators are used for drag reduction selection of VG design and shape plays a vital role for optimum reduction of drag. Among four discussed designs of VG's above, the triangle-shaped vortex generator gives the best results. As the VG height raises above the height of boundary layer. The VG's height ranges from 2 to 6 mm, if the height exceeds this range self-drag gets added. From this paper, we conclude that results with triangle-shaped vortex generator with height 6 mm shows excellent characteristics of drag reduction without hampering the performance of the downforce.

References

1. Subramani T (2012) Study of air pollution due to vehicle emission in tourism center. Int J Eng Res Appl 2(3)
2. Siva, V. Loganathan (2016) Design and aerodynamic analysis of a car to improve performance. Middle-East J Sci Res 133–140
3. Koike M, Nagayosh T Research on aerodynamic drag reduction by vortex generators. Technical Papers
4. Naveen, Prakkash V, Kannan S (2015) Design of a custom vortex generator optimization of vehicle drag and lift characteristics. IJISET—Int J Innov Sci Eng Tech 2(9)
5. Govindhrajan R, Parammasivam KM, Sathya Narayanan S (2013) Design of vortex generators for light transport vehicles (LTV) using CFD. The Eighth Asia-Pacific conference on wind engineering, 10–14 Dec 2013, Chennai, India
6. Rupesh A, Muruga lal Jeyan V, Jeyan L, Ram Mohan VM, Praveen Kumar K, Abhishek T, Ashish T, Reddy KVVM, Reddy GM (2020) Comparative study on wind tunnel calibrating instruments. Adv Metrol Measur Eng Surf Lecture Notes Mech Eng book series (LNME)— Springer, Singapore, 2, June 2020, pp 139–147, ISSN 2195-4356
7. Rupesh A, Muruga lal Jeyan V (2020) Performance evaluation of a two hole and five hole flow analyzer for subsonic flow. Int J Adv Sci Tech 29(5), 7512–7525. May 2020, ISSN 2207-6360
8. Rupesh A, Muruga lal Jeyan JV, Uthaman S (2020) Design and analysis of five probe flow analyser for subsonic and supersonic wind tunnel calibration. In: IOP conference series: materials science and engineering, vol 01, Issue 715, pp 1–7. January 2020, ISSN 1757-899X

Transmission Efficiency of Polymer Spur Gears Meshing with Polymer as Well as Metal Spur Gears

Akant Kumar Singh, Siddhartha, and Sanjay Yadav

Abstract Polymer gears are replacing metal gears in various applications nowadays. Polymer gears are deployed in lightweight applications and frequently used in robotic field. Various type of movement takes place in robot. Therefore, transmission efficiency (TE) is a key concerned for robot motion. Transmission efficiency very much depends on the pinion and gear materials. Gear tooth surface temperature affects the transmission efficiency of polymer gears. In the current work, Acrylonitrile Butadiene Styrene (ABS) gears are manufactured through injection molding. Transmission efficiency is investigated for ABS to ABS gear pairs and ABS to steel gear pairs. Fabricated gears are run at various speeds of 600, 800, 1000, and 1200 rpm and different torque values of 0.8, 1.2, 1.6, and 2 Nm for investigating the TE. Test gears are made to run up to 1.2×10^5 rotations during each experiment. The result finding shows that ABS to steel gear pairs have high transmission efficiency as compared to ABS to ABS gear pairs.

Keywords ABS gears · Transmission efficiency · Injection molding · Polymer gear test rig

1 Introduction

Thermoplastic materials are used to fabricate the polymer gears. Polymer gear possesses some significant edges over the metal gears in terms of quieter operations, lower inertia, lower coefficient of friction, and most importantly the lower cost. Due to these characteristics, plastic gears are now replacing metal gears in plethora of industrial applications. However, their applications are limited to low and medium load conditions only. Utilization of the plastic gear enhances the efficiency of the mechanical systems due to an overall reduction in the weight of the system [1]. Now

A. K. Singh (✉) · S. Yadav
Department of Mechanical Engineering, I.T.S Engineering College, Greater Noida 201308, India
e-mail: akant.me@its.edu.in

Siddhartha
Department of Mechanical Engineering, NIT Hamirpur, Hamirpur, HP 177005, India

a day, there are various applications where plastic gears are used. Though, the study regarding TE of plastic gears is not explored much so far. It has been observed by Walton et al. [2, 3] that TE of polymer gears is very much influenced by load and speed. It is found that the material of gears and their geometries also affect the TE of these gears.

Lots of work has been done on plastic gears in the last decade [4]. It has been observed by Senthilvelan and Gnanamoorthy [5] that TE of carbon fiber filled polymer composite gear improved as compared to neat gear. It happens because thermal peculiarity and gear tooth stiffness improved by reinforcing the fibers. It has also been observed that the addition of nano-clay fillers also improves the TE of plastic gears [6]. Some researchers have used the compressed air at the mating surface to improve the TE of plastic gears and almost 2% of enhancement is achieved in TE [7]. The effect of tooth deformation and gear tooth wear rate on transmission efficiency is investigated by Nagarajan and Rayudu [8]. Error in transmission due to the geometry of polymer gear is studied by Luscher et al. [9]. It has been observed in the study of Mertens and Senthilvelan [10] that TE of polymer gears is enhanced by adding carbon nanotubes in gear material. They have done the experiment on nanotube filled polypropylene spur. Kodeeswaran et al. [11] have done the experimental as well as numerical estimation of TE of polymer gears.

Reinforcement of fibers in polymer gear alters the performance of polymer gear very much. It improves the performance of the polymer gears by reducing the wear and temperature at the mating surfaces of polymer gear teeth [12–14]. Also, fiber-filled polymer composite gears have improved TE [2, 5]. Addition of fibers in polymer gears increases the damping characteristics of these gears which affects the transmission efficiency [15]. TE is also explored by the researchers for different materials [16–18]. A novel FGM based polymer spur gear has been fabricated by Singh and Siddhartha [19]. It has been observed that FGM based gears possess better TE in comparison to conventional polymer gears. Transmission efficiency has been observed for various plastic gears fabricated with different materials. Maximum investigations are done for the polymer to metal gear pair. However, it has been found from literature that transmission efficiency has not been explored much for a polymer to polymer gear pair. Therefore, the focus of this study is to investigate the TE of polymer-polymer gear pair and compared it with the polymer-steel gear pair.

2 Materials and Methodology

2.1 Gear Manufacturing

In this study, the plastic gears are manufactured through Injection molding technique. These gears are fabricated using ABS material. A dryer is used for heating ABS materials at 100 °C for 4 h to eliminate the moisture content. Injection pressure of

80 MP is used to fabricate gears. A pictorial view of a fabricated gear is presented in Fig. 1.

2.2 Polymer Gear Test Rig

The testing of the gears is carried out by using a customized gear test rig. The testing of the polymer gears is done with similar as well as with their steel counterparts. Specifications of polymer and steel gears are the same. Polymer test rig is manufactured by Bangalore based company DUCOM Instruments. A pictorial view of the test rig is provided in Fig. 2. The torque is measured by torque sensors which are acting

Fig. 2 Pictorial view of test rig

on driver and driven gears. Accuracy of the torque sensor is ±0.2%. Temperature was continuously measured with the help of an infrared sensor during experimentation. Temperature sensor is just fitted above the contact surface of driver and driven gear pairs. List count of the temperature sensor is 1 °C and it can measure the gear tooth surface temperature up to 130 °C.

2.3 Transmission Efficiency

Transmission efficiency (TE) of polymer to polymer and polymer to steel gear pairs is examined. Transmission efficiency is calculated using Eq. 1 by neglecting the power loss at couplings and bearings.

$$TE = \text{Driven Gear Torque/Driver Gear Torque} \qquad (1)$$

3 Results and Discussions

3.1 Influence of Speed and Torque on TE of Polymer Gears

Materials of pinion and gear play an important role in the TE. TE is also affected by torque and speed. Variation in the TE and surface temperature of polymer gear is shown in Fig. 3a, b. Variation is observed due to the torque at different speeds of 600 and 1200 rpm. It is evident from Fig. 3 that increment in gear tooth surface temperature as well as reduction in TE is observed with increase in torque. Polymer gear tooth flexibility affects the temperature of the gear tooth very significantly. Gear tooth surface temperature increases with an increase in the torque which ultimately results in the deflection of gear teeth. This deflection causes a reduction in the torque of the test gear that finally results in a reduced TE of the test gears [3] which is observed after the accomplishment of 1.2 million cycles.

It is observed from Fig. 3 that TE of polymer - steel gears pair is higher as compared to polymer–polymer pair for 600 rpm as well as 1200 rpm speed. It occurs due to lower temperature of gear tooth surface in case of polymer - steel gears pair. Polymer—polymer and polymer—steel gear pairs have high TE at 600 rpm while decrement in TE is seen for both gear pair at 1200 rpm as shown in Fig. 3a, b. This may happen because the higher temperature of gear tooth surface at the speed of 1200 rpm bases less TE for both gear pairs. The temperature at the surface of polymer - steel gear pair is less because steel gear has higher thermal conductivity. Whatever heat is generated because of the meshing of the gear teeth surface of ABS gear dissipates quickly. However, it does not happen for polymer–polymer gear pair. Both are the polymer material having less thermal conductivity causes high surface
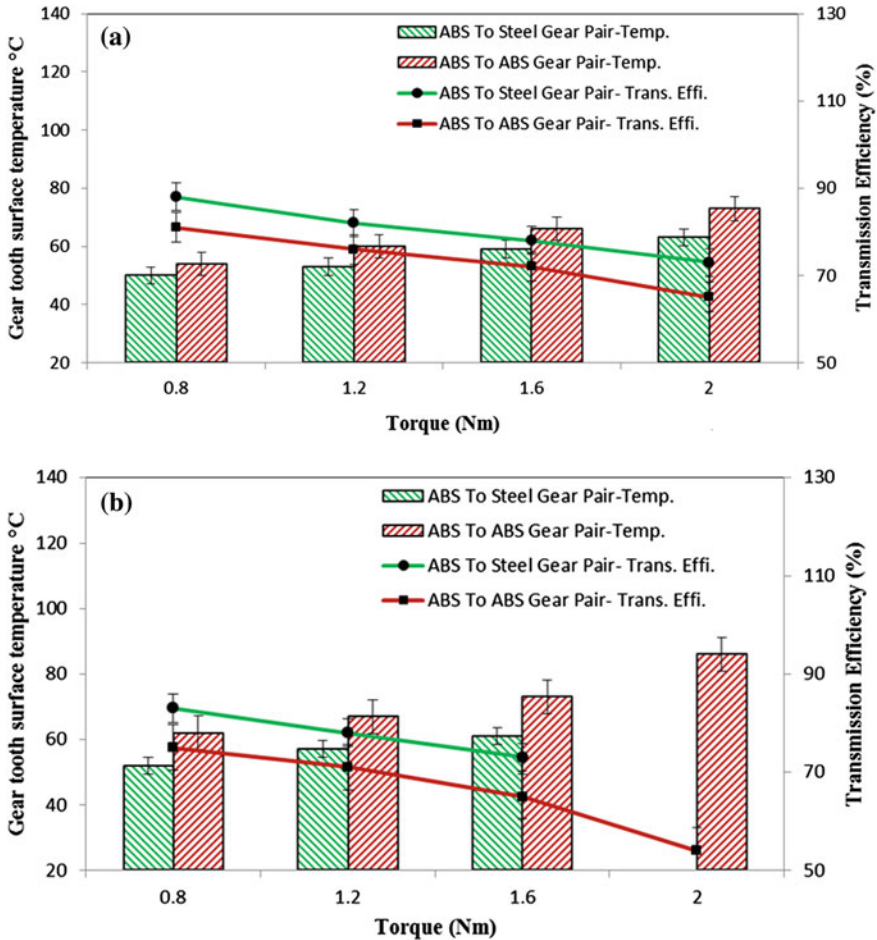
Fig. 3 **a** Transmission efficiency of gear pairs at speed of 600 rpm, **b** transmission efficiency of gear pairs at speed of 1200 rpm

temperature. It is observed from Fig. 3b that ABS gear having contact with metal gear failed at 2 Nm torque and 1200 rpm speed. ABS gear tooth becomes soft at 2 Nm torque due to tooth surface temperature and they were not able to sustain the impact came from the metal gear causes in the failure of a polymer gear tooth. However, that impact is not experienced by gear tooth in the case of polymer to polymer gear tooth meshing results no failure. TE of polymer to polymer gear pairs and polymer to steel gear pairs are reduced by 17% and 12%, respectively at 600 rpm and 19% and 16%, respectively at 1200 rpm with an increase in the torque value from 0.8 to 1.6 Nm.

TE of polymer to polymer gear pairs and polymer to steel gear pairs does not get influenced much by the variation of speed, as witnessed in Fig. 4. Thus, it is clear
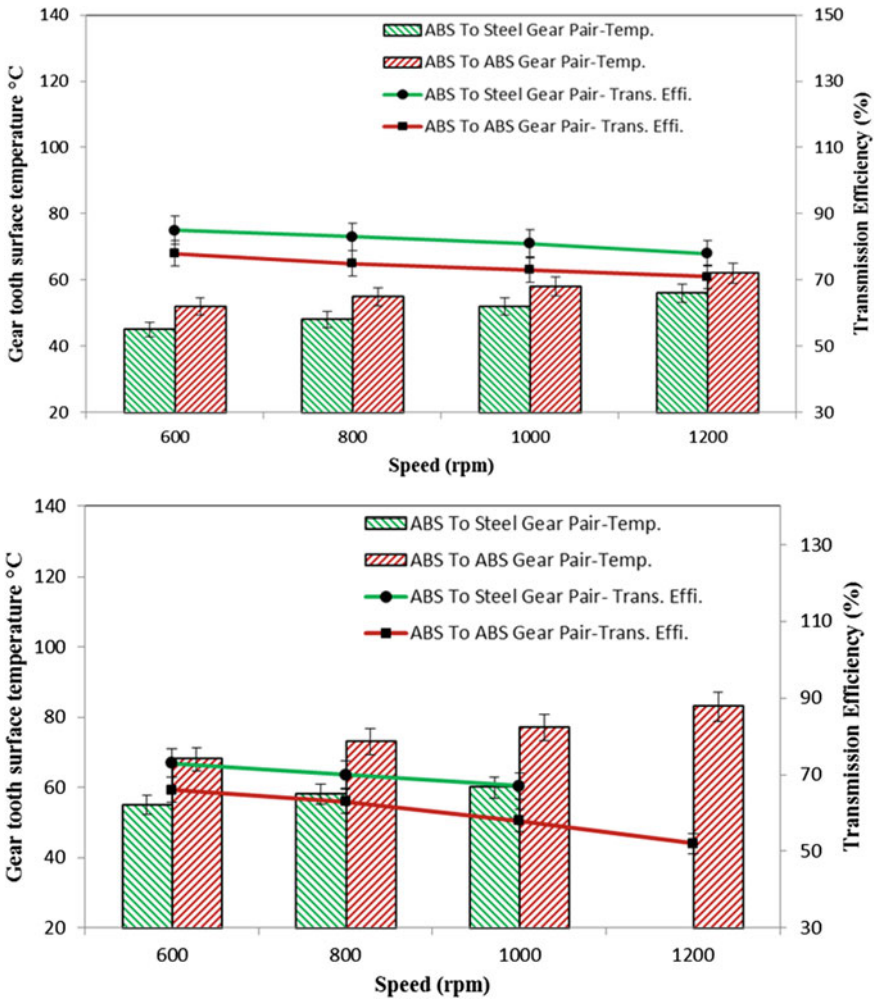
Fig. 4 **a** Transmission efficiency of gear pairs at 0.8 Nm torque, **b** transmission efficiency of gear pairs at 2 Nm torque

that TE of polymer to polymer gear pairs and polymer to steel gear pairs decreases with an upsurge in speed. Same results are also observed by Walton et al. [2, 3] for various polymer materials used to manufacture gears. TE of polymer to polymer and polymer to steel gear pair is low for 2 Nm torque as compared to 0.8 Nm torque for each constant speed which is shown in Fig. 4a, b. This may happen because of a higher temperature at the surface of both gear pairs at the torque of 2 Nm. TE of polymer to polymer gear pair and polymer to steel gear pair decreases marginally from 6 to 10% when the speed rises from the speed of 600 to 1200 rpm.

At 0.8 Nm, polymer to steel gear pair has 8% higher TE as comparison to polymer–polymer pair at the speed of 1200 rpm. However, at a constant torque of 2 Nm, polymer - steel gear pair have 12% higher TE as compared to polymer–polymer pair at the speed of 1000 rpm. Hence, the result finding shows that the polymer – steel gear pair performs better than the polymer–polymer gear pair up to 1000 rpm and 1.6 Nm torque.

4 Conclusions

Conclusions from this study are shown below:

- ABS material-based spur gears are manufactured by injection molding process.
- TE is less influenced by speed rather than torque for both gear pairs.
- Polymer to steel gear pair has higher TE as compared to polymer to polymer gear pair.
- ABS gear having contact with metal gear failed at 2 Nm torque and 1200 rpm speed due to generation of high gear tooth surface temperature and impact came from the metal gear.
- Polymer to polymer gear pair has minimum transmission efficiency at 2 Nm torque and 1200 rpm speed.

References

1. Adams CE (1986) Plastic gearing: selection and application (2nd edn). Marcel Dekker, New York
2. Walton D, Cropper AB, Weale DJ, Meuleman PK (2002) J Eng Tribol 216:75–92
3. Walton D, Cropper AB, Weale DJ, Meuleman PK (2002) J Eng Tribol 216:93–103
4. Singh AK, Siddhartha, Singh PK (2017) J Eng Tribol https://doi.org/10.1177/1350650111771595
5. Senthilvelan S, Gnanamoorthy R (2009) J Eng Tribol 223:925–928
6. Kirupasankar S, Gurunathan C, Gnanamoorthy R (2012) Maters Des 39:338–343
7. Mertens AJ, Senthilvelan S (2015) J Mat Des Appl 230:515–525
8. Nagarajan GVN, Rayudu (1987) Proceedings of the 7th world congress on the theory of machines and mechanisms Sevilla, Spain pp 1335–1338
9. Luscher A, Houser D, Snow C (2000) J Inject Molding Technol 4:177–190
10. Mertens AJ, Senthilvelan S (2016) J Mat Des Appl. https://doi.org/10.1177/1464420716654308
11. Kodeeswaran M, Suresh R, Senthilvelan S (2016) Int J Power Trains 5:246–263
12. Gurunathan C, Kirupasankar S, Gnanamoorthy R (2011) J Eng Tribol 225:299–306
13. Kurokawa M, Uchiyama Y, Iwai T, Nagai S (2003) Wear 254:468–473
14. Singh PK, Siddhartha, Singh AK (2017) Maters Today 4:1606–1614
15. Senthilvelan S, Gnanamoorthy R (2006) Polym Test 25:56–62

16. Singh AK, Siddhartha, Singh PK (2018) Maters Today 5:18038–18044
17. Singh AK, Siddhartha, Singh PK (2018) Adv Engg Desig 4:269–277
18. Singh AK, Siddhartha J (2019) Engg Tribol. https://doi.org/10.1177/1350650119886233
19. Singh AK, Siddhartha (2017) Poly Compos. https://doi.org/10.1002/pc.24682

Structural Analysis on the Separated and Integrated Differential Gear Case for the Weight Reduction

Jaesun Lee , Jungho Han, and Sunil Kumar Sharma

Abstract The development of lightweight vehicle components has been studied for a long time due to strict exhaust emission regulations and fuel efficiency. The purpose of this study is to improve the performance and weight reduction of the differential gear case due to the change from the conventional type to the integrated type. Through the 3D modeling and the finite element analysis, the static stress analysis was performed for each load condition. Based on the results, the structural safety analysis results confirmed that the collision criteria were satisfied and the possibility of improving the performance and lighter weight of the products was confirmed.

Keywords Differential case · Integrated diff.case · Structural analysis · FEM analysis

1 Introduction

The vehicle differential gear is a device that distributes the number of revolutions of different wheels properly when the car moves forward or turns on the uneven surface of the road. It is a device that equally distributes the number of revolutions of the left and right driving wheels or the front and rear drive axles for smooth driving or transmits an equal torque to the rotating shafts during steering. The differential gearcase is a device that protects the differential gear from impact and moves with

J. Lee (✉) · J. Han
School of Mechanical Engineering, Changwon National University, Changwon 51140, Korea
e-mail: jaesun@changwon.ac.kr

S. K. Sharma
Extreme Environment Design and Manufacturing Innovation Center, Changwon National University, Changwon 51140, Korea

Department of Mechanical Engineering, Amity School of Engineering and Technology, Amity University, Noida, Uttar Pradesh, India

S. K. Sharma
e-mail: sksharma10@amity.edu

175

the ring gear of the differential. Differential gears and differential gear cases have many different shapes and sizes according to the shape of structure and type of the vehicle, and there are various design variables to improve the driving stability and ride comfort of the vehicle.

Many researchers have worked in the area of include differential gear in different applications [1–14] i.e. vehicle [15–24], gear system [25–35], etc. A differential gear for vehicles is a combination of four rotating bevel gears (two pinion gears, two side gears), which are connected to the drive shaft of the car to control the rotation of both wheels as the car progresses. Looking at the principle of the differential gear, when driving straight, only the left and right two side gears rotate and the pinion gear does not move. When the vehicle moves forward on the uneven surface or rotates in a curved section, the pinion gear existing above and below rotates to adjust the rotation speed and rotation speed of the side gear. The vehicle differential gearcase is a device that protects the differential gear from impact and moves with the ring gear of the differential. When power is transmitted from the power shaft to the ring gear, the ring gear rotates and the vehicle moves while rotating the side gears on both sides of the case [1, 2].

In the case of the separated differential gear case, the upper and lower parts are manufactured by casting process of spheroidal cast iron, respectively, and then manufactured through surface assembly and assembly process. There are many parts and the production process is complicated and heavy. There is a possibility of defects due to manufacturing defects and human error that can occur during assembly. In order to overcome the disadvantages of the separate differential gear case, the integrated differential gear case was designed. In the case of the integral differential gear case, there is a possibility of defects because it is difficult to accurately manufacture the internal and external shapes through the casting process due to the characteristics of the bending. However, since the integral differential gear is made of a single part, the structure is simple and lightweight, and the mechanical properties are improved [3].

In this study, the integrated differential case is designed to improve the structural properties and reducing weight for improving fuel efficiency. The integrated differential case is analyzed with load cases which are simulated for impact cases.

2 Differential Gearcase Design and Modeling

The manufacturing of the differential gear case for the vehicle is finalized through the necessary machining process according to the internal and external positions such as turning, grinding, and planar processing. In the case of the separate differential gear, the tolerance of the upper and lower parts of the differential gear case manufactured through the casting process is checked to determine whether there is a step, and the inner and upper gears are assembled to complete the final differential gear. In the case of the integral differential gear, it is not divided into upper and lower parts, so the gear is inserted into the integral differential gear manufactured through the

casting process and fixed by using laser welding together with the fixing part. The material used for the integral differential gear is spheroidal cast iron, HB 170–241. The material is mainly used for the power transmission system of the vehicle, and the shape is manufactured through the casting process, and the connecting part is processed by grinding.

In order to eliminate the unnecessary elements of existing differential gear case models and to manufacture an integrated differential gear case for miniaturization and lightweight, miniaturization and lightening of differential gear proceed and through structural design program before production of a prototype to examine its stability [4, 5]. The integrated differential gear case was 3D modeled. In addition, 3D modeling was conducted to compare the stability of the separate and integrated differential gear cases. The separate differential gear case model measures 138 mm and 162 mm in weight and 6.137 kg in weight, respectively, and uses CATIA V5 R20 for the structural design program (Fig. 1). The all-in-one differential gear case model weighs 169 mm and 156 mm, respectively, and weighs 4.4 kg. Although there was little change in size, it satisfied the conditions when lightweight was advanced. At this time, the weight could be reduced by 28% (Table 1).

(a)   (b)
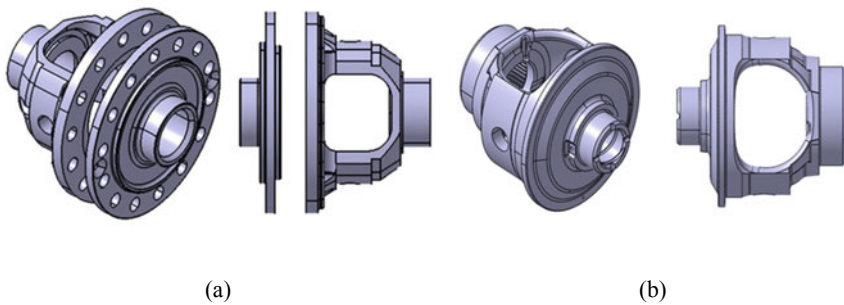
Fig. 1 Differential gearcase modeling **a** separated differential case and **b** integrated differential case

Table 1 Material properties of separated and integrated differential cases

Part name	Material	Young's Modulus (GPa)	Poisson' ratio	Density (kg/m^3)	Tensile strength (MPa)	Yield strength (MPa)
Cup cover	FCD600	200	0.275	7.86	600	370
Integrated diff case	GCD500	169	0.27	7.10	500	320
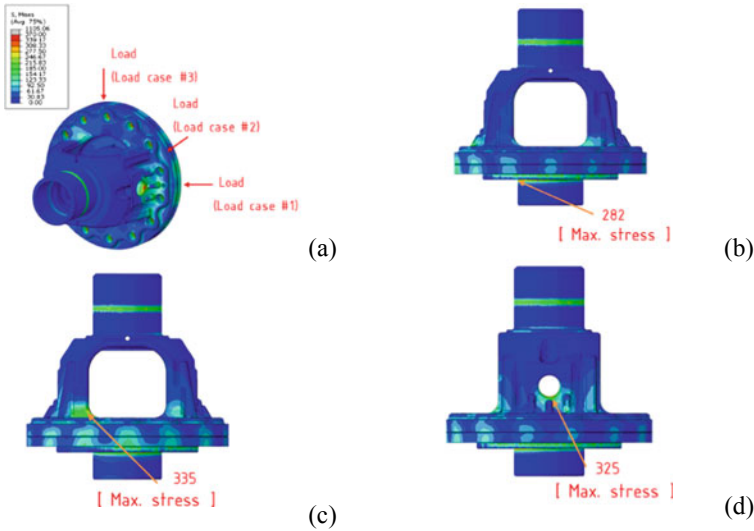
Fig. 2 Separated differential gearcase structural analysis with respect to loadcase: **a** loading information for loadcase, **b** loadcase#1analysis result, **c** loadcase#2analysis result and **d** load-case#3analysis result

3 Differential Gearcase Structural Analysis

3.1 Separated Differential Gearcase Analysis

The maximum stress was calculated when the differential gear case and the ring gear were connected with fixed boundary conditions and additional loads were applied to the ring gear in three directions of 0, 45, and 90 degrees along with the boundary conditions. The maximum stress locations and stress values occurring in the separate differential gear case for each external force are shown in Fig. 2. The results of the stress analysis showed that the maximum stress was the highest in the case of Load case # 2, and the part that received the maximum stress in each case appeared differently according to the shape of the product.

3.2 Integrated Differential Gearcase Analysis

Since the boundary condition is given by pressure, the pressure corresponding to the external force is set based on the area of each region. After adding each boundary condition, additional fixed boundary conditions for structural analysis are added. A boundary condition was added to fix the displacement in the z-axis direction so that rotation did not occur at the ring gear connection. In addition, considering the rotation
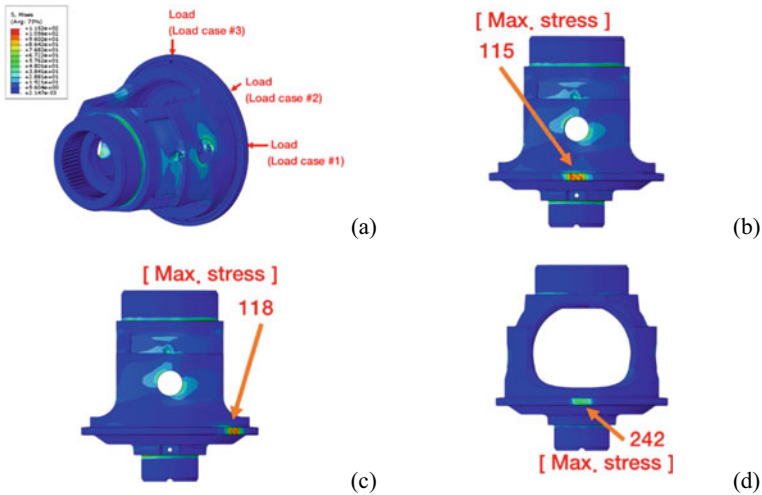
Fig. 3 Integrated differential gearcase structural analysis with respect to loadcase: **a** loading information for loadcase, **b** loadcase#1analysisresult, **c** loadcase#2analysis result and **d** loadcase#3analysis result

of the differential gear, an external force that gives torque to one of the rotating shafts was set.

The maximum stress was calculated when the differential gear case and the ring gear were connected with fixed boundary conditions and additional loads were applied to the ring gear in three directions of 0, 45, and 90° along with the boundary conditions. The maximum stress locations and stress values occurring in the integral differential gear case for each external force are shown in Fig. 3. The results of the stress analysis showed that the maximum stress was the highest in the case of Load case # 3, and the part under the maximum stress appeared in each case according to the shape of the product. Unlike the case of load case # 2 in the case of the separate differential gear case, the maximum stress is the highest in load case # 3 90° in the case of the integral differential gearcase. When compared with the model it can be seen that a significantly lower maximum stress value appears.

4   Conclusions and Discussions

The design change from the existing one-piece differential gear case model to an integrated differential gear case reduced the weight change by 28% while minimizing the size change. Structural analysis was performed to analyze the effect of structural safety due to the reduced weight, and as a result, the structural safety was confirmed. In addition, further research is needed to enable optimal shape design through structural optimization.

References

1. Veeranjaneyulu C, Babu Hari U (2012) Design and structural analysis of differential gear box at different loads. Int J Adv Eng Res Stud 1:65–69
2. Khan A, Verma S (2015) Design and analysis of automobile central differential having two-different side gear. Int J Sci Res Dev 3(4):2321–0613
3. Chen L, Zhang D, Chen W, Hu F, Huang M (2013) Lightweight design of differential case based on particle swarm optimization algorithm. Trans Chin Soc Agric Eng 29(9):24–31
4. Güler T, Demirci E, Yıldız AR, Yavuz U (2018) Lightweight design of an automobile hinge component using glass fiber polyamide composites. Mater Test 60(3):306–310
5. Zhang Y, Lai X, Zhu P, Wang W (2006) Lightweight design of automobile component using high strength steel based on dent resistance. Mater Des 27(1):64–68
6. Bhardawaj S, Chandmal Sharma R, Kumar Sharma S (2019) A survey of railway track modelling. Int J Vehicle Struct Syst 11 (5)
7. Bhardawaj S, Sharma R, Sharma S (2020) Ride analysis of track-vehicle-human body interaction subjected to random excitation. J Chin Soc Mech Eng 41(2):236–237
8. Bhardawaj S, Sharma RC, Sharma SK (2020) Analysis of frontal car crash characteristics using ANSYS. Mater Today Proc 25:898–902
9. Bhardawaj S, Sharma RC, Sharma SK (2020) Development in the modeling of rail vehicle system for the analysis of lateral stability. Mater Today Proc 25:610–619
10. Bhardawaj S, Sharma S, Sharma R (2020) Development of multibody dynamical using MR damper based semi-active bio-inspired chaotic fruit fly and fuzzy logic hybrid suspension control for rail vehicle system. In: Proceedings of the institution of mechanical engineers, Part K: journal of multi-body dynamics
11. Dao DK, Ngo V, Phan H, Pham CV, Lee J, Bui TQ (2020) Rayleigh wave motions in an orthotropic half-space under time-harmonic loadings: a theoretical study. Appl Math Model 87:171–179
12. Goyal S, Anand CS, Kumar S, Chandmal R (2019) Thin-walled structures crashworthiness analysis of foam filled star shape polygon of thin-walled structure. Thin-Walled Struct 144
13. Kanth Choppara R, Chandmal Sharma R, Kumar Sharma S, Gupta T (2019) Aero dynamic cross wind analysis of locomotive. IOP Conf Ser Mater Sci Eng 691:012035
14. Lee J, Ngo V, Phan H, Nguyen T, Dao DK, Cho Y (2019) Scattering of surface waves by a three-dimensional cavity of arbitrary shape: analytical and experimental studies. Appl Sci 9(24):5459
15. Palli S, Koona R, Sharma SK, Sharma RC (2018) A review on dynamic analysis of rail vehicle coach. Int J Veh Struct Syst 10(3):204–211
16. Park J, Lee J, Jeong S-G, Cho Y (2019) A study on guided wave propagation in a long distance curved pipe. J Mech Sci Technol 33(9):4111–4117
17. Park J, Lee J, Le Z, Cho Y (2020) High-precision noncontact guided wave tomographic imaging of plate structures using a DHB algorithm. Appl Sci 10(12):4360
18. Park J, Lee J, Min J, Cho Y (2020) Defects inspection in wires by nonlinear ultrasonic-guided wave generated by electromagnetic sensors. Appl Sci 10(13):4479
19. Sharma RC, Palli S, Sharma SK, Roy M (2017) Modernization of railway track with composite sleepers. Int J Veh Struct Syst 9(5):321–329
20. Sharma RC, Sharma S, Sharma SK, Sharma N (2020) Analysis of generalized force and its influence on ride and stability of railway vehicle. Noise Vibr Worldwide 51(6):95–109

21. Sharma RC, Sharma SK (2018) Sensitivity analysis of three-wheel vehicle's suspension parameters influencing ride behavior. Noise Vibr Worldwide 49(7–8):272–280
22. Sharma RC, Sharma SK, Palli S (2018) Rail vehicle modelling and simulation using lagrangian method. Int J Veh Struct Syst 10(3):188–194
23. Sharma SK (2019) Multibody analysis of longitudinal train dynamics on the passenger ride performance due to brake application. Proc Inst Mech Eng Part K: J Multi-body Dyn 233(2):266–279
24. Sharma SK, Kumar A (2014) A comparative study of Indian and worldwide railways. Int J Mech Eng Robot Res 1(1):114–120
25. Sharma SK, Kumar A (2018) Disturbance rejection and force-tracking controller of nonlinear lateral vibrations in passenger rail vehicle using magnetorheological fluid damper. J Intell Mater Syst Struct 29(2):279–297
26. Sharma SK, Kumar A (2016) Dynamics analysis of wheel rail contact using FEA. Proced Eng 144:1119–1128
27. Sharma SK, Kumar A (2017) Impact of electric locomotive traction of the passenger vehicle Ride quality in longitudinal train dynamics in the context of Indian railways. Mech Indust 18(2):222
28. Sharma SK, Kumar A (2018) Impact of longitudinal train dynamics on train operations: a simulation-based study. J Vibr Eng Tech 6(3):197–203
29. Sharma SK, Kumar A (2018) Ride comfort of a higher speed rail vehicle using a magnetorheological suspension system. Proc Inst Mech Eng Part K: J Multi-body Dyn 232(1):32–48
30. Sharma SK, Kumar A (2017) Ride performance of a high speed rail vehicle using controlled semi active suspension system. Smart Mater Struct 26(5):055026
31. Sharma SK, Phan H, Lee J (2020) An application study on road surface monitoring using DTW based image processing and ultrasonic sensors. Appl Sci 10(13):4490
32. Sharma SK, Saini U, Kumar A (2019) Semi-active control to reduce lateral vibration of passenger rail vehicle using disturbance rejection and continuous state damper controllers. J Vibr Eng Tech 7(2):117–129
33. Sharma SK, Sharma RC (2018) An investigation of a locomotive structural crashworthiness using finite element simulation. SAE Int J Commer Veh 11(4):02–11–04–0019
34. Sharma SK, Sharma RC (2018) Simulation of quarter-car model with magnetorheological dampers for ride quality improvement. Int J Veh Struct Syst 10(3):169–173
35. Sharma SK, Sharma RC, Kumar A, Palli S (2015) Challenges in rail vehicle-track modeling and simulation. Int J Veh Struct Syst 7(1):1–9

A Study on the Performance Evaluation of Hydraulic Tank Injectors

Sunho Choi, Jaesun Lee , and Sunil Kumar Sharma

Abstract The military scout vehicle has been developed, and it is widely used as the main operating system of the army in the field. Recently, the development of an existing military armored vehicle is being converted into an NBC reconnaissance vehicle and input into electric power through structural and performance changes. Injectors are supplied exclusively by advanced companies overseas, which constitute the upper thermal weapon turning device of NBC reconnaissance vehicles. In this study, the study reflecting the shape design and structural characteristics of the hydraulic tank injector was carried out. Analysis of the required performance of the group was carried out through analysis of the sludge flow and structural analysis according to the flow of the internal oil. As a result of the structural design for the shape optimization of the injector, the performance is improved by changing the size of the inlet and outlet.

Keywords Oil tank · Injector · Structure analysis · Fluid analysis · Optimization

1 Introduction

The K200A1 is an armored vehicle used by the Republic of Korea Army, Air Force and Marine Corps. Currently, 1700 infantry transport armored vehicles and 800 affiliated vehicles are in operation [1–8]. This is evolving into a number of derived vehicles, including anti-aircraft defense, rescue, command and chemical and biological systems. The role of armored vehicles is a trend that requires and improves the protection of infantry and in each field.

S. Choi · J. Lee (✉)
School of Mechanical Engineering, Changwon National University, Changwon 51140, Korea
e-mail: jaesun@changwon.ac.kr

S. K. Sharma
Extreme Environment Design and Manufacturing Innovation Center, Changwon National University, Changwon 51140, Korea

Department of Mechanical Engineering, Amity School of Engineering and Technology, Amity University, Noida, Uttar Pradesh, India

In the case of K200 armored vehicles, which have been operated and produced since the late 1980s and were treated for regeneration, the problem of the hydraulic system has been continuously raised that the oil leaks, cupolas and pylons are not working properly due to age [9–28]. All of the internal components of the oil tank of the new Korean CBR armored vehicles (K216A1) and K200 armored vehicles are imported from Germany's MAHLE Behr, which is the original manufacturer, and supply and demand are difficult due to the export control items of the countries concerned. In 2018, K261A1 Korea's new CBR armored vehicle was required for localization, and in December 2019, localization development was approved. In order to realize self-defense, it is necessary to secure stable financing sources through localized development of domestic system companies [29–38]. There are no R&D cases for hydraulic tanks and injectors of hydraulic tanks of K200 armored vehicles.

In this study, the required performance analysis was carried out through the FEM analysis of the injectors of the K200-type armored vehicle.

2 Finite Element Modeling of Injector

2.1 Oil Tank Injector Geometry

The injectors inside the hydraulic tanks of K200 armored vehicles were modeled after 3D shape precision measurements and analyses. SM45C was used for the material of the injector inside the hydraulic tank. Details are omitted because of the characteristics of military supplies. The shape of the injector inside the hydraulic tank is shown in Fig. 1.

(a)   (b)   (c)

Fig. 1 Schematic of oil tank injector, **a** real injector, **b** 3D model in CATIA, **c** meshing model in ANSYS

Table 1 Material property of SM45C

Material	Young's modulus (GPa)	Poisson's ratio	Density (kg/m^3)	Tensile strength (MPa)	Yield strength (MPa)
SM45C	206	0.29	7600	625	530
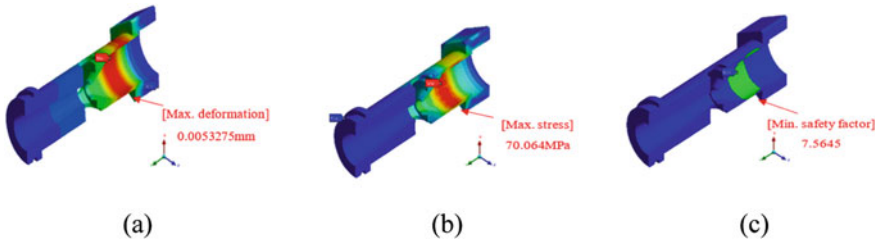
Fig. 2 Structure analysis of injector, **a** total deformation, **b** equivalent-stress, **c** safety factor

2.2 Meshing of Injector

The structure of injector was modeled by means of box-type assembly. In the primary circumstance, a mass unit was used to simulate the counterbalance. In this analysis, subspace method clubbed with preconditioned conjugate gradient (PGC) solver is preferred over subspace method. This method is also called as power dynamics method which is used for large models up to 10,00,000 degrees of freedom (DOF). The total number of nodes is 598,273, and elements are 112,477.

3 Result and Discussion

3.1 Structure Analysis

It was found that the actual max-total deformation, max-equivalent stress and min-safe factor were concentrated in the nozzle area in the injector. The results were reflected in the optimal shape design to improve internal weak areas and performance. The structure analysis results are as shown in Table 1 and Fig. 2.

3.2 Modal Analysis

Modal analysis was performed up to sixth order, and natural frequencies and shapes were generated according to each mode. In the case of actual armored vehicles, numerous parts are combined, so resonance should be feared. Otherwise, the

Table 2 Nature of frequency

Mode	1	2	3	4	5	6
Natural frequency (kHz)	7.466	7.467	11.799	11.805	14.217	17.133
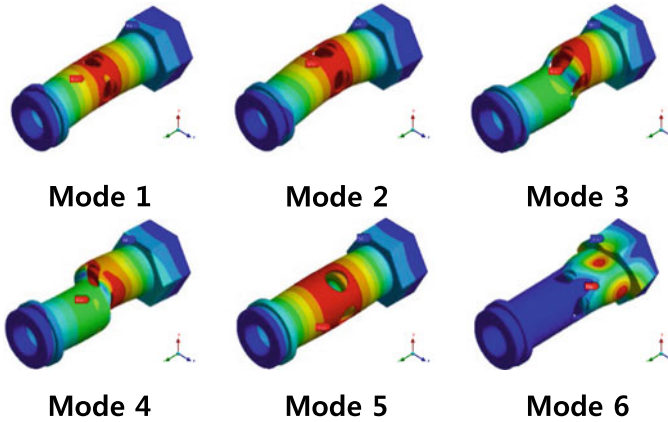
Fig. 3 Modal analysis of injector

hydraulic system will leak again. The modal analysis results of natural frequency are as listed in Table 2, and the shapes of deformations are shown in Fig. 3.

3.3 Flow Analysis

The injector is with the fluid in the hydraulic tank. In the case of older armored vehicles, various impurities and hydraulic oil are mixed, which may cause contamination of hydraulic oil and loss of hydraulic system. To prepare for this, the impurities filtering function through its own geometry was added. Flow velocity and pressure are concentrated in the nozzle area of the injector. The flow properties are listed in Table 3, and the flow analysis results are as shown in Fig. 4.

Table 3 Material property of hydraulic oil

Material	Density (kg/m^3)	Viscosity (kg·m^{-1} s^{-1})	Initial velocity (m/s)	Inlet/outlet pressure (kPa)
Hydraulic oil ISO 46	871	0.04	0.5	100
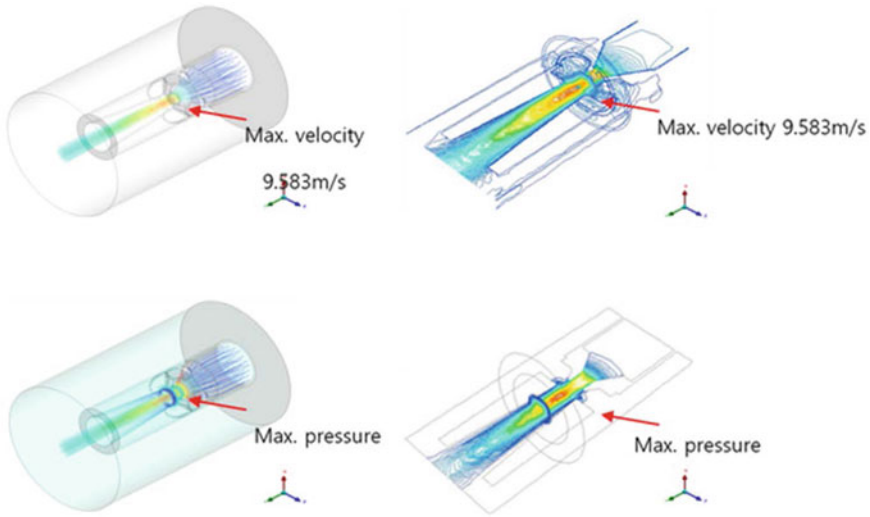
Fig. 4 Flow analysis of injector

3.4 Volume of Fluid Analysis

For the injectors inside the oil tank, the three-phase flow condition (three-phase) is a mixture of working oil, sludge and air. Volume of fluid (VOF) is used to calculate the flow at the boundary. Using this method, we checked the volume and the change in fluid volume and phase, and we used the prediction of the actual sludge path to see if the filtering function operates normally. The result is as shown in Fig. 5.

4 Conclusion

In this study, structural stability of the design model was ensured through analysis through pressure and external boundary conditions considering the internal hydraulic pressure of the injectors. Based on the results of the modal analysis, resonance avoidance design was made considering the frequency of vibration applied to the injectors.

Impurities in the fluid can be filtered through the shape of the injectors themselves. We applied welding technology to prevent hydraulic oil leakage and developed internal cross-sectional polishing process to prevent internal pressure loss and bubbles. This not only increased efficiency and durability, but also reduced load throughout the hydraulic system and further secured durability. In this study, the optimum shape derivation and design techniques were developed through FEM analysis and flow analysis. Additional research is needed to lighten up the products and apply new materials.
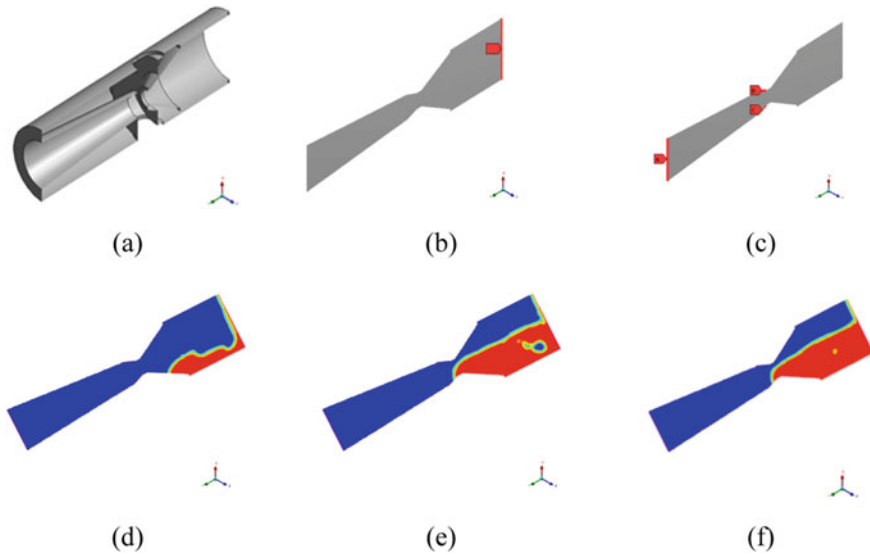
Fig. 5 Volume of fluid analysis, **a** injector model inside view, **b** inlet boundary setting, **c** outlet boundary setting, **d** initial step, **e** sludge filtering, **f** final step

Injection to the internal hydraulic pressure and to pressure and external boundary conditions through the analysis results, the design model of the structure stability was. Based on the results of the modal analysis, further research is needed for the design of resonant avoidance, lightening and applying new materials to account for the number of vibrations applied to the injector. The hydraulic tank was able to filter out impurities in the fluid through the shape of the injector itself. Also, the working hydraulic oil leakage prevention for welding technologies is applied, and the internal pressure loss and air bubbles on the internal end face polishing process were developed. This not only increased efficiency and durability, but also reduced load and added durability to all hydraulic systems. The design variables considered for the hydraulic tank inside the infuser to computational analysis and flow analysis through optimal geometry drawing and design skills developed will.

References

1. Schouveiler L, Brydon A, Leweke T, Thompson MC (2004) Interactions of the wakes of two spheres placed side by side. Eur J Mech B/Fluids 23:137–145. https://doi.org/10.1016/j.eur omechflu.2003.05.004

2. Overvelde JTB, Bertoldi K (2014) Relating pore shape to the non-linear response of periodic elastomeric structures. J Mech Phys Solids 64:351–366. https://doi.org/10.1016/j.jmps.2013.11.014
3. Park J, Lee J, Jeong S-G, Cho Y (2019) A study on guided wave propagation in a long distance curved pipe. J Mech Sci Technol 33:4111–4117. https://doi.org/10.1007/s12206-019-0806-z
4. Zhu B, Lee J (2019) A study on fatigue state evaluation of rail by the use of ultrasonic nonlinearity. Materials (Basel) 12:2698. https://doi.org/10.3390/ma12172698
5. Jeong K, Lee J, Kim T, Cho Y (2017) Aircraft component defect monitoring by the use of patch magnetostrictive EMAT. J Vis 20:847–858. https://doi.org/10.1007/s12650-017-0427-5
6. Lee J, Achenbach JD, Cho Y (2018) Use of the reciprocity theorem for a closed form solution of scattering of the lowest axially symmetric torsional wave mode by a defect in a pipe. Ultrasonics 84:45–52. https://doi.org/10.1016/j.ultras.2017.10.011
7. Li W, Cho Y, Lee J, Achenbach JD (2013) Assessment of heat treated inconel X-750 alloy by nonlinear ultrasonics. Exp Mech 53:775–781. https://doi.org/10.1007/s11340-012-9681-6
8. Lee J, Cho Y (2017) Evaluation of interface defects in inaccessible reactor shrink fit nozzle welds using ultrasonic waves. Energies 10:589. https://doi.org/10.3390/en10050589
9. Bhardawaj S, Chandmal Sharma R, Kumar Sharma S (2019) A survey of railway track modelling. Int J Vehic Struct Syst 11 (5)
10. Bhardawaj S, Sharma R, Sharma S (2020) Ride analysis of track-vehicle-human body interaction subjected to random excitation. J Chin Soc Mech Eng 41(2):236–237
11. Bhardawaj S, Sharma RC, Sharma SK (2020) Analysis of frontal car crash characteristics using ANSYS. Mater Today: Proc 25:898–902
12. Bhardawaj S, Sharma RC, Sharma SK (2020) Development in the modeling of rail vehicle system for the analysis of lateral stability. Mater Today: Proc 25:610–619
13. Bhardawaj S, Sharma S, Sharma R (2020) Development of multibody dynamical using mr damper based semi-active bio-inspired chaotic fruit fly and fuzzy logic hybrid suspension control for rail vehicle system. Proc Inst Mech Eng Part K: J Multi-body Dyn
14. Dao DK, Ngo V, Phan H, Pham CV, Lee J, Bui TQ (2020) Rayleigh wave motions in an orthotropic half-space under time-harmonic loadings: a theoretical study. Appl Math Model 87:171–179
15. Goyal S, Anand CS, Kumar S, Chandmal R (2019) Thin-walled structures crashworthiness analysis of foam filled star shape polygon of thin-walled structure. Thin-Walled Struct 144
16. Kanth Choppara R, Chandmal Sharma R, Kumar Sharma S, Gupta T (2019) Aero dynamic cross wind analysis of locomotive. IOP Conf Ser Mater Sci Eng 691: 012035
17. Lee J, Ngo V, Phan H, Nguyen T, Dao DK, Cho Y (2019) Scattering of surface waves by a three-dimensional cavity of arbitrary shape: analytical and experimental studies. Appl Sci 9(24):5459
18. Palli S, Koona R, Sharma SK, Sharma RC (2018) A review on dynamic analysis of rail vehicle coach. Int J Vehic Struct Syst 10(3):204–211
19. Park J, Lee J, Jeong S-G, Cho Y (2019) A study on guided wave propagation in a long distance curved pipe. J Mech Sci Technol 33(9):4111–4117
20. Park J, Lee J, Le Z, Cho Y (2020) High-precision noncontact guided wave tomographic imaging of plate structures using a DHB algorithm. Appl Sci 10(12):4360
21. Park J, Lee J, Min J, Cho Y (2020) Defects inspection in wires by nonlinear ultrasonic-guided wave generated by electromagnetic sensors. Appl Sci 10(13):4479
22. Sharma RC, Palli S, Sharma SK, Roy M (2017) Modernization of railway track with composite sleepers. Int J Vehic Struct Syst 9(5):321–329
23. Sharma RC, Sharma S, Sharma SK, Sharma N (2020) Analysis of generalized force and its influence on ride and stability of railway vehicle. Noise Vibr Worldwide 51(6):95–109
24. Sharma RC, Sharma SK (2018) Sensitivity analysis of three-wheel vehicle's suspension parameters influencing ride behavior. Noise Vibr Worldwide 49(7–8):272–280
25. Sharma RC, Sharma SK, Palli S (2018) Rail vehicle modelling and simulation using lagrangian method. Int J Vehic Struct Syst 10(3):188–194

26. Sharma SK (2019) Multibody analysis of longitudinal train dynamics on the passenger ride performance due to brake application. Proc Inst Mech Eng Part K: J Multi-body Dyn 233(2):266–279
27. Sharma SK, Kumar A (2014) A comparative study of Indian and worldwide railways. Int J Mech Eng Robot Res 1(1):114–120
28. Sharma SK, Kumar A (2018) Disturbance rejection and force-tracking controller of nonlinear lateral vibrations in passenger rail vehicle using magnetorheological fluid damper. J Intell Mater Syst Struct 29(2):279–297
29. Sharma SK, Kumar A (2016) Dynamics analysis of wheel rail contact using FEA. Proced Eng 144:1119–1128
30. Sharma SK, Kumar A (2017) Impact of electric locomotive traction of the passenger vehicle Ride quality in longitudinal train dynamics in the context of Indian railways. Mech Industr 18(2):222
31. Sharma SK, Kumar A (2018) Impact of longitudinal train dynamics on train operations: a simulation-based study. J Vibr Eng Tech 6(3):197–203
32. Sharma SK, Kumar A (2018) Ride comfort of a higher speed rail vehicle using a magnetorheological suspension system. Proc Inst Mech Eng Part K: J Multi-body Dyn 232(1):32–48
33. Sharma SK, Kumar A (2017) Ride performance of a high speed rail vehicle using controlled semi active suspension system. Smart Mater Struct 26(5):055026
34. Sharma SK, Phan H, Lee J (2020) An application study on road surface monitoring using DTW based image processing and ultrasonic sensors. Appl Sci 10(13):4490
35. Sharma SK, Saini U, Kumar A (2019) Semi-active control to reduce lateral vibration of passenger rail vehicle using disturbance rejection and continuous state damper controllers. J Vibr Eng Tech 7(2):117–129
36. Sharma SK, Sharma RC (2018) An investigation of a locomotive structural crashworthiness using finite element simulation. SAE Int J Commer Vehic 11(4):02-11-04–0019
37. Sharma SK, Sharma RC (2018) Simulation of quarter-car model with magnetorheological dampers for ride quality improvement. Int J Vehic Struct Syst 10(3):169–173
38. Sharma SK, Sharma RC, Kumar A, Palli S (2015) Challenges in rail vehicle-track modeling and simulation. Int J Vehic Struct Syst 7(1):1–9

A Two-Field Formulation in Isogeometric Analysis to Alleviate Locking

Dhiraj S. Bombarde, Arup Nandy, and Sachin S. Gautam

Abstract In recent past, isogeometric analysis (IGA) has gained significant popularity as a numerical technique in computational mechanics. The systematic framework of IGA allows maintaining the exact geometry during discretization regardless of how coarse the mesh is, and furthermore, it also eliminates the dependency on computer-aided design (CAD) once the initial mesh is created. IGA often referred as a generalized version of finite element analysis (FEA) or with a different perspective FEA can be seen as a special case of IGA. Though IGA performs superior to FEA in several ways, it does exhibit similar limitations sooner or later like its FE counterpart. One such limitation is locking which appears during the analysis of thin structural parts and for incompressible or nearly incompressible material. However, on the promising side, the techniques available in FEA to tackle such limitations can be successfully modified to work with IGA as well. In the present work, a two-field hybrid formulation is explored in the framework of IGA which performs convincingly well in situations where the problem demands incompressibility or near incompressibility of material or to solve problems of beam/plate/shell geometries and so on. As per our best knowledge, the stated method is yet to be studied in context of IGA, despite the fact that the same formulation will eliminate different types of locking. Finally, the proposed formulation has been successfully implemented on several examples with promising results.

Keywords Isogeometric analysis · Two-field variation principle · Hybrid stress NURBS elements · Locking

D. S. Bombarde (✉) · A. Nandy · S. S. Gautam
Department of Mechanical Engineering, Indian Institute of Technology Guwahati, Guwahati, Assam 781039, India
e-mail: dhiraj.bombarde@yahoo.com

A. Nandy
e-mail: arupn@iitg.ac.in

1 Introduction

The concept of IGA was introduced by Hughes et al. in 2005 with the notion of integrating CAD with FEA [1]. The preliminary idea was to incorporate non-uniform rational B-splines (NURBS) into the framework of IGA. NURBS are extensively used in engineering design with advantages of modeling free form surfaces, accurately representing conic sections like circle, sphere, cylinder, etc., and existence of numerous effective and numerically stable algorithms. Along with these, they also retain essential mathematical properties like non-negativity of basis functions, linear independence, partition of unity, and variation diminishing property [2]. Due to the above merits, NURBS became a foundation for an IGA background. Since its introduction in 2005, IGA has been widely practiced along different directions. Ever since, IGA proved to be a powerful method, which out-performs FEA in most of the numerical aspects.

This is being said that existing limitations in conventional FEA may pass on to its more generalized version, i.e., IGA. Even though IGA performs superior to FEA in several ways, it does exhibit similar limitations sooner or later like its FE counterpart. One such phenomenon is locking which appears during the analysis of thin beam, plates, or shells and incompressible material behavior [3]. However, on the bright side, remedies that exist to overcome these limitations in conventional FEA can be successfully modified to work with IGA. Various methods such as selective or reduced integration, $\bar{B}$ and $\bar{F}$ methods, enhanced assumed strain methods (EAS), assumed natural strain methods (ANS), solid shell elements, and many more which were initially developed to tackle locking issue in FEA work promising with IGA as well [13]. Each of these methods has their advantages along with certain limitations. Furthermore, most of these mixed formulations are strain-based approach, and less focus has been given to the stress-based formulation.

In this paper, we are proposing a class of hybrid stress formulation, which was initially implemented in FEA to overcome the locking in thin plate and shell problems, into the framework of NURBS based IGA. These hybrid elements are derived based on a two-field mixed variational principle, one being displacement and other is stress. Elements developed by this theory perform quite well irrespective of the type of locking. The same element can be used in situations where problem demand incompressibility, or near incompressibility of material or to solve plate/shell geometries and so on [4–9]. Another advantage of hybrid formulation is no energy, or work principle or variational norms has been violated, and hence, mathematically robust formulation is obtained. This paper highlights the concepts involved in hybrid IGA formulation and successful implementation of the stated method on numerous benchmark examples.

2   A Brief Overview of a Conventional Single Field IGA Formulation

Let us consider domain Ω with boundary Γ. Boundary Γ is composed of two disjoint regions such that $\Gamma = \Gamma_u \cup \Gamma_t$ where Γ_u is displacement boundary and Γ_t is traction boundary. The governing equation for the problem is given as

$$\nabla \cdot \boldsymbol{\tau} + \boldsymbol{f} = 0 \text{ on } \Omega, \tag{1}$$

$$\boldsymbol{\tau} \boldsymbol{n} = \boldsymbol{t} \text{ on } \Gamma, \tag{2}$$

$$\boldsymbol{u} = \boldsymbol{u}_0 \text{ on } \Gamma_u, \tag{3}$$

$$\boldsymbol{t} = \bar{\boldsymbol{t}} \text{ on } \Gamma_t \tag{4}$$

where $\boldsymbol{\tau}$ is the Cauchy stress tensor, $\boldsymbol{n}$ is the unit outward normal to Γ, $\bar{\boldsymbol{t}}$ is traction defined on boundary Γ_t, and $\boldsymbol{f}$ is the body force vector [10]. Similar to conventional FEA, IGA uses the same basis functions to approximate both dependent variable as well as geometry, but IGA selects the basis which are capable of representing the geometry exactly. For the stated two-dimensional problem, the displacement and its variation are approximated with bivariate NURBS basis functions (R_I) as,

$$\boldsymbol{u} = \sum_{I=1}^{n_{cp}^e} R_I U_I = \boldsymbol{R} \boldsymbol{U} \quad \therefore \delta \boldsymbol{u} = \sum_{I=1}^{n_{cp}^e} R_I \delta U_I = \boldsymbol{R} \delta \boldsymbol{U} \tag{5}$$

where I is the global numbering associated with the control point net. n_{cp}^e is the total number of control points per element.

Let $\tilde{\boldsymbol{\epsilon}}$ and $\boldsymbol{\sigma}$ be the engineering form of strain and stress components such that $\boldsymbol{\sigma} = \boldsymbol{C}\tilde{\boldsymbol{\epsilon}}$ and $\tilde{\boldsymbol{\epsilon}}(\boldsymbol{u}) = \boldsymbol{B}\boldsymbol{U}$. Following the similar approach as standard FEA, NURBS based isogeometric element stiffness matrix ($\boldsymbol{K}^e$), element displacement vector ($\boldsymbol{U}^e$), and element force vector ($\boldsymbol{F}^e$) are formed and assembled over the complete domain [11].

3   The Two-Field Hybrid Stress IGA Formulation

Hybrid finite elements are the most accurate class of finite elements as compared to displacement-based elements. They are not prone to different types of locking and performs well, even when the problem demands almost incompressibility or incompressibility, or in case of thin geometries. The presented hybrid elements are developed with the two-field mixed finite element formulation where stress and

displacement are considered as the field variables. Such formulations differ from plate and shell theories in a sense that rather going for complex derivations, one can achieve a similar accuracy with the convenience of displacement-based formulation, and moreover, it is not limited to thin structures. In view of computational efficiency, the proposed formulation is expensive. However, this limitation is compensated with coarse mesh accuracy as well as the versatility of the method to be used in a wide variety of problem domains without introducing any special treatments into the formulation.

Let $\delta\boldsymbol{u}$ and $\delta\boldsymbol{\sigma}$ represents the variation of the displacement field $\boldsymbol{u}$ and stress field $\boldsymbol{\tau}$, respectively, in such a way that,

$$V_{\boldsymbol{u}} = \left\{\delta u_i \in \boldsymbol{H}^1(\boldsymbol{\Omega}), \quad i = 1, 3 : \quad \delta\boldsymbol{u} = 0 \text{ on } \Gamma_{\mathrm{u}}\right\}, \tag{6}$$

$$V_{\boldsymbol{\tau}} = \left\{\delta\sigma_{ij} \in \boldsymbol{L}^2(\boldsymbol{\Omega}), \quad i, j = 1, 3 : \quad \delta\boldsymbol{\sigma} = \delta\boldsymbol{\sigma}^{\mathrm{T}}\right\} \tag{7}$$

After enforcing Eqs. (1), (4) and $\boldsymbol{\epsilon} = \frac{1}{2}\left[(\nabla\boldsymbol{u}) + (\nabla\boldsymbol{u})^t\right]$ in a weak sense, with Eq. (2) and $\boldsymbol{\tau} = \boldsymbol{C} : \boldsymbol{\epsilon}$ imposed in a strong sense and if $(\delta\boldsymbol{u}, \delta\boldsymbol{\sigma}) \in (\boldsymbol{V}_{\boldsymbol{u}} \times \boldsymbol{V}_{\boldsymbol{\tau}})$ denotes the variations of displacement and stress fields, respectively, then the weak enforcement of the equations governing the stated two-dimensional problem yields in

$$\int_{\Omega} \delta\boldsymbol{u} \cdot (\nabla \cdot \boldsymbol{\tau} + \boldsymbol{b})\mathrm{d}\Omega + \int_{\Gamma_t} \delta\boldsymbol{u} \cdot (\bar{\boldsymbol{t}} - \boldsymbol{t})\mathrm{d}\Gamma + \int_{\Gamma} \delta\boldsymbol{\sigma} : \left[\int \boldsymbol{\epsilon}(\boldsymbol{u}) - \boldsymbol{C}^{-1}\boldsymbol{\tau}\right]\mathrm{d}\Omega = 0 \ \ \forall(\delta\boldsymbol{u}, \delta\boldsymbol{\sigma}) \in (\boldsymbol{V}_{\boldsymbol{u}} \times \boldsymbol{V}_{\boldsymbol{\tau}}) \tag{8}$$

By using the identity $\nabla \cdot (\boldsymbol{\tau}^{\mathrm{T}}\delta\boldsymbol{u}) = \delta\boldsymbol{u} \cdot (\nabla \cdot \boldsymbol{\tau}) + \nabla\delta\boldsymbol{u} : \boldsymbol{\tau}$, the symmetry of stress tensor followed by the divergence theorem, and after satisfying the two cases $(\delta\boldsymbol{u}, \delta\boldsymbol{\sigma}) = (0, \delta\boldsymbol{\sigma})$ and $(\delta\boldsymbol{u}, \delta\boldsymbol{\sigma}) = (\delta\boldsymbol{u}, 0)$, the above equation simplifies to

$$\int_{\Omega} \delta\boldsymbol{\sigma}_c^{\mathrm{T}}\left[\bar{\boldsymbol{\epsilon}}_c(\boldsymbol{u}) - \boldsymbol{C}^{-1}\boldsymbol{\tau}_c\right]\mathrm{d}\Omega = 0 \ \ \forall\delta\boldsymbol{\sigma}_c, \tag{9}$$

$$\int_{\Omega} [\bar{\boldsymbol{\epsilon}}_c(\delta\boldsymbol{u})]^{\mathrm{T}}\boldsymbol{\tau}_c\mathrm{d}\Omega = \int_{\Omega} \delta\boldsymbol{u}^T\boldsymbol{b} \ \mathrm{d}\Omega + \int_{\Gamma_t} \delta\boldsymbol{u}^{\mathrm{T}}\bar{\boldsymbol{t}}\mathrm{d}\Gamma \ \ \forall\delta\boldsymbol{u} \in \boldsymbol{V}_{\boldsymbol{u}}, \tag{10}$$

where $\bar{\boldsymbol{\epsilon}}_c$ and $\bar{\boldsymbol{\tau}}_c$ denotes the strain tensor and stress tensor, expressed in engineering form. The interpolation for displacement ($\boldsymbol{u}$) and its variation ($\delta\boldsymbol{u}$) are given by Eq. (5), and stress fields ($\boldsymbol{\tau}_c$) and its variations ($\delta\boldsymbol{\sigma}_c$) are interpolated as

$$\boldsymbol{\tau}_c = \boldsymbol{P}\widehat{\boldsymbol{\beta}}, \delta\boldsymbol{\sigma}_c = \boldsymbol{P}\widehat{\boldsymbol{\gamma}} \tag{11}$$

Next important entity in presented formulation is the stress interpolation matrix ($\boldsymbol{P}$). Choice of $\boldsymbol{P}$ significantly affect the accuracy of the solution. For the proposed

class of hybrid formulation, P is derived as per the guidelines specified by Jog [4, 6] corresponding to NURBS basis functions rather than Lagrangian basis functions. Moreover, contrary to conventional two-field FEA formulation, P is defined in master space rather than in a parametric space. Its mapping to the physical space is taken care by the transformation matrix (T) derived from a combination of Jacobians relating the corresponding spaces. Jacobian which relates the master space and the physical space is $J = J_1 J_2$, where J_1 and J_2 are the Jacobians for mapping master space to parametric space and parametric space to physical space, respectively.

Let $P(\widetilde{\xi}, \widetilde{\eta})$ be the stress interpolation matrix in a master space $(\widetilde{\xi} - \widetilde{\eta})$. T is the transformation matrix which maps P to the physical space $(x - y)$ in such a way that,

$$P(x, y) = T P(\widetilde{\xi}, \widetilde{\eta}) \tag{12}$$

Finally, substituting Eqs. (5), (11), and (12) into Eqs. (9), (10), and invoking the arbitrariness of δu and $\delta \sigma$, Eqs. (9) and (10) can be written into a matrix form as,

$$\begin{bmatrix} -H & G \\ G^T & 0 \end{bmatrix} \begin{bmatrix} \widehat{\beta} \\ U \end{bmatrix} = \begin{bmatrix} \widehat{g} \\ \widehat{f} \end{bmatrix} \tag{13}$$

where with B as the strain displacement matrix, and S indicating the material compliance matrix. The matrix entities of Eq. (13) can be derived as,

$$H = \int_\Omega P^T S P \mathrm{d}\Omega, \, G = \int_\Omega P^T B \mathrm{d}\Omega, \, \widehat{g} = 0, \quad \widehat{f} = \int_\Omega R_u^T b \mathrm{d}\Omega + \int_{\Gamma_t} R_u^T \overline{t} \mathrm{d}\Gamma \tag{14}$$

Eliminating $\widehat{\beta}$ in the system of Eq. (13) leads to

$$KU = \widehat{f} \text{ where, } K = G^T H^{-1} G \tag{15}$$

Since the stress interpolations are chosen in such a way that they are not necessarily continuous across element boundaries, H^{-1} is performed at the element level (Ω_e). Thus, the elemental stiffness matrix is given by

$$K_e = G_e^T H_e^{-1} G_e \text{ where } H_e = \int_{\Omega_e} P_e^T S P_e \mathrm{d}\Omega, \, G_e = \int_{\Omega_e} P_e^T B_e \mathrm{d}\Omega, \tag{16}$$

4 Numerical Examples

4.1 Straight Cantilever Beam

In the first example, a linear elastic behavior of a two-dimensional straight cantilever beam is investigated in order to test reliability of the proposed formulation under locking situation. The problem is composed of a straight beam subjected to vertical traction on one end and fixed on the other end as illustrated in Fig. 1. F_y is the magnitude of the load at the free end, v is Poisson's ratio, and E is Young's modulus. The thickness of the beam is considered significantly small as compared to other dimension to activate the transverse shear locking effect in conventional IGA formulation. Different meshes are used in the analysis, starting from the coarsest (linear NURBS basis with only one element) to quadratic and cubic basis obtained from degree elevation of the coarsest mesh followed by h-refinement. One such mesh is shown in Fig. 2. From the Timoshenko-beam theory, vertical displacement at 'A' can be calculated as 216.3024 mm.

The proposed formulation is implemented to numerically compute the vertical displacement at point 'A' alongside reference solution, and the results are presented in Fig. 3. It can be clearly seen that the conventional IGA with linear NURBS basis locks severely, and significant high number of elements are needed to get the solution which is to some extent near to the analytical solution. On the other hand, the proposed hybrid IGA formulation converges to the solution in fairly coarse mesh. Though,
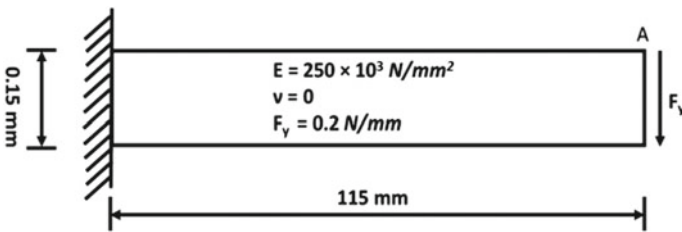
Fig. 1 A straight cantilever beam, material data, and boundary conditions
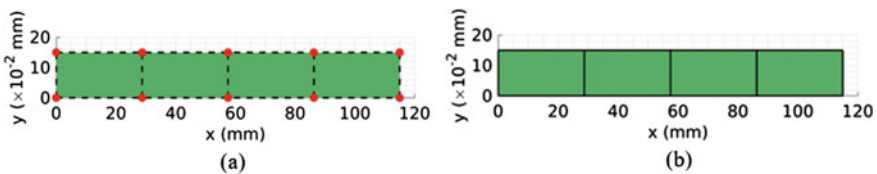
Fig. 2 **a** A physical geometry along with control point mesh, **b** discretized domains consisting four linear NURBS elements obtained by h-refinement of coarsest mesh ($\Xi = \{0, 0, 1, 1\}$, $H = \{0, 0, 1, 1\}$, $p = 1$, $q = 1$ where Ξ, H and p, q are knot vector and degree of basis function in ξ and η direction. Control points = (0, 0), (115, 0), (0, 0.15), (115, 0.15) with weights = 1)
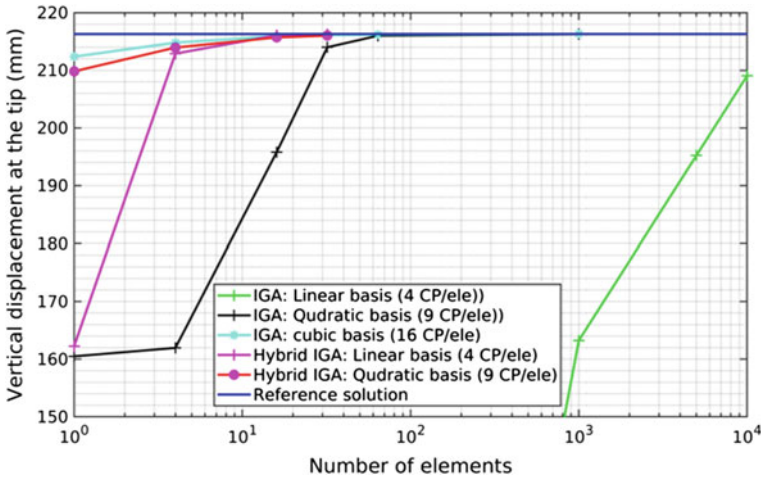
Fig. 3 Comparison of conventional and hybrid IGA for thin cantilever beam

higher order basis functions converge to the solution with less number of elements even in conventional IGA, the proposed hybrid IGA formulation out-performs the results with better coarse mesh accuracy alleviating the transverse shear locking.

4.2 Cook's Membrane Problem

The stated benchmark problem is admired in various literatures to test the performance of the numerical formulation for nearly incompressible material under combined bending and shear as a typical case of volumetric locking [12]. The Cook's membrane problem consists of a tapered plate fixed at one end and subjected to a uniformly distributed shear loading on the other end under plane strain condition. The setup and the boundary conditions are described in Fig. 4. F_y is the magnitude of the load at free end, v is Poisson's ratio, and E is Young's modulus. Similar to the previous problem, this has been solved with both conventional and proposed formulation for different mesh sizes and order of NURBS basis functions. One such mesh is illustrated in Fig. 5.

Vertical tip displacement at point 'A' is computed for various mesh sizes and order of NURBS basis functions and documented in Fig. 6. Once again, the conventional IGA with linear NURBS basis is severely susceptible toward volumetric locking. Higher order IGA though reduces the effect of volumetric locking but with additional computing cost. On the other hand, hybrid IGA performs well irrespective of order of basis function. For the matter of fact, even with linear basis and significant coarse mesh, the proposed formulation is tending to perform promisingly.

Fig. 4 A Cooks's membrane problem, material data and boundary conditions

$E = 250\ N/mm^2$
$v = 0.4999$
$F_y = 6.25\ N/mm$

16 mm

44 mm

48 mm

(a)

(b)
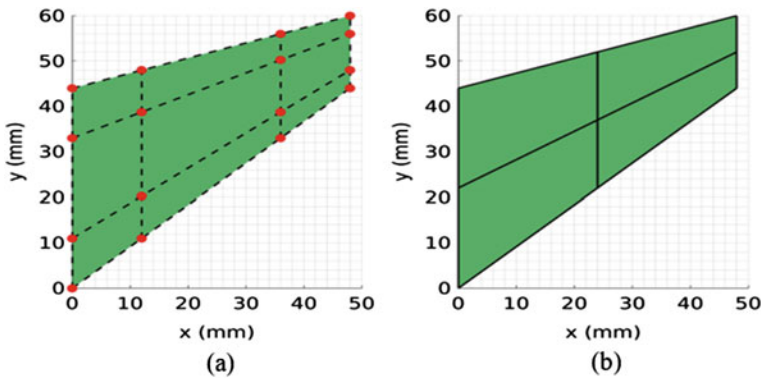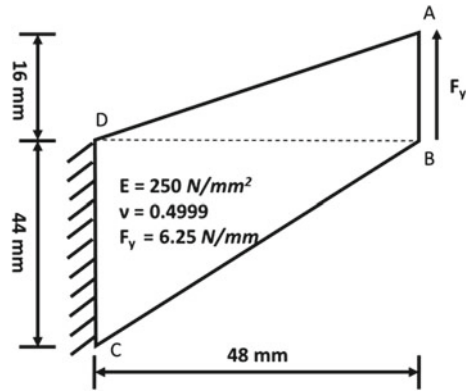
Fig. 5 a A physical geometry along with control point mesh, **b** discretized domains consisting four quadratic NURBS elements obtained by order elevation followed by h-refinement of coarsest mesh ($\Xi = \{0, 0, 1, 1\}$, $H = \{0, 0, 1, 1\}$, $p = 1, q = 1$ where Ξ, H and p, q are knot vector and degree of basis function in ξ and η direction. Control points = (0, 0), (48, 44), (0, 44), (48, 60) with weights = 1)

5 Conclusion

In this paper, a two-field hybrid stress formulation is implemented in context of NURBS based IGA to alleviate different types of locking in two-dimensional linear elastic problems. The results for typical benchmark locking problems confirm the effectiveness of the proposed method. A relatively simple formulation, comprising only displacement degree of freedom at the global level, works well for analyzing nearly incompressible problem domains as well as for thin plate and shell problems. Another added advantage is that the same formulation can be implemented for standard problems (absence of locking effect) without affecting the solution accuracy.

Fig. 6 Comparison of conventional and hybrid IGA for Cook's membrane problem
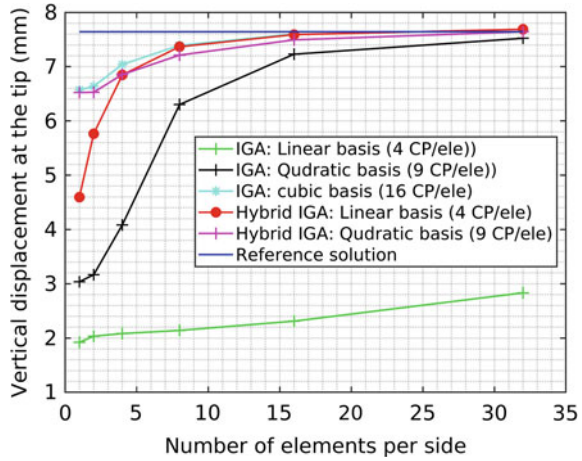
Extension of the proposed formulation for two-dimensional nonlinear domain and eventually to three-dimensional linear and nonlinear domain would be of interest for further study.

References

1. Hughes TJR, Cottrell JA, Bazilevs Y (2005) Isogeometric analysis: CAD, finite elements, NURBS, exact geometry and mesh refinement. Comput Methods Appl Mech Eng 194:4135–4195
2. Piegl L, Tiller W (1997) The NURBS book, 2nd edn. Springer, NewYork
3. Echter R, Bischoff M (2010) Numerical efficiency, locking and unlocking of NURBS finite elements. Comput Methods Appl Mech Eng 199:374–382
4. Jog CS (2005) A 27-node hybrid brick and a 21-node hybrid wedge element for structural analysis. Finite Elem Anal Des 41:1209–1232
5. Jog CS, Kelkar PP (2006) Non-linear analysis of structures using high performance hybrid elements. Int J Numer Methods Eng 68:473–501
6. Jog CS (2010) Improved hybrid elements for structural analysis. J Mech Mater Struct 5:507–528
7. Agrawal M, Nandy A, Jog CS (2019) A hybrid finite element formulation for large-deformation contact mechanics. Comput Methods Appl Mech Eng 356:407–434
8. Roychowdhury A, Nandy A, Jog CS, Pratap R (2014) Hybrid elements for modelling squeeze film effects coupled with structural interactions in vibratory MEMS devives. CMES 1:1–15
9. Jog CS, Nandy A (2015) Conservation properties of the trapezoidal rule in linear time domain analysis of acoustics and structures. J Vib Acoust Trans ASME 137:1–17
10. Bathe KJ (1996) Finite element procedures. Prentice-Hall, New Jersey
11. Agrawal V, Gautam SS (2018) IGA: a simplified introduction and implementation details for finite element users. J Inst Eng Ser C
12. Elguedj T, Bazilevs Y, Calo VM, Hughes TJR (2008) B bar and F bar projection methods for nearly incompressible linear and non-linear elasticity and plasticity using higher-order NURBS elements. Comput Methods Appl Mech Eng 197:2732–2762
13. Nguyen VP, Anitescu C, Bordas SPA, Rabczuk T (2015) Isogeometric analysis: an overview and computer implementation aspects. Math Comput Simul 117:89–116

Influence of Process Parameters on Reinforcement Height of Tungsten Inert Gas Welded Joints for Low Carbon Steel AISI 1010 Plates

R. P. Singh, Ashu Kumar Verma, Abhishek Mishra, and Abhishek Chauhan

Abstract In this work, Tungsten Inert Gas Welding process was used to analyze the effect of input process parameters on reinforcement height of the weld. The input process parameters were used as current, voltage, speed of welding, and the feed rate. Low carbon steel AISI 1010 plates of dimensions 75 mm × 50 mm × 5 mm were used to obtain the weld. Total of 16 pairs of plates was welded to obtain 16 welds using the tungsten inert gas welding process. At first current, voltage, and speed of welding were kept at constant values and the feed rate was varied one by one as 2.12 mm/s, 4.23 mm/s, 6.35 mm/s, and 8.47 mm/s, respectively, for 4 welds. In each case, the reinforcement height was measured. This was used to investigate the effect of feed rate on reinforcement height. In a similar manner other 3 sets, each having 4 welds were used to investigate the effect of welding speed, welding voltage, and welding current on reinforcement height respectively by keeping other variables at some fixed values. The results were tabulated and were expressed in 4 diagrams to investigate the effect of feed rate, welding speed: welding voltage and welding current on reinforcement height in each case. Generally, the reinforcement height increased with increase of current, voltage, and feed rate and decreased with welding speed in the present work.

Keywords Tungsten inert gas welding · Reinforcement height · Weld bead · Input process parameters · Travel speed · Welding torch

1 Introduction

Welding is used to join different materials permanently in which at the interface of the workpieces, melting and solidification take place. There are several methods of welding, in which some use and some do not use filler materials [1]. Tungsten inert gas welding is used to join the materials sometimes with and sometimes without filler materials [2]. The aim of the formation of any joint is to make it strong enough

R. P. Singh · A. K. Verma (✉) · A. Mishra · A. Chauhan
Department of Mechanical Engineering, GLAU, Mathura 281406, India
e-mail: ashu.verma_me17@gla.ac.in

to sustain the loads applied to it. If we consider different joining processes, welding is the cheapest of all [3]. All the materials cannot be welded by a single method as the weldability of different materials differs from the applied welding process. Therefore, the different welding processes are used in the manufacturing and general machine repair work [4]. During welding very high temperature is developed, so if nonconsumable electrode is to be used a material having a very high melting point is required [5]. Tungsten has a very high melting point and will not melt during welding. The process in which tungsten is used as an electrode is known as tungsten inert gas welding process. In this process, a mixture of argon and helium gasses is used to form a shielding atmosphere to protect the weld metal from atmospheric gasses. At high temperatures the atmospheric gasses may react with the hot weld metal and form contaminations [6]. Very sensitive materials that cannot be welded with other processes can be welded efficiently using tungsten inert gas welding process due to strong shielding atmosphere. During the Second World War, this process was developed to weld aluminum, magnesium, stainless steel, and mild steel, etc. efficiently [7]. Tungsten inert gas welding process generally works on constant current characteristics as in manual welding the control overvoltage is difficult, so constant voltage process becomes difficult [8]. If the tungsten electrode is connected to the negative terminal of DC current supply, the heat received by the electrode is only 30% of total heat generated and the life of electrode is more [9]. The main input welding parameters are welding current, voltage, speed of welding, and feed rate. These parameters control the structural and mechanical properties of the weld. If the voltage is increased the arc length increases and weld width also increases. The welding current has direct effect on heat supplied to the weld area and depth of penetration. Speed of welding reduces the heat input and feed rate affects the volume deposited on bead. The mechanical properties depend on the structure of the weld. The macroscopic structural output parameters of welding are weld width, depth of penetration, and reinforcement height. Reinforcement height should be optimum. It should not be very large to reduce the stress concentration, but the metallurgical concept allows the large value of the reinforcement height. In this way, the determination of optimum reinforcement height is very important and should be researched.

2 Experimental Procedure

The experiments were performed in the welding science and technology lab of the GLA University, Mathura. The welding of specimens was done with the help of a tungsten inert gas welding process. The specimen pieces were cut from a large thin low carbon steel AISI 1010 plate having 50 mm width and 5 mm thickness, with the help of a power hack saw. The dimensions of the specimens were taken as 75 mm × 50 mm × 5 mm. The specimens were cleaned with the help of rough and hard papers to remove rust, dust, and contaminated surface layers. The sensitivity analysis of the input parameters on the reinforcement height with 4 input welding parameters

requires 16 welded pieces in this work. To obtain 16 welds, thirty-two pieces, each of dimensions 75 mm × 50 mm × 5 mm were cut. Two pieces were welded in the butt position to obtain the required bead. The used power source was a rectifier from which the power was supplied to the workpieces with the help of a system having torch and tungsten electrode. An electric arc was developed between the workpiece and the tungsten electrode. The energy was supplied through the arc and a column of highly ionized gas and metal vapors. The temperature of more than 20,000 °C is developed in TIG welding process. The high amount of heat, so developed was used to melt the material and to form the joint. The schematic diagram of a TIG welding system is shown in Fig. 1, and some welded pieces are shown in Fig. 2.

In this work four input welding variables selected were current, voltage, speed of welding, and feed rate. The sensitivity analysis can be done if all the input parameters are fixed and only one parameter is altered and the effect of this alteration is analyzed.
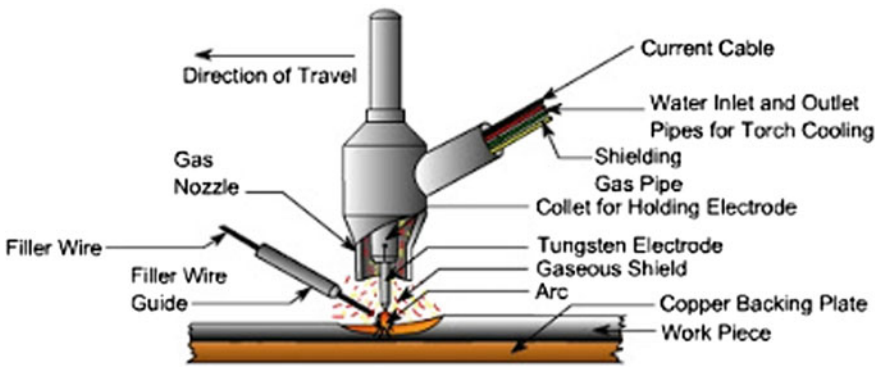
Fig. 1 Schematic diagram of TIG welding system [4]
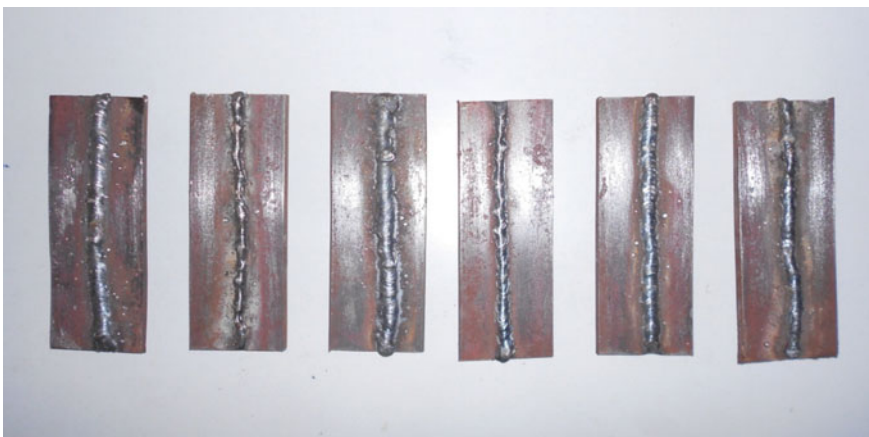
Fig. 2 Some welded pieces

At first, four sets of welds were obtained by having welding current at 150 A, welding voltage at 9.6 V, welding speed at 1.91 mm/s. Only feed rate was altered as 2.12 mm/s, 4.23 mm/s, 6.35 mm/s, and 8.47 mm/s, respectively, for the welding process. Four sets of welds were obtained by having welding current at 100 A, welding voltage at 9 V, and feed rate at 2.12 mm/s. Only welding speed was altered as 1.19 mm/s, 1.44 mm/s, 1.82 mm/s, and 1.91 mm/s respectively for the welding process. Four sets of welds were obtained by having welding current at 100 A, welding speed at 1.19 mm/s, and feed rate at 8.47 mm/s. Only welding voltage was altered as 9 V, 9.6 V, 10 V, and 10.5 V, respectively, for the welding process. Other four sets of welds were obtained by having welding voltage at 9.6 V, welding speed at 1.44 mm/s, and feed rate at 6.35 mm/s. The only welding current was altered as 100 A, 125 A, 150 A, and 200 A respectively for the welding process.

These data were arranged in Table 1. After welding, all the weld beads obtained were sectioned transversely at two surfaces in such a way that the middle portion, 1 mm thick containing weld, heat-affected zone, and base metal were selected for investigation. The welds are generally not proper at the start and at end of the work-pieces due to several reasons, so these portions are removed. The sectioned parts were ground with the help of emery belt grinders of grades 0, 2, and 3 so that weld bead dimensions become clear and visible. The ground portions were polished with double disk polishing machine. Etching process was done to the polished pieces with the help of a mixture of 2% nitric acid and 98% ethyl alcohol solution. The reinforcement height was measured for every weld with the help of digital sliding

Table 1 Variation of reinforcement height with current, voltage, speed of welding and feed rate

S. No.	Current (A)	Voltage (V)	Welding speed (mm/s)	Feed rate (mm/s)	Reinforcement height (mm)
1	150	9.6	1.91	2.12	0.38
2	150	9.6	1.91	4.23	0.65
3	150	9.6	1.91	6.35	0.87
4	150	9.6	1.91	8.47	1.03
5	100	9	1.19	2.12	0.60
6	100	9	1.44	2.12	0.55
7	100	9	1.82	2.12	0.47
8	100	9	1.91	2.12	0.45
9	100	9	1.19	8.47	1.90
10	100	9.6	1.19	8.47	1.91
11	100	10	1.19	8.47	1.93
12	100	10.5	1.19	8.47	1.99
13	100	9.6	1.44	6.35	0.79
14	125	9.6	1.44	6.35	0.87
15	150	9.6	1.44	6.35	0.96
16	200	9.6	1.44	6.35	0.98

caliper and arranged in Table 1. The effect of individual parameters on reinforcement height can be easily analyzed with this table.

3 Result and Discussion

The effect of individual parameter on the reinforcement height can be understood with the help of Figs. 3, 4, 5, and 6 and can be summarized as:

3.1 Effect of Feed Rate on Reinforcement Height

The measurements of reinforcement height for all the weld beads were done using a sliding digital caliper. The results were written in Table 1. From the table sensitivity analysis was done. If the input current, input voltage, and welding speed were fixed

Fig. 3 Effect of feed rate on reinforcement height
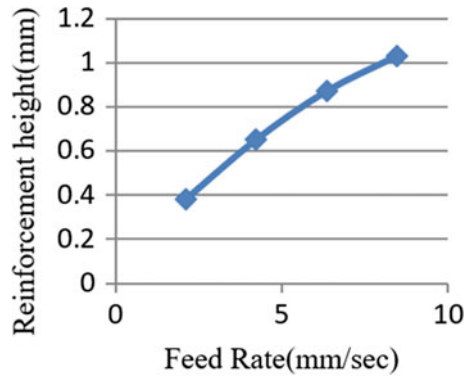
Fig. 4 Effect of welding speed on reinforcement height
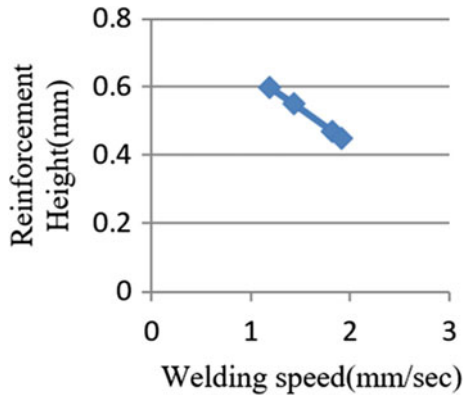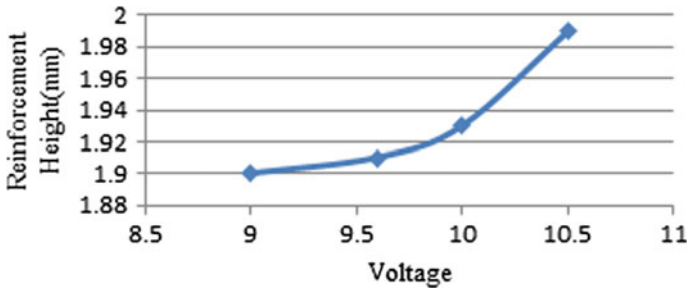
Fig. 5 Effect of voltage on reinforcement height
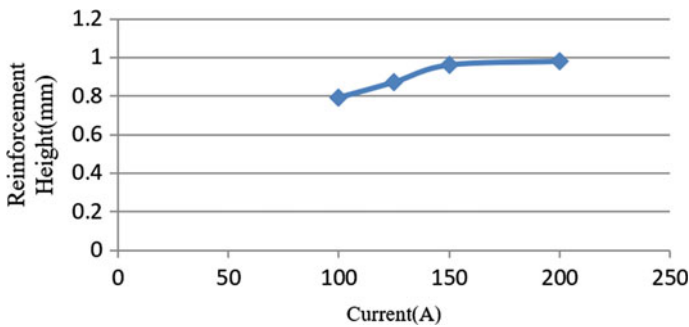
Fig. 6 Effect of current on reinforcement height

at 150 A, 9.6 V, and 1.91 mm/s; respectively, and only feed rate was increased, then the general trend for all the experiments under our study the reinforcement height increased with increase of feed rate. If the feed rate was increased from 2.12 mm/s to 4.23 mm/s the reinforcement height increased from 0.38 mm to 0.65 mm, if the feed rate was increased from 4.23 mm/s to 6.35 mm/s the reinforcement height increased from 0.65 mm to 0.87 mm, if the feed rate again increased from 6.35 mm/s to 8.47 mm/s, the reinforcement height again increased from 0.87 mm to 1.03 mm. these variations were shown in Fig. 1. Actually when feed rate increases more electrode melts per unit time hence the volume of weldment increases. The input power is proportional to the product of current and voltage and reciprocal to speed of welding. In this case, these three variables are fixed at some value so the net heat per unit time is fixed. If feed rate increases, then the same heat is used to melt more volume hence the temperature of the molten volume becomes lower. Due to this reason, the heat is unable to penetrate to more depth. The volume of weld is the function of product of weld width, reinforcement height, and depth of penetration. If the depth of penetration decreases this implies that the product of weld width and reinforcement height will increase, hence increase in reinforcement height is according to the convention.

3.2 Effect of Welding Speed on Reinforcement Height

If welding current, voltage, and feed rate were fixed at 100 A, 9 V, and 2.12 mm/s respectively and only speed of welding was varied. The general trend of change of reinforcement height was its reduction with increase in welding speed.

Heat rate can be expressed by the equation:

$$H = \frac{VI}{v} \tag{1}$$

where $H =$ heat rate in J/mm,
$V =$ welding Voltage in Volts,
$I =$ Welding Current, in Ampere,
$v =$ Welding speed in mm/s.

This can be explained as if the speed of welding increases the heat rate decreases and hence melted volume also decreases which results in reduction of some dimensions of the bead as the volume of weld is proportional to the product of weld width, reinforcement height, and depth of penetration. If the speed of welding was increased from 1.19 mm/s to 1.44 mm/s, the reinforcement height decreased from 0.60 mm/s to 0.55 mm/s, if welding speed was increased from 1.44 mm/s to 1.88 mm/s, the reinforcement height decreased from 0.55 mm to 0.47 mm, if the welding speed was further increased from 1.44 mm/s to 1.82 mm/s the reinforcement height further decreased from 0.47 mm to 0.45 mm. In our selected study range the reinforcement height decreased with increase in welding speed. This is according to the convention as less volume and heat rate is possessed by the weld in this case resulting in small reinforcement height as the product of the three bead dimensions is proportional to the volume of the bead.

3.3 Effect of Welding Voltage on Reinforcement Height

If the welding current, welding speed, and feed rate were fixed at 100 A, 1.19 mm/s, and 8.47 mm/s, respectively, and only the value of welding voltage was increased. The change in reinforcement height increased with increase in voltage for our study range of voltage. When voltage changed from 9 V to 9.6 V, the reinforcement height increased from 1.90 mm to 1.91 mm, if voltage was increased from 9.6 V to 10 V the reinforcement height increased from 1.91 to 1.93 mm, if the welding was again increased from 10 V to 10.5 V the reinforcement height again increased from 1.93 mm to 1.99 mm. This can be explained with the help of equation number 1, according to which as the voltage increases the input heat increases, and the volume of melted material increases which results in an increase of some dimensions of the bead. As due to the increase of voltage the distance between electrode tip and workpiece increases hence same heat is distributed at larger area. Actually, the arc is in the form of a cone whose vertex lies at the tip of the electrode, hence with increase

of distance between workpiece and the tip of electrode the surface area covered by molten metal increases, hence the depth of penetration does not increase if welding voltage is increased, so reinforcement height increases. This implies that the variation is according to the convention.

3.4 Effect of Welding Current on Reinforcement Height

If the value of welding voltage, speed of welding, and feed rate were kept as fixed at 9.6 V, 1.44 mm/s, and 6.35 mm/s and only the value of welding current was changed. The reinforcement height changed every time. If the current was increased from 100 to 125 A, the reinforcement height increased from 0.79 mm to 0.87 mm, if current was increased from 125 to 150 A, the reinforcement height increased from 0.87 mm to 0.96 mm, if the current was further increased from 150 to 200 A, the feed rate again increased from 0.96 mm to 0.98 mm. This indicates that reinforcement height increases with increase of current for the range of our study. It can be explained as the current is increased the input heat increases and melted volume increases so some bead dimensions will increase as the product of the three bead dimensions is proportional to the volume of the bead. This can be explained by equation number 1, due to increase of current heat rate increases but this heat is more utilized to increase the depth of penetration. The product of depth of penetration, reinforcement height, and weld width is proportional to the volume of the weld, so reinforcement height increases, which may be smaller in some cases as in that condition the depth of penetration may increase more. This implies that the variation of reinforcement height with current is according to the convention.

4   Conclusions

From investigations and sensitivity analysis, it is clear that the welding process is a complicated one and there is no exact relationship between input and output variables. Only a general trend can be observed. The volume of the weld bead is the function of weld width, reinforcement height, and depth of penetration. If this volume increases, all the dimensions may not increase but some increase and some may decrease. The general trend can be concluded as:

Reinforcement height increases if current of welding is increased.
Reinforcement height increases if voltage of welding increased.
Reinforcement height decreases if speed of welding is increased.
Reinforcement height increases if feed rate increased.

This research can be very much helpful as the strength of any weld is dependent on its reinforcement height, if reinforcement height is very large it will produce stress concentration and the weld will be very weak and if reinforcement height is very less the material becomes weak considering the metallurgy. The metallurgical

consideration says that due to the welding operation some metallic properties may degrade so to bear larger load larger area is needed. The two different concepts compel us to search for an optimum value of the reinforcement height. If optimum value of reinforcement height is obtained the maximum strength of the weld can be achieved.

References

1. Juang SC, Tarng YS (2002) Process parameter selection for optimizing the weld pool geometry in the tungsten inert gas welding of stainless steel. J Mater Process Technol 122: 33–37
2. Xi-he W, Ji-tai N, Shao-kang G, Le-jun W, Dong-feng C (2009) Investigation on TIG welding of SiCp-reinforced aluminum–matrix composite using mixed shielding gas and Al–Si filler. Mater Sci Eng: A 499(1):106–110
3. Qinglei J, Yajiang L, Puchkov UA, Juan W, Chunzhi X (2010) Microstructure characteristics in TIG welded joint of Mo–Cu composite and 18–8 stainless steel. Int J Refract Metal Hard Mater 28(3):429–433
4. Hussain AK, Lateef A, Javed M, Pramesh T (2010) Influence of welding speed on tensile strength of welded joint in TIG welding process. Int J Appl Eng Res, Dindigul 1(3):518–527
5. Sakthivel T, Vasudevan M, Laha K, Parameswaran P, Chandravathi KS, Mathew MD, Bhaduri AK (2011) Comparison of creep rupture behaviour of type 316L (N) austenitic stainless steel joints welded by TIG and activated TIG welding processes. Mater Sci Eng, A 528(22):6971–6980
6. Tseng KH, Hsu CY (2011) Performance of activated TIG process in austenitic stainless steel welds. J Mater Process Technol 211(3):503–512
7. Narang HK, Singh UP, Mahapatra MM, Jha PK (2011) Prediction of the weld pool geometry of TIG arc welding by using fuzzy logic controller. Int J Eng Sci Technol 3(9):77–85
8. Karunakaran N (2012) Effect of pulsed current on temperature distribution, weld bead profiles and characteristics of GTA welded stainless steel joints. Int J Eng Technol 2(12)
9. Li D, Shanping Lu, Dong W, Li D, Li Y (2012) Study of the law between the weld pool shape variations with the welding parameters under two TIG processes. J Mater Process Technol 212:128–136

Dynamics of Annular Liquid Sheets Using Feature Correlation Velocimetry (FCV)

Kizhakkelan Sudhakaran Siddharth

Abstract Liquid sheets find relevance in atomization point of view owing to its effect on the droplet distribution. As a general thumb rule, coarser droplets are formed from thicker sheets relative to finer droplets from thinner liquid sheets upon disintegration. Experimental quantification of the dynamics of liquid sheets has been a challenge over a long period. Imaging and subsequent post-processing have been successful in quantifying the velocity of liquid sheets. Towards this line, a non-intrusive method called Feature correlation velocimetry has been successful in determining the velocity of liquid sheets. The technique relies on the advection of short wavelength corrugations formed on the surface of liquid sheets when interacted upon by ambient gas. The present article gives a detailed report on the procedure followed in FCV analysis of an annular liquid sheet by demonstrating the technique on the swirling liquid sheet exiting a Gas Centered Swirl Co-axial injector. The technique gives spatio-temporal values of the velocities over the range of images considered. An estimate of the sheet thickness can also be obtained from the flow rates based on the velocities obtained from FCV analysis. FCV has the added advantage that it provides an insight into the unsteady behavior of liquid sheets.

Keywords Liquid sheets · Annular liquid sheet · High-speed imaging · Feature correlation velocimetry (FCV) · Pivlab® · **Velocity distribution** · Sheet thickness

1 Introduction

Quantification of the dynamics of liquid sheets has been a challenge over a long period [1]. From an atomization point of view, quantifying the thickness is very crucial. This can be attributed to the effect of thickness of the liquid sheet on the droplet distribution [2, 3]. Thicker sheets upon fragmenting produce relatively coarser droplets compared to thinner sheet which produces finer drops. The empirical relation of SMD $\propto t^{0.75}$

K. S. Siddharth (✉)
Amity University, Dubai, UAE
e-mail: ssudhakaran@amityuniversity.ae

between the Sauter Mean Diameter (SMD) and the sheet thickness (t) developed by Rizk and Lefebrve was one of preliminary works indicating the dependence [4, 5].

Techniques like Particle Imaging Velocimetry (PIV) have found wide acceptance in quantifying the motion of liquid sheets (annular sheets in particular) due to its non-intrusiveness and higher accuracy compared to other conventional techniques [6–9]. Similarly, imaging and various edge detection methods implementing cross-correlation have found success in the context of annular liquid sheets for the same purpose [10–15]. Towards this direction, Siddharth and co-workers developed a non-intrusive and relatively cheaper technique similar to PIV recently [16]. The technique called Feature Correlation Velocimetry relies on the displacement of corrugations which are naturally formed on the surface of liquid sheets. A correction as reported by the authors would lead to the determination of velocities without relying on seeded particles. Other notable recent works in this context are the novel non-invasive technique of Partial Coherent Interferometry developed by Shan and Chen [17], as well as the focus on the features of a circular liquid sheet by the simultaneous use of front and top views of Volume Laser-Induced Fluorescence (VLIF) detailed by Vegad and co-authors [18, 19].

This paper details the procedure followed in applying Feature Correlation Velocimetry (FCV) on the high-speed images of annular liquid sheet in analyzing the dynamics of an annular liquid sheet.

2 Feature Correlation Velocimetry (FCV)

When a liquid sheet interacts with ambient gas, corrugations are naturally formed on the surface of the sheet. These corrugations get advected along with the sheet. When captured using a high-speed camera, these corrugations appear as features on the liquid sheet. Feature correlation Velocimetry(FCV) utilizes the advection of short wavelength corrugations (sharp features) to quantify the velocity values at different spatial locations of a liquid sheet [16]. The technique uses sharp features as passive tracerscounterpart to seeded particles in Particle Imaging Velocimetry (PIV). The current article is a detailed write-up on the procedure followed in calculating the velocity of liquid sheets at different spatial locations from raw high-speed images using FCV. The method has been depicted over an annular liquid sheet exiting a GCSC injector at one particular flow condition (100 lpm of water and 6 lpm of compressed air). The steps taken during the analysis and the care in each step for quantifying the sheet thickness has been detailed in the following sections. The velocity determination of the liquid sheet is performed by cross-correlation of the successive high-speed images and utilizing the frame rate. The open-source Matlab® program developed by Thielicke and Stamhuis named PIVlab® has been implemented for the same [20, 21]. The images used in the report are from the study conducted on the spray exiting a Gas Centered Swirl Co-axial Injector (GCSC) done by Siddharth and co-authors [22].
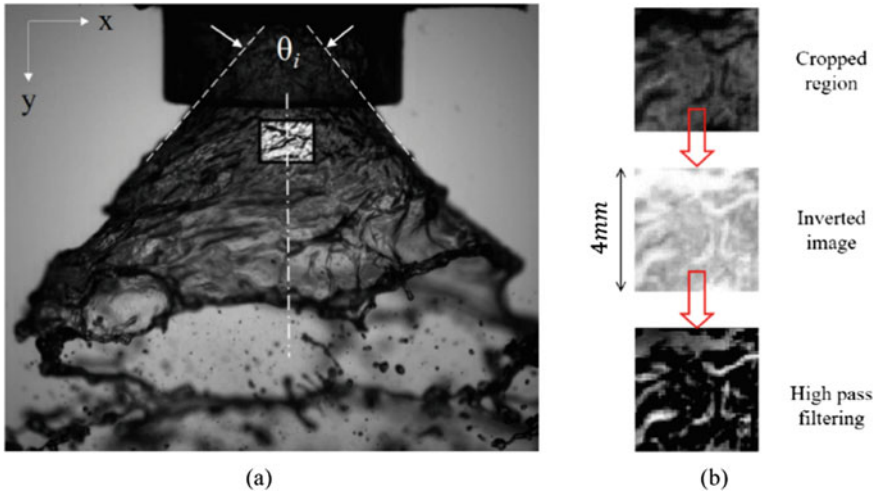
Fig. 1 The Region of Interest (ROI) chosen in the annular swirling sheet exiting a GCSC injector [22]. The ROI is chosen appropriately to avoid the curvature effect. The chosen ROI is of 4 mm × 4 mm

Gas Centered Swirl Co-axial injectors along to the category of gas-assist co-axial injectors where the atomization is due to the shearing action of a fast-moving central gas jet on the inside of an outward swirling annular liquid sheet [22, 23]. The annular sheet resembles a hollow frustum of a cone. The current study details the procedure, its advantages, and its limitations in quantifying the dynamics of an annular liquid sheet, by taking the spray exiting a GCSC injector as an example. The setup is the same as the one used by Siddharth and co-workers [22]. High-speed imaging was used in capturing the motion of the annular sheet. The near field images of the exiting annular sheet used in the study were captured at 6000 fps using $SA4$ Photron® high-speed camera using Shadowgraphy technique. A Tamron® 180 mm $f/3.5$ lens was utilized. A pulsed LED lighting provided crisp images of the annular sheet. Figure 1 shows a high-speed image of the annular sheet exiting the GCSC injector at a combination of 100 lpm of water and 6 lpm of compressed air. 1000 successive high-speed images have been used in the current study.

2.1 High-Speed Imaging and Inversion

FCV requires high-speed images of the liquid sheet to properly capture the naturally formed features [16]. Generally, the imaging can be either by shadowgraphy (also referred to in literature as bright field photography) or by dark-field photography. The latter refers to imaging using a black background and lighting from the front side. It should be noted that the corrugations appear as black features in shadowgraphy and

as white features in dark-field imaging. The advection of the corrugations is the focus of the technique. In the current article, shadowgraphy images captured were used due to the set-up constraints. This required inversion of the images as a preprocessing step. This is because of the fact that PIVlab® cross correlates the displacement of sets of white pixels among image pairs.

2.2 Choosing the Region of Interest (ROI)

The region of interest should be chosen such that the edge effects doesn't alter the determination of velocity distribution. The images are batch cropped accordingly to ensure the same. In the context of annular liquid sheet, additional care should be taken while choosing the Region of Interest (ROI), as the curvature effect would lead to incorrect results. For this reason in the present context, the ROI for the annular liquid sheet exiting GCSC injector has been chosen closer to the injector exit, along the spray centerline, and small enough to avoid the curvature effect of the swirling annular sheet. The ROI chosen as depicted in the [22] is shown in Fig. 1a. The cropped region is 4 mm × 4 mm in real units.

2.3 Cross-Correlation Using PIVlab®

The cross-correlation of the successive high-speed images is performed using the open-source Particle imaging software PIVlab® developed by Theielick and Stamhuis [19, 20]. The necessary steps to be performed during the analysis inPIVlab®are as follows:

Image preprocessing The primary step can be considered to be the most important one. When a liquid sheet interacts with ambient gas, corrugations of varying wavelength are formed on the surface of the sheet. The advection velocity of the short wavelength corrugations is the ones closer to the velocity of the liquid sheet. The other corrugations will be having velocities more deviated from the sheet velocity. So, it is necessary that the images are filtered and the corrugations which are not short enough are eliminated from the raw images before cross-correlating. The inbuilt high pass filters in *PIVlab*® has been utilized for the same. The 25 px filter has been used (details as reported in [20]). The effect of using high pass filters in the ROI is shown in Fig. 1b. The filtered image (bottom most) can be seen to be only consisting of sharp features in contrast to the raw image (topmost image) having corrugations of all range of wavelengths.

PIV settings and Analyzing The preprocessing step is followed by assigning the interrogation windows and the number of passes. The more is the number of passes, more is the accuracy of the method but at the expense of computational time required. The final pass was suitably chosen not to be extremely small so that noises were not incorporated additionally [20, 21]. The ROI in the current study was equivalent to

Fig. 2 The average representative velocity field obtained from **PIVlab**® after cross-correlation. Total of 144 vectors is obtained based on the interrogation windows assigned. The vectors can be seen to be directed in the direction of the swirl of the annular liquid sheet. Each vector represents the spatial locations at which velocity information along the set of 1000 images can be retrieved.
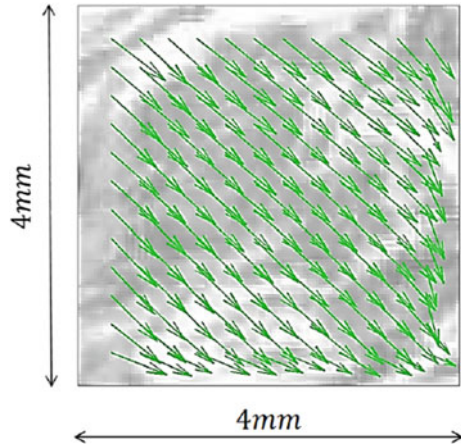
150×150 pixels. Four passes of 72×36 pixels, 36×18 pixels, 24×12 pixels, and 18×9 pixels were assigned.

Calibration and vector validation *The cross-correlation was followed by calibration (with reference to the parent image) to obtain these velocity values in real units. The time gap (in seconds) derived from the frame rate (*fps*) at which the images are captured is then utilized to get the velocity values. The assigned interrogation sizing for the passes as per the passes mentioned previously, provided us with* 144 *velocity vectors equally spaced in the ROI.* Figure 2 shows the resultant average velocity vector plot of the ROI after the validation phase. All the individual vectors represent the different spatial locations where velocity information is available in the current scenario. A total of 999 image sets are obtained from the 1000 images used for cross-correlation. *These number of velocity vectors were obtained automatically from the software.*

The vectors obtained after cross-correlation include also erroneous vectors which refer to the vectors that lie outside the practical possible velocity value of the annular sheet as per the particular flow condition. These incorrect vectors in the present context include the vectors that have risen from poor cross-correlation at different time instances due to several factors. These erroneous vectors arise from either the corrugations dying out by the time it reaches/passes the ROI (or) a corrugation grown in the ROI during the cross-correlation of two successive images. Due to the large deviation of such vectors from possible velocity values, they can be easily spotted and are removed manually from the velocity set. It should be mentioned that these incorrect vectors only contributed to nearly 2–3% of the entire velocity values. The erroneous vectors were eliminated during the vector validation phase.

Moving forward, out of the 144 velocity vectors, the vectors along the edges are prone to errors. This can be attributed to the reason that corrugations move in and out of the ROI in successive images. The frame rate initially is chosen (6000 fps) was such that the corrugations remain in the ROI for at least three successive images. This ensured the fact that the velocity values achieved along the spray centerline are

Fig. 3 Cell-wise representation of the ROI. Out of the 144 velocity vectors, the vectors at the sides of the unit cell has been avoided for quantification purpose. The blue cells represent the spatial locations which are the least error-prone among the 100 velocity vectors
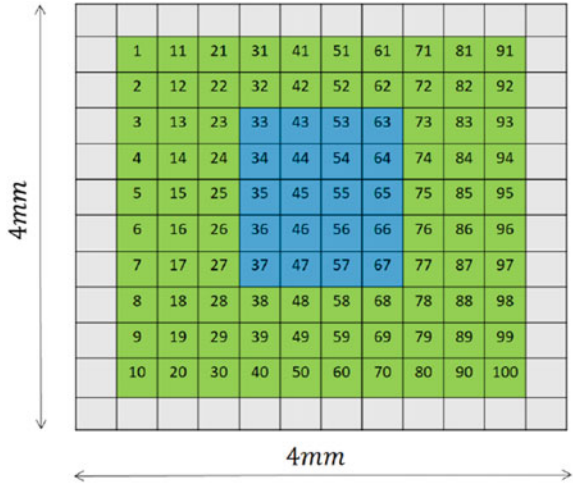
free from such errors. A cell-wise depiction of the ROI for better understanding is shown in Fig. 3.

3 Results and Discussion

For the reasons stated in the previous section, the average value of the velocity values obtained in the blue boxes has been only been used from each image pair. In this case of the swirling annular liquid sheet, both the x and y components of the sheet at the spatial location chosen can be obtained from the PIVlab® results. The x– component refers to the swirl velocity of the annular liquid sheet and the y– component refers to the axial velocity of the same (Fig. 4).

4 Conclusions

Feature Correlation Velocimetry is a non-intrusive technique for quantifying the dynamics of liquid sheets. The article briefs the procedure followed in applying the technique for quantifying the dynamics of an annular sheet exiting a GCSC injector. The preprocessing step is the most important step in the analysis. This is to ensure that that each image consists of only short-wavelength corrugations prior to cross-correlation of the same. Corrugations of other wavelengths will contribute to incorrect values of the liquid sheet and should be removed thereby. In addition, the Region of Interest (ROI) should be chosen properly along the spray/sheet centerline while applying the technique on annular sheets. This is to avoid the curvature effects of the
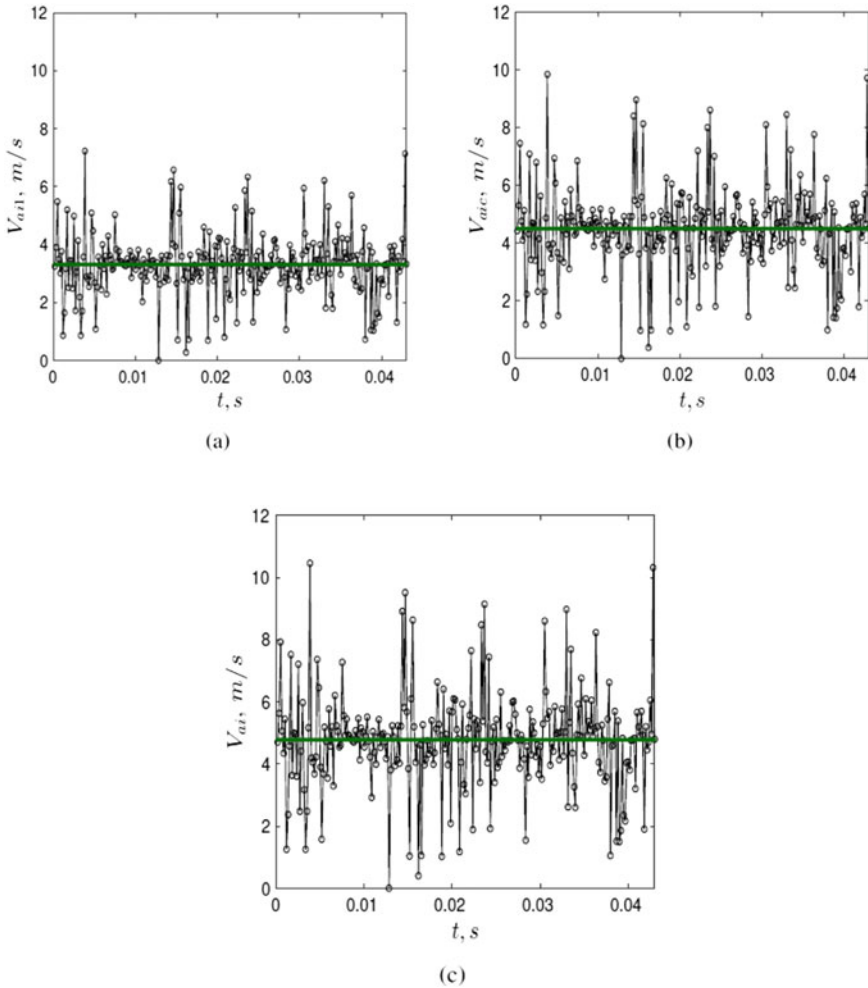
Fig. 4 The procedure of correction performed on the axial velocities obtained post-cross-correlation of images in **PIVlab®**

annular sheet. Finally, the inclination of the sheet with the imaging plane should also be accounted for while retrieving the axial component of the liquid sheet (Fig. 5).

The technique of FCV finds an advantage over conventional PIV in that it is relatively cheaper and easier to implement in liquid sheets. Also, the technique does not use any seeded particles but relies on the advection of naturally formed short-wavelength corrugations. The unsteadiness of liquid sheet can also be quantified using the technique which refers to the flapping nature of the sheet physically. By using the FCV values, the technique can also be extended to get an estimate of the sheet thickness by making use of the operating flow conditions and the injector dimensions.
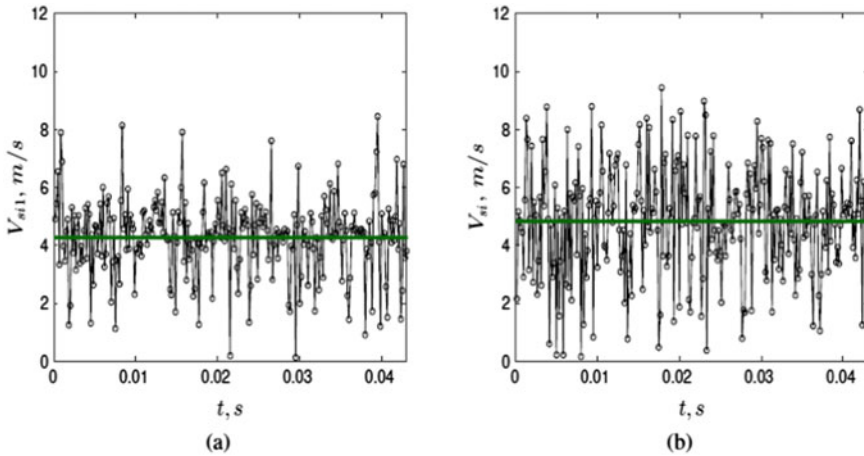
Fig. 5 The procedure of correction performed on the swirl velocities obtained post-cross-correlation of images in **PIVlab**®

References

1. Taylor GI (1959) The dynamics of thin sheets of fluid. Disintegration of fluid sheets. Proc R Soc London. Ser A. Math Phys Sci 253(1274) :313–321
2. Lefebvre A (1988) Atomization and sprays 1040
3. Lefebvre AH (1992) Twin-fluid atomization: Factors Influencing mean drop size. Atom Sprays 2(2)
4. Rizkalla AA, Lefebvre AH (1975) The influence of air and liquid properties on airblast atomization 316–320
5. Rizk NK, Lefebvre AH (1980) The influence of liquid film thickness on airblast atomization 706–710
6. Adrian RJ (1991) Particle-imaging techniques for experimental fluid mechanics. Annu Rev Fluid Mech 23(1):261–304
7. Willert CE, Gharib M (1991) Digital particle image velocimetry. Exp Fluids 10(4):181–193
8. Westerweel J (1997) Fundamentals of digital particle image velocimetry. Meas Sci Technol 8(12):1379
9. Emrich RJ (1983) Flow field measurement by tracer photography. Exp Fluids 1(4):179–184
10. Rayleigh L (1891) Some applications of photography 249
11. Duke D, Honnery D, Soria J (2010) A cross-correlation velocimetry technique for breakup of an annular liquid sheet. Exp Fluids 49(2):435–445
12. Wahono S et al (2008) High-speed visualization of primary break-up of an annular liquid sheet. Exp Fluids 44(3):451–459
13. Berthoumieu P, Lavergne G (2001) Video techniques applied to the characterization of liquid sheet breakup. J Visual 4(3):267–275

14. Fu Q-F, Yang L-J, Yuan-yuan Qu (2011) Measurement of annular liquid film thickness in an open-end swirl injector. Aerosp Sci Technol 15(2):117–124
15. Faazil AB, Eapen AM, Sudhakaran SK (2020) Disintegration of liquid sheets and quantification of its dynamics. In: 2020 advances in science and engineering technology international conferences (ASET). IEEE, New York, pp 1–6
16. Siddharth KS, Panchagnula MV, Tharakan TJ (2017) Feature correlation velocimetry for measuring instantaneous liquid sheet velocity. J Fluids Eng 139(9)
17. Shang W, Chen J (2019) A Partial Coherent Interferometry for measuring the thickness of a dynamic liquid sheet. Int J Multiph Flow 116:15–25
18. Vegad CS, Kumar A, Chakravarthy SR (2020) Visualization of features of atomizing circular liquid sheet using simultaneous Volume Laser-Induced Fluorescence. Exp Thermal Fluid Sci 112:109947
19. Vegad CS, Kumar A, Chakravarthy SR (2020) Experimental study of a free-surface circular liquid sheet using planar laser-induced fluorescence. Exp Fluids 61(2):46
20. Thielicke W, Stamhuis EJ (2014) PIVlab-time-resolved digital particle image velocimetry tool for MATLAB. In: Published under the BSD license, programmed with MATLAB 7.0.246, R14
21. Thielicke W (2014) The flapping flight of birds: analysis and application. University of Groningen, Diss
22. Siddharth KS, Panchagnula MV, Tharakan TJ (2017) Effect of gas swirl on the performance of a Gas Centered Swirl Co-axial injector. Atom Sprays 27(8)
23. Siddharth KS (2020) Gas Centered Swirl Co-Axial (GCSC) injectors relevant to rocket propulsion applications. In: 2020 advances in science and engineering technology international conferences (ASET). IEEE, New York, pp 1–6

Vibration and Acoustic Method for Detection of Cracks in Bearings: A Critical Review

Siddique Khan, Rajeev Kumar, Manpreet Singh, and Jujhar Singh

Abstract This paper discusses the acoustic and vibration techniques used for the diagnosis of crack in bearings. Cracks result in severe problem which may affect the bearing and leads in sudden breakdown of machines. Traditional vibration techniques are unable to determine the crack at early stages and also result in inaccurate data analysis due to the impact of operating conditions like speed, stiffness, and coupling on resultant harmonics. Even a minor deformation results in rapid release of strain energy which produces acoustic emission which is used for diagnosing insignificant cracks before their severe effect and used for early detection of cracks. In number of cases, the damage is been reported to initiate from inside of the surface that makes it undetectable using vibrational techniques as no change in geometry is reported, whereas it can be easily detectable with AE techniques. Various signal processing techniques are discussed and compared for a better understanding of the raw signals.

Keywords Acoustic emission · Crack diagnosis · Bearings · Vibration

1 Introduction

Rotating and reciprocating parts are the basic part of any manufacturing industry, normally in any industrial process, electric motors generate a broad range of mechanical challenges which triggers over 70% of rotating machinery vibration faults. Misalignment and imbalance are the main causes of vibration in rotatory machines. Misalignments cause a decrease in the efficiency of the motor and misaligned machinery is more prone to failure due to increased loads on bearings and couplings. As exact alignment is not possible but can be adjusted in an acceptable range which can avoid any damage or failure in machines and results in increased durability of

S. Khan (✉) · R. Kumar · M. Singh
Department of Mechanical Engineering, Lovely Professional University, Phagwara, India
e-mail: sidkhan8055@gmail.com

R. Kumar · J. Singh
Department of Mechanical Engineering, Inder Kumar Gujral Punjab Technical University, Ibban, India

machines. There are various reasons behind misalignment which causes machines instability like thermal distortion of machines, asymmetry in applied loads, improper assembly of machines, unequal settlement of the foundation, etc.

Most traditional techniques for Shaft Angular Misalignment (SAM) detection are carried out using vibration analysis but speed, stiffness, and coupling type have a strong effect on the vibration signature which may result in inaccurate data analysis. There are a lot of methods which is used to detect misalignment or imbalance by measuring various crucial parameters like pressure, temperature, vibrations but not good for early detection and localization of faults. Jalan and Mohanty [1] developed a model-based technique for the diagnosis of the rotor-bearing system by considering residual vibration of rotor-bearing system. This method can be used in large rotating machines like turbines, gearboxes, etc. for early detection, localization, and diagnosis of faults. Sudhakar and Sekhar [2] works on model-based methods that are widely used for the identification of faults in rotating systems because of their ability to identify both location and severity of faults. Here equivalent load minimization method is used in which fault is identified by minimizing the difference between equivalent loads and theoretical loads. One limitation of this method is that error is increased by a decrease in the number of measured vibrations. Researchers also work on different types of techniques used to identify the misalignment, Simm [3] developed a method to monitor shaft misalignment and positional changes using a laser-based measurement method. This method is suitable for on-job operation monitoring because of being non-contact detection of misalignment. This method is used to measure shaft tolerances up to 0.02 to 0.3 mm which depends upon the rotational speed of the machine. Ferrando Chacon [4] used the Acoustic Emission technique for the detection of misalignment which is conducted under different operating conditions to analyze the effect on AE and vibration signature. This paper concluded that AE when combined with envelope analysis, shows more consistency, steadiness, and higher Signal to Noise Ratio (SNR) for detection of SAM. Tonks and Wang [5] applied temperature monitoring technique using an infra-red thermometer which can be further used for online temperature monitoring of misaligned shaft couplings. This concludes that the temperature change is the direct effect of misalignments. As misalignment of shafts leads in temperature rise, Mohanty and Fatima [6] applied this phenomenon by using a thermal imaging camera for fault detection. Further, the temperature variation is studied according to different load, speed, and misalignment, and found that by monitoring temperature rate misalignment can be diagnosed. This technique can be used in windmills gearboxes located at elevated heights where the traditional method is not convenient.

2 Detection of Crack

Every component that fails passes through a process of elastic and plastic deformation, which releases energy in various forms, that energy can be used for detection of crack initiation. In context to phenomenon of energy release, Bashir et al. [7]

developed a mathematical method for detection of acoustic energy produced during crack growth of rolling element steel-bearing. During the experiment, it is found that the acoustic emission amplitude amplifies from 9.8×10^{-12} m to 29×10^{-12} m, and duration increases from 0.1 to 1 υs as the crack growth is becoming critical. Fourier transform is used for predicting the range of frequencies within which detectable AE is analyzed. Due to uneven, excessive loads and bad lubrication spalling takes place which keeps on damaging the bearing surface. Li et al. [8] helps in predicting the occurrence of spalling using Discrete Wavelet Transform (DWT). DWT is used to capture information from both time and frequency characteristics. As the occurrence of spalling comes near the values of wavelet coefficients increase through which prediction of spalling can be possible by monitoring the signature of wavelet coefficient maximum values. Wavelet transform and envelope analysis are widely used for different applications, here [9] use this for condition monitoring and early fault diagnosis. Early detection plays an important role in condition-based maintenance and predictive maintenance. As AE technique is highly sensitive for high frequency and low energy signals. The AE signals passed through FFT to create power spectrums are continuously changing the characteristics with growing crack. It is found that the harmonic spectra of rotation speed and bearing cage frequency are excited by crack growth which can be used for early fault diagnosis and condition monitoring. Wu and Huang [10] performed the FFT analysis of displacement spectrums that helps in extracting features and can be used as a good parameter to detect the crack depth and its location. The crack depth and bending moment at the crack location are directly proportional to the vibration amplitude [11].

Condition monitoring and early fault diagnosis of bearings is the most crucial part for any rotating machines that cause machine. Hemmati et al. [12] divided the condition monitoring into four stages, statistical analysis, fault detection, crack size, and prognostics. Here, the effect of loading conditions, speed, and crack size on AE signals using the design of experiment (DOE) method are analyzed. The algorithm is based on kurtosis and Shannon entropy to acquire better results using the wavelet packet transform (WPT) and envelope detection. Detection of faults in case of non-stationary signals with noise is a challenging task, Soleimani and Khadem [13] introduces a new technique, phase space reconstruction is implemented to study the change in chaotic behavior due to various faults. For better classification of faults Lyapunov exponent, approximate entropy with correlation dimension is applied and for intelligent identification of different types of faults, and the results are analyzed using neural networks. While dealing with real-life application, usually the recorded signals are mixed with noise which may lead to inaccurate data analysis, the developed method can be used for extracting features signals from noisy and weak signals, it is seen that the proposed method can enhance noisy signals and capture signals with the accuracy of 97% and in case of calculating crack sizes, it shows the maximum error of 10%.

Acoustic Emission technology is widely accepted as a complementary tool for condition monitoring of bearings, Elforjani and Mba [14] uses AE measurements to monitor the growth and propagation in a bearing. As a lot of mechanical industries are equipped with low speed rotating machines. For instance, the interaction of

surface asperities and impingement of the bearing rollers over a defect on an outer race will result in the generation of acoustic emission. These emissions propagate on the surface of the material as Rayleigh waves and are measured with an AE sensor. AE is known for detecting cracks at incipient stage, in few cases, it is seen that the first crack initiates beneath the surface that is undetectable by vibrational techniques, however, AE techniques can successfully able to detect that cracks earlier before the cracks reaches the surface. If the crack propagates to the surface it will end up in spalling and deteriorates the bearing due to the introduction of debris in a lubricant. Fuentes [15] uses Gaussian mixture models for probabilistic modeling due to variational change in operational conditions and noise. As AE is highly affected by operating conditions like temperature, load, and lubrication that cause misleading in detectability of cracks. References [16, 17] discusses another technique for fault diagnosis of slow speed bearings with minimum speed up to 10 rpm under different loading conditions. Relevance vector machine (RVM) and Support vector machine (SVM) is presented for faults diagnosis of slow speed bearings. This study shows that RVM is performing better for fault diagnosis of slow speed bearings and also found that the AE signals produce better results than vibration signals considering accuracies. There are various studies on detection of fault due to particle contamination in slow-speed bearings using acoustic emission, whereas it lacks while fault diagnosis of high-speed bearings. It is shown by Schnabel [18] that signals produced by plastic deformation is used to identify the particle contamination therefore it detects the faults. AE detection of faults depends on the ratio between the transient signals and signals produced due to plastic deformation. In case of high-speed bearings, the excessive transients force signals deteriorate the signals produced by plastic deformation whereas for slow speed bearings the effect of transient signals reduces and results in detecting particle contamination. Extracting features from the raw vibrations signals is still a challenging task for fault diagnosis of rolling element bearing, as normal and traditional techniques concentrate on pattern of classifier with single domain feature, Yan and Jia [19] addresses this issue and introduce a new technique that is based on optimized SVM with multi-domain feature. This algorithm is subdivided into three stages, and the last stage uses PSO-SVM model that is used for identification of multiple fault conditions**. The accuracy of PSO-SVM is 91% i.e., comparably higher than other different classifiers. Saidi et al. [20] uses SVM classifier and higher-order spectrum for pattern recognition for bearing fault detection, nonlinear and non-gaussian characteristics can be analyzed using this technique. Here, third-order spectrum is extracted for detecting different types of bearing faults, then the extracted signals are fed into SVM to obtain the severity of bearing faults. Samanta et al. [21] compares the two different types of classifiers for bearing fault detection i.e., artificial neural networks (ANNs) and SVMs for analysis from time-domain vibration signals. Results show that the performance of SVM is better than ANN and training time for SVMs is comparably less than ANNs. Liu et al. [22] proposed a new technique that is composed of empirical model decomposition (EMD), distance evaluation technique, and wavelet support vector machines for condition monitoring of roller element bearings. Here, WSVM algorithm is constructed using morlet and Mexicans wavelet kernel functions and found out to be more robust and accurate with

better generalization ability. Sinou [23] shows the effects of cracks on the stability of non-linear rotor system, behavior of rotor-bearing system due to various vibration influencing parameters like crack depth, crack location, disk position, stiffness of supports, and shafts rotational speed. It is found that an increase in crack size tends to increase the instability of the system. Sampaio and Nicoletti [24] presented an experimental NN & EDBA model that shows that the vibration amplitude increases with an increase in size of defect with good confidence. It has been seen that surface defect, load and speed have a significant effect on vibration amplitude apart from the damping factor.

Detection of cracks in shafts is important as the damage can lead to machine failure with costly repairs and loss of productive time. Gómez et al. [25] uses Wavelet transform to analyze the vibration signals captured from the accelerometer. It is seen that large variation in energy is recorded at $1\times$, $2\times$, and $3\times$ but after comparing with theoretical results is found that $3\times$ component is the indication of cracks in rotor-bearing system. Probability of detection of cracks increases with an increase in rotational speed. Qi et al. [26] develops a method for diagnosing misalignment for machines under varying speed by transforming non-stationary time-domain signals to quasi-stationary signals. Order tracking technique used to resolve non-stationary signals and EEMD captures the speed profile of shaft, with the combination of neural networks and wavelet-based technique and the proposed method proved out with better detection capability while dealing with non-stationary signals. Desavale and Mali [27] uses Approximated entropy for detection of cracks in rotating shafts but with at least a speed of 33% and 50% of critical speed to capture the data with the presence of irregularities. This technique can distinguish between the type of faults. Other vibration-based methods detect cracks length above 10% of shaft diameter whereas this method can detect cracks with 5% of shaft diameter, but one limitation is that for different direction and orientation of cracks it shows weak effects on vibration signals. Smith and Zhao [28] introduces asymptotic approach that is used for sub-space detection approach for imbalance in stationary structures but here this technique is adapted for rotating machines with constant speed. Shrivastava and Mohanty [29] presents the model-based method for detection of unbalance in rotor-bearing system using a combination of Kalman filter and recursive least square method for input force estimation. Reduced-order model is used which results in fast processing of signals. Shrivastava and Mohanty [30] again presents a joint input state estimation technique for diagnosing unbalance in rotor-bearing system but they lack while capturing the signals of high-speed rotors. Traditional methods for vibration analysis depend on the positioning of sensors for signal acquisition that arises some sort of problem. Yao et al. [31] introduces the novel technique for misalignment detection without using additional sensors i.e., Virtual Phase Diagram (VPT) method. In VPT diagram the relation between load torque and current is obtained. Misalignment can be detected by analyzing the spectrum analysis of current whereas the fault feature extraction is carried out by EEMD algorithm combined with phase angle diagram to make VPT diagram, that finally results in evaluating angle offset and misalignment detection.

Modern rotating machineries comprised of multiple rotors and bearing that introduces high non-linearity and non-stationary vibrations in the system. To deal with non-stationary signals HHT is an effective signal processing technique used, that is the combination of HT and EMD. While dealing with multi-frequency signals, HHT results in generation of IMFs that turns out to meaningless IFs. One of the drawbacks of HHT, it cannot able to characterize the high-frequency feature of non-stationary signals. To overcome this problem new method is developed by Xiong [32] combines the HHT with Kurtogram that is fourth-order spectral analysis tool. Kurtogram generates the monochromatic signals using non-stationary intra and inter wave modulation components form original signals. The combination of HHT and Kurtogram is successfully able to extract the hidden features of multi-frequency and non-stationary signals.

Time and frequency domains are made for diagnostics of roller element bearings as well as the vibration signature of healthy and defected bearings are compared. Here, High-Frequency Resonance Technique (HFRT) method is employed on frequency domain analysis for further monitoring. The proposed method can be used to find the ideal sensor position and signal processing technique, considering the rotational speeds, structural effects, and loading conditions at the beginning of an industrial condition monitoring application. Chandra and Sekhar [33] works on three different techniques for detection of faults, i.e. STFT (Short-Time Fourier Transform), CWT, and HHT (Hilbert Huang Transform) and later compared for better detection technique. It is found that the analysis time for HHT is comparably less, but CWT is better while dealing with noisy data. It is concluded that misalignment leads to generation of sub-critical speeds at $0.5\times$ and also at other sub-harmonics while the transverse cracks lead to generation of strong sub-harmonics at $0.5\times$ while weak at other sub-harmonics. Pandya et al. [34] works on fault diagnosis of roller element bearing which is based on AE, HHT, and data mining tool. The time domain approach is represented using FFT of IMF from HHT for obtaining a better signal response. K-nearest neighbor method with asymmetric proximity function (APF) is used as an efficient data mining classifier 96.67% and also overcomes drawbacks, i.e., KNN requires more computational time and memory. Peng et al. [35] develop an effective method by combining WPT with HHT for IMF, the technique shows that the enhanced HHT results in better resolution in time and frequency domain as well as comparably good computing efficiency than scalogram but may mislead the results due to ripple phenomenon in frequency. Multi fault detection is used to extract the fault feature of weak signals as these signals are mixed up with high amplitude vibration which results in weak signals undetectable and causes the fault unapproachable. Thereby, Teng et al. [36] works on the Cepstrum method to differentiate the various frequency components as well the Complex wavelet transform (CWT) is used to detect the weak signals buried in high-level vibrations. It decomposes and demodulated the signals simultaneously with the help CWT that provides the multi-scale enveloping spectrogram (MuSEnS).

Vashisht and Peng [37] introduces a switching control strategy that is a combination of STFT and active control which helps in detecting small cracks in rotor-bearing system. It is determined that the vibration amplitude in the pre-resonance region is

increased by switching control strategy while decreases with the application of active control. Hoshi [38] developed a cost-effective method for detecting initiation and propagation of cracks to prevent sudden failure and arrest of rotatory machines. To monitor the crack or detection of bearing faults AE, RMS, spectrum analysis, envelope analysis, and wavelet transformation are applied. Rolling contact fatigue damage is not only the cause behind the bearing faults, Elasto-Hydro-Dynamic lubrication film also deteriorates due to some common causes like overloading, contamination of dust, chip, and coolant penetration, etc. Brkovic et al. [39] works on early fault detection techniques to avoid failure of components and degraded efficiency which results in high energy consumption. This technique is comprised of standard vibration signal analysis in addition to standard deviation and logarithmic energy entropy as a measure of average energy and degree of disorder, respectively. Compared to few other detection techniques, this leads others by their simplicity and accuracy level. While working on different techniques few literatures uses multiwavelets and EMD for compounds faults diagnosis but facing issue while mode mixing and overestimation of harmonics. Considering this issue [40] works on empirical wavelet transform duffing oscillator technique in which EWT can extract signals at fully adaptive wavelet basis in different modes and further the signals is passed via duffing oscillator to observe chaotic motion using poincar mapping with accurate results. Hence, this method will perform better for compound faults decoupling diagnosis.

3 Conclusion

This review paper on detection of cracks concludes that the Acoustic Emission (AE) energy release is one of the most effective phenomena that can be used for crack diagnosis bearings. AE technique can detect the crack at early stages which are one of the major advantages because it allows you to prevent the sudden breakdown of machines. In number of cases, the damage is been reported to initiate from inside of surface that makes it undetectable using vibrational techniques as no change in geometry is reported, whereas it can be easily detectable with AE techniques. An acoustic emission is due to the rapid release of strain energy which means any minor deformation results in acoustic emission.

Lot of techniques for crack diagnosis fail while detecting slow speed bearings but AE can successfully detect the cracks and provides better and reliable results comparably. Cracks result in instability of Rotor bearing system (RBS), with an increase in crack size the instability increases rapidly, as well probability of crack detection increases with increase in rotational speeds, it is also seen that the AE can detect crack better than other vibrational techniques in terms of reliability and accuracy as well it is also seen that the wavelet representation is more sensitive than FFT. Many modern machineries have multiple bearings and rotors system that leads to complex and non-stationary signals, to deal with these type of signals HHT is one of the effective algorithms, but it fails while computing multi-frequency signals. As there are various algorithms for analysis of raw data signals, HHT is found out to

take comparably lesser time but in case of noisy signals, CWT can easily extract features with high accuracy.

References

1. Jalan AK, Mohanty AR (2009) Model based fault diagnosis of a rotor-bearing system for misalignment and unbalance under steady-state condition. J Sound Vib 327(3–5):604–622
2. Sudhakar GNDS, Sekhar AS (2011) Identification of unbalance in a rotor bearing system. J Sound Vib. 330(10):2299–2313
3. Simm A, Wang Q, Huang S, Zhao W (2016) Laser based measurement for the monitoring of shaft misalignment. Meas J Int Meas Confed 87:104–116
4. Ferrando Chacon JL, Artigao Andicoberry E, Kappatos V, Asfis G, Gan TH, Balachandran W (2014) Shaft angular misalignment detection using acoustic emission. Appl Acoust 85:12–22
5. Tonks O, Wang Q (2017) The detection of wind turbine shaft misalignment using temperature monitoring. CIRP J Manuf Sci Technol 17:71–79
6. Mohanty AR, Fatima S (2015) Shaft misalignment detection by thermal imaging of support bearings. IFAC-PapersOnLine 28(21):554–559
7. Bashir I, Bannister R, Probert D (1999) Release of acoustic energy during the fatiguing of a rolling-element bearing. Appl Energy 62(3):97–111
8. Li Y, Billington S, Zhang C, Kurfess T, Danyluk S, Liang S (1999) Adaptive prognostics for rolling element bearing condition. Mech Syst Signal Process 13(1):103–113
9. Gu D, Kim J, Kelimu T, Huh SC, Choi BK (2012) Evaluation of the use of envelope analysis and DWT on AE signals generated from degrading shafts. Mater Sci Eng B Solid-State Mater Adv Technol 177(19):1683–1690
10. Wu MC, Huang SC (1998) Vibration and crack detection of a rotor with speed-dependent bearings. Int J Mech Sci 40(6):545–555
11. Singh G, Kumar R, Singh M, Singh J (2017) Detection of crack initiation in the ball bearing using FFT analysis. Int J Mech Eng Technol
12. Hemmati F, Orfali W, Gadala MS (2016) Roller bearing acoustic signature extraction by wavelet packet transform, applications in fault detection and size estimation. Appl Acoust 104:101–118
13. Soleimani A, Khadem SE (2015) Early fault detection of rotating machinery through chaotic vibration feature extraction of experimental data sets. Chaos, Solitons Fractals 78:61–75
14. Elforjani M, Mba D (2009) Natural mechanical degradation measurements in slow speed bearings. Eng Fail Anal 16(1):521–532
15. Fuentes R, Dwyer-Joyce RS, Marshall MB, Wheals J, Cross EJ (2020) Detection of sub-surface damage in wind turbine bearings using acoustic emissions and probabilistic modelling. Renew Energy 147:776–797
16. Widodo A et al (2009) Fault diagnosis of low speed bearing based on relevance vector machine and support vector machine. Expert Syst Appl 36(3 PART 2):7252–7261
17. Han T, Liu Q, Zhang L, Tan ACC (2019) Fault feature extraction of low speed roller bearing based on Teager energy operator and CEEMD. Meas J Int Meas Confed 138:400–408
18. Schnabel S, Marklund P, Larsson R, Golling S (2017) The detection of plastic deformation in rolling element bearings by acoustic emission. Tribol Int 110:209–215
19. Yan X, Jia M (2018) A novel optimized SVM classification algorithm with multi-domain feature and its application to fault diagnosis of rolling bearing. Neurocomputing 313:47–64
20. Saidi L, Ben Ali J, Fnaiech F (2015) Application of higher order spectral features and support vector machines for bearing faults classification. ISA Trans 54:193–206
21. Samanta B, Al-Balushi KR, Al-Araimi SA (2003) Artificial neural networks and support vector machines with genetic algorithm for bearing fault detection. Eng Appl Artif Intell 16(7–8):657–665

22. Liu Z, Cao H, Chen X, He Z, Shen Z (2013) Multi-fault classification based on wavelet SVM with PSO algorithm to analyze vibration signals from rolling element bearings. Neurocomputing 99:399–410
23. Sinou JJ (2007) Effects of a crack on the stability of a non-linear rotor system. Int J Non Linear Mech 42(7):959–972
24. Sampaio DL, Nicoletti R (2016) Detection of cracks in shafts with the approximated entropy algorithm. Mech Syst Signal Process 72–73:286–302
25. Gómez MJ, Castejón C, García-Prada JC (2016) Crack detection in rotating shafts based on 3 × energy: Analytical and experimental analyses. Mech Mach Theory 96:94–106
26. Qi X, Yuan Z, Han X (2015) Diagnosis of misalignment faults by tacholess order tracking analysis and RBF networks. Neurocomputing 169:439–448
27. Desavale RG, Mali AR (2016) Detection of Damage of Rotor-bearing Systems Using Experimental Data Analysis. Procedia Eng 144:195–201
28. Smith B, Zhao Q (2015) Modal structure imbalance fault detection for rotating machines. IFAC-PapersOnLine 28(21):1420–1425
29. Shrivastava A, Mohanty AR (2018) Estimation of single plane unbalance parameters of a rotor-bearing system using Kalman filtering based force estimation technique. J Sound Vib 418:184–199
30. Shrivastava A, Mohanty AR (2019) Identification of unbalance in a rotor system using a joint input-state estimation technique. J Sound Vib 442:414–427
31. Yao Y, Li Y, Yin Q (2019) A novel method based on self-sensing motor drive system for misalignment detection. Mech Syst Signal Process 116:217–229
32. Xiong X, Yang S, Gan C (2012) A new procedure for extracting fault feature of multi-frequency signal from rotating machinery. Mech Syst Signal Process 32:306–319
33. Chandra NH, Sekhar AS (2016) Fault detection in rotor bearing systems using time frequency techniques. Mech Syst Signal Process 72–73:105–133
34. Pandya DH, Upadhyay SH, Harsha SP (2013) Fault diagnosis of rolling element bearing with intrinsic mode function of acoustic emission data using APF-KNN. Expert Syst Appl 40(10):4137–4145
35. Peng ZK, Tse PW, Chu FL (2005) A comparison study of improved Hilbert-Huang transform and wavelet transform: Application to fault diagnosis for rolling bearing. Mech Syst Signal Process 19(5):974–988
36. Teng W, Ding X, Zhang X, Liu Y, Ma Z (2016) Multi-fault detection and failure analysis of wind turbine gearbox using complex wavelet transform. Renew Energy 93:591–598
37. Vashisht RK, Peng Q (2018) Crack detection in the rotor ball bearing system using switching control strategy and short time fourier transform. J Sound Vib 432:502–529
38. Hoshi T (2006) Damage monitoring of ball bearing. CIRP Ann - Manuf Technol 55(1):427–430
39. Brkovic A, Gajic D, Gligorijevic J, Savic-Gajic I, Georgieva O, Di Gennaro S (2017) Early fault detection and diagnosis in bearings for more efficient operation of rotating machinery. Energy 136:63–71
40. Jiang Y, Zhu H, Li Z (2015) A new compound faults detection method for rolling bearings based on empirical wavelet transform and chaotic oscillator. Chaos, Solitons Fractals 89:8–19

Experimental Investigation of a Stress Wave Force Balance System

Raj Pal Singh and Kishan Pal Singh

Abstract The measurement of acting forces on a flying aerodynamic vehicle is troublesome. The measured forces are used to determine the performance of the flying vehicle. However, the measurement of forces in flying conditions have a big challenge due to a very short testing duration, i.e., barely a fraction of milliseconds and the requirement of quick response sensors for forces measurement. In the present study, an experimental investigation has been carried out for a short duration to measure the strength and nature of signal induced in aerodynamic structure and stress wave force balance. Experiments have been carried out by employing an aerodynamic model, which consists of a stress bar attached with a hemispherical model at one end. The information of the characteristic behavior of stress bars for different geometries and materials in one-dimensional impulsive environments has been determined. A simulation model has been developed using ANSYS software and evaluates the existing stress wave force balance for verification of results obtained from the experimental investigation.

Keywords Stress wave force balance · Semiconductor strain gauge · Impulsive behavior · Stress force · Stress bar and hemispherical

Nomenclature

FEM   Finite Element Method
HB   Hypervelocity Ballistic
IIT   Indian Institute of Technology
SSG   Semiconductor Strain Gauge
SWFB   Stress Wave Force Balance

R. P. Singh
Department of Mechanical Engineering, S.D.E.C, Ghaziabad, UP, India

K. P. Singh (✉)
Department of Mechanical Engineering, Mangalayatan University, Aligarh, UP, India
e-mail: kishan.amu@gmail.com

1 Introduction

Space science has a great importance nowadays. Many countries are focusing on development of their space sciences, and few of them have established their own rocket and satellite launching pads. They have improved their space science capabilities and also working on research projects related to spacecrafts and satellites improvements. Therefore, the wind tunnels are being built to analyze behavior of the aerodynamic spacecraft structure at high speed. The structure design of an aerospace body thus hinges greatly upon the hypersonic tests conducted in the wind tunnels. The recent interest in hypersonic testing has motivated researchers, engineers, and scientists working in this field and has brought into focus once again the requirement for suitable ground test capabilities to assist in accepting of the complex physical phenomenon that complement high-speed flight. Stress wave generates in forced motion in the portion of a deformable medium. As elements of the medium are deformed, the disruption is transmitted from one point to another subsequent point and the disturbance or stress wave produced in the confined medium. Stress wave force balance was first proposed by Sanderson and Simmons (1991). The authors presented a technique for measuring the drag force in hypersonic impulse conditions with the test time duration of 1 ms or less [1]. In the experiment, the balance force referred as stress wave force balance involves attaching the test model to a long elastic sting and suspending the arrangement such that there is no restriction to move in the direction of the drag force. The system of the aerodynamic model and its support structure behaves like a linear dynamic system.

Tuttle et al. (1995) tested a short model of hypersonic impulse condition for the measurement of drag force using stress wave force balance [2]. The experimentation was conducted on a 15° semi angle cone whose length was 450 mm and mass of 1.75 kg. It measured the drag at Mach number 5 using stress wave force balance. Joarder et al. (2003) designed and tested a free-floating internally mountable balance system [3]. Minimal friction ball bearings are used for ensuring the free-floating condition of the model during tunnel testing. Finite element modeling and computational fluid dynamics are used in the design and calibrating the new balance system. The measured experimental drag force at the blunt leading edge of flat plate at stagnation enthalpy of 0.7 MJ/kg and nominal Mach number of 5.75 matches well with the results obtained from simulated finite element method. Robinson et al. (2010) has designed and employed an internal stress wave force balance in a shock tunnel [4]. In this work, the measured force is in the order of milliseconds for the blunt cone of 303 mm long and half cone angle of 100 with an accuracy of $\pm 6\%$. Computational fluid dynamics estimation indicates the success of the three-component force balance. Authors also show that a higher accuracy of the recovered forces and moment loads are attained using an external force balance.

Bommana (2012) obtained the results using an accelerometer, laser vibro-meter, and semiconductor strain gauge for five dissimilarity impulse forces applied to the tip of the model [5]. He modeled the structure using finite element modeling software and achieved the corresponding strain, acceleration, and velocity responses. In addition,

an evaluation between the experimental work and the simulation work has been done. Dave (2013) carried out an experimental study by employing an aerodynamic model, which consists of a stress bar attached with a hemispherical model at one end and other end connected with a rod [6]. Three intrusive type sensors, i.e., semiconductor strain gauge, piezo film, and accelerometer, are used for measurement and instrumentation. The strain is measured by using semiconductor strain gauge and piezo film; both the sensors are mounted on the surface of the stress bar at the same distance from ends but at different locations.

Pallekonda et al. (2014) developed an experimental setup to distinguish the applicability and calculation of a laser-based extrusive technique along with the established intrusive accelerometer constructed method for impulsive force measurement. Accelerometer recognized measurements are found to calculate precisely the magnitude and sequential nature of the force [7]. Luo et al. (2015) developed a new signal decomposition wave system fitting method with accelerometer free. This devised system was used to remove vibration waves of low frequency [8]. It could decompose the balance signal and distinct vibration waves without the influence on the DC component; whether the cycle of the sample signal was complete or not. As an average signal post-processing tool in JF-12, the application results show that it works reliably with high accuracy, and it can explain puzzling signals encountered in JF-12.

Jiang et al. (2016) planned a trimaran hull to observe the hydrodynamic characteristics of tunnel and its impact on the hull body. The devised prototype was tested for Froude number ranging from 0.90 to 5.87 [9]. A finite volume method was used to simulate the frontward motion of the hull with two degrees of freedom for Froude number more than 3.16. The hull has a noticeable hydrodynamic performance wave profile, dynamic lift, longitudinal center of pressure, and flow vectors in the tunnel region at various Froude numbers. Liu et al. (2017) investigated the dynamic responses generated by using variable load on a train body [10]. The applied pressure at the marked points on both sides of the train body are about the same. Whenever it goes under dynamic loads in the tunnel, the lateral acceleration on the roof is significantly more than that of the underframe. The vibration acceleration components in horizontal and vertical direction are 33.8% and 47.2% more than those for a train operating in open air, respectively.

Boutemedjet et al. (2018) conducted an experiment in a high Reynolds number blow down wind tunnel in three speed regimes as subsonic, transonic, and supersonic to obtain the accuracy of the rolling moment measurement in wind tunnel tests [11]. The rolling moment analyzed on a missile prototype using mono block strain gauge balance. The anticipate rolling moment values obtained in the test were expressively less than the balance rolling moment measuring element full scale. To check the correctness of the balance measurement, a sensitive one-component transducer formed. Rolling moment is measured using the balance and the sensitive transducer simultaneously. Experimental data obtained using the balance and the transducer were compared. The obtained results reveal that the balance data agree very well with the sensitive one-component transducer data. Balakalyani and Jagadeesh (2019)

developed and evaluated for measuring drag, lift, and pitching moment over hyper-velocity ballistic in a hypersonic shock tunnel [12]. The two-hypervelocity ballistic models HB 1 and HB 2 are used in experimentation at different angles of incidents at nominal Mach numbers of 5.78 and 8.31. The force balance is provided with rubber supports to ensure unrestrained motion of the model during the hypersonic free-stream flow. The results reveal that measured values of force and moment coefficients match well with the theoretical values estimated using modified Newtonian theory for HB 1 and HB 2 models.

So far as discussed in literature, different techniques are used to address various aspects of the design problems associated with hypersonic flight. However, none of them are able to define nature and strength of signals induced in the aerodynamic structure. Therefore, the aim of this study has been set to access the nature and strength of the signal induced. In the present study, the stress wave force balance uses for measurement of forces in an impulsive condition is investigated here. An experimental setup is devised to investigate stress wave force balance experimentally. This setup comprises a hemispherical Aluminum metal block of 50 mm diameter and a 150 mm stress bar made from brass alloy. An encapsulated type of semiconductor strain gauge is used to calculate the intrusive type of measurement technique. A digital oscilloscope is used to record the signal coming from the semiconductor strain gauge and the impact hammer. These recorded signals show in the wave shape of the time versus voltage signal which is converting into strain.

2 Experimentation

The experimentation is performed in two phases. In first phase, an experimental setup was fabricated and deploy in the favorable conditions of experimentation. Sensors were calibrated and a number of test conduct and record reading. In the second phase, a numerical simulation performed using finite elements method and computational fluid dynamics software with adequate boundary conditions for verifying the recorded reading from the experimental setup.

2.1 Numerical Simulation

The objective of the simulation modeling is observing the response of the model for an applied impulse signal. The optimum length of a model is the maximum length for a specific strain gauge location beyond which the signal sensed by the strain gauges is not affected by interference from the reflected stress wave. In other words, it is the maximum length for which the time of travel of the stress wave from the model tip to the strain gauge location, the time of travel from the strain gauge location to the end of the stress bar and time of travel for reflected back to the same point, are equal. The stress wave force balance is calculated by numerical simulation method
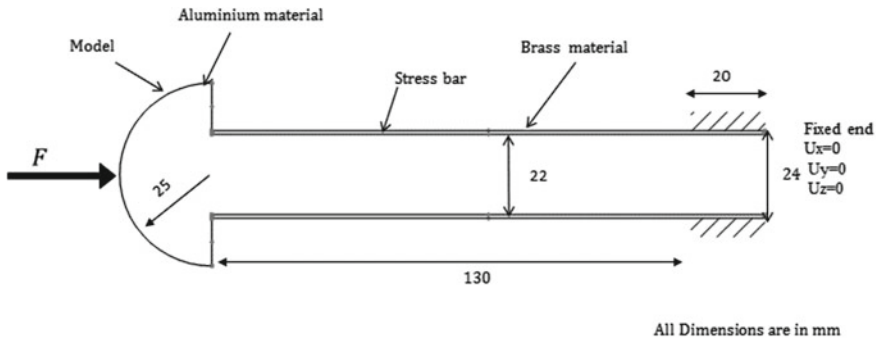
Fig. 1 Schematic diagram of the experimental model used in this study

using an experimental model of hemispherical-shaped aluminum block of 50 mm diameter and 150 mm lengthened brass material stress bar as shown in Fig. 1.

The obtained strain was plotted for a node at the location where the strain gauges were presumed to be placed. For the sake of assumption, the strain gauge location was fixed at 20 mm apart from the interface between the model and the stress bar. By analyzing the strain versus time graphs for a given model length at that specific node, the correct length for which the strain gauge reading showed interference could be determined.

2.2 ANSYS Model Definition and Meshing

The section view of the model was created in the ANSYS software and swept about the longitudinal axis to generate three-dimensional as shown in Fig. 2. Subsequently, it was meshed with the free mapping tool, and material properties were defined for the model and the stress bar. The material properties assigned to the model and stress bar during simulation are given in Table 1. Fixed condition to the threaded part of the stress bar is provided as the boundary conditions during the simulation of fixed
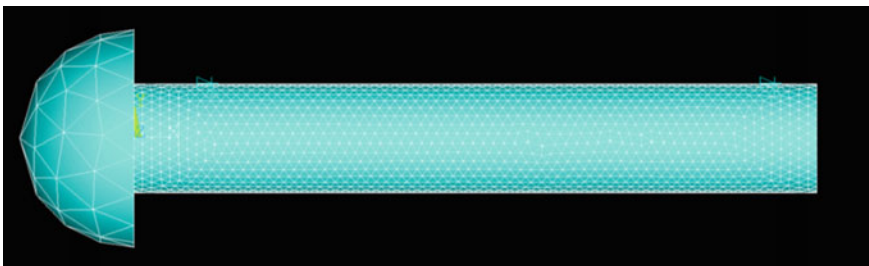
Fig. 2 Meshed hemispherical model in ANSYS

Table 1 Material properties of model and stress bar

S. No.	Material	Young modulus (E) (GPa)	Density (ρ) (kg/m^3)	Poisons ratio (ν)
1	Aluminum	70	2770	0.29
2	Brass	100	8400	0.33

case, whereas a rubber of 6 mm is attached to the threaded portion and inner surface of the rubber is made fixed for simulating the free flying condition.

The material properties of the model are given in Table 1.

The choice of material for the model as aluminum is justified, since it is in lightweight and less dense than other metals mostly. This means that an aluminum model can respond quickly in the free-flying test section even to a low intensity load. Other materials such as ferrous alloys, zinc, and copper are far denser than aluminum, and this restricts their quick response to an applied load in a free flying section. On a broader scale, it is aluminum and its many alloys; such as duralumin used for aerospace applications.

One more hemispherical model of aluminum having radius 15 mm attached with a stress bar of brass having diameter 14 mm, thickness of 1 mm, and length of 41 mm which is fabricated and equipped with stiffness dominated balance that is chosen for current analysis purpose which is shown in Fig. 3. The balance also includes a threaded section made on the stress bar for fixing it in the end flange. Initially, FEM simulation has been carried out so as to estimate the position of the strain gauge for a higher magnitude of the strain and for longer test duration. Transient finite element analysis has been carried out for the above model using ANSYS 14.5 software version for a simulation time of 2 ms which corresponds to the range of experimental test in stress wave force balance system.
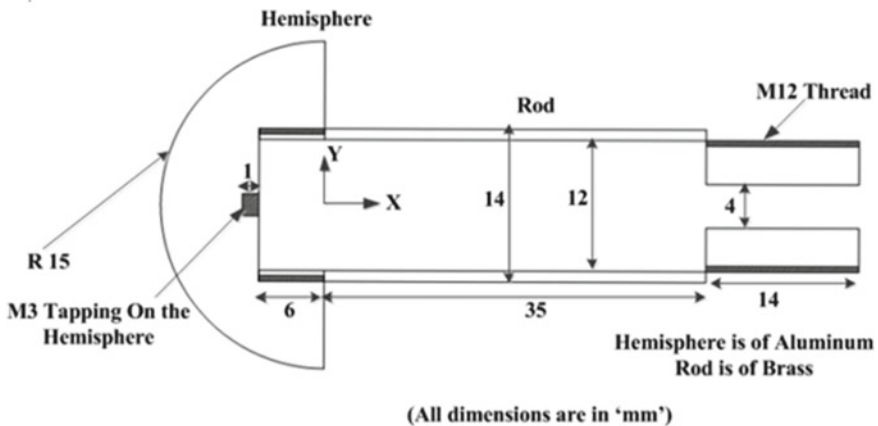
Fig. 3 Second schematic diagram of the experimental model
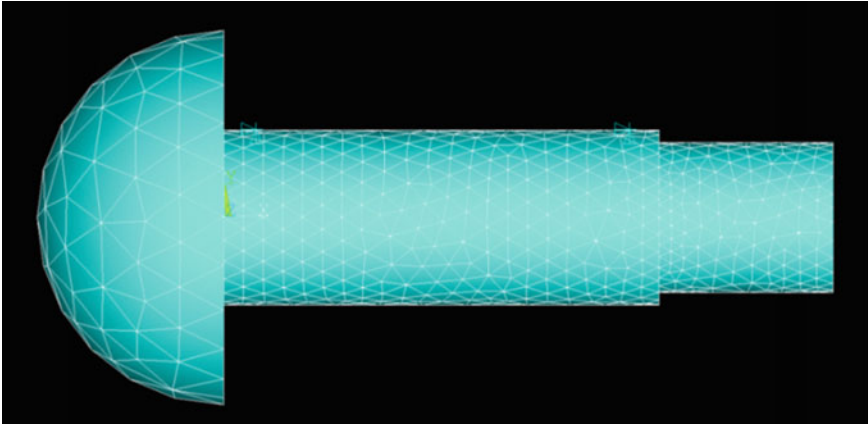
Fig. 4 Second meshed conical model in ANSYS

During meshing for the test model, a ten-node tetrahedral element is used. After the detailed mesh independence studies, the number nodes obtained are 89,500. The material properties assigned to the model and stress bar during simulation are given to a fixed condition for the threaded part of the stress bar and provided as the boundary conditions during the simulation of fixed case. A rubber of 6 mm is attached to the threaded portion, and the inner surface of the rubber is fixed for simulating the free-flying conditions. The detailed mesh of the model is shown in Fig. 4.

During simulation, different magnitudes of impulse forces are applied at the tip of the model and corresponding dynamic strain along horizontal direction at discrete points on the stress bar are measured for both types of boundary conditions. The comparison of the strain magnitude for both the cases is carried out for a load application of 20 N, which has been shown in Fig. 4. From the figure, it can be concluded that the strain gauge should be mounted at a distance of 5 mm from the end of the model for ensuring a higher magnitude of strain.

3   Experimental Setup

The experimental setup as shown in Fig. 5 was settled in the fluid mechanics laboratory of mechanical engineering department, IIT, Guwahati. It consists of a metal span held by a sliding block and the length of the span can adjust with the help of a bolt. The sliding block is fabricated to an angle section for the support of wooden beams. The wooden beam can be fixed with the help of a bolt. The span base is fixed to the iron bed with the help of bolt and nut arrangement. The wooden beam suspends the configuration horizontally. Care should be taken such that the model should be in the horizontal position free from external effects like noise or atmospheric disturbances. The model is suspended by the two stainless steel wires and the wires are fitted to
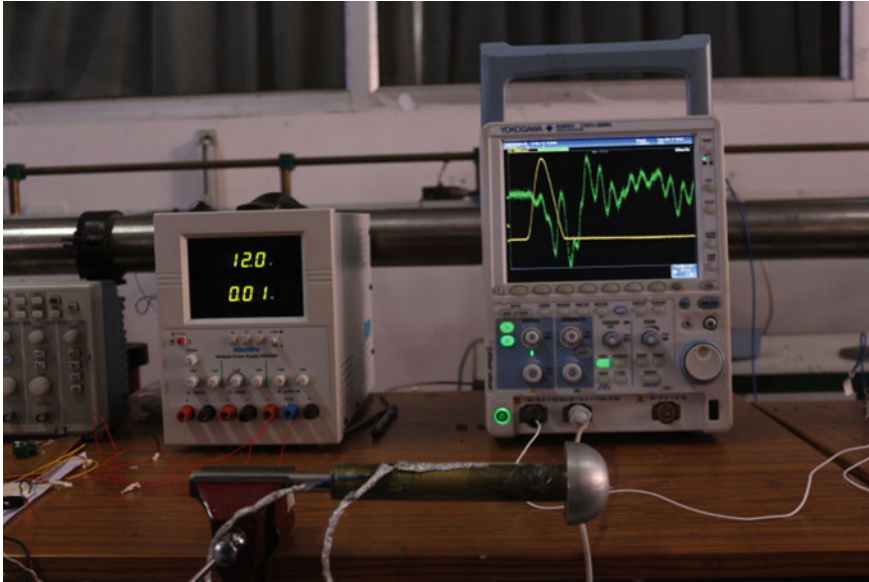
Fig. 5 A pictographic view of experimental setup used for experimentation

the two hooks attached at the top of the frame. The accelerometer is fitted to the model in the tap hole with connection to an impact hammer and both are connected to the signal conditioner. The instruments as oscilloscope, signal conditioner, impact hammer, semiconductor strain gauge, and instrumentation amplifier were used for measurement.

4   Results and Discussion

Impact hammer is used to apply impulse forces on the hemispherical model. Impact is applied in the longitudinal direction of the bar to propagate waves in one dimension only. The different signal data are visualized and measured from the oscilloscope. The response plots are drawn from the signal data measured from the oscilloscope multiplying with the corresponding sensitivity factor of each individual sensor. The response's accuracy is up to 1 ms.

Experiments perform on a model of stress bar of length 150 mm made of brass and 50 mm hemispherical-shaped aluminum block. The sensors used for monitoring response signals are semiconductor strain gage, which is fixed 20 mm from the reference axis. For this set of experimental combinations, two force input signals, and their corresponding strain, the force–time histories are measured and draw graphs.
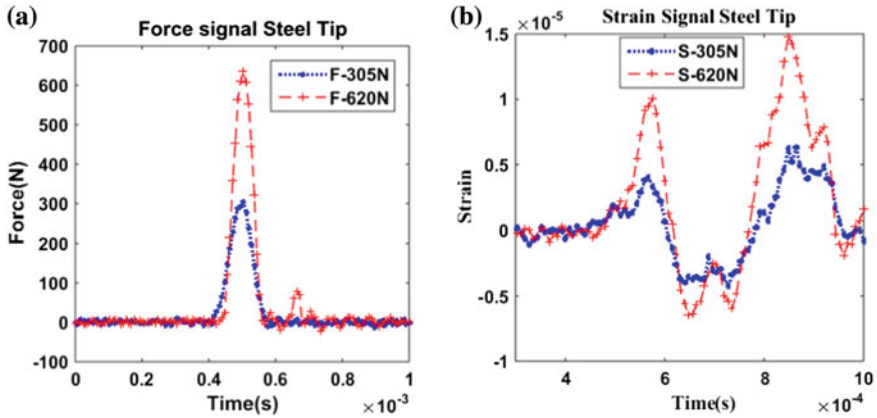
Fig. 6 **a** Force–time signal response **b** Strain–time signal response

The force–time response and strain–time response are generated from the impact hammer for two impulsive forces 305 N and 620 N investigated with the help of an oscilloscope and graphically represented in Fig. 6.

- It is observed from the graphical representation Fig. 6a, b that the maximum value of force and strain attains for the same time duration, i.e., $(0.4 \text{ to } 0.6) \times 10^{-3}$ s and $(0.8 \text{ to } 1) \times 10^{-3}$ s, respectively.
- The force signal obtained from impact hammering of two distinct impulsive forces and their corresponding measured strain signal will be highest.

The force–time response and strain–time response for free-flying conditions generated from impact hammering for two impulsive force 400 N and 500 N investigate with the help of an oscilloscope and graphically represented in Fig. 7.

- It is deliberated from Fig. 7a, b that the maximum value of force and strain attains for the same time duration, i.e., $(0.8 \text{ to } 1) \times 10^{-3}$ s and $(1 \text{ to } 1.2) \times 10^{-3}$ s, respectively.
- The force signal obtained from impact hammering of two distinct impulsive forces and their corresponding measured strain signal will be the highest.

Experiments perform one more configuration of hemispherical models of aluminum having radius 15 mm attached with a stress bar of brass having diameter 14 mm, thickness of 1 mm, and length of 41 mm. The sensors used for monitoring response signals are semiconductor strain gage, which is fixed 20 mm from the reference axis. For this set of experimental configuration, three force input signals, and their corresponding strain; the force–time responses are measured and draw graphs.

The force–time response and strain–time response for free-flying conditions generated from impact hammering on a steel tip for three impulsive forces 80 N, 160 N, and 190 N investigate with the help of an oscilloscope and represented graphically in Fig. 8.
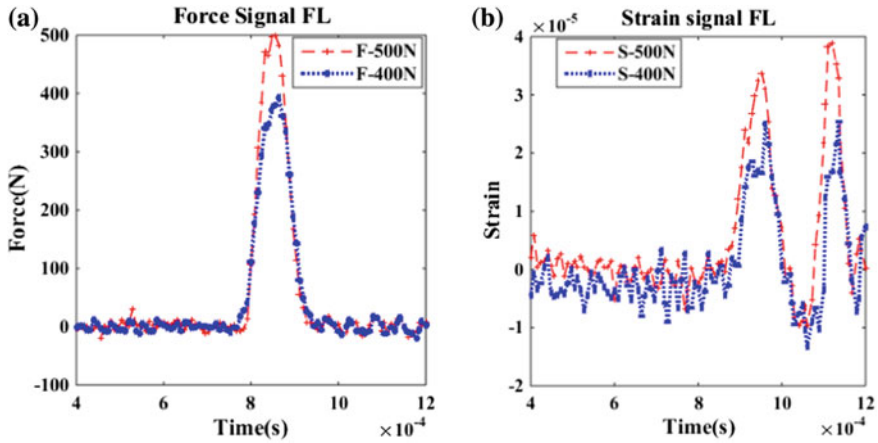
Fig. 7 **a** Force–time signal response **b** Strain–time signal response
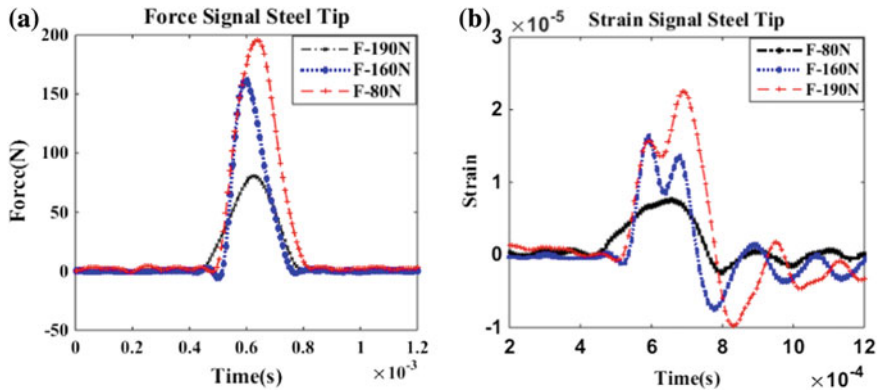
Fig. 8 **a** Force–time signal response **b** Strain–time signal response

- It is deliberated from Fig. 8a, b that the maximum value of force and strain attains for the same time duration, i.e., (0.6 to 0.8) $\times 10^{-3}$ s and (0.6 to 0.8) $\times 10^{-3}$ s, respectively.
- The force signal obtained from impact hammering of two distinct impulsive forces and their corresponding measured strain signal will be the highest.
- The graph line follows the same trajectory from the beginning time to the end of trajectory, i.e., 1.2 ms.

Figures 9a, b and 10a, b compare the result obtained from experimental setup and simulation using finite element method. Figures 9 and 10 show the magnitude of strain has peak values at 1 ms for both experimental setup as mentioned above two impulsive forces 400 N and 500 N and three impulsive forces 80 N, 160 N, and 190 N, respectively.
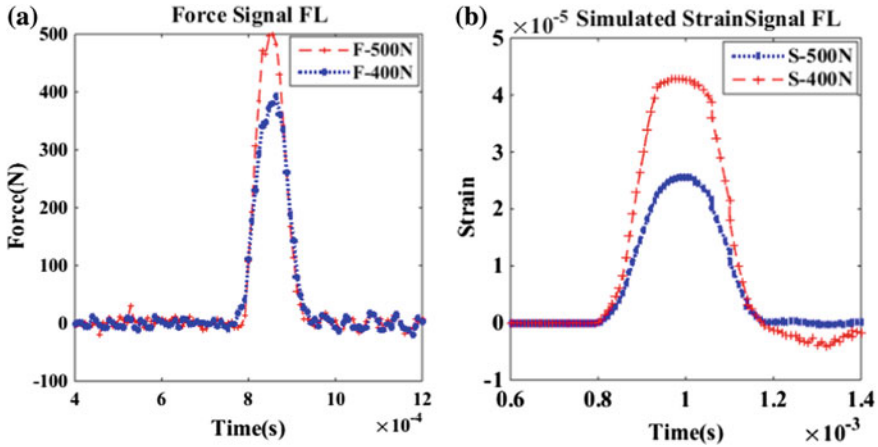
Fig. 9 **a** Force–time signal response **b** Strain–time signal response
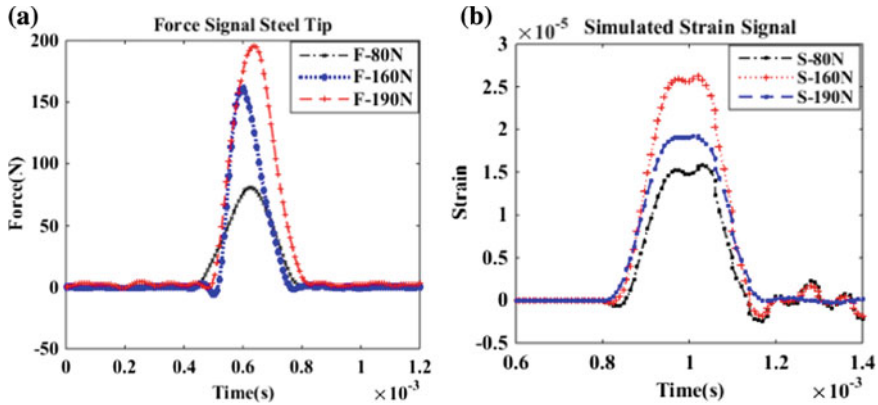
Fig. 10 **a** Force–time signal response **b** Strain–time signal response

5 Conclusion

In the present work, stress wave force balance for the hemispherical model and the stress bars has been studied. The hemispherical model is fabricated of aluminum metal, and the stress bars is made of brass, copper, and mild steel. Apropos to graphical representation, it can be concluded that the nature of signals for each individual sensor is distinctive and highly repetitive. The strength of strain signals is depending on the impulse force act on the aerodynamic structure as well as the distance travelled by the stress wave inside the stress bar. These waves propagate and reflect within the model and the stress bar. In this very short duration, no steady state of force equilibrium can be achieved. After the careful inspection of the recovery force–time

responses and strain–time responses recorded from the oscilloscope, it can be easily concluded that for the same time duration; force and strain values have achieved their maximum value.

References

1. Simmons JM, Sanderson SR (1991) Drag balance for hypervelocity impulse facilities. AIAA J 29(12):2185–2191
2. Tuttle SL, Mee DJ, Simmons JM (1995) Drag measurements at Mach 5 using a stress wave force balance. Exp Fluids 19(5):336–341
3. Joarder R, Jagadeesh G (2003) A new free floating accelerometer balance system for force measurements in shock tunnels. Shock Waves 13(5):409–412
4. Robinson MJ, Schramm JM, Hannemann K (2010) Design and implementation of an internal stress wave force balance in a shock tunnel. CEAS Space J 1(1–4):45–57
5. Pallekonda (2011) Design and analysis of Single Component Accelerometer Balance for High Speed Aerospace Applications, M. Tech thesis
6. Bommana (2012) Experimental Investigation of a Stress Wave Force Balance System for Aerospace Application, M. Tech thesis
7. Dave (2013) parametric studies of stress wave force for short duration measurements M. Tech thesis
8. Luo C, Wang Y, Wang C, Jiang Z (2015) Wave system fitting: a new method for force measurements in shock tunnels with long test duration. Mech Syst Sign Process 62–63:296–304. https://doi.org/10.1016/j.ymssp.2015.02.024
9. Jiang Y, Sun H, Zou J, Hu A, Yang J (2016) Analysis of tunnel hydrodynamic characteristics for planing trimaran by model tests and numerical simulations. Ocean Eng 113:101–110. https://doi.org/10.1016/j.oceaneng.2015.12.038
10. Liu TH, Chen ZC, Chen XD, Xie TZ, Zhang J (2017) Transient loads and their influence on the dynamic responses of trains in a tunnel. Tunnell Underground Space Technol 66:121–133. https://doi.org/10.1016/j.tust.2017.04.009
11. Boutemedjeta A, Samardži M, Ćurčić D, Rajić Z, Ocokoljić G (2018) Wind tunnel measurement of small values of rolling moment using six-component strain gauge balance. Measurement 116:438–450. https://doi.org/10.1016/j.measurement.2017.11.043
12. Balakalyani G, Jagadeesh G (2019) An accelerometer balance for aerodynamic force measurements over hypervelocity Ballistic models in shock tunnel. Measurement 136:636–646. https://doi.org/10.1016/j.measurement.2018.12.099

Fatigue Life Prediction of Front Axle of Truck at Different Crack Directions Using ANSYS

Rajesh P. Verma and Shivani Pant

Abstract The front axle is an important part of vehicle suspension system. The front axle of materials AISI 1045, AISI 1053, and Structural steel is analyzed with the help of ANSYS. The AISI 1045 material exhibits comparatively greater von-misses stress and deformation. The critical area of axle is determined, which provides a failure-prone zone and a basis to introduce a crack at this region for study. The critical zone of the axle is found under the plate spring sheet. The failure often propagates due to the developed crack in axle and the direction of appearance of crack may be different in different conditions. The fatigue life of axle is determined for different crack angles. The fatigue life of front axle is decreasing with increase in crack angle. The vertical crack direction is found more dangerous direction in front axle.

Keywords Front axle · Crack direction · Fatigue life · ANSYS

1   Introduction

The front axle beam is one of the major parts of vehicle suspension system. About 30–40% of total vehicle weight is taken up by front axle. The front axle is mainly subjected to the combination of shear stresses and bending stresses. The failure prevention of front axle of a vehicle is prime concern of a designer. The failure often propagates due to the developed crack in axle. The direction of appearance of crack may be different in different loading conditions. Therefore, a detailed analysis of effect of crack direction on failure of axle is required to understand the failure phenomena. However, Zhang et al. [1] studied the influence of crack on the fatigue life of front axle of heavy-duty truck, still more investigation is required.

Finite element (FE) method is a powerful technique to analyze a mechanical component. Shao et al. [2] obtained stress concentration region at critical section of drive axle housing of mining dump truck using FE analysis. The region obtained by FE analysis coincides with the region obtained in practice. Topac et al. [3] analyzed

R. P. Verma (✉) · S. Pant
Department of Mechanical Engineering, Graphic Era Deemed to Be University, Dehradun, Uttarakhand, India
e-mail: rajesh_diva1@yahoo.in

successfully the damaged wheel disc to obtain stress distribution and possible failure initiation region using FE analysis. In another work, Topac et al. [4] also used FE method to predict the critical section of rear axle housing prototype, where high-stress concentration and lower fatigue life existed. The obtained critical section showed the same pattern of Von-Misses stress distribution as obtained in practice. Many more researchers [5–8] have applied FE method successfully to analyze the different mechanical components.

This paper studies the effect of crack direction on failure of front axle of a truck by FE analysis using ANSYS workbench software. Firstly, the material having better strength was identified among the most used materials (AISI 1045, AISI 1053, and Structural steel) for front axle. The critical section was obtained based on the greater stress and deformation. Finally, the effect of direction of crack at critical zone on fatigue life was analyzed.

2 Methodology

The front axle modal was prepared in the CREO software and was imported to the ANSYS for all types of analysis. The objective of the work was to estimate the fatigue life of front axle of truck having a crack at different angles. The work was planned in the following manner:

(i)   Comparative study of different material (AISI 1045, AISI 1053, and Structural steel) of front axle
(ii) Identification of critical zone of front axle
(iii) Inclusion of crack at different angles at critical zone of front axle
(iv) Investigation of fatigue life of front axle containing cracks at different angles

The base length of the half of modal was 736 mm and width were 80 mm. Two circular holes were made at each end of the front axle to align the wheels to the front axle with the help of stubaxle. The FE model (Fig. 1a) consists of 27,731 nodes and 187,202 elements with 8 mm grid size. The uniform distributed load was applied on the plate spring seat of front axle which is 22500 N. Movement constraints of X, Y, Z are applied on the left support arch, and movement constraints of X, Z are applied on the right support arch as shown in Fig. 1b.

3 Comparative Study of Different Material of Front Axle

The axle models of three different materials (AISI 1045, AISI 1053, and Structural steel) were simulated in ANSYS environment to obtain von-misses equivalent stress pattern and deformation pattern. The mechanical properties of materials used in analysis are listed in Table 1.

(a)

A Force=22500 N
B Displacement
C Displacement 2

(b)
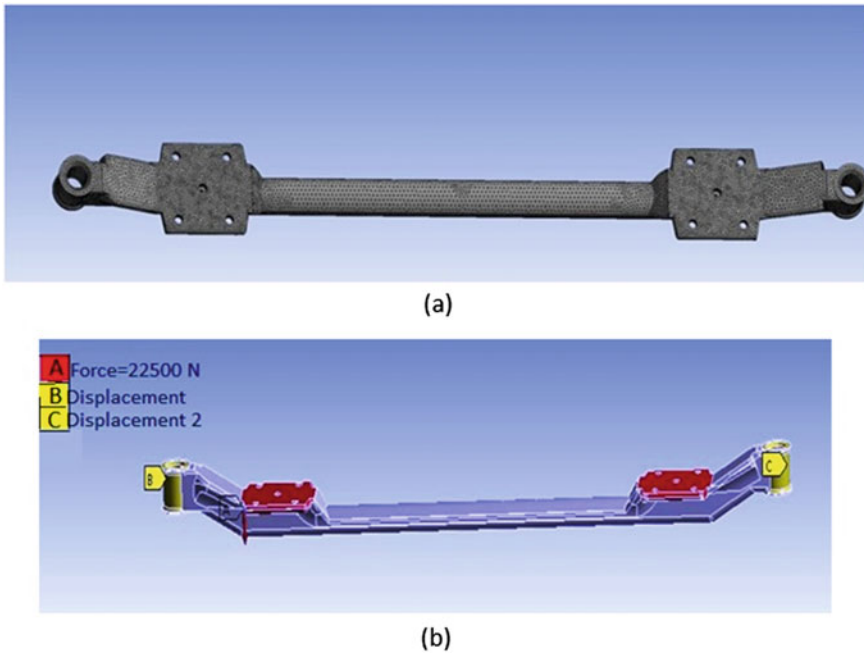
Fig. 1 **a** Mesh generation **b** boundary condition applied

Table 1 Mechanical properties of materials

Material	Density (g/cc)	Young modulus (GPa)	Poission ratio	Tensile ultimate strength (MPa)	Yield strength (MPa)
AISI 1045	7.87	200	0.29	585	310
AISI 1053	7.70	190	0.27	650	350
Structural steel	7.85	207	0.30	400	250

Figure 2 shows the von-misses stress pattern and deformation pattern of the materials respectively. The maximum stress of 291.62 MPa, 273.27 MPa and 279.75 MPa has appeared in axle of material of AISI 1045, AISI 1053, and structural steel respectively. As displayed in Fig. 2, the ultimate deformation is 12.058 mm, 12.034 mm, and 12.033 mm in axle of material of AISI 1045, AISI 1053, and structural steel respectively. The comparison of maximum stress and ultimate deformation of the three materials are shown in Fig. 3.
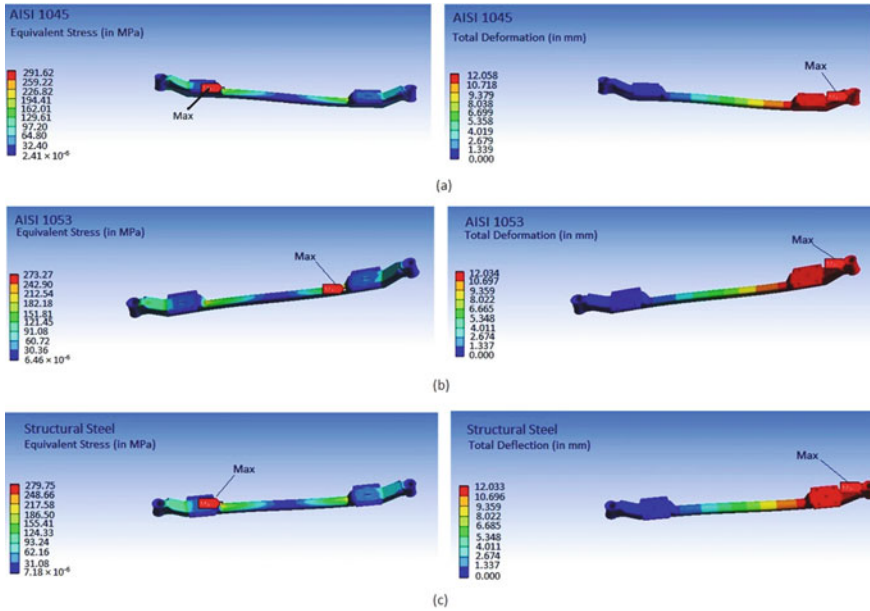
Fig. 2 Equivalent Stress (Von Misses stress) and total deformation in front axle made of (a) AISI 1045 (b) AISI 1053 (c) Structural Steel
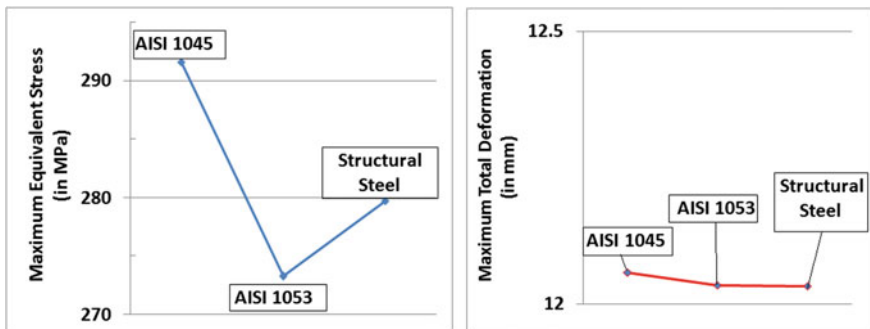
Fig. 3 Comparison of maximum von misses stress (equivalent stress) and maximum deformation of materials

4 Identification of Critical Zone of Front Axle AISI 1045

From Fig. 2, we can find that the maximum stress and ultimate deformation occurs under the plate spring sheet for all three materials. That is because the site has greater stress concentration. Therefore, this section is considered a critical (danger) section of front axle.

Fig. 4 Critical zone (danger zone) of front axle
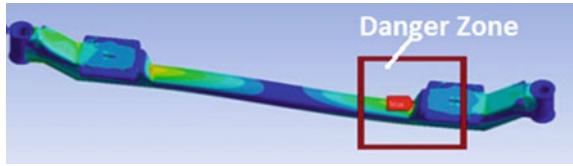
Among the three materials, AISI 1045 shows greater von-misses equivalent stress and deformation. So the AISI 1045 material is considered for further investigation in the present work. The critical zone of front axle made of AISI 1045 is shown in Fig. 4.

5 Inclusion of Crack at Different Angles at Critical Zone of Front Axle

An internal crack (of length 8 mm) of different angles ($\theta = 0°$, 10°, 20°, 30°, 40°, 50°, 60°, 70°, 80°, and 90°) with axle axis was generated at critical zone in the CAD modal as shown in Fig. 5. The front axle made of AISI 1045 was taken to study the effect of crack direction on failure. The crack angle $\theta = 0^0$ refers to crack along axle axis direction and $\theta = 90°$ refers to the crack perpendicular to axle axis direction.
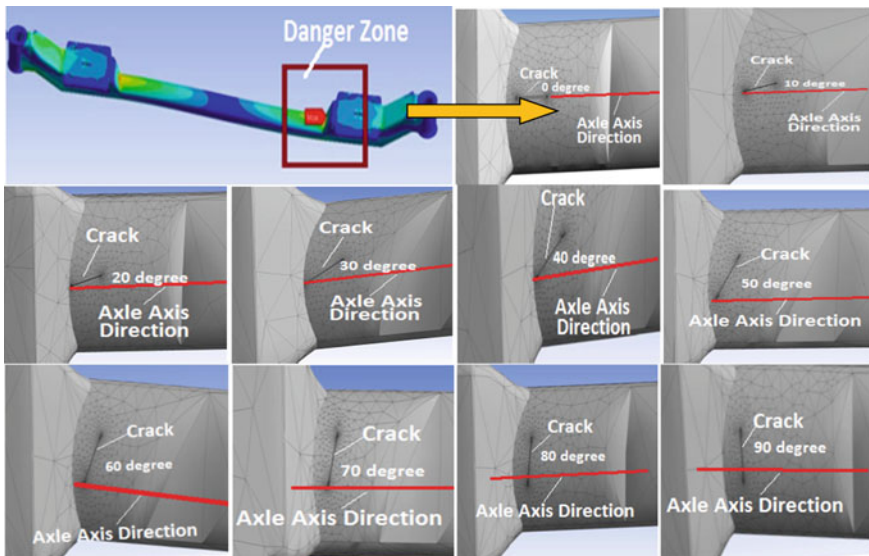
Fig. 5 Different crack direction (0°, 10°, 20°, 30°, 40°, 50°, 60°, 70°, 80°, 90° from axle axis direction) in critical zone of axle

6 Analysis of Front Axle Containing Cracks at Different Angles

The fatigue life of the axle was estimated for different crack angles using ANSYS. The estimated fatigue life of axle with crack direction at $\theta = 0°$ using ANSYS is compared with the experimental value of fatigue life of CT specimen (as per ASTM E647-08) under tensile load. The fatigue load was kept at tension-load equivalent to 30% of ultimate tensile strength with stress ratio 0.1 and frequency 10 Hz. The estimated and experimental values are presented in Fig. 6. The difference in estimated value (by ANSYS) and experimental value is below 10%. Therefore, it may be concluded that the life estimated by ANSYS is very close to the experimental value. So in further investigation of life of axle with different crack direction, ANSYS was applied assuming that the trend of the result will be similar to the experimental result.

The effect of crack direction on the fatigue life of front axle is shown in Fig. 7. From Fig. 7, it is observed that the fatigue life of the axle decreases with the increase of crack angle. The life is reduced drastically up to crack angle $\theta = 20^0$.

The trend of decreasing fatigue life may be understood by the direction of major principal stress. The major principal stress in the analysis was found along axle axis, and so the crack at $\theta = 0°$ exhibits slower crack propagation (i.e. longer fatigue life), whereas the crack at $\theta = 90°$ (perpendicular to major principal stress) propagates very easily. The literature [1, 4] also reflects the fact that the fatigue life of cracked components is greater along with major principal stress.

Fig. 6 Comparison of fatigue life obtained by ANSYS and experiment for crack angle 0°
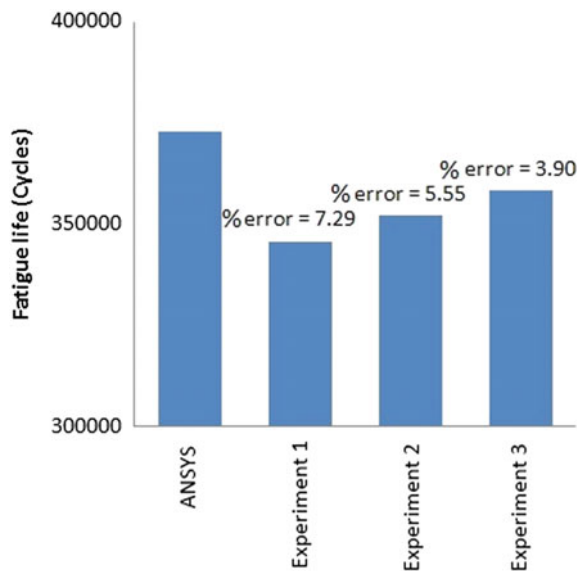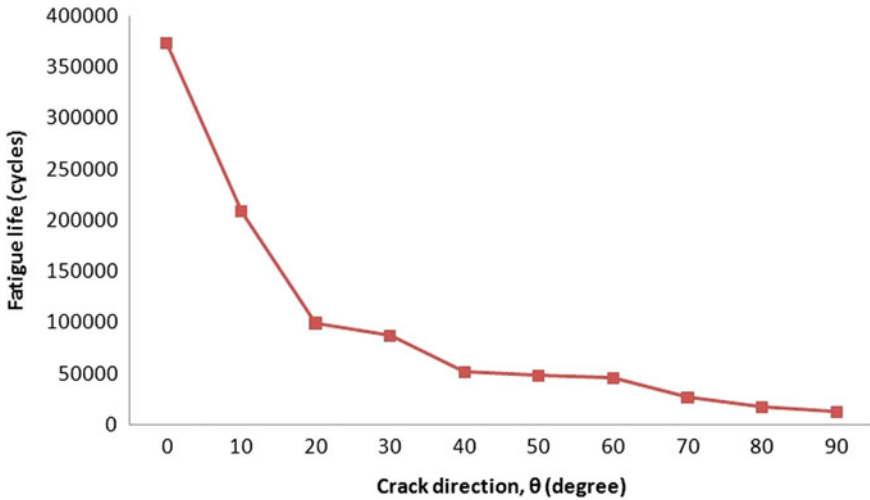
Fig. 7 Variation of fatigue life at different crack angles

7 Conclusion

From the present work, the following conclusions are made:

(i) AISI 1045 material exhibits comparatively greater von-misses stress and deformation.

(ii) The critical zone of the axle is found under the plate spring sheet for all three materials; AISI 1045, AISI 1053, and structural steel.

(iii) The fatigue life of front axle is predicted using ANSYS and it was found very close to the life recorded by the experiment (with less than 10% error).

(iv) The fatigue life of front axle is decreasing with an increase in crack angle (crack direction with respect to the axle axis).

(v) The crack with crack angle more than 20^0 in front axle reduces the fatigue life of axle drastically.

(vi) The axle with vertical crack (crack perpendicular to axle axis) exhibits lesser fatigue life and so vertical crack direction ($\theta = 90°$) is found the more dangerous direction of crack in front axle.

References

1. Zhang M, Ji X, Li L (2016) A research on fatigue life of front axle beam for heavy-duty truck. Adv Eng Softw 91:63–68
2. Shao Y, Liu J, Mechefske CK (2011) Drive axle housing failure analysis of a mining dump truck based on the load spectrum. Eng Fail Anal 18(3):1049–1057

3. Topaç MM, Ercan S, Kuralay NS (2012) Fatigue life prediction of a heavy vehicle steel wheel under radial loads by using finite element analysis. Eng Fail Anal 20:67–79
4. Topaç MM, Günal H, Kuralay NS (2009) Fatigue failure prediction of a rear axle housing prototype by using finite element analysis. Eng Fail Anal 16:1474–1482
5. Senalp AZ, Kayabasi O, Kurtaran H (2007) Static, dynamic and fatigue behavior of newly designed stem shapes for hip prosthesis using finite element analysis. Mater Des 28:1577–1583
6. Xu Z, Mamtimin G, Cheng W (2009) Finite element analysis to fatigue life of the S-shape bellows. Press Vessel Technol 26(2):21–25
7. Peng Y, Zhi-yong HAO (2007) Fatigue life prediction based on finite element and multibody dynamics co-simulation. J Zhejiang Univ 41(2):325–328
8. Nan C, Jianzhong S, Xun C, Zheng Y, Keshan L (2009) Accelerated fatigue bench test of driving axle housing based on FEA. In: International conference on measuring technology and mechatronics automation, pp 3–6

Automatic Handbrake System to Reduce Theft Problem of Vehicle

Sagar Saini, Shubham Mishra, R. K. Tyagi, and Preeti Joshi

Abstract In this work, automatic hand brake system which reduces the theft problem of vehicles has been designed and fabricated. This system works similar to the central locking system in which the car is locked by a remote-control system, and this automatic handbrake system also uses the remote-control system to lock and unlock the rear brakes of the car, thus providing a better security to the vehicle and reduce the human effort by automating the handbrake system. This automatic hand brake system is found to be better than the central locking system used in the current vehicles as this system provides the locking by electrical as well as mechanical means. The present hand brake system consists of attachments which make it an antitheft device for the vehicles. This device also helps in reducing the cost of the locking system of the vehicle with better security.

Keywords Antitheft · Locking system · Central locking

1 Introduction

The current handbrake system is modified effectively to provide a feasible solution for reducing the human effort, which is applied during the locking of the manual handbrake. This handbrake system is used as a safety device for the cars while parking, and this also provide an excellent braking effect. This system is simple in operation and hence reduces the braking time. Thus, this system successfully replaces the conventional handbrake system and reduces the error in operating the handbrake manually [1, 2].

The manual handbrake system different than conventional handbrake in construction which consists of two sets of wire which are pulled during the braking operation to lock the rear wheels. When we pull these cables, they transfer the applied force on the braking pad which rubs themselves against the drum walls or disks to stop the running wheel. Some vehicle even has the separate braking system which is operated

S. Saini · S. Mishra · R. K. Tyagi (✉) · P. Joshi
Amity University, Noida, Uttar Pradesh, India
e-mail: tyagirk1@gmail.com

251

manually by a handbrake lever. Currently, the manual handbrake system is replaced by electronic parking brake, which is also known as automatic handbrake system [3]. In this braking system, when we press the electronic button, the DC motor runs and pulls the braking pads toward the disk or drum walls. So, this handbrake system is made automatic by using the combination of rack and pinion gear mechanism and electronic proximity sensors.

In this handbrake system, the manual handbrake system is made automatic, which is operated with the ignition system of the vehicle. This provides safety while riding on the slopes and hilly areas. This automatic handbrake system is operated with the help of the key of car, i.e., initially, this braking system is in locked condition, but as soon as the key is rotated and the car's ignition system is ON, the brakes gets unlocked automatically. Thus, this handbrake system reduces the human efforts and human errors which occur while parking or driving the vehicle [4, 5]. This system is entirely automatic in operation during the application of the brake, along with this it also provides the unique features like "HOLD" perform which are very helpful on the inclined roads, thus providing the better safety and pleasure for the driver as well as the vehicle during the drive and stop condition. This system is much more advance and effective than the traditional braking system which is operated manually, so it has a vast scope and would be used in all the vehicles in future [6–9]. This system can be used in any vehicle today by just spending a small amount of money as it provides many practical uses and safety features.

The main aim of the present work is to reduce the theft problem of the vehicles and to reduce the human effort in applying the handbrake by automating the handbrake system. This system works similar to the central locking system in which the car is locked by a remote-control system, so in the similar way, this automatic handbrake system also uses the remote-control system to lock and unlock the rear brakes of the car, thus providing a better security to the vehicle and reduce the human effort by automating the handbrake system. This system is very cost-effective and efficient, so that it can be used in any existing vehicle as a safety device.

1.1   Components

12 V DC Motor: A DC motor is an electrical machine that converts electrical energy into mechanical energy. In this system, the DC motor is used to move the handbrake lever automatically during the operation of braking, i.e., to lock and unlock the rear wheel. This DC motor provides sufficient torque for the operation of the braking system. DC motor provides electricity from the car battery which is charged by the alternator connected to the flywheel of the engine. This motor consumes approximately 5Amp current at 12 V.

Worm and Worm Wheel: A worm and worm wheel is a gear arrangement in which a worm wheel meshes with a worm gear to transfer the torque generated from the rotation of the DC Motor effectively and efficiently in perpendicular direction. The two elements of this gear arrangement are worm wheel and worm screw, which
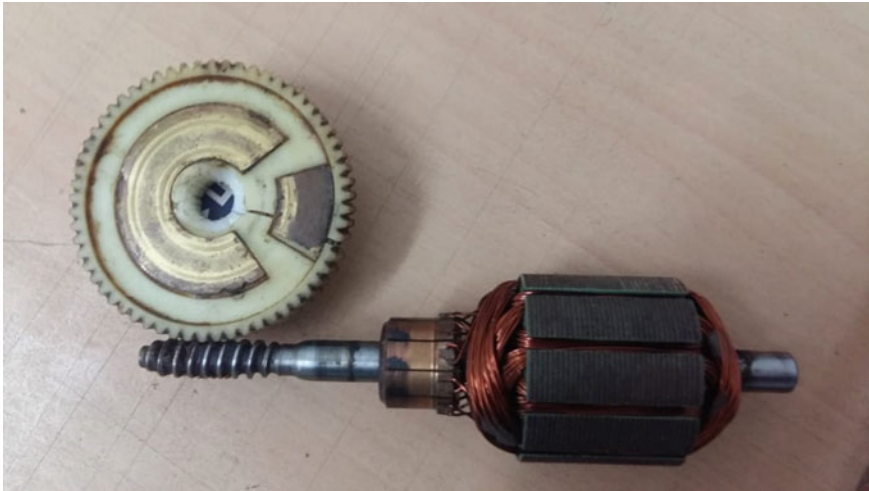
Fig. 1 Worm and worm wheel arrangement

are shown in Fig. 1. Figure 1 clearly shows the actual meshing and arrangement of the worm wheel and worm screw. We have used the worm and worm wheel gear arrangement in this system because it can multiply the torque produced from the rotation of the DC motor by approx. 50 times and on the other hand slowing down the speed of the motion of the handbrake lever. This gear arrangement has a unique locking mechanism in which we can rotate the worm wheel by meshing it with the worm screw, but we cannot rotate the worm screw with the worm wheel, and thus, this gear arrangement can be used to lock the handbrake lever, as we can move the handbrake lever only with the help of remote-control system.

Relay: Relays are electrical switch which open or close with the help of electrical signals (shown in Fig. 2). Relays are used in this project to ON and OFF DC motor, which is used for moving the handbrake lever up and down (i.e., engaging and disengaging the brake). The low voltage supply to the relay is the signal for switch OFF, whereas on the other hand a high voltage supply to the relay is to ON the motor and moves the handle at the required position. For making this system more efficient, a highly sensitive relay is required, which can sense a minimal fluctuation or difference in the input voltage/supply voltage.

2 Mechanism

In this project, the handbrake is actuated with the help of the combination of worm and worm wheel gear mechanism and remote-control system. When we press the lock button on the remote-control system, then the remote control sends the radio signal to the control system attached to the handbrake in the car. Then, control system activates
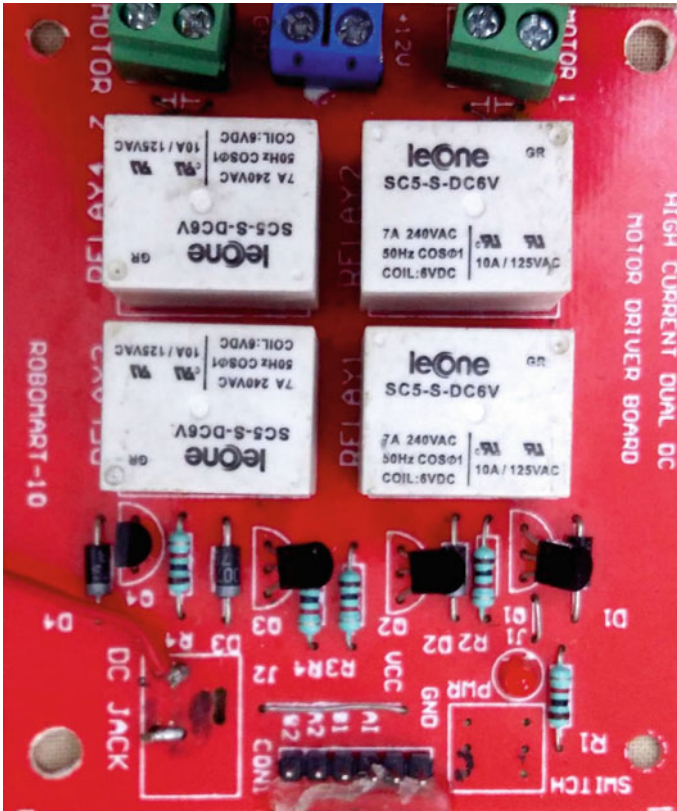
Fig. 2 Relay circuit board

the DC motor, which further rotates the worm and worm wheel gear mechanism and the handbrake lever moves up and locks the rear wheel. In a similar manner when we press the unlock button on the remote of the control system, the handbrake lever moves down disengaging the rear wheel brakes.

3 Calculation of Design Parameters

The specifications of DC motor and brake wire are mentioned in Tables 1 and 2. The force applied by handbrake lever can be calculated using the relation: Torque = Force × Distance

$$\text{Force} = 166.67 \text{ N}$$

Force applied by the handbrake lever = 166.67 N.

Table 1 DC motor specification

Voltage required by the motor	12 V
Torque generated by the motor	5 Nm
Spindle rotation	360°
RPM of motor	65
Motor arm length (x)	3 cm

Table 2 Brake wire specification

Material of wire	Stainless steel wire cable (7 × 7)
Diameter of wire	2 mm
Tensile strength of wire	905 MPa

The braking load (BL) can be calculated as:

$$BL = \frac{(\text{Tensile Strength of wire} \times \prod \times (\text{Wire Diameter})^2)}{4}$$

$$BL = \frac{\left(905 \frac{N}{mm^2} \times 3.14 \times (2\,mm)^2\right)}{4}$$

$$BL = 2843\ N$$

$$BS = \frac{(\text{Tensile Strength of wire} \times \Pi \times (\text{Wire Diameter})^2)}{4 \times 9.8}$$

$$BS = \frac{\left(905 \frac{N}{mm^2} \times 3.14 \times (2mm)^2\right)}{4 \times 9.8 \frac{N}{kg}}$$

$$BS = 290\ kg$$

The braking force can be calculated as:

F_n = Clamping force applied by brake pads.

μ = Coefficient of friction (a nominal value of 0.4 is assumed for fully conditioned pads of standard material)

$$F_b = 2 \times \mu \times F_n$$

$$F_b = 2 \times 0.4 \times 150\ N$$

$$F_b = 120\ N$$

As we can see in the above calculations that the force produced by motor in much higher than the force required for effective braking, hence this will work efficiently and effectively.

4   Assembled Model

Figure 3a shows the actual model of automatic handbrake system in which the hand-brake lever attaches with the assembly system, which consists of worm and worm wheel gear mechanism which is further attached with DC motor. The motion of the DC motor is controlled with the help of a remote-control system by using the radio waves. This project also provides an additional feature along with the automatic handbrake system in which a separate locking mechanism is used along with the above-described assembly system, which is shown in Fig. 3b.

This locking mechanism consists of a rotary gear with teeth and a lock gear which rotates radially. The motion of lock gear is controlled by a lever attached in a perpendicular direction, and this complete locking mechanism is operated manually by the user. This feature is mainly helpful when the vehicle is parked on the slope as if we unlock the rear wheels with the automatic handbrake system by a remote-control system, then the vehicle will move along the slope which will cause accident of the vehicle. But if we lock the rear wheel by both mechanisms, i.e., automatically locking mechanism and manually, then if we unlock the handbrake with remote-control system then also the rear wheel is locked by the manual locking system which keeps the vehicle at the same position along the slope and saves the vehicle from the accident.
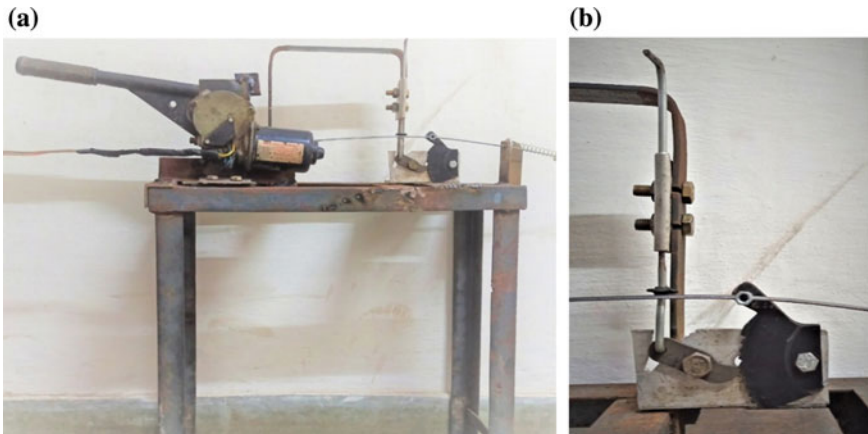
Fig. 3 **a**, **b** Different views of assembly model of automatic handbrake system

5   Conclusion

In this work, automated handbrake system is designed and fabricated, which reduces the human effort and provides better security to the vehicle. In this system, the handbrake is operated with the help of remote-control system, i.e., locking and unlocking of the rear wheels can only be done with the help of remote. This system uses a worm and worm wheel gear mechanism which has a unique locking mechanism in which the worm wheel gear can be rotated with the worm gear, but worm gear cannot be rotated with wheel gear. This device also helps in reducing the cost of the locking system of the vehicle with better security.

References

1. Naveen Kumar B, Lokesh Raj K, Ramerow Jacob R, Santhosh B (2014) Design of seatbelt activated handbrake system in cars. Int J Mech Prod Eng 2(10):53–55 (2014)
2. Thivagar S, Kumar CN (2016) Automatic hand brake system. Int J Eng Res General Sci 4(1):214–221
3. Dharia SS, Bhopale SS, Kumbhar PP, Pathak KS (2016) Advancements in automatic hand brake system. In: 4th international conference on science, technology and management, pp 193–201
4. Maske AB, Tuljapure SB, Satav PK (2016) Design & analysis of parking brake system of car. Int J Innov Res Sci Eng Technol 5(7):12,578–12,590
5. Ishak MR, Bakar ARA, Belhocine A, Taib JM, Omar WZW (2016) Brake torque analysis of fully mechanical parking brake system. Mater Today Proc 94:487–497
6. Dalvi RE, Sutar RG, Karke PH, Satpute JB (2017) Design and development of hand brake release system. Global Res Dev J Eng 2(6):280–284
7. Gopan G, Gopikrishnan EJ, Cherian GJ, Samuel JS, Sreejith R (2017) Development of automatic hand brake system. Int J Innov Res Sci Technol 3(11):328–332
8. Ugale VJ, Gade SD, Pagar SS, Shirsath SD, Aher SS (2017) Safety belt operated pneumatic handbrake. Int J Res Appl Sci Eng Technol 5(5):1730–1733
9. Khubalkar R, Kumar S, Jadhav K, Regundawar V, Phatangare A (2017) Modification and implementation of automatic hand brake system using sensor 6(4):4098–4102

Investigation of Tensile and Flexural Properties of Epoxy-Based Reinforced with Sugarcane Trash and Kevlar Pulp Filler Hybrid Polymer Composite

Mohit Vishnoi (ID)**, A. N. Veerendra Kumar** (ID)**, Neeraj Verma** (ID)**, and T. G. Mamatha** (ID)

Abstract Many investigators had carried out experiments in the field of material science in order to create various new materials for providing considerable improvement in mechanical properties by decreasing the cost without harming our eco-system by inculcating these points This paper presents the fabrication and investigation of tensile & flexural properties of filler reinforced hybrid composite using sugarcane trash and kevlar pulp filler in an epoxy matrix. The fabrication of composites was done using the compression molding technique on different weight fractions of the reinforcements. Specimens were prepared by using 20 wt% sugarcane trashes and varying percentage (0, 3, 6, 9 and 12%) of kevlar pulp in the material. Tensile and flexural tests had been performed on the developed hybrid composite and experiment results revealed that the percentage elongation and percentage of deflection of the developed hybrid composite decrease with increasing kevlar weight percentage while there was increase in tensile strength, young's modulus, flexural strength of the developed hybrid composite with increasing kevlar weight percentage and properties such as maximum tensile strength of 22.83 N/mm^2, maximum Young's modulus of 1029.71 N/mm^2 and maximum flexural strength of 61.72 N/mm^2 were observed in 12 wt% Kevlar pulp specimen.

Keywords Epoxy · Natural filler-sugarcane trash · Kevlar pulp trash · Compression molding process

M. Vishnoi (✉) · A. N. Veerendra Kumar · N. Verma · T. G. Mamatha
Department of Mechanical Engineering, J S S Academy of Technical Education, Noida 201301, India
e-mail: vishnoi.mohit06@gmail.com

A. N. Veerendra Kumar
e-mail: anvkumar38@gmail.com

N. Verma
e-mail: neerajverma@jssaten.ac.in

T. G. Mamatha
e-mail: mamathatg@jssaten.ac.in

1 Introduction

Currently, Composite materials are extensively used in multiple applications in engineering structures that consist of automobiles, aero-planes, spacecraft, buildings, bridges, sports equipment, industries, etc. Composite material's application was initiated in the aerospace industry in 1970s but currently, it is booming rapidly also in automobile industries due to headway in technology, composites materials are substituting metallic automotive components. Natural filler has gained use as reinforcement in the polymer matrix composite due to an increase in concern headed for the environment. By the use of natural fillers as an additive for composite materials provide an adequate consequence for enhancing their work and utilizations due to biodegradability, profusion, low cost with a high specific strength. It is also helpful due to lower density the mass of composite is dropped by the value of natural filler [1]. Sugarcane trash is an amply existing waste that can be used as natural filler in the polymer reinforced matrix composites. It is obtained from agricultural waste and can be employed as filler in the composite materials.

Epoxy resins are one of the most applicable classes of thermosetting plastic, which are excessively used as a matrix for reinforced polymer composite materials and structural adhesive. It showed enhancement in resistance to fatigue and microcracking also it does not form volatile products [2]. According to current research on properties and preparation of reinforced polymer matrix composites using a natural filler such as bamboo, sugarcane, kenaf, jute, and pineapple were implements [3–5].In current tradition, it has been observed that natural fiber composites have used in both interior and exterior components in automobile especially in car manufacturing, this accomplish two causes of companies, i.e., to lower the overall weight of the vehicle which leads to increase in the fuel efficiency and feasibility of manufacturing process is also enhanced. It is utilized in numerous organizations like Mercedes Benz, Daimler Chrysler, Toyota, and perusing to spread the uses of normal fiber composites.

Singha et al. has concluded that particle reinforcement of hibiscus sab-dariffa in urea formaldehyde is found to be more effective as compared to fibre reinforcement [2]. Limcharoen et al. have revealed that kevlar pulp increases the tensile modulus by appreciable value when its added more than 5 wt% [3]. Padmanbhan et al. has resulted that at different percentages of aloe vera and sugarcane trash as reinforcement different properties yield maximum magnitude [4]. Ramesha et al. has concluded that the different combination provides different maximum properties hence every combination such as glass + jute, glass + jute + sisal have its own significance [5].

2 Possible Materials

2.1 Epoxy

Epoxy is either any of the fundamental parts or the relieved finished results of epoxy gums, just as a conversational name for the epoxides useful gathering [1]. Epoxy gums, otherwise called poly-epoxies, are a class of receptive pre-polymers and polymers which contain epoxides gatherings. Epoxy saps might be responded (cross-connected) either with themselves through synergist homo-polymerization, or with a wide scope of co-reactants including poly-utilitarian amines, acids (and acid anhydrides), phenols, alcohols, and thiols. These co-reactants are regularly alluded to as hardeners or curatives, and the cross-connecting response is generally alluded to as restoring. Response of poly-epoxies with themselves or with poly-useful hardeners shapes a thermosetting polymer, frequently with high mechanical properties, temperature, and concoction opposition. Epoxy has a wide scope of utilizations, including metal coatings, use in hardware/electrical parts/LED, high tension electrical separators; paintbrushes producing, fiber-fortified plastic materials.

2.2 Epoxy Hardener (Araldite HY 951)

Hardener is utilized as dissolvable. Hardeners are substances that are added to polymers for helping in restoring composites. Hardeners are utilized to improve the physical properties of epoxy saps, for example, attachment, impact strength, and to change the viscosity of the polymer network. It additionally improves life, lower exotherm, and diminishes shrinkage. Utilization of Epoxy Hardeners

- Adhesives
- Solvent-free, high coatings
- Marine and mechanical coatings
- Surface tolerant introductions for metallic substrate
- Pipeline and tank coatings

2.3 Filler

Fillers are the particles added to materials to

- Lower the utilization of costly folio material
- Better the properties of the blend material.

    Filler has two types:
    Natural filler: Sugarcane—Rice Husk, Wheat Husk, coconut coir, sugarcane trash, sisal, jute, etc.

Fig. 1 Sugarcane trash

Synthetic filler: Glass, carbon, etc.
Advantages of natural filler over synthetic filler:

- Availability of renewable natural resources
- Satisfactory high specific strength and lightweight
- Low Cost and bio-degradability
- Eco-friendly.

2.4 Sugarcane Trash

Sugarcane Trash can be utilized as filler material. It is a brilliant biomass asset in sugar-creating nations around the world. The measure of sugarcane rubbish relies upon the plant assortment, age of the yield at reap, and soil and climate conditions. Sugarcane Trash can potentially be converted into heat and electrical energy. This trash contains 28.6%-natural carbon, 0.35–0.42% nitrogen, 0.04–0.15% phosphorous, 0.42–0.50% potassium. The sugarcane garbage consolidation in the dirt impacts the physical, substance, and natural properties of the dirt. Sugarcane trash is shown in Fig. 1.

2.5 Kevlar Pulp

Kevlar is the enrolled trademark for a para-aramid manufactured fiber, identified with different aramids, for example, Nomex and Technora created by Stephanie Kwolek at DuPont in 1965, this high-quality material was first economically utilized in the mid-1970s as a substitution for steel in racing tires. Ordinarily, it is spun into ropes

Fig. 2 Kevlar pulp

or texture sheets that can be utilized thusly or as a fixing in composite material segments.

Presently, Kevlar has numerous applications, going from bike tires and dashing sails to body protection, in light of its high elasticity to-weight proportion; by this measure, it is multiple times more grounded than steel. It is additionally used to make present-day drumheads that withstand high effect. At this point when utilized as a woven material, it is reasonable for securing lines and other submerged applications. Kevlar pulp is shown in Fig. 2.

3 Material Selections

3.1 Matrix: Epoxy (LY 556) with Hardener (HY951)

The base material is selected is a thermo-set polymer that is epoxy because of the following reasons:

1. Low Thermal Conductivity.
2. Better strength besides many other polymers.
3. Low density, hence lightweight.
4. Nontoxic.
5. Least effect of atmospheric composition.
6. Low cost besides other polymers and good availability.

3.2 Reinforcement: Sugarcane Trash and Kevlar Pulp

The fillers selected are sugarcane trash and Kevlar pulp and it is obviously taken for:

1. Sugarcane trash is totally biodegradable after disposal.

2. Both have fairly lightweight
3. Good Strength.
4. Least cost, apparently
5. Very high availability.

3.3 Physical Properties of Materials

Density of Epoxy = 1250 kg/m^3 (As per Supplier Manual).
Density of Sugarcane trash = 600 kg/m^3 (As per Supplier Manual).
Density of Kevlar Pulp = 300 kg/m^3 (As per Supplier Manual).

3.4 Design Calculation for Mould:

3.4.1 Specimen Size

Tensile Test: 150 * 10 * 4.5 mm^3 (As per ASTM D3039-76).
Flexural Test: 60 * 10 * 4.5 mm^3 (As per ASTM – D2344-84).
Volume of material = (150 * 10 * 4.5) * 4 + (60 * 10 * 4.5) * 4 = 47,250 mm^3
= 4.725 × 10^{-5} m^3.

3.4.2 Specimen Compositions

(Sample compositions are shown in Table 1).
C1: Epoxy (LY 556) + 20 wt% Sugarcane Trash.
C2: Epoxy (LY 556) + 20 wt% Sugarcane Trash + 3 wt% Kevlar Pulp.
C3: Epoxy (LY 556) + 20 wt% Sugarcane Trash + 6 wt% Kevlar Pulp.
C4: Epoxy (LY 556) + 20 wt% Sugarcane Trash + 9 wt% Kevlar Pulp.
C5: Epoxy (LY 556) + 20 wt% Sugarcane Trash + 12 wt% Kevlar Pulp.

Table 1 Sample composition

Component	Mass of epoxy (gm)	Mass of sugarcane trash (gm)	Mass of Kevlar pulp (gm)	Mass of hardener (gm)
C1	47.25	5.67	–	4.73
C2	45.48	5.67	0.43	4.55
C3	43.71	5.67	0.85	4.37
C4	41.93	5.67	1.28	4.19
C5	40.16	5.67	1.70	4.02

Fig. 3 Mould drawing
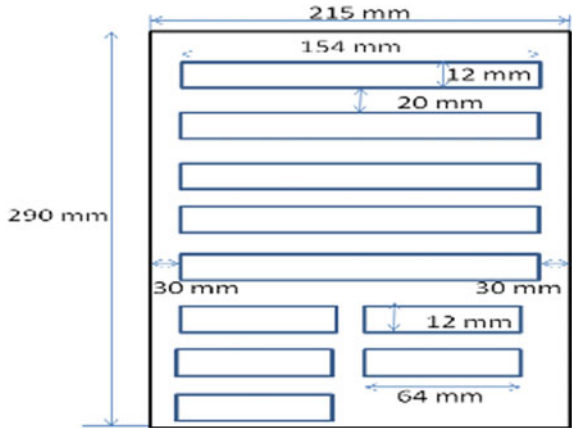
Fig. 4 Mould after pouring

3.4.3 Specification of Mould

- Length = 215 mm
- Breadth = 290 mm
- Thickness = 4 mm
- Volume = $(215 \times 290 \times 4) = 249{,}400$ mm^3

The drawing of the mould used for the fabrication of hybrid composite is shown in Fig. 3 and the mould after pouring has been shown in Fig. 4.

3.4.4 Final Specimens

***C1: Epoxy (LY 556)+ 20 wt% Sugarcane Trash*as** shown in Fig. 5.

Fig. 5 C1 specimens with epoxy & 20 wt% sugarcane trash

C2: Epoxy (LY 556)+ 20 wt% Sugarcane Trash+ 3 wt% Kevlar Pulp shown in Fig. 5.

C3: Epoxy (LY 556)+ 20 wt% Sugarcane Trash+ 6 wt% Kevlar Pulp

The specimen with Epoxy, 20 wt% Sugarcane Trash & 3 wt% Kevlar Pulp and Epoxy, 20 wt% Sugarcane Trash wt% Kelvar Pulp is shown in Fig. 6.

C4: Epoxy (LY 556) + 20 wt% Sugarcane Trash + 9 wt% Kevlar Pulp

C5: Epoxy (LY 556) + 20 wt% Sugarcane Trash + 12 wt% Kevlar Pulp

The specimen with Epoxy, 20 wt% Sugarcane Trash & 9 wt% Kevlar Pulp and Epoxy, 20 wt% Sugarcane Trash & 12 wt% Kevlar Pulp is shown in Fig. 7.

Fig. 6 C2 and C3 specimen

Fig. 7 C4 and C5 specimen

4 Experimentation and Results

4.1 Universal Testing Machine

The universal testing machine is shown in Fig. 8 which has capacity of UTM on which we performed testing: 10 kN. Specimen is shown in Fig. 9.

Fig. 8 Universal testing machine

Fig. 9 Specimen for tensile test

Tensile test

The tensile strength of a material is the most extreme measure of tensile stress that it can take before failure. The ordinarily utilized example for malleable test is the dog bone-type. During the test, a uni-axial load is applied through both the ends of the specimen. The component of the example is $150 * 10 * 4.5$ mm^3. Regular focal points when testing a material include extreme elasticity; counterbalance yield quality which speaks to a point just past the beginning of lasting twisting; and the crack or break point where the example isolates into pieces. The malleable test is acted in the all-inclusive testing machine and results are broke down to ascertain the elasticity of composite.

Standard dimension for testing

Dimension of sample $150 * 10 * 4.5$ mm^3 (As per ASTM D3039-76) and a sample is shown in Fig. 9 (Table 2).

The tensile strength of hybrid composite was increasing with an increase in Kevlar (wt%) as shown in Fig. 10. Tensile test had been carried out on C1, C2, C3, C4, and

Table 2 Composition of different samples

S. No.	Test parameter/specimen	Tensile strength (N/mm^2)				Average result (N/mm^2)
		1 Specimen	2 Specimen	3 Specimen	4 Specimen	
1	C1 (0% Kevlar)	14.54	11.34	19.88	14.30	15.02
2	C2 (3% Kevlar)	23.24	15.78	8.48	15.91	15.86
3	C3 (6% Kevlar)	16.66	20.30	15.32	20.84	18.28
4	C4 (9% Kevlar)	18.73	15.39	20.27	20.79	18.80
5	C5 (12% Kevlar)	24.70	23.41	20.71	22.50	22.83

Fig. 10 Graph between tensile strength and Kevlar content
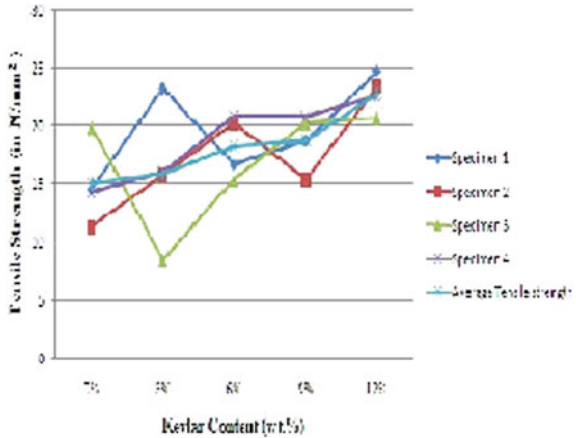
Table 3 Compositions of various samples

S. No.	Test parameter/specimen	Young's modulus (N/mm^2)				Average result (N/mm^2)
		1 Specimen	2 Specimen	3 Specimen	4 Specimen	
1	C1 (0% Kevlar)	849.92	621.10	1013.37	849.92	833.58
2	C2 (3% Kevlar)	1111.44	817.24	686.48	915.30	882.61
3	C3 (6% Kevlar)	882.62	1176.82	849.92	1046.06	988.85
4	C4 (9% Kevlar)	947.99	947.99	1078.75	1046.05	1005.20
5	C5 (12% Kevlar)	1013.37	1046.06	1013.37	1046.06	1029.71

C5 Specimens. Four specimens are tested of identical composition. The observation of Young's Modulus for various compositions had been tabulated in Table 3.

Graphical Representation of the test results is shown in Fig. 11.

The Young's Modulus of hybrid composite was increasing with increase in Kevlar weight percentage.

Tensile test had been carried out on C1, C2, C3, C4, and C5 Specimens. Four specimens are tested of identical composition. The observation of % Elongation for various compositions had been tabulated in Table 4.

Graphical Representation of test results is shown in Fig. 12.

The % elongation of hybrid composite was decreasing with increase in Kevlar weight percentage.

Flexural test

Flexural quality is characterized as a material's capacity to oppose deformation under load. The short-shaft shear (SBS) tests are performed on the composites tests to assess the estimation of Flexural Strength. It is a 3-point twist test, which by and large advances failure by interlaminar shear. This test is led according to ASTM
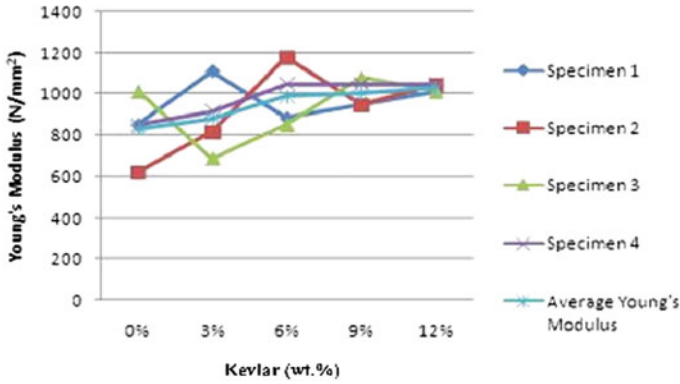
Fig. 11 Graph b/w Young's Modulus and Kevlar content (wt%)

Table 4 Compositions of various samples

S. No.	Test parameter/specimen	% Elongation				Average result
		1 Specimen	2 Specimen	3 Specimen	4 Specimen	
1	C1 (0% Kevlar)	1.93	2.20	2.20	1.73	2.02
2	C2 (3% Kevlar)	2.33	1.87	1.27	2.00	1.87
3	C3 (6% Kevlar)	1.70	1.80	1.93	1.93	1.84
4	C4 (9% Kevlar)	1.73	1.67	2.00	1.87	1.82
5	C5 (12% Kevlar)	1.65	1.75	2.07	1.70	1.79
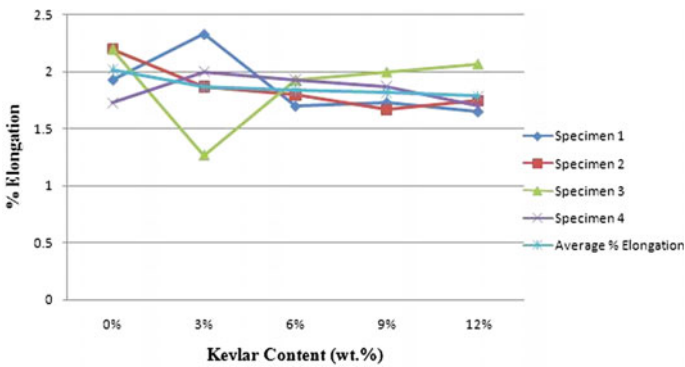
Fig. 12 Graph between % Elongation and Kevlar content (wt%)

standard utilizing UTM. The stacking plan is appeared in the figure. The component of the example is $60 * 10 * 4.5$ mm^3. Notwithstanding, early flexural tests regularly invigorated qualities that were impressively lower than the tensile strength. One purpose behind this was the stacking focuses in flexural test rigs intended for metals frequently caused confined harm which started untimely disappointments. In any case, in any event, when this flawed test technique was amended, low-stress failures despite everything happened. It was then viewed as this was on the grounds that in materials with poor in-plane shear resistance and with compression strength that were lower than the tensile strength, it was shear as well as compression damage modes that started the untimely flexural failures.

The flexural strength is measured by the following formula:

$$\text{Flexural Strength} = 3PL/2bt^2$$

where P = Maximum Load in newtons, b = width of specimen, t = depth of specimen in mm, L = Length of specimen between supports in mm.

The flexural strength of hybrid composite was increasing with increase in Kevlar weight percentage.

Flexural test had been carried out on C1, C2, C3, C4, and C5 Specimens. Four specimens are tested of identical composition (Fig. 13).

The observation of flexural strength for various compositions had been tabulated in Table 5.

Flexural test had been carried out on C1, C2, C3, C4, and C5 Specimens for finding the deflections. Four specimens are tested of identical composition.

Graphical Representation of test results is shown in Fig. 14.

Flexural Strength of hybrid composite was increasing with increase in Kevlar weight percentage.

The observation of % Deflection for various compositions had been tabulated in Table 6.
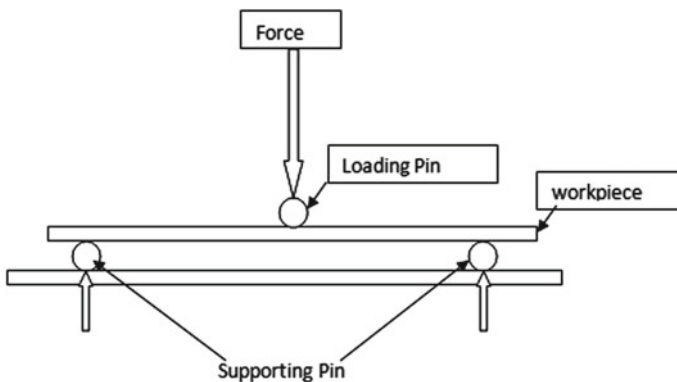
Fig. 13 Three-point flexural test

Table 5 Compositions of various samples

S. No.	Test parameter/specimen	Flexural strength (N/mm²)				Average result (N/mm²)
		1 Specimen	2 Specimen	3 Specimen	4 Specimen	
1	C1 (0% Kevlar)	56.71	45.74	38.78	46.94	47.04
2	C2 (3% Kevlar)	48.92	40.15	69.60	40.64	49.83
3	C3 (6% Kevlar)	56.66	46.88	43.67	67.67	53.72
4	C4 (9% Kevlar)	45.95	56.41	61.06	78.17	60.40
5	C5 (12% Kevlar)	57.36	59.21	86.33	44.00	61.72
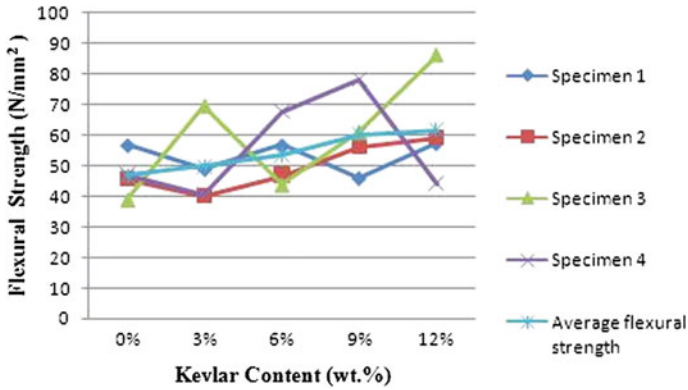
Fig. 14 Graph between flexural strength and kevlar content (wt%)

Table 6 Compositions of various samples

S. No.	Test parameter/specimen	% Deflection				Average result
		1 Specimen	2 Specimen	3 Specimen	4 Specimen	
1	C1(0%Kevlar)	3.75	3	2	3.75	3.13
2	C2(3% Kevlar)	1.5	1.5	3	2.5	2.13
3	C3(6% Kevlar)	0.75	1.5	2	3.5	1.94
4	C4(9% Kevlar)	2.25	1.25	1.3	2.75	1.89
5	C5(12% Kevlar)	1.85	1.5	1.75	2	1.76

Graphical Representation of test results is shown in Fig. 15.

% Deflection of hybrid composite was decreasing with increase in Kevlar weight percentage.
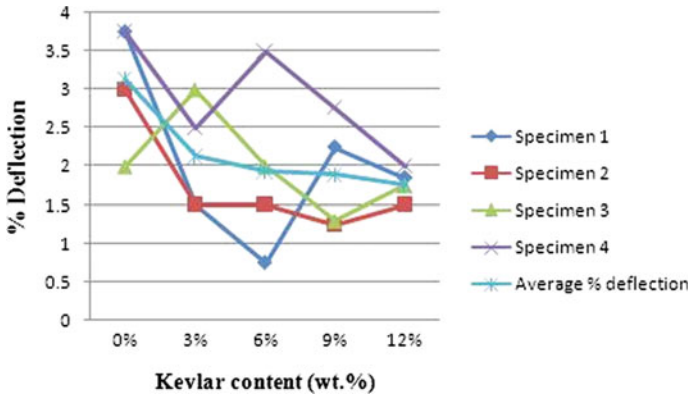
Fig. 15 Graph b/w % deflection and kevlar content (wt%)

5 Conclusion and Scope of Future Work

5.1 Conclusion

- A series of Hybrid composites had been developed by keeping sugarcane Trash weight percentage constant (20 wt%) and varying Kevlar pulp weight percentage (0, 3, 6, 9 and 12%) filler.
- Tensile tests and flexural tests were successfully carried as per the ASTM Standard using Universal testing Machine on developed hybrid composite.
- The test results had been tabulated in Tables as well as graphical representation of test results was also shown using appropriate graphs.
- As Kevlar pulp weight content % increases the tensile strength, young's modulus & flexural strength of the hybrid composite increases.
- As Kevlar Pulp weight content % increases the % elongation and % deflection of the hybrid composite decreases.
- Maximum tensile strength of 22.83 N/mm^2, maximum Young's modulus of 1029.71 N/mm^2 and maximum flexural strength of 61.72 N/mm^2 were observed in C5 (12 wt% Kevlar pulp) specimen.

5.2 Scope of Future

In this paper have tried kevlar and sugarcane combination in epoxy resin and prepared a hybrid polymer composite. In the future different natural fibers like hibiscus sabdariffa, sisal, jute, rice husk, aloe-vera, etc. can be added to get better strength of the material. Determination of effect of Kevlar Pulp and sugarcane in polyester or urea formaldehyde resin matrix is also a future scope of our project.

References

1. Rout AK, Satapathy A (2012) Study on mechanical and triboperformance of rice-husk filled glass-epoxy hybrid composites. Elsevier 41:131–141
2. Singha AS, VThakur K (2008) Mechanical properties of natural fibre reinforced polymer composites. Indian Acad Sci 31:791–799
3. Bualek-Limcharoen S, Nakinpong T (1997) Kevlar pulp-thermoplastic elastomer composites: morphology and mechanical properties. J Sci Soc Thailand 23:101–114
4. Padmanbhan RG, Ganpathy M (2015) Investigation of mechanical behavior of bagasse (sugarcane)—Aloevera as hybrid natural fibre composites. Int J Res Appl Sci Eng Technol 3:13–20
5. Ramesha M, Palanikumar K, Hemachandra Reddy K (2013) Mechanical property evaluation of Sisal-jute-glass fiber reinforced polyester composites. Elsevier 48:1–9

Ultrasonic Vibrations Assisted Turning (UAT): A Review

Govind S. Ghule and Sudarshan Sanap

Abstract To execute the demanding environmental liability, the analysis in the recent time has been centered on embracing endurable techniques in manufacturing sectors. In recent days, hardened materials and their alloys are extensively used in various industries like automobile, aeronautics, power, and defense. But machining of these materials is a bit troublesome with the conventional process (CT), as it directly results in high cutting forces, high machining stresses, excessive tool wear, increment in temperature, and poor surface finish. In concern of an equivalent, ultrasonically assisted turning (UAT) has been cultivated as an unconventional technique that uses low-energy, high-frequency ultrasonic vibrations which are superimposed on the cutting tool for the removal of unwanted material from a workpiece to produce a desired high precision product. The ultimate purpose of this review article is to underline the benefits of UAT and to publicize UAT by composing a path for making the overall system financially efficient and environment-friendly by shrinking footprints of carbon.

Keywords Conventional turning · Ultrasonic vibratory tool (UVT) · Ultrasonically assisted turning · Surface roughness · Cutting forces · Tool wear

1 Introduction

Given the continuous advancement in the modern engineering processes, many of the manufacturing industries are remodeling themselves to various endurable and advanced machining techniques. In the case of conventional turning (CT), the major hindrance which is being faced is poor machinability. High cutting forces, high machining stresses, excessive tool wear, increment in the temperature and poor surface finish are the main hold-downs of the machining industries [1]. In many

G. S. Ghule (✉)
MIT-ADT University, Pune, Maharashtra, India
e-mail: govindghulemasterofengineering@gmail.com

S. Sanap
Mechanical Engineering Department, MIT-SOE, MIT-ADT University, Pune, Maharashtra, India

of the cases, coolant fluids are also consumed for the lubrication purpose to dissipate the amount of heat being generated. This attempt also accommodates reduction in the tool wear hence having betterment in tool life. But importantly these coolant fluids are pricey and are very difficult to handle and dispose of as well resulting in an increment in machining costs. Thus, dry machining operations are financially effective and environment-friendly as it accommodates the shrinking of carbon footprints [2, 3]. In concern of all the of this, nowadays, a new unconventional technique, i.e., ultrasonic vibrations system, is widely used in various manufacturing sectors like ultrasonic welding [4], ultrasonic-assisted drilling [5], ultrasonic-assisted milling [6, 7], ultrasonic emulsification, and ultrasonic cleaning and in medical applications too. Ultrasonic vibration system uses sound velocity which is over and above 16,000 Hz and also is out of audible range of human hearing of an average person [8–10].

2 Hard Turning

Hard turning is the process where the machining tasks are carried on the workpiece whose hardness is over 45 HRC with compelling tractability and with higher material removal rates, and thus, it has wide focal points over-grinding operation [11]. The suggestion to the machining of hard turning dependent on the level of hardness and its depth if it is case hardened. In many of the cases, it is performed without the utilization of coolants coming about into a positive effect on the natural display. This technique egests the series of functioning which are necessary for the production of component thereby lessening the cycle time and subsequent in the betterment of productivity. Studies have demonstrated that with the usage of effective nose radii, feed rate or the recent tool insert mechanization, hard turning operation will result in the improvised surface finish when contrasted with the grinding operation [11, 12]. For the most part higher cutting speed, small depth of cut and low feed rates are selected for smoother surface finishing operation.

From the most recent couple of decades, the distinctive materials which are hard turned on a standard premise contingent on the application are steel alloys, bearing steels, die steels, case hardened steel, satellite and aerospace alloys and automotive industries [13]. While completing the hard machining activities, productive and efficient cutting parameters must be chosen by legitimate planning of the analysis as its impact will be straightforwardly conferred on surface finish, dependability and assembling proficiency of the framework. Because of tangled shared association among cutting tool and the workpiece with hardness over 45 HRC, the amount cutting forces developed are also likewise immense. Therefore as per norms, the cutting tool material should have good strength to sustain these forces and low wear property [14]. While performing machining operations on hardened steel, ceramic tools and polycrystalline cubic boron nitride (PCBN); PVD covered carbide inserts and sintered tungsten carbides are utilized as cutting devices. Accomplishment in hard turning activity relies upon not many of the significant angles including machine rigidity

nature, work holding inflexibility, astounding vibration damping qualities and so on [15].

3 Ultrasonically Assisted Turning

Ultrasonically assisted turning (UAT) is the current unconventional technique that uses low-energy, high-frequency ultrasonic vibrations which are overlaid on the cutting tool (besides the relative motion between tool and workpiece) for the removal of chips (unwanted material from workpiece) to produce a required high accuracy product. The basic assembly of ultrasonically assisted turning (UAT) is consisting of transducer, booster, and horn as shown in Fig. 1. The ultimate function of considering piezoelectric transducer is that it converts electrical energy into mechanical energy, i.e., mechanical vibration in the range of around 20 kHz and amplitude of 100 microns [16, 17].

Similarly, the function of the booster is to enhance the amplitude of vibration and the stepped horn acts as an amplifier as well as a tool holder. This complete assembly of piezoelectric transducer, booster, and stepped horn is known as an ultrasonic vibratory tool (UVT). UAT is generally classified by directions of vibrations as mentioned in Fig. 2. These vibrations are in feed (axial) direction, longitudinal (tangential) direction, and transverse (radial) direction [18]. To mention the variation between conventional turning (CT) and ultrasonically assisted turning (UAT), the researchers have been introducing multiple types of UAT setups and proclaimed indicative enhancements especially in cutting forces, surface finish, reduction of noise, tool wear reduction, etc.

Also, all the while operations on UAT much lesser amount of stresses are getting generated in the workpiece. The stress distribution in UAT and CT, the effect of cutting speed on residual stresses, and resemblance of cutting forces in UAT and CT are as shown in Fig. 3a–c [19].
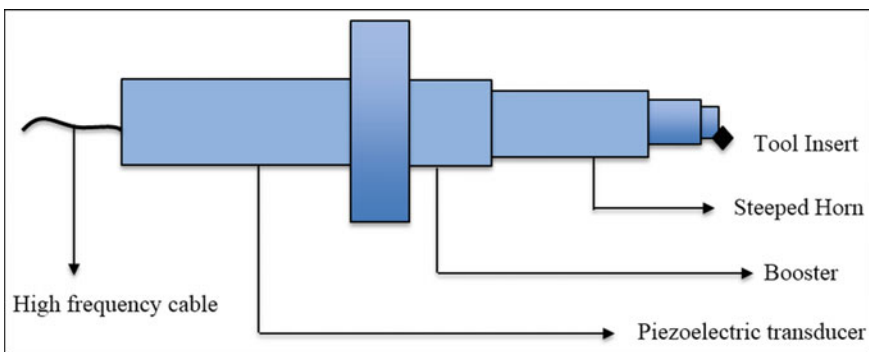
Fig. 1 An assembly of UVT system [16]
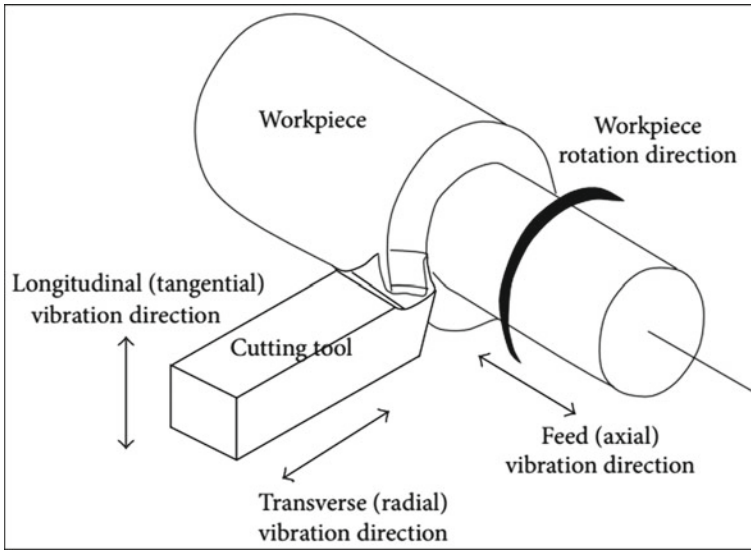
Fig. 2 Principal vibration directions in UAT [18]

When these ultrasonic vibrations are enforced in tangential direction during machining operation [8, 9],

Tangential direction:

$$V_c = \pi N D < V_t = 2\pi a f \qquad (1)$$

where.

V_c = cutting speed during turning operation,

N = workpiece rotational speed,

D = diameter of the workpiece,

V_t = tip velocity,

a = amplitude of vibration,

f = frequency of vibration.

4 Process Measurement Parameters

4.1 *Measurement of Surface Roughness and Cutting Forces*

Kim et al. [20] have proposed the experimental investigation of turning of SiCp/Al with a compound machining approach (UAT) using minimum quantity lubrication (MQL) and correlated it with convention turning (CT). The results of simulation have been compared with experimental readings, and it showed that surface contour

(a)

(b)

(c)
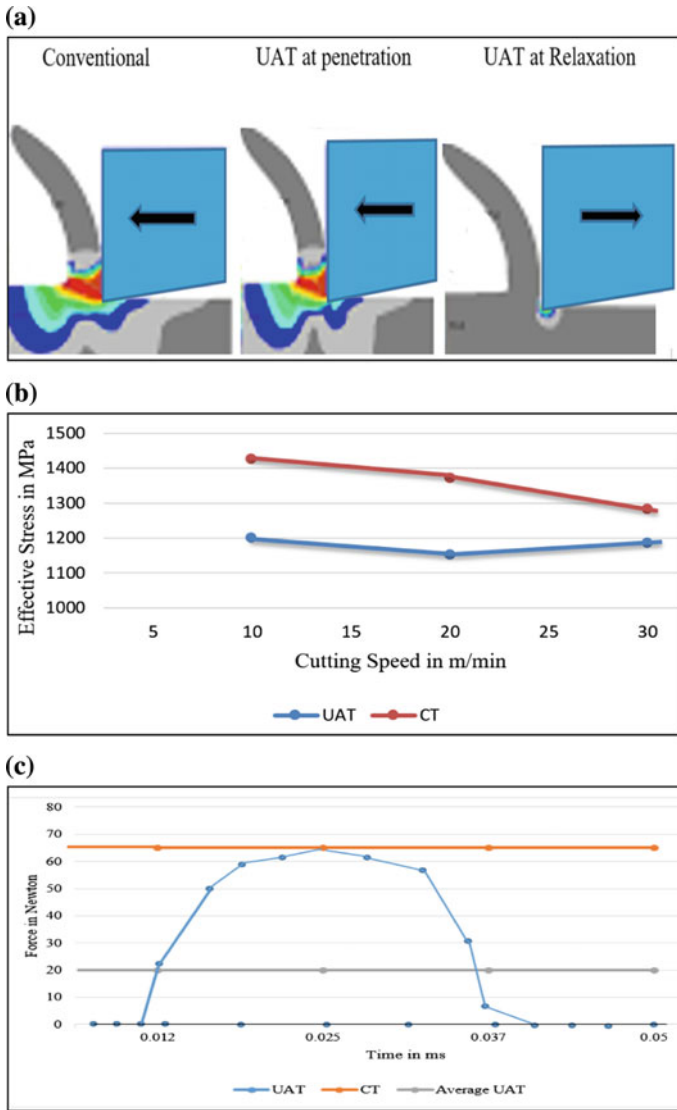
Fig. 3 **a** Stress distribution in UAT and CT [19], **b** Effect of cutting speed on stresses [19], **c** Comparison of cutting forces [19]

demonstrates a decrement in surface roughness by considering UAT when differentiated with CT. With the implementation of UAT, the amount of surface roughness decremented with a 12% increment in Ra for turning operation carried out with the use of minimum quantity lubrication (MQL). Researchers have also claimed that in UAT machining operation, there is a decrement in cutting forces in the tangential

direction by 68% and in the radial direction by 66%. The lowest value of appreciable decrement in forces was in feed direction which was 25%.

Xiangyu et al. [21] have presented a cutting-extrusion phenomenon with UVT for Ti-6Al-4V alloys. The results have indicated that with the due presence of vibrations in complicated geometries, the value of Ra was no larger than 0.4 µm.

Wei Bai et al. [22] have studied the consequent outcome of compound machining on Inconel 718 with the use of ultrasonic vibration on machinability and structural integrity. They claimed that there is a reduction of surface roughness with UAT in the picture when there is an increment in the feed rate along with the depth of cut. Researchers also proposed the suitable parameters of machining (speed, feed, and depth of cut) with critical speed higher than that of cutting speed, low feed rate value and depth of cut; in addition to overhead amplitude of vibration can abate the cutting forces in UAT.

Wang et al. [23] have experimented with the surface roughness in feed direction in ultrasonic elliptical vibration-assisted turning on Inconel 718 and claimed that Ra and Rz values are greater as compared to conventional turning. Researchers have also proposed ultrasonic vibrations deduct the effect of cutting force when cutting speed is beyond the ultimate value of ultrasonic speed.

Vivekananda et al. [24] have proposed the FEM analysis to calculate the natural frequency of the stepped-shaped horn made up of mild steel with stainless steel [SS304] as a workpiece and carbide tool insert. They have successfully claimed the reduction in surface roughness value in UAT as compared with CT. Along with the same researchers have investigated that the percentage of decrement in the cutting forces in UAT is 8.16–53.89% if correlated with conventional turning.

Nestler et al. [25] have experimented using aluminum matrix composites (AMCs) with UAT in the perpendicular (radial) direction or the direction of cutting; claiming an advancement in residual stresses in compression.

Muhammad et al. [26] have proposed hot ultrasonically assisted machining for turning of β-Ti alloys. They have experimentally claimed that surface roughness has been improvised in hot convention turning (HCT) and hot ultrasonically assisted turning (HUAT) when compared with conventional turning (CT) and ultrasonically assisted turning (UAT). Researchers also have proposed the cutback in cutting forces in HUAT is superior to in HCT as of differentiated with UAT and CT for the steady measure of heat outfitted to the workpiece.

Maurotto et al. [27] have differentiated machinability of Ti-15-3-3-3 and Ni-625 alloys in turning operation with ultrasonic-assisted vibration by using sintered carbide coated tool insert, suggesting the marginal betterment in the surface quality of Ni-based alloy than Ti-based alloy. Researchers have claimed that the material removal rate (MRR) is 2–3 times more in UAT than in CT for the same amount of cutting forces.

Llanos et al. [28] have proposed the experimental analysis of the reduction in cutting force during ultrasonically assisted turning of Ti6Al4V. Carbide inserts of CCMT 060204-MF 1115 make of Sandvik is used for carrying out the test. Researchers have concluded with empirical expressions that acknowledge calculating the effect of cutting force decrement in UAT with a better degree of accuracy.

Aouici et al. [29] investigated the effects of cutting parameters on cutting forces and surface roughness in machining of hardened steel. For this investigation, they used the material which has a hardness of 50 HRC. Experimentation was carried out using the CBN tool insert. They observed the effect of cutting conditions on machining parameters, namely cutting forces and on surface roughness, respectively, by an application of analysis of variance (ANOVA). With an application of response surface methodology (RSM) and hence a quadratic regression model, relationship of the cutting parameters and the machining parameters is processed. The desirability of all models is closed to 1. Results indicate that the depth of cut demonstrates higher cutting forces as compared to cutting speed and feed.

Kim et al. [20] have experimented on metal matrix composite, i.e., SiC-reinforced aluminum (SiCp/Al), which is ideally used in distinct aerospace applications. Experimental outcomes demonstrated betterment in UAT when differentiated with CT for surface topography and cutting forces.

4.2 Measurement of Tool Wear

Bai et al. [30] have experimented on metal matrix composites-SiCp/Al by comparing dry UAT with conventional turning using cemented carbide and a polycrystalline diamond (PCD) tool insert. Researchers quoted both adhesive and abrasive wear found on the cemented carbide tool in conventional turning (CT) and in ultrasonically assisted turning (UAT) too. But in conclusion, the topography of the machined part procured in UAT with the WC tool was pretty superior to that obtained with the PCD tool.

Basavarajappa et al. [31] proposed SiC-reinforced metal matrix composites (hard ceramics) intricate tool wear, hence confining its prevalent application in engineering.

Zhong et al. [32] proposed that increment in SiC volume fraction in metal matrix composites (MMC) precede to augment tool resulting in flank wear increment of the machined material. Researchers have claimed that tool wear was to be the basic hindrance in turning operation of MMCs, under an exceedingly scratchy nature of rigorous particulate reinforcements.

Rehman et al. [33] have experimented with the effects of tool wear by using variable cutting conditions on workpiece material as Ti-15V3Al3Cr3Sn and cutting tool as a coated carbide insert (AlTiN) as an in both CT and UAT. Researchers have quoted that as there is an increment in cutting speed from a lesser amount to incremented amount, there is a reduction in the contact between tool and workpiece in UAT. As an outcome of this, high temperatures got generated in the region of the cutting area, which influenced tool life by an increment in the tool wear in UAT machining as compared to CT.

Nath et al. [34] proclaimed the incremented value of tool wear in the CT method. Nonetheless, UAT was found to associate the inappreciable rate of wear for an increase in feed rate along with the cutting speed. It was justified that the rate of abrasive wear was over and above the other wear. The frequent friction between the

workpiece and the tool insert concluded in additional abrasive wear in convention methodology. Nonetheless, the intermittent cutting operation of UAT granted the tool to have aerodynamic lubing for the decrement in the temperature while cutting and therefore slighter tool wear was discovered. Additionally, acceleration in tool wear was justified to be so much minor in UAT; however, the damage value of the cutting tool insert in the conventional methodology demonstrated a sheer increment with the time required for machining operation.

Lotfi et al. [35] developed a model to anticipate tool wear rate along with the amount of heat allocation on tool inserts in standard, rotary, and ultrasonically assisted rotary turning strategies. To exemplar, the rate of flank wear, an updated Usui wear rate model which incorporates a clearance angle of tool insert, is arranged. Furthermore, a chain of experiments is performed to authenticate the system, by contrasting the forecasted and calculated flank wear rates that can be presented to be in smart correspondence. In line with the outcomes of the simulation, circumscribed heat within the tool–chip contact region throughout exemplar turning is divided within the periphery of the tool principal edge in rotary turning. Researchers claimed that due to the presence of detachment span in ultrasonic-assisted rotary turning, the overall duration for the thermal conduction phenomenon within the region of contact lessens, leading to a considerable and substantial decrement in the rate of tool wear.

Singh et al. [36] experimented with the consequence of cutting parameters on the surface topography in turning of hardened materials. For this study, AISI 52,100 was used as a workpiece material and mixed ceramic as a cutting tool insert with a distinct nose radius and effectual value of rake angles. Results revealed that the cutting parameters, i.e., cutting speed, feed, effective rake angle, and nose radius, are the elementary affecting factors, which influenced the surface topography. This system was advantageous in the selection of the cutting tool geometry and operating conditions for the essential surface finish quality.

4.3 Measurement of Residual Stresses

Sharma et al. [37] have proposed an experimental XRD analysis for residual stresses minimization in UAT with 4340 hardened steel as a workpiece. The experiments were performed to advance a mathematical model for residual stresses which is dependent on the methodology of the response surface. The results of ANOVA interpreted that the amount of feed rate considerably influences the residual stress origination.

Munoz-Sanchez et al. [38] investigated practically and arithmetically the influence of crater and flank wear on the topography, residual stresses are generated while operating on Inconel 718 at invariable cutting speed, feed rate, and depth of cut. Researchers claimed that residual stresses on the surface were superior while there is an increment in the flank wear. By distinction, residual stresses on the surface with the biggest crater wear were not up to along with the tiniest crater wear utilized in the respective experiments.

Xiangyu et al. [21] have claimed that when operating parameters, vibration parameters, and tool geometry are suitably decided, a cutting-extrusion development can turn up once high-speed ultrasonic vibration turning with Ti-6Al-4V alloys. This cutting-extrusion development may consequent during a compressive surface residual stress instead of a tensile in CT turning.

5 Conclusion

This paper reviewed the literature and interpreted in detail about the benefits of ultrasonically assisted turning (UAT) when compared with conventional turning (CT). It has been found that the UAT method is an applicable methodology to prevail a better quality surface topography and with lesser demand of cutting forces. This method is befitting for hardened materials and also for ordinary scope material in engineering like stainless steel which are widely used by manufacturing industries. Along with this, the study of tool wear and residual stresses in ultrasonically assisted turning has also been reviewed.

References

1. Sharma V, Pandey PM (2016) Recent advances in ultrasonically assisted turning: A step towards sustainability. Int J Cogent Eng 3
2. Brehl DE, Dow TA (2008) Review of vibration-assisted Machining. Precis Eng 32:153–172
3. Madhavulu G, Ahemad B (1994) Hot machining process for improving metal removal rates in turning operation. J Mater Process Technol 44:199–206
4. Lei Y, Luo Y, Cheng C, Xiao GB (2014) Effect of traces of CO_2 on arc-ultrasonic TIG welded MGH956 alloy. Mater Manuf Process 29(8):1004–1010
5. Celaya LN, de Lacalle L, Campa FJ, Lamikiz A (2010) Ultrasonically assisted turning of mild steels. Int J Mater Prod Technol 27:131–139
6. Sherrit SAA, Gradzio M, Dolgin BP, Chang XBZ, Bar-Cohen Y (2002) Novel horn designs for ultrasonic/sonic cleaning welding, soldering, cutting and drilling. In: Proceedings of the SPIE smart structures conference, vol 4701, p 34
7. Verma GC, Pandey PM, Dixit US (2018) Modelling of static machining force in axial ultrasonic-vibration assisted milling considering acoustic softening. Int J Mech Sci 136:1–16
8. Outeiroa JC, Costesa JP, Kornmeierb JR (2013) Cyclic variation of residual stress induced by tool vibration in machining operations. Proc CIRP 8:493–497
9. Kuo KL (2009) Ultrasonic vibrating system design and tool analysis. Trans Nonferrous Metals Soc China 19:225–231
10. Xu YS, Zou P, Yang XL, He Y (2013) Study on an ultrasonic generator for ultrasonically assisted machining. Adv Mater Res 797:320–325
11. Aouici H, Yallese MA, Belbah A (2013) Experimental investigation of cutting parameters influence on surface roughness and cutting forces in hard turning of X38CrMoV5-1 with CBN tool. Indian Academy of Sciences, Sadhana 38:429–445
12. Boucha K, Yallese MA (2010) Statistical analysis of surface roughness and cutting forces using response surface methodology in hard turning of AISI 52100 bearing steel with CBN tool. Int J Refractory Metals Hard Mater 28:249–361

13. Pal A, Choudhury SK, Chinchanikar S (2014) Machinability assessment through experimental investigation during hard and soft turning of hardened steel. In: 3rd international conference on materials processing and characterization, vol 6, pp 80–91
14. Guddat J, Saoubi RM (2011) Hard turning of AISI 52100 using PCBN wiper geometry inserts and the resulting surface integrity. In: 1st international conference on surface integrity, vol 19, pp 118–124
15. Gaurav Bartarya SKC (2012) Effect of cutting parameters on cutting force and surface roughness during finish hard turning AISI 52100 grade steel. In: 5th CIRP conference on high performance cutting, vol 1, pp 651–656
16. Vivekananda K, Arka GN, Sahoo SK (2014) Design and analysis of ultrasonic vibratory tool (UVT) using FEM, and experimental study on ultrasonic vibration-assisted turning (UAT). Proc Eng 97:1178–1186
17. Vivekananda K, Arka GN, Sahoo SK (2014) Finite element analysis and process parameters optimization of ultrasonic vibration-assisted turning (UVT). Proc Mater Sci 6:1906–1914
18. Rajput P, Siddiquee AN, Sharma R (2015) Experimental study of ultrasonically assisted turning of AISI 52100 based on Taguchi method. Int J Recent Res Aspects 2:42–47
19. Kumar MN, Kanmani Subbu S, Vamsi Krishna P, Venugopal A (2014) Vibration assisted conventional and advance machining: a review. Proc Eng 97:1577–1586
20. Kim J, Bai W, Roy A, Jones LCR, Ayvar-Soberanis S, Silberschmidt VV (2019) Hybrid machining of metal-matrix composite. In: 17th CIRP conference on modelling of machining operation, vol 82, pp 184–189
21. Xiangyu Z, Zhenghui L, He S, Deyuan Z (2018) Surface quality and residual stress study of high-speed ultrasonic vibration turning Ti-6Al-4V alloys. IN: 4th CIRP conference on surface integrity, vol 71, pp 79–82
22. Bai W, Roy A, Sun R, Silberschmidt VV (2018) Effect of hybrid machining on structural integrity of aerospace-grade materials. In: 8th CIRP conference on high performance cutting, vol 77, pp 163–166
23. Wang Q, Wu Y, Gu J, Lu D, Ji Y, Nomura M (2016) Fundamental machining characteristics of the in-base-plane ultrasonic elliptical vibration assisted turning of Inconel 718. In: 18th CIRP conference on electro physical and chemical machining, vol 42, pp 858–862
24. Vivekananda K, Arka GN, Sahoo SK (2014) Finite element analysis and process parameters optimization of ultrasonic vibration assisted turning (UVT). In: 3rd international conference on materials processing and characterization, vol 6, pp 1906–1914
25. Nestler A, Schubert A (2014) Surface properties in ultrasonic vibration assisted turning of particle reinforced aluminium matrix composites. In: 2nd CIRP conference on surface integrity, vol 13, pp 125–130
26. Muhammad R, Maurotto A, Roy A, Silberschmidt VV (2012) Hot ultrasonically assisted turning of β-Ti alloys. In: 5th CIRP conference on high performance cutting, vol 1, pp 336–341
27. Maurotto A, Muhammad R, Roy A, Babitsky VI, Silberschmidt VV (2012) Comparing machinability of Ti-15-3-3-3 and Ni-625 alloys in UAT. In: 5th CIRP conference on high performance cutting, vol 1, pp 330–335
28. Llanos I, Campa A, Iturbe A, Arrazola PJ, Zelaieta O (2018) Experimental analysis of cutting force reduction during ultrasonic assisted turning of Ti6Al4V. In: 8th CIRP conference on high performance cutting, vol 77, pp 86–89
29. Aouci H, Yallese MA, Belbah A, Ameru MF (2013) Experimental investigation of cutting parameters influence on surface roughness and cutting forces in hard turning of X38CrMoV5-1 with CBN tool. Sadhana 38:429–445
30. Bai W, Roy A, Sun R, Silberschmidt VV (2019) Enhancement machinability of SiC-reinforced metal matrix composite with hybrid turning. J Mater Process Tech 268:149–161
31. Basavarajappa S, Chandramohan G, Paulo Devim J (2007) Application of Taguchi techniques to study dry sliding wear behavior of metal matrix composites, vol 28, pp 1393–1398
32. Zhong ZW, Lin G (2006) Ultrasonically assisted turning of aluminium based metal matrix composite reinforced with SiC particles. Int J Adv Manuf Technol 27:1027–1081

33. Rehamn A, Maqsood S (2015) Finite element analysis of tool wear in ultrasonically assisted turning. In: 4th international conference on aerospace science and engineering, vol 23, pp 1800–1810
34. Nath C, Rahman M (2008) Effect of machining parameters in ultrasonic vibration cutting. Int J Mach Tools Manuf 48:965–974
35. Lotfi M, Amini S, Aghaei M (2018) 3D FEM simulation of tool wear in ultrasonically assisted rotary turning. Int J Ultrasonic 88:106–114
36. Sharma V, Pandey PM (2016) Optimization of machining and vibration parameters for residual stresses minimization in ultrasonic assisted turning of 4340 hardened steel. Int J Ultrasonic 70:172–182
37. Singh Rao D, Paruchuri VR (2007) A surface roughness prediction model for hard turning process. Int J Adv Manuf Technol 32:1115–1124
38. Munoz-Sanchez A, Canteli JA, Cantero JL, Miguelez MH (2011) Numerical analysis of the tool wear effect in the machining induced residual stresses. Simul Model Pract Theory 19:872–886

Correlation Between Anthropometric Measurements and Muscle Performance Based on Endurance Test

Mohd Mukhtar Alam, Abid Ali Khan, and Mohd Farooq

Abstract The purpose of this paper is to evaluate the correlation between anthropometric measurements and muscle performance based on endurance test at 50% MVC. Eight VT protocols (based on the different combinations of vibration frequency (35 and 45 Hz), amplitude (3 g $\pm$ 0.5 g, and 9 g $\pm$ 0.5 g), and exposure duration (30 and 60 s)) were given to the participants from two groups (56/group): persons with a sedentary lifestyle (SL) and a group of construction workers (CW) for 4 days. EMG signals were acquired from four muscles, namely flexor carpi ulnaris (FCU), flexor digitorum superficialis (FDS), extensor carpi radialis brevis (ECRB), and extensor carpi ulnaris (ECU) of the right forearm. The results showed a significant correlation ($p < 0.001$) between MVC grip strength with age, height, palm length, palm circumference, and forearm circumference for both groups. In addition, endurance time was significantly positively correlated ($p < 0.05$) with height and palm length for SL group, whereas for CW group with age, weight, palm length, palm circumference and forearm length. It can be concluded that Pearson's correlation test suggested forearm circumference followed by weight and palm circumference was the most influential factor affecting the grip strength and palm length generally served as a better predictor for grip endurance time.

Keywords Grip strength · Endurance time · Neuromuscular efficiency and electromyography · Anthropometry

M. M. Alam (✉) · A. A. Khan · M. Farooq
Ergonomics Research Division, Department of Mechanical Engineering, ZHCET, Faculty of Engineering & Technology, Aligarh Muslim University, Aligarh, India
e-mail: mukhtaralam143@gmail.com

A. A. Khan
e-mail: abidak71@yahoo.com

M. Farooq
e-mail: mohdmmfarooq@rediffmail.com

1 Introduction

Grip strength is often used as an indicator of overall physical strength and health in a clinical setting because grip is important for many daily activities [1, 2]. Many occupations rely on grip to perform important tasks. Food packers, assembly line workers, and many other manual industrial workers may use repetitive or forced gripping on a regular basis [3, 4]. Other occupations require lifting and holding heavy loads with relatively static grips. Grip strength assessment can help identify individuals with hand or forearm fatigue and helps determine the improvements made during the course of treatment and rehabilitation [1, 5].

Grip strength is widely accepted as an indicator of maximal hand strength and is a measure of active muscle contraction in both the hand and forearm. Grip strength was significantly correlated with disabled and/or injured upper limb function [6]. Posture affects grip strength and grip endurance time [7–9], but the supination posture was the most effective grip position [7]. Kattel et al. [9] found that maximum grip strength occurs at 0° upper arm abduction and 135° elbow flexion and the wrist is neutral. In addition, grip strength is a function of age and curve [10]. It increases from childhood to puberty, peaks between the ages of 20 and 40, and declines slowly with age [6, 10]. Therefore, the present study was designed to evaluate the correlations with anthropometric measurements between MVC grip strength, grip endurance at 50% MVC, and EMG activity in FDS, FCU, ECRB, and ECU muscle.

2 Methods

2.1 Participants

Participants were selected from two groups (56 group): a sedentary lifestyle (SL) and a group of construction workers (CW). Only those who did not report a history of hand, wrist, or forearm dysfunction, or other neuromuscular problems, were selected. The experimental protocol was explained to each participant, and they give their written consent. The experimental protocol was approved by the departmental ethics committee (Ref. No. EC/60/2017). Table 1 shows the basic anthropometric measurements of the participants.

2.2 Experimental Rig

A spring-loaded vibrating plate was designed to support the forearm in supine posture for the vibration exposure. The vibrator (model: Max JS113, brand: M/s Manipol Massager Medicare Products Inc. India) was attached in the center underneath the

Table 1 Basic anthropometric measurements of the participants

Groups	Age (years)	Weight (kg)	Height (cm)	Palm length (cm)	Palm circumference (cm)	Forearm length (cm)	Forearm circumference (cm)
SL	28.6 ± 5.8	69.9 ± 11.8	172.6 ± 5.9	10.7 ± 0.7	21.6 ± 1.1	26.5 ± 1.1	25.8 ± 2.3
CW	31.3 ± 9.4	60.1 ± 8.1	163.1 ± 5.6	10.6 ± 0.4	22.3 ± 1.4	24.7 ± 1.2	25.3 ± 1.7

vibrating plate consisting of a small DC motor with an eccentric head. That was encased in a metal housing and whose frequency was between 15 and 65 Hz.

2.3 Protocol and Procedure for the Experiment

The participants were asked to sit on a height-adjustable chair and were asked to squeeze the grip dynamometer (twice, with a 2-min rest period to record the MVC), in supine posture before and after vibration exposure (BVE) to maximum capacity [11, 12]. The height of the chair was adjusted so that the participant's right arm was in the coronal plane with a 0° abduction ensuring an elbow angle of 90°–130°. The grip Jammer (Model: G100) was directly interfaced with 8-channel participant unit Data LINK using cable H2000 (Make: Biometrics Ltd. UK) and connected with the laptop through USB1800 connecting lead. Then after 5 min of rest, the grip endurance time at 50% MVC (taking reference as maximum value of both trials) before and after vibration exposure was measured, and simultaneously, the EMG signals were obtained using Data LINK for subsequent analyzes. Further, four bouts of VT as per the VT protocol (Table 1) with a rest of 60 s after each bout were given to each participant. However, after performing the VT before recording the MVC grip strength and endurance time, each participant was given a 15-min rest period.

2.4 Surface EMG Recording and Analyses

Active differential surface EMG electrodes (SX230, M/s Biometrics Ltd. UK) with center-to-center distance of 20 mm were used to record the EMG signals at a sampling frequency of 1024 Hz [13]. The reference electrode was attached to the wrist of the non-dominant hand. In accordance with the SENIAM protocol [14], the electrodes were placed on flexor carpi ulnaris (FCU), flexor digitorum superficialis (FDS), extensor carpi radialis brevis (ECRB), and extensor carpi ulnaris (ECU) muscles of the right forearm. The EMG data was recorded and analyzed in line with the previous in-house study [13].

3   Results

Pearson's correlation test was performed using IBM SPSS version 20.0 (Table 2) on the data to evaluate the correlation of MVC grip strength, grip endurance time, neuromuscular efficiency, and normalized EMG RMS considering as dependent variables between anthropometric measurements.

Table 2 Pearson's correlation (r) between dependent variables and co-variates for both groups

Groups	Co-variates	MVC	ET	Neuromuscular efficiency				% Normalized EMG RMS			
				FDS	FCU	ECRB	ECU	FDS	FCU	ECRB	ECU
SL	Age	0.374**	0.013	0.198**	0.013	0.360**	0.276**	−0.012	0.044	0.092	0.015
	Wt	0.607**	0.072	0.236**	0.108	0.472**	0.412**	−0.087	0.045	0.009	0.082
	Ht	0.292**	0.118*	0.084	0.015	0.202**	0.231**	−0.055	0.201**	−0.015	−0.058
	PL	0.148*	0.214**	−0.003	0.021	0.054	0.173**	−0.033	0.076	−0.010	−0.164**
	PC	0.470**	−0.015	0.170**	0.042	0.260**	0.276**	−0.083	0.106	0.032	0.064
	FL	−0.018	0.075	0.252**	0.139*	−0.121*	0.137*	−0.079	0.011	0.040	0.027
	FC	0.611**	0.011	0.234**	0.067	0.475**	0.347**	−0.084	0.064	0.077	0.124*
SSCW	Age	−0.3**	0.176**	−0.083	−0.039	−0.116	−0.134*	−0.003	−0.050	0.205**	0.085
	Wt	−0.003	0.149*	0.041	0.026	−0.048	0.010	0.093	−0.039	0.156**	0.048
	Ht	0.125*	0.015	−0.115	−0.076	−0.102	−0.122*	0.058	0.060	−0.017	0.039
	PL	−0.21**	0.197**	0.023	0.130*	0.019	0.080	0.16**	0.134*	−0.035	0.265**
	PC	0.359**	0.126*	0.023	0.077	0.034	0.070	0.068	−0.010	−0.131*	−0.178**
	FL	−0.037	0.227**	−0.19**	0.061	0.009	−0.101	0.046	0.026	−0.109	−0.041
	FC	0.219**	0.065	−0.029	0.047	0.070	0.057	0.136*	−0.16**	−0.047	−0.101

Note ** ($p < 0.01$), * ($p < 0.05$) (2-tailed). *Wt.* weight; *Ht.* height; *PL* palm length; *PC* palm circumference; *FL* forearm length; *FC* forearm circumference; *MVC* maximal voluntary contraction; *ET* endurance time; *FDS* flexor digitorum superficialis; *FCU* flexor carpi ulnaris; *FCU* flexor carpi ulnaris; *ECRB* extensor carpi radialis brevis; *ECU* extensor carpi ulnaris

3.1   MVC Grip Strength and Endurance Time

MVC grip strength had a significant correlation with age, weight, height, palm length, palm circumference, and forearm circumference for SL group (Table 2). However, a significant negative correlation for CW group with age and palm length and a significant positive correlation with height, palm circumference, and forearm circumference was found. In addition, endurance time was significantly positively correlated with height and palm length for SL group, whereas for CW group with age, weight, palm length, palm circumference, and forearm length as shown in Table 2.

3.2   Neuromuscular Efficiency (NME)

Neuromuscular efficiency was significantly correlated with age in FDS, ECRB, and ECU; weight in FDS, ECRB, and ECU muscles; height in ECRB and ECU muscles; palm length in ECU muscle; palm circumference in FDS, ECRB, and ECU muscles; forearm length in FDS, FCU, ECRB, and ECU muscles; and forearm circumference in FDS, ECRB, and ECU muscles for SL group. However, NME was negatively significantly correlated for CW group with age in ECU muscle, height in ECU muscle, and forearm length in FDS muscle and positively significantly correlated with palm length in FCU muscle as shown in Table 2.

3.3   % Normalized EMG RMS

% normalized EMG RMS had a significant correlation with height in FCU muscle, palm length, and forearm circumference in ECU muscle for SL group. In addition, for CW group % normalized EMG RMS had a significant correlation with age and weight in ECRB muscle, palm length in FDS, FCU, and ECU muscles, palm circumference in ECRB and ECU muscles, and forearm circumference in FDS and FCU muscles (Table 2).

4   Discussion

Grip strength assesses the hand's ability to exert force at maximum capacity and is also a measure of active muscle contraction of the intrinsic and extrinsic muscles of the hand and forearm. In addition, the grip strength is significantly correlated with the function of the upper limbs in disabled and injured people. Wu et al. [7], during a survey on 482 adults in Taiwan, reported significant correlations between grip strength with gender, age, and palm length. They added that palm length, after

gender and age, was the most influential factor affecting grip strength. Fiebert et al. [15] also agree that palm length is strongly correlated with grip strength. Farahi and Jadidian [16] found that hand length, palm length, palm circumference, forearm length, and forearm circumference were significantly correlated with grip strength. Interestingly, the current results show that age, height, palm length, palm, and forearm circumference have significant correlation with grip strength on both groups. In addition, forearm circumference ($r = 0.611$, $p < 0.001$) followed by weight ($r = 0.607$, $p < 0.001$) and palm circumference ($r = 0.470$, $p < 0.001$) in SL group was the most influential factor affecting the grip strength. However, a significant negative correlation between grip strength with age and palm length was found in the CW group. This may be due to the fact that participants in the CW group were older than those in the SL group. In addition, grip strength is a function of age and curve [10]. It increases from childhood to puberty, peaks between the ages of 20 and 40, and declines slowly with age [6, 10].

Heidi and Jonathan [17] found significant difference between age and grip strength ($p < 0.001$) and no significant correlation between age and grip endurance time ($r = -0.13$, $p = 0.38$). Nicolay and Walker [8] concluded that, in contrast to strength, variability in anthropometry was independent of relative grip endurance. They also concluded that forearm and hand measurements were found to be better predictors of grip strength than height and weight, as reported in this study. Contrary to current results, no significant correlation of the palm circumference ($p = 0.108$) with the grip strength and the forearm circumference ($p > 0.05$) with the grip strength and the endurance time has been reported [11]. These discrepancies in findings may be due to differences in experimental approaches, devices for measuring grip strength, or the methods used to measure anthropometric variations. Interestingly, present results showed that endurance time was significantly positively correlated with height and palm length for SL, whereas for CW group with age, weight, palm length, palm circumference, and forearm length. Therefore, it can be confirmed that grip strength and grip endurance are factors that depend on the variability of anthropometry.

Furthermore, no studies so far have investigated a correlation between anthropometric variability with neuromuscular efficiency and normalized EMG RMS. In addition, present study showed that NME was positively and significantly correlated with anthropometric measurements in most muscles of the SL group. However, the CW group had a negative correlation between NME with age and height in ECU and forearm length in FDS muscle. But, there was a positive correlation between NME and palm length in FCU muscle. In addition, palm length and forearm circumference were the most influential parameters significantly correlated with normalized EMG RMS and NME, respectively.

5   Conclusions

It can be concluded that Pearson's correlation test suggested forearm circumference followed by weight and palm circumference was the most influential factor affecting the grip strength and palm length generally served as a better predictor for grip endurance time.

Conflicts of Interest The authors declare that they have no conflict of interest.

References

1. Boissey P, Bourbonnais D, Carliotti M, Gravel D, Arsenault B (1999) Maximal grip force in chronic stroke subjects and its relationship to global upper extremity function. Clin Rehab 13:354–362
2. Massey-Westrop N, Rankin W, Ahern M, Krishnan J, Hearn T (2004) Measuring grip strength in normal adults: reference ranges and a comparison of electronic and hydraulic instruments. J Hand Surgery 29:514–519
3. Gurram R, Gouw G, Rakheja S (1993) Grip pressure distribution under static and dynamic loading. Exp Mech 33:169–173
4. Dubrowski A, Carnahan H (2004) Grip force when grasping moving cylinders. Int J Ind Ergon 34:69–76
5. Alam MM, Khan AA, Farooq M (2018) Effect of whole-body vibration on neuromuscular performance: A literature review. Work 59(4):571–583
6. Shiffman L (1992) Effects of aging on adult hand function. Am J Occup Ther 46:785–792
7. Wu S-W, Wu S-F, Liang H-W, Wu Z-T, Huang S (2009) Measuring factors affecting grip strength in a Taiwan Chinese population and a comparison with consolidated norms. Appl Ergon 40:811–815
8. Nicolay CW, Walker AL (2005) Grip strength and endurance: Influences of anthropometric variation, hand dominance, and gender. Int J Ind Ergon 35:605–618
9. Kattel B, Fredericks T, Fernandez J, Lee D (1996) The effects of upper extremity posture on maximum grip strength. Int J Industr Ergon 18:423–429
10. Hinson M, Gench B (1989) The curvilinear relationship of grip strength to age. Occupat Therapy J Res 9:53–60
11. Alam MM, Khan AA, Farooq M, Bhardwaj S (2016) Effect of one week intervention of vibratory massage therapy on forearm grip strength and endurance. In: 14th international conference on humanizing work and work environment HWWE-2016, pp 91–95. NIT Jalandhar
12. Khan AA, Sullivan LO, Gallwey TJ (2009) Effects of combined wrist flexion/extension and forearm rotation and two levels of relative force on discomfort. Ergonomics 52(10):1265–1275
13. Farooq M, Khan AA (2014) Effects of shoulder rotation combined with elbow flexion on discomfort and EMG activity of ECRB muscle. Int J Ind Ergon 44:882–891
14. Hermens H, Freriks B, Merletti R, Stegeman D, Blok J, Rau G, Hagg G (1999) SENIAM: European recommendations for surface ElectroMyoGraphy: results of the SENIAM project. Roessingh research and development, Enschede, The Netherlands: SENIAM
15. Fiebert I, Roach K, Fromdahl J, Moyer J, Pfeiffer F (1998) Relationship between hand size, grip strength and dynamometer position in women. J Back Musculoskeletal Rehab 10:137–142

16. Fallahi AA, Jadidian AA (2011) The effect of hand dimensions, hand shape and some anthropometric characteristics on handgrip strength in male grip athletes and non-athletes. J Hum Kinet 29:151–159
17. Heidi C, Jonathan A (1996) Tongue strength and endurance in different aged individuals. J Gerontol: Med Sci 51(5):247–250

Virtual Environment Design of Railway Wagon for Prototype Analysis and Simulation

Shivendra Nandan [ORCID]**, Satyajeet Kant, Rishikesh Trivedi, Javed Ahmad, and M. Maniraj**

Abstract Railway is an expeditiously developing research field, and significant efforts are being carried with the focus of enhancing their liability and up-gradation of railway systems by substantially reducing associated costs and introducing new features with material research along with software prototype analysis for prediction of progressive dynamic nature of railway model. Using virtual environment, tedious task can switch from time-based vehicle prototype to event-driven modeling software prototype. This research is aimed for proving analysis effectively and fulfilling criteria of national and international standards. To design and assembly of virtual prototype of model is done by using application of modeling software. To develop an efficient modern prototype model of wagon needs to perform variable mode as well as linear shaped mode modeling to finalize the design of wagon on track. Based on analysis, the change in material of wagon from steel alloys to aluminum alloys was analyzed by virtual dynamic software prototyping results that reduction in longitudinal creep force by 5.99–7.65%, wheel-set normal force by 4.7–8.5%, vertical forces by 8.32% and normal forces by 6.01%. This method is completely in the favor of prototyping economy. The components of the railway wagon can easily be designed and modified with the application of Software. By using this process, a real-time analysis of prototype is to be finding which reflects the optimized environment for analysis, and according to that, the prototype can be developed at the minimum of cost and time.

Keywords Tracks · Dynamic loading · Maintenance · Prototype · Locomotives · Simulation · Balancing · Material research · Ultrasonic testing

Abbreviations

CNG   Compressed natural gas
DA   Dynamic augment

S. Nandan (✉) · S. Kant · R. Trivedi · J. Ahmad · M. Maniraj
Galgotias University, Greater Noida, UP 201308, India
e-mail: shivendranandan@gmail.com

FAC   Fatigue allowance criteria
FOS   Factor of safety
IR   Indian Railways
LNG   Liquefied natural gas
MPa   Mega Pascale
SDB   Self-discharging bogie
UST   Ultrasonic testing

1 Introduction

In this research, we are developing a railway wagon prototype in consideration of balancing of tracks for the different loading conditions, by which optimum dimensions can be integrated to the wagon, and testing of railway prototype wagon has been rolled out on track. If actual faults correspond to damage indexes, collection of data is available to assess and examine the overall system operation [1]. The railway cars can be designed to operate at various speeds in one accordance with side bearings to ensure driving mode [2]. The track derailment occurs due to wheel-set loss, and induced stresses cause support structure failure. These studies can be carried by FEA analysis [3–5].

Universal Mechanism Software and Ansys Software are used to analyze wagon parameters. And in present research work, aluminum alloy study is focused which has greater strength and less self-weight as compared to existing systems. And it can replace the current iron-alloy material in future. Also reduction in vertical forces tends to less material wear and corrosion.

The purpose of prototype design is to be maximizing the versatility of containers, swap body wagons, trailers and passenger bogies to be free movement within rail transport network of most standard gauge in relation to accommodate a mix model of inter-modulus [6].

2 Research Methodology

In methodology, various stages of wagon design are to be involved:

1. Concept and detailed design,
2. Prototype testing and design validation,
3. Optimum speed and oscillation trial,
4. Open track line introduction of wagons.

Wagon dimensions for drawings and diagrams arrangement are necessary input in the software for study of load distribution with consideration upon FOS, DA and FAC along with specific component fatigue life. IR system suitability for loading and

unloading methods becomes enhanced by opting material research. The multi-body system modeling can also be carried with same methodology [5].

3   Design and Analysis of Wagon

Structure plan of prototype is drawn by standard dimensions of IR gauge, and components are prepared. Then all components are assembled to develop final prototype (refer Fig. 1), and section view of prototype is extracted into files for the analysis of body.

3.1   Design Aspects

A wheeled bogie is a wagon. According to engineering mechanics, chassis of a vehicle attached to wheel carrying framework on a locomotive or carriage train is termed as bogie. And structure of bogie underneath a train to connect each wagon with a certain degree of rotation around axis. The axles designed for heavy loading conditions vary up to five, but most of them built up with two axles. And, bogies are used with span bolsters to make connection and load equalization for the developed prototype.

Fig. 1 View of prototype wagon

3.2   Wagon Assembly

The assembly of wagon is done by using universal mechanism, SolidWorks and pro/e software. These are most appropriate way of design and prepare blueprints by assembly. As the wagons are unloaded by means of gravity and there is no external assistance. It is necessary to fill railroad level for self-discharging bogies.

4   Simulation and Analysis

This work is mainly focused on steel and aluminum material, which is analyzed dynamically and statically. Most of this part is done by using PTC Mathcad and Ansys analysis [2].

The followed steps are as follows:

1. Extraction of design assembly,
2. Assigning boundary conditions,
3. Define material properties,
4. Load and stress analysis,
5. Fatigue life cycle study,
6. Simulation of component.

4.1   Force Calculation on Each Surface

The forces acting on the wagon body depend upon the type of material, which is under consideration for transportation. Likewise,

(a) Solid matter: coal, ferrous material, industrial products, etc.,
(b) Liquid matter: milk, petroleum, water, etc.,
(c) Gases: CNG, LNG and other gases.

Apart from these, human beings are also under consideration for the analysis of the force. So, we refer Table 2, for the different material values which are to be analyzed for the pressure or force calculation on the wagon prototype. Here are given some values of respective matters for the 110 m^3 volume of space, for which, these boundary conditions need to specify according to material properties (refer Table 1) for simulation of prototype. The load and boundary conditions are applicable according to particular analysis as temperature for thermal analysis, loads for structural analysis and both conditions in combined analysis of frame.

- Linearly elastic behavior of material is in nature.
- There is no nonlinearity.
- The theory of small deflection can be used, damping needs not to be included, and it is assumed that there is no possibility of the structure excitation.

Table 1 Load analysis table

Parameters	Aluminum (unit)	Steel (unit)
Mod. of elasticity	$7.01e^{-10}$ (N/m^2)	$2.741e^{-11}$ (N/m^2)
Density	2693.5 (kg/m^3)	8012.2 (kg/m^3)
Stress on yield	$4.92e^8$ (N/m^2)	$4.21e^8$ (N/m^2)
Mod. of shear	$2.32e^{10}$ (N/m^2)	$8.329e^{10}$ (N/m^2)
Endurance limit	0.51	0.39
Poisson's ratio	0.34 (unitless)	0.33 (unitless)
Strength	290 (MPa)	403 (MPa)

Table 2 Loading material values

Product	Density (kg/m^3)	Mass = Density × Volume (kg)
Anthracite coal	1490	163,900
Water	1000	110,000
Bituminous coal	1354	148,940
Ballast	1206	132,660
CNG	0.87	95.7
Lignite coal	1287	141,570

- The wagon structure type can be either constrained in type or unconstrained in type.

Force calculation equation on each surface,

$$F = ma \tag{1}$$

Based on the acceleration, the applicable forces on the prototype can be calculated, and further simulation of the prototype proceeded for the optimum dimension of coaches. But simulation on prototype produces the results given in Table 3. The stress analysis results are shown in Fig. 2.

The UDL and compressive forces applied on the prototype axis for finite element analysis, and these stress analyses further carried for virtual analysis.

Table 3 Material loading conditions

Material	Total deformation	Stress	Strain
Aluminum	0.092691	0.52364	$6.25e^{-6}$
Aluminum alloy	0.072325	0.49635	$5.98e^{-6}$
Alloy steel	0.025964	0.54308	$2.02e^{-6}$
Steel	0.034602	0.56812	$2.92e^{-6}$
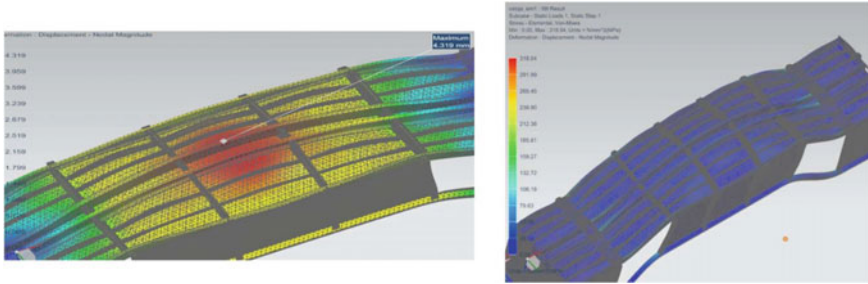
Fig. 2 Load and stress analysis of freight wagon in FEA

4.2 Simulation Result on Materials

After performing the Ansys material simulation, the following data is obtained.

These are the materials which are used as body material of wagon. So, as we obtained that aluminum or its alloy can replace the steels in future and become an integral part material of wagons.

5 Balancing of Track and Ultrasonic Testing

Track geometry is 3D in construction, and layout of track may be straight or curvature in nature. A variety of gauge systems are available based on the track geometry and expressed in terms of separate layouts as horizontal layout and vertical layout. A reference rail line is the base point for measurement. Balancing of track achieved when train speed and track support amount are in balance, which justifies the equilibrium of centrifugal forces with centripetal force. And rail wheel force normal to track plane has same for inside and outside rail [7].

Our study focuses on rail inspection by automated ultrasonic testing method, where track failures can be easily identified and detect the surface as well as internal defects by ultrasonic defectoscopy, and on different angles, several transducers are provided to enable detection of defects at different orientations. And graphical record of inspection displayed on monitor [3].

6 Material Research

Aluminum and steel are compared for wagon material for the analysis of static-dynamic analysis and stress values correspond to load. As seen that, equivalent longitudinal creep and lateral creep on track curve are tangent [1]. Further normal force and vertical force effect for both steel alloys and aluminum alloys (refer Table 3) for

Table 4 Load combination calculation

Load case	F_{YPmax} [kN]	F_{YP} [kN]	F_{Y1max} [kN]	F_{Z1max} [kN]	F_{X1max} [kN]
1st	774.98	0	0	0	0
2nd	0	402.67	171.52	0	0
3rd	0	402.67	171.52	96.55	0
4th	0	402.67	171.52	0	42.13

Fig. 3 Wheel-set forces in point load applications
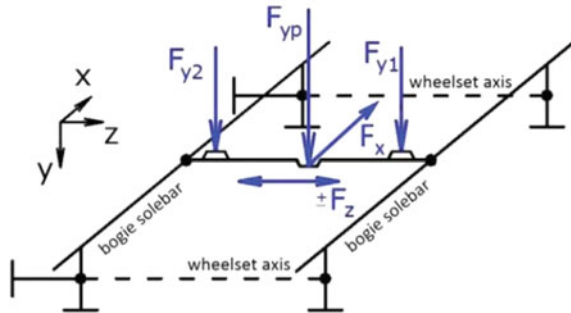
different components of bogie is analyzed. Other properties are also under consideration, i.e., corrosive strength, wear resistance, etc. which affects the dynamic strength of material. For these materials, various load combination applied for calculation as referred in Table 4.

Based on the load combination for wheel-set forces on frame (as mentioned in Table 4 and Fig. 3), the data is used for various calculations, i.e., creep, fatigue and normal load analysis of the prototype.

7   Conclusion

Based on the design, simulation, testing and material research, the following results are achieved when aluminum alloy is used as wagon material, and these % reductions of force values are reflected:

(a) Vertical forces of wheel set are reduced by 8.32% whereas normal forces are reduced by 6.01%.
(b) Longitudinal creep is reduced by 6.23–7.85%, and lateral creep is reduced by 5.5–8.32%.
(c) Fatigue strength less variability tends a longer component life, and due to less fluctuation, more reliable components are introduced.

So above results concluded that aluminum alloy is more reliable and economical as wagon material as compared to steel.

8   Future Scope

It is a wide field of work and finding solution for lot of challenges of transport model. Many types of commodities are transported by wagons, trailers and containers, which need to be optimized and implemented by new design prototype analysis. Because analysis by virtual software is provide more accurate data and requirement of real environment feasibility of prototype can be fulfilled.

References

1. Zboinski K (1998) Dynamical investigation of railway vehicles on a curved track Euro- pean. J Mecha-A/Solids 17(6):1001–1020
2. Gerlici J et al (2019) Analysis of the possibility of the use of tough side bearers in the covered wagons designed for light weight loads transportation. Transp Res Proc 40:694–702
3. Kochak RS, Sharma A (2001) Development of virtual prototype domestic container railcar. In: 16th EuropeanMDIUsers'Conference, Berchtesgaden, Germany, 14–15November 2001
4. Xu L et al (2018) Development of a railway wagon track interaction model. Mech Syst Sign Process 100:877–898
5. Vatulia G et al (2017) Structural improvements in a tank wagon with modern software packages. Proc Eng 187:301–307
6. Nandan S et al (2020) Design, analysis and prototype development of railway wagons on different loading conditions. Elsevier SSRN, pp 1–8, March (2020)
7. Koziak S et al (2019) Virtual software testing and certification of railway vehicle from the point of view of their dynamics. Transp Res Proc 40:729–736

Finite Element Analysis of HDPE-Based Hybrid Nanocomposite for Potential Use as Liner Material for Total Hip Prosthesis

Dannana Dimple, Medha Shruti, Nitesh Dhar Badgayan, and Santosh Kumar Sahu

Abstract The current investigation limits to analysis of metallic stem and high-density polyethylene (HDPE) based hybrid nanocomposite used as acetabular cup liner material. The structural analysis of stainless steel stem was carried out in ANSYS workbench GUI at various neck angles, i.e., 100, 110, 120, 130 and 140^0, with a load of 3700 N. The results show that the maximum value of equivalent von Mises stress was 0.336 GPa, which decreased by 29, 38, 39 and 56% for 110, 120, 130 and 140^0 stem angles, respectively. The best stem angle was chosen which showed the least equivalent von Mises stress, and further analysis of $140^°$ acetabular cup was performed for various human actions, i.e., cycling, jogging, stairs down, stairs up, stand up and walking. The results concluded that with HDPE/0.25 MWCNT/0.15 h-BNNP hybrid nanocomposite as liner material, the maximum value of equivalent von Mises stress was lower than the safer value for acetabular cup material for all human actions.

Keywords Finite element analysis · Total hip prosthesis · Acetabular cup · HDPE

1 Introduction

Hip arthroplasty is a procedure in which a painful hip joint with arthritis is removed with surgery and replaced with an artificial joint. This procedure reduces pain and induces normal movement in cases of wear and tear of these joints. Components of hip replacement surgery include femoral stem with ball, articulating against acetabular component as shown in Fig. 1a [1]. The femoral stem possibly will be cemented or press fit into the bone. The selection of materials plays a major role in longevity of the transplant apart from weight reduction. Thermoplastic polymeric material is precisely

D. Dimple · M. Shruti · S. K. Sahu (✉)
Department of Mechanical Engineering, Amrita School of Engineering, Bengaluru, Amrita Viswa Vidyapeetham, India
e-mail: sksahumech@gmail.com

N. D. Badgayan
Department of Mechanical Engineering, Centurion University of Technology & Management, Odisha, India
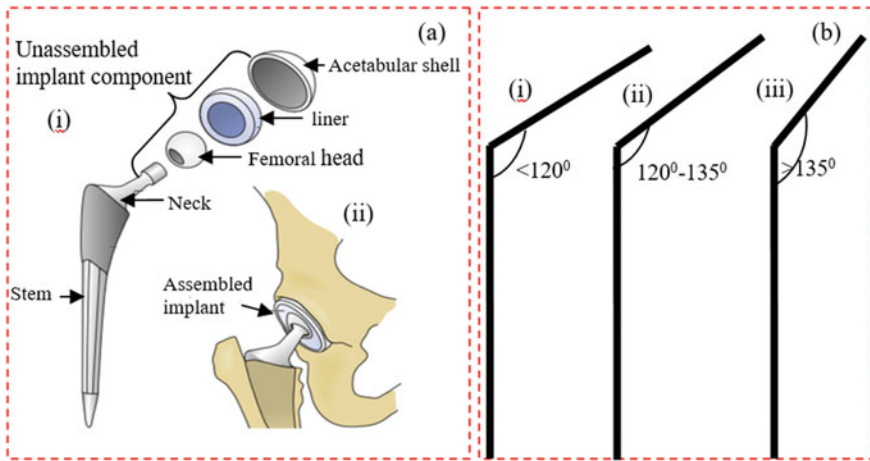
Fig. 1 **a** Components of total hip prosthesis (i) un-assembled, (ii) assembled view, b) (i) coxavara, (ii) normal, (iii) coxavalga neck angle [1]

being the best solution compared to metallic one [2–4]. High-density polyethylene (HDPE) is one such example of thermoplastic polymer that has drawn enormous interest to researchers in recent years due to lightweight, corrosion resistance, chemical inertness and bio-compatible [5, 6]. However, it possesses inherent loopholes like low wear resistance, low stiffness and strength which hinder its application in biomedical implants. HDPE-based hybrid nanocomposite is one such example with improvised property due to synergistic effect of individual nanofiller has widened the application areas from engineering to biomedical industries [7]. Followings are the brief discussions on HDPE-based polymer nanocomposites and hybrid relevance to mechanical and tribological performance to be suitable use in implant material.

Saleh et al. [8] reported on effect of alumina on tensile properties of HDPE composite. It was observed that there is an increase in elastic modulus with loading of above 7 wt% of alumina nanoparticle. Sahu et al. [9] studied on tribological and dynamic nano-mechanical properties of HDPE composite reinforced with multidimensional carbon nano-filler such as nano-diamonds (NDs), multi-walled carbon nanotubes (MWCNTs) and graphite nanoplatelets (GNPs). It was found that HDPE/0.1 GNP/ND hybrid nanocomposite exhibited the least plasticity index and hence acclaims highest wear resistance among the composites. Badgayan et al. [10] studied the dynamic mechanical and thermal properties of HDPE composite reinforced with MWCNT and h-BNNP composites. It was noted that hardness, impact toughness and stiffness HDPE/0.25 MWCNT/0.15 h-BNNP hybrid nanocomposite were increased by 172, 190 and 50% in comparison with virgin HDPE. Lin et al. [11] reported on mechanical, dynamic mechanical and thermal properties of HDPE-based composite reinforced with 0.1–10% graphite nanoplatelets (GNP) and 0.05–1.5% graphene oxide (GO). There is 56, and 23% increase in elastic modulus and maximum stress is noted at 10% GNP, which acclaims the best among composites.

Sahu et al. [12] reported on nanomechanical properties of HDPE composite using nanoindentation technique. It was observed that 0.1 GNP/ND showed the stiffest material among the composites.

Badgayan et al. [13] evaluated on dynamic nanomechanical properties of HDPE composite reinforced with CNT and h-BNNP nanomaterials. It was observed that, at 10 Hz, the best elastic property was noted for 0.1 CNT composite where loss modulus decreased by 23.52% in comparison with virgin HDPE. Based on literature survey, it was found that HDPE with 0.25 MWCNT/0.15 h-BNNP hybrid filler system showed the superior mechanical, tribological performance and also biocompatible that best suitable for liner material in acetabular cup [9]. The current investigation is oriented toward finite element simulation of acetabular cup with above liner material. The current study acclaims novel as none of the work reported on acetabular cup with above liner material. The finite element analysis using ANSYS 14 software is used to simulate the result with variation of stem angle (angle at neck region), i.e., 100 to 140 degrees at 10 degrees of increment as shown in Fig. 1b. The limitation of stem angle variation is looked from literature Byrne et al. [1]. The best stem angle is chosen, and further analysis is performed on acetabular cup at various human actions, i.e., cycling, jogging, stairs down, stairs up, stand up and walking.

2 Materials and Methods

2.1 Materials

Material for stem is *stainless steel* and for outer shell part of acetabular cup virgin HDPE is used. The liner part in acetabular cup is HDPE/0.25 MWCNT/0.15 h-BNNP hybrid nanocomposite. The material properties for the above materials are chosen from literature Sahu et al. [14] and Badgayan et al. [15] and shown in Table 1. Perfectly plastic model is assumed for the analysis of stem and acetabular cup.

Table 1 Materials property [14, 15]

Component	Material	Young's modulus (GPa)	Poisson's ratio (μ)	Density (g/cm^3)	Tensile yield strength (MPa)
Stem	Stainless steel	210	0.27	8	215
Acetabular cup(Outer shell)	HDPE	1	0.42	0.964	29.7
Acetabular cup (Liner)	HDPE/0.25 MWCNT/0.15 h-BNNP	1.5	0.43	0.964	42
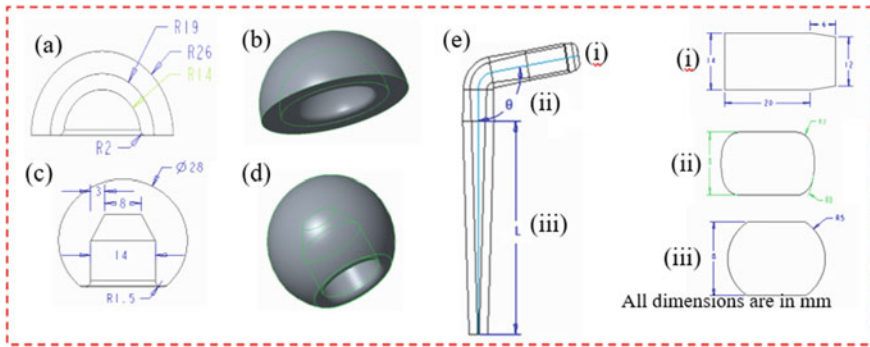
Fig. 2 **a**, **c** Geometry of outer shell and femoral head; **b**, **d** modeling of outer shell and femoral head; **e** geometry of stem and its cross-section

2.2 Modeling and Finite Element Analysis of Stem and Acetabular Cup

Stem and accetabular cup are modeled in PTC Creo 3.0. The details of design and 3D modeling of stem and acetabular cup are shown in Fig. 2a–e. Finite element simulation of stem and acetabular cup is performed using ANSYS 19 workbench GUI under static structural in project schematic. Figure 3a shows the modeled stem with its boundary conditions. The length of 100 mm below the neck of stem is fixed in all degrees of freedom, as it should be inserted to femoral bone. A load of 3700 N applied at the head part of stem. The load has chosen as suggested by literature Li et al. [16], i.e., five times the patient's body weight. Similar loading conditions are adopted for all stem designs, i.e., variation of neck angle, i.e., from 100 to 140 degrees. Deformation results and equivalent von Mises stresses are to be found out from the analysis. Among the results, the best neck angle of stem is adopted for stress analysis of acetabular cup study, where it showed least value of von Mises stress and particularly with uniform distribution of stress where chance of failure is least. The meshing for stem structures was performed using triangular elements. The mesh convergence study is also performed to evade any mesh size dependency before
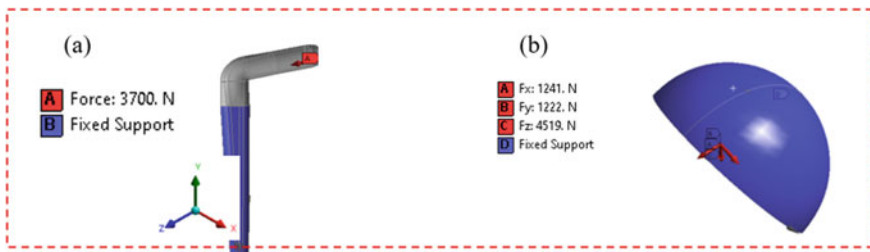
Fig. 3 Boundary and load condition of **a** stem; **b** acetabular cup
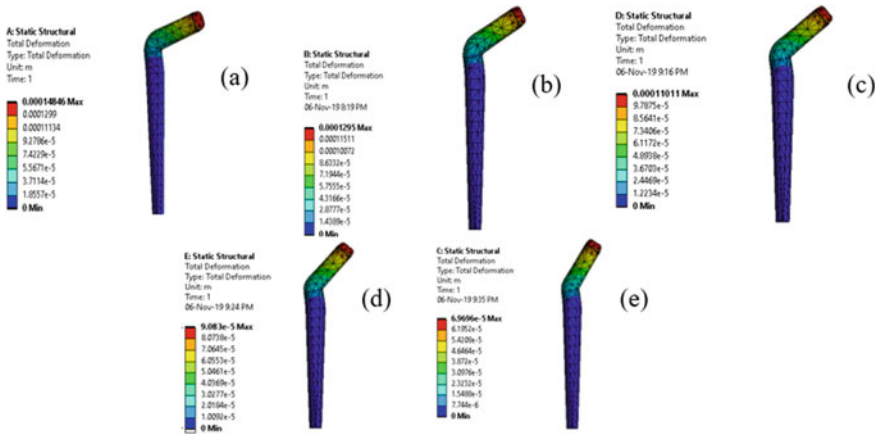
Fig. 4 Deformation results at **a** 100; **b** 110; **c** 120; **d** 130; **e** 140º stem angle

proceeding for analysis. There were a total of 1338 elements and 2607 nodes are considered for stem analysis. The next stage of analysis is combination of stem with acetabular cup, which is also performed ANSYS 19 workbench GUI. Figure 3b shows the acetabular cup with its boundary conditions by hiding the stem part meant for simplification. The outer part of the acetabular cup that has to be fixed to acetabulum bone hence arrested in all degrees of freedom. The liner of the acetabular cup that has to be fitted to femoral head is given loading at different human actions, i.e., cycling, jogging, stairs down, stairs up, stand up and walking. The loading values in each action are looked at form literature [17]. The meshing for stem structures is also performed using triangular elements. Likewise, for stem, the mesh convergence study is also performed on cup to evade any mesh size dependency before proceeding for analysis. There was a total of 370 elements and 791 nodes which are considered for analysis acetabular cup (Figs. 4, 5, 6, 7).

3 Results and Discussion

Figure 4 shows the deformation distribution results, and Fig. 7a shows the highest values of deformation results at different angles of stem, i.e., 100, 110, 120, 130 and 140°. The highest deformation is observed at the loading point and decreases continuously toward the fixed point. The highest deformation at 100° is 0.149 mm, which decreased by 13, 26, 39, 53% at 110, 120, 130 and 140° of stem angles, respectively. In order to spot the highly stressed areas, the stress distribution results are found and shown in Fig. 5.

Figure 7b shows the maximum equivalent von Mises stress at different angles of stem, i.e., 100, 110, 120, 130 and 140°. It is observed that the stressed areas are spotted toward fixed point and lowest at the loading point. It is observed that, at 100^0,
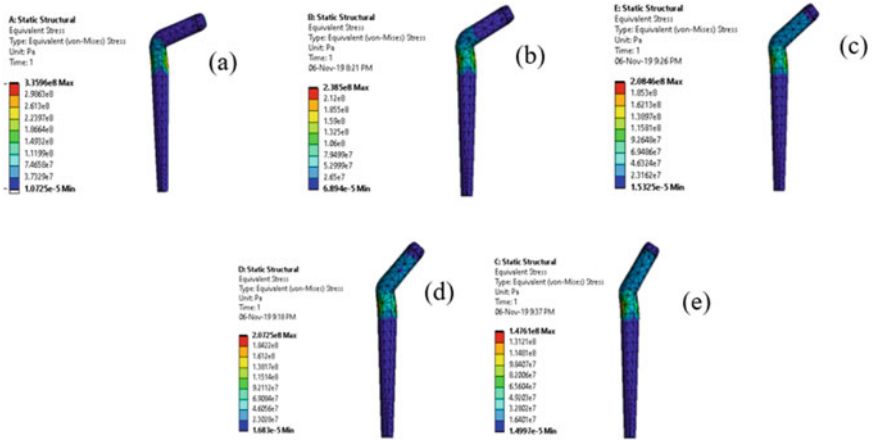
Fig. 5 Stress distribution results at **a** 100; **b** 110; **c** 120; **d** 130; **e** 140º stem angle
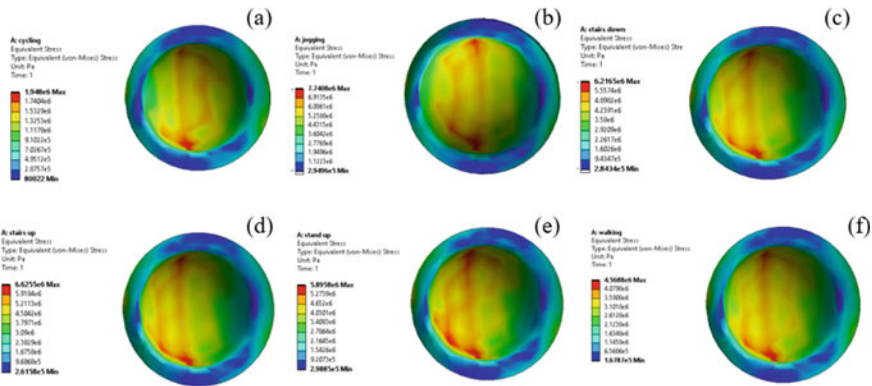
Fig. 6 Stress distribution results on liner of acetabular cup during **a** cycling; **b** jogging; **c** stairs down; **d** stairs up; **e** stand up; **f** walking
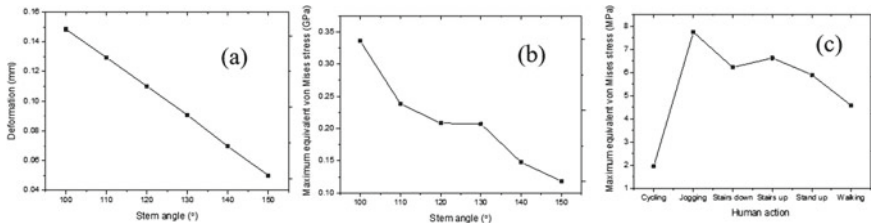
Fig. 7 **a** Deformation versus stem angle; **b** maximum equivalent von Mises stress versus stem angle; **c** maximum equivalent von Mises stress versus various human actions

Table 2 Load acting during various human actions [16]

Load direction	Cycling	Jogging	Stairs down	Stairs up	Stand up	Walking
F_x (N)	−420	−1241	−1085	−1164	−1578	−831
F_Y (N)	−1131	−4519	−3662	−3876	−3480	−2709
F_Z (N)	−357	−1222	−855	−1067	−612	−536
F_t (N)	1258	4843	3913	4185	3869	2885

s

the maximum value of equivalent von Mises stress is 0.336 GPa, which decreased 29, 38, 39 and 56% for 110, 120, 130 and 140° stem angles, respectively. The decrease in stress with increase in stem angle can be attributed to stress concentration or stress raisers at neck of the stem, where there is chance of failure which is severe. However, with increase in angle, the stress distribution is uniform that hinders the stress and decreases the chance of failure at neck, which can be seen in Fig. 5. Hence, the higher angle is preferred over lower angle of stem. Figure 6 shows the stress distribution results for acetabular cup with HDPE/0.25 MWCNT/0.15 h-BNNP hybrid nanocomposite as liner material at different human action. It is observed that the maximum value of equivalent von Mises stress is 7.74 MPa as shown in Fig. 7c, which seen during jogging, followed by stairs up, stairs down, stand up, walking and cycling. The results indicate that, with HDPE/0.25 MWCNT/0.15 h-BNNP hybrid nanocomposite as liner material, the maximum value of equivalent von Mises stress is lower than the safe value for acetabular cup as shown in Table 2.

4 Conclusion

The structural analysis of stainless steel stem at various stem angles, i.e., 100, 110, 120, 130 and 140 degrees, was performed using ANSYS workbench GUI. The best stem angle was chosen for further analysis of acetabular cup with HDPE/0.25 MWCNT/0.15 h-BNNP hybrid nanocomposite as liner material at various human actions, i.e., cycling, jogging, stairs down, stairs up, stand up and walking. Based on the investigation, following conclusion can be drawn;

1. The stem angle at neck angle of 140^0 showed the least equivalent von Mises stress, which is chosen for further analysis of acetabular cup.
2. The maximum value of equivalent von Mises stress for acetabular cup is 7.74 MPa, which seen during jogging, followed by stairs up, stairs down, stand up, walking and cycling.
3. The liner material, i.e., HDPE/0.25 MWCNT/0.15 h-BNNP hybrid polymer nanocomposite stress distribution results, showed that the maximum value of equivalent von Mises stress is lower than the safe value for acetabular cup at all human actions, which is ideal liner material for total hip prosthesis.

It is concluded that acetabular cup with HDPE/0.25 MWCNT/0.15 h-BNNP hybrid polymer nanocomposite as liner material at an angle of 140° the implant is safe to use. The further experimental investigations will add feasibility of the above implant material which opens new avenues in research.

References

1. Byrne DP, Mulhall KJ, Baker JF (2010) Anatomy and biomechanics of the hip. Open Sports Med J 4:51–57
2. Sahu SK, Badgayan ND, Samanta S, Sahu D, Sreekanth PSR (2018) Influence of cell size on out of plane stiffness and in-plane compliance character of the sandwich beam made with tunable PCTPE nylon honeycomb core and hybrid polymer nanocomposite skin. Int J Mech Sci 148:284–292
3. Sahu SK, Badgayan ND, Sreekanth PSR (2020) Numerical investigation on the effect of wall thickness on quasistatic crushing properties of nylon honeycomb structure. Mater Today Proc https://doi.org/10.1016/j.matpr.2019.12.351
4. Badgayan ND, Sahu SK, Samanta S, Sreekanth PSR (2020) An insight into mechanical properties of polymer nanocomposites reinforced with multidimensional filler system: a state of art review, Mater Today Proc 24(2):422–431 [In press]
5. Badgayan ND, Sahu SK, Samanta S, Sreekanth PSR (2018) Assessment of nanoscopic dynamic mechanical properties and BCN triad effect on MWCNT/h-BNNP nanofillers reinforced HDPE hybrid composite using oscillatory nanoindentation: an insight into medical applications. J Mech Behav Biomed Mater 80:180–188
6. Sahu SK, Badgayan ND, Samanta S, Sreekanth PSR (2020) Experimental investigation on multidimensional carbon nanofiller reinforcement in HDPE: an evaluation of mechanical performance. Mater Today Proc 24(2):415–421 [In press]
7. Fouad H, Elleithy R, Othman YA (2013) Thermo-mechanical, wear and fracture behavior of high-density polyethylene/hydroxyapatite nano composite for biomedical applications: effect of accelerated ageing. J Mater Sci Technol 29(6):573–581
8. Saleh M, Al-Hajri Z, Popelka A, Javaid ZS (2020) Preparation and characterization of alumina HDPE composites. Materials 13(1):250–262
9. Sahu SK, Badgayan ND, Sreekanth PSR (2019) Understanding the influence of contact pressure on the wear performance of HDPE/multi-dimensional carbon filler based hybrid polymer nanocomposites. Wear 438:102824–102834
10. Badgayan ND, Sahu SK, Samanta S, Sreekanth PSR (2019) Evaluation of dynamic mechanical and thermal behavior of HDPE reinforced with MWCNT/h-BNNP: an attempt to find possible substitute for a metallic knee in transfemoral prosthesis. Int J Thermophys 40(10):93–113
11. Lin S, Anwer MA, Zhou Y, Sinha A, Carson L, Naguib HE (2018) Evaluation of the thermal, mechanical and dynamic mechanical characteristics of modified graphite nanoplatelets and graphene oxide high-density polyethylene composites. Compos Part B: Eng 132:61–68
12. Sahu SK, Badgayan ND, Samanta S, Sreekanth PSR (2018) Quasistatic and dynamic nanomechanical properties of HDPE reinforced with 0/1/2 dimensional carbon nanofillers based hybrid nanocomposite using nanoindentation. Mater Chem Phys 203:173–184
13. Badgayan ND, Samanta S, Sahu SK, Siva SV, Sadasivuni KK, Sahu D, Sreekanth PSR (2017) Tribological behaviour of 1D and 2D nanofiller based high densitypoly-ethylene hybrid nanocomposites: a run-in and steady state phase analysis. Wear 376:1379–1390
14. Sahu SK, Badgayan ND, Samanta S, Sreekanth PSR (2018) Dynamic mechanical thermal analysis of high density polyethylene reinforced with nanodiamond, carbon nanotube and graphite nanoplatelets. Mater Sci Forum 917:27–31

15. Badgayan ND, Sahu SK, Samanta S, Sreekanth PSR (2018) Assessment of bulk mechanical properties of HDPE hybrid composite filled with 1D/2D nanofiller system. Mater Sci Forum 917:12–16
16. Li X, Li D, Lian Q, Guo H, Jin Z (2010) The effect of stem structure on stress distribution of a custom-made hip prosthesis. Proceed Instit Mech Eng Part H: J Eng Med 224(11):1275–1284
17. Heidari BS, Davachi SM, Moghaddam AH, Seyfi J, Hejazi I, Sahraeian R, Rashedi H (2018) Optimization simulated injection molding process for ultrahigh molecular weight polyethylene nanocomposite hip liner using response surface methodology and simulation of mechanical behavior. J Mech Behav Biomed Mater 81:95–10

Design and Analysis of Metal-To-Metal Contact Bolted Flange Joint Using FEA Tool

Tanuj Joshi , **Ravikant Sharma, Om Parkash, and Aaditya Gupta**

Abstract Chemical and petroleum industries are striving for a better module of flanges for reducing the stress and higher temperature distribution to keep it safe for long-time prevention from the leakage. CAD and CAE tools like SolidWorks and Ansys are one of the best solutions for providing better information for improving the mechanical and thermal properties of the flange. Flanges are characterized in terms of rating (strength and sealing capacity). In present work, metal-to-metal gasket has been used for achieving minimum stress, providing high sealing capability, and to make amends for unloading impact due to external and internal loading. 317L stainless steel, ASTM A387 Grade 22 Class 2 steel, and ASTM A193M B16 materials are used for flange, gasket, and bolts, respectively. A 3D nonlinear finite element model is established for analyzing the complex behavior of MMC-type gasket flange under combined loading of internal pressure and thermal constraints. This present study shows MMCG model, which is able to serve better gasket performance in terms of temperature, pressure, and leakage reduction.

Keywords Sealing · MMCG · Leakage · Temperature

Abbreviations

CAD   Computer Aided Design
MMCG   Metal-to-Metal Contact Gasket
ASTM   American Society for Testing and Materials
CAE   Computer Aided Engineering
MMC   Metal-to-Metal Contact
ASME   American Society of Mechanical Engineering

T. Joshi (✉) · R. Sharma · O. Parkash · A. Gupta
Amity University Haryana, Gurugram 122413, India
e-mail: tanujjoshi15@gmail.com

1 Introduction

A flange is a way of connecting pipes, valves, pumps, and other equipment to shape a piping device. These are made by bolting them together. Gasket offers a seal that is between flanges. Flanges are used for connecting joints which incorporate attaching a pipe to fittings, valves, and mechanical equipment. Flanges are ranked through the rating system; higher the rating leads higher the maximum allowable pressure limit. Metal-to-metal contact (MMC)-bolted flanged joint, which seems among gasket centering ring and flange facing, is extensively used in nuclear and petrochemical industries [1]. Gasket outer metal ring is compressed after bolt-up and the stored energy into the gasket is in the form of stress due to internal pressure, bending moment, and creep which resulting in a low leakage [2].

Kraus [3] anticipated a model to forecast the time required by means of the bolts to diminish from high stress to some minimum level. Experimental results show that the gasket relaxation took place at some stage in the primary 15 min after the tightening of the joint bolts. The increment of compression leads to the leakage and at the same time instant, creep has a tendency to fill up the gap [4]. Bolt tightening is a considerable factor for flange joint assembly resulted after conducted the bubble leak testing method [5]. Weight loss throughout thermal exposure effects gasket properties, such as relaxation, compression stress, tensile strength, and tightness [6].

Initially, FE analysis of a distinctive bolted flanged joint was carried out by strain-hardening creep law. Due to ignorance of gasket in the assembly, accurate results were not been obtained [7]. These experiments set up a fundamental for using the gasket which leads to leakage control and strengthens the joints. The study of gasket creep-relaxation consequences onto the bolted flanged joints conclude that gasket experiences a drop in its initial compressive stress. Creep-relaxation of flanged joints enhanced by temperature incensement [8]. The analytical outcomes cautioned that the thickness of the flange and stiffness of the gasket have an extremely good impact on stress distribution [9].

Schneider et al. [10] uses a beam theory model to solve flanges with MMC, which was quickly accepted by ASME. For modeling and analysis of a flange model using FEM software is carried out by Shoji and Nagata et al. [11] in which analysis execution is controlled by Ansys Parametric Design Language. Flange with different surface profile was modeled and analyzed and it resulted that for achieving 'no-leak' condition, a flange having positive taper angle, elliptical hub, and thickness is of at least six instances of bolt diameter [12]. Flange thickness and bolt diameter have a predominant effect on bolt tension forces [13]. Temperature changing into flange at axial and radial expansion causes the load variation [14]. Flange configuration with a (+) ive slope results in an increment of leakage rate with the allowance of bolts [15]. Pindera and Sze [16] explain the impact of the bolts with washers on the MMC flange and concluded that higher rigidity of the bolts reduces bolt load. Some experiments resulted that contact stress distribution into flange and gasket have a dominant effect on the sealing of bolted flange joints [17].

Spiral-wound gasket for the pipe flange analyzed by Sawa et al. [18] and new-fangled gasket constraints acquired by using the elastic theory of axis-symmetry. If a gasket modulus of elasticity decreases or thickness increases, than the contact stress distribution should be uniform. Vishwanath et al. [19] analyse bolted flange with gasket by changing the thickness of flange from 44.4 to 55 mm and resulted that bolt preload changes from 35 to 75% of yield stress. For obtaining the uniform stress, the number of bolts must be 6, 8 and 12 bolts. A 3D nonlinear finite element model of flange joint with MMC-type gasket analyzed for internal pressure and thermal loading by Ma et al. [20], which concluded that gasket stress decreases due to rotation of flange and joint thermal expansion. The leakage pressure is predicted through full- and small-scale tests of metal-to-metal contact flange and proposed a design tool to optimize the flange geometry and maximize the leakage pressure [21]. The analysis resulted that when gasket stress reaches to the gasket yield stress, the sealing performance of bolted flange will increase significantly [22]. As the world moving through advancement in order to enrich the efficiency higher as possible, which is only possible by using some advance material for the mechanical system. Concidering this theme as a central idea, in present work, the new materials are utilized with the same boundary condition and observed that the new material demonstrates the better stress distribution, less deformation, and higher life in both into mechanical and thermal loading.

2 Material and Method

A 3D model of metal-to-metal contact (MMC)-bolted flanged joint assembly which consists of flange (3″ NPS Weldneck Flange 300# RF Sch-STD), gasket (3″ NPS Flat ASME B16.5 300#) and bolt (Hexbolt 3/4″ UNC (or M20) * 110 long) is designed and imported to CAE software package for testing (maximum stress, strain, total deformation and thermal analysis). The finite element technique is used for the simulation of the flange assembly. The assembly domain is discretized into a finite set of elements before simulation. Simulation can be solved by using the steps depicted into Fig. 1, which are as follows:

2.1 Material

Earlier studies consider specific material for the flange assembly. Flange, gasket, and bolt comprise of materials like 2.25Cr1Mo (ASTM A387 Grade 22 Class 1 Steel), ASTM A193M B7, and ASTM A240 316L, respectively. For the present study, some advance materials are used for flange, bolt, and gasket metal rings which are 2.25Cr1Mo (ASTM A387 Grade 22 Class 2 Steel), ASTM A193M B16, and ASTM A240 317L, respectively. The new materials have high tensile strength, long service life, high corrosion resistivity, high machinability, higher temperature, good

Fig. 1 Process flowchart
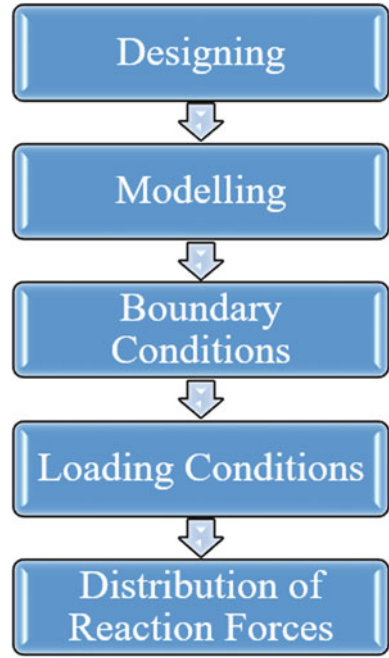
Table 1 Mechanical properties [24–26]

Material	Density (g/cm^3)	Young's modulus (GPa)	Poisson's ratio	Ultimate strength (MPa)	Yield strength (MPa)
317L stainless steel	7.9	200	0.28	550	250
ASTM A387 Grade 22 Class 2 steel	7.9	190	0.29	600	350
ASTM A193M B16	17.81	-	0.28	860	795

surface stability, mechanical loading, and toughness. An additional air column is used between flange and bolt for thermal analysis which has equivalent thermal conductivity (Tables 1, 2).

2.2 Methodology

The primary step in pre-processing consists of developing a 3D CAD model of flange assembly using SolidWorks 3D modeling software package. Dimensions of a flange

Table 2 Thermal properties [24–26]

Material	Maximum temperature (°C)	Thermal conductivity (W/m–°K)	Thermal Expension (μm/m–°K)	Sp. Heat (J/kg–°K)
317L stainless steel	1010	14	17	470
ASTM A387 grade 22 Class 2 steel	620	40	13	470
ASTM A193M B16	–	40	–	120
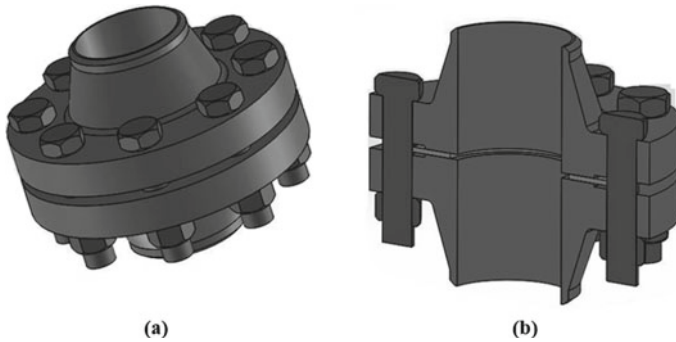
Fig. 2 **a** 3D model of flange assembly, **b** Sectional view of flange assembly

(3″ NPS Weldneck Flange 300# RF Sch-STD), gasket (3″ NPS Flat gasket ASME B16.5 300#), and bolt (Hexbolt 3/4″ UNC (or M20) * 110 long) illustrate into the following Fig. 2 a and b. After creating parts, assembly and drawing of flange setup were saved in.sldprt extension format, assembly file has extension name.sldasm and for drawing file it is.slddrw. Flange assembly setup has three main components, i.e., flange, gasket, and bolt.

2.3 Meshing

Specifically, meshing in workbench provides durable and easy that will primarily help facilitate the process of mesh generation. The discretization of a long linear body to a certain finite number of elements is known as meshing. Discretize shapes are known as an element which attached with another element at corners with nodes. Structural analysis and thermal analysis have the element SOLID 185 and SOLID 70, respectively. Meshed model of flange assembly depicted into Fig. 3.

Fig. 3 Meshed model of
flange
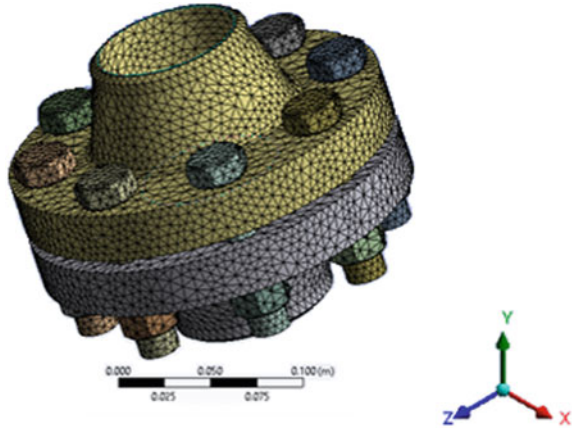
2.4 Boundary Condition

Constraints are applied to the lower portion and both sides of the model. As of only
the axial behavior of the gasket metal ring is considered; therefore, no interaction
takes place between the gasket and metal rings. As per the analysis, the bolts and
nut must be fixed and standstill at the compression load which is known as a bolt
pretension. A compression force is applied onto the inner wall and compensating
pressure onto the inlet of the flange pipe depicted in Fig. 4 a, b, and c, respectively.
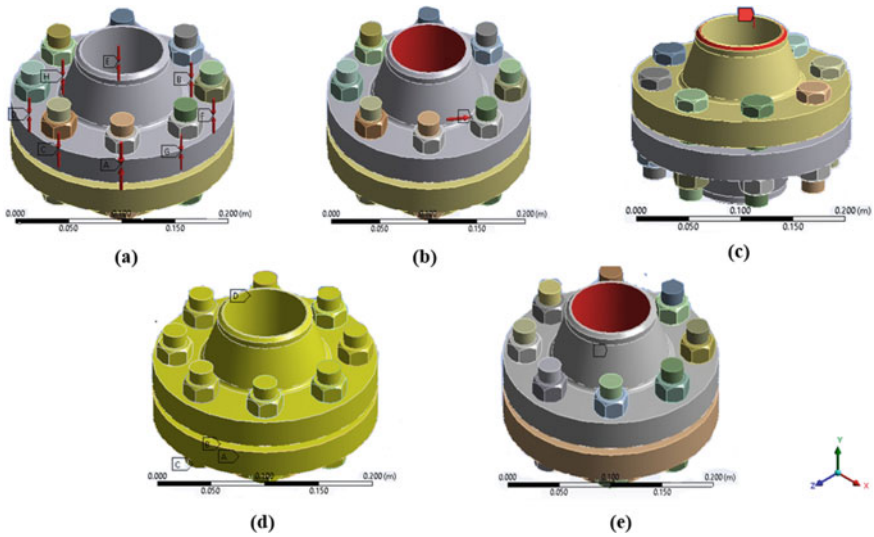
Fig. 4 a Bolt pretension, **b** 5 MPa pressure at inner walls, **c** Compression pressure over flange
assembly, **d** Convection Coefficient and **e** Temperature applied to the inner wall

Steady-state thermal analysis is assumed for analyzing of the flange. The present analysis considers the variation of internal temperature from 200 to 500 °C having a constant external temperature of 20 °C shown in Fig. 4e. 5800 and 32 W/m2°C are the convective heat transfer coefficient for the inner and outer surface of flange portrays into Fig. 4d.

3 Result and Discussion

3.1 Result

After setting up, all the arrangements and boundary conditions are applied over the flange. Bolt load varies due to pressure increment. In present work, internal pressure varies from 0 to 5 MPa and gives us the analytical result of maximum stress at the inner and outer diameter of the gasket depicted in Fig. 5, which illustrates that the maximum stress at outer and inner diameter is 62.067 and 9.5238 MPa, respectively. Figure 6 expresses the relation between the leakage follow up by the increment of internal pressure. The deformation due to incensement of the pressure from 0 to 5 MPa leads to larger deformation at inner and lesser to the outer gasket diameter. Figures 7 and 8 illustrate deformation and the maximum deformation at the inner and outer diameter of the gasket, respectively.

Figures 9and10 illustrate the temperature distribution and average temperature with the varying internal temperature from 200 to 500 °C for a bolt, flange, outer ring, and shell, respectively.
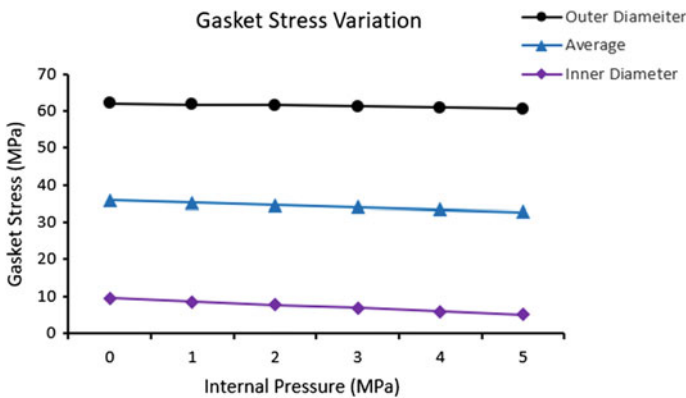
Fig. 5 Gasket stress variation
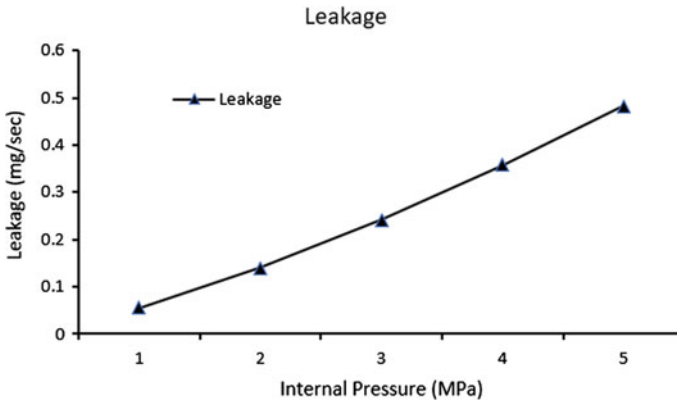
Fig. 6 Leakage variation
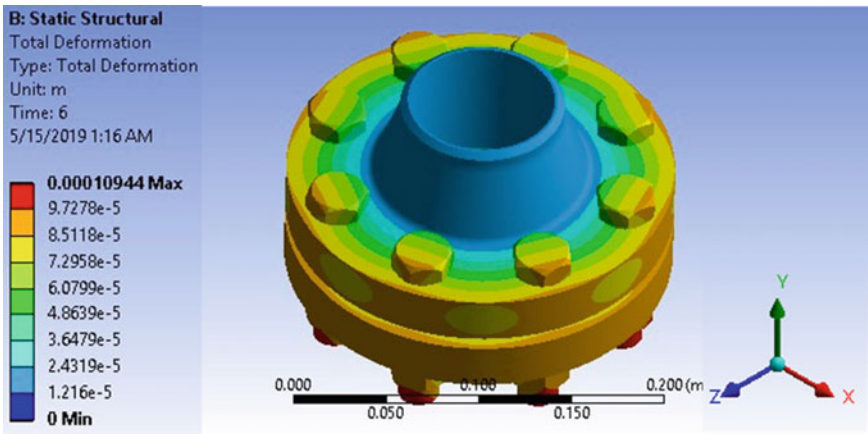
Fig. 7 Maximum deformation on bolted flange

3.2 Validation

The aftereffect of computed gasket stress for the 3″ NPS Weldneck Flange 300# RF Sch-STD model is validated with the published data by Ma et al. [23], which portrays into Fig. 11. This figure illustrates that the maximum and minimum average gasket stresses are 35.79 and 32.80 MPa, respectively. On the other hand, the model used by Ma et al. (2013) shows higher average stress having minimum and minimum gasket stress 57.50 and 51 MPa, respectively. It is found that the present simulation results of designed joints are able to serve better gasket performance on the basis of its reduced stress in the inner and outer diameter of the gasket..
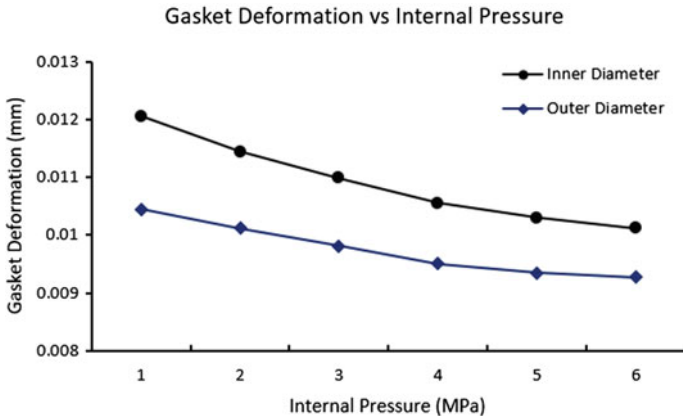
Fig. 8 Gasket deformation versus internal pressure variation in outer and inner diameter
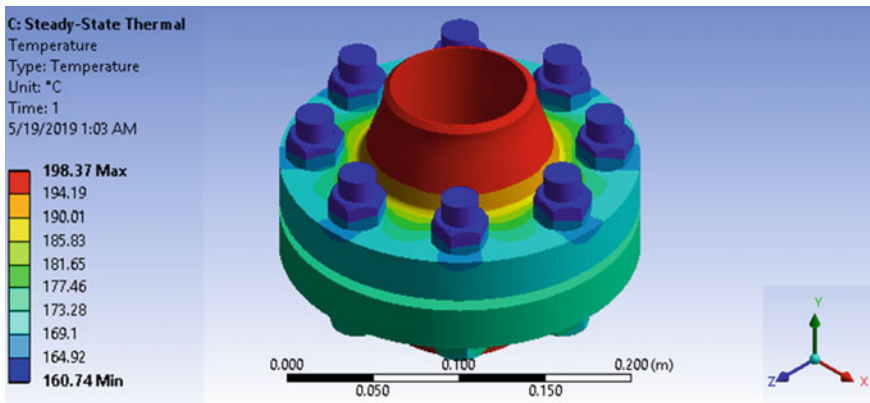
Fig. 9 Temperature distribution at flange assembly

4 Conclusion

A 3D finite element model of (MMC) gasket flange assembly is designed and analyzed for combined internal pressure and thermal loading. From that analysis, following conclusions have been drawn:

- MMC gasket is effective in reducing the unloading effect causes by internal and external compression effect.
- The flange lifted upwards because of the thermal expansion in the outer ring which leads to decrement in gasket stress.
- 317L stainless steel, ASTM A387 Grade 22 Class 2 steel provides better efficiency into thermal loading and lowering down the maximum stress.
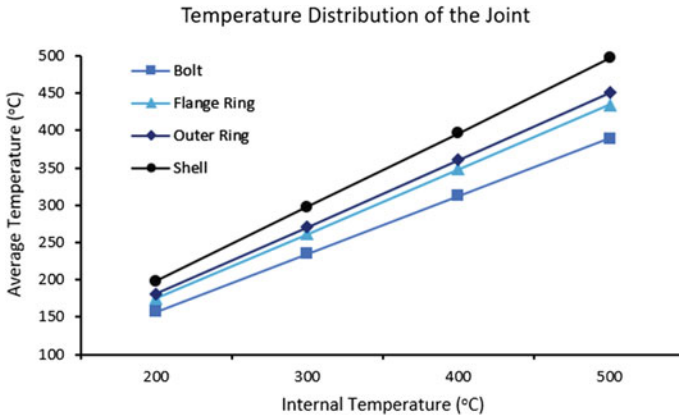
Fig. 10 Average temperature of the joint components at different internal temperature cases
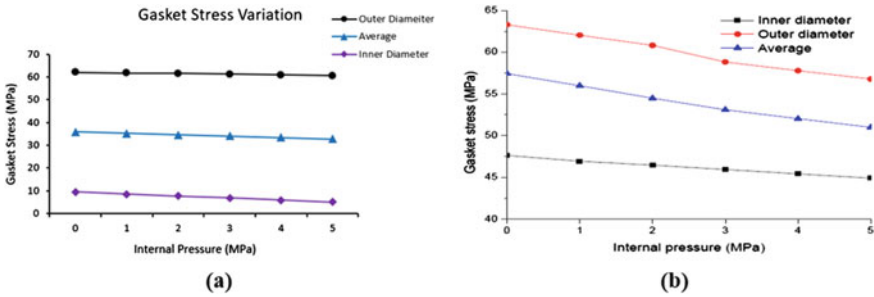
Fig. 11 Gasket stress variation **a** Present study and **b** Ma et al. [23]

References

1. Webjörn J (1967) Flange design in Sweden, ASME Paper 67-PET-20
2. Waters EO, Westrom DB, Rossheim DB, Williams FSG (1937) Formulas for stresses in bolted flanged connections. Trans ASME 59:161–167
3. Kraus H (1980) Creep analysis. Wiley, New York, NY
4. Bazergui A (1984) Short term creep relaxation behavior of gaskets. Gaskets," Welding Research Council Bulletin No. 294, New York, NY
5. Kondo K, Tsubaki S, Sawa T, Kikuchi T, Omiya Y (2012) FEM stress analysis and the sealing performance evaluation in bolted flange connections with ring joint gasket subjected to internal pressure: effect of scatter in bolt preloads. In: ASME 2012 pressure vessels and piping conference, American Society of Mechanical Engineers Digital Collection, pp 147–154
6. Marchand L, Derenne M, Bazergui A (1990) Weight loss correlation for sheet gasket materials. In: Proceedings, pressure vessel and piping conference, Nashville, Tennessee, pp 77–84
7. Fessler H, Swannell JH (1974) Prediction of the creep behaviour of a flanged joint. In: Proceedings, conference on creep behaviour of piping, Institution of Mechanical Engineers, pp 39–49

8. Bouzid A, Chaaban A, Bazergui A (1995) The effect of gasket creep-relaxation on the leakage tightness of bolted flanged joints. ASME J Pressure Vessel Technol 117(1):71–78
9. Do T, Bouzid H, Dao T-M (2008) Effect of bolt spacing on the circumferential distribution of gasket contact stress in bolted flange jonts. J Pressure Vessel Technol 133. https://doi.org/10.1115/ICONE16-48634
10. Schneider RW (1968) Flat faces flanges with metal-to-metal contact beyond the bolt circle. ASME J Eng Power 90(1):82–88
11. Shoji Y, Nagata S (2002) Analysis of gasketed flanges with ordinary elements using apdl control. Toyo Engineering Corporation
12. Abid M, Nash DH (2004) A parametric study of metal-to-metal contact flanges with optimised geometry for safe stress and no-leak conditions. Int J Press Vessels Pip 81(1):67–74
13. Tafheem Z, Amanat KM (2015) Finite element investigation on the behavior of bolted flanged steel pipe joint subject to bending. J Civil Eng (IEB) 43(1):79–91
14. Nechache A, Bouzid A-H (2005) Creep effect of attached structures on bolted flanged joint relaxation. In: Proceedings of the ASME 2005 pressure vessels and piping conference. High pressure technology, nondestructive evaluation, pipeline systems, student paper competition. Denver, Colorado, USA. July 17–21, ASME, vol 5, pp 207–215
15. Lewis LV, Fessler H, Hyde TH (1987) Determination of initial gaps between flat flanges without gaskets. Proc Inst Mech Eng Part A 201:267–277
16. Jofriet JC, Sze Y, Thompson JC (1981) Further studies of the interface boundary condition for bolted flanged connections
17. Krishna M, Shunmugam MS, Prasad N (2007) A study on the sealing performance of bolted flange joints with gaskets using finite element analysis. Int J Pressure Vessels Piping 84:349–357 https://doi.org/10.1016/j.ijpvp.2007.02.001.
18. Sawa T, Ogata N, Nishida T (2002) Stress analysis and determination of bolt preload in pipe flange connections with gaskets under internal pressure. J Pressure Vessel Technol 124(4):385–396
19. Kharat H, Gadewar SP, Gawande SH (2017) Numerical and experimental investigation of structural gasketing approach for gearbox flange. Int Rev Mech Eng 11(7)
20. Ma K, Zhang Y, Zhang L, Guan K (2014) Behavior of bolted joints with metal-to-metal contact type gaskets under bolting-up and loading conditions. Proc Inst Mech Eng Part E: J Process Mech Eng 230. https://doi.org/10.1177/0954408914547931
21. Bertini L, Beghini M, Santus C, Mariotti G (2009) Metal to metal flanges leakage analysis. In: ASME 2009 pressure vessels and piping conference, American Society of Mechanical Engineers, pp 149–158
22. Kondo K, Omiya Y, Tsubaki S, Sawa T (2014) FEM stress analysis and sealing performance evaluation in bolted flange connections with metal flat gasket subjected to bending moment and internal pressure. In: Computer technology and bolted joints, vol 2
23. Ma K, Zhang Y, Zhang L, Guan K (2013) Behavior of flange joints under combined internal pressure and thermal loading: the case of using metal-to-metal contact type gaskets. In: Proceedings of the ASME 2013 pressure vessels and piping conference. Computer technology and bolted joints, Paris, France. July 14–18, 2013, vol 2, V002T02A024, ASME
24. AZO Material Science https://www.azom.com/article.aspx?ArticleID=4837
25. AZO Material Science https://www.azom.com/article.aspx?ArticleID=8262
26. Boltport Fasteners LLP https://boltport.com/specifications/astm-a193m-grade-b16/

Investigation of Types of Technical Levitation and Mathematical Modeling of the Action of Many Composites Non-contact Electromechanical Mechanism

F. M. Matmurodov, Basant Singh Sikarwar, and Mohit Bhandwal

Abstract In this work, a comparative analysis is provided for technological indicators of various methods of technical levitation. Later, mathematical model was formed for particular cases of the gap of electromagnetic levitation and many composite non-contact mechanisms. This analysis mechanics creates effective contactless mechanisms which help us many aspects of energy and material saving.

1 Introduction

The number "Zero" was the first introduced by an Indian scientist, not a narrow "zero" about it 200 years later German scientist introduced in circulation. In the eighth century, our ancestor Al-Khwarizmi introduced the combination of Circulation 0 and 1. This action is now called after our scientist "Al-Khwarizmi"—"Al-Gorithm". This algorithm "01" invented by Al-Khwarizmi is considered the basis of this chip, which uses these chips of mobile phones, computers, and television, and precious equipment [1]. The operating system of these digital technologies is only understood to be "01" and its combinations. Al-Khwarizmi also wrote the book "Al-Jabr", which is now called "Algebra" in mathematics. Our encyclopedist Abu RayhonBeruni, a great scientist of the eleventh century and principle of the Academy of Sciences "Ma'mun 2", lived and worked in India. He wrote his scientific work "India" when he was on Indian soil.

F. M. Matmurodov (✉)
Italian Turin Polytechnic University, Tashkent, Uzbekistan
e-mail: matmurodov@yahoo.com

B. S. Sikarwar
Department of Mechanical Engineering, Amity University, Noida, Uttar Pradesh, India

M. Bhandwal
Department of Mechanical Engineering, Amity University, Tashkent, Uzbekistan

Drawing on this common scientific history between the India and Kazakhstan, we have been continuing our scientific collaboration and discussions at this International Conference. Non-contact mechanisms in technology play a very important role. This mechanism neglects contact friction, improves power transmission in power drives, etc. If we mechanics create effective contactless mechanisms, there will be a big turn in the world economy [1, 2].

The theory and technique of levitation of contactless suspension of solids in electric and magnetic fields using different types of non-contact hangers, existing and under development at present, are discussed. The condition in which a solid body "floats" in the power field of the suspension without any mechanical contact with surrounding bodies is called levitation [1, 6].

The word "levitate" comes from the English word "levitate"—soaring, rising in the air. That is, levitation is the overcoming of the object of gravity when it soars and does not touch the support, not repelling from the air, not using jet propulsion. From a physics point of view, levitation is the stable position of the object in the gravitational field, when the force of gravity is compensated and there is a return force that provides the object with stability in space.

Magnetic suspension devices are extremely expensive at this time. One of the ways to increase their efficiency is the use of superconductors, which, when cooled to temperatures close to absolute zero, completely lose electrical resistance [3]. Despite the wonderful possibilities of superconductors, it is very difficult to apply them. Keeping large magnets in tanks with extremely cold liquids is very expensive. To keep liquids cold, huge cold factories will be required that will raise the cost of superconducting magnets to sky-high heights and make their use disadvantageous. Powerful magnetic fields that can keep cars and trains on weight will become so cheap that even "planning cars" may prove to be economically viable.

2 Methodology

In the work, methods of analysis of the levitation process are used and its various methods are studied. The method of comparative analysis shows the technological indicators of various methods of technical levitation. Mathematical modeling has investigated particular cases of the gap of electromagnetic levitation of a multi-component non-contact mechanism. Discussion of various ways of technical levitation is shown in Fig. 1 [5].

Magnetic levitation can be realized in three ways: by using a permanent magnet, an electromagnet, and a superconductor magnet. The easiest way is to use an intermediary (magnetic intermediary). Aerodynamic levitation, as opposed to optical levitation, is "firmly on its feet" in the field of macro—and microtechnology. In one of the varieties of this method, the word "air cushion" is again present. It is very easy to get an air cushion. It is sufficient to drill many holes in the carrier substrate and blow compressed air through them (Fig. 1d). The lifting force of the air balances
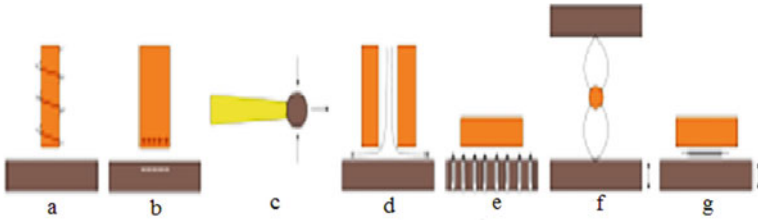
Fig. 1 Technical levitation principles [5]: **a** magnetic **b** electric **c** optical **d** Bernoulli principle **e** air cushion **f** standing wave **g** near field

the weight of the product and it starts to "soar" in the air. The disadvantage of this method is that it has no centering effect.

In a standing wave (Fig. 1e), small objects may "hang" at the pressure points between the transmitter and the reflector. In the near field, the reflector is replaced by the levitating object (Fig. 1e). Forces arising in an acoustic standing wave are able to keep objects weighing several grams suspended in the gas atmosphere and in other earth conditions.

Isobe et al. [2] proposed a new non-contact transport system that combines two levitation principles: aerodynamic and acoustic. As mentioned earlier, the aerodynamic air cushion has a fundamental disadvantage: instability in the horizontal direction due to the lack of a centering effect. In a combined transport system, this disadvantage has become a virtue. The silicon wafer "soars" in the air due to the aerodynamic forces and is transported by an acoustic viscous flow induced by a standing wave when deformed by the discastator (Fig. 2).

Comparative characteristics of different methods of technical levitation are given in Table 1. Magnetic and electrostatic methods of levitation are likely to yield somewhat in the near future, as they are difficult to apply to all kinds of materials. In addition, they usually require automatic control and regulation systems.
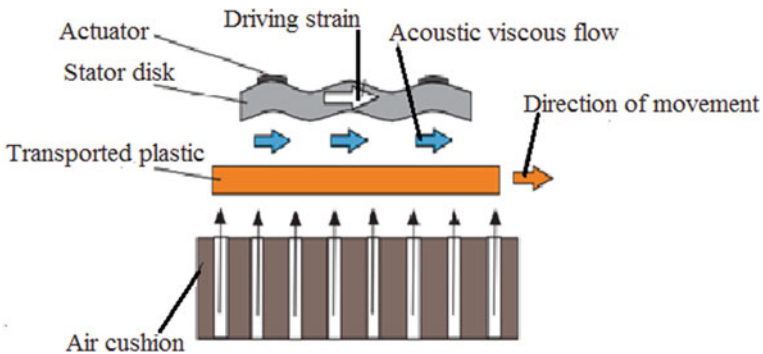
Fig. 2 Principle of combined non-contact transport

Table 1 Comparison of different methods of technical levitation

Levitation method	Shape and size of the object	Micro movement ability	Maximum lifting capacity	Stability
Electro-magnetic	No restrictions.	Moving non-conductive parts when metal devices are connected to them (mechanical contact)	Not limited	Unstable without automatic regulation and control system
Electrodynamic	Not applicable to microelectronic components	Low transport capacity; difficult access to parts	Not limited	Stable
Electrostatic	–	–	Not limited	Unstable with automatic control system and controls. The destabilizing effects are induced by triboelectricities
Optical	Small spherical-shaped particles with a diameter up to 50 mkm	Very large restrictions on particles and their environment.	0.1–1 nN	oscillations fade better in liquids; instability due to thermal effects in the surrounding space
Bernoulli's principle	Objects containing minimum one flat surface	Weak lateral stability	–	Transverse stability disorder—wiggle (plate does not remain parallel to the nozzle surface)
Air cushion	Flat objects	No transverse stability	0,1–10 H	Horizontal instability due to lack of centering effect
Standing Wave	Different shape; size smaller than one eighth of the wavelength	Gripping, orientation positioning and release of parts with radial centering force	10 mN	Axial stability; natural centering effect, like Bernoulli in principle; orientation is controlled by field asymmetry; the acoustic flow is a cause of destabilizing force

Table 1 (continued)

Levitation method	Shape and size of the object	Micro movement ability	Maximum lifting capacity	Stability
Near Field	Flat objects; preferably thin plates	Grabbing and transporting parts in a tidal wave	Not limited.	The centering effect is achieved by adjusting the type of oscillation

Optical levitation is limited to very small and relatively transparent particles in a transparent environment. It is clear that the restrictions on the nature of the particles and the environment so far have made it unacceptable to use in relation to modern micro assemblies. This method generates forces of 1nN, which are too small to manipulate components larger than 100 mkm. Although, everything flows, everything changes. Nanotechnology is developing at an unpredictably high rate. In relation to MEMS, these conclusions are already becoming false.

The choice remains between aerodynamic and ultrasonic acoustic levitation. This conclusion is reached by the authors of the article [1]. But aerodynamic levitation, unfortunately, "gives" us bad transverse stability and requires complex execution, because it needs an external source of compressed air. Ultrasonic acoustic levitation is not yet as widely used as the method based on Bernoulli's equation. Standing wave levitation is more preferable for gripping, orientation, positioning, and releasing small pieces of different shapes. Near-field levitation is more suitable for traffic control and transport of flat workpieces.

Urazaev emphasizes in his work [5] "As a result, another conclusion suggests itself—there is no perfection in the world. Although you can still get a little closer to perfection. On the part of industrial scientists, the mainstream in the field of technical levitation is most likely hidden behind the word "combinatorics". As a result of the successful combination of two or more alternative systems, as a rule, new technical solutions appear that combine the advantages and eliminate the disadvantages of their components"

Mathematical modeling of the action of a multi-component non-contact electromechanical mechanism: Neyman and Neyman [3] argued that "A promising area of research in the field of electromagnetic levitation is the improvement of machines and mechanisms with increased energy based on an electromagnetic drive of vibrational motion operating in near-resonance and resonant modes with a frequency of up to 100 Hz. "Increasing the efficiency of such electric drives is possible only if a rational choice of the interconnected parameters of the electric, magnetic and mechanical subsystems is necessary, for the analysis of whose work, even at the design stage, there is a need for dynamic calculation." Carry out a dynamic calculation allows you to find the necessary parameters of electromagnetic levitation.

Given that the dependence of the stabilizing force on transverse misalignment within zero to half the pole width of a linear line, the target function and limit can be represented as follows

$$S = \frac{P_y}{m} + m_\varphi^{-1}, \tag{1}$$

$$\frac{\partial P_z}{\partial z} \geq \frac{0,4 P_{y0}}{a}, \tag{2}$$

where S is the target function, P_y—lifting force, P_{y0}—rated lifting force, m—suspension electromagnet mass, m_φ^{-1}—ferromagnetic rail running mass, P_z—stabilizing force, a—suspension electromagnet pole width.

The mathematical model of the first-level suspension electromagnet is obtained based on the following assumptions: the thickness of the magnetic core is constant, the magnetic resistance of the magnetic core sections is negligible, and the scattering and bubbling fluxes are insignificant. Within the framework of these assumptions, the expression of the suspension electromagnet mass in the form of induction function in the working gap is obtained

$$m = \frac{4l\delta\rho_{ob}}{\mu_0 J_g} B + 25\rho_{ob} \left(\frac{2\delta^3 \alpha}{\mu_0^3 J_g^3 k_3} \right)^{1/2} B^{1/2}$$

$$+ \frac{\rho_m \mu_0^2 P_{y0}^2 x_\varphi^{1/2}}{B_g l} B^{-3} + \frac{(2\alpha + 1) P_{y0} \rho_m}{B_g} \left(\frac{2\delta k_\varphi \mu_0}{J_g k_3 \alpha} \right)^{1/2} B^{-1/2}, \tag{3}$$

As a special case, we consider the gap of electromagnetic levitation of a many composite non-contact mechanism. The design scheme for the formation of the levitation clearance of the action of a many composite electromechanical mechanism (Fig. 3). We mathematically simulate the actions of a lot of composite non-contact electromechanical mechanism [4].

$$\begin{cases} u(t) = ir + \frac{d\psi(i,x)}{dt} \\ m_1 \frac{dx_1^2}{dt^2} + b_1\left(\frac{dx_2}{dt} - \frac{dx_1}{dt}\right) - \ldots - b_{n-1}\left(\frac{dx_n}{dt} - \frac{dx_{n-1}}{dt}\right) \\ + k_1(x_1 - x_0) - \ldots - k_n(x_{n-1} - x_n) = -f_{tr1}\text{sign}\frac{dx_1}{dt} + f_{emj}(i,x) \\ m_2 \frac{dx_2^2}{dt^2} + b_2\left(\frac{dx_3}{dt} - \frac{dx_2}{dt}\right) - \ldots - b_n\left(\frac{dx_n}{dt} - \frac{dx_{n-1}}{dt}\right) \\ + k_1(x_1 - x_0) - \ldots - k_n(x_{n-1} - x_n) = -f_{tr2}\text{sign}\frac{dx_2}{dt} \\ - \\ m_n \frac{dx_n^2}{dt^2} + b_n\left(\frac{dx_n}{dt} - \frac{dx_{n-1}}{dt}\right) - \ldots - b_n\left(\frac{dx_n}{dt} - \frac{dx_{n-1}}{dt}\right) \\ + k_1(x_1 - x_0) - \ldots - k_n(x_{n-1} - x_n) = -f_{trn}\text{sign}\frac{dx_n}{dt} \\ M \frac{dx_0^2}{dt^2} + b_0\left(\frac{dx_1}{dt} - \frac{dx_0}{dt}\right) - b_0\frac{dx_0}{dt} - k_1(x_1 - x_0) + k_0 x_0 = 0 \end{cases} \tag{4}$$

Using the equation systems of our action three-component electromechanical mechanism
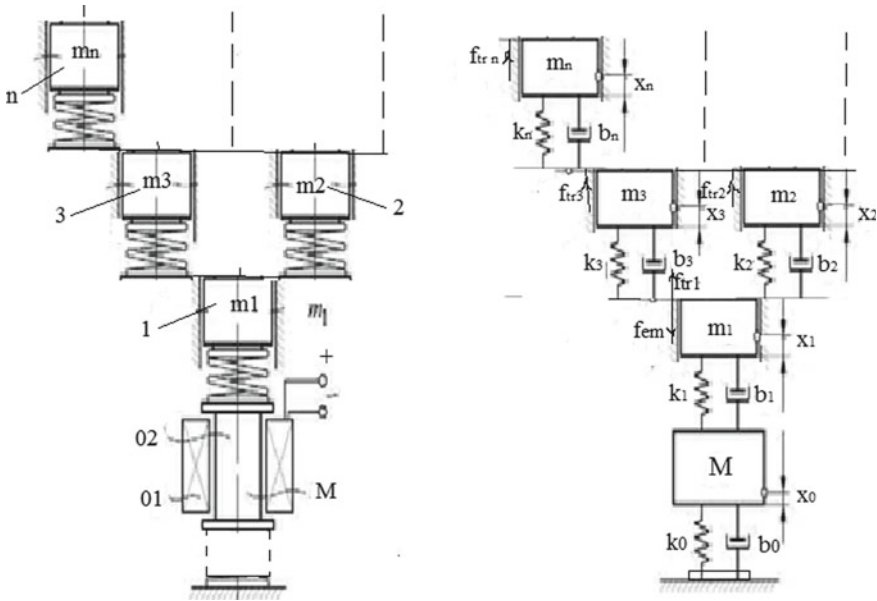
Fig. 3 Calculation scheme of action of many composite electromechanical mechanism

$$
\begin{cases}
u(t) = ir + \frac{\mathrm{d}\psi(i,x)}{\mathrm{d}t} \\
m_1 \frac{\mathrm{d}x_1^2}{\mathrm{d}t^2} + b_1\left(\frac{\mathrm{d}x_1}{\mathrm{d}t} - \frac{\mathrm{d}x_0}{\mathrm{d}t}\right) - b_2\left(\frac{\mathrm{d}x_2}{\mathrm{d}t} - \frac{\mathrm{d}x_1}{\mathrm{d}t}\right) + \\
k_1(x_1 - x_0) - k_2(x_2 - x_1) = -f_{tr1}\mathrm{sign}\frac{\mathrm{d}x_1}{\mathrm{d}t} + f_{em1}(i,x) \\
m_2 \frac{\mathrm{d}x_2^2}{\mathrm{d}t^2} + b_2\left(\frac{\mathrm{d}x_3}{\mathrm{d}t} - \frac{\mathrm{d}x_2}{\mathrm{d}t}\right) + k_2(x_2 - x_1) = -f_{tr2}\mathrm{sign}\frac{\mathrm{d}x_2}{\mathrm{d}t} \\
M \frac{\mathrm{d}x_0^2}{\mathrm{d}t^2} + b_0\left(\frac{\mathrm{d}x_1}{\mathrm{d}t} - \frac{\mathrm{d}x_0}{\mathrm{d}t}\right) - b_0\frac{\mathrm{d}x_0}{\mathrm{d}t} - k_1(x_1 - x_0) + k_0 x_0 = 0
\end{cases}
\tag{5}
$$

$u(t)$—voltage on the coil winding, r-active resistance of the coil, $\mathrm{d}\psi(i,x)$—values of threading clutch, $f_{\mathrm{emj}}(i,x)$—force forcing electromagnetic force, $f_{tr1\ldots T}$—force of dry friction $1\ldots n$ nodes, $x_1 \ldots x_n$—generalized coordinates of linear motion of the center of masses $1\ldots n$ nodes, $m_1 \ldots m_n$—connected masses $1\ldots n$ nodes, M -, $k_0 \ldots k_n$—coefficients of elastic bonds stiffness $0\ldots n$ nodes, $b_0 \ldots b_n$—coefficients of viscous friction of elastic bonds $0\ldots n$ nodes. Solve the last three compiled equations

$$
\begin{cases}
u(t) = ir + \frac{\mathrm{d}\psi(i,x)}{\mathrm{d}t} \\
m_1 \frac{\mathrm{d}^2 x_1}{\mathrm{d}t^2} + b_1\left(\frac{\mathrm{d}x_1}{\mathrm{d}t} - \frac{\mathrm{d}x_3}{\mathrm{d}t}\right) - b_2\left(\frac{\mathrm{d}x_2}{\mathrm{d}t} - \frac{\mathrm{d}x_1}{\mathrm{d}t}\right) \\
+ k_1(x_1 - x_3) - k_2(x_2 - x_1) = -f_1 \, \mathrm{sign}\frac{\mathrm{d}x_1}{\mathrm{d}t} + f(=i,x) \\
m_2 \frac{\mathrm{d}^2 x_2}{\mathrm{d}t^2} + b_2\left(\frac{\mathrm{d}x_2}{\mathrm{d}t} - \frac{\mathrm{d}x_1}{\mathrm{d}t}\right) + k_2(x_2 - x_1) = -f_1 \, \mathrm{sign}\frac{\mathrm{d}x_2}{\mathrm{d}t} \\
M \frac{\mathrm{d}^2 x_3}{\mathrm{d}t^2} + b_1\left(\frac{\mathrm{d}x_1}{\mathrm{d}t} - \frac{\mathrm{d}x_3}{\mathrm{d}t}\right) + b_3\frac{\mathrm{d}x_3}{\mathrm{d}t} \\
- k_1(x_1 - x_3) + k_3 x_3 = 0
\end{cases}
\tag{6}
$$

Let's consider private cases. $x_3 = 0$ so the equations take the form

$$\begin{cases} u(t) = ir + \frac{d\psi(i,x)}{dt} \\ m_1 \frac{d^2 x_1}{dt^2} + b_1 \frac{dx_1}{dt} - b_2\left(\frac{dx_2}{dt} - \frac{dx_1}{dt}\right) \\ \quad + k_1 x_1 - k_2(x_2 - x_1) = -f_1 \operatorname{sign} \frac{dx_1}{dt} + f(i,x) \\ m_2 \frac{d^2 x_2}{dt^2} + b_2\left(\frac{dx_2}{dt} - \frac{dx_1}{dt}\right) + k_2(x_2 - x_1) = -f_2 \operatorname{sign} \frac{dx_2}{dt} \\ -b_1 \frac{dx_1}{dt} - k_1 x_1 = 0 \end{cases} \quad (7)$$

If from the expression we find it $x_1 == C_1 e^{\frac{-k_1 \cdot t}{b_1}}$ and put it on the following system of equations and get

$$m_2 \frac{d^2 x_2}{dt^2} + b_2 \frac{dx_2}{dt} + k_2 x_2 + f_2 \operatorname{sign} \frac{dx_2}{dt} = C_1\left(k_2 - b_2 \frac{k_1}{b_1}\right)e^{\frac{-k_1 t}{b_1}} \quad (8)$$

$$b_2 \frac{dx_2}{dt} + k_2 x_2 = C_1\left(m_1 \frac{k_1^2}{b_1^2} - k_1 \frac{b_2 k_1}{b_1} + k_1 + k_2\right) \cdot e^{\frac{-k_1 t}{b_1}} - f_1 - f(i,x) \quad (9)$$

Take away both equations of each other and get

$$m_2 \frac{d^2 x_2}{dt^2} + f_2 \operatorname{sign} \frac{dx_2}{dt} = C_1\left(-2k_1 - m_1 \frac{k_1^2}{b_1^2}\right)e^{\frac{-k_1 t}{b_1}} + f_1 + f(i,x) \quad (10)$$

These expressions are the same values $\operatorname{sign}\frac{dx_2}{dt}$ we integrate.

$$x_2 = \frac{1}{m_2}\left[C_1 \frac{b_1^2}{k_1^2}\left(-2k_1 - m_1 \frac{k_1^2}{b_1^2}\right)e^{\frac{-k_1 t}{b_1}} + (f_1 + f(i,x)) \cdot \frac{t^2}{2}\right]$$

$$+ \left\{\begin{array}{l} 0, \ \operatorname{sign}\frac{dx_2}{dt} = 0 \\ 1, \ \operatorname{sign}\frac{dx_2}{dt} > 0 \\ -1, \ \operatorname{sign}\frac{dx_2}{dt} < 0 \end{array}\right\} \cdot \frac{t^2}{2} + C_2 t + C_3 \quad (11)$$

Here, the general solution will be in the following form

$$\begin{cases} x_1 == C_1 e^{\frac{-k_1 \cdot t}{b_1}} \\ x_2 = \frac{1}{m_2}\left[C_1 \frac{b_1^2}{k_1^2}\left(-2k_1 - m_1 \frac{k_1^2}{b_1^2}\right)e^{\frac{-k_1 t}{b_1}} + (f_1 + f(i,x)) \cdot \frac{t^2}{2}\right] \\ \quad + \left\{\begin{array}{l} 0, \ \operatorname{sign}\frac{dx_2}{dt} = 0 \\ 1, \ \operatorname{sign}\frac{dx_2}{dt} > 0 \\ -1, \ \operatorname{sign}\frac{dx_2}{dt} < 0 \end{array}\right\} \cdot \frac{t^2}{2} + C_2 t + C_3 \\ x_3 = 0 \end{cases} \quad (12)$$

where C_1, C_2, C_3—constant coefficients.

We accept that the values k_0, b_0 means magnetic bonds or magnetic gaps. There are no contact frictions at the pole of the magnetic gap. Means this model describes electromagnetic non-contact mechanisms.

3 Conclusions

From the analysis of technological indicators of various methods of technical levitation, we can say that each method has its advantages and disadvantages. From the point of view of technological requirements, you can choose and use the appropriate method of levitation. The best and most promising technical levitation combined and combined technical levitation. In cases where several types of technical levitation are used, a highly effective form of levitation is created. Mathematical modeling of the action of the gap of electromagnetic levitation of a multi-component non-contact mechanism allows you to find the necessary dynamic and geometric parameters. Using a mathematical model, you can find the gaps of electromagnetic quantities, a contactless mechanism. This model will help car designers to calculate this type of mechanism.

References

1. Vandalaele V, Lambert P, Delchambre A (2005) Non—contact handling in microassembly: acoustical levitation. Precision Eng 29(4):491–505
2. Isobe H, Fushimi M, Oosuka M, Kyusojn A (2007) Non-contact transportation of flat panel substrate by combined ultrasonic acoustic viscous and aerostatic forces. Int J Precision Eng Manu-f 8(2):44–48
3. Neyman LA, Neyman VY (2015) Matematicheskaya model' elektromekhanicheskoy sistemy kolebatel'nogo dvizheniya s uprugimi svyazyami.« Vestnik IGEU » Vypusk 6
4. Matmurodov FM, Matmurodov FF (2018) Beskontaktnyye i dempfiruyushchiye mekhanizmy. Monografiya –T: « Fan va texnologiya, 184C
5. Urazayev V (2007) Tekhnicheskaya levitatsii—metody obzorov. Tekhnologii v elektronnoy promyshlennosti, vol 6
6. Sizov R (2015) Real magnetic charges in the substance, ferrogravitation and technical levitation. J Modern Phys 6:1591–1561

Advance Fatigue Analysis of an Auto Rickshaw Rear Axle Shaft

Durgeshwar Pratap Singh, Jyoti Joshi, Narendra Gariya, Rajesh P. Verma, and Chandra Kishore

Abstract In India, mostly auto rickshaws are used as the most cost-effective and easily available public transport, and because of its frequent usage, the failure of its rear axle shafts is a common problem. Studies and research on failure analysis of rear axle shafts reveal the problem during dynamic and uncertain loading. So, there is a huge scope for research on fatigue failure analysis of the rear axle shaft of the auto rickshaw to minimize the problem that leads to fatal road accidents. The function of the rear axle shaft of an automobile is to transmit power to the wheels. The rear axle shaft is subjected to cyclic loading, torsion loading, and the load due to the weight of the vehicle and passengers. The scope of the present paper is to find out the fatigue life due to cyclic loading and to find out the natural frequency of vibration of the rear axle shaft to predict the safe working condition for it. The tool used is ANSYS 14.0. AISI 4140 steel is considered as it is the most common material used in the manufacturing of rear axle shaft in auto rickshaws. Results show that the minimum and maximum life cycle of the shaft is 4544 and 106 cycles, respectively. The natural frequency of vibration varies from 92.18–515.19 Hz for the first six modes of vibration. These results will help in determining the suitable material for the manufacturing of the rear axle shaft.

Keywords Shaft · Fatigue · Rickshaw · FEM · Failure

1 Introduction

Nowadays, automobiles are the easiest, fastest, and safest way of transportation. Automobile can be classified on various categories like based on usage, wheels, drive, types of engines, fuels, etc. An auto rickshaw is a three-wheeler, rear-drive vehicle which is commonly used in local transportation, for goods as well as for public transport. It is very undesirable for the failure of any component of the automobile,

D. P. Singh · J. Joshi · N. Gariya (✉) · R. P. Verma · C. Kishore
Department of Mechanical Engineering, Graphic Era Deemed to Be University, Dehradun 248002, Uttarakhand, India
e-mail: navigk.me@gmail.com

but the axle shaft, which is subjected to moment and very high vibration, its failure is very frequent in a three-wheeler, which leads to loss of human and money too.

The author tries to analyses the component of the powertrain of the high-speed train, as they need to be highly reliable with long service life. In high-speed trains, the tripod shaft, which is installed on power boogies, is responsible for the transportation of motor power to the axles and experiences torsional load constantly. The author carries out the torsional fatigue analysis of the tripod stand, to predict its lifetime by understanding the results of the accelerated life test method [1, 2]. The author conducted a failure analysis of the bus drive shaft of a fleet of 40 buses, which consists of six different drive designs. Only one identified design is observed to be failed. The microscopic examination of the fractured surface of the drive shaft is done to determine the mode of failure. A FEM technique is used to predict the fatigue life, and results show the presence of high-cycle fatigue [3]. The author carried out the thermal and fatigue stress analysis of submerged compound steel pipes. The compound pipe is of three layers, the inner layer is of API 5L X70 steel, the middle layer is of polypropylene, and the outer layer is of concrete. Results indicate that the stresses and the deformation are in the safe zone, and thermal stresses can isolate the inner layer of the compound steel pipe from the outside temperature [4, 5].The author performs the analysis of portal axle, which is a gearbox designed especially for the off-road driving condition. They modeled the spur gear in the portal axle and performed the simulation to estimate the vehicle's actual motion. They carried out the modal analysis using the FEM technique, for a combination of three different gear train system, designed for the portal axle. The three different gear train combinations are one with two idler gears, second with one idler gear, and third with no idler gear [6]. In this study, the author carried out the experimental and theoretical modal analysis of the rotor system with crack. They varied the depth of the crack and obtain the values of stress level for various defects [7].

Within this study, the author performs the fatigue analysis of a 3 MW electric motor shaft in which crack is detected after approximately fifteen months of service. The defect was found in the motor shaft which is used to operate a reciprocation gas compressor. Detailed failure analysis is carried out which shows the presence of sulfide inclusion and causes the fatigue crack which is initiated by the quench crack. The study also reveals the presence of axial and angular crack along the surface of the shaft [8, 9]. In this study, the author investigates the crankshaft of an IC engine for a passenger car. They develop the three-dimensional CAD model of engine parts using CATIA V5, and analysis is carried out in the ANSYS. Obtained stress value helps to improve the design of crankshaft by weight reduction [10, 11].

In this study, we are performing structural analysis of the rear axle shaft of an auto rickshaw to determine the stress distribution over the shaft and the natural frequency of vibration of the shaft for AISI 4140 material. In real practice, the shaft is subjected to high moments and strong vibration. So, we are performing fatigue analysis to predict the life cycle of the shaft, and to determine the natural frequency of vibration of the shaft, vibration analysis is carried out. The shaft is fixed at one edge, and another edge is subjected to a moment while all other loads are neglected.

To perform this study, finite Element method (FEM) technique is utilized. Within the FEM technique, the CAD model of the shaft is discretized into small elements that are connected by points called nodes. Stiffness matrix is developed for each element, and finally, a relationship is developed between displacement and applied forces utilizing the global stiffness matrix developed to form the elemental stiffness matrices. The relation is shown below

$$\left\{F^g\right\} = \left[K^g\right]\left\{U^g\right\} \tag{1}$$

where $[F]$ is a vector of applied force, $[K]$ is a global stiffness matrix, and $[U]$ is a nodal displacement vector [12, 13].

Model of the rear axle shaft is developed using SolidWorks 2018, and then, the CAD file is imported into ANSYS 14 where fatigue and vibration analysis is carried out. The length of the rear axle shaft is 1000 mm with a 20 mm diameter. Splines are of rectangular cross-section with $(47 \times 5 \times 3)$ mm dimensions. The CAD model and mesh model of the rear axle shaft is shown in Fig. 1. The meshing of the model
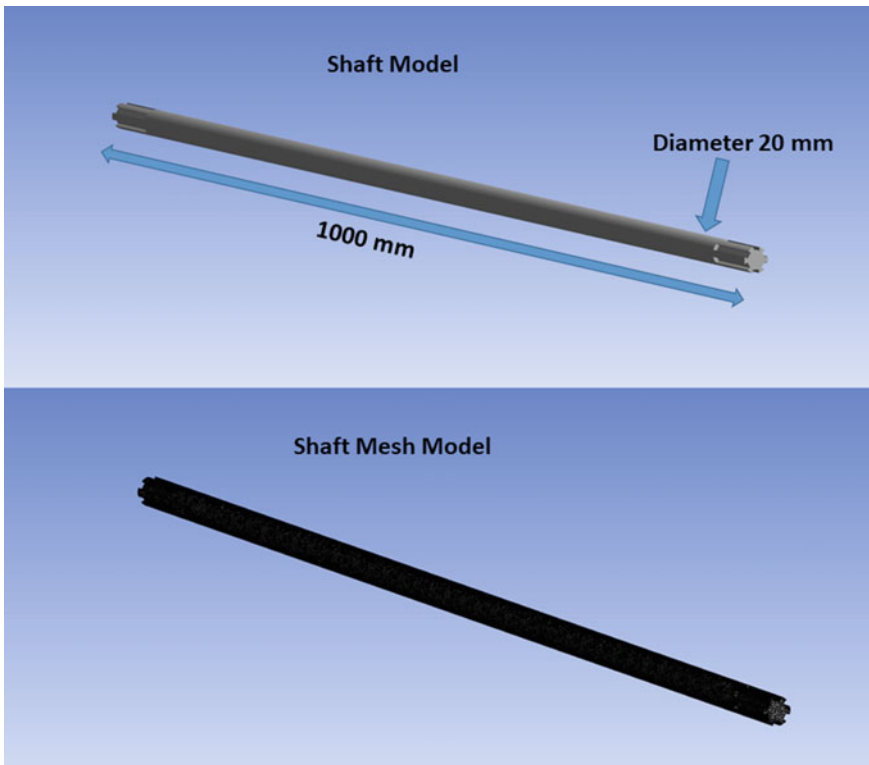
Fig. 1 CAD and mesh model of the rear axle shaft

Table 1 Mechanical properties of AISI 4140 steel

Material	Young's modulus	Poisson's ratio	Density	Shear modulus	Bulk modulus	Ultimate tensile strength
AISI 4140 steel	833 (MPa)	0.3	7850 (kg/m^3)	7.69 e + 04 (MPa)	1.66 e + 05 (MPa)	4.6 e + 02 (MPa)

is done using quadratic elements, and total no. of nodes and elements are 46,488 and 23,307, respectively

As the rear axle shaft is subjected to high vibration, vibration analysis is carried out to determine the natural frequency of vibration of the rear axle shaft, to predict the safe working environment. The relation to calculate the natural frequency of vibration is given by Manral et al. [14].

$$\omega = \sqrt{\frac{k}{m}} \tag{2}$$

where k is the stiffness, m is the mass, and w is the natural frequency of vibration of the shaft.

2 Materials Properties

AISI 4140 steel is used for the manufacturing of rear axle shaft of auto rickshaw and shaft's fatigue analysis, steel is considered. The mechanical properties of steel are provided in Table 1.

3 Boundary Condition

In this study, an analysis of the rear axle shaft of auto rickshaw is carried out. Axle shaft is subjected to high torsion as well as high bending load, and therefore, analysis of shaft is very important to understand the behavior of shaft under different loading conditions. In our study, shaft is assumed to be fixed from one side while the other end is subjected to a moment of 108.675 Nm as it is the maximum torque produced by the auto rickshaw at the highest speed as shown in Fig. 2. All other loads are neglected, as we want to analyze shaft when it is subjected to moment only, to predict the life cycle and stress and deformation experienced by the shaft.

To determine the natural frequency of vibration of the rear axle shaft, shaft is considered to be fixed from both sides.
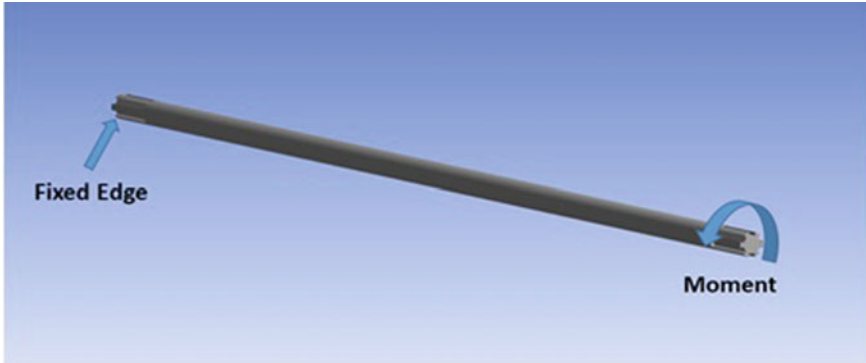
Fig. 2 Rear axle shaft subjected to moment

4 Results

Rear axle shaft (AISI 4140 steel) of an auto rickshaw shaft is assumed to be fixed at one side and subjected to a moment on the other side. Fatigue analysis is carried out to predict the life cycle of the rear axle shaft. The expected life cycle of the rear axle shaft is shown in Fig. 3.

The minimum analyzed life cycle of rear axle shaft is 4544 cycles, whereas the estimated maximum life cycles is 1×106 cycles.

The total deformation of the shaft under moment is shown in Fig. 4.

The stress distribution over the shaft subjected to moment is shown in Fig. 5.

The values of minimum and maximum stress, deformation, and life cycles is given in Table 2.
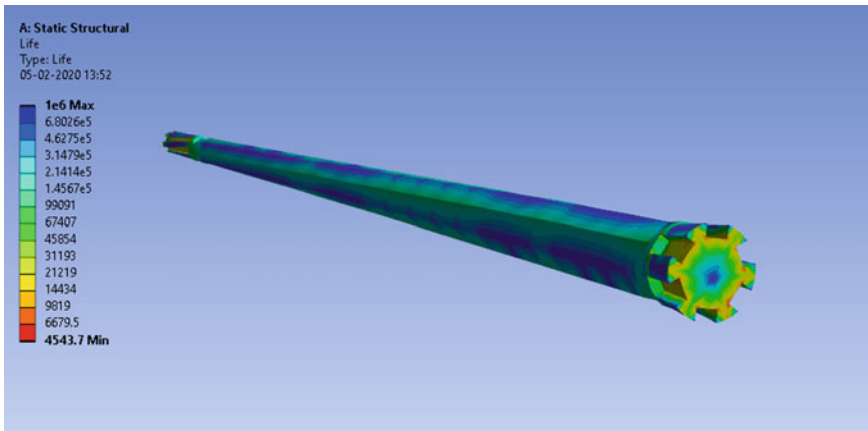
Fig. 3 Life cycle of rear axle shaft
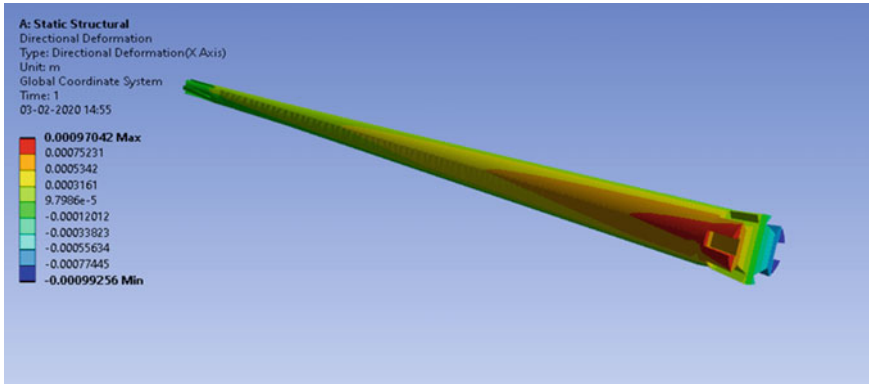
Fig. 4 Total deformation of the rear axle shaft
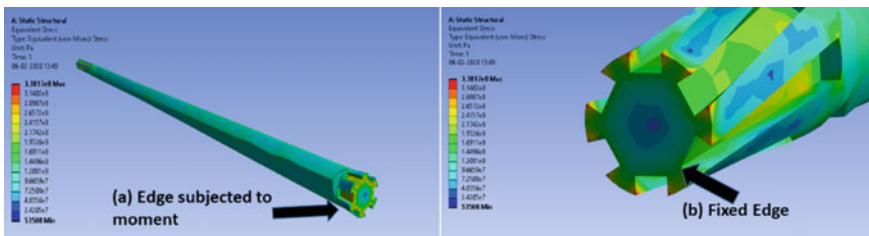
Fig. 5 a Stress distribution over edge subjected to moment **b** Stress distribution over the fixed edge

Table 2 Values of life cycle, stress, and deformation of the rear axle shaft

Parameters	Minimum	Maximum
Life cycle (Cycles)	4544	1×10^6
Deformation (mm)	−0.99	0.97
Stress (Pa)	53,508	3.38×10^8

When fatigue analysis is carried out for rear axle shaft, maximum stress is generated at the vertices of the splines at the fixed edge, due to the moment applied at another end. The moment causes the shaft to go under high stress at the edges as shown in Fig. 5a The maximum stress is generated at the vertices of the splines, which is 338 MPa. The maximum deformation is observed at the loading end which is 0.97 mm (Fig. 5b). Under the applied boundary condition, the rear axle shaft will work for at least 4544 cycles and it can withstand 1×106 cycles before its failure.

Moreover, vibrational analysis for the first six modes is carried out for the shaft under both ends fixed boundary conditions. The first six mode shapes are shown in Fig. 6.

The natural frequencies for the first six modes of vibration of rear axle shaft are given in Table 3.
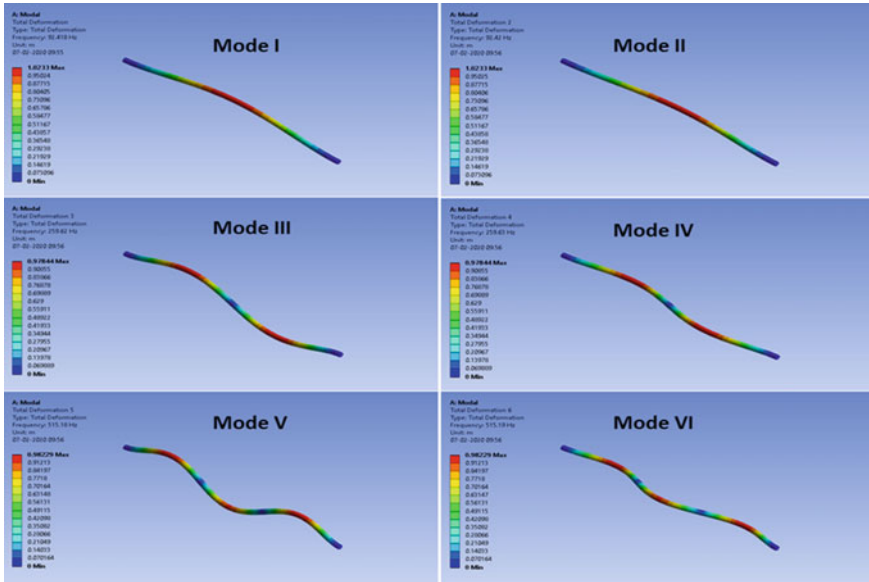
Fig. 6 Mode shapes for the first six modes of vibration

Table 3 Natural frequencies of vibration for different modes

Modes	Frequency (Hz)
I	92.418
II	92.42
III	259.62
IV	259.63
V	515.18
VI	515.19

The above analysis shows the first six modes of vibration for rear axle shaft under both ends fixed conditions. The natural frequency of vibration for shaft varies from 92.418 to 515.19 Hz. The color contour in the mode shapes shows the deformation level. Blue color indicates minimum deformation while the red color indicates maximum deformation. As we know, the rear axle shaft is fixed at two ends and revolves around its longitudinal axis. In real practice, the shaft is subjected to high vibration, because of which its vibration analysis is very important for understanding its behavior under high vibration.

5 Conclusion

The following conclusions have been made from the study. The fatigue analysis is carried out for the rear axle shaft to predict its life cycle. The rear axle shaft under a moment of 108.675 Nm and one edge fixed condition can withstand a life cycles of a maximum of 1×10^6 cycles. Analysis shows the stress and deformation distribution over the shaft, which can be considered for the selection of material for the manufacturing of the axle shaft. Modal analysis shows mode shapes and the natural frequency of vibration for the first six modes. These results can also help to optimize the best material for the shaft which can withstand the high vibration because the external excitation force of relatively higher frequency can create resonance and can damage the shaft, which will be disastrous.

References

1. Lee J-H, Cho H-Y (2018) An experimental study of the lifetime of a tripod shaft with torsional fatigue using an accelerated life test method. Int J Precis Eng Manuf 19(9):1399–1404
2. Das S, Mukhopadhyay G, Bhattacharyya S (2015) Failure analysis of axle shaft of a fork lift. Case Stud Eng Failure Anal 3:46–51
3. Duffner DH (2006) Torsion fatigue failure of bus drive shafts. J Failure Anal Prevent 6(6):75–82
4. Raafat E et al. (2019) Fatigue and thermal stress analysis of submerged steel pipes using ANSYS software. Ocean Eng 193:106574
5. Rivera JA, Aguilar E, Cárdenas D, Elizalde H, Probst O (2016) Progressive failure analysis for thin-walled composite beams under fatigue loads. Compos Struct 154:79–91
6. Ooi JB et al. (2012) Modal and stress analysis of gear train design in portal axle using finite element modeling and simulation. J Mech Sci Technol 26.2:575–589
7. Zakhezin AM, Malysheva TV (2010) Experimental and theoretical modal analysis of constructions with fatigue cracks. J Mach Manuf Reliabil 39(5):478–484
8. Stafford SW, Trueba L (2015) Fatigue cracking of a 3-MW electric motor shaft. J Failure Anal Prevent 15(2):211–218
9. Thejasree P, Dileep Kumar G, Leela Prasanna Lakshmi S (2017) Modelling and analysis of crankshaft for passenger car using ANSYS. Materials Today: Proceed 4.10:11292–11299
10. Tscharnuter D (1999) Numerical simulation of vibrations for the design of a rear axle. In: High performance scientific and engineering computing, Springer, Berlin, Heidelberg, pp 167–176
11. Avikal S, Bisht A, Sharma D, Hindwan H, Yadav S, Kumar KN, Thakur P (2020) Design and fatigue analysis of front axle beam of a heavy duty truck using ansys. Materials Today: Proceed
12. Manral ARS, Gariya N, Bansal G, Singh HP, Rawat A (2020) Computational stress analysis of chicken feather fibre (CFF) with epoxy-resin matrix composite material. Materials Today: Proceed
13. Manral AR, Gariya N, Kumar KN (2020) Material optimization for femur bone implants based on vibration analysis. Materials Today: Proceed
14. Manral ARS, Gariya N, Bansal G, Singh HP, Negi P (2020) Structural and modal analysis of chicken feather fibre (CFF) with epoxy-resin matrix composite material. Materials Today: Proceed

Modal Analysis of Humerus Bone Using FEA

Check for updates

Rushali Pant, Brijesh Yadav, Mohit Gundwal, Chandra Kishore, and Pravin P. Patil

Abstract The main objective of this paper is to deduce the effect of vibration on human hand. The longest bone in the arm is the humerus bone that connects the elbow to the shoulder. Finite element method is used to carry out the simulation on the humerus bone. The results of simulation give the natural frequencies of the bone under varying boundary conditions. The natural frequencies are used to generate the mode shape result for six modes. FEA software Solid Edge is used to create a profile of humerus bone and the simulation is carried out in ANSYS 14.5.

Keywords Humerus bone · FEA · Vibration · Natural frequency

1 Introduction

Any form of vibration that a human body is exposed to is called the human vibration. Type of vibration that affects the human body is hand-arm vibration or whole body vibration. To reduce the health risk and increase the comfort for an individual, it is important to study these vibrations. Workers subjected to continuous vibrations can develop disorders such as nerve disorder, clotting in blood circulatory system, numbness in fingers and thumbs, disordered shape of bones in hands and wrists. Whole body vibrations may cause stomach troubles or affect the spine.

Humerus bone is the longest bone in the human hand which joins the shoulder to the elbow. The shoulder and elbow of the hand act as cups connected by cylindrical shaft. Many research work has been done over the past 50 years in this field.

R. Pant (✉) · M. Gundwal
Graphic Era Hill University, Dehradun, India
e-mail: vrushalipant28@gmail.com

B. Yadav · C. Kishore · P. P. Patil
Graphic Era (Deemed to Be) University, Dehradun, India
e-mail: Yadav.brijesh9995@gmail.com

2   Literature Review

Pelker et al. performed a study on the femur bone subjected to dynamic loading [1]. Huiskes and Chao performed simulation for studying biomechanics of hand-arm system [2]. Radwin and Armstrong conducted an industrial study to avert the hazards caused by human vibrations [3]. Paddan and Griffin analyzed transmission of vibrations from seat to the human head and procure its mechanical, physiological and psychological aspects on the whole body [4].

Holmlund et al. performed an experiment to deduce the effect of vibrations on impedance of human body in sitting position [5]. The results show that the impedance increases with the frequency up to 5 Hz and then start to decrease in a complex manner. Lings and Leboeuf-Yde have given the literature review for WBV and lower back pain [6]. From the study it was established that there exists a direct relation between whole body vibration and back pain. Methods that could be used to reduce the back pain caused by external vibrations were also discussed in the review. Dong et al. have introduced a method to determine the vibration energy absorbed in the palm and fingers of hand-arm vibration system. Experiment was performed for frequencies ranging from 16 to 1000 Hz [7].

Dong et al. have performed various test to find the resonance frequency of hand-arm system [7]. It was found that resonant frequency for human hand-arm system varies from 20 to 50 Hz. Khalil et al. carried out experiment based on Fourier analysis to deduce the resonance frequency and mode shape results of femur bone [8]. Analytical approach was also used for the same purpose. Mathematical model generated used 59 elements for performing the analysis. Frequency used in the experiments was within the range of 250–7300 Hz.

3   CAD Model of Humerus Bone

CT scan data collected from the hospital was analyzed and used to construct the CAD model of humerus bone. The modeling of the bone is done using the software Solid Works (2013). To perform the vibrational analysis of the bone, the bone shaft is considered to be cylindrical and the shoulder and elbow joints are modeled as hemispherical cups, keeping the elbow cup smaller than the shoulder cup (Fig. 1). This is done to simply the designing as well as the analysis procedure as the actual geometry of the bone is complex. However, the properties of the bone are kept same to predict the actual bone results. The meshed model of humerus bone is shown in Fig. 2. Length of the shaft is 250 mm and shaft radius is 8.33 mm. The elbow and shoulder cup radius are 24.99 and 33.32 mm respectively [9].
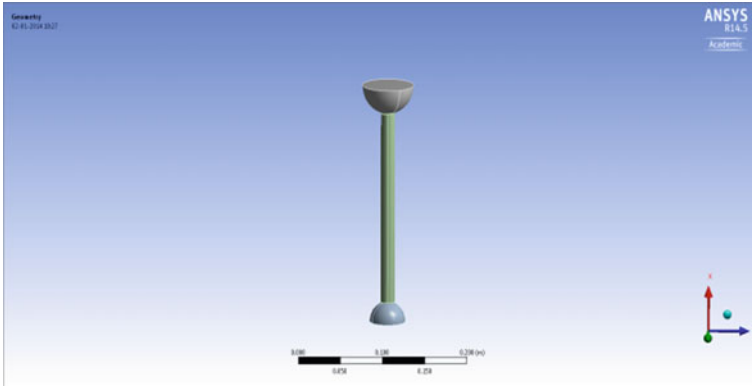
Fig. 1 Cad model of humerus bone

Fig. 2 Meshed model of humerus bone

4 Boundary Conditions and Material Property

Analysis of humerus bone is carried out under three boundary conditions. The first condition of analysis is both side free condition. The second is fixed-fixed. And the last boundary condition used for analysis is one end fixed and one end-free boundary condition. For the free-free condition, the DOF are allowed to variations, i.e., both the shoulder and elbow cups are free at the joints. For fixed-fixed boundary condition, the cups at the shoulder and elbow are constrained. Under the third boundary condition of one side fixed and one side free, the shoulder cup is kept fixed and the elbow cup is free for variations. The results of all three boundary conditions are analyzed and compared. It is found that the second boundary condition of both side fixed gives the more accurate outcomes and also explains the human hand-arm biodynamic precisely. Vibration mode shapes for first six modes are considered in our analysis.

Table 1 Mechanical properties of humerus bone [9]

Mechanical properties	Mathematical value
Young's modulus	17.2 GPa
Poisson's ratio	0.30
Density	1900 kg/m3

Three boundary conditions applied are free-free, one side fixed and both side fixed. The degree of freedom in free-free conditions is exposed to variations and in case of fixed-fixed all degree of freedom are obliged in boundaries. Zadpoor [9] Mechanical properties of humerus bone are shown in Table 1.

5   Modal Analysis

Modal analysis is a step by step approach for identifying all possible failures in a design. Modal analysis can be used to deduce the fundamental or natural frequency for six modes and respective mode shapes of any design. Natural or fundamental frequency is the frequency of a physical system at which it starts vibrating. Modal analysis simulation can be used to generate the modal shape of any vibrating system. The three boundary conditions are used to carry out the simulation in ANSYS 16.2 [10]. The natural frequency and mode shape results for first six modes are deduced.

The resonant frequencies for all three conditions are given in Table 2. The simulated results when compared with the experimental results show that the fixed-fixed condition gives more precise results for humerus bone analysis. Therefore, for further analysis, we choose this condition. The natural frequency for this condition for mode one is 565.47 Hz.

Of many reasons for fracture in the humerus bone, we consider external excitation as a main reason for fracture. Fracture may occur in the bone when the natural frequency is paired with the external excitation frequency. The range of resonant frequency of humerus bone is 565.47 and 3081.2 Hz. The analysis results

Table 2 Natural frequency of humerus bone under varying conditions

Mode	Both side fixed (N.F) (Hz)	Both side free(N.F) (Hz)	One side fixed–one side free (N.F) (Hz)
1	565.47	0	53.133
2	573.49	0	53.454
3	1573.2	$7.8953e^{-004}$	423.61
4	1587.1	$1.4904e^{-003}$	425.79
5	3063.9	15.468	527.72
6	3081.2	15.832	1200.5
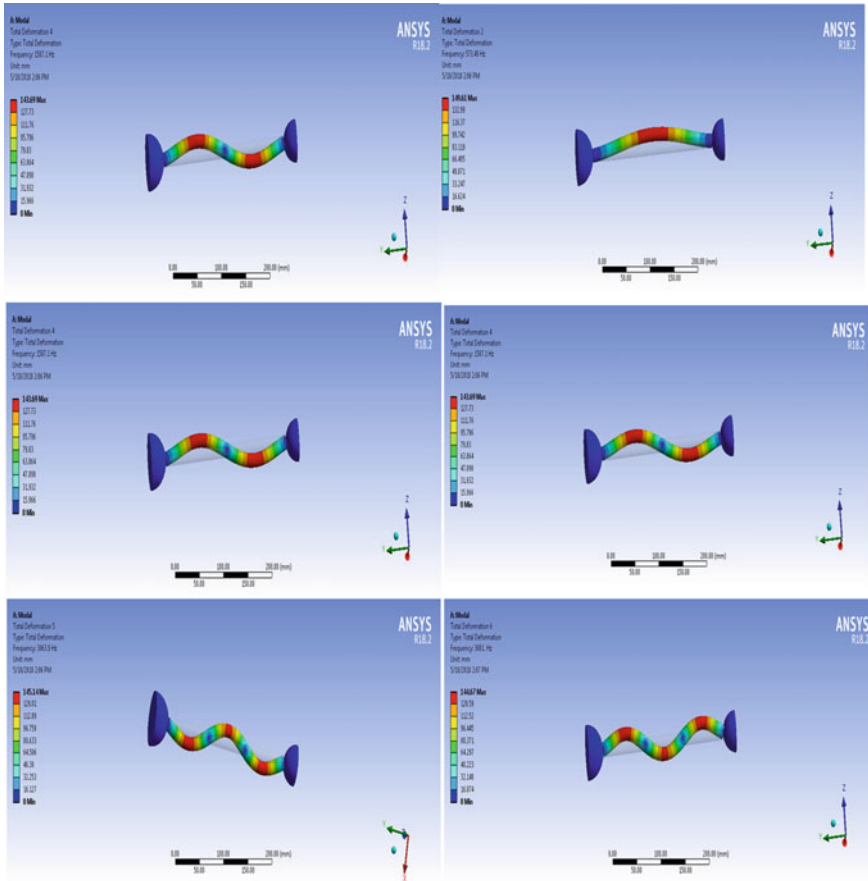
Fig. 3 Different modes shape of the humerus bone model (both side fixed boundary condition)

are compared with the experimental results deduced by Khalil et al. and validated. The experimental value for the frequency is given between 250 and 7239 Hz [8].

Mode shape result for both side fixed condition is given in Figs. 3, 4 shows the mode shape result for both side free condition and Fig. 5 shows the mode shape for one side free and one side fixed condition. Figure 6 shows the graph plot for frequency of three boundary condition.

6 Result and Discussion

The results obtained by carrying out the following analysis shows that the continuous hand-arm vibrations and sudden loading during accidents are responsible for bone
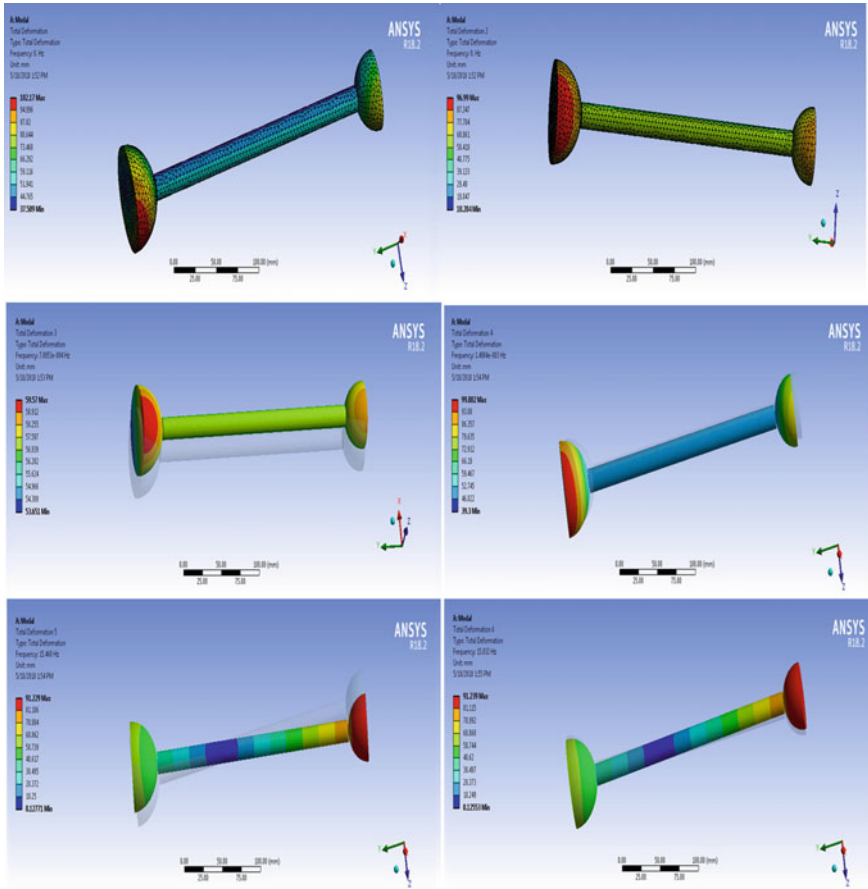
Fig. 4 Different mode shape of the humerus bone model (both side free boundary condition)

fracture. The area most prone to failure is joints and the bone shaft. The following results have been obtained during analysis of humerus bone. Solid three-dimensional model has been prepared for simulation. The first six fundamental frequencies and the respective mode shape of humerus bone were determined using three different boundary conditions. The natural frequency deduced from the modal simulation is in the range of 0–805.9 Hz for free-free condition. Under both side fixed condition, the range of frequency is 565.47–5321.2 Hz. For one side fixed and one side free, the frequency is between 53.133 and 2229.5 Hz.
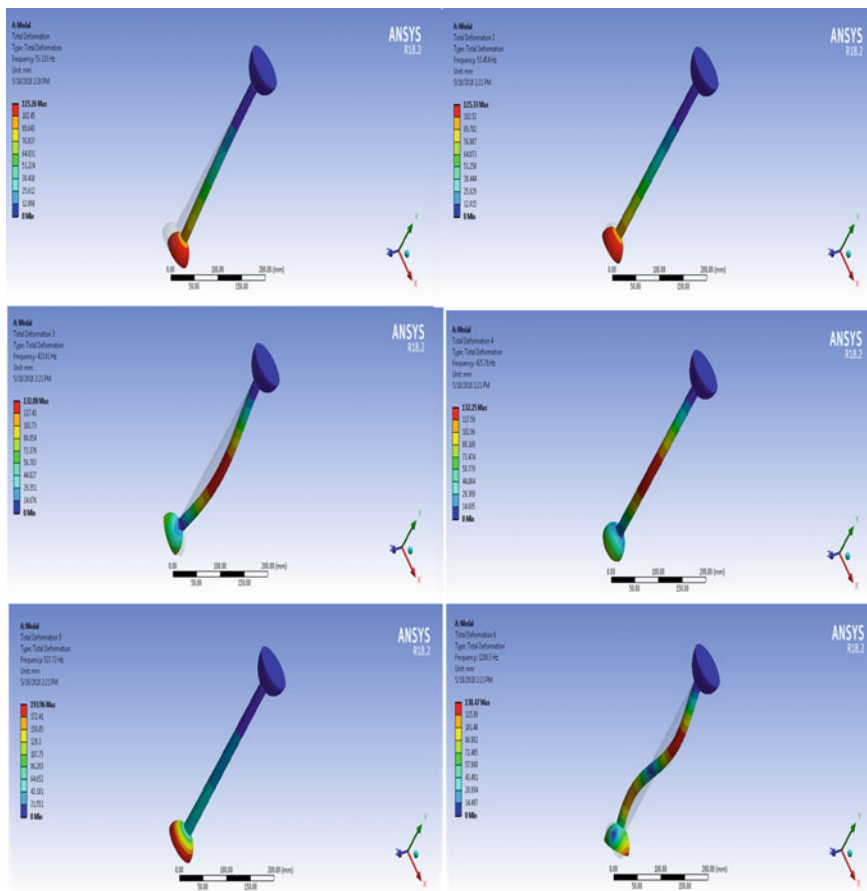
Fig. 5 Different mode shape of the humerus bone model (one side fixed–one side free boundary condition)
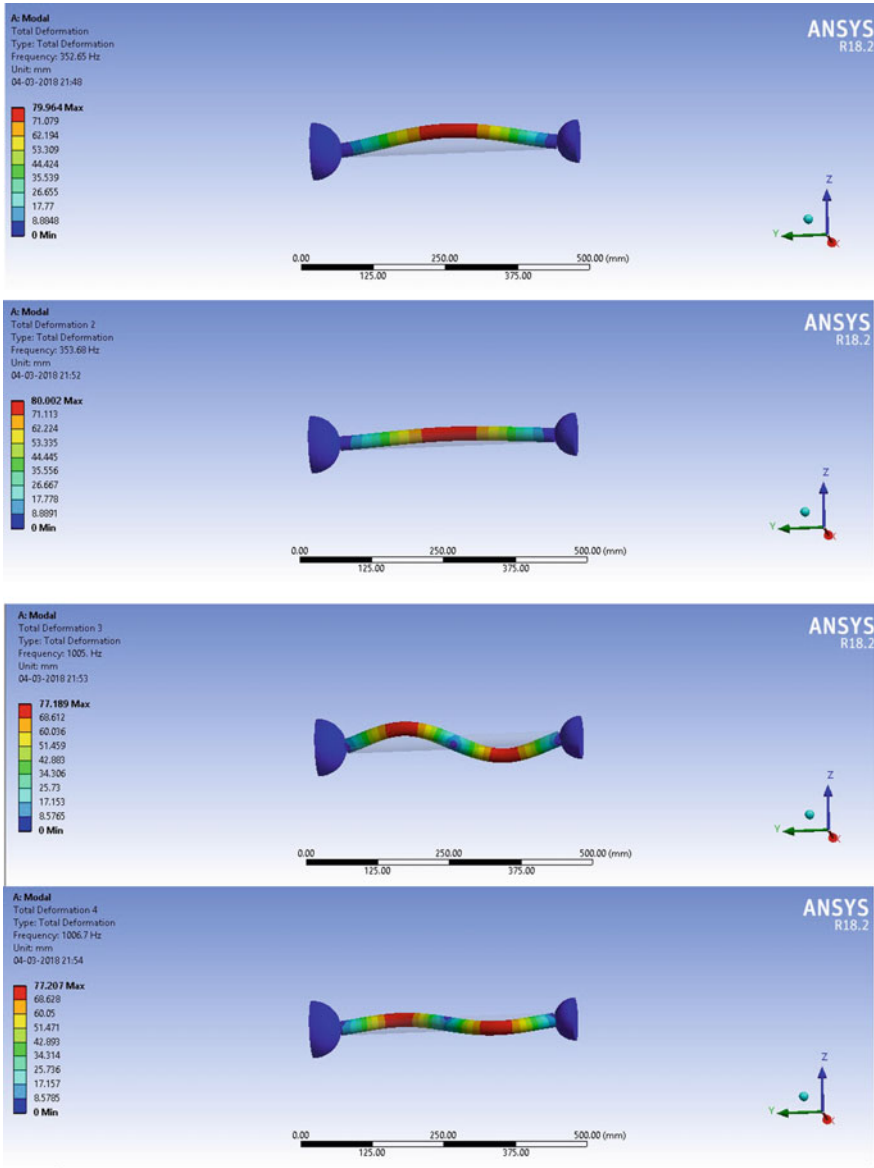
Fig. 6 Different mode shape of the humerus bone model (one side fixed–one side free boundary condition)
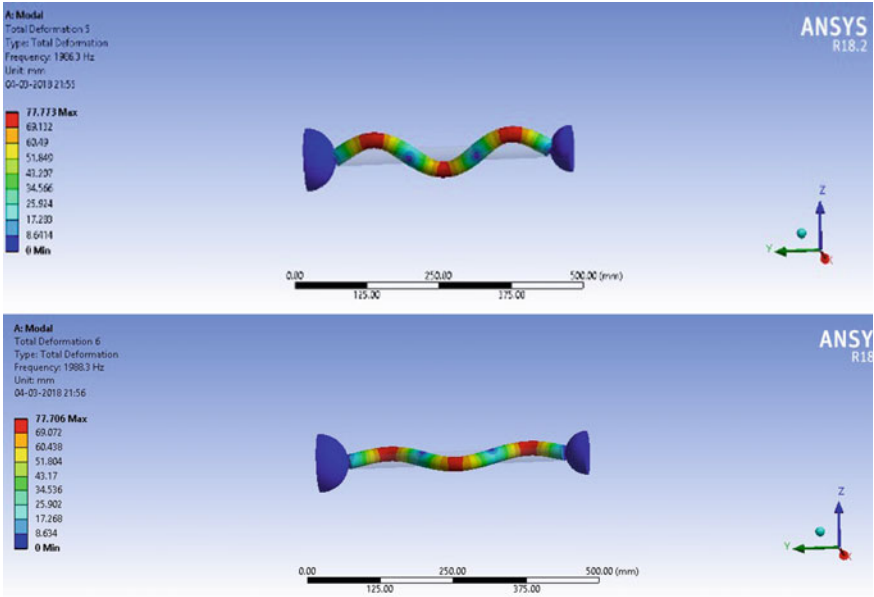
Fig. 6 (continued)

References

1. Pelker RR, Saha S (1983) Stress wave propagation in bone. J Biomech 16:481–489
2. Huiskes R, Chao EYS (1983) A survey of finite element analysis in orthopedic biomechanics: the first decade. J Biomech 16:385–409
3. Radwin RG, Armstrong TJ (1985) Assessment of hand vibration exposure on an assembly line. Am Ind Hyg Assoc J 46:211–219
4. Paddan GS, Griffin MJ (1998) A review of the transmission of translational seat vibration to the head. J Sound Vibra 215:863–882
5. Holmlund P, Lundstrok RM, Lindberg L (2000) Mechanical impedance of the human body in vertical direction. J Appl Ergonom 31:415–422
6. Lings S, Leboeuf-Yde C (2000) Whole-body vibration and low back pain: a systematic, critical review of the epidemiological literature 1992-1999. Int Arch Occup Environ Health 73:290–297
7. Dong RG, Schopper AW, McDowell TW, Welcome DE, Wu JZ, Smutz WP, Warren C, Rakheja S (2004) Vibration energy absorption (VEA) in human fingers-hand-arm system. Med Eng Phys 26:483–492
8. Khalil TB, Viano DC, Taber LA (1981) Vibrational characteristics of the embalmed human femur. J Sound Vibr 75:417–436
9. Zadpoor AA (2006) Finite element method analysis of human hand arm vibration. Int J Sci Res 16:391–395
10. ANSYS R 14.5 (2013) Academic, Structural analysis Guide

Tribological Study on Comparing the Effect of Wedge- and Flat-Shaped Pin Using SAE20W40 Lubricant

Roshan Jha, Savneet Singh, Shahjad Khan, Rohit Kumar, and R. C. Singh

Abstract Researchers are continuously involved in developing mechanisms and material to deplete friction and wear at the tribo-pair and finally reduce the energy losses applicable in industries and use in transportation. The reliability and performance of mechanical systems are affected by the relative motion that is responsible for friction and wear. Modeling and analysis were achieved using Solid works and Minitab. The experiment had been executed to investigate the influence of wedge-shaped surface on fluid film lubrication. The wear rate and coefficient of friction were obtained/garnered/procured for (i) plain pin and (ii) wedge-shaped pin by conducting the test on the pin on disc tribometer for SAE20W40 lubrication conditions. A set of experiments was performed, with pin material being mild steel on cast iron disc. The variables were load, velocity, time, and track diameter. Surface and material characterization were carried out to obtain the effect of phenomena. The results showed that the coefficient of friction and wear rate obtained was less in case of wedge-shaped pin comparatively to plain pin.

Keywords Lubrication · Wear · Fluid film · Friction · Wedge shape · Modeling · Tribometer

List of Symbols

L = linear distance travelled (m)
d = diameter of disc used in experiment (mm)
N = speed of rotating disc (rpm)
T = time taken to travel length (sec)

R. Jha (✉) · S. Singh · S. Khan · R. Kumar · R. C. Singh
Department of Mechanical Engineering, Delhi Technological University, Delhi, India
e-mail: Roshanjha2997@gmail.com

1 Introduction

Tribology effects of tribo-pairs are the relevant considerations for the industrialization of the materials and its uses. Various researches are being carried out in the field of material categorization and its properties for being used in the industries. As per Reynold's equation, the pressure is generated on the wedge-shaped surface which helps in reducing the friction force and wear on the surface [1]. This research compared the properties of the flat and wedge-shaped pin using wet lubrication. The properties of flat and wedge-shaped pin are compared using the operation length of 1 km to be constant while changing other parameters such as velocity, load, track diameter using the Taguchi method on Minitab software. The lubrication used is SAE20W40 in the experiment as it provides the viscosity range of 20 during operation. The benefit of using the lubricant is that it allows for the high viscosity, high thermal stability, and high anti-wear properties during operation [2]. Tribo-pairs are being tested on the pin on disc tribometer to know the factor such as frictional force and wear on the pin; the friction force is being calculated as the operation is carried out during the operation while the wear is determined using the weight analysis of pin before and after the experiment. Weight is measured using precision weighing machine. Pin on disc tribometers is used to graph the frictional force and wear at a data point and is being used for the analysis of the experiment [3].

Tribological process occurs due to the two bodies relative motion and the changes occurred with the passage of time are physical as well as chemical changes and hence the laws governing are both physical and chemical in nature. As the process is a function of time it produces both the geometrical and composition al changes in the bodies which resulted in energy related output such as friction, wear, and viscosity. Due to adverse effect of this outputs on the bodies it had been a major concern for the researchers in tribology. The method employed is either surface coating or the surface generation to reduce the effects. To provide the surface optimization in case of surface coating is achieved through eight wear design developed by Matthews et al. [4] and Franklin and Dijkman [5],which synchronises the selection of metallic materials, surface treatments and coatings during the initial stages of engineering design altogether. But the limitation of surface coating lied in the fact that the all surface coating requires the proper analysis of the surface of two bodies and their combined physical and chemical properties. Where this limitation had been rectified through the use of surface generation which requires the surfaces of the bodies to present in certain manner so as to provide the lubrication higher effect and helpful in creating higher load carrying capacity. The alignment of surfaces had been developed and been studied in the paper.

The primary objective of this study was to obtain the wear and friction for plane and wedge shaped pin and hence compare them to find out, which pin has low wear and coefficient of friction under wet condition.

2 Literature Review

Surface textures are proved to improve the tribological properties of the material for the plane sliders [6]. The journal [6] tried to enhance the property of the plane sliders during hydrodynamic lubrication using different textures on the surface. The experiment performed was done on four surface textures, namely circle, eclipse, triangle and chevron where the triangle surface outperforms all the three surfaces validated the wedge-shaped phenomenon.

In the journal, [7] experiments were performed to find out the best surface for texture formation during the hydrodynamic lubrication. The data obtained was for different surfaces and the efficiency of texture for different surfaces. The result obtained showed that the plane sliders for maximum load-carrying capacity should contain surface texture ~70%, whereas, for the convergent shaped surface, the surface texture depends on the convergent ration which should be between 0.066<k>4. The surface texture should limit to be ~30% for maximum load-carrying capacity. The data obtained also validated that the wedge-shaped surface provide the pressure difference and is self-sufficient for load-carrying, whereas the surface texture is essential for improving the maximum load-carrying capacity of the plane sliders. The cavitation pressure is also significant in the case of the plane sliders, whereas it is negligent in the case of the wedge-shaped surfaces.

In the journal, [8] pressure distribution was studied for hydrodynamic plain journal bearing. The maximum pressure is obtained at midline in axial direction and at the boundary, the pressure is zero.

The journal, [9] experiments were performed to compare the wear pattern for dry and wet testing. It showed that the lubricant forms a thin layer of film between two contact surfaces and hence reduces wear. Different types of lubricants can be tested.

In the journal, [10] study was done to find out the dependence of coefficient of friction on contact pressure and sliding speed. The results showed that the coefficient of friction increases with decreasing both contact pressure and sliding speed.

3 Development

3.1 Computer Aided Design

Cad model of the pin and disc was created using the SolidWorks^{TM} 2017 (Fig. 1). The cad model depicted the wedge-shaped pin of chamfer of $\tan^{-1}$ 2 degree. The dimension of the pin selected is 35*6.25*6.25 mm. The disc developed was of 165 mm diameter, and there are 4 extruded cut on both surfaces with dimension 8 mm diameter and 4.5 mm length; furthermore, the cut was being extended through the surface with a diameter of 4 mm.
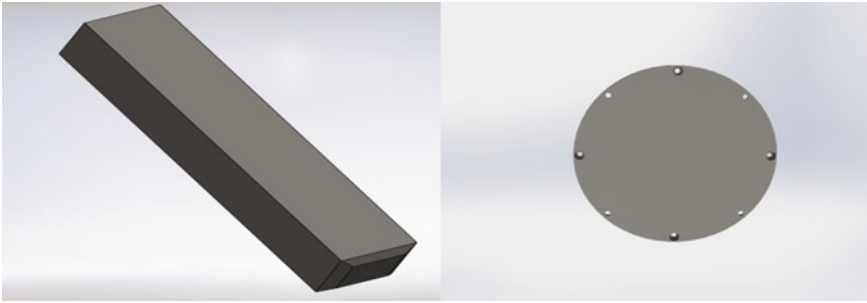
Fig. 1 Cad model of the pin and disc

3.2 Development of Pin and Disc

The development of the pin was done through a 6.25*6.25 mm beam of mild steel and the length was taken as 35 mm. Surface grinders were used to give a chamfer of $\tan^{-1}$ 2 degrees on the surface. Sectioning of pin from all four sides was done. The vertical and horizontal lengths being sectioned were 1 and 0.5 mm. For disc, cast iron was used.. The holes were made with drilling attachment in the lathe machine using 8 mm diameter for 4.5 length and 4 mm diameter for the 3.5 mm length. The surfaces of the disc were faced for about 2 mm length.

3.3 Taguchi Design

The experiment was performed considering the design of the experiment(doe) approach. For this, the Taguchi designed is preferred for the consideration of loss function and provides the stable variation among all factors. This experiment was carried out using the three-level factor design on the Taguchi function. For the purpose, Minitab[R] 19 was used and elements included are the speed, load and track diameter of the disc (Fig. 2). The table created was used to run the specimen for the calculated time for 1 km operational length

4 Experimental Analysis

4.1 Pressure Analysis

The pressure difference developed between the convergent-shaped relative moving bodies was plotted using MATLAB inputs of dimension. MATLAB has been used

	C1	C2	C3	C4	C5	C6	C7	C8
	speed(rp...	load(kg)	track dia....					
1	400	2	100					
2	400	4	120					
3	400	6	80					
4	500	2	120					
5	500	4	80					
6	500	6	100					
7	600	2	80					
8	600	4	100					
9	600	6	120					
10								
11								

Fig. 2 Taguchi method on minitab

in this project to simulate pressure conditions arising because of the hydrody-namic lubrication. 1000 iterations were carried out to generate the pressure plot in MATLAB. Wedge action has been created by the wedges on the pins and average clearance value has been given in the input of the MATLAB program corresponding to different wedges on the pins used (Fig. 3). The viscosity of different fluid used to start from air to other lubricating fluids were given as input in the program for corresponding fluids. The pressure distribution from the program is in compliance with Reynold's assumptions regarding hydrodynamic lubrication.
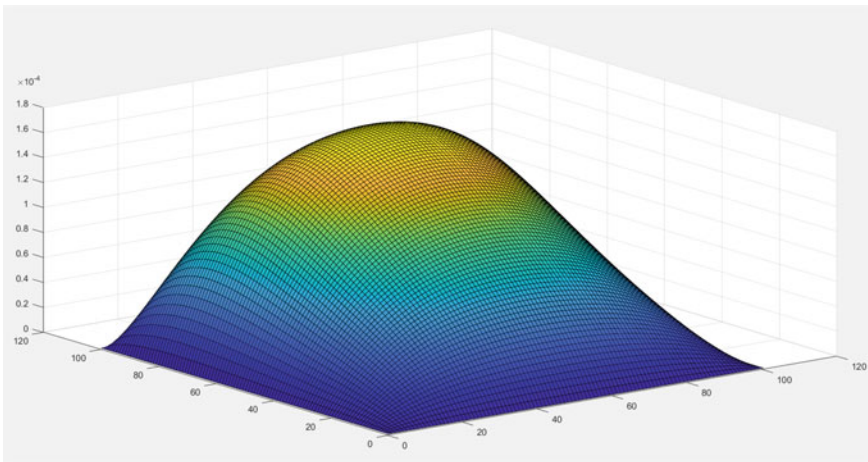
Fig. 3 MATLAB model for pressure analysis on the wedge-shaped pin

The MATLAB code for generation of pressure profile used here is

```
N=100; % number of nodes in X-dir.
M=100; % number of nodes in Z-dir.
C = 0.030; % radial clearance in mm.
Z1=6.5; % Length in axial direction(mm).
X1 =6.5; % Length in sliding direction.
delxbar = 1/N;
delzbar = 1/M;
const1 = X1*X1/(Z1*Z1);
ITER = 1000; % Number of iterations.
for I=1: N+1
for J=1:M+1
p (I, J) =0.0; % Assigning zero pressure at every i, j node.
end
end
sum (1) =0.0;
for K = 1: ITER
sumij=0.0;
for I=2:N
X(I)=1/N*(I−1);
h=2/3*(2−X(I));
hm=2/3*(2−X(I)−0.5*delxbar);
hp=2/3*(2−X(I)+0.5*delxbar);
hm1=2/3*(2−X(I)−delxbar);
hp1=2/3*(2−X(I)+delxbar);
cubh=h*h*h;
cubhm=hm*hm*hm;
cubhp=hp*hp*hp;
const2 = (cubhp+cubhm+2*const1*cubh);
A=const1*cubh/const2;
CA=cubhp/const2;
D=cubhm/const2;
E=-0.5*delxbar*(hp1-hm1) *C/(const2*X1);
for J=2:M
Z(J)=1/M*(J−1);
p(I, J)=A*p(I, J+1)+A*p (I, J−1) + CA*p (I+1, J) + D* p(I−1, J)−E;
sumij=sumij+p (I, J);
end
end
sum (K+1) =sumij;
percentage = abs(sum(K+1)-sum(K))/abs(sum(K+1));
if percentage < 0.0001
break
end
```

Table 1 Time calculation for different load (L), speed (N), and track diameter (D)

Speed(rpm)	Load(kg)	Track Dia. (mm)	Time(sec.)
400	2	100	478
400	4	120	398
400	6	80	597
500	2	120	319
500	4	80	477
500	6	100	382
600	2	80	398
600	4	100	320
600	6	120	265

end
$y = K$
surf(p); % Plot pressure in 3-D

4.2 Experimental Setup

Pin on disc tribometer used to validate the pressure analysis given by Reynold's equation. The variation in wear and frictional force was small in wedge-shaped pin as compared to the flat plate. The variation was recorded for 9 observations with the observational 1 km length. The time calculated for all the observation was being done using the Formula (Table 1).

$$L = \frac{\pi \, \mathrm{DNT}}{60,\,000}$$

The data obtained was used in the WINDUCOM software to run the experiment on the pin on disc tribometer for the desired period. The operation was performed using the above-said conditions and the graph for frictional force and wear rate analysis done on the observations. The wear analysis was done using weight analysis.

5 Results and Discussions

The data obtained were recorded for 9 observations and the graph was plotted for both the wedge-shaped pin (Fig. 4) and the flat surface pin (Fig. 5). The graph showed the variation among initial weight, final weight, and wear occurred in the process. The weight analysis for both the surfaces showed that the weight change occur in the flat surface pin is more as compared to the wedge-shaped pin.
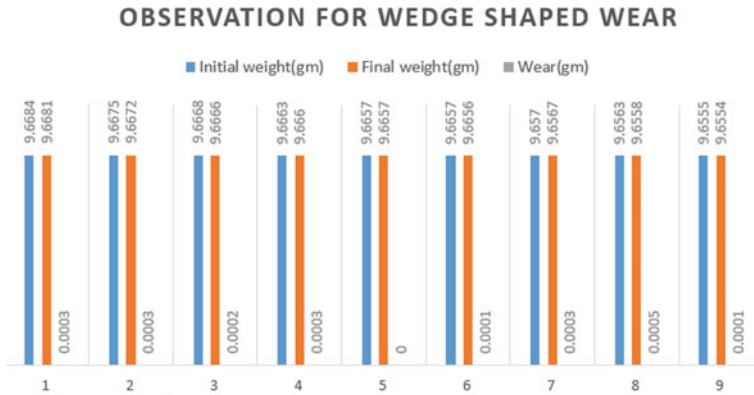
Fig. 4 Weight analysis for the wedge-shaped pin
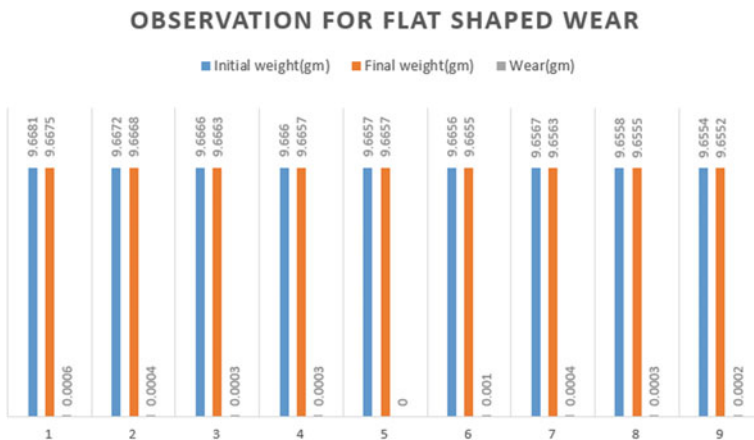
Fig. 5 Weight analysis for flat surfaced pin

The wear was calculated by taking the weight before and after each observation on the wedge-shaped surface and the flat surface. The data obtained were used in the bar graph to show the change between the two surfaces (Fig. 6).

The coefficient of friction was analyzed for all the observations and the graph was plotted to compare the differences between the wedge-shaped pin and flat-shaped pin. The observation was shown on the same graph for two observations and the comparison was made. The graph plotted showed various lines which represent the coefficient of friction for two observations of plane and wedge surfaces.

Data obtained (Fig. 7) was depicted by four lines, which represent the 2 observations. The red line denoted the wedge surface coefficient of friction for the First observation while the green line denoted the coefficient of friction for plane surface and it had shown that the coefficient of friction is more for the plane surface as

WEDGE WEAR V/S FLAT WEAR
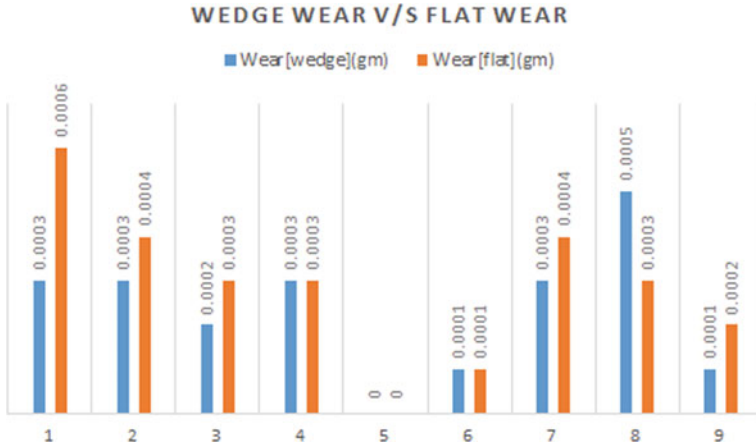
Fig. 6 Graph between the wedge-shaped pin and flat surface pin
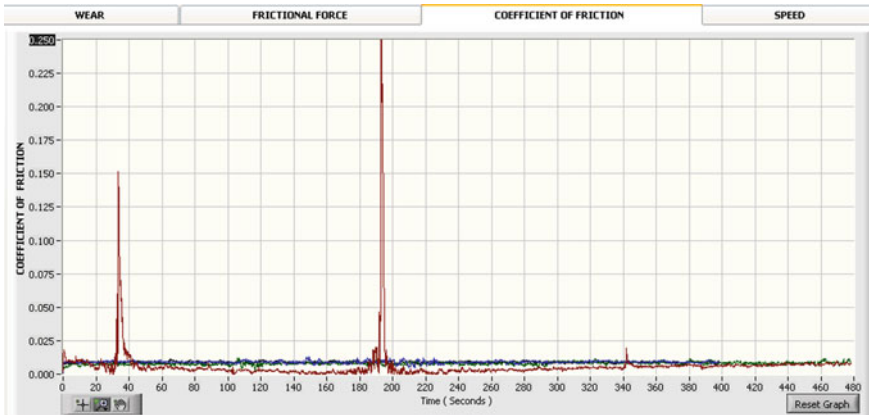
Fig. 7 Graph comparing 400 rpm, 2 kg, 100 mm, 478 s setup and 400 rpm, 4 kg, 120 mm, 398 s setup for wedge and plane surface pin

compared to wedge surface. Similarly, the data were recorded for Second observation through blue(wedge) and black(plane) line and the result is in accordance with the theory.

The data obtained (Fig. 8) denoted the Third and Fourth observation. The red line here represented the coefficient of friction for the wedge shape of Third observation, whereas the green line showed the coefficient of friction for the plane surface pin. The data obtained for Fourth observation showed the change in trend as blue (plane) and black (wedge) as plane surface coefficient of friction is lesser as compared to the wedge shape. This can be resulted due to the accumulation of wear debris that made the graph more zig-zag and a higher coefficient of friction in the data.
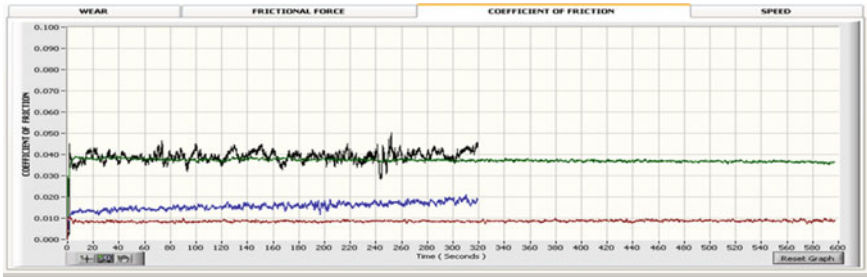
Fig. 8 Graph comparing 400 rpm, 6 kg, 80 mm, 597 sec-3rd setup and 500 rpm, 2 kg, 120 mm, 319 s setup for wedge and plane surface pin
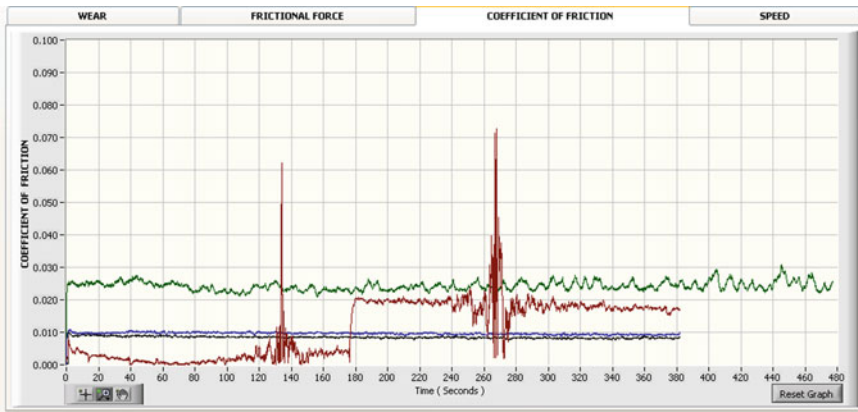
Fig. 9 Graph comparing 500 rpm, 4 kg, 80 mm, 477 s setup and 500 rpm, 6 kg, 100 mm, 382 s setup for wedge and plane surface pin

Data obtained for Fifth and Sixth observations (Fig. 9), Seventh and Eighth observations (Fig. 10), and Nineth observation (Fig. 11) clearly depicted that the coefficients of friction for wedge-shaped surface were lass as compared to plane surfaces shown above with change in trend for Fifth observation which resulted in the zero wear for the observation. In the Sixth and Eigth observation (Fig. 9 and Fig. 10), the blue line is for the wedge surface and black for the plane surface. In observation 9 (Fig. 11), the blue line depicted for the plane surface and red denoted the wedge surface. In Seventh observation, the red line meant the wedge surface and green represented the plane surface whereas for the Fifth observation, green denoted the wedge surface and red denoted the plane surface.

All the data shown above in the graph showed the trend that the coefficient of friction for wedge surface was coming less as compared to the plane surface for same observation with the change in trend for Fourth and Fifth observations which can result in the same wear or no wear as shown in bar graph. The reasons for the spike in the coefficient of friction were justified as sometimes the surface of the pin
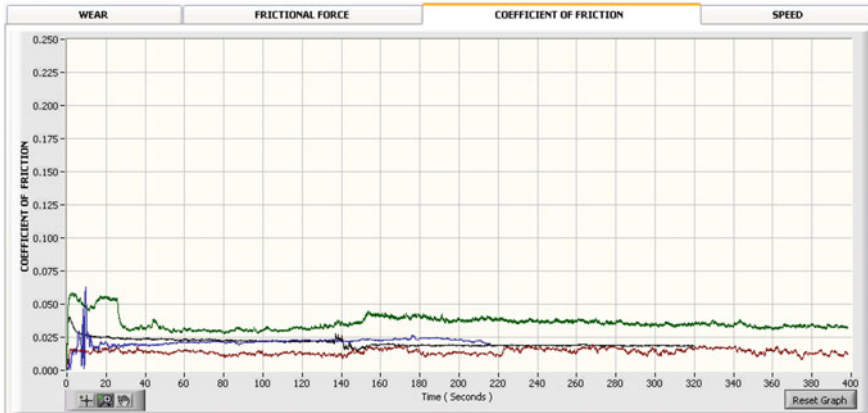
Fig. 10 Graph comparing 600 rpm, 2 kg, 80 mm, 398 s setup and 600 rpm, 4 kg, 100 mm, 320 s setup for wedge and plane surface pin
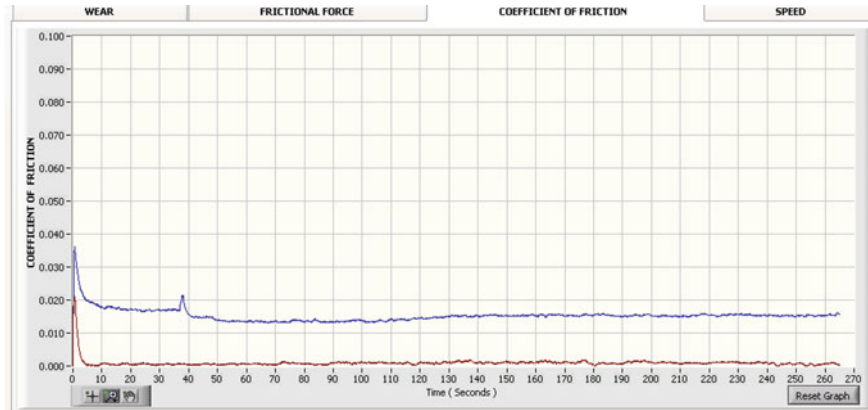
Fig. 11 Graph comparing 600 rpm, 6 s, 120 mm, 265 s setup for wedge and plane surface pin

and disc are not entirely in contact also the accumulation of debris particle during the experiments gives rise to such spikes.

6 Conclusion

In this study, the experiments were conducted to show the comparison between the wedge-shaped pin and the plane pin on the basis of wear and coefficient of friction using lubricant. It was found that the wear in case of wedge-shaped pin was less as compared to plane pin in most of observations and it was obtained from weight

measurements. While in some observations, the wear for both pins is negligible. The study of coefficient of friction was done with the help of graph, where it was seen that the coefficient of friction for wedge-shaped pin is less than plane pin for most of the time throughout the graph. While at some point of time, a high peak is obtained for the coefficient of friction for wedge pin, which can be due to the wear debris or the worn out particles The graph obtained for the observations showed that the frictional force rapidly increases after some data point and then becomes constant for the entire process. The data obtained showed that the frictional force first increases due to the accumulation phenomenon and then becomes constant for the entire process. Also, the hydrodynamic lubrication validated the point that the lubrication reduces the wear to a much greater extent than the frictional force. For further research, pins of different sizes can be taken into use. The effect of temperature and humidity can be studied to see their effect on wear and friction. Different types of coatings can be implemented on both pin and disc.

The present study was based on Reynold's equation without considering the Navier stroke equation for the fluid which incorporated the inertia factor in the system. Also the study was based on the ambient room temperature while different conclusions can be drawn through the use of temperature dependency of the fluid as temperature is related to the viscosity variation in case of hydrodynamic lubrication.

7 Summary

The study clears the fact that the wet lubrication on the wedge-shaped surface provides a reduction in the frictional force and wear of the tribo-pairs. The significance of the result obtained lies in the fact that the maintenance cost is reduced by using the convergent relative moving bodies. The objective of the experiment is achieved with the experimental data error. The difference in the result obtained can be accompanied to the fact of accumulation of oil particles from lubricant to the pin surface. The materials used in the experiment mild steel(pin) and cast iron(disc) are interchangeable in nature in the field of tribology due to similar properties and are used in various industries applications like automobile industries.

Various researches have been done in the field of the tribology to explain the friction and wear phenomenon and reduce the cost associated with it. The furthermore study such as coating, different wedge angle, and different wedge surfaces in the field of the wedge-shaped pin can be done to improve the findings of the experiment. The wedge-shaped pin can also be made using different materials so as to find out the material needed to lessen the frictional force and wear of the tribo-pairs

References

1. Stachowiak GW, Batchelor AW (2014) In: Engineering tribology, 4th edn, Butterworth-Heinemann Publication, Oxford
2. Lysyannikov AV, Shram VG (2016) The mechanism of lubricants protective layers formation in friction sliding. In: International conference on industrial engineering, Elsevier, Tehran
3. Hoic M, Hrgetic M (2016) Design of a pin-on-disc-type CNC tribometer including an automotive dry clutch application. Mechatronics 000:1–13
4. Matthews A, Holmberg K, Franklin S (1993) A methodology for coating selection. In: Dowson D et al (ed) Thin films in tribology (Proceedings of 19th leeds–lyon. symposium on tribology, Leeds, UK, 8–11 September 1992), Elsevier Tribology Series, vol 25, Elsevier, Amsterdam, 1993, pp 429–439
5. Gropper D (2016) Hydrodynamic lubrication of textured surfaces: a review of modeling techniques and key findings. Tribol Int 94:509–529
6. Uddin MS (2016) Design and optimization of a new geometric texture shape for the enhancement of hydrodynamic lubrication performance of parallel slider surfaces: Biosurface Biotribol 2:59–69
7. Mane RM, Soni S (2013) Analysis of hydrodynamic plain journal bearing. In: COMSOL conference
8. Sharma A, Singh N, Rohatgi P (2013) Study of wear pattern behavior of aluminum and mild steel discs using pin on disc tribometer. Europ J Appl Eng Sci Res
9. Wahlström J (2019) A pin-on-disc tribometer study of friction at low contact pressures and sliding speeds for a disc brake material combination. Results Eng 4:100051
10. Hirani H (2016) Fundamentals of engineering tribology with applications. Cambridge University Press, Cambridge. https://doi.org/10.1017/CBO9781107479975

Structural Analysis of a Typical Foldable Bicycle Using CAE Tools

Arjun Singh Bisht, Shwetank Avikal, Rohit Singh, K. C. Nithin Kumar, and Anoop Singh Rawat

Abstract In today's life, transportation is the most important, but the use of automobiles nowadays seems to be creating more problems. The major problems are pollution, unavailability of conventional fossil fuels. The usage of bicycles had health benefit, and it is environmentally friendly. Only we required minimum initial investment and no maintenance cost. The currently available bicycles are either costly or heavy. The objective of this work is to design and analysis of foldable bicycle. We considered two different cases in the design; first case in the frame is modeled without joints and another with joints. The load of 2000 N is applied, and it is found that the second case is best suited, and stress is minimum as compared to the first case.

Keywords FEA · Foldable cycle · CAE · Stress analysis · Al-6061

1 Introduction

Transportation is becoming one of the most important issues for the people who are traveling a shorter distance. It is time-consuming and tedious. It is because of the sudden increase in automobiles [1]. Cycling is always considered one of the most popular daily transportation tool for the shorter distance, it is flexible and low cost [2]. Currently, available bicycle materials are heavy this makes them heavy, and they are difficult to carry. These bicycles are costly and difficult for the common man to purchase. These require large space to keep it and most of them are not foldable [3]. Folding mechanisms vary from different configuration to configuration. This configuration is mainly based on speed, folding speed, weight, compactness, and

A. S. Bisht · S. Avikal (✉) · R. Singh
Department of Mechanical Engineering, Graphic Era Hill University, Dehradun, India
e-mail: shwetank.avikal@gmail.com

K. C. Nithin Kumar
Department of Mechanical Engineering, Graphic Era Deemed to Be University, Dehradun, India

A. S. Rawat
L M Thaper School of Menagement, Thaper University, Patiala, India

cost. There are different notable complex foldable motion analyses, and components involved in the motion are demand more complex design requirements. The choice of model, apart from cost considerations, is a matter of resolving the various practical requirements: a quick, easy fold, a compact folded size, or a faster but less compact model [5].

The design criteria generally consider with respect to frame design are low cost, less weight, functionality, safety, durability, and so on. A number of researches have been done to solve these problems [6].

In this present study, a specific set design criterion is formulated for the foldable bicycle and exiting bicycle configurations are evaluated to understand their limitations. A folding bicycle is a bicycle designed to fold into a compact form, facilitating transport, and storage [12]. When folded, the bikes can be more easily carried into buildings, on public transportation (facilitating mixed-mode commuting and bicycle commuting), and more easily stored in compact living quarters or aboard a car, boat, or plane [4].

2 Materials and Method

The materials and methods are more important in any design and analysis. In any design, we need to consider all the necessary required design parameters, and once the preliminary design is made, a feasibility study is required to perform to validate the design. Our main motive is to reduce the cost and enhance the strength of the material, and for that, we are doing several analysis on materials where we get the best and affordable material to make the foldable bicycle with respect to strength [7].

Later, we designed the 3D frame on the software (Solid Edge), and to make bicycle fold, we made a hinge joint again in the software solid edge. Then, we had cut the bicycle from the middle to join the hinge joint to make bicycle foldable. After that, we did the analysis on the software or better to say testing on the software (computer-aided design) ANSYS. And we did a lot of testing and analysis on the joint and frame of the bicycle with the help of computer-aided design.

2.1 Materials Selection

Material selection is the most important step in any designing process. If the material is selected wrongly than the design is not valid. There are mainly two aluminum alloy 6061, 7071, and 7005 used in the cycling industry because of their availability and properties. Two other alloys, 6066 and 6069 are also used, but on a smaller scale. In our study, we selected the aluminum 6061 alloy. This is used in making the bicycle frame. It is lightweight and high strength [8, 9]. This alloy is cast by missing different metals especially magnesium as its primary metal. 6.61 is cheaper than any aluminum alloys. The strength of the bicycle is not so important. Based on the thickness, we

Table 1 Material properties of Al 6061

E (GPa)	γ	ρ (g/cm3)
68.9	0.33	2.7

can able to obtain the required strength by varying the thickness of the frame [10, 11]. The material properties are given in Table 1.

Young's modulus (E): Young's modulus states the relationship between stress and strain in a material. It measures the stiffness of the material.

Poisson's ratio (γ): *Poisson's ratio* measures the deformation in the material in a direction perpendicular to the direction of the applied force.

Density (ρ): *Density* is the weight of a substance for a specific volume.

2.2 Modelling

A three-dimensional model of frame is prepared using Solid Edge modeling. Frame design using solid edge is shown in Fig. 1, hinge joint is shown in Fig. 2, and frame

Fig. 1 Frame designed using solid edge

Fig. 2 Hinge joint
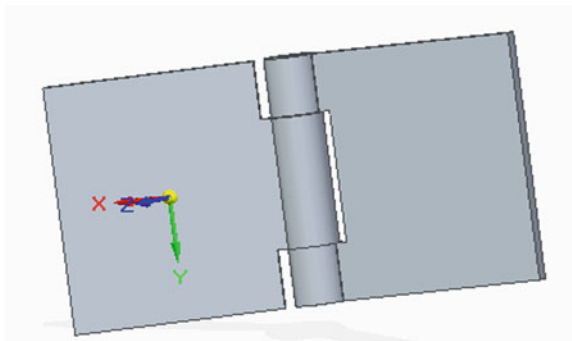
Fig. 3 Frame with hinge joint

with hinge joint is shown in Fig. 3. The clamp is designed such a way that the hinge can be locked with less effort.

3 Result and Discussion

ANSYS FEA code enables the designers to analyze the mechanical components accurately. In this work, a frame of foldable bicycle has been designed in Solid Edge, and an analysis has been done at ANSYS structural analysis software. After designing of frame analysis of bicycle frames, it has been done with joints and without joints at 2000 N force.

Analysis of aluminum alloy frame (without joints) at 2000 N force and the result obtained are shown in Figs. 4 and 5; (Table 2).

Analysis of aluminum alloy frame (with joints) at 2000 N force and the result obtained are shown in Figs. 6 and 7; (Table 3).

The factor of safety is taken as 800 N, and the forces that were acting on the bicycle frame is at the seat post and at the handle mount rod.

The results show that the fatigue life of the aluminum alloy 6061 is decreasing very less after adding the joint, and the stress value at the joints is also low.
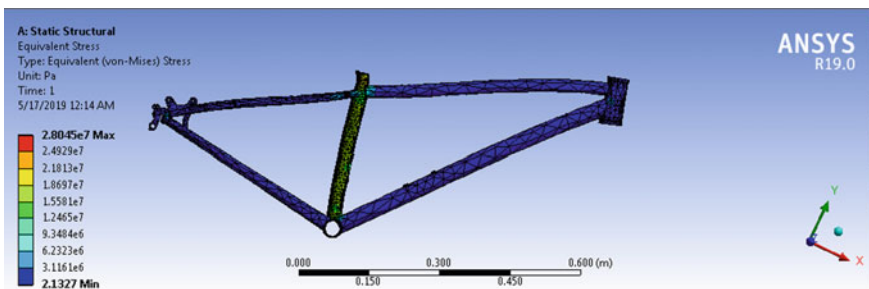
Fig. 4 Stress value at 2000 N force without joint
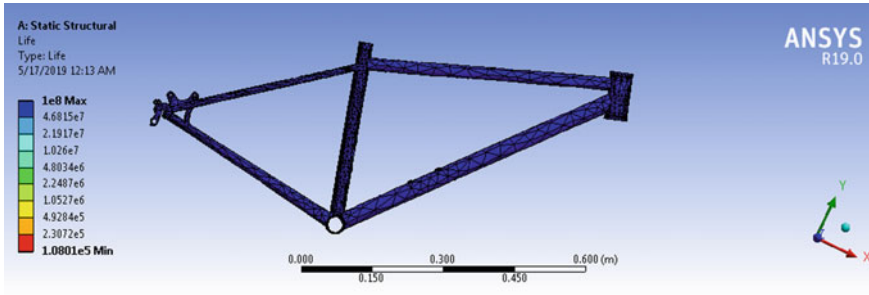
Fig. 5 Life of frame at 2000 N without joints

Table 2 Results at 2000 N force without joints

Solutions	Min	Max
Fatigue life (cycle)	1.0801 e^5	1 e^8
Stress (Pa)	2.1327	2.8045 e^7
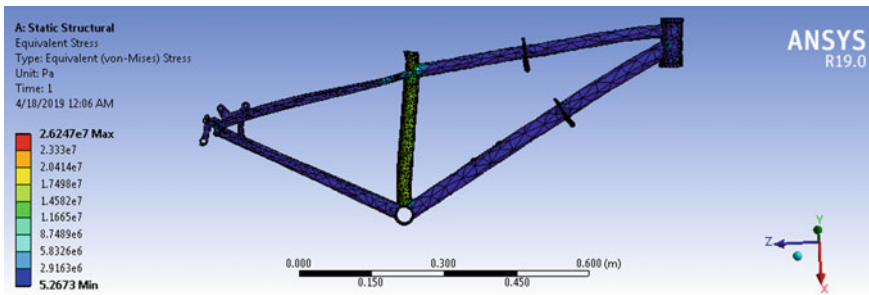
Fig. 6 Value of stress at 2000 N with joints
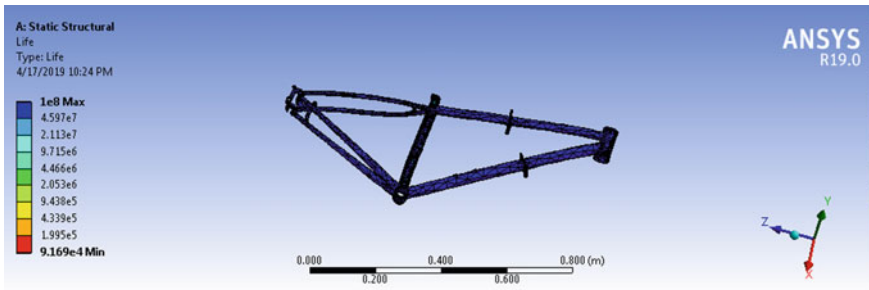
Fig. 7 Frame life at 2000 N with joints

Table 3 Results at 2000 N force with Joints

Solutions	Min	Max
Fatigue life (cycle)	9.169 e^4	1 e^8
Stress (Pa)	4.5126	2.8045 e^7

4 Conclusions and Future Work

For making the bicycle more affordable and without losing its strength the best material, we selected aluminum alloy of 6061 grade because it is cheap and has high strength. The hinge joint is applied in this cycle because it is easy to manufacture through welding and gives a low-stress value and easy to fold. As well as it is eco-friendly, lightweight, and foldable, it is easy to carry and store everywhere in your cars and store inside the house. The results show that the fatigue life of the aluminum alloy 6061 is decreasing very less after adding the joint and the stress value at the joints is also low. In future, researchers can do the cost analysis and cost optimization of bicycle using optimization techniques like Genetic Algorithm, TLBO, etc.

References

1. Ankush MH, Sharad PB, Bhavesh AB (2020) Design of single fork of folding bicycle. Int J Modern Eng Res (Ijmer) 6(5):64–70
2. Arunachalam M, Arun Prakash R, Rajesh R (2020) Foldable bicycle: evaluation of existing design and novel design proposals. Arpn J Eng Appl Sci 9(5):706–710
3. Chien-Cheng Lin, Song-Jeng Huang, Chi-Chia Liu (2020) Structural analysis and optimization of bicycle frame designs. Adv Mech Eng 9(12):1–10
4. Soden PD, Millar MA, Adeyefa BA, Wonc YS (1986) Loads stresses and deflections in bicycle frames. J Strain Anal Eng Des 21(4):185–195
5. Soden PD, Adeyefa BA (1979) Forces applied to a bicycle during normal cycling. J Biomech 12(7):527–541
6. Hoes MJAJM, Binkhorst RA, Smeekes-Kuyl AEMC, Vissers ACA (1968) Measurement of forces exerted on pedal and crank during work on a bicycle ergometer at different loads. Internationale Zeitschrift für angewandte Physiologie einschließlich Arbeitsphysiologie 26(1):33–42
7. Kanasagara P, Mandliya J, Bhatt K, Bhandari R (2020) Design and fabrication of tricycle fold around the bag and utilized as a trolley. Int Res J Eng Technol (Irjet) 05(11):486–494
8. Maleque MA, Hossain MS, Dyuti S (2011) Material properties and design aspects of folding bicycle frame. In: Advanced materials research vol. 264. Trans Tech Publications Ltd., pp 777–782
9. Nikhil YP, Aitavade EN (2020) Static structural analysis of foldable frame for bicycle using finite element method. Int Res J Eng Technol(Irjet) 6(10):1190–1193
10. Shelke M, Tingne A, Chandrakar S, Bharti P, Meshram V, Dahikar T (2020) Design methodology to fabricate foldable bicycle. Int J Res Appl Sci Eng Technol(Ijraset) 6(Iii):1751–1755
11. Shaikh S, Shaikhnag YA, Surangiwala M, Khan SA, Shaikh F (2020) Literature review for design of elliptical bicycle. Int J Sci Eng Technol Res(Ijsetr) 5(1):275–281
12. Liu XJ, Wang J, Yu WY et al (2011) Analysis and optimum design of rider-bicycle mechanisms: design of bicycle parameters for a specified rider. Sci China Technol Sci 54:3027–3034

Modeling and Analysis of Composite Bullet-Resistant Jacket

Sashi Kant, Tanuj Joshi ⓘ, and Ravikant Sharma

Abstract Armor industries are striving for the better safe body vests having a high-impact energy-absorbing capacity. CAD and CAE tools like SolidWorks and FEA code ANSYS provide us approximate solution in order to giving us the better knowledge for improving the bullet-resistant capability of vest. This work attempts to compare and analyses of mostly used material for bulletproof vest, i.e., kevlar, carbon-epoxy, and spectra. The 14 combinations of these fiber materials were analyzed using design and analysis tools. The spectra-carbon/epoxy-kevlar-spectra-kevlar (SEKSK) is the best option for the vests showing superior results comparing with other combinations. At the point when a bullet projectile strikes body shield, it transmits its energy until such time as the bullet has been stopped. The best arrangement of the fiber's cloth is identified in the vest based on using total deformation, Von Mises stress results, when it is subjected to a .220 Swift bullet impact. This study provides the important information for researchers and industries for development of better-quality bullet-resistant vest by utilizing superior combination of different fiber cloth.

Keywords SolidWorks · Ballistic · ANSYS · Kevlar · Bullet

1 Introduction

A bullet-resistant vest or ballistic vest is also known as a bulletproof jacket. It is an item of personal armor that is used for absorbing the impact and reduce (stop) penetration into the body. Body covering has been utilized in workforce assurance for quite a long time since the Roman Empire (145 B.C.) [1] to till now, i.e., 2018. The ballistic body-protective layer encountered a quick development amid the advanced fighting, and the essential quality requirements are: to stop the entrance of weapon into the human body and to scatter the effect vitality [2]. These days a ballistic body shield is

S. Kant
NIET, Greater Noida 201306, India

T. Joshi (✉) · R. Sharma
Amity University, Gurugram 122413, Haryana, India
e-mail: tanujjoshi15@gmail.com

generally utilized by furnished administrations, law requirement, and security work-force. With the advancement of military tasks, weapons, and ammo, the body shield is required not exclusively to have better ballistic assurance, but also additionally, it must be lightweight and adaptable to guarantee the wearer's portability and solace. These days, a ballistic body shield is generally utilized by furnished administrations, law requirement, and security workforces. In the mid-twentieth century, advances of the equipment and innovations in assemblies led to the emergence of highly developed materials, such as nylon, aramid, and polyethylene with a large module. Further improvements to the ballistic performance of a sensitive body shield are apparent to be gradually difficult to achieve, due to increasing financial expenditure for the development of fresh ballistic products and the lengthy-term marketing of them [3].

Usually, the layering of multiple layers of the corresponding texture was used to produce fine body armor. Generally, the bulletproof vest consists 10 to 50 layers which leads its weight to approximately 20–25 kg. [4]. Crossbreed boards for ballistic body defensive layers have turned into an undeniably fascinating point to analysts for a long time. Ballistic corps strengthening is a class of protective clothing that protects the human body against the metal parts of hand-held and explosive weapons [5], usually employed by the military and regulating workforce authorizations. The basic condition is that the wearer is extraordinarily versatile and comfortable with practical loads of ballistic certainty. It means that the ballistic framework protection layer must respect the frame of the consumer, as it should be dispersing their load over the frame to restriction the person's weariness, give good enough breathability to broadened use, and should not meddle with or confine the consumer's portability [6].

The ballistic dimensions of the frame-protective layer chests are usually used as a cover for vital organs. The use of non-bending material such as polymer composite, creative, metal, silicon carbide (SiC), and boron carbide (B4C) panels generated through the difficult overlay of the board [7]. It is unbending and thicker and is widely used in the lightweight car coverage, conflict shields, and shooting guarantee for foundation [8]. The texture layers of a ballistic proof jacket change from 10 to 50 with loads of around 3–10 kg, depending on the cover-point and the yarn test [9].

For a long time, composite materials have been used for mechanical problems and are deliberately manufactured for one package of a kind, consisting of vehicle parts, brandy goods, aviation parts, and buyers and within the marine and petroleum businesses [10]. Metal parts that have composite sections can be supplanted with the help of aluminum parts to 60 to 80% by the weight of the section, and 20 to 50% by the weight. Today, the effects of composites for some construction packages are the material of choice [11]. The glass fiber fortified polymer was first developed in 1940. From 1965 onward, most research is initiated on composite materials. The composite materials give high quality and in addition lessening in part weight which enhances the execution of segments and additionally sparing of materials for assembling a segment. S-glass fiber is mostly utilized composite in nowadays situation [12].

The most widely recognized strategy to create a lattice composite is called hot squeezing technique [13]. Sujith et al. [14] investigate Boron fiber, Kevlar 149, and spectra 900 in order to determine the deformations and stresses at 950 m/s speedy

bullet. Its outcome is that spectra 900 fibers with minimal distortion and stress under bullet effects are the best compared with Boron and Kevlar 149. It demonstrates greater strength, chemical reactions resistance, and negligible sensitivity to humidity. Defense sectors, aircraft parts, fiber optics, and protecting layers are the application field of kevlar, spectra, and carbon fibers because of high strength and comparatively less reactant. Increment into the efficiency of the jacket can be obtained by using graphene, UHMWPE, Dyneema. Dyneema SB61 is good for creating bulletproof vests because they are waterproof and light in weight [15].

Composite demonstrates the enhancement of the material properties of the bulletproof jackets. Johns Abraham et al. [16] tested warp around composite using ANSYS at three different speed, i.e., 180, 250, and 350 m/s. The wrapped model shows minimum material deformation and a maximum bullet deformation. Fasil Mohiuddin [17] demonstrates the tensile force of K29 and K49 fibers which are eight times higher than that of steel and comparatively lightweight. Abhishek Kushwaha et al. [18] uses graphene and kevlar 149 and tested for 8 mm thick composite armor at a velocity of 928 m/s. This shows that graphene is the best reinforcement for the ballistic resistant material as compared to the kevlar 149 fiber with minimum deformation of 3.04 mm and max. principal stress 9140.3 MPa. Kevlar composite is best for minor applications like stab armor having a combination of kevlar with rubber armor because of its cost-effectiveness [19].

Nyanor et al. [20] use different sequence and thickness of layers in the form of a sandwich and simulated TWIP steel, water, and PP-PE polymer layers. The three of the four models simulated were able to stop a 9 mm bullet having a speed of 360 m/s without penetration of the inner plate.

2   Material and Method

In the work, a 3D model of composite and bullet assembly is developed and imported to the CAE software package for testing (evaluation and conception of bullet-resistant composite ballistic analyses). The solver is based on the technique of finite elements. The domain is discretized into a limited set of control volumes before simulation. Simulation can be solved in some steps as follows (see Fig. 1):

2.1   Material

Kevlar 149, carbon fiber epoxy, and spectra materials are used because their properties are best suited for manufacturing the bulletproof composite. Kevlar® is a natural fiber inside the aromatic polyamide circle of relatives. Kevlar® combines high electricity, high modular power, toughness, and thermal equilibrium with an entirely distinctive mixture. The latest spectra® fiber technology was created to deliver highly satisfactory, super-sturdy, and extremely lightweight fibers to blankets, aviation, and
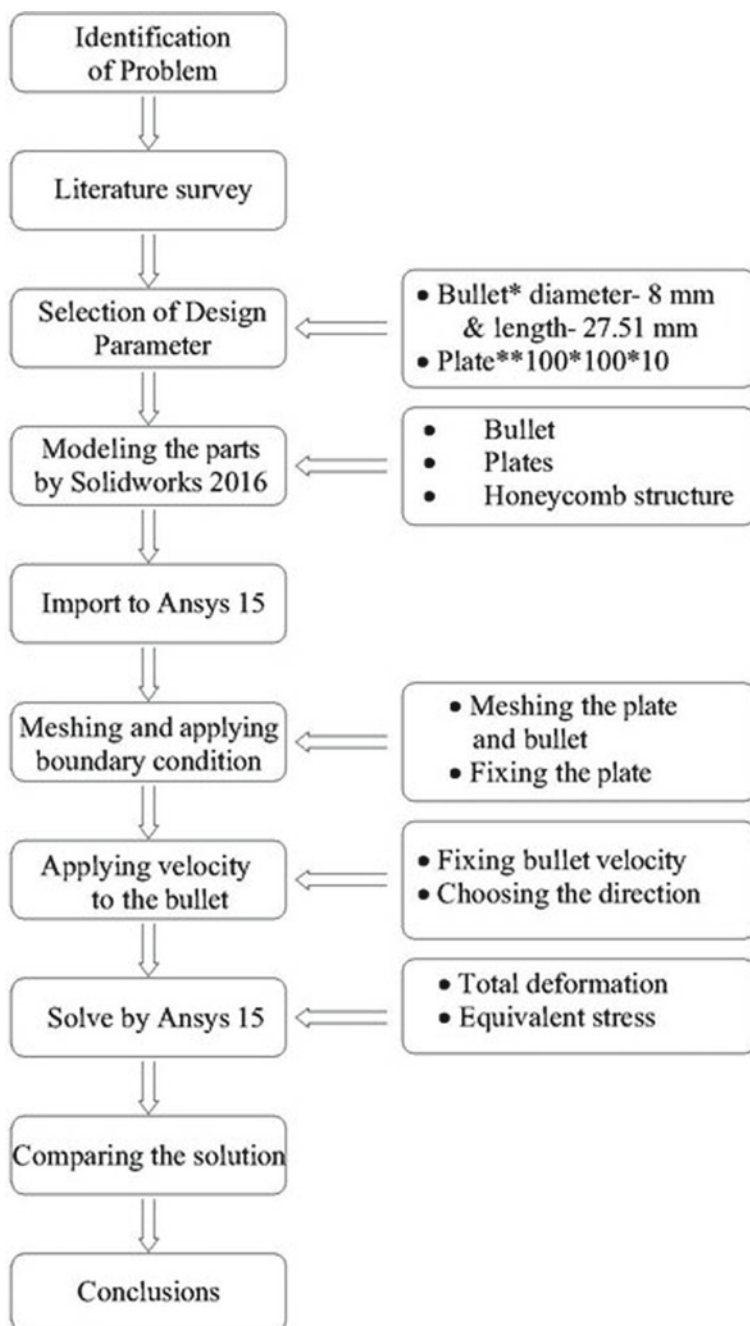
Fig. 1 Process flowchart
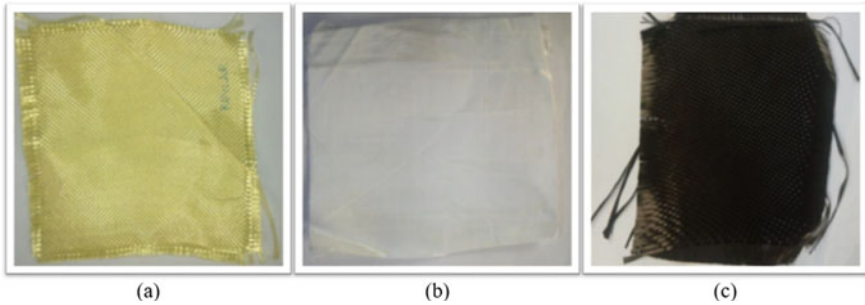
Fig. 2 Materials for composite **a** kevlar, **b** spectra, and **c** carbon fiber epoxy

Table 1 Mechanical properties [13]

Material	Density (g/cm^3)	Young's modulus (GPa)	Poisson's ratio	Yield strength (GPa)
Kevlar	1.44	124	0.36	3.6
Spectra	0.97	132	0.31	1.2
Carbon epoxy fiber	1.8	135	0.33	2.25

excessive wearing of products. Carbon fiber epoxy and resin mixture has higher characteristics than both substances alone and is being used as substitutes more and more for particularly heavy metal substances. All three materials are depicted into Fig. 2, and Table 1 provides a list of materials used for bulletproof analysis into the FEM software package.

2.2 Methodology

Into the initial step of preprocessing is to develop a 3D CAD model of ballistic setup using SolidWorks 3D modeling software package. After creating sketches, parts, assembly, and drawing of ballistic setup, it is saved in.sldprt extension format, assembly file has extension name.sldasm, and for drawing file, it is.slddrw. The ballistic setup has two main components, first is bullet, and the second one is assembly fiber as depicted in Fig. 3. All dimensions are in mm. Bullet has a diameter of 8 mm and a length of 27.51 mm. Fiber cloths assembly has a total thickness of 10 mm, having each fiber of 2 mm thickness.
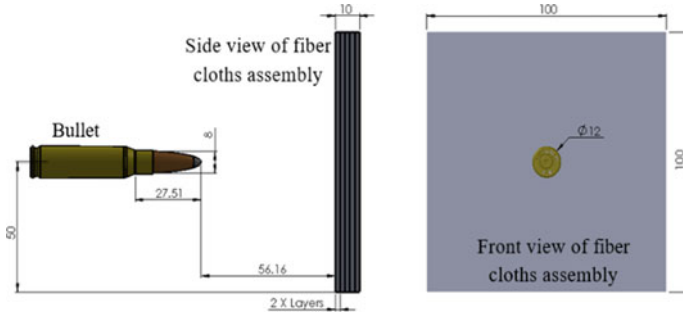
Fig. 3 CAD model of bullet and layered fiber
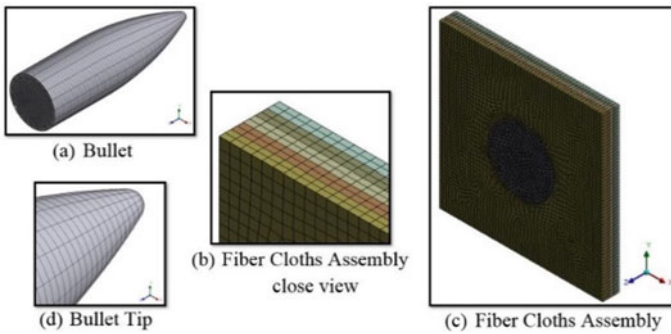
Fig. 4 Meshed model of bullet and layered fiber

2.3 Meshing

Meshing in Workbench generally provide durable and easy specifically that will mainly help to facilitate the mesh generation process. Discretized shapes are known as an element attached to other elements at corners with nodes. Meshing view of fiber cloths and bullets is shown in Fig. 4. This fine mesh file contains 19106 nodes and 13420 elements of tetrahedral shape. A material property of bullet is applied using fatigue data at zero mean stress which comes from 1998 ASME BPV Code, Sect. 8, Div. 2, Table 5-110.1. This data is used from ANSYS library.

2.4 Boundary Condition

Fix support is applied at four sides of the composite plate, and 1250 m/s velocity is applied to bullet which is depicted into Fig. 5.
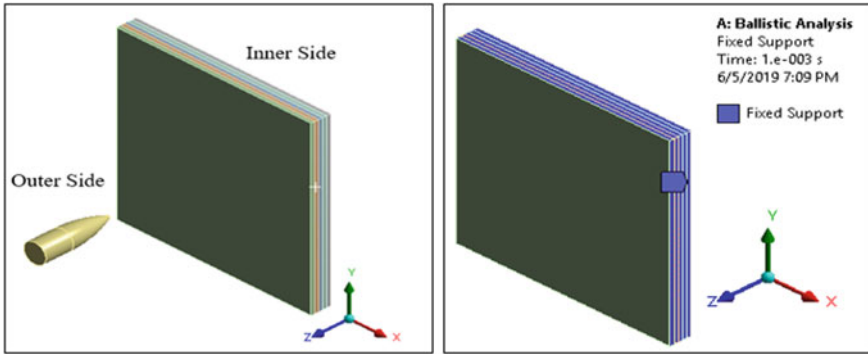
Fig. 5 Boundary conditions of layered fiber

3 Result and Discussion

3.1 Results

In this paper, various investigations of a different combination of composite ballistic layers having 2 mm thickness for kevlar 149, spectra, and carbon/epoxy fiber were carried out. In order to get the optimum results, the Johnson–Cook model is utilized for study. For the 14 types of combinations, these layers were used instances of the investigations which were considered in the present work see Fig. 6. Depth of penetration by the bullet over SSEKK and SEKSK composite is depicted into Fig. 7. Table 2 shows various combinations of the composite used for investigation.

In the wake of breaking down, all the 14 variations of the composite bulletproof combinations, we get the results that are tabulated into Table 3 and graphically presented into Fig. 8. Table demonstrates the consequence of all the variation of different fiber composites.

3.2 Validation

In collaboration with the laboratory, experiments were carried out, and the experimental results were analyzed and compared with CAE software package results. At the research laboratory, after performing an experiment on kevlar fiber, 0.127 mm penetration was observed. Virtual analysis with the same inputs on FEA code ANSYS software was carried out, and 0.14698 mm penetration was observed which is depicted in Fig. 9. The experimental results found to be approximately 15% variations of the software analysis depicted into Fig. 10 which indicates that the analysis report is within optimum validation.
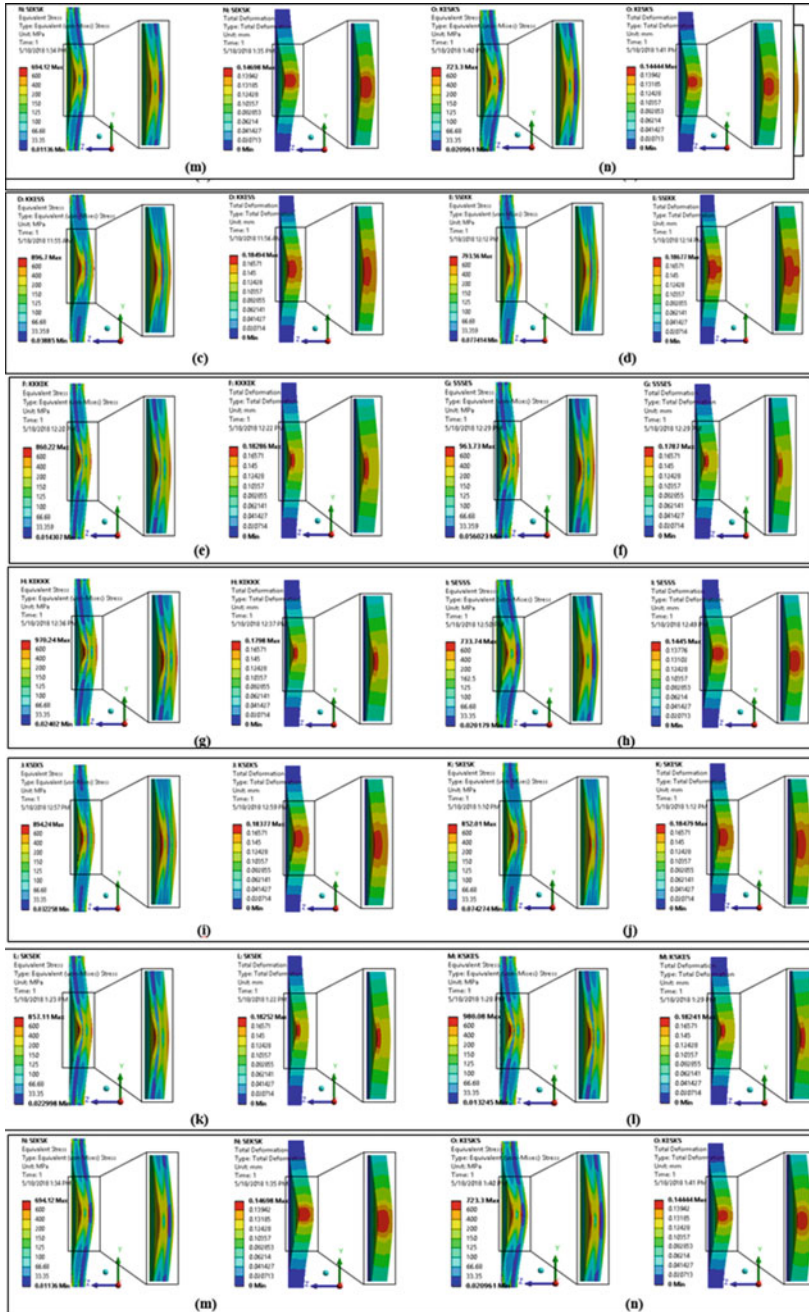
Fig. 6 Max. stress and max. deformation of composite fiber **a** KKEKK, **b** SSESS, **c** KKESS, **d** SSEKK, **e** KKKEK, **f** SSSES, **g** KEKKK, **h** SESSS, **i** KSEKS, **j** SKESK, **k** SKSEK, **l** KSKES, **m** SEKSK, and **n** KESKS
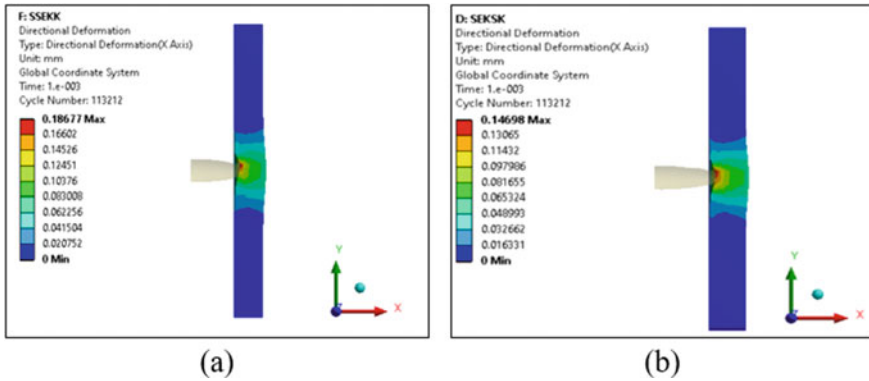
Fig. 7 Composite penetration depth **a** SSEKK and **b** SEKSK

Table 2 Layered composite variants

Name of layer composite	Inner first layer	Inner second layer	Middle layer	Outer second layer	Outer first layer
KKEKK	Kevlar	Kevlar	Carbon/Epoxy	Kevlar	Kevlar
SSESS	Spectra	Spectra	Carbon/Epoxy	Spectra	Spectra
KKESS	Kevlar	Kevlar	Carbon/Epoxy	Spectra	Spectra
SSEKK	Spectra	Spectra	Carbon/Epoxy	Kevlar	Kevlar
KKKEK	Kevlar	Kevlar	Kevlar	Carbon/Epoxy	Kevlar
SSSES	Spectra	Spectra	Spectra	Carbon/Epoxy	Spectra
KEKKK	Kevlar	Carbon/Epoxy	Kevlar	Kevlar	Kevlar
SESSS	Spectra	Carbon/Epoxy	Spectra	Spectra	Spectra
KSEKS	Kevlar	Spectra	Carbon/Epoxy	Kevlar	Spectra
SKESK	Spectra	Kevlar	Carbon/Epoxy	Spectra	Kevlar
SKSEK	Spectra	Kevlar	Spectra	Carbon/Epoxy	Kevlar
KSKES	Kevlar	Spectra	Kevlar	Carbon/Epoxy	Spectra
SEKSK	Spectra	Carbon/Epoxy	Kevlar	Spectra	Kevlar
KESKS	Kevlar	Carbon/Epoxy	Spectra	Kevlar	Spectra

4 Conclusion

The design and analysis (simulation) process of the five-layered composite materials of thickness 10 mm is subjected to calculating deformation and stress. From the above analysis, the following results are obtained:

- The SEKSK composite, which can wear the projectile force of bullet velocity 1250 m/s, shows less stress 694.12 MPa Fig. 6(m) among the above 14 combinations.

Table 3 Composite layers and results

Composite layer arrangement	Max. stress (MPa)	Max. deformation (mm)
KKEKK	804.45	0.18642
SSESS	893.47	0.18329
KKESS	896.70	0.18494
SSEKK	793.56	0.18677
KKKEK	894.24	0.18377
SSSES	825.01	0.18479
KEKKK	860.22	0.18286
SESSS	963.73	0.1787
KSEKS	970.24	0.1798
SKESK	733.74	0.1485
SKSEK	857.11	0.18252
KSKES	980.08	0.18241
SEKSK	694.12	0.14698
KESKS	723.30	0.14444
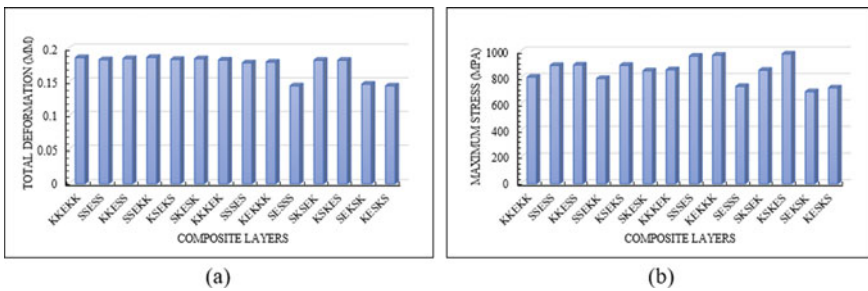
Fig. 8 Composite layer **a** total deformation and **b** maximum stress

- The minimum depth of penetration, i.e., 0.14698 mm, was observed into material combination SEKSK which makes it highly suited for the bulletproof vest.
- The maximum depth of penetration, i.e., 0.18677 mm, were observed into material combination SSEKK which makes it less suited for the bulletproof vest.
- Therefore, SEKSK is said to be the best combination for bulletproof composite, and its capability under heavy-duty work is comparatively good as compared to other composite materials.
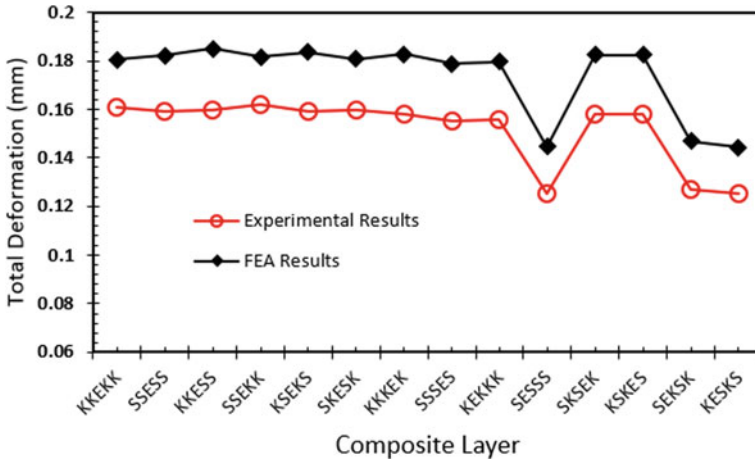
Fig. 9 Validating analytical results with experimental results
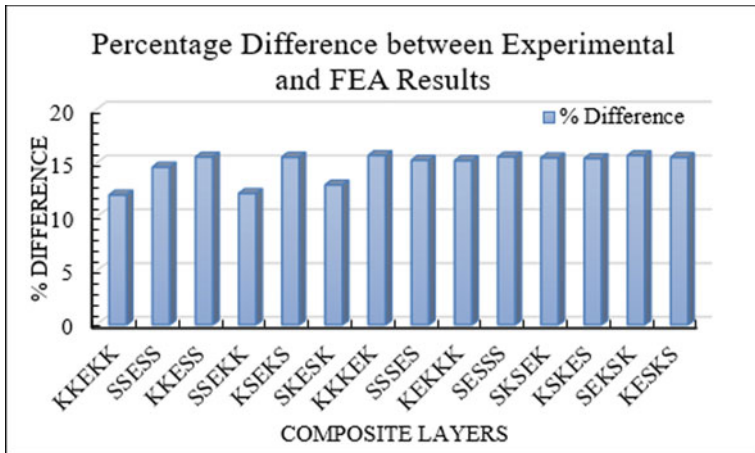
Fig. 10 Percentage difference between experimental and FEA results

References

1. Mark R (1982) Analysis of long-range bullet entrance holes atomic absorption spectrophotometry and scanning electron microscopy. J Forensic Sci 27(1):92–112
2. Rajan S, Reddy C (1997) Assessment of tensile behavior of boron carbide/AA2024 alloy metal matrix composites. Int Conf Compos Mater Character 4(2):160–163
3. Pushpa B, Sriram (1997) Ballistic protective clothing: an overview. Indian J Fiber Textile Res 22(1):274-291
4. Raftenberg M (2004) Modeling thoracic blunt trauma towards a finite-element-based design methodology for body armor. U. S. Army Research Laboratory, Aberdeen Proving Ground, MD 21005–5069

5. Gopalakrishnan S, Senthil (2011) Failure analysis of ballistic material. Int Conf Adv Mater Eng 15(1):95–100
6. Ramawat S, Thorat D, Prashant (2012) Simulation of bullet impact on bullet resistant steel plate. J Simul Driven Innov 1(1):1–13
7. Thiyagarajan K, Martin L, Elayaraja N, Sivaprakasam P (2014) Modelling of kevlar-Al alloys and finite element simulation of mechanical properties. ARPN J Eng Appl Sci 9(5):599–607
8. Regassa Y, Likeleh G, Uppala R (2014) Modeling and simulation of bullet resistant composite body armor. Int J Res Stud Sci Eng Technol 1(3):39–44
9. Emayavaramban E, Raj P (2014) Finite element analysis of different composite materials using multi continuum method. IOSR J Mech Civil Eng (IOSR-JMCE) 11(5):94–99
10. Kumaravel S, Venkatachalam A (2014) Development of nylon, glass/wool blended fabric for protective application. IOSR J Polym Textile Eng 1(4):5–9
11. Siriphala P, Veeraklaew T, Kulsirikasem W, Tanapornraweekit G (2014) Validation of finite element models of bullet impact on high strength steel armors. WIT Trans State of the Art Sci Eng 75(1):63–71
12. Fernando E, Niles S, Morrison A, Pranavan P, Godakanda I, Mubarak M (2015) Design of a Bullet-proof vest using shear thickening fluid. Int J Adv Sci Technical Res 1(5):434–444
13. Oleivi J, Hussein A, Ahmed S (2015) Experimental and numerical analysis of bulletproof armor made from polymer composite materials. Eng Tech J 33(33):1583–1597
14. Sujith S, Chethan, Sandeep D, Sanjay S, Shaik B, Sowmyashree S (2015) Impact analysis of bullet on different bullet proof materials. Int J Mech Indus Technol 3(1):303–310
15. Kumar N (2016) Bulletproof vest and its improvement–a review. Int J Sci Develop Res 1(1):34–39
16. Abrahm J, Kumar S, Sankar S (2016) Finite element simulations of ballistic impact on glass fiber composite. Int J Eng Res Technol 5(9):521–526
17. Mohiuddin F (2017) Experimental investigation on mechanical properties of kevlar fiber. Int Res J Eng Technol 4(7):3466–3473
18. Kushwaha A, Kushwaha P, Nagayach N (2018) Impact analysis of bullet on different ballistic resistant material using Ansys. Int J Recent Technol Sci Manage 12(1):33–42
19. Varunkumar D, Ramalingam K (2018) Impact analysis of bullet on different ballistic resistant material using Ansys. Int Conf Recent Trends Eng Appl Sci Manage 8(2):438–448
20. Nyanor P, Hamada A, Hassan M (2018) Ballistic impact simulation of proposed bullet proof vest made of TWIP steel, water and polymer sandwich composite using FE-SPH coupled technique. Key Eng Mater 302–313

The Effect of Dynamic Snapping on Critical Buckling Load Prediction of an Axially Compressed Cylindrical Shell Using Energy Barrier Method

Suhas Ankalkhope, Sandeep Jose, Amal S. Siju, and Kiran D. Mali

Abstract The non-repeatability of cylindrical shell buckling experiments is a limiting factor in their stability characterization. The need for high-fidelity estimates of the buckling loads of shell structures is of critical importance for reliance or to increase payload capability. The recent studies on cylindrical shell buckling show that the energy barrier method can be used as a nondestructive and noninvasive technique for determining the shock sensitivity and stability of thin-walled structures. However, the dynamic snapping which is observed during the determination of the energy barrier remains to be a hurdle that needs to be addressed before standardizing this technique as a non-destructive testing methodology for the prediction of the buckling load-carrying capacity of axially compressed cylindrical shells. In the present study, numerical analyses were carried out to investigate the snapping mechanism that is observed during the determination of the energy barrier.

Keywords Buckling of cylindrical shell · Energy barrier method · Dynamic snapping · Bifurcation

1 Introduction

Cylindrical shell structures find numerous aerospace applications because of their high efficiency in carrying the load while keeping the lowest possible weight. The buckling of an axially compressed cylindrical shell, in particular, has gained a lot of attention because of its utilization in rocket shells and in space vehicles. The lack of predictability of the buckling load of a cylindrical shell owing to its sensitivity to geometric imperfections is the major challenge that aerospace engineers are trying to address even today. The existing guideline for the design of cylindrical shells based on the recommendations by NASA SP-8007 [1] is found to be conservative and designers are looking forward to better guidelines. Several avenues such as single perturbation load approach, artificial neural network prediction, probabilistic

S. Ankalkhope (✉) · S. Jose · A. S. Siju · K. D. Mali
BITS Pilani K K Birla Goa Campus, Goa, India
e-mail: suhas.ankalkhope@gmail.com

perturbation load approach, vibration correlation technique are being pursued in this regard [2–7]. Among the different approaches, the energy barrier method is gaining a lot of attention recently [8–11].

The energy barrier method is a non-destructive, non-evasive technique that can be used for predicting the buckling load-carrying capacity of axially compressed cylindrical shells. Information about the structure's stiffness and robustness against buckling in terms of energy and other force parameters can be arrived using this technique. In simple terms, the energy barrier is the energy that needs to be supplied to drive the shell over buckling, and the determination of this energy barrier in a way helps us to find the buckling load-carrying capacity of the structures. The concept of energy barrier is based on the finding that the lowest energy barrier that a perfect shell needs to overcome to change into a buckled configuration has the shape of a dimple [10].

Experimentally, this single dimple can be easily achieved by probing a pre-compressed cylindrical shell by a displacement controlled probe as shown in Fig. 1.

To measure the energy barrier the cylindrical shell is axially compressed under different prescribed axial loads. Typically the axial loads are chosen to be 0.2 P_{cr} to 0.5 P_{cr}, where P_{cr} is the critical buckling load from classical theory. Such a shell is then subjected to probing (poking) from the side by using a poker. The poker force and poker displacement are recorded and the energy barrier can be obtained from the area under a plot between poker force and poker displacement as shown in Fig. 2a, b. The relationship between poker force and poker displacement is a nonlinear stiffening/softening type. Such curves between poker force and poker displacement for different levels of prescribed axial loads can be constructed on a 3D graph. This 3D plot can be used as an effective tool for assessing the stability characteristics of an axially compressed cylindrical shell [11]. For example, the critical buckling load can be obtained by extrapolating the curves corresponding to the lowest energy barriers. In addition to obtaining the critical buckling load, several features of the

Fig. 1 **a** A cylindrical shell under axial compression subjected to lateral poking **b** Simple dimple observed during poking
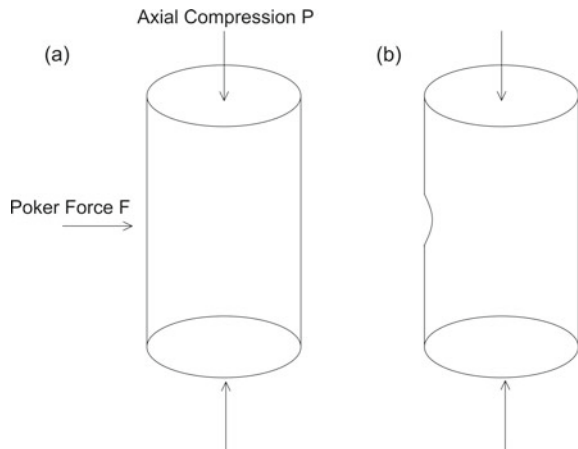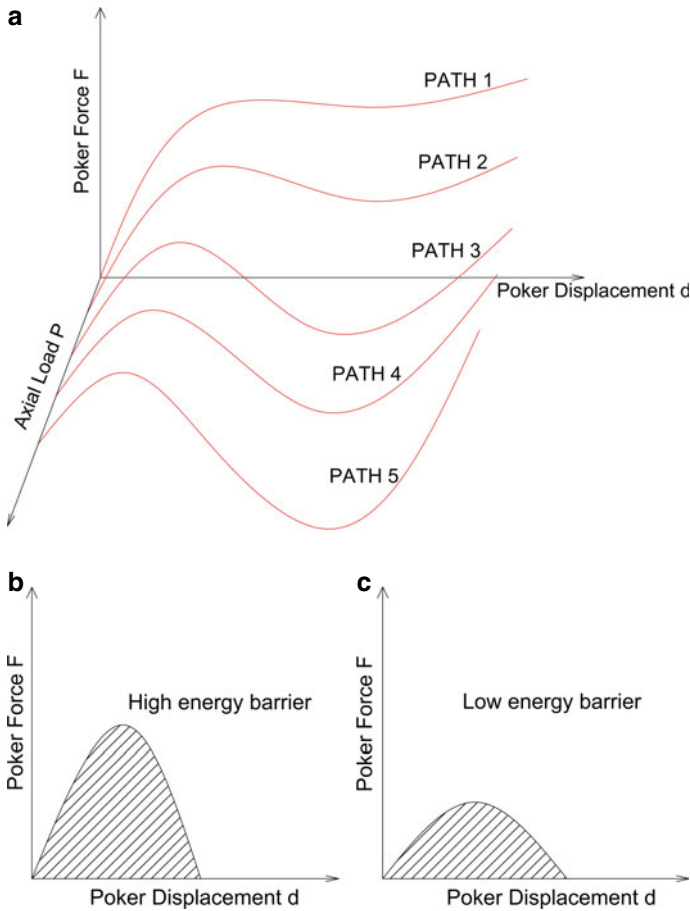
Fig. 2 **a** Energy barriers obtained for different levels of axial compression: For low levels of axial compression, the slope of the curve remains positive as indicated by PATH 1. If the level of the axial compression is further increased the slope of the curve may drop to zero or even negative as indicated by PATH 2–3 leading to the formation of a stable dimple. For further increase in axial load, the curves may cross zero poker force axis and reemerge leading to the formation of a stable dimple as shown by PATH 4–5. **b** Illustration of the energy barrier for different magnitudes of axial compression. The leftmost figure shows the energy barrier for a cylindrical shell subjected to lower magnitudes of pre-compression load compared to the right one

shell stability such as shock sensitivity of the cylindrical shell can be obtained from this plot. However, a major drawback of the stability plot is that, some of the regions is affected by the snapping and bifurcations as shown in Fig. 3. A better understanding of the bifurcations that are occurring in this region is necessary to assess the stability of the cylindrical shell.

In the present numerical study, 3D stability plot is constructed for the cylindrical shell of dimensions 54 mm diameter, 107 mm height, and 0.106 mm thickness.

Fig. 3 Snapping and
bifurcations in the stability
response of a structure
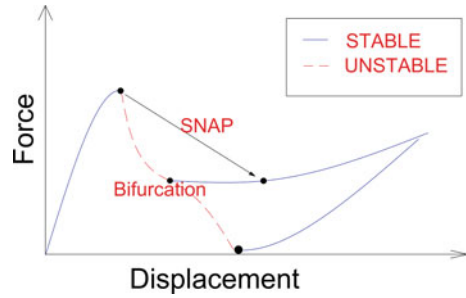
The regions in the plot where snapping is expected are identified. Some possible
bifurcation mechnisms that can be expected in this region are identified.

2 Numerical Model

Numerical modeling is carried out using the commercial software ABAQUS. The
cylindrical shell is modeled using S4R-4 nodded shell elements having reduced
integration feature [12]. A total of 36,400 elements is used in the shell model; the
number of elements used is decided based on a convergence study. The size of the
elements used is well below the recommended mesh size $0.5 \sqrt{Rt}$, where R is the
radius and t is the thickness of the cylindrical shell. The cylindrical shell is given
the material properties of Aluminium, E-70 GPa, $u-0.3$ and is assumed to remain
elastic throughout the loading. The poker is assumed be a rigid body. The shell edges
are assumed to be clamped, i.e., all degrees of freedom except the translation in the
axial direction for the top edge of the shell is restrained. 'Rigid body' connections
are used to link the end nodes of the shell to a reference point which are located at
the shell edge centers. The axial loads are applied at the top reference point. The
interaction between the cylindrical shell and the poker is modeled as a 'Surface to
surface' contact.

   The cylindrical shell buckling can be modeled using Static General/Dynamic/Riks
analysis procedures in Abaqus. In the present study, 'Static General' analysis is
adopted for carrying out the numerical simulations considering the quasi-static nature
of the axial compression and lateral poking. For the stabilization of the solution 'Arti-
ficial damping' with damping factor, 1×10^{-6} is adopted. Figure 4 shows the numer-
ical model used in the present study. As the static general algorithm traces marginally
stable paths, exact reproduction of the numerical results using experimental methods
may not be feasible.

Fig. 4 Numerical modeling of the axial compression and poking

3   Results and Discussion

Figure 5 shows the response of the cylindrical shell to lateral poking for different levels of axial compression. The results obtained here are qualitatively in agreement with experimental studies of [11] and numerical studies of [13]. Important regions in the graph are marked *A*, *B*, *C*. The region '*A*' represents the safe zone where the

Fig. 5 Poker force versus poker displacement for various levels of axial compression
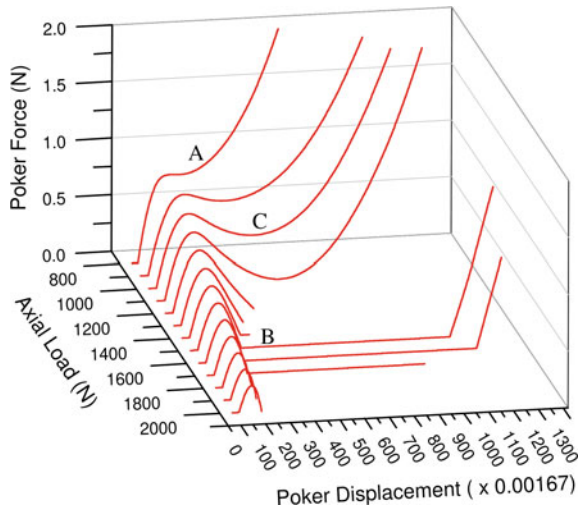
cylindrical shell will remain stable irrespective of the poker load and displacement. The slope of the curves in region 'A' remains always positive, i.e., the stiffness offered by cylinder in this region is always positive. The curves in region 'C' have positive slope initially which becomes marginally negative and again becomes positive for rest of the part. In region 'B', the curves initially having positive slope reach a maximum and then drop to zero. Region 'B' represents the shock-sensitive region where the shell is prone to exhibit an unstable post-buckling response if it is subjected to poking. On the other hand, the region 'C' represents areas where the marginally stable response to external disturbances can be expected. Since weight efficiency is a major requirement in aerospace applications, the shell design should be based on the stability of the shell corresponding to region 'C'.

An important feature of the shell stability in the region 'C' is that the shell may undergo snapping. Since snapping is primarily a nonlinear dynamics phenomenon and is prone to poker dynamics, it needs to be addressed for effectively characterizing the shell stability in this region. In addition to snapping, the cylindrical shell may also exhibit bifurcations or branch switching in the region 'C'. Some of the types of bifurcations that may be expected during the lateral poking are discussed in Fig. 6.
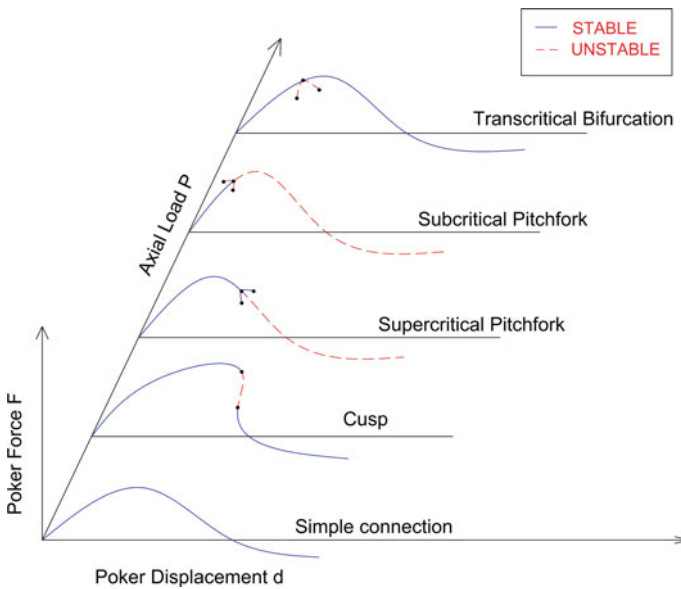
Fig. 6 Expected bifurcations in the stability plot during lateral poking for different levels of axial compression

4 Conclusions and Potential Lessons

The non-destructive testing procedure for the cylindrical shells can drastically improve the reliability of these structures used in a variety of applications. For example, the primary force that may cause buckling failure of a rocket shell structure during its take off is axially compressive in nature. Also, the reliability of shell structures used in other sensitive applications like atomic research can be analyzed using the insights gained into the stability of the shell. The energy barrier approach has the potential to be used as a non-destructive testing procedure. The present paper discusses some of the complications that can arise during the stability characterization of a cylindrical shell using the energy barrier approach. The major challenge in adopting energy barrier method as a potential non-destructive, non-evasive technique, to assess the stability of cylindrical shells, is to address the snapping that may arise during the lateral poking.

References

1. Peterson JP, Seide P, Weingarten VI (1965) NASA-SP-8007: buckling of thin-walled circular cylinders, Technical report. NASA Langley Research Center, Hampton, VA, USA
2. Wagner HNR, Hühne C, Niemann S, Khakimova R (2017) Robust design criterion for axially loaded cylindrical shells-simulation and validation. Thin-Walled Struct 115:154–162
3. Kriegesmann B, Jansen EL, Rolfes R (2016) Design of cylindrical shells using the single perturbation load approach–potentials and application limits. Thin-Walled Struct 108:369–380
4. Wang B, Du K, Hao P, Tian K, Chao YJ, Jiang L, Xu S, Zhang X (2019) Experimental validation of cylindrical shells under axial compression for improved knockdown factors. Int J Solids Struct 164:37–51
5. Tahir ZR, Mandal P (2017) Artificial neural network prediction of buckling load of thin cylindrical shells under axial compression. Eng Struct 152:843–855
6. Meurer A, Kriegesmann B, Dannert M, Rolfes R (2016) Probabilistic perturbation load approach for designing axially compressed cylindrical shells. Thin-Walled Struct 107:648–656
7. Arbelo MA, de Almeida SFM, Donadon MV, Rett SR, Degenhardt R, Castro SGP, Kalnins K, Ozoliņš O (2014) Vibration correlation technique for the estimation of real boundary conditions and buckling load of unstiffened plates and cylindrical shells. Thin-Walled Struct 79:119–128
8. Gerasimidis S, Virot E, Hutchinson JW, Rubinstein SM (2018) On establishing buckling knockdowns for imperfection-sensitive shell structures. J Appl Mech 85:091010
9. Thompson JMT, Hutchinson JW, Sieber J (2017) Probing shells against buckling: a non-destructive technique for laboratory testing. Int J Bifurcation Chaos 27(14):1730048
10. Horak J, Lord GJ, Peletier MA (2006) Cylinder buckling: the mountain pass as an organizing centre. SIAM J Appl Math 66:1793–1824
11. Virot E, Kreilos T, Schneider TM, Rubinstein SM (2017) Stability landscape of shell buckling. Phys Rev Lett 119:224101
12. ABAQUS 6.14, Abaqus/ CAE User's Guide

13. Haigui F (2019) Critical buckling load prediction of axially compressed cylindrical shell based on non-destructive probing method. Thin–Walled Struct 139:91–104

Vibration and Stress Analysis of Spur Gear Train by Using Ansys

Anunay Kumar, Yashwardhan Sahi, Swet Chandan, and P. Suresh

Abstract Spur gear is very important component of the machine which follows the mechanical operation under some loading conditions. The gear is used with some assemblies which are called gear train mechanism. To withstand the loads the material as well as the parameters of the gear train must be specific. So, in this paper, the gear train of stainless steel and some specific parameters is designed in Solidworks and further simulation is done in Ansys 18.0 under some loading conditions. The simulation contains two types of analysis i.e. vibration and stress analysis. By doing these analyses the result shows that at 500 N–m of moment at gear the stress at the tooth and shaft is 72.91 MPa and 294.7 MPa respectively which are within the yield tensile limit of the used material.

Keywords Spur gear · Gear train · Stainless steel · Vibration analysis · Stress analysis

1 Introduction

Spur gears are very simple in design that can be easily designed to manufacture. The teeth of the spur gears are commonly parallel to the axis of the gear. Since the spur gears are simple in design, easy to manufacture, easy to design, and most economical gear. This gear can be included as smoother and quietest one, can produce a lot of power and highly effective. It works efficiently at low and moderate speed but at high speed, it becomes noisy and creates vibration.

There is a need for at least two gear combinations in portal axle gearbox in order to give high off-set in between input and output gear. The portal axle is basically designed for 4-wheeled vehicles. The portal axle gives greater ground clearance in off-road circumstances for driving. Hence, the simulation of the designed gear for portal gear gives the idea of actual motion [1]. While the designing of gears for portal axle a dynamic response consider is critical. The modal response is dynamic

A. Kumar (✉) · Y. Sahi · S. Chandan · P. Suresh
School of Mechanical Engineering, Galgotias University, Sector 17-a, Yamuna Expressway, Greater Noida, Gautam Buddh Nagar 201310, India
e-mail: theanunay@gmail.com

response for designed gears for portal axle that is for periodic or quasi-periodic situation give the noise analysis and structural response to vibration. The modal response can predict the behavior of the dynamic input in the structure. Sometimes under such conditions structure stress may be high and create structure deficiencies [2].

It is very necessary to analyze the gear stress in transmission system which is a result built the idea of contact stress and bending stress which often need. FEM is elected for the different types of complicated structure's stress and strain analysis as well as of gear. In the intervening time, the stress distribution on the surface of gear leads to the surface fatigue of gear [3].

There has been performed an experiment in order to examine the numeric value of thin spur gear of truck gearbox as a result to get bending fatigue. The modeling and simulation with the use of FEM lead to gear stress analysis in order to get static and dynamic load disorders [4].

There has been developed a two-dimensional and three-dimensional meshing gear to analyze the stress analysis using FEM in order to collect gear tooth bending stress and surface stress over distributed surface. Further, the stress obtained with the FEM analyses equates with the Lewis bending stress equation and Hertz contact stress equation. This comparison gives the basic knowledge of the behavior of gears in operation that in what way the stress is distributed from one mesh to another [5, 6].

2   Design, Modeling, and Parameters

Generally, steel, bronze, aluminum, stainless steel, cast-iron, and non-metallic phenolic are used as the material for the manufacturing of spur gear. In this paper, Stainless Steel is used as the material for both gears as well as the axles. The physical properties are arranged below in Table 1:

There are some important parameters which are required to design a spur gear which is listed below along with their values:

Based on the parameters of design given in Table 2 and shown in Fig. 1, gear is designed and analyzed on designing software Solidworks and Ansys18.0 [7]. Figure 2 shows the single gear design and meshing spur gears while Fig. 3 is the arrangement of the spur gears and the axle. At the smaller axel input is provided and at the larger one the output will be obtained.

Table 1 Material properties for gear

Material	Young's modulus of elasticity in GPa	Poisson ratio	Density in kg/cm^3	Ultimate tensile strength in MPa		Tensile strength in MPa
Stainless steel	197	0.27–0.30	7.86		785	396

Table 2 Design parameters

Parameters	Value in cm
Dedendum circle dia.	7.50
addendum circle dia.	8.40
Pitch circle dia.	8.00
Tooth thickness	0.63
Addendum	0.40
Dedendum	0.50
Fillet radius	1.00
Diametral Pitch	2.50
Top side of tooth	0.25
Face width	4.00
No. of teeth	20
Circular pitch	1.26
Width of space	0.63
Shaft length	10&20
Shaft Dia.	3.00
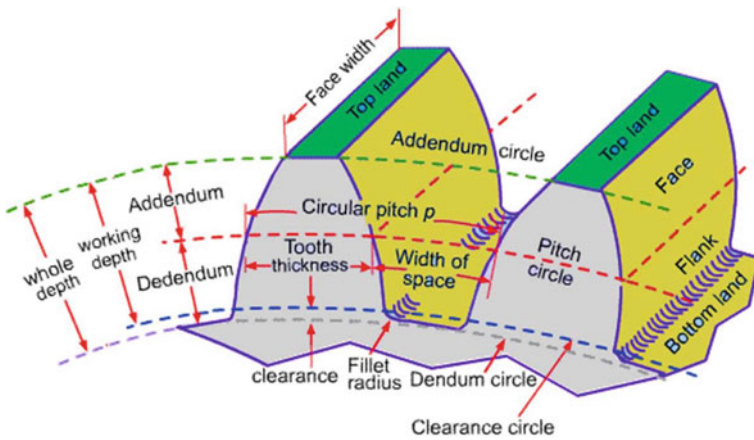
Fig. 1 Nomenclature of the gear [8]

There are two types of analysis is done for the vibration as well as stress. For the vibrational analysis, a modal system in Ansys is used and boundary conditions are applied to design, the shafts at the gears are made to cylindrical support (Fig. 4). For the stress analysis, static structural system is used and the boundary conditions are applied to the design. The shafts at the gear are made to cylindrical support while a moment (500 N–m) is provided at the input shaft.

Based on the boundary conditions the stress and deformation at the gear shaft and gear are obtained with the help of ANSYS 18.0.
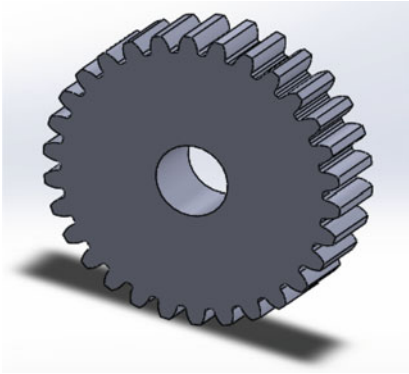
Fig. 2 Spur gear design
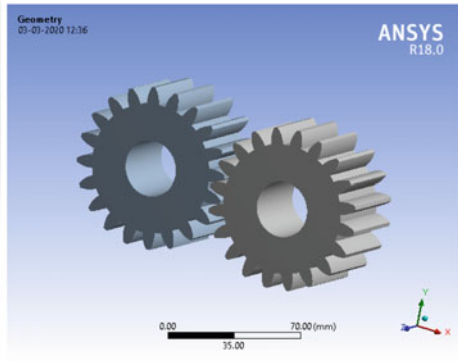
Fig. 3 Spur gear with axle
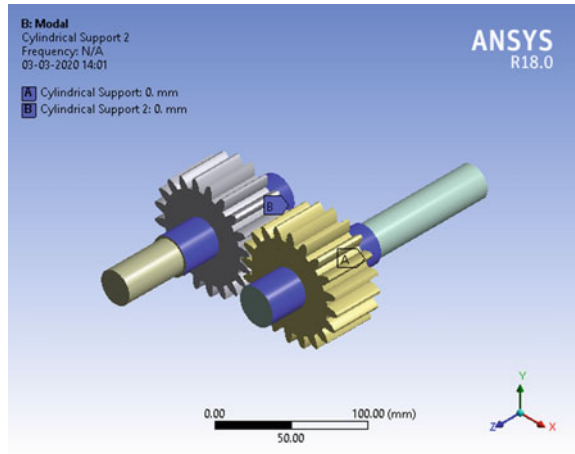
Fig. 4 Spur gear with boundary conditions for modal analysis
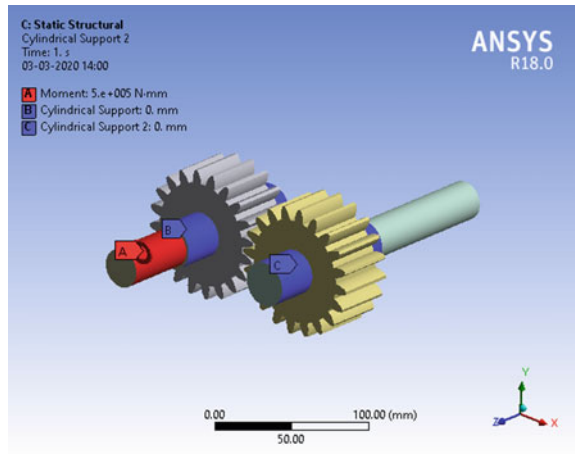
3 Result and Discussion

After applying the boundary conditions the vibrational analysis is done for the gear train and the result is obtained as six modes of frequencies:

Figure 5 shows the deformation of the gear train in first six modes of frequency. It shows the component behavior at the certain natural frequencies which are arranged in Table 3.

Based on the data the graphs are drawn in which first graph (Fig. 6) shows the variation of frequency w.r.t. different modes while second graph (Fig. 7) shows deformation in the gear train w.r.t. different modes.

The result from another analysis system the stress is analyzed in which cylindrical support is provided at the shaft at the gear and moment of 500 N–m is applied to one gear and as the result the stress is obtained at the shaft as well as at the gear tooth.
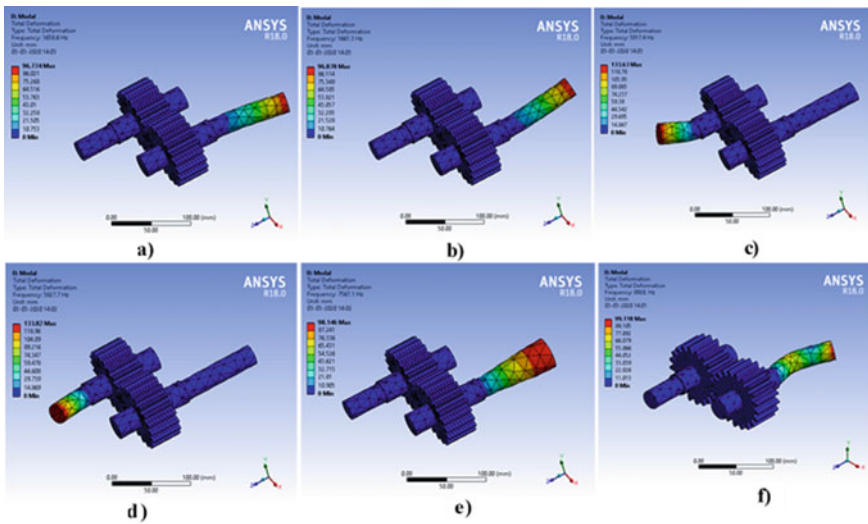
Fig. 5 Six mode shapes of the design. **a** 1st mode **b** 2nd mode **c** 3rd mode **d** 4th mode **e** 5th mode **f** 6th mode

Table 3 Deformation and frequency at six modes

Mode	Frequency in Hz	Deformation in mm
First	1658.6	96.77
Second	1661.3	96.88
Third	5817.4	133.63
Fourth	5827.7	133.82
Fifth	7567.1	98.15
Sixth	8920	99.12

Fig. 6 Frequency w.r.t modes
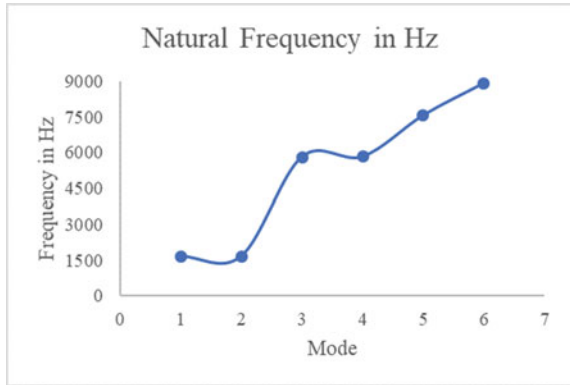
Fig. 7 deformation of shaft w.r.t modes
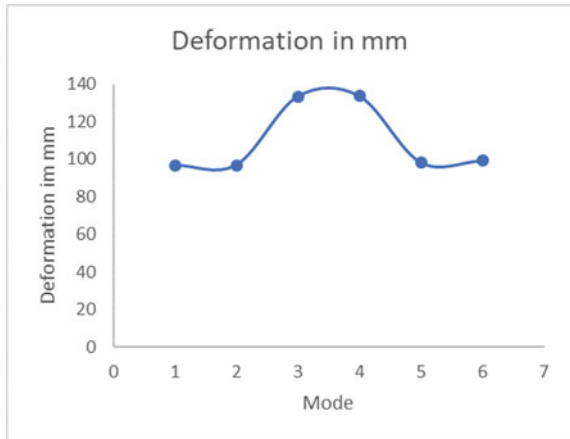
Fig. 8 Deformation on the shaft at loading condition
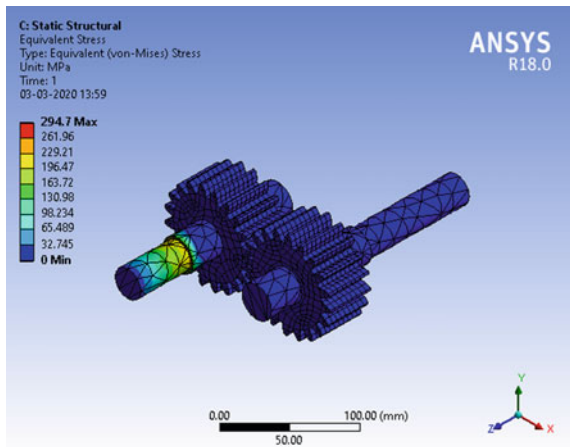
Fig. 9 Stress on the teeth of gears at loading condition
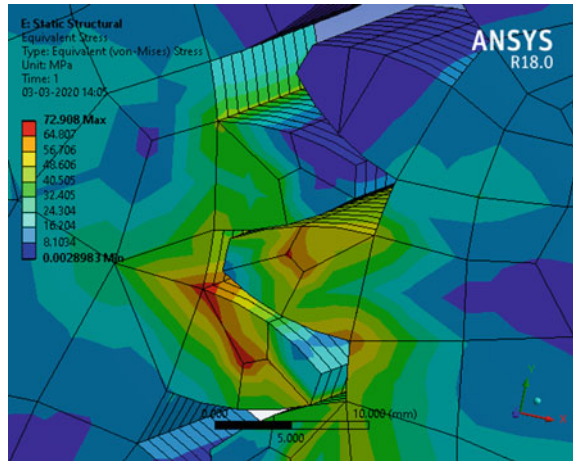
The stress at the shaft is 294.70 MPa (Fig. 8) while at the tooth during operating condition is 72.91 MPa (Fig. 9) which is less than the yield tensile strength of the material used. This shows that the design is safe under the loading condition and it will not fail.

4 Conclusion

In this paper, gear train is designed and the simulations are done. The designing is done in Solidworks and the simulation is done in Ansys software. Two types of simulations are done in this paper. First, the vibrational analysis is done which results six modes of frequencies along with deformation on the shaft. Second, the stress analysis is done in the gear train by applying boundary conditions and 500 N–m moments to one gear. It is obtained that the stress at the shaft is 294.7 MPa while at the gear tooth the stress is found 72.91 MPa. The obtained stresses are less than the yield tensile stress of the gear material which means the gear train will not fail at that loading conditions.

References

1. Bruns T, Schafer E (2010) Modelling and identification of an all-terrain vehicle. Int J Vehicle Syst Modell Test 2(3):276–295
2. Lu J, Litvin FL, Chen JS (1995) Load share and finite element stress analysis for double circular-arc helical gears. Math Comput Model 21:13–30
3. Litvin FL, Chen JS, Lu J, Handschuh RF (1996) Application of finite element method for determination of load share. Trans ASME J Mech Des 118:561–567

4. Litvin FL, Lian Q, Kapelvich AL (2000) Asymmetric modified spur gear drives: reduction of noise, localization of contact, simulation of meshing and stress analysis. Comp Meth App Mech Eng 188:363–390
5. Mohamed Nabi S, Ganesan N (1993) Static stress analysis of composite spur gears using 3D-finite element and cyclic symmetric approach. Compos Struct 25(1–4):541-546
6. Lin T, Ou H, Li R (2007) A finite element method for 3D static and dynamic contact/impact analysis of gear drives. Comput Methods Appl Mech Eng 196(9–12):1716–1728
7. ANSYS 18.0 (2017), https://www.ansys.com/
8. Vinodh Reddy C (2015) 'Gear Terminology', me-mechanicalengineering.com. https://me-mechanicalengineering.com/gear-terminology/. Accessed Oct 7 2015

Recent Researches on the Failure of Spur Gears—Literature Review

Ankit Yadav, Pawan Kumar Singh Nain, and M. Maniraj

Abstract Gears are important mechanical machine component used for transmission. The properties of gears are influenced due to loading, speed of rotation, etc. These factors result in gear failures like wear, fatigue, pitting, etc. Various researches have been carried out to find out the behavior of gears made up of different types of materials. Some research has been done to improve the strength, wear characteristics, and life cycle of the gear. These researches were carried out experimentally with the help of various machines as well as with the help of numerical models. This paper reviews the recent researches carried out on the failure of spur gears.

Keywords Fatigue · Wear · Gear

1 Introduction

Gears are machine elements that transmit motion by means of successively engaging teeth. The gear teeth act like small levers. It is one of the most important parts of the machinery used in industry. They are widely used due to their many advantages like high transmission efficiency, reliable operation, compact structure, etc. Its application can be found from a small clock to complicated aerospace accessories. During transmission, gears are subjected to different amounts of forces due to which they are prone to different types of failure like wear, fatigue, pitting, spalling, etc. Researches have been done to improve the strength and the behavior of gears depending upon the demand by the industries when they are subjected to different parameters with different effects. Researchers are keen to solve these problems of failure of gears so that their life cycle can be increased.

A. Yadav (✉) · P. K. S. Nain · M. Maniraj
Galgotias University, Greater Noida, UP, India
e-mail: ankityadav2108@gmail.com

2 Background

The gears have been used for mechanical transmission for a long time. While transmitting power, the gear generates stresses at the mating points over the teeth, which causes various types of failures in gear. Researches have been done on various materials of gears under different conditions to analyze their behavior. Previously, the gear analysis was generally based upon the experimental approaches and various types of failures were analyzed. Nowadays, the analysis part has become very easy due to computers. Now, we can easily analyze the gear or any other mechanical structure with the help of various softwares. So, in spite of using the experimental approach, we can go for a software approach for analysis.

3 Recent Researches Regarding the Failure of Gears

Suhaghar calculated the wear and service life of varying fiber weight percentages, i.e., 5, 10, 15, and 20% of Madar and Bauhinia Racemosa fiber-reinforced polyester gears. These are the natural fibers that are found from the branches of the tree. Glass fiber-reinforced nylon and acetal gears are manufactured, and some relation was made between wear and surface temperature. Based on the researches, it was concluded that to improve the failure of gears generally due to root and pitch fracture, and these natural fibers were used. The composite gears were rolled and slide against nylon gear with the help of gear test rig, and the results of the test were compared with unreinforced polyester gear. For testing, different amount of torque was provided, i.e., 4, 8, 12, and 16 Nm and results were observed. After the test, it was concluded that the wear rate for composite gears while running with nylon gears was less as compared to unreinforced polyester gears. With an increase in torque, the plastic deformation increases. The service life of composite gear is increased by 16.67% [1].

Bharti Sarita used polyamide 66 and steel gear to check the effect on their surface due to lubricant. The gear was manufactured with the help of injection molding. A power absorption test rig was used to carry out the testing. The effect of lubricant and without lubricant on the gear was checked. The lubricant used was Standard automotive gear oil (SAE 75W85). The gears were provided with various amount of loads, ranging from 1.8 to 4.5 Nm with different parameters taken into consideration like the rotational speed of 800 rev/min. The results indicated that the gear tooth temperature estimated at 4.5 Nm load was 32% greater than that at 1.8 Nm load under dry conditions. Under various load conditions, i.e., 1.8–4.5 Nm, lubricated gears life increased by 66–200%. The lubricant also helped in dissipating the heat at the tooth surface of the gear [2].

Praveen Silori estimated fatigue life along with understanding the stresses which were concentrated on the root of AISI4041 Alloy Steel and Ti6242s. The modeling of gear was done on Solid Edge V19 with the parameters selected accordingly.

For analyzing the stresses on the tooth radius of gear, different gears of varying radiuses like 0.8, 1, 1.2, 1.4 mm were modeled. The analysis and the meshing of gears were done on ANSYS 14.0 for different materials. FEA was done for different tooth radiuses for different materials. The gear assembly was meshed by a solid 186 element. Certain parameters, assumptions, and boundary conditions were given to the system. After the analysis, it was found that for the AISI4041 root radius 0.8 and 1.4 mm were best for design and manufacturing. And for Ti6242S alloy, a 1 mm tooth radius was best suited. The fatigue life and safety factor for Ti6242S alloy were best. These gears can be used for high-temperature applications [3].

Paras Kumar used the AGMA approach to investigate pitting and bending fatigue failure along with the tooth profile of Case Hardened and through-hardened gears. AGMA approach results were compared with FEA results. The tests revealed that case hardened gears delayed pitting, but it increases the chances of bending fatigue failure. The probability of pitting/bending fatigue was highest in the single tooth contact region, and the chances for contact fatigue failure were more in comparison to bending fatigue failure. Through hardened gear showed better bending fatigue life while the case-hardened gear showed better contact fatigue life [4].

Wei Li investigated the effect of shot peening on the contact fatigue strength characteristics of 20CrMnMo carburized gear and hardened gears using up-down test method and grouping test method. The fatigue limit stress values under different reliability were obtained. The results concluded that the contact fatigue strengths of gears increased by 14.56%. The values of gears with or without shot peening processes were 1810 MPa and 1580 MPa, respectively [5].

You Lv investigated the effect of micro-shot peening on the fatigue behavior of Laser melted W6Mo5Cr4V2 steel gear. Both the gears were used for study by laser surface melted (LSM) and laser surface melted and micro-shot peened (LSMMP). The materials used for shot particles were high carbon steels and ceramics. Different materials were used for shot accordingly with different peening time, ranging from the 20 to 100 s. The fatigue behavior was tested using the Forschungsstelle für Zahnräder und Getriebebau (FZG) back-to-back spur gear test machine. The results concluded that the fatigue strength of micro-shot-peened gears was more as compared to laser surface melted gears. The properties of LSMMP did not change with an increase in peening time [6].

Mao investigated the effect of surface temperature and load on the polymer composite gear. The gears used for testing were polymer composite gears running against each other. Acetal and composite (55% nylon, 30% glass fibers, and 15% PTFE as an internal lubricant) were used. The experimental test rig was designed to measure the wear and endurance limit of the gear. The experiment was carried out with different temperatures, different load capacity, and different geometries of gear. A critical torque value was calculated with the help of its surface temperature. The results concluded that the gear performance was totally dependent on the load capacity. With an increase in torque, the wear rate increased. The wear rate of gear was low when it was operated under the critical value [7].

Senthilvelan investigated the effect on the unreinforced and glass fiber-reinforced Nylon 6 spur gears due to the rotational speed. A power absorption-type gear test

rig was used to test the gears at different rotational speeds, i.e., 600, 800, 1000, 1200 rpm, different torque levels, i.e., 1.5, 2, 2.5, 3 Nm and different stress levels, i.e., 8, 15, 20, 25, 30 MPa, respectively. The results concluded that with an increase in rotational speeds, the stress increases, and surface temperature of the gear increases, which causes weakening in gear due to which the gear life decreases. The stress rates were small at low speeds and the gear and gear root cracking were considered to be the only failure modes [8].

Masaya Kurokawa investigated the behavior of various types of carbon fiber-reinforced polyamide gears. The materials used in this paper were polyamide 12(PA12), polyamide 6(PA6), polyamide 66(PA66), polyamide 46(PA46) with carbon fiber-reinforced Polyamide, and in the presence of grease. The test specimens, i.e., the pellets, were dehumidified at 80 °C for 24 h and then injection molded into a gear. The gear testing apparatus was used to investigate the behavior. The apparatus absorbs the power with the help of a powder brake. About 0.5 gm of grease was applied on the teeth surfaces before starting the test. Many properties of gears were investigated in this paper, like load-bearing capability, wear properties, sound properties. The results concluded that PA 12/CF gears were found superior to other gears. Such gears had the highest load-bearing potential and the wear property was found excellent in these gears, the sound properties were also considered to be the strongest as they were the most quiet during the engagement [9].

Anand Mohan investigated the bending fatigue performance of symmetric gears 20°/20° and asymmetric gears 20°/34° of unreinforced and 20% glass fiber-reinforced polypropylene materials with the help of servo-hydraulic fatigue testing machine. The gear teeth was subjected to constant loading and deflection. The results concluded that the bending load capacity increased due to the addition of glass fibers, and the load-carrying capacity of 20°/34° asymmetric gears was better than 20°/20° symmetric gears, due to more gear tooth width at the root region [10].

Dhanashekaran investigated the wear characteristics of sintered spur gear under unlubricated conditions. A MATLAB program was developed to check the changes occurring on the contact point of gear per mesh cycle. Wear prediction was made with the help of Archard's wear formula. The gears used for investigation were Fe–C–Cu, Fe–C–Cu–3%MoS$_2$, and Fe–C–Cu–5%MoS$_2$. The test was conducted on the power absorption-type gear test machine. The gears were subjected to different torques ranging from 1 to 2.5 Nm with the rotational speed of 800 rpm until tooth breakage or 20×10^4 cycles. Experimental results were validated with the predicted methodology. The results concluded that the wear was maximum at the dedendum of the tooth. The addition of MoS2 improved the wear characteristics of the gear like improvement of part density, hardness, strength, and wear resistivity. And the results were quite similar to the predicted results [11].

Ken Mao investigated the wear performance of non-reinforced polyoxymethylene (POM), and 28% glass fiber-reinforced POM (GFR POM). The gears are manufactured using injection molding. A polymer composite gear test rig was specially designed for the test. The difference in the performance of both types of gears was observed. Both the gears were running against each other, i.e., polymer against polymer. The test was carried out with POM gear pairs that were provided with 3Nm

initial torque, and this torque keeps on increasing with 0.5Nm with every 20,000 cycles, and based on that, results were taken into consideration. For GFR POM, initial torque was taken as 6 Nm, and increased by 1 Nm for every 20,000 cycles, and results were observed. The results concluded that 28% of GFR POM showed better performance compared to non-reinforced POM, with about 50% better load capacity. The wear rate of non-reinforced gears increased at high speed above transition load because gear operating temperature reached to the material melting point [12].

4   Conclusion

To complete the requirements of organizations and industries, various researches on the design and analysis of gear have been brought into consideration. Different researchers have used different materials for manufacturing the gears, depending upon the requirements. The effects on the behavior of gears under different operating conditions have been investigated. It is observed that composite gear wear rate is less as compared to unreinforced polyester gear. For high temperature applications, alloys like Ti6242S tooth radius 1 mm, AISI4041 root radius 0.8 mm, and 1.4 mm are preferred. The polyamide 12 carbon fiber gears were found superior to other such gears. Researchers have investigated various forms of failure in gears like wear, fatigue due to load, speed, etc. To avoid the failure in gears and to increase the gear life- lubrication of gear, load capacity, rotational speed, gear tooth width, surface temperature of gear play a major role. It is also seen that fatigue strength increases with micro shot and shot peening processes in the gear. In this review paper, we have summarized the effects of failure in gears, and to resolve these problems, certain methods have been provided by the researchers to increase the gear life.

References

1. Sudhaghar S The wear behaviour and service life of Madar and Bauhinia Racemosa reinforced polyester hybrid composites for gear applications. Mater Today Proc. https://doi.org/10.1016/j.matpr.2019.2019.07.738
2. Sarita B Effects of lubricant on the surface durability of an injection-molded polyamide 66 spur gear paired with a steel gear. Tribol Int. https://doi.org/10.1016/j.triboint.2019.02.050
3. Silori P (2015) Finite element analysis of traction gear using ANSYS. Mater Today Proc 2:2236–2245. https://doi.org/10.1016/j.matpr.2015.07.243
4. Kumar P (2017) Fatigue failure prediction in spur gear pair using AGMA approach. Mater Today Proc 4:2470–2477
5. Li W Experimental investigation on the effect of shot peening on contact fatigue strength for carburized and quenched gears. Int J Fatigue. https://doi.org/10.1016/j.ijfatigue.2017.09.015
6. Lv Y Effect of microshotpeened treatment on the fatigue behaviour of laser- melted W6M05Cr4V2 steel gear. Int J Fatigue. https://doi.org/10.1016/j.ijfatigue.2017.01.017
7. Mao K (2007) A new approach for polymer composite gear design. Wear 262:432–441. https://doi.org/10.1016/j.wear.2006.06.005

8. Senthilvelan S (2007) Effect of rotational speed on the performance of unreinforced and glass fiber reinforced Nylon 6 spur gears. Mater Des 28:765–772. https://doi.org/10.1016/j.matdes.2005.12.002
9. Kurokawa M (2003) Performance of plastic gear made of carbon fiber reinforced polyamide 12. Wear 254:468–473. https://doi.org/10.1016/S0043-1648(03)00020-6
10. Anand Mohan N (2014) Preliminary bending fatigue performance evaluation of asymmetric composite gears. Mech Mach Theory 78:92–104. https://doi.org/10.1016/j.mechmachtheory.2014.03.006
11. Dhanasekaran S (2008) Gear tooth wear in sintered spur gears under dry running conditions. Wear 265:81–87. https://doi.org/10.1016/j.wear.2007.08.025
12. Mao K (2019) The wear resistance improvement of fiber-reinforced polymer composite gears. Wear 426–427:1033–1039. https://doi.org/10.1016/j.wear.2018.12.043

Effect of Seat Cushion Stiffness on Human Comfort

Rohit Kumar, Sachin Kalsi, and Ishbir Singh

Abstract Human body encounters different types of vibration conditions while traveling, performing activities, driving, playing, etc. that results in discomfort and becomes a necessity to work in this domain. In this current study, harmonic analysis has been performed while applying a vibration in a vertical direction while human subjects sitting in sitting posture with backrest support on automotive seats. A 4-layered human subject CAD model of mass 76 kg has been developed to resemble with the realistic properties of human subject that includes shape with proper dimensions and biodynamic properties of bone, organs, muscle, and skin. For cushion material of seat Polyurethane foam has been used with its stiffness and damping properties. The study has been performed on human subject sitting on a seat cushion with varying thickness of fixed backrest at angle of 0° and excited with magnitude of 1.0 m/s^2 in the frequency range 0–20 Hz. The seat-to-head transmissibility (STHT) has been evaluated using FEM and found that the maximum value of transmissibility effect is 3.12 at frequency of 6 Hz; but then decreases due to stiffness and damping of the cushion material of seat and backrest. It has been found from the current study that seat cushion has good vibration absorbing properties due to which there observed a less effect of vibration at more value of cushion thickness and also, it has been analyzed that the backrest cushion can also result in improving the human body ride comfort.

Keywords Sitting posture · FEM · Harmonic response · Frequency · Damping · Transmissibility

R. Kumar · S. Kalsi
Department of Mechanical Engineering, Chandigarh University, Punjab, India

I. Singh (✉)
Department of Mechanical Engineering, Gulzar Group of Institutes, Punjab, India
e-mail: ishbir@rediffmail.com

409

1   Introduction

In the current modern era, humans expect comfort in their life while working, traveling, sitting, as well as sleeping also, etc. While traveling by any type of vehicle or automotive-like bus, car, tractor, train, ship, etc. people expect that vehicles provide the best comfort level. But in all these environments, the human subjects get vibration by the contact area which causes discomfort and some health issues. So, automotive seats are designed to provide a good comfort level and ensure to have less risk factors. But the vibration generated has the opposite effect on the human body. The vibration effect also depends on the intensity of vibration, time, body posture, human body type, etc. Some adverse effects of the vibration are low back pain when continuously exposed to low-frequency vibration, changing in heart rate, muscular contraction and fatigue in the human body caused by suppression of motor reflexes, losses of eye vision, musculoskeletal disorders like spline fracture, insensitivity to some body parts during driving, etc. [1]. These effects show the WBV (whole-body vibration) is harmful to the human body and found to be a very important factor in automotive ride comfort.

Related to this work, lots of research has been performed in the field of vibration for analysis of vibration effect on the human subject using different sitting postures. Mohajer et al. [2], Hou [3], Toward and Griffin [4] conducted the study on human subjects using variant biodynamic models. Barbeau [5], Ebe and Yamasaki [6], Corbridge and Griffin [7] conducted a study on seat cushions and their effect on human subject. Liang and Chiang [8], Cho and Yoon [9], Shakhlavi et al. [10], Chalotra et al. [11] conducted a study on biomechanical model of the human body to evaluate the biodynamic responses to vertical vibration and transmitted accelerations for the seated position. Nupur et al.[12], Mehta and Tiwari [13] performed a study on tractor seats and human subjects. Vijay Prasad et al. [14], Witkiewicz and Zielinski [15] performed a study on foam composites. Kim et al. [16], Valentini and Vita [17], Grujicic et al. [18], Singh et al. [19], Kitazaki and Griffin [20], Patel et al. [21] performed a study on human subject to observe the effect of vibrations and a method to reduce it under variant conditions.

It has been absorbed from the current existing literature that there still a requirement to further study the transmissibility of human subjects in sitting posture by considering the stiffness and damping parameters of cushion material. As the cushion material has been more effective while evaluating about the comfort level of human subject. In the current study, a study has been performed on an Indian male human subject of mass 76 kg using 95th percentile anthropometric data of male population by replacing cushion material with spring and damper. The transmissibility of human subjects has been evaluated while a whole-body vibration has been applied in a vertical direction using FEM method.

2 Methodology

A realistic human body has been represented with a four layers CAD model i.e., bones, organs, muscles, and skin using 95th percentile Indian anthropometric data [22–24] with human subject in sitting posture. A seat has been considered with available cushion material properties as per literature. The material properties of all these organs and different layers of human subjects have been taken from existing literature. The effect on transmissibility from seat to head has been evaluated and observed while a cushion material has been represented with spring along with damping properties.

2.1 3D Solid Model of the Human Subject with Seat Cushion

The 3D solid model is the human subject in sitting posture that has been considered for harmonic analysis. The human subject has been designed by considering by taking 95th percentile Indian anthropometric data. This CAD model of human subject has been introduced four-layer concept that includes bones, organs, muscles, and skin. The bones have been considered as layer 1, organs as layer 2, muscles as layer 3, and skin as layer 4. The biomechanical properties of the human subject have been considered from existing literature [25–28].

The average thickness of the skin layer has been considered to be 1 mm from existing literature [28]. The layers of the 3D solid model of human subjects give a brief explanation of the human body which can be a better outcome during FEM analysis. In layer 2, organs have been considered the heart, liver, lungs, and stomach have been considered because these organs are mostly affected by the vibration. The biomechanical properties of the human subject have been considered from existing literature shown in Table 1. The average properties of each layer have been mentioned that helps to give better outcomes of FEM analysis in sitting posture. 4 layers of the human subject give a detailed representation of a human subject and make it real as like as a human. The solid model within sitting posture has been designed with the help of solid works 2018 as shown in Fig. 1a.

Table 1 Biomechanical and mechanical properties of human subjects & seat cushion [25–28]

Type	Density (kg/m3)	Young's modulus (MPa)	Poisson ratio
Bone	1700	12000	0.3
Organ	1065	0.06	0.3
Muscles	1062	13	0.3
Skin	1100	0.15	0.46
Polyurethane foam (Coir rubber foam) Seat cushion	62.25	0.3	25
Polyurethane foam (Coir rubber foam) Backrest seat cushion	58.23	0.3	25

(a)   (b)
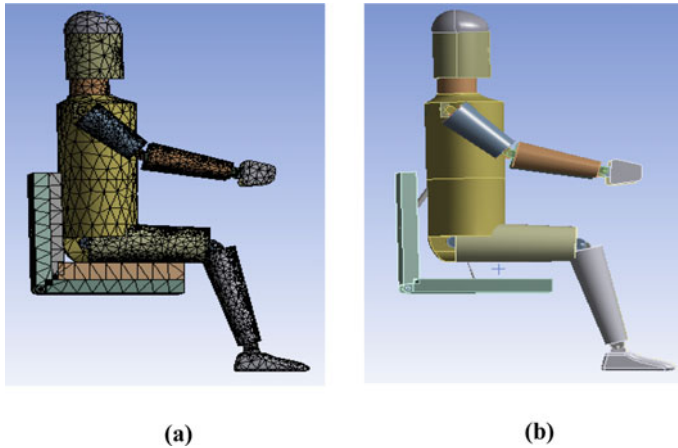
Fig. 1 **a** Meshed model; **b** representation of seat cushion

Now, these days there is so much comfort in the automotive seat because of the suspension system in the vehicle seat. So in this paper, simulation has been performed on the solid model that is shown in Fig. 1a, and vibration effect has been analyzed on the seat cushion in the vertical vibration with the 0° angle of the backrest and thickness of the seat and the backrest cushion. The cushion's mechanical properties and their dimension have been considered from the existing literature [13–15, 18, 29]. The cushion has been considered that has been generally used in the different types of automotive. The selected cushion material of different mechanical properties and thickness i.e., coir rubber foam (polyurethane foam) [13] that materials are hard which are generally laminated with medium density polyurethane foam for use as the automotive seats are used to increase comfort level [13]. It has been found that 60–70% of human body mass depends upon the body shape, size, and posture in the seat. So the seat pan cushion is compressed with high forces and the seat backrest cushion due to vertical vibration as compared to fore-aft and lateral vibration under different dynamic conditions [30]. So, generally, it is recommended that the thickness of the seat pan cushion must be greater than backrest cushion. So in this study, seat pan cushion thickness has been considered greater than backrest cushion. The density of the cushion material has been considered according to the thickness of the cushion and the damper and stiffness have been taken from existing literature that cushion used in the automotive. The frame of the seat has been considered as the medium carbon steel material from existing literature [31] that has been generally used in automotive, whose density is 7850 kg/m^3, young's modulus is 20700 MPa, and the Poisson ratio is 0.3 [32].

Figure 1a shows the meshing of the solid model where the tetrahedral mesh has been considered due to the complex structure of the solid model. There are multiple segments in the model due to which there is error in other meshing types but in the

tetrahedral mesh, by considering automatic mesh size, there is found to be no error in the meshing.

Tetrahedral element has triangular shape where it has 4 faces, 4 vertices, 6 edges, and bounded by 4 triangular faces where tetrahedral volume mesh generated automatically. By these properties of tetrahedral mesh, it becomes flexible with any type of complex model [33]. In this paper, harmonic analysis has been performed on reverse engineering of the automotive seat with a human subject. So before the suspension system in automotive, there was also less vibration effect on the human subject due to seat cushion and their properties. In Fig. 1, a male subject is seated on the seat, and properties of seat material used in this simulation study shown in Table 1, which are considered for the seat cushion. Figure 1b shows the suspension of the seat cushion with their stiffness and damping coefficient in the backrest foam and seat foam.

In Fig. 1b, cushion has been replaced with the spring that shows the suspension of the seat with their property. It shows the actual motion of human subjects according to their comfort. Spring has been connected from the backrest seat to the back of the male subject that helps to give comfort to back during traveling. And the second spring has been connected from seat foam to hip where the thickness of the seat foam becomes greater than backrest foam for increasing comfort level. During traveling backrest foam gives comfort to back body part but seat foam gives whole body comfort and it also reduces the vibration effect. Therefore, in this study, analyze the effect of vibration generated from the road profile and the automotive. In this study, the harmonic analysis has been considered on the head where the seat, feet, and backrest become fixed that has been shown in Fig. 1b. The boundary conditions have been considered as the analysis of transmissibility from seat to head where the seat and feet are assumed to be fixed. The human subject seated in the vertical direction with backrest support in only vertical direction has been considered for excitation [19]. The excitation magnitude 1 m/s^2 [34] has been considered and the frequency range lies within 0–20 Hz the human body suffers from ill-effects like motion sickness and lower back pain in this frequency range which are commonly found in vehicle drivers [35].

3 Result and Discussion

In this study, seat-to-head transmissibility has been analyzed that is a complex ratio of the motion of the head to the exciting acceleration motion at the seat-body interface. The result obtained after performing harmonic analysis to find out the Seat to Head Transmissibility (STHT) of male subject seated on an automotive seat where there is no suspension system and the seat cushion have their vibration absorber properties have shown in Fig. 2.

In the current study, transmissibility has been analyzed from seat to head, it has been found that the head has high magnitudes of transmissibility and the maximum peaks lies at the frequency of 6 Hz, the first peak lies from 5 to 7 Hz, and reduction of transmissibility peak at frequency 8 Hz, and then after the 2nd peak at 12 Hz

Fig. 2 Comparison of the results
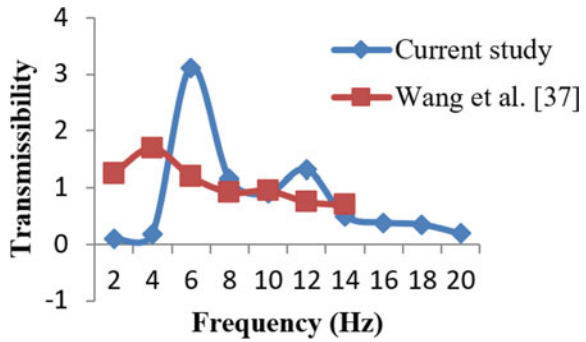
and the transmissibility peak is reduced to lower than 14 Hz for head shown in Fig. 2. The cushion, backrest cushion, and their shock absorber properties reduce the frequencies. The transmissibility peak values can be decreased by increasing the foam damping. Therefore, when the floor excitation frequency is applied, minimum transmissibility at this frequency can be achieved by selecting proper stiffness and damping coefficients of the seat cushion and backrest cushion to minimize the vibration transmission to the human body and maximize the ride comfort [36]. The current result has been validated with the experimental result of Wang et al. [37], the authors evaluated the seat to head transmissibility (STHT) on 12 human subjects in different sitting postures i.e., without backrest support, vertical backrest support, and inclined backrest support in vertical and fore-and-aft direction at excitation of 0.25, 0.5, and 1.0 m/s^2 between 0 and 15 Hz frequency range. A helmet-strap-mounted accelerometer mounting system was designed to measure the effect of vibration along the three translational axes. The vibration effect in vertical excitation at 1 m/s^2 rms that the first and maximum primary peak lies at frequency 5 Hz and the second peak lies between frequencies range 8–12 Hz and continuously decrease. It might be due to the different biomechanical properties of 12 human subjects and the different stiffness and damping coefficient of the seat cushion and backrest cushion.

Comparing the current study result with a study conducted by Wang et al. [37] shows maximum transmissibility effect i.e., 1.78 at 5 Hz in a validated result and 3.12 at 6 Hz frequency in the current study. After the primary peak in both studies, another peak is 0.95 at 10 Hz in validated paper and in current study another peak at 12 Hz is 1.32. After the comparison, it has been found that there is an approximate value with the existing literature. There is a difference in the result due to different models and different positions of hand and leg and also this may be due to variation in properties of model and difference in body structure dimensions which has been used in the study.

4 Conclusion

This study has been performed to analyze the human body response to vibrations on the automotive seat by using reverse engineering. For this work, coir rubber foam has been considered where the seat has seat cushion and backrest cushion in vertical angle but there is no suspension system. In FEM analysis, human body response has been analyzed using measured seat-to-head biodynamic response in the vertical direction with excitation magnitude 1.0 m/s^2 rms in the frequency range 0–20 Hz. There is a peak value of the transmissibility effect that shows that the highest magnitude of 3.12 is lies at 6 Hz frequency and then it decreases due to stiffness and damping of the seat cushion and backrest cushion. By comparing the current results with validated results and found to be approximately near to each other. So this study showed that seat cushion has good vibration absorber properties due to which there found to be less effect of vibration without seat suspension system and also showed that the backrest cushion can improve the human body ride comfort.

References

1. Griffin MJ, Erdreich J (1991) Handbook of human vibration, no. 4. J Acoust Soc Am 90:2213–2213
2. Mohajer N, Abdi H, Nahavandi S, Nelson K (2017) Directional and sectional ride comfort estimation using an integrated human biomechanical-seat foam model. J Sound Vib 403:38–58
3. Hou Z (2014) Study on the vertical vibration of an occupant—seat cushion system. In: Internoise 2014—43rd international congress on noise control engineering: improving the world through noise control
4. Toward MGR, Griffin MJ (2009) Apparent mass of the human body in the vertical direction : effect of seat backrest. J Sound Vib 327(3–5):657–669
5. Barbeau R, Weisser T, Dupuis R, Aubry E, Baudu S (2019) Assessment of the impact of sub-components on the dynamic response of a coupled human body/automotive seat system. J Sound Vib 459:114846
6. Ebe K (2004) Effect of foam characteristics at backrest and underneath thighs on vibration transmission and seating comfort. Technical report, Bridgestone Corporation, Chemical Automotive Components Development Department, pp 3729–3732
7. Corbridge C, Griffin MJ (1989) Seat dynamics and passenger comfort. SAGE J 203(1):57–64
8. Liang C, Chiang C (2008) Modeling of a seated human body exposed to vertical vibrations in various automotive postures. Ind Health 46(2):125–137
9. Cho Y, Yoon Y (2001) Biomechanical model of human on seat with backrest for evaluating ride quality. Int J Ind Ergon 27(5):331–345
10. Shakhlavi SJ, Marzbanrad J, Tavoosi V (2018) Various vehicle speeds and road profiles effects on transmitted accelerations analysis to human body segments using vehicle and biomechanical models. Cogent Eng 3(1):1–17
11. Chalotra PP, Chand SK, Kumar P, Saran VH (2013) Comparision of the transmission whole-body vibration to the body segments of standing subjects holding handle and handrail. MIT Int J Mech Eng 3(1):63–68
12. Nupur Y, Tewari VK, Thangamalar R, Kumari S, Kumar A (2013) Translational vibration evaluation of tractor seats for ride comfort. Agric Eng Int CIGR J 15(4):102–112
13. Mehta CR, Tewari VK (2002) Vibrational characteristics of tractor seat cushion materials and ride comfort. J Low Freq Noise Vib Active Control 21(2):77–85

14. Vijayprasad S, Bidarakatti SR, Naikar S, Rathod AK, Hiremath PGS (2017) Characterization of mechanical and physical properties of polyurethane cored sandwich. Int J Res Appl Sci Eng Technol 5(6):1163–1176
15. Witkiewicz W, Design S, Protection E (2006) Properties of the polyurethane (PU) light foam. Adv Mater Sci 6(2):10
16. Kim TH, Kim YT, Yoon YS (2005) Development of a biomechanical model of the human body in a sitting posture with vibration transmissibility in the vertical direction. Int J Ind Ergon 35(9):817–829
17. Vita L, Valentini PP (2002) DAViD—a multybody virtual dummy for vibrational com-fort analysis of car occupants. In: NATO science series 103, 3–8. Kluwer Academic Publisher, Holland
18. Grujicic M, Pandurangan B, Arakere G, Bell WC, He T, Xie X (2009) Seat-cushion and soft-tissue material modeling and a finite element investigation of the seating comfort for passenger-vehicle occupants. Mater Des 30(10):4273–4285
19. Singh H, Singh A, Singh S (2018) Investigation of occupational whole-body vibration exposure among Indian tractor drivers investigation of occupational whole-body vibration exposure among Indian tractor drivers Amandeep Singh*, Lakhwinder Pal Singh and Sarbjit Singh Harwinder Singh
20. Kitazaki S, Griffin MJ (1998) Resonance behaviour of the seated human body and effects of posture. J Biomech 31(2):143–149
21. Patel PSD, Shepherd DET, Hukins DWL (2008) Compressive properties of commercially available polyurethane foams as mechanical models for osteoporotic human cancellous bone. BMC Musculoskeletal Disorders 7(9):5–11
22. Chakrabarti DK (1997) Indian anthropometric dimensions. For ergonomic design practice. National Institute of Design, Ahmedabad, pp 30–93
23. Chaurasia BD (2006) Human anatomy regional and applied dissection and clinical lower limb, abdomen & pelvis, 4th edn, vol 2. CBS publishers & distributers
24. Chaurasia BD (2004) Human anatomy regional and applied dissection and clinical up-per limb and thorax, 4th edn, vol 1. CBS publishers & distributers
25. Guo LX, Dong RC, Zhang M (2016) Effect of lumbar support on seating comfort predicted by a whole human body-seat model. Int J Ind Ergon 53(1):319–327
26. Choi APC, Zheng YP (2005) Estimation of Young's modulus and Poisson's ratio of soft tissue from indentation using two different-sized indentors: finite element analysis of the finite deformation effect. Med Biol Eng Comput 43(2):258–264
27. Hasgall PA, Di Gennaro F, Baumgartner C, Neufeld E, Lloyd B, Gosselin MC, Payne D, Klingenböck A, Kuster N (2018) IT'IS database for thermal and electromagnetic parameters of biological tissues, Version 4.0, IT'IS
28. Dong R, He L, Du W, Cao Z, Huang Z (2019) Effect of sitting posture and seat on biodynamic responses of internal human body simulated by finite element modeling of body-seat system. J Sound Vib 438:543–554
29. Kumbhar P, Li N, Xu P, Yang J (2014) Optimal seat dynamic parameters determination for minimizing virtual driver's fatigue. SAE Int 1(1):877
30. Pywell JF (1993) Automotive seat design affecting comfort and safety. SAE Tech Papers 4(06):448–452
31. William D, Callister J, David GR (2015) Fundementals of materials science and engineering, 5th edn. Wiley binder version, USA
32. Kitazaki S, Griffin MJ (1997) Resonance behaviour of the seated human body and effects of posture. J Biomech 31(2):143–149
33. Filipovic N (2020) Computational modeling of dry-powder inhalers for pulmonary drug delivery. Comput Model Bioeng Bioinf 257–288
34. Harsha SP, Desta M, Prashanth AS, Saran VH (2014) Measurement and bio-dynamic model development of seated human subjects exposed to low frequency vibration environment. Int J Veh Noise Vib 10(2):1–24
35. ISO 2631-1 (1997) International Standard ISO 2631-1, 2nd edn. ISO, Switzerland

36. Kumbhar O, Xu P, Yang J (2013) Evaluation of human body response for different vehicle seats using a multibody biodynamic model. SAE Int 2(1):0994
37. Wang W, Rakheja S, Boileau PE (2006) Effect of back support condition on seat to head transmissibilities of seated occupants under vertical vibration. J Low Freq Noise Vib Acive Control 25(4):239–259

Fabrication and Mechanical Characterization of Aluminium Alloy Reinforced with Silicon Carbide and Fly Ash

Chayan Arora, Mohit Gupta, Ayush Kaushik, Jeevan Singh Bisht, and Pallav Gupta

Abstract Aluminium-based metal matrix composites are among one of the most widely matrix composites which are used in automobile sector, aerospace, and other engineering applications. In present study, Al-based metal matrix composite is manufactured and reinforced by silicon carbide and fly ash at various weight percentages. The aluminium matrix composite (MMC) is made with the help of stir casting method. In this paper, the mechanical properties like hardness, impact strength of Al MMC are investigated for different mass percentages of fly ash and silicon carbide. It has been observed through this study that the hardness and impact strength are increased when weight percentage of SiC and fly ash is increased. The mechanical test result of block 3 (Aluminium 95%, SiC 5%, fly ash 5%) shows increased strength and hardness. It is expected this study will be effective in the evolution of lightweight composites for aerospace industries and in shipping industries applications.

Keywords Metal matrix composites · Stir casting · Fly ash · Silicon carbide

1 Introduction

In the present era, with the highly modernized technology, there is a demand of the advanced engineering composites for different engineering applications. To fulfil such need, MMC, i.e. metal matrix composite is one of best source. Composite materials are among the best and effective solution for such requirement. The main constituent of the composite is called as matrix and the other element is known as reinforcement. Elements which are reinforced in metal matrix lead to foundation of reinforced composites. Composites possess high characteristic than individual element [1–4]. There are variety of metal which can be used for metal matrix such as aluminium, titanium, magnesium, copper, and their alloy. The opportunity of aluminium-based matrix composite is better than other reinforced counterpart reason of combining aluminium, SiC, and fly ash to get the desirable property of the entire

C. Arora · M. Gupta · A. Kaushik · J. S. Bisht (✉) · P. Gupta
Department of Mechanical Engineering, ASET, Amity University, Noida, Uttar Pradesh, India
e-mail: jsbisht1@amity.edu

419

element. Aluminium will act as continuous phase in aluminium-based metal matrix composite and other reinforcement elements will act as discontinuous phase. The process that we will use for mixing the reinforcement in aluminium metal matrix is stir casting. The aim of present work is to produce matrix composite of aluminium reinforced with silicon carbide and fly ash by the method which is stir casting and to observe the effect of different percentage distribution of fly ash and SiC on the mechanical behaviour of metal matrix composite. The material retains their identities in the composite that is they are not mixed or unite completely into each other even though they perform [2–5].

In this paper, Aluminium metal matrix composite is created in which SiC and fly ash are reinforced in Al-based MMC. Silicon carbide-based aluminium matrix composite had been developed over time due to supreme properties like light in weight and wear resistance and hardness. They are used in much application such as aerospace, aircraft, automobile, and electronic industry. The metal matrix composite is developed by mixing SiC and fly ash in a different weight percentage with aluminium 6063 by the stir casting method. There are various possibilities of obtaining of metal matrix composites (MMCs) with uniform and not changing during the process of creating a reinforcement phase [6]. There are many casting methods but stir casting method is mostly preferred because the process is simple and flexible. Stir casting helps to provide quality mixing of particles because of the vortex created in the surface of the melt. This technique is one of the most effective and inexpensive of all the available manufacturing methods for MMC [6–10]. Fly ash is among the cheapest and low-density reinforcement. The use of fly ash in composite helps in reducing crack problems. Fly ash possesses high electrical resistance and low thermal conductance. As fly ash possesses low density, it can be helpful for producing lightweight-insulated composites. Use of fly ash reinforcement in aluminium casting reduces the cost, decreases density, and increases hardness, stiffness, wear, and abrasion resistance. The silicon carbide has high strength, high hardness, and high stiffness. Silicon-reinforced aluminium metal matrix composites are used in many industries because of its lightweight and high strength and stiffness. The composite containing silicon carbide (reinforcement) and aluminium (matrix) has effective more load carrying capacity [11–13].

The mechanical characterization (tests are performed) of the composite with different percentage composition of silicon carbide and fly ash is carried out to know the change in strength and hardness. The test performed in this paper is impact Charpy and hardness test. The impact Charpy test is used to provide the shock absorbing capability of material subjected to sudden applied shock loads. It helps to determine the rupture energy, modulus of rupture, and notch impact strength whereas the hardness is determined with the help of Rockwell hardness test (HRB number).

Table 1 Composition of Al6063

Element	Silicon	Iron	C	Mg	Chromium	Zn	Ti	Al
Weight (%)	0.4	0.20	0.05	0.05	0.06	0.10	0.08	98. 6

Table 2 Composition of SiC

Elements	SiC	Si	SiO$_2$	Fe	Al	C
Weight (%)	98.5	0.3	0.5	0.08	0.1	0.3

2 Materials

2.1 Aluminium Alloy 6063

Aluminium is among widely available metal available on earth's crust, which comprises 8% of its weight which is widely used in main matrix element in composite material. Aluminium 6063 alloy has the magnesium and silicon as the alloying element (Composition shown in Table 1). Al6063 possesses excellent properties as it is also heat treatable and can be welded easily. Al6063 can be used in architectural fabrication, used for windows and door frames, pipes, and used for making aluminium furniture.

2.2 Silicon Carbide

SiC is a semiconductor which comprises of Silicon (Si) and Carbon (C). SiC is also called carborundum. Silicon carbide maintains its strength to a high temperature range approaching to 1600–1700 °Cwithout any strength loss [6]. When SiC is mixed in aluminium-based matrix composites, SiC helps to improve the toughness of the composite along with making composite corrosion free with high wear resistance. It is one of the finest abrasives ever produced and is useful in fabrication of different materials such as tools, the automobile parts, wear resistance parts of pumps, and rocket engine and is also used in making led's. Composition of silicon carbide is given in Table 2.

2.3 Fly Ash

Fly ash is one of the cheapest and easily available reinforcement materials available in coal industry with lower density, as fly ash is the waste left out when coal burns in the power plants [6, 7]. Its composition is given in Table 3. The main advantage

Table 3 Composition of fly ash

Element	SiO_2	Al_2O_3	Fe_2O_3	CaO	LoI
Weight (%)	40	20	25	8	5

of fly ash is that fly ash reduces crack problems and can be used as an admixture. It is much cost effective as it is easily available in industries where coal is used fly ash is an environmentally friendly material.

3 Casting Method

3.1 Stir Casting

The stir casting is a liquid-state method with the help of which composites are fabricated, in which a reinforcement is mixed with a metal matrix which is in a molten state by means of stirring with the help of stirrer [2, 8]. The MMC fabricated in this paper was carried out with the help of stir casting. A stir casting machine consists of an electric furnace and a stainless-steel stirrer shown in Fig. 1. Stirrer is stirred at different speeds which are regulated by the meter assembled on the machine. While fabricating MMC, the equal distribution of the reinforcing material in the matrix metal is obtained by stir casting method as to carry out good bonding between reinforcement and matrix.

Why stir casting is preferred over other casting method:

- Process is simple and flexible.
- Stir casting can be used in mass production [6].
- The stir casting technique can be used to provide homogeneous mixing of particles reinforced in metal matrix.
- This technique helps in fabrication of large-sized component.

Fig. 1 Stir casting machine

4 Experimental Procedure

In this study, we used Al6063 aluminium as the matrix phase whereas silicon carbide powder and fly ash powder are used as the reinforcement, and the composites were produced by stir-casting method. In this method, SiC and fly ash are preheated in crucible of graphite material having melting point near about (3600 °C) in muffle furnace at 400° for 1 h so that excess moisture and entrapped gases can be removed from the SiC and fly ash but before preheating the reinforcement crucible is preheated for 15–20 min to remove moisture from crucible (shown in Figs. 2 and 3). At the same time, aluminium is kept in preheated crucible and preheated at 400 °C for 30 min in electric furnace after which the temperature is raised slowly to 720 °C on which aluminium starts melting. When aluminium is melted completely, then stirrer is placed inside the crucible and stirring of the melt is done. When the vortex is

Fig. 2 Preheating of crucible
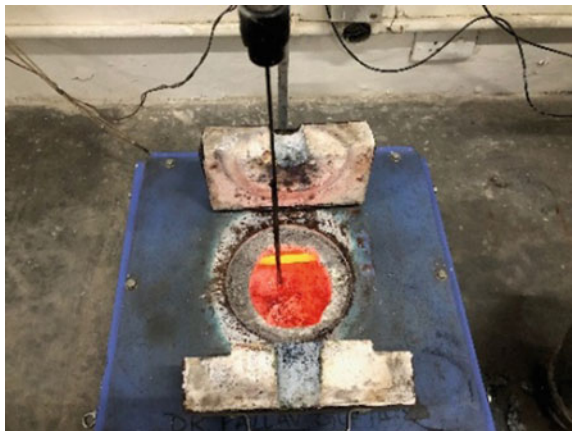
Fig. 3 Preheating of SiC and fly ash in crucible
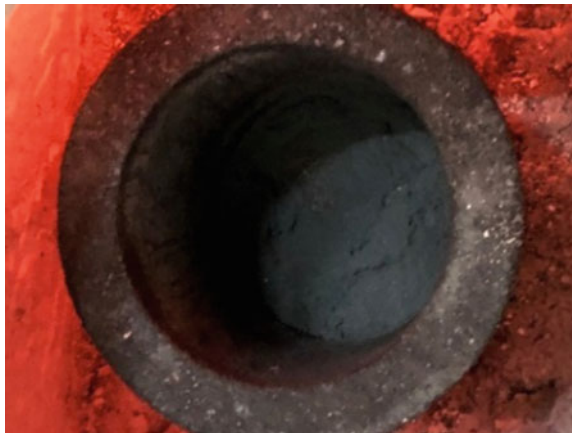
Table 4 Different samples with their weight %

$AlSiC_1$	96% Al6063 + 2% SiC + 2% Fly ash
$AlSiC_2$	94% Al6063 + 3% SiC + 3% Fly ash
$AlSiC_3$	90% Al6063 + 5% SiC + 5% Fly ash

formed at the centre surface of the melt due to stirring then the preheated reinforced (i.e. silicon carbide and fly ash) are being added from the side of the vortex to the molten aluminium [7–9].

Vortex method helps in providing uniform distribution of reinforcement into metal matrix composite; the vortex is developed because of the pressure difference between the inner most and outer most surface of the melt. It was advised that the turbine stirrer should be placed 35% liquid below and 65% liquid above melt to minimize the porosity level [5, 10, 11]. Stirring is done to allow mixing of reinforcement and aluminium. Continuous stirring is done for 5–7 min so that the reinforcement get distributed into the aluminium matrix phase properly. After mixing, the Al matrix composite reinforced with SiC and fly ash is poured in the die kept in sand pool. Similar process is carried out for different composition of SiC and fly ash for different specimens. After the casting is carried out successfully then machining of the part is done to provide surface finish for Charpy test; the specimen size should be of 55 mm × 10 mm × 10 mm. Then mechanical characterization (tests are performed) of the composite with different weight percentage composition are carried out to know the change in strength performed on different machines (shown in Table 4).

5 Results and Discussion

5.1 Impact Charpy Test

It is the test which is used to provide the shock absorbing capability of material subjected to suddenly applied shock loads. It determines the rupture energy, modulus of rupture, and notch impact strength. The test specimen is held in clamp device. A hammer-like pendulum hits the specimen with certain force. The specimen before and after performing the test is shown in Figs. 4 and 5. This impact can be seen on impact measuring gauge. For impact Charpy test, the dimension of the part should be 5 mm × 10 mm × 10 mm and notch is being made at an angle of 45° [2]. The observed readings of the Charpy test are given in Table 5. The graph in Fig. 6 shows the results of Charpy test.

Fig. 4 Specimens before
testing performed

Fig. 5 Specimens after
testing performed

Table 5 Readings of impact
Charpy test

Sample No	Reading 1 (J/mm^2)	Reading 2 (J/mm^2)	Mean average (J/mm^2)
AlSiC$_1$	3.125	3.246	3.1855
AlSiC$_2$	3.525	3.45	3.4875
AlSiC$_3$	3.624	3.532	3.578

5.2 Rockwell Hardness Test

Rockwell test is among the commonly used hardness test method used to measure
or used to identify the hardness of any substance with higher accuracy than other
methods. This test can be used for testing hardness of any metals.

Fig. 6 Shows the effect of impact Charpy test on specimen

IMPACT CHARPY TEST
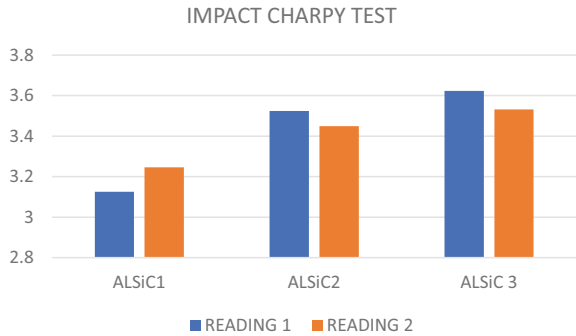
Table 6 Readings of rockwell hardness test

Sample No	Reading 1	Reading 2	Mean average
AlSiC$_1$	66	50	58
AlSiC$_2$	72	68	70
AlSiC$_3$	76	72	74

The Rockwell test helps to measure the depth of the indentation produced by a load on an indenter. The force is applied to sample by use of diamond or ball indenter. The load breaks the surface to lower down the effect of the finish of the surface.

The test is carried out when initially a of minor load of 10 kgf is and then major load is applied and is left to penetrate for 20 s, the load is released and the scale reading is noted down (as on B scale) then the calculation is carried out be determine the HRB number (Table 6 shows the readings). Results of Rockwell test are plotted in Fig. 7.

Fig. 7 Shows the effect of Rockwell hardness test on specimen

ROCKWELL HARDNESS TEST
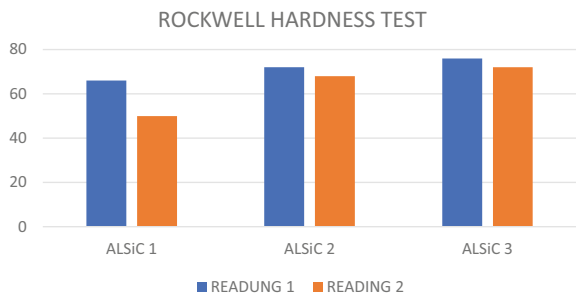
6 Conclusion

(a) Hybrid composite by varying SiC and fly ash has been fabricated by the stir casting method.
(b) The research shows that hardness increases when the weight percentage of SiC and fly ash is increased.
(c) Study shows that impact strength starts increasing when weight percentage of SiC and fly ash is increased.
(d) The study shows that use of fly ash for fabrication of composites is useful and effective way of make industrial waste into industrial wealth.

References

1. Mohan V, Kori SA, Sridhar BR, Padasalgi Shrishail B (2012) Synthesis and characterization of aluminium alloy A356 and silicon carbide metal matrix composite. In: 2nd international conference on industrial technology and management (ICITM 2012), IPCSIT, vol 49, pp 752–756. IACSIT Press, Singapore
2. Paulraj D, Majeed SA, Rajendran R (2017) Influence of nano TiO2 particles on the properties and behaviour of A356 aluminium metal matrix composites (No. 2017-28-1986). SAE Technical Paper
3. Spasova D, Radev R, Atanasov N, Yankova R (2019) Investigation to obtain complex relief MMC with metal matrix Al and Cu reinforcement phase. Adv Mater Process Technol 5(3):394–400
4. Clyne TW, Hull D (2019) An introduction to composite materials. Cambridge University Press
5. Kumar D, Phanden RK, Thakur L (2020) A review on environment friendly and lightweight magnesium-based metal matrix composites and alloys. Mater Today Proc
6. Singh V, Prasad RC (2004) Tensile and fracture behavior of 6061 Al-SiCp metal matrix composites. In: International symposium of research students on materials science and engineering, pp 20–22
7. Hatch JE (1984) Properties and physical metallurgy. Am Soc Metals 134–199
8. Jayashree PK, Shankar MG, Kini A, Sharma SS, Shetty R (2013) Review on effect of silicon carbide (SiC) on stir cast aluminium metal matrix composites. Int J Current Eng Technol 3(3):1061–1071
9. Kataria R, Singh RP, Sharma P, Phanden RK (2020) Welding of super alloys: a review. Mater Today Proc
10. Kok M (2005) Production and mechanical properties of Al2O3 particle-reinforced 2024 aluminium alloy composites. J Mater Process Technol 161(3):381–387
11. Garg P, Jamwal A, Kumar D, Sadasivuni KK, Hussain CM, Gupta P (2019) Advance research progresses in aluminium matrix composites: manufacturing & applications. J Mater Res Technol 8(5):4924–4939
12. Reddy PS, Kesavan R, Ramnath BV (2018) Investigation of mechanical properties of aluminium 6061-silicon carbide, boron carbide metal matrix composite. Silicon 10(2):495–502
13. Nair SV, Tien JK, Bates RC (1985) SiC-reinforced aluminium metal matrix composites. Int Metals Rev 30(1):275–290

Mechanical Regenerative Braking System for Higer Bus

Dabi Beyen, Ramesh Babu Nallamothu, Anantha Kamal Nallamothu, and Seshu Kishan Nallamothu

Abstract Many efforts have been made in finding alternative energy sources rather than based on petroleum fuels due to its intermittency and increase in price. The other approach is to use the available energy effectively by minimizing energy wastage and recycling energy by using regenerating devices. During braking the vehicle, the kinetic energy of the vehicle converted into heat energy and wasted to the environment. This braking energy can be stored in regenerating devices such as the flywheel, high voltage battery, and flat spiral spring before it converted into heat. The restored energy can be reused to restart the vehicle or for acceleration. This work aimed to design and analyze MRBS for Higer bus using a flat spiral spring as an energy storage device. This MRBS is designed for Ankai Higer bus operated in Addis Ababa that delivers about 55 passengers per trip beyond the manufacturer limit 40 passengers. According to the result, the energy stored in the flat spiral spring is inversely proportional to both spring length and the vehicle speed. The spring efficiency for the spring length of 2000 mm or 2 m moving at 40 km/h is greater than 45%. The CAD model of the planetary gear assembly was developed using CATIA VR5 and Solid-Works software and the model imported into ANSYS 16.0 for structural analysis in ANSYS workbench. From the analysis, the result for stress, strain, and deformation distribution had drawn. The AAK compact alternator is also connected to one end of the ring gear to get an output of around 1.7 kW (1680 W). The electric energy regenerated can be used to recharge the battery or to fulfill the electric need of the vehicle. It is recommended to the automotive industries, automotive manufacturers, and the universities to motivate and fund the researchers to investigate to develop environmentally friendly and technologically advanced regenerative brake system.

D. Beyen
Department of Mechanical Engineering, Wolkite University, Gubrei, Wabe Bridge, Ethiopia
e-mail: dabi.beyen@yahoo.com

R. B. Nallamothu (✉)
Mechanical Systems and Vehicle Engineering Department, SoMCME, Adama Science and Technology University, Adama, Ethiopia
e-mail: rbnallamothu@gmail.com; ramesh.babu@astu.edu.et

A. K. Nallamothu · S. K. Nallamothu
School of Industrial and Information Engineering, Politecnico di Milano, Milan, Italy

1 Introduction

The regenerative braking system was a past idea and a recently focused researchable concept that needs more attention from automotive industries/manufacturers/and any other concerning bodies since it has its own contribution in combating the future energy demand deficiency problem that may occur due to intermittence of the fossil fuel. This system also needs a technological advance to give the necessary output and to bring a continuous solution to the problem. Regenerative braking is a device that helps to convert braking energy into another form of energy and stores the energy for later use by the driver to start the vehicle from rest or for accelerating vehicle. The amount of stored/captured/energy by the regenerative device depends on the efficiency of the device and the amount of braking torque/force [1–5]. On the other hand, a storage system is used to store a part of the kinetic energy of the vehicle for a shorter duration in a regenerative braking system. Power transmission is used to direct the energy which otherwise generally dissipated in the brakes storage system during deceleration [1, 6, 7]. In a conventional vehicle, due to the friction between brake pads and brake drums, the kinetic energy of the vehicle is converted into heat. This generated heat gets carried away by the wind stream into the atmosphere. Thus, vehicle kinetic energy gets wasted. More the amount of energy wasted more the duration of the application of the brakes and more the frequency of the application of brakes [1, 4, 6]. The energy storage system stores the energy for a shorter duration until the vehicle needs it back.

The conversion system converts the stored energy back into kinetic energy and used for restarting or accelerating the vehicle. The type of storage, the efficiency of the drive train, drive cycle, and inertia of the vehicle determine the amount of energy that can be stored. City-bound driving leading to very frequent braking has the higher potential of energy saving due to more energy wastage under normal conditions [1, 4, 5]. A successful regenerative braking system ideally should have the following properties [1, 3, 8–10]

- High energy conversion efficiency,
- High energy storage capacity per unit weight and volume,
- High power rating with short energy transmission time,
- No complicated control system,
- With higher smoothness of power delivery from the regenerative braking system,
- The rate of absorption and storage of energy is proportional to braking,
- With the shorter delay and less amount of energy loss over a wide range of road speeds and wheel torques.

The mechanical regenerative braking system (MRBS) is an assembly of planetary gear systems that contain sun gear in center, planetary gear in between, and ring gear

Fig. 1 MRBS assembly drawing
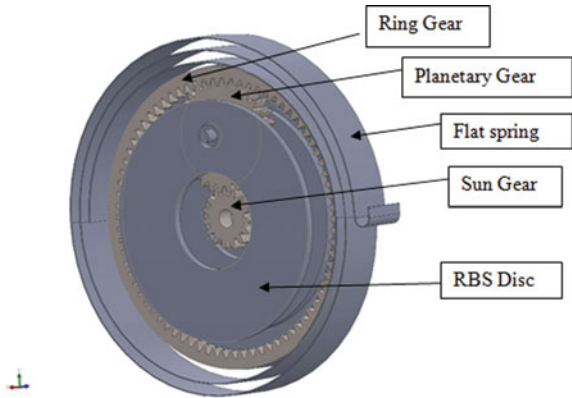
at the outside. The sun gear relates to the wheel axle in the wheel hub and transfers the axle rotation to the planetary gear. The planetary gear translates on the ring gear until the brake pedals depressed. As soon as the normal brake pedal depressed, the regenerative brake disk also depressed simultaneously. The regenerative brake depression stops the planetary gear from translating and transfers the motion to the ring gear. The ring gear on its turn starts to rotate on its axis and transfer to the external flat spiral spring. The flat spiral spring is attached to the outside of ring gear on one side, and the assembly covers on the other side. Following the turning of the ring gear, the spring winds up and starts to store the braking energy in the form of strain energy. The braking energy stored remains until it needs to start the vehicle from rest or to accelerate the vehicle. When the vehicle comes to rest finally the spring is controlled from returning by the mechanism allow the only a single direction of rotation the ring gear in the negative spin direction. This controlling mechanism/one-way clutch stays on until the accelerator pedal depressed. Model is shown in Fig. 1.

During the forward driving or accelerating the vehicle, the system is idling. This means the ring gear remains at rest, and the planetary gear translates on the stationary ring gear. At this moment, the system does not restore the energy, and this non-energy restoring cycle is known as idling time. This mechanism is an easy and simple mechanism which can be easily removed and inspected when failed it can be replaced with the new one.

The gear ratios between gears mate:

- Between the sun and planetary gear $= 2$
- Between the planetary and ring gear $= 2.5$
- The overall gear ratio $= 2 \times 2.5 = 5$.

Higer bus is (Fig. 2) one of the transport means operated in our capital city Addis Ababa/Finfine and it is neighbor Oromia region cities. Specifications of Higer bus are given in Table 1.

Fig. 2 Higer bus
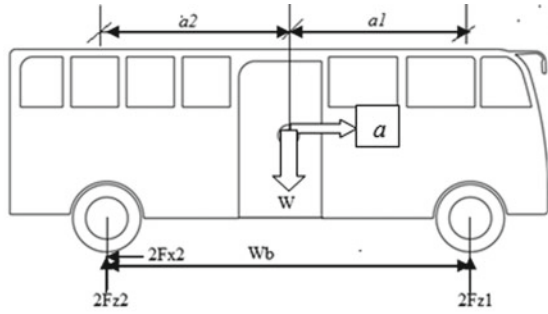
Table 1 Specifications of the Higer bus

Model	HK6669K
Overall dimensions (mm)	6620 × 2250 × 2795
Wheel drive	Rear-wheel drive (2RWD)
Type of fuel	Diesel
Maximum vehicle speed	120 km/h
Wheelbase (mm)	3308
Axle (front/rear)	Rated load 2500 kg/4500 kg

2 Braking Forces

Air Resistance (R_a) for a Rear-Wheel Drive (RWD)

$$R_a = \frac{1}{2} \times \rho_a \times C_D \times A_{FP} \times v^2$$

where, $\rho_a = \frac{P_a}{R_a \times T_a} \approx 1.05$ kg/m^3 is the density of the local air in k/m^3.

$C_D \approx 0.3$ to 0.6 is the drag coefficient (0.42 for Higer Bus).

$A_{FP} = SF \times W_2 \times H$ is the projected frontal area in m^2.

where, $SF \approx 0.75$ to 0.85 is the Shape Factor.

Rolling Resistance (R_{rl}) for a Rear-Wheel Drive (RWD)

$$Rxf + Rxr = fr(Wf + Wr) = fr \cdot W$$

where

Rxf   Rolling resistance of the front wheels,
Rxr   Rolling resistance of the rear wheels,
fr   Rolling resistance coefficient,
W   Weight of the vehicle.

Grade Resistance (*R*g) for a Rear-Wheel Drive (RWD)

$$R_g = mg \times \sin \phi = W \times \sin \phi$$

where

W   is the weight of the vehicle in '*N*',
ϕ is the angle of inclination or slope.

3   Spur Gear Structural Analysis (ANSYS 16.0)

(i)   The stress, strain, and deformation analysis of sun, planetary, and ring gear is making the ring gear fixed support. ANSYS analysis results are shown in Fig. 3a–d.

(ii) The stress, strain, and deformation analysis of sun, planetary, and ring gear is making the ring gear frictionless support. ANSYS analysis results are shown in Fig. 4a–d.

4   Conclusion

This work aims to explore, analyze, and improve the brake efficiency, fuel economy of the vehicle, and reduce emission without affecting/compromising/the vehicle performance by restoring the braking energy in the flat spiral spring and using it during restart from rest or acceleration. This MRBS is designed for Ankai Higer bus operated in Addis Ababa, Ethiopia. The bus delivers about 55 passengers per trip beyond the manufacturer limit 40 passengers due to the transportation facility shortage in Addis. There is a repeatedly braking and releasing of brake pedal during the delivery of passengers on the trip that causes much energy to lose as a form of heat to the environment. The mechanical regenerative braking system is the system designed to recover, permanently store, and release the energy safely when needed.

According to the result, the energy stored in the flat spiral spring is inversely proportional to both spring length and the vehicle speed. The spring efficiency for the spring length of 2000 mm or 2 m for the bus moving at 40 km/h is greater than 45%. But the efficiency drops when the length of the spring exceeds 2000 mm or 2 m. The finite element analysis of the designed components is done using ANSYS 16.0,
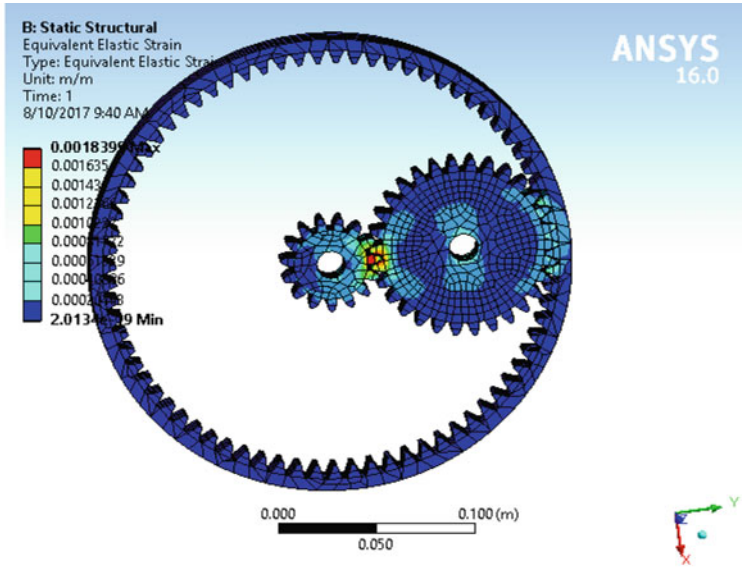
a) Equivalent strain
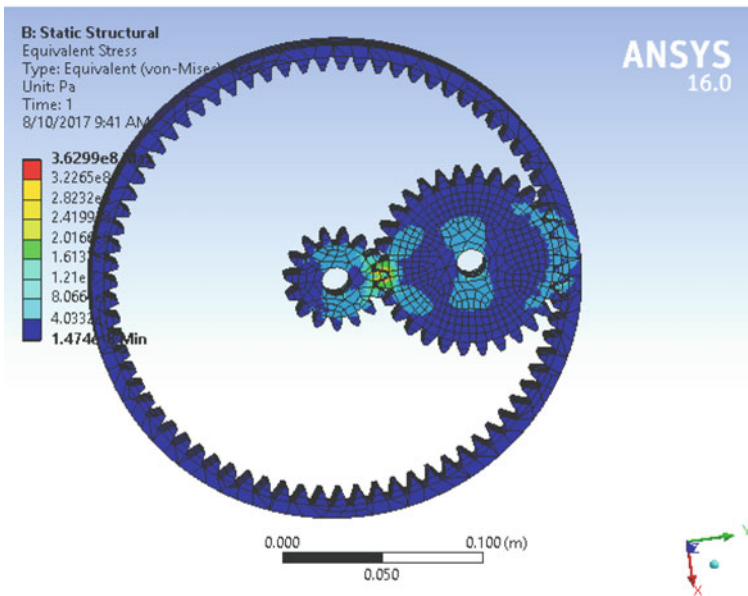
b) Equivalent Stress

Fig. 3 Structural analysis (ring gear fixed)
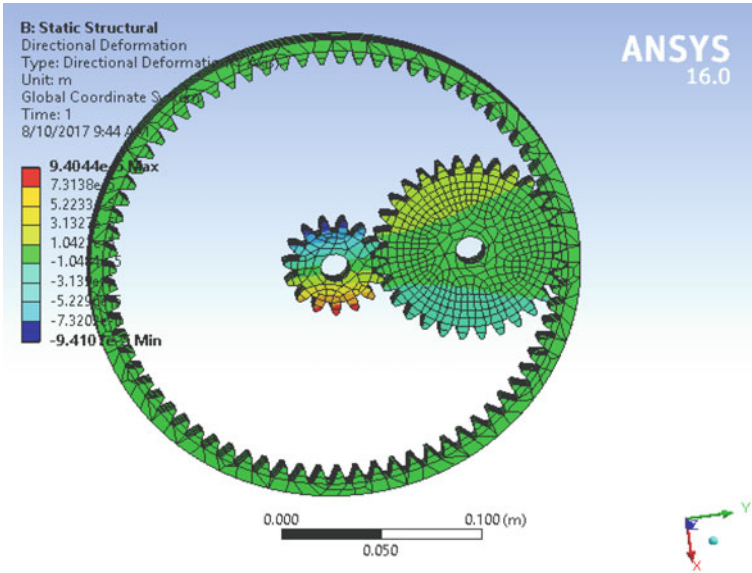
c) Directional Deformation
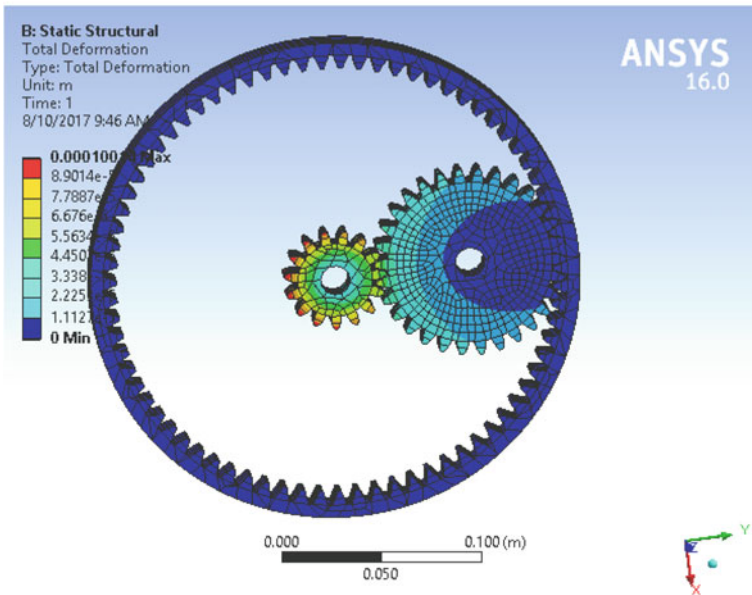
d) Total Deformation

Fig. 3 (continued)
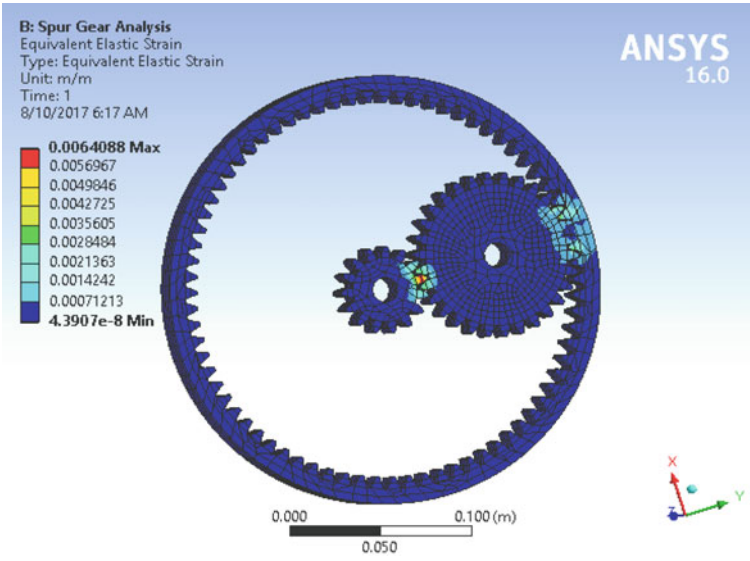
a)   Equivalent Strain
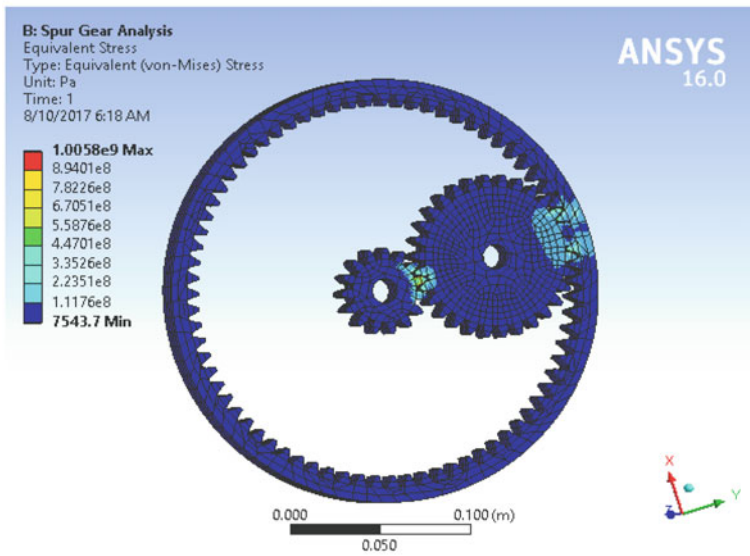
b)   Equivalent Stress

Fig. 4 Spur gear structural analysis
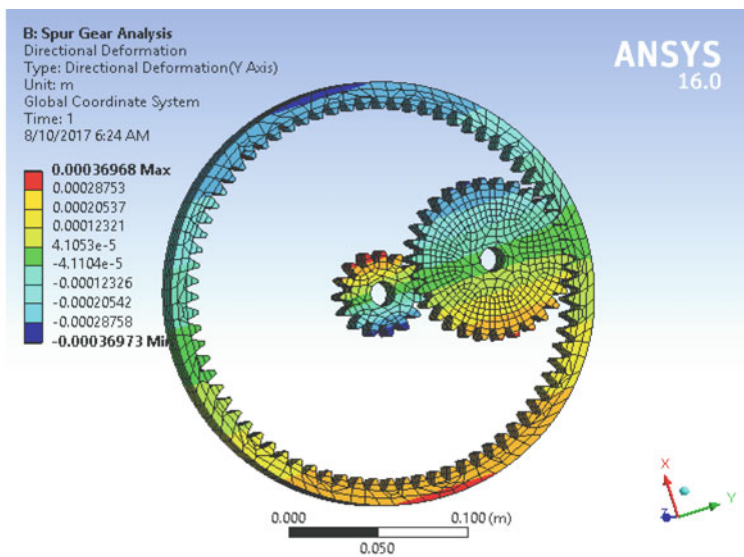
c)   Directional Deformation
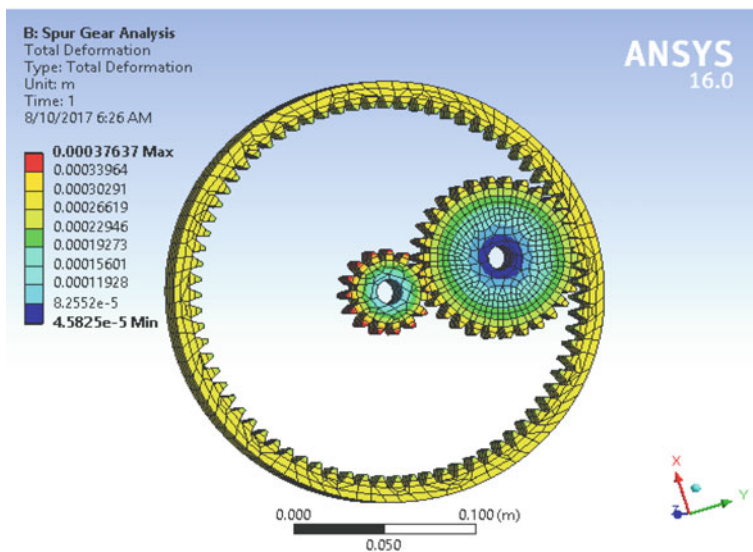
d) Total Deformation

Fig. 4   (continued)

which shows that the stresses and strains developed are well within the permissible limit. From the AAK compact alternator, connected to one end of the ring gear 1.7 kW (1680 W) electric power is also captured. The electric energy regenerated can be used to recharge the battery or to fulfill the electric power need of the vehicle. The energy that is needed to be dissipated/lost/during braking is secured and stored in a flat spiral spring and the alternator in the form of torsion force and electric energy, respectively. The MRBS is a compact assembly and can be installed in the wheel hub. The operations of MRBS are done gradually by the use of one-way clutch to make sure the use of system safe and control the energy loss. Future study in this field will result in design which is environmentally friendly and technologically advanced system that electronically controlled. The energy storing capacity and the size of the device also can be improved by using supercapacitor in the future.

References

1. Clegg SJ (1996) A review of regenerative braking systems. The University of Leeds, Institute of Transport Studies, White rose, p 25
2. Khurmi RS, Gupta JK (2005) Machine design textbook, 1229 pp. Eurasia Publishing House (PVT) LTD
3. Veh Int J Innov Technol Res 2(30):981–984
4. Singh S (2004) Spur gears in "mechanical machine design-II," 1st edn, pp 243–311. ISBN 98-93-5014-266-0
5. Mahadevan K, Balveera Reddy K (2014) Spring and gear design, design data handbook
6. Schmid H, Jacobson (2014) Fundamentals of machine elements, 3rd ed. CRC Press
7. Jazar RN (2012) Vehicle dynamics: theory and applications, Dept. of Mechanical Engineering Manhattan College Riverdale, NY 10471. springer.com, New York
8. Author Guide (2015) IskraAvtoelektrikad.d.ALTERNATORS, Manual of users, London
9. Karaveer V (2013) Modeling and finite element spur gear analysis. Int J Current Eng Technol
10. Gujar RA, Bhaskar SV (2013) Shaft design under fatigue loading by using modified goodman method. Int J Eng Res Appl (IJERA) 3(4):1061–1066. ISSN: 2248-9622, www.ijera.com

Some Numerical Investigation of Frame for Human-Powered Flywheel-Equipped Cycle Rickshaw

Fikru Tadele Kankie, Ramesh Babu Nallamothu, Seshu Kishan Nallamothu, and Anantha Kamal Nallamothu

Abstract Recent awareness in fossil fuel depletion due to large consumption with regard to population number growth from time to time and environment degradation due to fossil fuel combustion emission has been generated. This research focuses on the design of human-powered flywheel-equipped cycle rickshaw. The operating mechanism of this vehicle is same as the upright bicycle. The study conducted by reviewing different related previous works. The main objective of this work is designing flywheel-equipped cycle rickshaw, to harvest kinetic energy lost during braking or slow down for later use. This is done by using a mechanism incorporated with flywheel and clutch system. The study is carried out for design of the frame. The frame of this work cycle rickshaw is designed by using both upright bicycle fit data and anthropometrics data to develop ergonomic and rigid frame. The models of the components are developed using CATIA after determining the dimensions of the components. The design considers both static and dynamic condition. For FE analysis, ANSYS 15 is used to find out total deformation, equivalent (von Mises) stress, maximum shear stress and factor of safety.

Keywords Cycle rickshaw · Frame · Finite element analysis · Human-powered · Flywheel · Pollution free · Cycle rickshaw performance

F. T. Kankie
School of Mechanical and Automotive Engineering, College of Engineering and Technology, Dilla University, Dilla, Ethiopia

R. B. Nallamothu (✉)
Mechanical Systems and Vehicle Engineering Department, SoMCME, Adama Science and Technology University, Adama, Ethiopia
e-mail: ramesh.babu@astu.edu.et; rbnallamothu@gmail.com

S. K. Nallamothu · A. K. Nallamothu
School of Industrial and Information Engineering, Politecnico di Milano, Milan, Italy

1   Introduction

The First Cycle rickshaw improvement project was launched in the early 1970s. In 1973, Stuart Wilson, an engineering lecturer at Oxford University, designed a differential for use in Indian rickshaws. The aim was to overcome the problem that only one of the rear wheels was driven. The following year a "Mark-2" version was produced which was completely redesigned rickshaw. This was named "Oxtrike". The main features of the Oxtrike were a 3-speed Sturmey-Archer gear (which allowed three gearings smaller, stronger wheels; chassis made of box section steel sheet; powerful foot brake and the differential [1]. The plan was to dispatch the vehicle in kit form for local assembly. Then as the Oxtrike became more widely used, kits would be limited to complex components which could not be locally made (e.g. 3-speed free wheel, etc.). Oxtrike was such a radically different design. Many of its components were unable in third world countries. Local rickshaw makers would have had to learn a completely new design [2, 3].

Since people come in a variety of sizes and their bodies are not built in the same proportion, "design for an average" (50th percentile) will not work. The goal of product design is to accommodate as many users as possible. A number of countries in the world have sampled sufficient numbers of their respective population to have developed a national anthropometric profile [4]. The bicycle and the human-powered vehicle industry currently generate no pollution. Human-powered vehicles or non-motorized transport, such as bicycle, tricycle or cycles rickshaws, are some of the purest forms of transportation [5]. Transport tricycles, also known as cycle rickshaws, are a three-wheeled tricycle design, pedalled by a human driver in the front, and with a back seat in the rear for passengers or for conveying goods [6].

It is related with economy that is utilized for movement of people and goods from one place to another. Various means of transportation can be self-propelled or manually driven. Every normal human being is using either one or the other form of transportation facilities available. Among transportation means, petroleum fuel-powered road transport is the nearest and flexible to people which allows even to operate from door-to-door over short distance at the most competitive prices. However, most road transportation, that is, internal combustion engine-based propulsion, uses petroleum fuel and it causes environmental impacts. Moreover, in this time, transportation of both goods and humans increased rapidly with regard to population and economic growth. Also, transportation is the backbone for development of civilization [7, 8].

This study helps to reduce environment degradation, noise and air pollution. Because unlike internal combustion engine propelled vehicle, flywheel-equipped cycle rickshaw is driven by human muscle power which is eco-friend, quiet and pollution free. The other aspect is that with growing population, there is still growing need for local transportation. If this need is entirely met through internal combustion engine propelled vehicles, there will be additional import requirement of petroleum

products. Also, flywheel-equipped cycle rickshaw, used as a mode of localized transport, can contribute to income generation and employment for uneducated unemployed youths, well-being of their families and to the country's economic development itself. This project is a way to design efficient human-powered vehicle that potentially will serve as a partial solution to these problems. This work goal was to design human-powered flywheel-equipped cycle rickshaw which is commuter vehicle. Design layout of cycle rickshaw is a delta-style with rear wheels drive for a single rider and three passengers. One of the most important requirements is that the vehicle must have an optimum strength, weight and low price. To achieve this goal, it is necessary to use the optimal material and suitable frame to ensure the required quality with the lowest cost and simple construction. Finally, to represent 3D model of new cycle rickshaw and its component CATIA V5 R20 software are used and ANSYS 15.07 used as well for FEM analysis. The main objective of this work is to frame human-powered flywheel-equipped cycle rickshaw for integrated ergonomically and possible lightweight frame.

2 Materials and Methods

The overall dimension of the frame has been determined from the anthropometric data of the 95% population and bicycle frame size that is from upright bicycle manufacturing manual data and standard machine elements. After all, needed dimension obtained 3D CAD modelling of the frame and components of cycle rickshaw generated in CATIA V5R20 and saved in CATIA format or IGIS format. That saved model is imported to ANSYS 15 to perform finite element analysis. In addition, that ANSYS space claim is used for cleaning and repairing the model created in CATIA software in order to increase mesh refinement and result accuracy.

2.1 Design Specifications

- Weight of vehicle below 70 kg
- Maximum load: 240 kg (rider plus two passengers each 80 kg).
- Wheelbase: up to 1.95 m.
- The new cycle rickshaw operating mechanism must be like bicycle except KERS.
- The frame of the new cycle rickshaw must be able to accommodate varying size of 95% population.
- The maximum speed of the vehicle not exceeding 30 km/h.
- The cycle rickshaw will be steered through the bicycle's handlebars at 1:1 steering ratio will be maintained.
- 610 mm (24 in.) both rear and front wheels.
- This new cycle rickshaw compatible with existing parts.
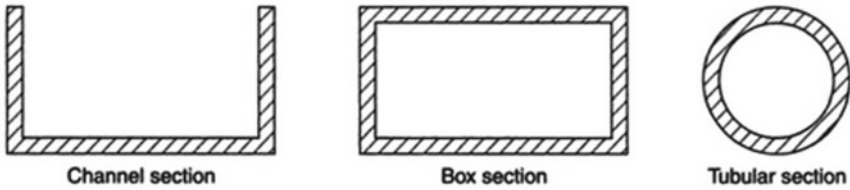
Fig. 1 Frame sections type

2.2 Frame Design

A cycle rickshaw frame is the main supporting structure to which all other components are attached. The main functions of a frame in cycle rickshaw are to support load of passengers, rider and mechanical components of cycle rickshaw and to deal with static and dynamic loads, without undue deflection. The various loads dealt with frame includes Weight of the other mechanical component, rider, passengers loads causing vertical bending of the member transmitted by going over uneven surfaces for Sudden impacts from collisions in order to support these all, loads the frame should be strong enough to withstand the rigorous force that will act on it but at the same time it should be as light in weight as possible to increase efficiency [8].

2.3 Frame Section

Generally, frame of a vehicle made from the following section such as channel, box and tubular section is shown in Fig. 1.

Channel section used in long member of the frame since it has good resistance to bending. Box section is used in short members of the frame, and it has good resistance to bending and torsion, while tubular section is used in the frame which subjected to torsion. Therefore, box section and tubular section are selected for this work base on load carrying character criteria.

2.4 Frame Geometry Analysis

Cycle rickshaw frame is composed of upright bicycle frame and rear lower passenger carriage frame. In order to determine overall length and width of cycle rickshaw frame, eleven dimensions of the human body are enough. See Fig. 2. Bicycle frame geometry is needed during cycle rickshaw design. For this work, upright bicycle frame has been selected based on 50% of the adult population size from road bikes on sale in the UK.

Fig. 2 Bicycle frame geometry
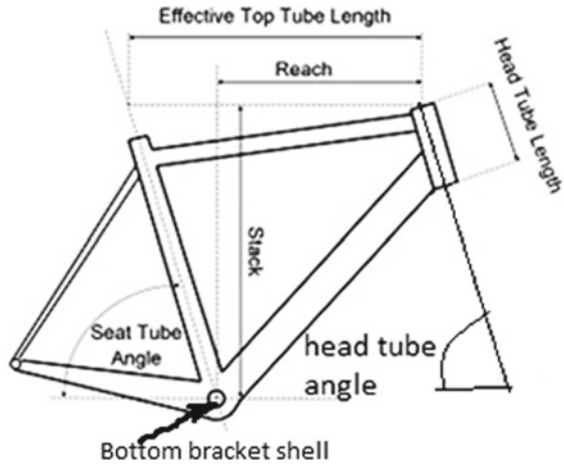
The height and inseam of the rider are 1719 mm and 816 mm, respectively, and then select the correct size of bike frame from table that is 54 cm.

2.5 Dimension for Passenger Carriage Frame

Rear total track width = number of passengers * hip breath of passenger + space for side support. From anthropometric, 95% data had been used for design. The cycle rickshaw passenger compartment carrying capacity is two passengers.

$$Reartotaltrackwidth = 2 \times 410mm + 50m = 870mm$$

Length of passenger compartment = Buttock-knee length + assume little free space of passage footrest and rear support.

$$Lengthofpassengercompartment = 660mm + 100mm = 760mm \approx 800mm.$$

2.6 CAD Modelling of the Frame

The four CAD model concepts of the frame were developed based on above frame size analysis data. That data obtained from anthropometrics selected bicycle frame size. This CAD models concept was developed on CATIA V5.

Two section types (i.e. box and tabular) have been used to develop CAD models and with standard section size of 35 mm diameter and 2.5 mm thick head tube, 30 mm

diameter tube with 1.5 mm thickness, for box section 1.5 mm thick and (30 × 30) mm, and (35 × 30) mm was used.

From four developed frame model concept model (d) concept has been selected based on its simple to construction, less welded parts, compatible free space at the centre of passenger carriage frame for purpose of mounting kinetic energy recovery system and less mass when it compared with other three model concept. The mass of each model concept is, for Fig. 3a 22.7 kg, Fig. 3b 19.3 kg, Fig. 3c 15.4 kg and Fig. 3d 11.7 kg, and this is obtained from CATIA after selecting frame that is steel. The CATIA software automatically calculates mass frame using material density and frame volume.

2.7   Frame Model

CAD model of flywheel-equipped cycle rickshaw frame has been prepared in CATIA V5 as shown below in Fig. 4. The dimensions were obtained from anthropometrics, bicycle frame size and other parts. The thickness size of each section of the frame is considered relative to steel bicycle and standard parts. The size of section used for modelling final frame is head tube (160 mm length, 35 mm diameter and 2.5 mm thickness), for top, down, seat stay and cross-tubes (square tube 30 × 30 (mm) and 1.5 mm thickness), for chain stay and passenger carriage tubes (rectangular tube 30 × 35 (mm) and 1.5 mm thickness), seat tube (30 mm diameter, 450 mm length and 1 mm thickness), BB shell (68 mm width, 42 mm outer diameter and 35 inner diameter), rear axle support plate (100 × 180 (mm) plate and 4 mm thickness), KERS support tube (20 mm outer diameter and 1.5 mm thickness) for further and detail dimension see Appendix D.

2.8   Frame Material

Material selection for human-powered vehicle frame applications plays very important role in providing the desired strength, endurance, safety, efficient performance and reliability to the vehicle. The selection of material for cycle rickshaw frame is done by detailed study of properties of material regarding strength, weight, manufacturability, cost and availability results found that steel alloy AISI 4340. But prefer to use AISI 4130 over the rest carbon steel because of its higher yield strength and corrosion resistant. AISI 4130 high strength-to-weight ratio is essential property because cycle rickshaw human-powered vehicle needs less weight frame to improve its performance.

Fig. 3 Flywheel-equipped cycle rickshaw frame model concepts
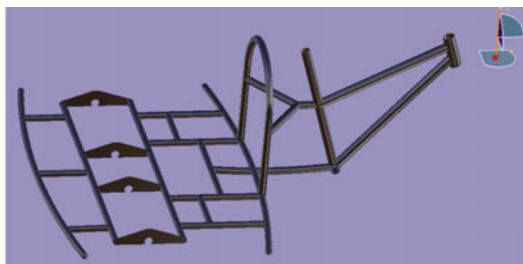
(a)
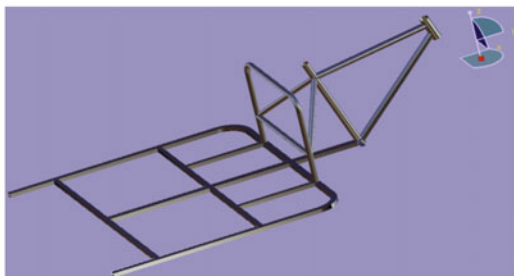
(b)
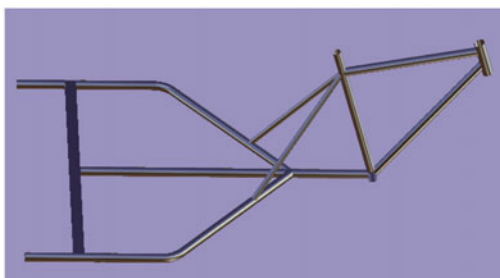
(c)
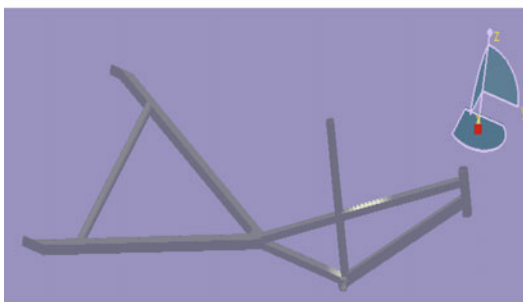
(d)
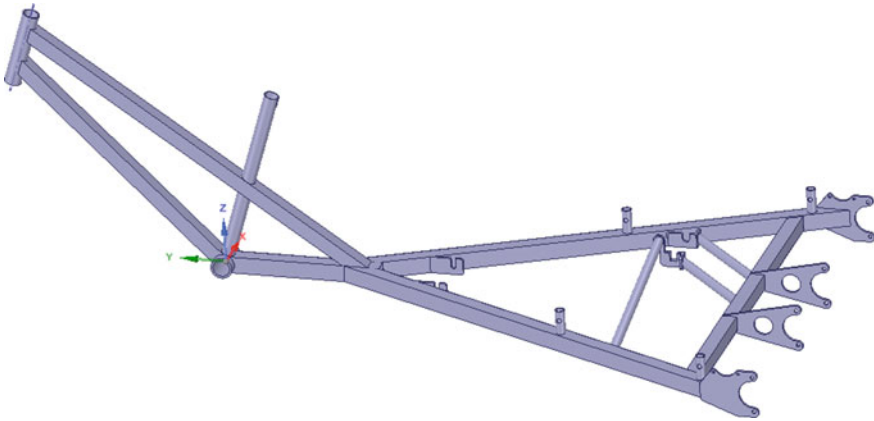
Fig. 4 Flywheel-equipped cycle rickshaw frame

2.9 Meshed Frame Model

Meshing for the new cycle rickshaw frame model was done using the automated ANSYS meshing refinement feature. That with fine relevance centre, fine smoothing and with 4 mm element size, these parameters controlled on ANSYS global mesh control features. Finally, the frame meshed to 430,832 nodes and 217,457 elements numbers. The meshed model is shown in Fig. 5.

2.9.1 Boundary Condition or Loading

The model is fixed in all degrees of freedom near the supports; fixed support is applied at bottom side of head tube and rear wheel axle support plates. The loading
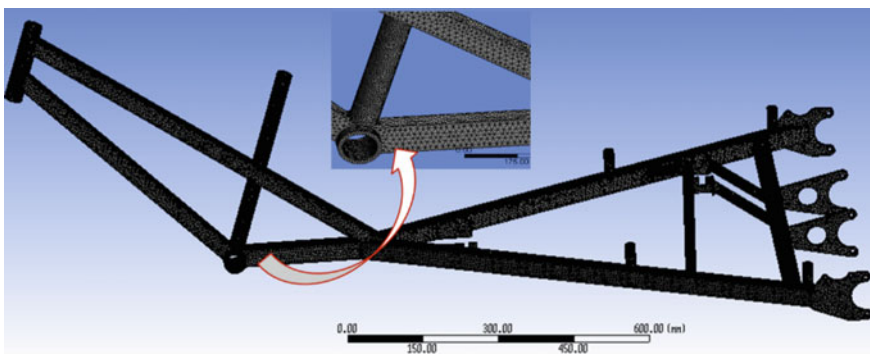
Fig. 5 Meshed new cycle rickshaw frame model
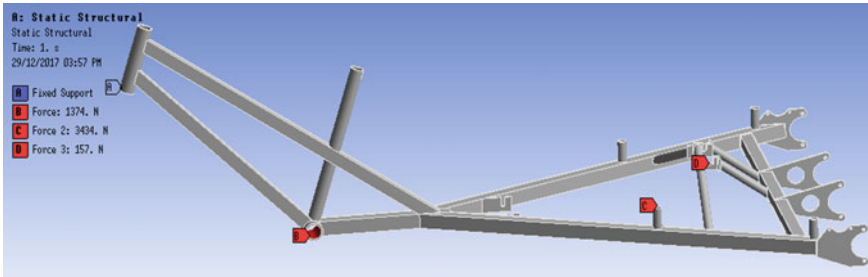
Fig. 6 Loading and boundary condition for static start-up

conditions are static start-up and steady-state pedalling. For those scenarios' analysis, simulation had been done in similar way except rider loading.

2.9.2 Static Start-Up

A 70 kg rider is applied maximum effort to bottom bracket to accelerate cycle rickshaw with 160 kg passenger on seat mount, 8 kg flywheel on mount and other mechanical components from stand position. For this scenario, the rider is out of the saddle. The cycle rickshaw frame is in vertical equilibrium with head tube (at A) and rear drive axle assembling plate hole were fixed (at A but for multiface selection ANSYS work bench label only one point). Figure 6 shows that the loading and boundary condition on a cycle rickshaw frame, this load is applied according to the design of frame, Also the boundary condition is applied at fixed position of a model which is consider as a supports, the load is applied considering weight shift during operating condition of cycle rickshaw it taken twice of static load on each load application point.

2.9.3 Steady State Pedalling

From total load of rider, 60% load (824 N) considered is applied on seat tube and 40% load (550 N) applied on pedal or BB bearing. But other loads are not changed and it is the same as case one. Those all loads are applied to negative Z-axis. Figure 7 shows load and boundary application on frame for steady state pedalling condition.

3 Results and Discussions

Finite element analysis is important to do a numerical simulation in order to find out how cycle rickshaw frame reacts when the rider, passengers and other mechanical system subject to weight load and dynamic load. In order to perform finite element
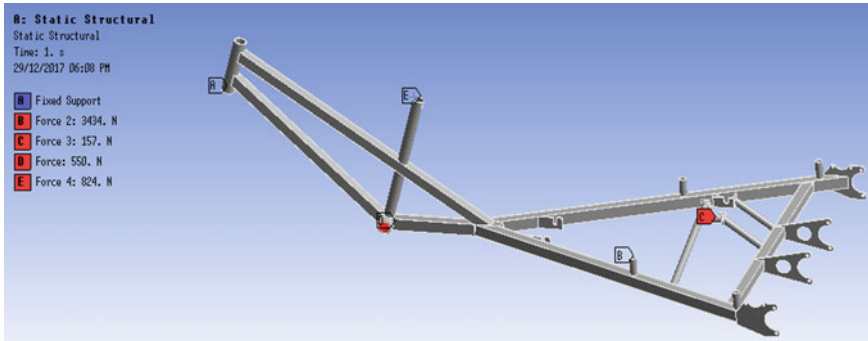
Fig. 7 Steady-state pedalling loading and boundary condition

analysis, FEA modelling process requires three types of input data such as geometry, material properties and loading. After modelling, the analysis of frame is done in ANSYS 15.07 workbench, for that purpose frame model is prepared in CATIA then it is imported to ANSYS workbench, and the file is imported from CATIA by file > import > IGS. To carry out the analysis, three scenarios are considering like start-up and stand pedalling.

3.1 *Result Analysis for Static Start-Up Condition*

The results are shown in Fig. 8a total deflection, Fig. 8b equivalent (von Mises) stress and Fig. 8c factor of safety, for static start-up condition in the frame when the load of 1374 N (at B), 3434 N (at C) and 157 N (at D) is applied for material AISI 4130. The red colour shows the maximum simulation value of those parameters and blue colour shows minimum simulation value of those parameters generated. But for factor of safety, blue colour shows maximum value and red colour shows minimum value.

3.2 *Result Analysis for Load for Steady Pedalling Condition*

Figure 9 shows the result of Fig. 9a total deflection, Fig. 9b equivalent (von Mises) stress and Fig. 9c factor safety for steady-state pedalling condition in the frame when the load of 824, 550, 3434 and 157 N is applied for material AISI 4130. The red colour shows the maximum simulation value of those parameters and blue colour shows minimum simulation value of those parameters generated. But for factor of safety, blue colour shows maximum value and red colour shows minimum value.

(a) Total deformation

(b) Equivalent Stress
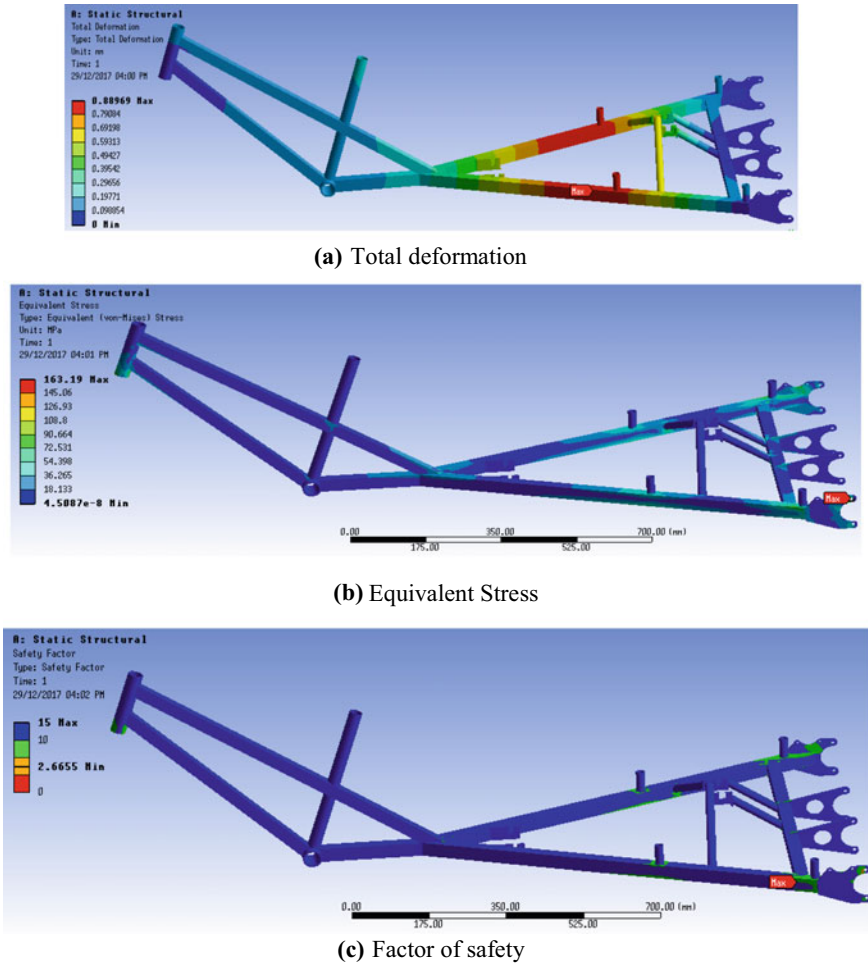
(c) Factor of safety

Fig. 8 **a** Total deformation. **b** Equivalent stress. **c** Factor of safety for static start-up condition in the frame

3.3 Comparison of Frame Static Structural Analysis Result

Static structural analysis of the cycle rickshaw frame is done on ANSYS workbench 15 for static start-up and steady-state pedalling condition. And the result of total deformation, equivalent (von Mises) stress and factor of safety obtained is tabulated below in Table 1.

From analysis result the total deformation under applied load of rider, passenger, other mechanical system weight and operational dynamic load the maximum total deformation obtained around front leg mount of passenger seat and magnitude of 0.88 mm for static start-up and 0.91 mm for steady pedalling condition as Fig. 8a red

(a) Total deformation

(b) Equivalent Stress
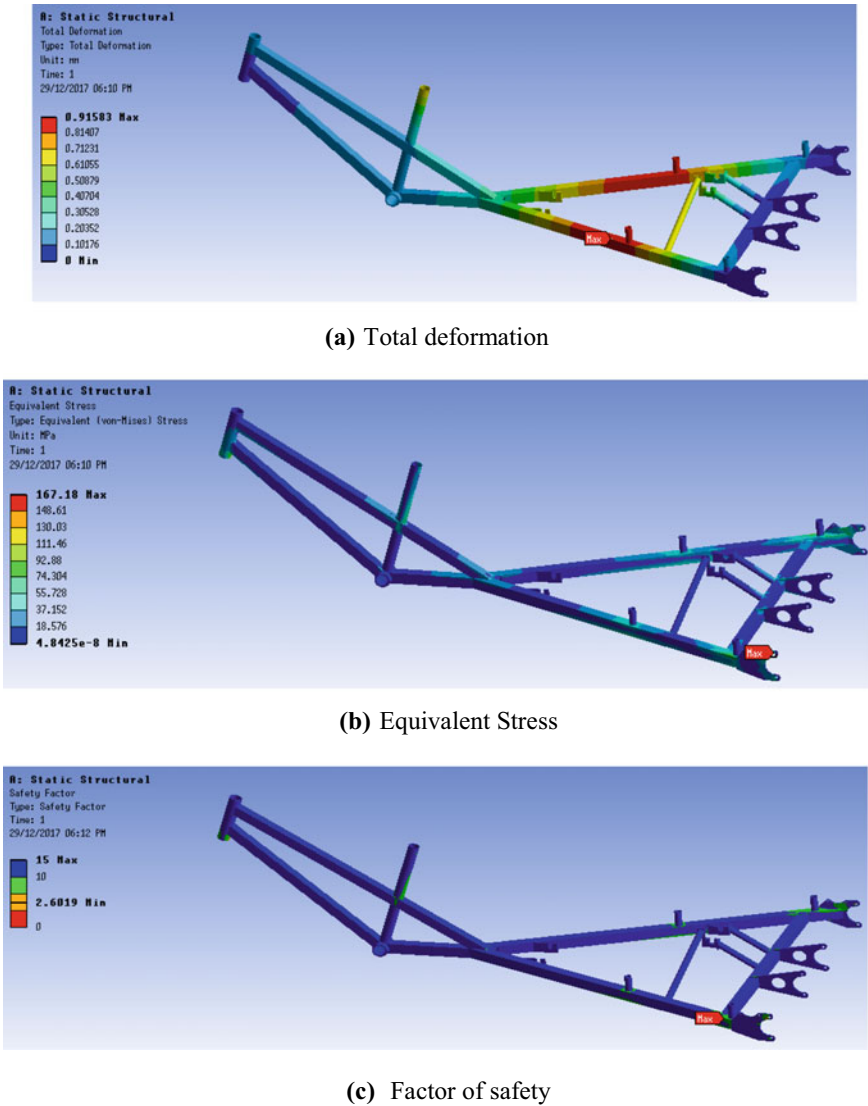
(c) Factor of safety

Fig. 9 **a** Total deformation. **b** Equivalent stress. **c** Factor of safety for steady-state pedalling condition in the frame

colour counter shows. For both conditions, maximum total deformation value is less than 1 mm and this indicates that cycle rickshaw frame stiffness is feasible under application of these loads. The simulation results for both static start-up and steady pedalling condition revealed that the maximum stress or equivalent (von Mises) stress generated on the frame is of the magnitude of 163.19 and 167.77 MPa reactively which is less frame material yield strength. These stresses found on rear axle mount

Table 1 Frame simulation result

	Static start-up		Steady-state pedalling	
	Maximum	Minimum	Maximum	Minimum
Total deformation (mm)	0.88	0	0.91	0
Equivalent stress (Von Mises stress) (MPa)	163.19	0.0027	167.77	0.00168
Factor of safety	15	2.67	15	2.60

plate. Also, the factor of safety of the frame for static start-up and steady pedalling condition on analysis was found to be of 2.67 and 2.6 reactively which means it can be considered practically feasible.

4 Conclusion

The frame of cycle rickshaw was designed on the basis of anthropometrics, and this makes vehicle comfortable for both passenger and rider. Also, integrated frame design increases stiffness and reduces the weight of the frame which in turn increases the performance of the vehicle. The frame was made of 35 mm circular head tube 30×30 square and 30×35 rectangular AISI 4130 steel tube with steering link constructed from 25 mm AISI 4130 steel tubing that successfully underwent a series of ANSYS static structural tests, and it was able to support a 6867 N vertical load (both static and dynamic loads). The maximum flywheel-equipped cycle rickshaw speed was 30 km/h. though that would increase with the addition of a larger front chain ring. The frame of flywheel-equipped cycle rickshaw can withstand both full static load and dynamic load up to 6867 N without any failure. The analysis shows that the equivalent stress of designed parts of flywheel-equipped cycle rickshaw is less than material stress which means the factor of safety is greater than one. It can be further improved by using automatic mechanisms.

References

1. Rahman BJM (2010) Non-motorised public transport. Aust Transp Res Forum 29:1–14
2. Menon S (2012) Design and analysis of kinetic energy recovery system in bicycles. Int J Innov Res Sci Eng Technol 2(8):42–45
3. Wegener M (1997) Sustainable transport. J Transp Geogr 3(5):177–190
4. Black JA (2002) Sustainable urban transportation: performance indicators and some analytical approaches. J Urban Plan Devel 128(4):83–107
5. Wilson SS (1974) The cycle rickshaw in appropriate technology. Oxford University 1(2):15–28
6. Javakumar Design and analysis of light weight motor vehicle flywheel. Int J Comput 4(7):2360–2365
7. Bawane SG (2012) Analysis and optimization of flywheel. Int J Mech Eng Robot 1(2):272–276

8. Sen PK (2015) Study on differential for optimum utilization in automobile. Int J Res Appl Sci Eng 3(5):353–357

Design and Simulation of Adaptive Low-Speed Electro-Pneumatic Frontal Impact Absorption System for Crossover Vehicles

Kaleab Ameneshewa, Ramesh Babu Nallamothu, Anantha Kamal Nallamothu, and Seshu Kishan Nallamothu

Abstract Vehicle frontal low-speed impact creates vehicle frontal component damage and driver injuries. In conventional vehicle frontal impact protection system, the frontal foam and reinforcing bar reduce the amount of damage and the degree of injuries, and it is the fact that heavier opponent needs stiffer structure and lighter opponent need less stiff structure but those structural components behave similarly in every crash situation. This work deals with using controlled pneumatic actuator as low speed and adaptable impact absorber in vehicle frontal impact absorption system in order to create dynamic behaviour of impact absorber and achieve sufficient damping during the event of crash. In this work, air spring dynamic property is simulated using ABAQUS simulation software and all controlling electrical and electro-pneumatic components behaviour is animated by using both Proteus 8 Professional and ARDUINO. To control the system, different electrical sensors, controllers and actuators are used. At the back of the air spring, the pressure sensor is mounted to control the amount of pressure needed in the air spring and the compressor control system is coded to pre-conditions to maintain the amount of pressure needed and to make idle the control system when the situation is in crash situation. The microcontroller is coded with the ARDUINO software by studying the real-time scenarios and it uses the input from the ultrasonic sensor to measure the distance between cars. In line with the ultrasonic sensing, the vehicle speed is sensed, and then the microcontroller compares the distance and the speed of the car and decides whether the car can achieve 0 kph within this distance or not. The result of electro-pneumatic shows a sufficiently good agreement with the physical parameter taken and the controlled system is able to execute and take action within 15 μs which is less than the impact duration for low-speed frontal crash and stiffer air spring column is maintained when

K. Ameneshewa (✉)
Department of Mechanical Engineering, Debre Berhan University, Debre Berhan, Ethiopia
e-mail: mv8kaleab@gmail.com

R. B. Nallamothu
Department of Mechanical Systems and Vehicle Engineering, Adama Science and Technology University, Adama, Ethiopia
e-mail: rbnallamothu@gmail.com; ramesh.babu@astu.edu.et

A. K. Nallamothu · S. K. Nallamothu
School of Industrial and Information Engineering, Politecnico Di Milano, Milan, Italy

453

the severity of crash is higher by comparing speed and distance between cars and less stiff air spring column is maintained when the severity of crash is minimum.

Keywords Vehicle frontal protection system · Frontal collision · Air spring

1 Introduction

Vehicle collision is a big challenge being faced by automotive field. In the design of an automobile, the most important task is to minimize the occurrence and consequences of automobile accidents. Automotive safety can be improved by "active" as well as "passive" measures. Active safety refers to technology which assists within the prevention of a crash. Passive safety includes all components of the vehicle that help to scale back the aggressiveness of the crash event. Crash protection priorities are directly proportional to the speed of the car when crash occurs: at speeds up to 15 km/h, the main goal is to minimize repair costs, at speeds between 15 and 40 km/h, the first aim is to protect pedestrians; at speeds over 40 km/h, the most important concern is to guarantee occupant protection [1–3].

The term "Crash Management System" is usually wont to describe the structural module consisting of the bumper and therefore the related attachments which hook up with the longitudinal beams of the car. Front bumpers are connected to the front chassis rail by a separate deformation element ("crash box"). Energy absorbers are loaded in compression or tension also because the bumper moves from a designed outer position toward the vehicle body and are operative to soak up the energy of the impact. After impact, these energy absorbers recover at various rates to return related to bumper assembly toward its original pre-impact position. Most of crash boxes are mechanical impact absorbers they did not return to their original position and shape after impact [4–6].

Pneumatic actuators are devices and they use controlled compressed air to create mechanical motion. It gives both linear movement and angular rotation with simple and continuously variable operational speed of the car. And also, it can be used as impact absorbers by controlled restricted flow [7–9].

2 Methodology

This work is done with the main objective of developing adaptive low-speed electro-pneumatic frontal impact absorption system for crossover vehicles. The air spring with various controlling electrical components is used. Air spring is simulated by using ABAQUES simulation software. Then, all the system components including mechanical components installation are done with the help of Proteus software. The controlling code is written in ARDUINO programming. After all the Arduino code is loaded in to Proteus microcontroller.

The response of the system simulated by varying different parameters such as

- The distance between cars
- Vehicle speed
- Air spring internal pressure.

2.1 Development of Electro-Pneumatic Impact Absorption System

Low-speed electro-pneumatic frontal impact absorption system is a system designed to reduce the occupant injuries and vehicle components damage during low-speed collision (30 kph). The system uses controllable damping element called air spring and controlling element called microcontroller by receiving the input data through sensors and send signals to the actuators.

2.1.1 Air Spring

Air springs consisting of actuators made of rubber or fabric and are supported by a compressed air column. These air springs are generally used as vibration isolators and as pneumatic actuators. Air springs do not consist of pistons, connecting rods, dynamic seals, etc. like pneumatic cylinders. This behaviour is good to make them suitable to handle various impacts and even off-centre impacts.

Air springs make use of the fact that air has elastic or springiness when compressed. Air springs are normally noise-free because of the virtue of their construction. Material properties of air spring are stated in Table 1.

Table 1 Air spring materials

Material	Parameters	Value of parameters
Steel	Elastic modulus	2.1e+5 MPa
	Density	7.8e−9 t/mm^3
	Poisson ratio	0.3
Rubber	density	1e−009
	Mooney–Rivlin parameters c01	80
	Mooney–Rivlin parameters c10	80
	TEMP	25
Air	Gas constant	287 J/kg K
	Temperature	−273.15 + 25 K

2.1.2 Terms in Air Spring

Assembly. Assembly of air spring includes the flexible member like rubber body, top plate and bottom plate.

Assembly volume. Air spring assembly volume is working volume exclusive of any external working volume.

Compression stroke. Compression stroke in air spring is reduction of height from its designed operational height.

Design load. Maximum static load expected to be acting on the spring under normal conditions.

Design height. The overall height of the air spring.

Effective area. The working area perpendicular to air spring output force. It is not the actual cross-sectional area of the air spring.

Reservoir volume. It is the volume of the reservoir which is located externally to the air spring and supplying the air for functioning of the air spring.

Vertical parameters to describe air spring vertical parameter.

- The elastic part is described by K_{ez}

$$K_{ez} = \left(\frac{1}{\frac{p_0 A_e 2^n}{V_{b0} + V_{r0}} + P_g \frac{dA_e}{dz}} + \frac{1}{K_{\text{aux}}} \right)^{-1} \tag{1}$$

- Viscous part is described by K_{vz}, $C_{z\beta}$, β and M.

$$K_{vz} = \left(\frac{1}{\frac{p_0 A_{e2} n}{V_{b0}} + P_g \frac{dA_e}{dz}} + \frac{1}{K_{\text{aux}}} \right)^{-1} - K_{ez} \tag{2}$$

- Mass (M) to describe the inertia of air in the surge pipe

$$M = 1_s A_s P \left(\frac{A_e}{A_s} \frac{V_{r0}}{(V_{b0} + V_{r0})} \right)^2 \tag{3}$$

- Nonlinear viscous damper $C_{z\beta}$, β

$$C_{Z\beta} = C_s K_{wz}^{1+\beta} = C_s \left(\frac{A_e}{A_s} \frac{V_{r0}}{(V_{b0} + V_{r0})} \right)^{1+\beta} \tag{4}$$

- equilibrium internal absolute air pressure is

$$P_0 = \frac{m_b g}{A_e} + P_a \tag{5}$$

2.2 Modelling of Air Spring Using Abacus

The air spring modelled in abacus is cylindrical in shape with inner diameter of 100 and 150 mm outer diameter. The idealization of the air spring consists of two metal discs of circular shape connecting with each other with a component made of rubber. The radius of the lower disc is 70 mm and the radius of upper disc is 72 mm and they are coaxial with a distance of 70 mm between them.

The fluid cavity is modelled using the surface-based fluid cavity capability, and to define cavity completely and ensure proper calculation in three-dimensional models, surface elements are defined along the bottom and top rigid disc boundaries of the cavity, even though no displacement element exists along those surfaces. Since two-dimensional surface elements are provided by abacus, structural elements were used instead of surface elements for modelling the rigid disc boundaries.

The rubber component is modelled as shell element, and the circular top and bottom plates are modelled as rigid element.

Boundary conditions and materials

- Fluid cavity inflated to a pressure at step one
- For bottom plate—U1 = U2 = U3 = UR1-UR2 = UR3 = 0
- For top plate—U1 = UR2 = UR3 = 0
- For top plate—U3 = UR1 = UR2 = 0
- For top plate—U2 = 30 cm
- Top plate and rubber body has tie contact
- Rubber body and bottom plate has tie at centre and surface-to-surface contact with the others (adjust slave surface to its initial position)
- Contact property between rubber body and bottom plate is rough
- Top plate is modelled as rigid body (adjust point to centre of mass at start of analysis)
- Bottom plate is modelled as rigid body.

2.3 System Control and Components

Ultrasonic sensors are a type of sensors used to measure the distance of an object from the point the sensor is placed. Ultrasonic waves are sound waves with frequencies higher than 20 kHz which cannot be heard.

Pressure sensor: Pressure is one of the most important physical parameters in fluid operation, and it is the force exerted on a unit of area.

Speed sensor uses the principle of variable reluctance magnetic sensing. In this, there is a coil wire wound around a cylindrical permanent magnetic core and is mounted on stationary hub carrier.

Quick exhaust valves work by providing a rapid exhaust of controlled air when placed directly onto an air cylinder after the control valve.

3   Results and Discussion

Speed has been identified as a key risk factor in road traffic injuries, influencing both the risk of a road crash as well as the severity of the injuries that result from crashes. Controlling vehicle speed can prevent crashes happening and can reduce the impact when they do occur, but collision occurs unintentionally so building a system to reduce the consequence is important.

It is the fact that injuries and damages during collision are directly proportional to the amount of kinetic energy generated during the motion of the vehicle, to minimize risk of injury and damage, and it is important to remove the kinetic energy as slowly and evenly as possible.

Kinetic energy is directly proportional to the mass and the square of the speed of the vehicle, so at different speed the vehicle will have different amount of kinetic energy. To remove this varying kinetic energy, it is important to develop adaptive kinetic energy removing system to reduce injuries and damages happen during collision. Figure 1a, b shows the undeformed and deformed shapes of air spring.

In simulation of air spring using abacus, an incompressible Mooney–Rivlin (hyper-elastic) material with c10 = 80, c01 = 80, d1 = 0 and temp = 25, and the steel with E = 210.0 Gpa and v = 0.3 is used. Figure 2a, b shows the material distribution in the model.

The simulation result in Fig. 3 shows the von Mises stress concentration on the inflated air spring when the spring is compressed about 30 cm in the negative y-direction, and as the graph Fig. 4 indicates the stress concentration is below the Tresca stress and we can say it is safe.

As the graph in Fig. 5 shows all the stress components during the simulation of air spring lies below the Tresca line, so it is safe to use the air spring with this range which is proportional with the required range.

(a) Undeformed shape of air spring   (b) deformed shape of air spring
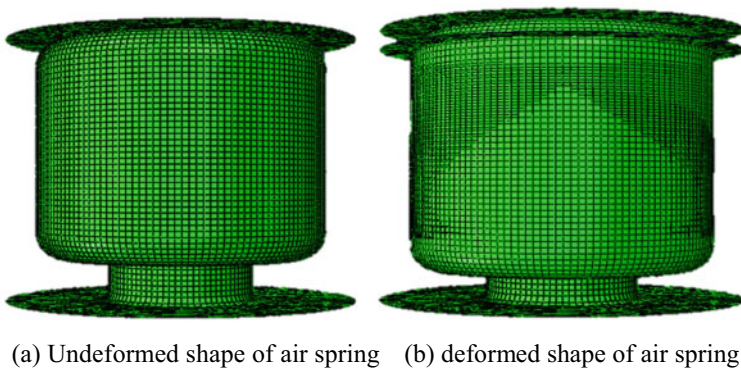
Fig. 1 **a** Undeformed shape of air spring and **b** deformed shape of air spring
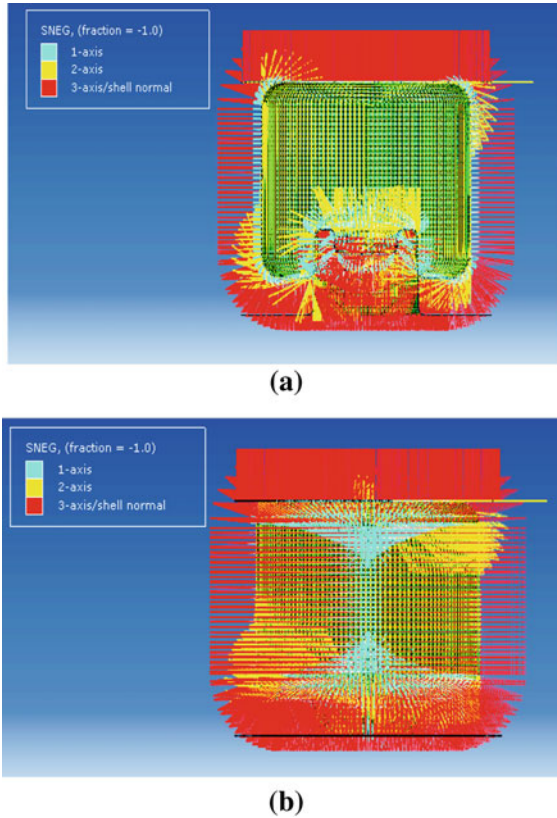
Fig. 2 a Material orientation on deformed shape sectional view and **b** material orientation on deformed shape

As indicated in the parameter, the air spring is first inflated to the required pressure level and then compressed in 30 cm in the negative y-direction, so the graph in Fig. 6a, b shows the characteristics in both steps. The effective area of the air spring change is negligible; pressure is directly proportional to the applied force so as the compression force increases the pressure also increases.

3.1 Spatial Displacement

When the air spring is compressed to 30 cm in the negative y-direction, the rubber body compressed in the same direction is shown in Fig. 7. The following result in Figs. 8, 9, 10, 11 and 12 shows the magnitude and the direction of displacement.
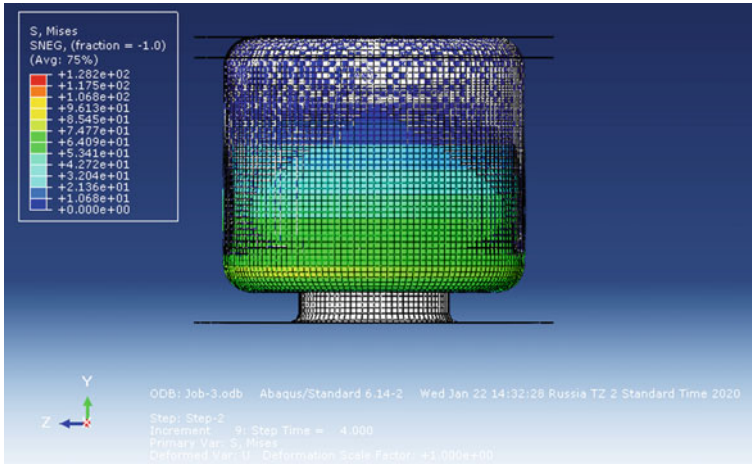
Fig. 3 Stress contour on the air spring
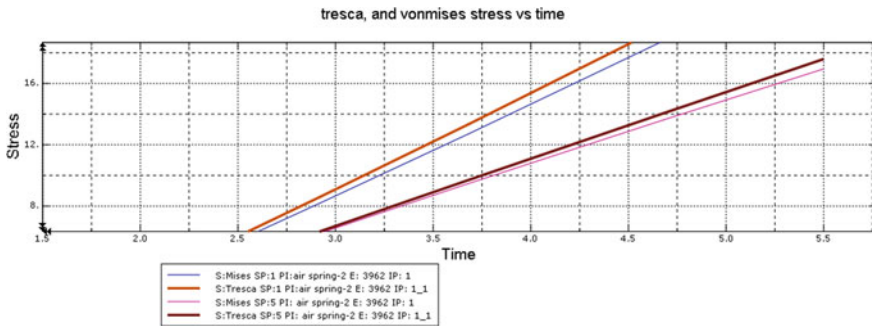
Fig. 4 Von Mises stress

4 Conclusion

To reduce the damage in the vehicle components and occupant injuries, adaptive electro-pneumatic system is used, and this designed system is mounted in the vehicle frontal structure. Then, the system operation is animated in Proteus 8 Professional result of electro-pneumatic shows a sufficiently good agreement with the physical parameter taken and the controlled system able to execute and take action within 15 µm which is less than the impact duration for low-speed frontal crash.

In this paper, the timely response of the system is observed. Air column unit can able to perform efficiently for low-speed crash impact load and the required amount of stiffness is achieved by varying the air pressure inside the air column unit, and impact energy damping is achieved by controlling the quick exhaust valve diameter.
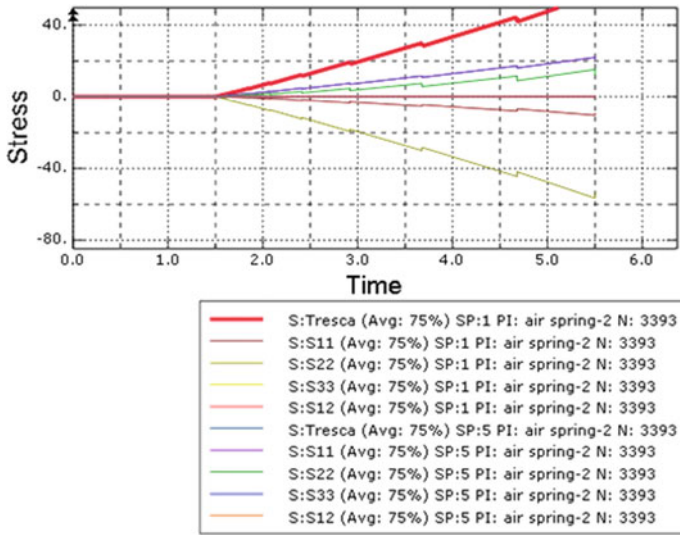
Fig. 5 Stress components
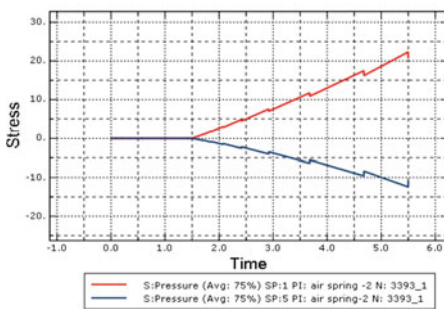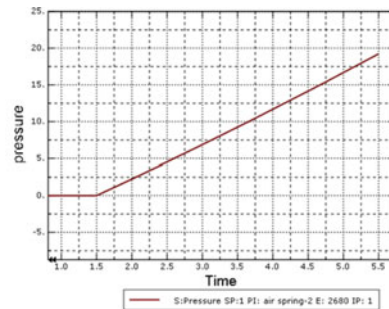
(a) Stress versus time　　　　　　　　　(b) ressure versus time

Fig. 6 **a** Stress versus time and **b** pressure versus time

To check the response and operation of the system, the following dynamic operation condition is simulated and the result is as follow:

- When both the speed and distance between colliding cars are minimum in this condition, the probability of crash between the cars is very low so the valve condition remains closed.
- When speed of the car is maximum and the distance between colliding cars is maximum, in such scenario, the vehicle is at 50 kph and the distance between the cars is 11 m apart then this condition is not enough to trigger the valve so the valve remains closed and the signal voltage reading is 0 V.
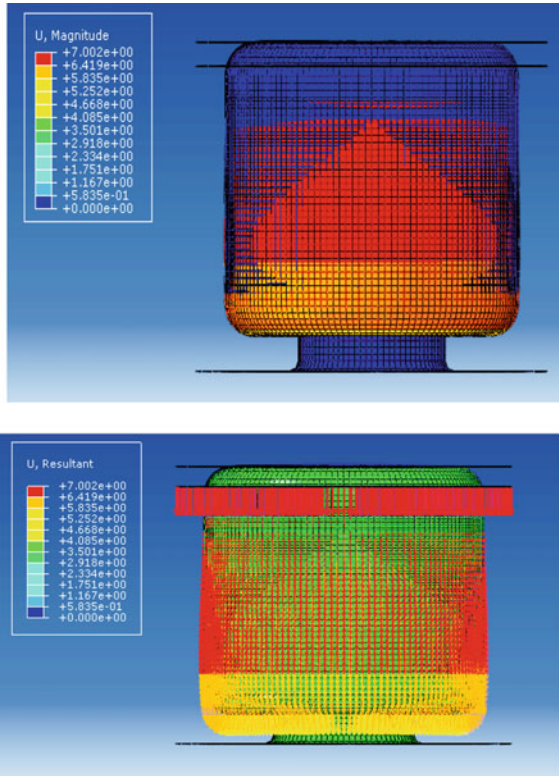
Fig. 7 Magnitude and symbols on air spring
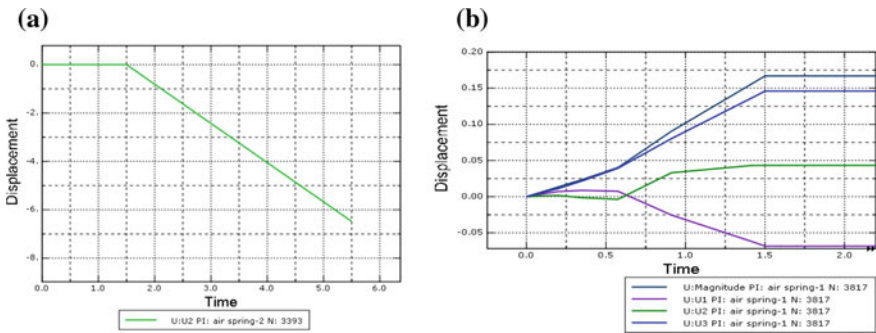
Fig. 8 **a**, **b** Displacement versus time
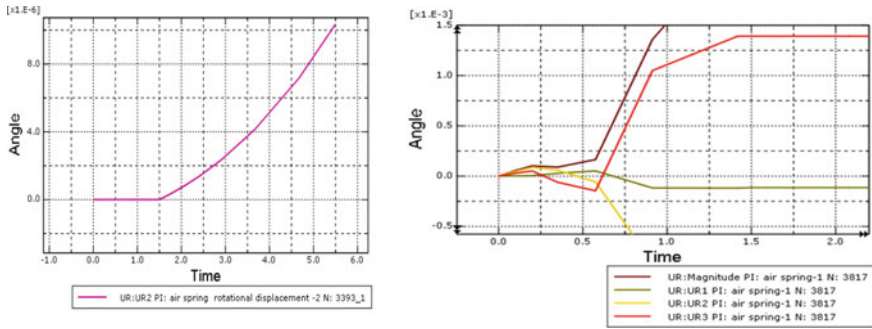
Fig. 9 Rotational displacement versus time
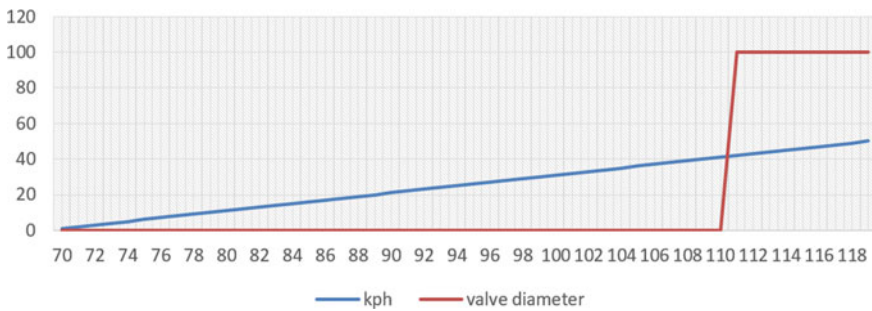
Fig. 10 Valve control solenoid operation with respect to speed of the car
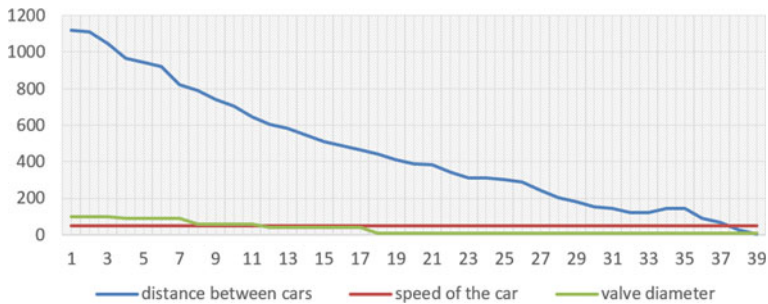
Fig. 11 Relationship between distance, speed and valve diameter

- When speed of the car is maximum and the distance between colliding cars is minimum, the system is checked by suddenly decreasing the distance between the car to 4 cm, and the speed of the car was at constant speed which is 50 kph and quick exhaust valve opens about 40%.
- When speed of the car is minimum and the distance between colliding cars is maximum in this extreme condition, the speed of the car suddenly drops to 8
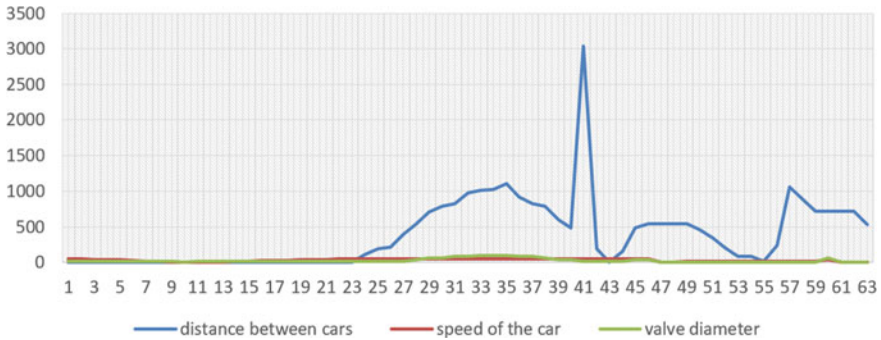
Fig. 12 Valve diameter versus damping

kph and the distance between the car rises to 11.1 m at this condition the system compares the actual condition and the pre-condition set and maintain the valve condition in closed state because the vehicle in motion has sufficient distance to bring the vehicle to 0 kph.

- When distance is constant but speed varies even if the speed of the car is increasing but the distance between the cars is constant or in a safe distance to bring the car to 0 kph, the valve remains in closed command.

References

1. Wakjira A, Nallamothu RB (2013) Microcontroller based rear-end anti-collision warning systems for vehicles. Glob J Eng Design Technol 2(6):14–21
2. Nagel G, Thambiratnam D (2002) Energy absorption and performance of a vehicle impact protection system. School of Civil Engineering, Queensland University of Technology, Australia, Physical Infrastructure Centre
3. Chen H, Yang Y, Wang L (2015) Vehicle Front structure energy absorbing optimization in frontal impact. College of Automotive Engineering, Shanghai University of Engineering Science, Shanghai
4. Ghasemnejad H, Hadavinia H, Marchant D, Aboutorabi A (2008) Energy absorption of thin-walled corrugated crash box in axial crushing
5. Witteman W (1999) Adaptive frontal structure design to achieve optimal deceleration pulses. Technische Universiteit Eindhoven Mechanics of Materials/Vehicle Safety the Netherlands Paper Number 05-0243
6. Jie L, Lin D (2014) Influence of material properties on automobile energy-absorbing components crashworthiness. College of Civil Engineering, Heilongjiang University, Harbin
7. Wykes NJ, Edwards MJ, Adrian Hobbs C (2004) Compatibility requirements for cars in frontal and side impact. Transport Research Laboratory United Kingdom Paper Number 98-S3-O-04
8. Jain S, Sreekumar M (2016) The preliminary design of a collision energy absorption system. Indian Institute of Information Technology Design and Manufacturing, Kancheepuram Melakottaiyur, Chennai
9. Nunes T (2017) Multi-objective design optimization of a frontal crash energy absorption system for a road-safe vehicle. Instituto Superior Técnico, Universidade de Lisbon, Portugal

Design and Analysis of Reaming Tool by Finite Element Modeling and Simulation

Aman Kumar

Abstract The reamers are rotary cutting tools extensively used in enlarging the previously drilled holes. Precision reamers find application in finishing operations and are very expensive. So, it is extremely important to design the reamer tool with utmost care taking into account all the factors involved so as to avoid any quality issue at later stage. The actual testing of tool may cost a lot which can be minimized by modeling and simulation of designed tool. So, this paper deals with the design of reamer tool using the design formulas and the second is the modeling of reamer through ANSYS 19.2 and then comparing the stress and strain developed by both the processes. It is a cost-effective method and by analyzing the different forces and stress developed it becomes easy to optimize the model which in turn increases the efficiency of the process.

Keywords Reamers · Finishing operations · Modeling · Simulation · Stress · ANSYS

1 Introduction

Economical design of machine tool has always been a challenge to design engineers. Industrial modernization has enabled us to produce more economical and better design with the help of advanced tools and techniques [1]. Reaming is a machining process used for enlarging and finishing the already drilled holes to very fine tolerance and is suitable for batch type of production [2], 3. A complete description about the special-purpose tools can be found in international manual [4]. For common machining applications, the average surface roughness is found to be in the range of 0.8–3.2 mm. Reamers with high accuracy can produce even better results which may close to 0.4 mm [6]. Figure 1 shows a typical reaming operation [5].

Much work pertaining to reaming tool modeling has been done [7–11]. Yang et al. worked on optimization and design of reamer tool for directional reaming of

A. Kumar (✉)
Department of Mechanical Engineering, UIET, Maharshi Dayanand University, Rohtak, India
e-mail: amanmdu526@gmail.com

Fig. 1 A typical reaming operation
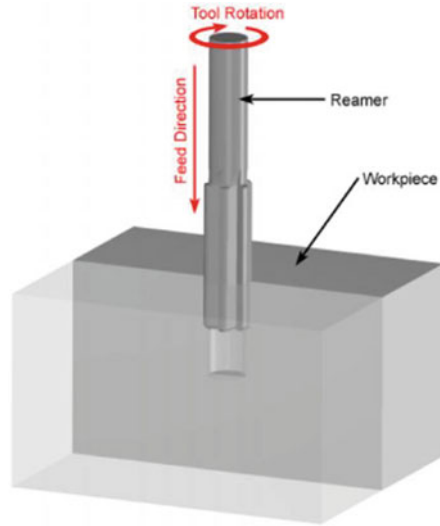
polycrystalline diamond compact which enhanced the performance of the reaming process [12]. Povolny et al. studied the reamer tool system performance under various types of load through FEM. They confirmed the system design with defined rigidity [13]. Reis et al. analyzed the technical and economic aspects of two manufacturing systems in drilling of compacted graphite iron (CGI) workpieces. This resulted in 40% reduction in machining time and 57% reduction in total cost [14]. The stress analysis of barrel reamer was evaluated through FEM by Baksa et al. They provided useful insights into boundary conditions required for performing numerical simulation of a barrel reamer [15]. Reaming improves the accuracy of a round hole enough to allow interchangeability. Reamers hold size consistently and can be applied to the metal-machining process with a minimum amount of skill. Reaming is a finishing operation and is not intended to remove a large amount of material. The speed of reaming is generally considered to be two-thirds of the speed used for drilling the same material. Reamers are most easily damaged than drills when subjected to chatter. Since rotating cutting tools are less likely to chatter when the cutting speed is reduced, reamers generally produce better results at lower cutting speeds. Reaming feeds are much higher than drilling feeds because there are more teeth in the reamer. Feeds vary from 0.0015 to 0.005 mm per flute per revolution, depending upon the size of the reamer. Reamer feeds that are too low can cause burnishing, glazing, or chatter. High feeds tend to reduce the accuracy of the hole and the quality of the finish.

2 Design for Tapered Shank Straight Fluted Machine Reamer

Outside Diameter (D): Hole resulting from reaming is bigger (overcut) than the reamer size. Consequently, reamer should be made smaller than the maximum permissible size of the reamed hole. The reduction in size (overcut) is usually 15% of the tolerance for the hole. The manufacturing tolerance for the reamer is confined to 35% of the tolerance for the hole.

Back Taper (t): Reamers are tapered down toward shank to provide axial clearance on teeth. The back taper ranges from 0.05 to 0.08 mm for hand reamers, and 0.04–0.06 mm for rigidly held machine reamers on diameter for the entire flute length. Back taper can be higher 0.06–0.08 mm if a floating holder is used for reamer.

Back Taper Flute End (D1): D1 = Minimum diameter of reamer − back taper t.

Lead (l): The length l of the lead chamfer depends upon the reaming allowance as well as the lead angle.

$$l = [(2.6 \text{ to } 2.8) \times A \times \cot \Phi] / 2 + (1 \text{ to } 3 \text{ mm})]$$

where

A Radial machining allowance (mm).
Φ Lead angle number of teeth (T): This depends upon the workpiece material.

Flutes: The type of flute depends upon the diameter D of hole and number of teeth T. The cylindrical land f ranges from Ø 0.1 for Ø 6 mm reamer to Ø 0.50 for Ø 50 reamer. Length of primary clearance ranges f_1 from 0.5 to 1.8 for same reamer sizes.

Flute length (L_f): It depends upon the diameter D of the hole.

$$L_f = 5D$$

Morse Taper (MT): It depends upon the diameter D of the reamer. Depending upon the Morse taper, the angle of taper of shank is calculated.

Shank Length (L): It depends upon Morse taper MT of the reamer.

Diameter of neck (d): It depends upon the diameter D of the reamer.

Overall Length of reamer (Lo): It depends upon the length of flute L_f, diameter of neck d, and the shank length L.

$$Lo = L_f + d + L$$

3   Methodology

3.1   Geometry of Tooth

The geometry of tooth was first designed as shown in Figs. 2 and 3, in AUTO-CAD software and was then transferred to ANSYS. By doing so, it was easy to find out the key points.
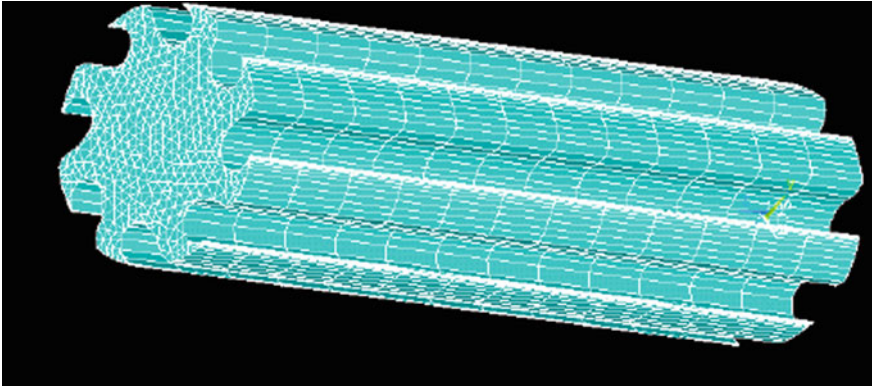
Fig. 2   Meshed volume of the complete profile of reamer cutter
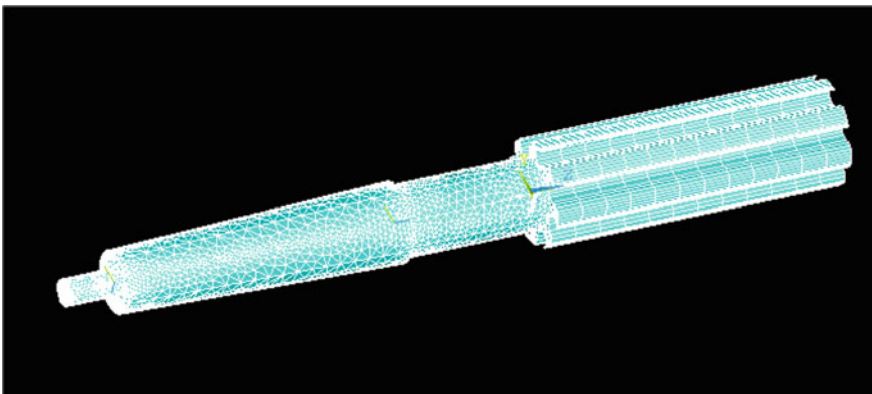
Fig. 3   Reamer profile after meshing

4 Analysis

4.1 Calculation

The maximum load which the reamer can undertake varies between 50 and 200 N. So the forces are taken in intervals of 25 N. Hence, the stress and strain have to be evaluated for 50, 75, 100, 125, 150, 175, 200 N. The stress and strain values for above loads are evaluated both through the design formulas and then through the ANSYS. Then, the values obtained from these methods are compared and if the values obtained through these values are almost comparable then there is no need for further optimization. FE Mesh is generated using Tetrahedral Solid Element with an element size of 3 mm. The model has 185,642 nodes and 94,652 elements. The reason for selecting tetrahedral element is that because they fit very well arbitrary-shaped geometries with their simple computations.

4.2 Calculation of Stress and Strain Values Through Design Formulas

Since mild steel is taken as the material, therefore Young's modulus (Y) for mild steel is 2×10^5 and the Poisson's ratio (υ) is 0.3. From the table, the change in diameter (ΔD) for Ø 30 hole is 3.96 mm.

Poisson's ratio $=$ Change in lateral dimension/Change in longitudinal dimension

$\Rightarrow 0.3 = (\Delta D/D)/(\Delta L/L)$

$\Rightarrow 0.3 = (3.96/30)/(\Delta L/L)$

$\Rightarrow (\Delta L/L) = [(3.96)/(30 \times 0.3)]$

$\Rightarrow (\Delta L/L) = 0.44$

Strain $= (\Delta L/L) = 0.44$

The maximum strain calculated is 0.44

Young's modulus $=$ Stress/Strain

$\Rightarrow 2 \times 10^5 =$ Stress/0.44

$\Rightarrow$ Stress $= 2 \times 10^5 \times 0.44$

$\Rightarrow$ Stress $= 88,000$ N/mm

The maximum stress calculated is 88, 000 N/mm

Hence for Ø 30 hole the maximum stress for all values of load 50, 75, 100, 125, 150, 175 and 200 N should be within 88,000 N/mm^2 and strain should be within 0.44 for all value's of load.

Fig. 4 Von Mises stress
nodal (50 N)
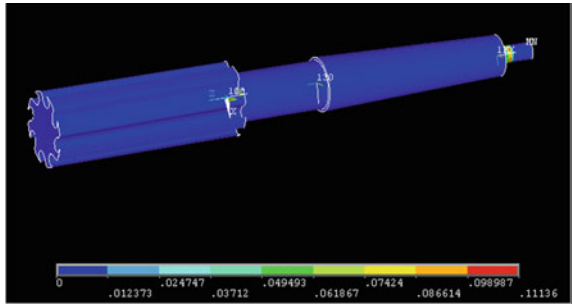
4.3 Calculation of Stress and Strain Values from ANSYS 19.2

Figures 4, 5, and 6 show simulation done for stress, strain, and displacement nodal
for 50 N load.

Von Miss stress nodal (Table 1).
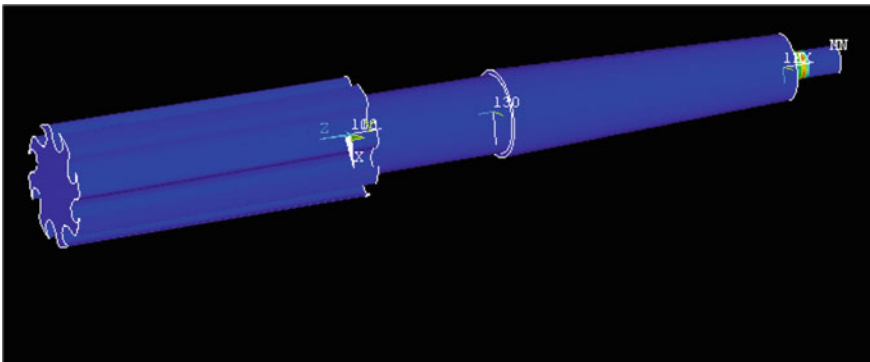
Fig. 5 Von Mises strain nodal (50 N)

Fig. 6 Displacement vector
nodal (50 N)
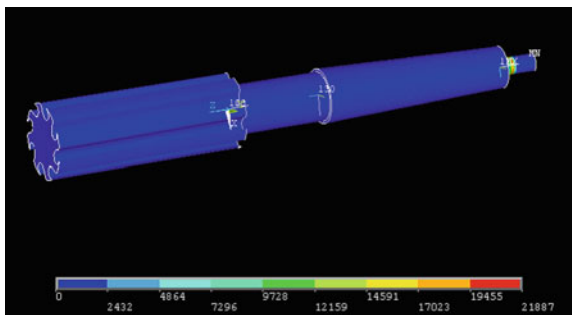
Table 1 Tabulation of stress and strain for the specified value of force

The results can be tabulated as shown below load/force (F)	Max. stress (N/mm^2)	Max. strain ($\Delta L/L$)	Displacement sum
50	21,887	0.11136	4.360
75	32,830	0.16704	6.541
100	43,774	0.22272	8.721
125	54,717	0.278401	10.901
150	65,661	0.334081	13.081
175	76,604	0.389761	15.261
200	87,546	0.445441	17.442

5 Conclusion

The study of optimization of a reaming tool in the form of machine reamer, using mild steel as the material, was undertaken with a view to analyze the stress and strain on the reaming tool during the operation. From the designing, it was found that maximum value of stress acting on reamer tool could be 88,000 N/mm^2 and maximum strain could be 0.44. On comparing these values with the one obtained from ANSYS for the same reamer was found well within the limits. The present study provides very effective way to get better results for economical design of reaming tool without undergoing costly actual testing however more accurate results can be obtained from dynamic analysis of reaming tool as well as its topographic optimization.

References

1. Pandit GP, Patil SB, Shinde RV, Amale SB (2017) Modelling and analysis of drilling jig for mounting casing of electric motor. Int J Eng Res Technol (IJERT) 6(02)
2. Karunanidhi S, Singaperumal M (2010) Design, analysis and simulation of magnetostrictive actuator and its application to high dynamic servo valve. Sensors Actuators 185–197
3. Verghese S, JPaul C, Karunanidhi S (2014) Int J Innov Res Adv Eng (IJIRAE) 1(8). ISSN: 2349-2163
4. Guhring (2006) International manual on advanced machine tools, 9th edn
5. Shingarwade RU, Chavan PS (2014) A review on mql in reaming. Int J Mech Eng Rob Res
6. De Chiffre L, Tosello M, Muller P (2009) Investigation on capability of reaming process using minimal quantity lubrication. CIRP J Manuf Sci Technol 2:47–54
7. Towfighian S, Behdinan K, Papini M et al (2007) Finite element modeling of low speed reaming vibrations with reamer geometry modifications. J Intell Manuf 18:647–661. https://doi.org/10.1007/s10845-007-0038-4
8. Bayly PV, Metzler SA, Schaut AJ, Young KA (2001) Theory of torsional chatter in twist drills: model, stability analysis and composition to test. J Manuf Sci Eng 123:552–561
9. Bayly PV, Young KA, Halley JE (1998) Dynamic simulation of reaming: theory, methods and application to the problem of lobed holes. Dyn Acoust Simul ASME Publ DE 98:245–252
10. Metzler SA, Bayly PV, Young KA, Halley JE (1999) Analysis and simulation of radial chatter in drilling and reaming. In: Proceedings of ASME DETC'99, (CD), Paper No. V1B8059

11. Towfighian S (2006) Finite element modeling of low speed reaming in the application of femoral canal preparation for intramedullary nailing. M.A.Sc. thesis, Ryerson University, Toronto, Canada
12. Yang Y, Yang Y, Liu X, Huang K, Ren H (2019) Optimized design and application of a directional reaming-while-drilling polycrystalline diamond compact bit. Eng Fail Anal 105:699–707
13. Povolny M, Fulemova J, Rehor J, Zatloukal T (2019) Study of clamping system plasticity for reaming tools. Annals DAAAM Proc 30
14. dos Reis A, da Silva RB, Silva LG, Machado ÁR, Arencibia RV, de Souza Ruzzi R, Jackson MJ, Zeilmann RP (2020) Analyses of two manufacturing systems in drilling of CGI: drilling and reaming× drilling. Int J Adv Manuf Technol 1–14
15. Baksa A, Ladányi G, Szirbik S, Virág Z (2019) Fem stress analysis of a barrel reamer. New Trends Prod Eng 2(1):178–185

Bond Graph Modeling and Simulation of a Differential Drive Mobile Robot

Jyoti Joshi, Rushali Pant, Narendra Gariya, Avi Raj Manral, and Pushpendra Kumar

Abstract Wheeled mobile robots (WMRs) are being used in many walks of life due to their simple structure and easy control. Furthermore, a differential drive robot is the simplest form of a WMR, which is having two independent actuators to drive its two tractive wheels. The steering is performed using the difference of velocities of two wheels; hence, two wheels velocities are manipulated in order to control the velocity and orientation of the robot. Modeling is the first step for the control system design. A kinematic model is not enough to represent the real behavior of the robot. Therefore, this paper deals with the dynamic modeling of a differential drive mobile robot. The model considers the multi-domain nature of the robot and includes electrical actuators and mechanical dynamics. A multi-domain graphical modeling tool called bond graph (BG) is used to develop the robot's model. The developed BG model is verified through simulation and the robot's motion is analyzed on the surfaces with different coefficients of friction.

Keywords Differential drive · Mobile robots · Bond graph

1 Introduction

A mobile robot is the robot whose base is not fixed such as wheeled, legged, drones, underwater mobile robots, etc. Wheeled mobile robots (WMRs) have increasingly been used in many applications due to their simple design. Some applications include transportation, industries, and disaster missions. WMRs can have different number of wheels such as two, three, four, and many more. A WMR with two tractive wheels on the same axle line is called differential drive robot, where orientation of the robot is obtained by different angular velocities of the two wheels. In addition, there may be one or two passive supporting wheels. In this work, we focus on dynamic analysis of a differential drive mobile robot.

J. Joshi · R. Pant · N. Gariya · A. R. Manral · P. Kumar (✉)
Department of Mechanical Engineering, Graphic Era Deemed To Be University, Dehradun 248002, Uttarakhand, India
e-mail: kumar.pushpendra@geu.ac.in

473

Modeling is the first step in analyzing a robot; further it is necessary to develop some control strategies. In the existing literature, kinematic models of differential drive robots have been analyzed for different controls [1–3]. Furthermore, dynamic models of differential drive robots have been developed for controller design [4, 5]. In [6], a controller is designed to solve the problem of trajectory tracking of a differential drive robot, where both the kinematic and dynamic models are considered.

Besides analytical models, graphical models are of interest to cope up with the complexity of a system. Among those graphical models, bond graph (BG) is a suitable graphical tool to model multi-domain complex systems [7]. On contrary to other graphical tools, BG represents edges carrying power not signal. BG has been used to model mobile robots [8, 9]. In the present work, we focus on BG modeling of a differential drive mobile robot considering its chassis, wheels, and actuators dynamics. The developed model is analyzed through simulation over various surfaces with different coefficients of friction.

The rest of the paper is organized in the following sections. Section 2 presents an introduction of BG modeling. The BG model of differential drive robot is developed in Sect. 3. Simulation results are presented in Sect. 4. Finally, the paper is concluded in Sect. 5.

2 Introduction to Bond Graph Modeling

Bond graph (BG) is a graphical modeling approach based on power exchange phenomena between systems. The power exchange is represented by a half arrow called power bond. This power bond carries two unified variables of power (P) namely, effort (e) and flow (f). Mathematically, it is represented by the relation:

$$P = ef \tag{1}$$

Since BG is based on the energy exchange, it can be applied to the systems of multi-domain nature such as mechanical, electrical, and thermal. The applications of BG in various domains with corresponding effort and power variables are described in Table 1.

Refer to Table 1, BG has been applied to various domains of physics because power (P) is common to all the domains. Therefore, power is exchanged between multi-domain physical systems using power bonds in BG. The multi-domain physical systems are modeled using unified BG elements, which are single port (source of flow SF and source of effort SE, resistance R, compliance C, and inertia I), double port (transformer TF and gyrator GY), and multi-port (common effort 0-junction and common flow 1-junction) elements. There comes a term called causality, which helps to determine the direction of effort and flow in a power bond. The main advantages of BG modeling include (i) multi-domain modeling tool, (ii) graphical tool, (iii) suitable to model complex systems, and (iv) can be used for control as well [7]. Therefore, in this work BG is used for modeling the differential drive mobile robot.

Table 1 Bond graph in different domains

Domain	Effort (e)	Flow (f)	Power (P)
Mechanical translation	Force (F)	Velocity (v)	$P = Fv$
Mechanical rotation	Torque (τ)	Angular velocity (ω)	$P = \tau\omega$
Electrical	Voltage (V)	Current (i)	$P = Vi$
Thermal	Temperature (T)	Entropy flow ($\dot{s}$)	$P = T\dot{s}$
Hydraulic	Pressure (p)	Mass flow rate ($\dot{q}$)	$P = p\dot{q}$

3 Bond Graph Modeling of the Differential Drive Mobile Robot

3.1 Description of the Robot

In this work, a WMR called differential drive robot is considered, which is having two active wheels on the same axle line and one or more passive supporting castor wheels. The active wheels are actuated by two independent direct current (DC) motors. The schematic diagram of the quadcopter is shown in Fig. 1.

Refer to Fig. 1, there are two coordinate frames, first one is the inertial frame $E\{x, y\}$ fixed to the earth, while second frame $CM\{x_b, y_b\}$ is the body-fixed frame attached to the center of mass (CM) of the robot. The CM of the robot is assumed to be located at the center point of the line joining the rotation axes of the two wheels. The angular velocities of the two wheels are represented by ω_1 and ω_2, for the left and the right wheels, respectively. The wheels' radii are equal and denoted by r. The linear velocities of wheels are represented by v_1 and v_2. The velocity of robot's CM is denoted by v, while its orientation is θ. The robot is having three degrees of freedom

Fig. 1 Schematic diagram of the differential drive mobile robot
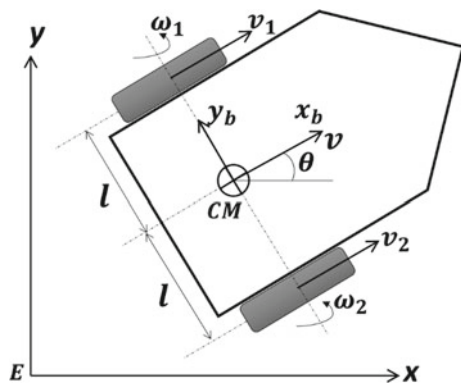
(DoF) in the two-dimensional (2D) plane. The three motions along the three DoF include longitudinal ($\dot{x}$), lateral ($\dot{y}$), and yaw ($\dot{\theta}$) motions. The steering of the robot is performed using the difference between the angular velocities of two wheels.

3.2 Kinematics of the Robot

The relationship between the body-fixed frame and the earth-fixed frame is given by the following transformation.

$$\begin{Bmatrix} \dot{x} \\ \dot{y} \\ \dot{\theta} \end{Bmatrix} = [R] \begin{Bmatrix} \dot{x}_b \\ \dot{y}_b \\ \dot{\theta} \end{Bmatrix} \tag{2}$$

where $[R]$ is the rotation transformation matrix between the inertial frame and the body-fixed frame, which is given by:

$$[R] = \begin{bmatrix} \cos\theta & -\sin\theta & 0 \\ \sin\theta & \cos\theta & 0 \\ 0 & 0 & 1 \end{bmatrix} \tag{3}$$

The nonholonomic constraint restricts the motion of the robot in y_b direction, hence, $\dot{y}_b = 0$. Also, we know $\dot{x}_b = v$. Finally, velocities in the inertial frame are given by:

$$\dot{x} = v\cos\theta \tag{4}$$

$$\dot{y} = v\sin\theta \tag{5}$$

The wheel velocities can be given by the following relations.

$$v_1 = v - l\dot{\theta} \tag{6}$$

$$v_2 = v + l\dot{\theta} \tag{7}$$

The wheels' linear velocities v_1 and v_2 are caused by the rotation of wheels with angular velocities ω_1 and ω_2.

3.3 Bond Graph Dynamic Modeling of the Robot

In this subsection, we will develop the dynamic BG model of the robot using the kinematic equations presented in the previous subsection. The kinematic constraints at some points automatically reflect in the BG dynamic model, because it is based on the energy flow between various points. In the present paper, the dynamic model of the robot considers the multi-domain components including electrical motors and the mechanical dynamics of the robot's CM. The robot's wheels are actuated by two independent DC motors. The following modeling assumptions are made: (i) the robot moves in a plane with three DoF, i.e., longitudinal, lateral, and yaw, (ii) rigid body dynamics is considered, (iii) since the robot moves in a known indoor environment, hence, suspension, roll, and pitch dynamics are ignored, and (iv) wheels are actuated by two independent DC motors. The BG model of the robot is developed in Fig. 2.

In Fig. 2, the half-headed arrows represent the power bonds in BG, while the full-headed arrows represent the measurements, say detector of flow (Df). Each Df is a sensor, which measures the flow at the junction where it is attached. Eight 1-junctions say, 1_v, 1_θ, 1_{i1}, $1_{\omega1}$, 1_{v1}, 1_{i2}, $1_{\omega2}$, and 1_{v2}, are corresponding to linear and angular velocities of CM, motor current, angular and linear velocities of the left and right motor-wheel systems, respectively. Two 0-junctions say, 0_{F1} and 0_{F2}, are corresponding to the left and right wheel forces, respectively. Theses wheels' forces F_1 and F_2 are transmitted to the robot's CM. Two 1-junctions say, 1_x and 1_y, are
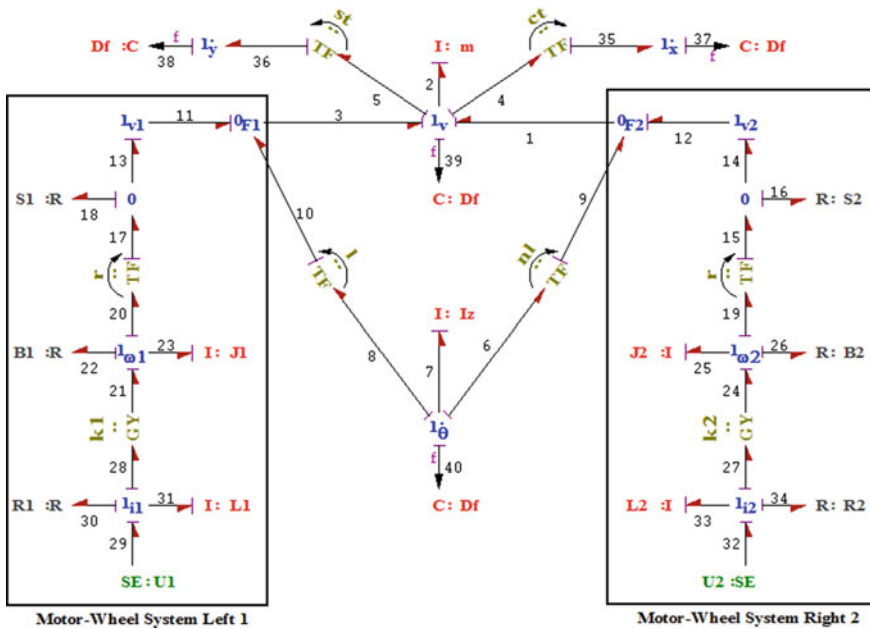
Fig. 2 Bond graph model of the differential drive mobile robot

corresponding to the longitudinal and lateral velocities of the robot in the inertial frame, the transformers TF moduli ct and st represent sin θ and cosθ, respectively.

Refer to BG in Fig. 2, there are various parameters related to the robot's dynamics. In CM dynamics, m and I_z are mass and rotary inertia of the robot; transformers TF moduli l and nl represent the robot's dimension, where nl means negative l. In the electrical part of the left motor-wheel system, U_1, i_1, L_1, R_1, and k_1 represent the input voltage, current, inductance, resistance, and motor constant, respectively. In the mechanical part of the left motor-wheel system, ω_1, J_1, and B_1 represent the angular velocity, rotary inertia, and viscous friction of the motor's rotor shaft. In the wheel-ground part of the left motor-wheel system, r and S_1 represent the wheels radius and the coefficient for the contact dynamics, which depends on the normal load and the friction between the wheel and ground. In the same way, different parameters in the right motor-wheel system can be defined. The expressions for the S_1 and S_2 are given as follows.

$$S_1 = S_2 = \frac{\mu mg}{2} \tag{8}$$

where μ is the friction coefficient between the wheel and ground. In this way, a complete dynamic model of the robot is developed which includes the actuators and the wheel-ground contact dynamics as well.

4 Simulation

The model is verified through simulation in a dedicated software for BG modeling and simulation called SYMBOLS [10]. Once BG model of a system is drawn in SYMBOLS, it automatically generates the equations of motion of the system, and simulation can be carried out (Fig. 3).

The aim of this simulation study is to verify the model and to analyze the dynamic behavior of the robot when it moves on various surfaces with different coefficients of friction. The following numerical values of the parameters are taken for simulation: $L_1 = L_2 = 0.05$ H, $R_1 = R_2 = 0.5$ Ω, $k_1 = k_2 = 0.1$ N-m/A, $J_1 = J_2 = 0.2$ kg/m^2, $B_1 = B_2 = 0.1$ N m s/rad, $r = 0.05$ m, $\mu = 0.6$, $m = 5$ kg, $l = 0.15$ m, and $I_z = 1.5$ kg m^2. First, same input voltage is given to both the motors, say 10 V. The results are shown in Fig. 4, where it can be observed that the robot moves along X direction in the straight line and there is no motion along Y direction, which is an expected behavior for the equal angular velocities of the wheels.

Now, the robot's behavior is analyzed for the different angular velocities of the wheel, the left wheel's motor is excited with $U_1 = 10$ V and the right one with $U_2 = 15$ V. The results are shown in Fig. 5, where we can see the expected behavior of the robot with positive anticlockwise orientation and circular trajectory.

In order to analyze the behavior of the robot over various surfaces, we have simulated the robot with different coefficients of friction, i.e., 0.5, 0.6, 0.7, and 0.8.
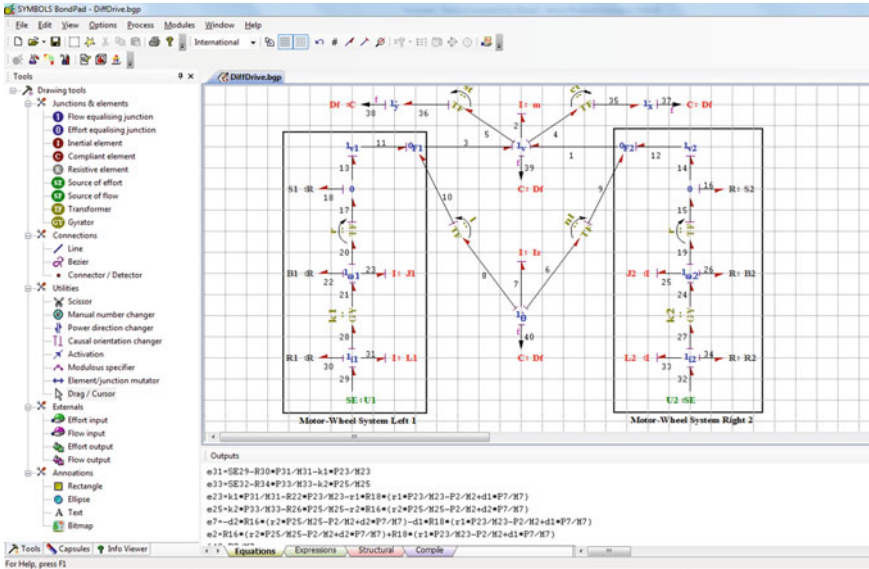
Fig. 3 BG modeling and simulation software SYMBOLS
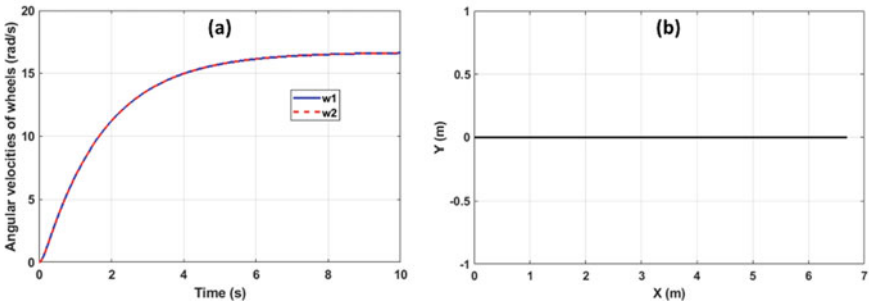
Fig. 4 Equal input voltage to both the motors: **a** angular velocities and **b** trajectory

The different input voltages are given to motors $U_1 = 10$ V and $U_2 = 15$ V. The results are shown in Fig. 6, where it can be seen that the changing values of friction coefficient affect the wheel forces, which leads to change in orientation and trajectory of the robot.
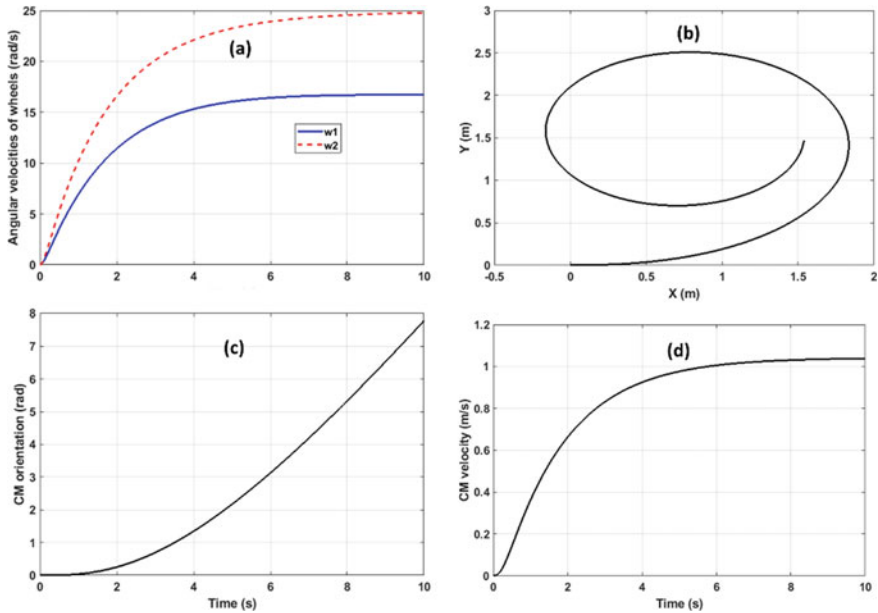
Fig. 5 Different input voltages to both the motors: **a** angular velocities, **b** trajectory, **c** orientation, and **d** velocity of the center of mass of the robot
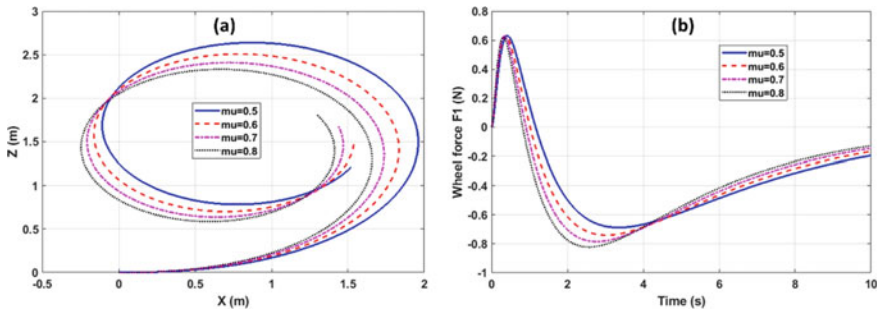
Fig. 6 **a** Trajectories and **b** left wheel forces for different values of coefficient of friction

5 Conclusion

This paper presents the dynamic model of a differential drive mobile robot using a graphical modeling tool called BG. The model considers the chassis, wheels, and actuators dynamics of the robot. The developed model is verified through simulation. The obtained simulation results show the expected dynamic behavior of the robot. Further, the robot's model is simulated over various surfaces with different friction

coefficients. For future work, it is interesting to use the developed BG model for control design with some faulty components.

References

1. Chung Y, Park C, Harashima F (2001) A position control differential drive wheeled mobile robot. IEEE Trans Industr Electron 48(4):853–863
2. Huang P, Zhang Z, Luo X, Zhang J, Huang P (2018) Path tracking control of a differential-drive tracked robot based on look-ahead distance. IFAC Papers OnLine 51(17):112–117
3. Yazdjerdi P, Meskin N (2018) Design and real-time implementation of actuator fault-tolerant control for differential-drive mobile robots based on multiple-model approach. Proc Inst Mech Eng Part I J Syst Control Eng 232(6):652–661
4. Alves TG, Lages WF, Henriques RV (2018) Parametric identification and controller design for a differential-drive mobile robot. IFAC Papers OnLine 51(15):437–442
5. Martins FN, Sarcinelli-Filho M, Carelli R (2017) A velocity-based dynamic model and its properties for differential drive mobile robots. J Intell Rob Syst 85(2):277–292
6. Abdulwahhab OW, Abbas NH (2018) Design and stability analysis of a fractional order state feedback controller for trajectory tracking of a differential drive robot. Int J Control Autom Syst 16(6):2790–2800
7. Mukherjee A, Karmakar R, Samantaray AK (2006) Bond graph in modeling, simulation and fault identification. IK International, New Delhi, pp 342–346
8. Kumar P, Merzouki R, Conrard B, Coelen V, Bouamama BO (2014) Multilevel modeling of the traffic dynamic. IEEE Trans Intell Transp Syst 15(3):1066–1082
9. Sahoo SR, Chiddarwar SS (2016) Dynamic modelling of four wheel skid mobile robot by unified bond graph approach. In: 2016 international conference on robotics: current trends and future challenges (RCTFC). IEEE, pp 1–6
10. Mukherjee A, Samantaray AK (2001) System modelling through bond graph objects on SYMBOLS 2000. Simul Ser 33(1):164–170

Investigating CVT as a Transmission System Prospect for Wind Turbine

Pranav Upadhyay, Suraj Pandey, Rachit Saxena, Yash Dixit, Vimal Yadav, Pikesh Bansal, and Shivam Sharma

Abstract Wind energy is a renewable source of energy besides being a clean source of energy. At a time when conservation of resources is the need of the hour, the better utilization of the present reusable sources should be the utmost priority. One of them being the wind turbines. A wind turbine is a device, which converts the energy of wind into mechanical energy, and this mechanical energy with the help of a generator is converted into electrical energy. The conservation of energy is at the top for a sustainable and quality environment and wind energy is one of the few yet best renewable resources. The vast potential of wind energy has never been in doubt however, access to abundance has always been a challenge. This paper covers the possibility of enhancing the existing methods of power transmissions and thereby the better efficient performance of the wind turbine The present electrical methods to cover for the variation in speed of the wind and variable input to the generator is doing a good job but this paper encroaches the mechanical aspect of the system something which has not been looked at while this time. The arrival of Continuously Variable Transmission (CVT) in the automobile industry was a breakthrough in automatic power transmission. We credit our inspiration and approach the CVT only, the ability to provide optimal gear ratio in varying conditions is what we engulfed upon. We are proposing the design of a system based on CVT to provide the solution to the varying input problem to the generator.

Keywords Wind turbine · Wind turbine transmission · Continuously variable transmission (CVT)

1 Introduction

The current ecological condition is a recent cause of worry for a large number of environmental activists. The two main reasons that appear to be the highlight, first, the increasing pollution and its ill effects and second, the unavailability or successful

P. Upadhyay (✉) · S. Pandey · R. Saxena · Y. Dixit · V. Yadav · P. Bansal · S. Sharma
Department of Mechanical Engineering, ABES Engineering College, Ghaziabad, India
e-mail: upad.pranav1202@gmail.com

483

usage of green sources of energy, which forces us to shift towards the conventional fuels such as coal, crude oil, etc. Solar energy and wind energy are the most common renewable energy resources. Out of them, solar energy has always been a center of development. But with the recent growing trends, wind energy is the fastest growing renewable source of energy. This has been the common center of discussion for researchers across the world.

In February 2019, an initial statistic was released by WWEA according to which the total wind turbine capacity worldwide touched 597 GW till the end of 2018. In the year 2017, a total of 52.552 MW was added worldwide whereas in 2018 only 50.100 MG were added. In 2017 the growth rate of new installations was around 10.8% and in the consecutive year of 2018, the growth rate of new installations was 9.1%. Estimated 6% of the worldwide demand for electricity will be covered by all the turbines installed worldwide by the end of 2018 [1]. With this increasing capacity several designs have been proposed and practiced for the transmission system of wind turbine. But, the demand for creating a simpler and more reliable system for transmission in wind turbines still exists. This paper reviews the various techniques used in designing the transmission techniques and presents an innovative solution to the existing transmission system which is inspired by the principle of working of Continuous Variable Transmission, commonly abbreviated as CVT. CVT has been a topic of research for wind energy researchers and has also proved its worth in the field of effective transmission of energy using mechanical engineering methods and power electronics. CVT bargains a range of gear ratios between anticipated boundaries. This gives more time for the engine to operate in the optimum range. Whereas, in a traditional gear setup, a lot of limitations pertaining to several fixed transmission ratios forces the engine to operate outside the optimum range.

2 Literature Review

Denis Alkan [2] investigated the possibility of using CVT as means of transmission and also covers the need to do so. The paper presents a comparative study of the existing power electronics method and conventional gearbox not only the cost basis but the performance as well. With the help of a designed mathematical model, the possibility of CVT has been confirmed by the help of analysis. The efficiency of the energy production of the wind turbine increases with CVT has been clearly shown with the results.

The above graph clearly shows the dependency of efficiency on factors like gear ratio and torque generation. Figure 1 concludes that the efficiency can be up to 98% in optimum cases, which according to this study occurs at wind speed greater than 7 m/s. But at a low speed, the CVT offers a much-improved performance and during the best and worst months, the performance is much better. The frequency control with the CVT system is a strong replacement for the existing expensive power electronics ultimately reducing the maintenance and overall cost. Though, the factors such as friction torque and mechanical efficiency of the CVT are not considered in this overall

Fig. 1 Measured
mechanical efficiency data of
30 mm GCI chain CVT
(Verdonschot 2009)
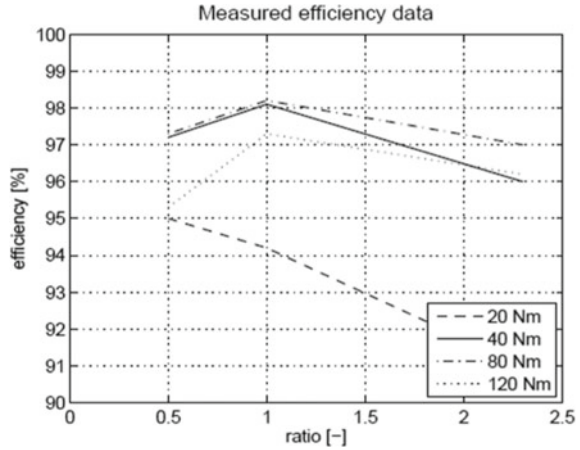
analysis. The heating effects and lubrication mechanism needs to be figured out and then needs a careful study, also the strength analysis of the system has not been done.

Verdonschot [3] has covered the possibility of maximum energy capture and limiting the dynamic loads while using CVT with the help of MATLAB/SIMULINK. The entire wind turbine model is prepared first consisting of every main component and suitable assumptions are made for further analysis. The specific set points and control points help in achieving the highest possible energy capture. The wind speed range is assumed based on the previous existing numbers and the algorithm is used. However, for controlling the system there is another series of operations, and the whole process is completed in two steps. The controlling method stated in the paper is sufficient for the application but on the aspect of limiting the dynamic loading other operations may offer more. The possibility of CVT with certain modifications is well established. Still, in order to attain and obtain the best out of the intended mechanism, the configuration and uncertainties need to be looked at and better backups and improved ideas will be needed to avoid sudden failure and below-par performance.

Vishnu Seelan [4] has investigated the design, analysis, and applications of CVT. The paper has expressed every component of the CVT in detail starting from high-density belt, set of cone pulleys, actuator, torque converter, and so on. Evidence of the multi advantages offered by CVT has been well proved in the present study. It provides not only an unlimited gear ratio but also without any "shift shock". VT helps in running the machine on its optimum RPM range, providing a quicker better acceleration with low cost and lower number of parts. However, everything is not so green about CVT as it has limitations as well. Problem of friction between the belt and pulley causes wear and tear, also the material used in manufacturing of the belt affects the torque transmitting capacity of the system. The transmission fluid used is also costly.

Cotrell [5] assessed the implementation of CVT in place of power electronics (PE) which is currently used across all types of wind turbines. The main advantage of CVT overpower electronics is that it can go through rapid ratio changes and can

also soak up torque spikes. Therefore, this offers an economical solution in place of power electronics. This paper also focuses on potential economic and performance benefits when CVT is used in conventional wind turbine systems. The analysis of this paper shows that when a CVT is used then it lowers the starting speed to 5 m/s which is usually 6.5 m/s when a CVT is not used. This lower speed provides an approximately 0.6% increase in energy production which is roughly 32 MWh per year.

Claudio Rossi et al. [6] considered the possibility of using power slit electric driven CVT as key to wind energy conversion system. It is installed between the gearbox and generator. The CVT has a planetary gear system along with an electric device. It allows maintaining the constant speed of the generator while controlling the turbine rotor speed. This concept provides a complete dynamic model of transmission which is based on CVT. It also provides a design criterion for the size of CVT that will be used in that system. The combination of CVT and generator provides the best solution. It is an epicyclic gearing also known as a planetary gear system. The CVT disassociates the variable speed output from the constant speed of the generating machine.

The reliability problems linked with the gearbox associated wind turbines were researched by Ragheb et al. [7]. It also points out that the Continuous Variable Transmission (CVT) generally used in the automobile sector can be of use in place of existing transmission systems in the wind turbines. Almost over 1000 damage claims were reported due to gearbox and had to be replaced by Allianz, the German industry giant as per German Insurance Association.

Mangialardi et al. [8] focusses on the conversion of wind energy into electrical power which is particularly problematic owing to the changes in wind speed. It states incorporation of Continuous Variable Transmission (CVT) in between a wind turbine and generator. It also focuses on the type of regulator or control system to be used for the CVT. It also provided proper proof of the advantages of using CVT as a Transmission system in locations with available wind data.

From the literature review, it is quite evident that the wind turbine efficiency is affected due to variable wind speed. The wind speed is variable throughout any area, this issue needs to be addressed. Many solutions related to this has been submitted is based on electronics, no mechanical design solution is prevalent. The authors have worked in this area and proposed a preliminary design for the resolution of this problem.

3   Problem Statement

The inability to utilize full potential of wind energy is primarily due to the varying speed of the wind. As stated earlier the problem is somehow reduced by the electrical systems but the power electronics used are very expensive. Also, the constant gear ratio from the gearbox arrangement limits the usability of the lower wind speed and thus restricting the complete efficient utilization. The life of gears is also a

factor in increased maintenance cost as well. The generators require the rotation speed in a certain bracket range for quality electricity. Due to this requirement, the limitations are there when the speed varies. The quality of electricity produced is directly proportional to the load and the rotor speed though in a limit but the dead-end is way too far. Wind turbine is a very big installation and it becomes very difficult to provide maintenance again and again in a short duration. So, the necessity to implicate new measures is pivotal for the natural growth in renewable energy and the environment as well. The CVT used in the wind turbine is the field of interest in wind energy. Though not much significant practical work has been done as of yet researches has been going on for quite some time. This paper has analyzed and covered maximum researches for a better upcoming ideas and perfect implementation of the project. The designed system is based on CVT and will provide an excellent solution to the existing problems and the possibilities are immense for the development of the wind turbine.

4 Proposed Solution

We are proposing a design that is an alternative to the traditional gearbox as used in wind turbines. Here, we have used a Cone CVT with slots cut throughout the surface of the cone, and teeth of suitable thickness will be inserted in those slots (shown in Fig. 2). Teeth, free to move between the slots, will be connected through a chain drive between the two cones (one being driver and the other being driven). Teeth connected together with a circular mechanism for constant movement along with the chain is used as a transmission system.
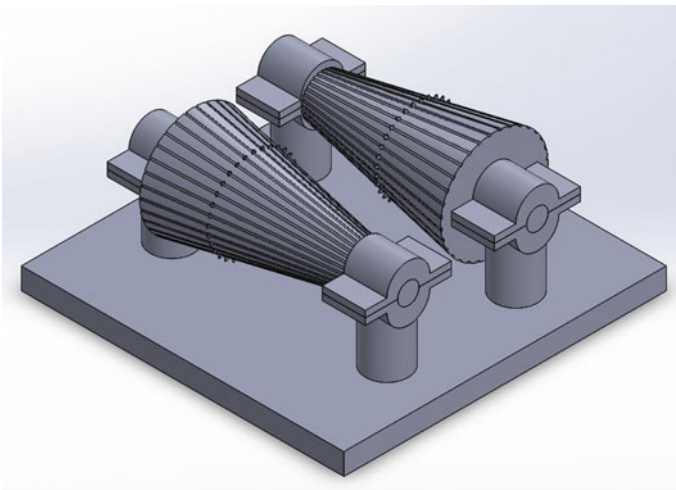
Fig. 2 Proposed design (isometric view)-designed in solid works 2018

5 Conclusion

In this review paper, the study of various research papers in context to the use of Continuously Variable Transmission as an alternative of gearbox in the wind turbines to provide a constant input to the generator of wind turbine is done. We are proposing a design that is an alternative to the traditional gearbox as used in wind turbines. Here, we have used a Cone CVT with slots cut throughout the surface of the cone, and teeth of suitable thickness will be inserted in those slots. Teeth, free to move between the slots, will be connected through a chain drive between the two cones (one being driver and the other being driven). The chain and sprocket mechanism may be used for the transmission from the variable output from the blades to provide a constant input to the wind turbine and thus eliminating fluctuations in the power output and also minimizing the use and reducing the cost of power electronics being used in the wind Turbines.

References

1. WWEA: Wind Power Capacity Worldwide Reaches 597 GW, 50,1 GW added in 2018, Press Release, https://wwindea.org/blog/2019/02/25/wind-power-capacity-worldwide-reaches-600-gw-539-gw-added-in-2018/. Accessed on May 2020
2. Alkan D (2012) Investigating CVT as a transmission system option for wind turbines KTH School of Industrial Engineering and Management Energy Technology, EGI-2011–2012, Division of Innovative Sustainable Energy Engineering, SE-100 44. Stockholm
3. Verdonschot M (2009) Modelling and control of wind turbines using a continuously variable transmission. Eindhoven University of Technology, Eindhoven
4. Seelan, V.: Analysis, design and application of continuously variable transmission (CVT). Int J Eng Res Appl 5(3)(Part-1):99–105 (2015). ISSN:2248-9622
5. Cotrell J (2005) Assessing the potential of a mechanical continuously variable transmission for wind turbines, golden. National Renewable Energy Laboratory, CO
6. Rossi C, Corbelli P, Grandi G (2009) W-CVT continuously variable transmission for wind energy conversion system. In: 2009 IEEE power electronics and machines in wind applications. Lincoln, NE, pp 1–10
7. Ragheb M (2011) Wind Turbine gearbox technologies, fundamental and advanced topics in wind power, Rupp Carriveau, IntechOpen
8. Mangialardi L, Mantriota G (1994) Automatically regulated CVT in wind power systems. Renew Energy 4(3):299–310

Optimization of the Suspension Parameters of a Quarter Car Model with Nonlinear Damper

Vipul Paliwal, Ritvik Dobriyal, Neeraj Sengar, and Pushpendra Kumar

Abstract Suspension system of a vehicle has always been an important part of design consideration in order to ensure passenger safety and ride comfort. Therefore, many studies have been performed for the suspension system analyses considering passive and active types of suspension. However, most of the vehicles are based on the passive suspension system. In this paper, a quarter car model is analyzed considering the passive suspension system, where the damper action is considered quadratic nonlinear. The main contribution of the paper is to optimize the design parameters, viz. spring stiffness and damper coefficient of the suspension in order to improve the ride comfort. Genetic algorithm is selected as the optimization tool. Finally, the model is verified through simulation in MATLAB/Simulink.

Keywords Quarter car model · Optimization · Modeling and simulation · Suspension

1 Introduction

Suspension system is one of the critical subsystems of a vehicle, which ensures not only the ride comfort but also the passenger safety. Many researchers devoted for improving the design of suspension systems. There are two types of suspension systems, namely active and passive. The active suspension system needs controlled input excitation power to reduce the effects of undesired oscillations due to road profile, and such type of suspension is used only in high-end vehicles due to their complexity and cost. Most of the vehicles use the passive suspension systems; in the present work, we focus on the dynamic analysis of the passive suspension system.

It is important to design the passive suspension system with optimum values of the elements such as spring stiffness and damping coefficient. In the existing literature, many works on the suspension system design have been found, which are detailed as follows. Lee [1] in his study tuned the damper by using the genetic

V. Paliwal · R. Dobriyal · N. Sengar · P. Kumar (✉)
Department of Mechanical Engineering, Graphic Era Deemed To Be University, Dehradun 248002, Uttarakhand, India
e-mail: kumar.pushpendra@geu.ac.in

algorithm and evaluated the optimized design parameters for damping force which resulted in the reduction in the acceleration of the sprung mass for the assumed vehicle suspension system. Mitra et al. [2] in their study used the genetic algorithm optimization technique to model a quarter car comprising of driver seat with driver body and found increase in the ride comfort by optimizing the suspension parameters like spring stiffness, tire stiffness, damping coefficient, and sprung mass acceleration.

Nagarkar et al. [3] presented a seat driver nonlinear quarter car model and determined the improvement in the ride comfort and health criterions using the non-dominated sort genetic algorithm (NSGA-II) technique. Chen et al. [4] presented the more accurate improved ride comfort model by introducing nonlinear damper, verified it with experiments and performed a bivariate analysis for finding out the sensitivity of suspension parameters to ride comfort. Puneet et al. [5] in their work determined the damping coefficient from the damper of the light motor vehicle and use those values in quarter car analysis to evaluate the ride comfort and road holding parameters using design of experiments.

Florea et al. [6] in their study optimized the suspension stiffness and damping coefficients by minimizing the sprung mass accelerations and displacements arising from kinematic factors. They excited the quarter car model of 2 D.O.F. by random road profiles having different road roughnesses and used genetic algorithm to obtain the required optimized results. Nagarkar et al. [7] implemented the genetic algorithm in the Mac person strut passive suspension system to minimize the vibration dose values (VDV), suspension space and sprung mass acceleration and displacement for better ride comfort. Maher et al. [8] in their study carried out the linear quarter car simulations and compared those results with the experimental results of passive suspensions which had shown reasonable unsprung mass amplitude frequency range for sinusoidal excitation.

Several researches had been performed in optimizing the parameters in quarter car suspensions using the genetic algorithm technique. Most of the previous researches are focused on optimizing the suspension system parameters having linear and nonlinear damper for providing the better ride comfort and road holding. Our present work focuses on the quadratic nonlinear damper in the passive suspension for optimizing the suspension parameters by utilizing the genetic algorithm technique. The quadratic nonlinear damper used in this study along with the genetic algorithm optimization technique has never used before in the previous researches of the quarter car suspension systems. The contribution of this work is that the optimized parameters can be considered in the automobile vehicle suspension systems for providing the improved ride comfort to the passengers and the driver.

The rest of the paper is organized in the following sections. The modeling of the quarter car model is presented in Sect. 2. Simulation results are discussed in Sect. 3. The paper is concluded in Sect. 4 with some future works.

2 Modeling

2.1 Suspension Parameters

In this work, a quarter car model is developed in order to analyze the performance of the suspension. The schematic diagram of the quarter car model is shown in Fig. 1. The quadratic nonlinear damping effect on the performance of suspension is studied using the quarter car model as shown in Fig. 1. The sprung mass is labeled as m_s and is suspended on the suspension spring labeled as k_s representing spring stiffness. The damper is labeled in Fig. 1 as c_s representing damping coefficient of suspension. The mass of wheel, wheel hub, and the adjoining suspension parts is lumped together as unsprung mass, labeled in Fig. 1 as m_u. This unsprung mass rests on the tire whose spring stiffness and damping coefficient are labeled in the figure as k_u and c_u, respectively. z_r is the vertical height from the road surface. z_s and z_u are the sprung mass and unsprung mass displacements, respectively.

The equations of motion for the quarter car model can be derived using Newton's second law of motion, and the second-order differential equations are given by:

$$\ddot{z}_s = -\frac{k_s}{m_s}(z_s - z_u) - \frac{c_s}{m_s}\mathrm{Sgn}(\dot{z}_s - \dot{z}_u)(\dot{z}_s - \dot{z}_u)^2 - g \tag{1}$$

Fig. 1 Schematic diagram of the quarter car model
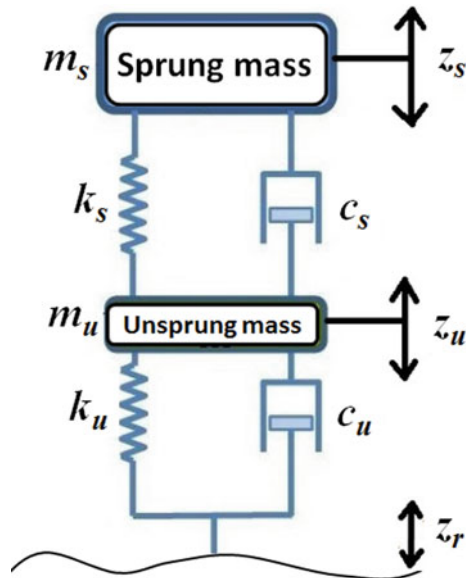
Table 1 Numerical values for the various parameters of the quarter car model

Parameter	Value
m_s	500 kg
m_u	30 kg
k_s	20,000 N/m
c_s	1500 N s/m
k_u	200,000 N/m
c_u	1 N s/m

$$\ddot{z}_u = \frac{k_s}{m_u}(z_s - z_u) + \frac{c_s}{m_u}\text{Sgn}(\dot{z}_s - \dot{z}_u)(\dot{z}_s - \dot{z}_u)^2 - \frac{k_u}{m_u}(z_u - z_r)$$
$$-\frac{c_u}{m_u}(\dot{z}_u - \dot{z}_r) - g \tag{2}$$

where first and second derivatives z_s, z_u, and z_r represent their velocities and accelerations, respectively. Sgn is the signum function. The numerical values of the parameters used in the study are given in Table 1.

2.2 Optimization

Genetic algorithm (GA) is an advanced tool for finding best solution in optimization of desired variables of an objective function. GAs are based on the procedure for searching of natural genetics and natural selection. This way of GA has struck several researches in natural science and engineering. Robustness of solution is the main objective of GA with the help of balance between efficiency and effectiveness of the solution. Goldberg [9] stated the principle and application of GA in engineering field. GA starts from initial population of possible outcomes, i.e., first generations. Reproduction (selection), crossover, and mutation are main operators for optimization of objective function of GA. However, there exist many other optimization techniques, but in this study, GA has been selected due to its ability of global search and easy implementation with good results [10]. GAs have been applied in the vehicle dynamic systems [11] including suspension system [12].

In the suspension system of the quarter car model, we are interested in improving the ride comfort, which can be realized by minimizing the acceleration of the sprung mass. Therefore, the optimization problem can be defined as follows:

$$\min_{k_s, c_s} \ddot{z}_s = f(z_s, z_u, z_r, \dot{z}_s, \dot{z}_u, k_s, c_s)$$

subjected to:

$$k_{s\,\min} \leq k_s \leq k_{s\,\max}$$

$$c_{s\,\min} \leq c_s \leq c_{s\,\max} \tag{3}$$

The fitness function for GA is based on the integral time absolute error (ITAE), where the absolute value of the sprung mass acceleration is multiplied by time, and its integration is performed for obtaining the ITAE value.

3 Simulation

The quarter car model is implemented in MATLAB/Simulink for analyzing the dynamic behavior over a road bump. The road bump profile is shown in Fig. 2a and the displacements of the sprung (z_s) and unsprung (z_u) masses are shown in Fig. 2b. In these results, the values of ks and c_s are not optimized and taken as given in Table 1. From these results, it can be observed that initially there is no displacement for two masses, but as the tire strikes the bump at 5 s, there are peaks for z_s and z_u. The sprung and unsprung masses start oscillating due to the effect of road bump, which leads to reduce in comfort for the driver and passengers. Therefore, it is necessary to reduce the amplitude of oscillations using suitable values of the parameters. Since drive comfort mainly depends on the sprung mass acceleration, hence, it is minimized by optimizing the values of suspension parameters, viz. k_s and c_s.

The values of k_s and c_s have been optimized using GA, and the population size and the number of generations take 50. The upper and lower bounds for k_s and c_s are taken as follows: $k_s = [10{,}000\ 30{,}000]$ and $c_s = [1000\ 3000]$. From the GA, the obtained optimized values are $k_s = 21{,}960$ N/m and $c_s = 1382$ N s/m. The results are shown in Fig. 3, where non-optimized and optimized results are compared.

From the simulation results in Fig. 3a, b, it can be observed that after applying the optimized values of k_s and c_s, amplitude of the sprung mass acceleration reduces which leads to improved ride comfort. In Fig. 3c, the amplitude of oscillations for sprung mass displacement is also reduced after optimization. Moreover, in Fig. 3d, the relative displacement between the unsprung mass and the road excitation is also reduced after optimization, which ensures better road holding capability.
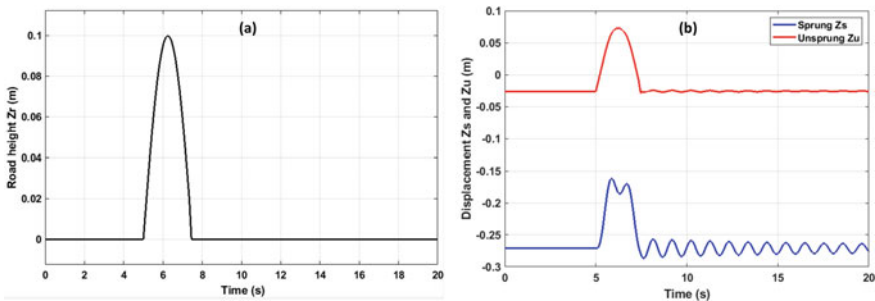
Fig. 2 **a** Road excitation and **b** displacements of the sprung and unsprung masses
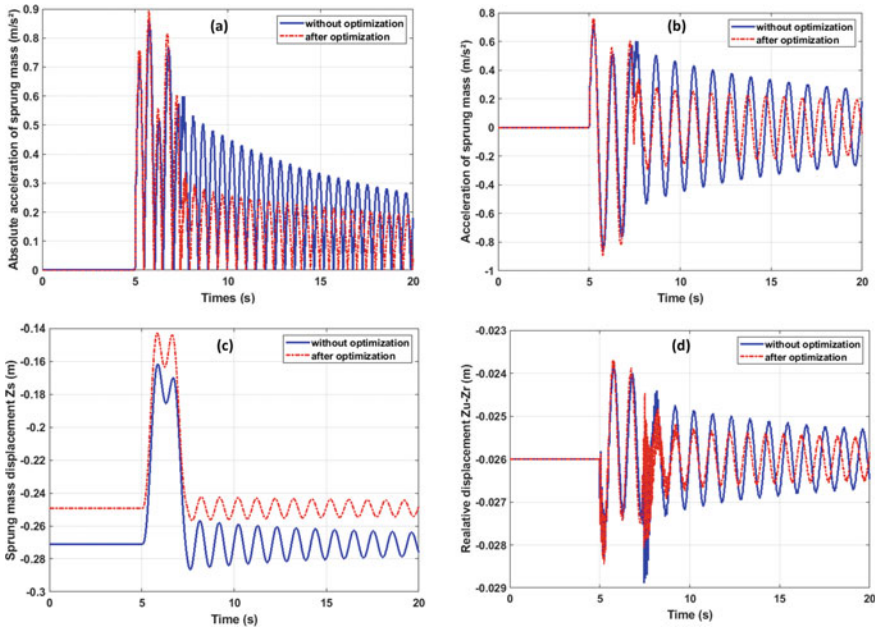
Fig. 3 Simulation results before and after the optimization **a** absolute acceleration of the sprung mass, **b** acceleration of the sprung mass, **c** displacement of the sprung mass, and **d** relative displacement between the unsprung mass and road height

4 Conclusion

The suspension dynamics of a vehicle is analyzed considering the nonlinear quarter car model. The suspension of the quarter car is modeled using a quadratic nonlinear damper. The performance of this nonlinear model is analyzed over a bumpy road. The optimization of the suspension parameters is performed using the genetic algorithm. From the simulation results, it can be concluded that the amplitudes of peaks are reduced for (i) sprung mass acceleration, (ii) sprung mass displacement, and (iii) relative displacement between the unsprung mass and road height, after incorporating the optimized values of k_s and c_s. Therefore, the optimized values of the suspension parameters resulted in improved ride comfort and road holding capability. For future work, it is interesting to analyze the performance of the suspension system over real road data.

References

1. Lee CT (2018) A study on the optimization design of damper for the improvement of vehicle suspension performance. J Drive Control 15(4):74–80
2. Mitra AC, Desai GJ, Patwardhan SR, Shirke PH, Kurne WM, Banerjee N (2016) Optimization of passive vehicle suspension system by genetic algorithm. Proc Eng 144:1158–1166
3. Nagarkar MP, Patil GJV, Patil RNZ (2016) Optimization of nonlinear quarter car suspension–seat–driver model. J Adv Res 7(6):991–1007
4. Chen K, He S, Xu E, Zhen W, Tang R (2019) Ride comfort analysis and multivariable co-optimization of the commercial vehicle based on an improved nonlinear model. IEEE Access
5. Puneet NP, Hegale A, Kumar H, Gangadharan KV (2019) Multi objective optimization of quarter car parameters for better ride comfort and road holding. In: AIP conference proceedings, vol 2200, No 1. AIP Publishing LLC, p 020046
6. Florea A, Cofaru I, Roman L, Cofaru N (2016) Applying the multi-objective optimization techniques in the design of suspension systems. J Digital Inf Manage 14(6)
7. Nagarkar MP, Patil VG (2016) Multi-objective optimization of LQR control quarter car suspension system using genetic algorithm. FME Trans 44(2):187–196
8. Maher D, Young P (2011) An insight into linear quarter car model accuracy. Veh Syst Dyn 49(3):463–480
9. Goldberg DE (2006) Genetic algorithms. Pearson Education India
10. Mirjalili S (2019) Genetic algorithm. In: Evolutionary algorithms and neural networks. Springer, Cham, pp 43–55
11. Jiang Y, Wu P, Zeng J, Zhang Y, Zhang Y, Wang S (2020) Multi-parameter and multi-objective optimisation of articulated monorail vehicle system dynamics using genetic algorithm. Veh Syst Dyn 58(1):74–91
12. Ramalingam M, Thirumurugan MA, Kumar TA, Jebaseelan DD, Jebaraj C (2019) Response characteristics of car seat suspension using intelligent control policies under small and large bump excitations. Int J Dyn Control 1–13

Estimation of Orthodontic Force Parameters with Developed Computer Application for *En-Masse* Retraction of Six Maxillary Anterior Teeth

Abhishek M. Thote, Rajesh V. Patil, and Sunita Shrivastava

Abstract In the current research study, a computer application (desktop software) was developed to determine orthodontic force application points to achieve *en-masse* retraction of six maxillary anterior teeth. In this type of tooth movement, retraction forces are applied with retraction spring by fixing it anteriorly and posteriorly. Based on other orthodontic force, moment and distance parameters, proper location of retraction spring attachment on anterior and posterior side is needed to ensure accurate application of orthodontic appliances. In this research study, the computer application (desktop software) based on simple trigonometric calculation was developed for the ease of estimation of location of required retraction force. This computer application can be used both in labial orthodontics (LaO) and lingual orthodontics (LiO) if other force, moment, and distance parameters are known. Due to simple user interface of computer application, the task of determination of force application points will be simplified for orthodontists which is desirable.

Keywords *En-masse* retraction · Six maxillary anterior teeth · Computer application · In vivo (clinical) testing

Nomenclature

C_{res} Center of resistance
P_f Anterior force application point of retraction spring
P_a Posterior teeth anchorage point of retraction spring
F_r Retractive force
Θ Angle of application of retractive force
M_c Counteracting moment

A. M. Thote (✉) · R. V. Patil
School of Mechanical Engineering, MIT - World Peace University, Pune, Maharashtra, India
e-mail: abhi.thote8@gmail.com

S. Shrivastava
Department of Orthodontics, Sharad Pawar Dental College, Wardha, Maharashtra, India

d^c Lingual distance of C_{res} of six maxillary anterior teeth from Iincisal edge (I)
h_c Apical distance of C_{res} of six maxillary anterior teeth from Iincisal edge (I)
d_f Lingual distance of point P_f from Iincisal edge (I)
h_f Apical distance of point P_f from Iincisal edge (I)
d_a Lingual distance of point P_a from Iincisal edge (I)
h_a Apical distance of point P_a from Iincisal edge (I)
h_{aw} Height of archwire level

1   Introduction

Orthodontic forces are applied to keep the teeth in well-organized structure [1]. Generally, teeth are protruded in many dental patients. In this orthodontic deformity, lips are protruded and face shape becomes convex in nature due to flaring of maxillary anterior teeth. In this case, *en-masse* retraction of maxillary anterior teeth is carried out by extracting both the pre-molar teeth [2].

Periodontal ligament (PDL) between tooth and bone should be protected in the orthodontic treatment. Hence, orthodontic force system should be optimized to ensure safety in teeth movement [3, 4].

The computed force parameters should be verified with a proper technique. Various biomechanical analysis methods are suggested by previous researchers like finite element analysis (FEA) [5], in vitro (laboratory) testing [6] and in vivo (clinical) testing [7], while in vivo (clinical) testing on respective patients is considered as a better treatment than others due to application on actual patients.

In the current research study, a computer application (desktop software) was developed to determine orthodontic force application points to achieve *en-masse* retraction of six maxillary anterior teeth. In this research study, the computer application (desktop software) based on simple trigonometric calculation was developed for the ease of estimation of location of required retraction force.

2   Development of Computer Application

In *en-masse* retraction, teeth are moved toward lingual (tongue) direction. The retractive force vector is generally inclined at a small angle θ with occlusal (horizontal) plane (OP). So, the net applied force can be divided into retractive (horizontal) force and vertical (intrusive) force. However, parallel (pure) retraction is achieved sometimes with $\theta = 0°$. Figure 1 represents retractive force with angle of application (θ) and different directions such as apical, occlusal, labial, and lingual as shown in this figure.

Figure 2 represents the necessary orthodontic force parameters for the *en-masse* retraction of six maxillary anterior teeth. In Fig. 2, all the considered points are
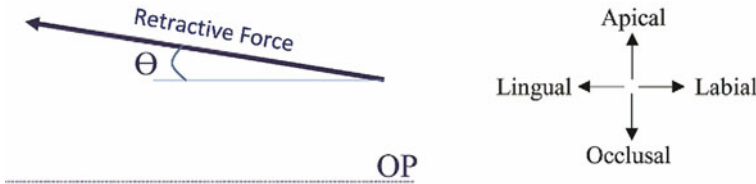
Fig. 1 Retractive force with angle of application (θ)
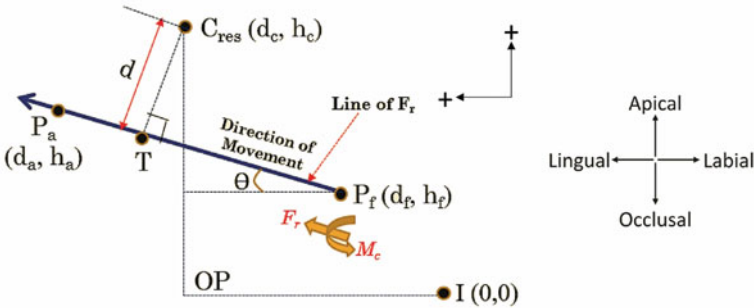
Fig. 2 Necessary orthodontic force parameters with reference points

projected on the sagittal, i.e., vertical plane and observed from the side (distal) view of teeth. The retractive force is applied with retraction spring from anterior attachment point (P_f) to posterior attachment point (P_a). The occlusal (horizontal) plane (OP) is assumed to be touching the incisal edge (I) of a maxillary central incisor tooth. The center of resistance (C_{res}) of six maxillary anterior teeth is considered to compute net (resultant) force system and it cuts the retraction force vector perpendicularly at a point T which is distance 'd' apart.

The manual computation of necessary force parameters is a very crucial task for orthodontists unlike engineers. Thus, the computer application is created in the current study using C++ programming language on Microsoft Visual Studio 2013 platform. Figures 3, 4 and 5 represent all the three screens of the computer application. There are certain input parameters (variables) which need to be entered in the computer application. The purpose of the study, i.e., "retraction of six maxillary anterior teeth" is displayed at the topmost location of all the three screens.

The first (starting) screen of the developed computer application is shown in Fig. 3. The diagram representing Fig. 2 is inserted in this first screen to represent necessary orthodontic force parameters with reference points. The certain values of distances are required to enter in this first screen by taking the projection of incisal edge (point I) as a reference. It includes the lingual (horizontal) distance (d_c) and the apical (vertical) distance (h_c) of C_{res} of six maxillary anterior teeth, lingual (horizontal) distance (d_f) of anterior spring attachment point or force application point (P_f), and the lingual (horizontal) distance (d_a) of posterior spring anchorage point (P_a). The
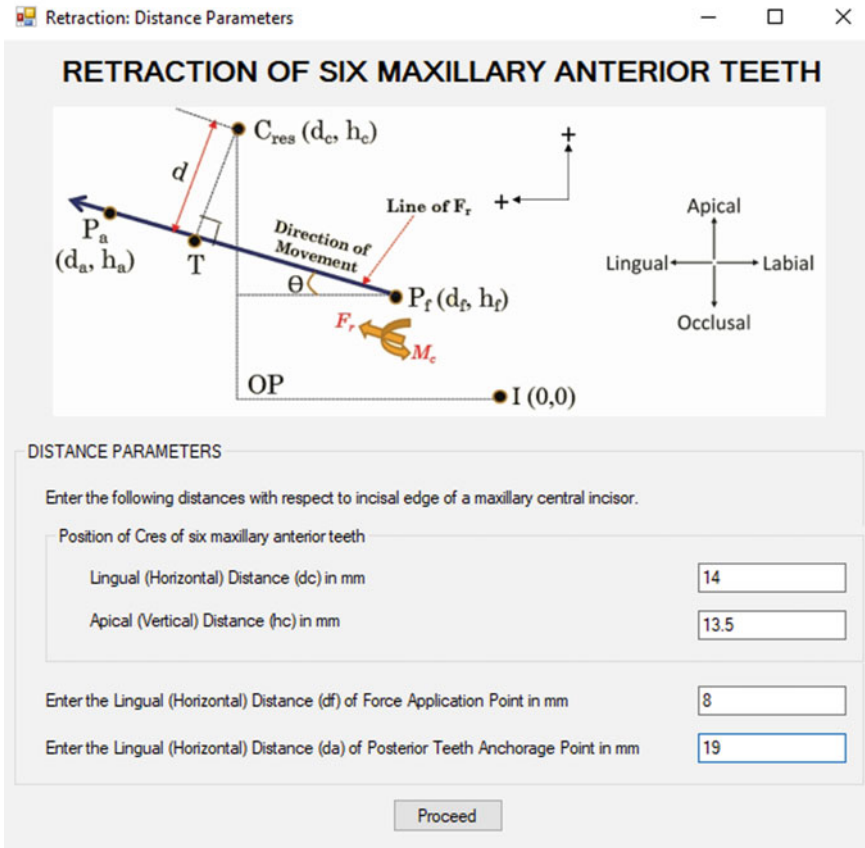
Fig. 3 First screen of the developed computer application

unit for distance values is taken as 'mm'. The resultant force system should be computed with respect to C_{res} so that single force should pass through it without any moment. Hence, position of C_{res} is a crucial factor. The approximate position of C_{res} is taken as 13.5 mm apical (vertical) and 14 mm lingual (horizontal) from the projected point I of incisal edge of a maxillary central incisor [8]. To proceed to next (second) screen of computer application, the person needs to click on 'proceed' tab (button) at the bottom of first screen.

The second screen of the computer application is shown in Fig. 4 with two notifications. The necessary force or moment parameters for half (three) anterior teeth needs to be entered. So, the same parameters must be applied for other three anterior teeth considering sagittal (vertical) plane as a dividing plane. Here, the person should enter the magnitude and angle (θ) of retractive force (F_r) in grams and degrees, respectively. Then, the height of archwire level (h_{aw}) in mm should be entered. Based on this value of h_{aw}, the computer application displays the permissible range of
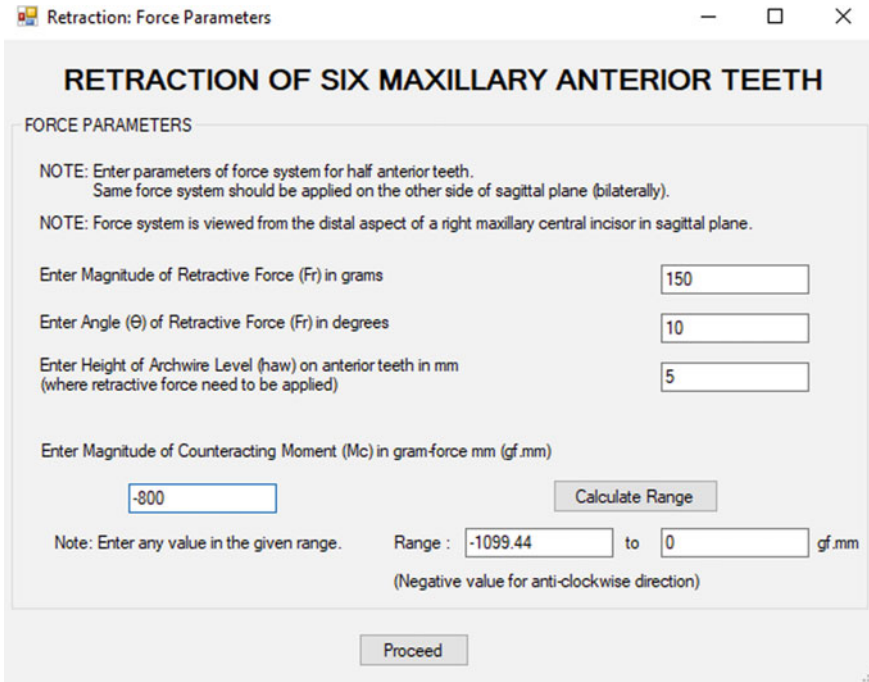
Fig. 4 Second screen of developed computer application
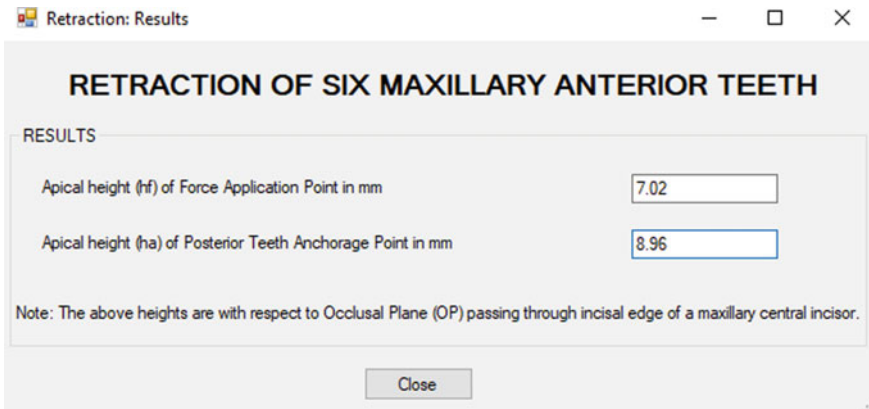
Fig. 5 Third (last) screen of developed computer application

required counteracting moment (M_c) in gram-force mm (gf.mm) after clicking on the button 'Calculate Range'. From this suggested range, the value of M_c applied by an orthodontic appliance should be entered in this second screen. The maximum desirable negative (–) value of M_c displayed in the software (first value in the suggested range) corresponds to estimation of minimum feasible value of h_f and h_a. The other entered value of M_c from the displayed range will estimate optimum values of h_f and h_a based on M_c and other parameters. To keep the lesser values of h_f and h_a, the retractive force (F_r) vector should pass occlusal to C_{res} which develops clockwise (+) moment M_f due to F_r. Hence, the negative (–) value of M_c should be entered to represent its anti-clockwise direction. All these parameters entered in first and second screens, i.e., d_c, h_c, d_f, d_a, F_r, Θ, h_{aw}, and M_c are input parameters. To proceed to next (third) screen of computer application, the person needs to click on 'proceed' tab (button) at the bottom of second screen.

Figure 5 represents the third (last) screen of the computer application. Based on all the input parameters as shown in first and second screens, the computer application displays the computed values of apical height (h_f) of anterior force application point (P_f) and apical height (h_a) of posterior teeth anchorage point (P_a) of retraction spring. These values of heights are the output parameters of the developed computer application which show distance values of retraction spring attachment points anteriorly and posteriorly from the occlusal (horizontal) plane (OP). At the lower portion of the third screen, 'Close' tab (button) is kept to close the running computer application.

3   Results

In vivo (clinical) testing is accomplished to validate the success of output parameters of developed computer application. For this purpose, input (given) and output parameters shown in Figs. 3, 4 and 5 are used. In this clinical testing of labial orthodontics (LaO), *en-masse* retraction movement of six maxillary anterior teeth was performed. For this purpose, 0.022 inch stainless steel labial MBT brackets and 0.019×0.025 inch archwire of stainless steel were used. The entire treatment time was nearly 9–10 months. Retractive forces are applied bilaterally. To keep proper anchorage, orthodontic force system was activated once in a month [9]. The gender and age of any patient are non-prime factors and included for illustrative reasons only.

Fig. 6a and b represents patient's teeth photographs (female with 17 years of age) prior and after orthodontic treatment, respectively.

From the after treatment results, it is clearly visible that the successful *en-masse* retraction of six maxillary anterior teeth is obtained in the patient. Hence, parameters computed with the aid of developed computer application can be considered as accurate.

The application of orthodontic force at a proper point is a key parameter for successful orthodontic treatment. In traditional method, orthodontists select the position of force application according to approximate judgment as per their expertise. However, it may lead to excess required time for successful treatment. Generally, this
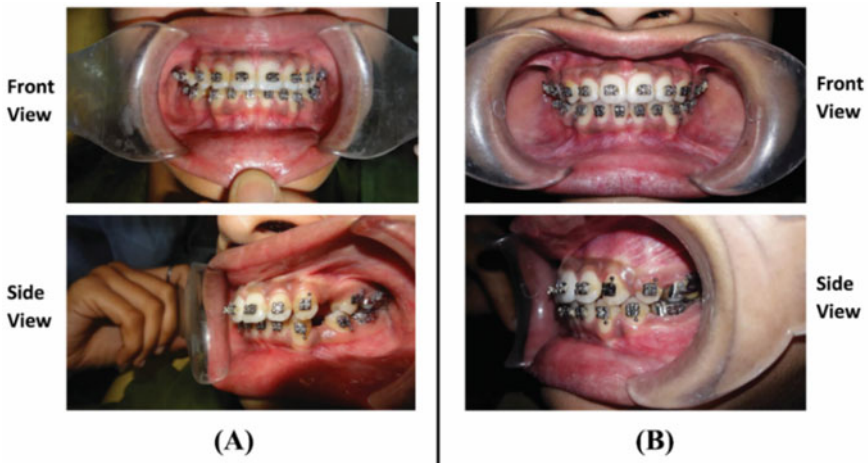
Fig. 6 Patient's teeth photographs (female with 17 years of age) **a** prior treatment and **b** after treatment

treatment needs one year. It is observed that the developed computer application is able to estimate proper positions of force application points which lead to successful clinical orthodontic treatment on the patient and treatment was completed in 9–10 months. Thus, the developed computer application plays a key role in shortening and optimizing treatment time. It is a considerable factor which leads to improvement in orthodontic treatment efficiency [10].

4 Discussion

In the developed computer application, the person needs to specify position of C_{res}, anterior and posterior horizontal distance of retraction spring attachment, i.e., d_f and d_a, respectively, magnitude and angle (θ) of retractive force (F_r), height of archwire level (h_{aw}). Based on these parameters, computer application suggests the necessary range of counter-acting moment (M_c). From this range, proper value of M_c needs to be entered as suggested by orthodontist by considering dimensions of brackets and archwires. Then, this computer application gives output parameters in terms of anterior and posterior vertical distance of retraction spring attachment, i.e., h_f and h_a, respectively.

All the aforementioned input parameters are based on magnitude and direction of retractive force (F_r) and counter-acting moment (M_c), retraction spring application points (P_f, P_a) and position of C_{res} of six maxillary anterior teeth. As suggested by orthodontists, all the aforementioned input parameters are needed to compute output parameters (h_f, h_a) for *en-masse* retraction orthodontic treatment.

In vivo (clinical) testing is accomplished to validate the success of output parameters of developed computer application. For this purpose, input (given) and output parameters shown in Figs. 3, 4 and 5 are used. In this clinical testing of labial orthodontics (LaO), *en-masse* retraction movement of six maxillary anterior teeth was performed successfully based on parameters computed by computer application. Hence, parameters computed with the aid of developed computer application can be considered as accurate.

In this study, in vivo (clinical) testing is carried out with labial archwires and brackets only. The detailed study with more clinical trials is needed in future for both labial orthodontics (LaO) and lingual orthodontics (LiO) treatment methods. Further, this computer application can be provided on internet platform so orthodontists can download it easily. Additionally, mobile application can be created in future to increment the users of this application by making it portable.

5 Conclusion

The highlighting points of this study are as follows:

- Due to simple user interface of the computer application, the task of determination of force application points will be simplified for orthodontists which is desirable.
- The task of computation of output parameters can be completed quickly (approximately within a minute).
- The developed computer application can be used both in labial orthodontics (LaO) and lingual orthodontics (LiO) if other force, moment, and distance parameters are known.
- In future, mobile application can be developed from this computer application to make it portable.

References

1. Park JH, Kook YA, Kojima Y, Yun S, Chae JM (2019) Palatal *en-masse* retraction of segmented maxillary anterior teeth: a finite element study. Korean J Orthod 49(3):188–193
2. Thote AM, Uddanwadiker RV, Sharma K, Shrivastava S, Reddy V (2020) Optimum force system for *en-masse* retraction of six maxillary anterior teeth in labial orthodontics. J Mech Med Biol 20(2):195006601–195006620
3. Kim T, Suh J, Kim N, Lee M (2010) Optimum conditions for parallel translation of maxillary anterior teeth under retraction force determined with the finite element method. Am J Orthod Dentofac Orthop 137:639–647
4. Brodsky JF, Caputo AA, Furstman LL (1975) Root tipping : a photoelastic- histopathologic correlation. Am J Orthod 67:1–10
5. Thote AM, Uddanwadiker RV, Sharma K, Shrivastava S (2016) Optimum force system for intrusion and extrusion of maxillary central incisor in labial and lingual orthodontics. Comput Biol Med 69:112–119

6. Desai SH, Gandhi FM, Patel K, Agrawal S (2019) Comparison of friction in sliding mechanics using different ligation methods on ceramic bracket with metal slot and epoxy resincoated stainless steel esthetic wire: An in vitro study. J Indian Orthod Soc 53(2):101–108
7. Yoshida N, Koga Y, Mimaki N, Kobayashi K (2001) In vivo determination of the centres of resistance of maxillary anterior teeth subjected to retraction forces. European J Orthod 23(5):529–534
8. Jeong GM, Sung SJ, Lee KJ (2009) Finite-element investigation of the center of resistance of the maxillary dentition. Korean J Orthod 39(2):83–94
9. Mckinney JR, Harris EF (2001) Influence of patient age and sex on orthodontic treatment: evaluations of Begg lightwire, standard edgewise, and straightwire techniques. Am J Orthod Dentofac Orthop 12:530–541
10. Liu Y, Wu Y, Yang C, Song J, Fan Y (2020) Biomechanical effects of corticotomy facilitated orthodontic anterior retraction: a 3-dimensional finite element analysis. Comput Method Biomech Biomed Eng 23(7):295–302

Comparative Analysis of Femur Bone's Compatible Materials by Finite Element Analysis (FEA) Tool

Vineet Kumar, Ahmad Reshad Bakhtari, Payal Himanshu, and Waseem Akhtar

Abstract In the present paper, the deformation of human femur bone with different materials under axial and bending loads is analysed. To perform this, a CAD model of the human femur bone has been developed by the help of CT scan imaging and SolidWorks, and then this model is used to develop an FEA model that consists of 3861 quadrilateral elements and 7201 nodes. The static structural model of analysis is used to analyse the developed model with three different materials properties (bone, titanium alloy and stainless steel) under different boundary conditions. For a range of axial and bending loads, the results are achieved. The sensitivity of the structure towards deformation for bone, titanium alloy and stainless steel is computed in this analysis. The achieved results give an understanding of the vulnerability of the three different materials towards deformation. Orthopedists can then take advantage of these results to select the right material for developing synthetic bones.

Keywords FEM · Femur bone · CAD model · Deformation · Stress concentration

1 Introduction

1.1 Finite Element Analysis

The finite element analysis (FEA) is a numerical technique and procedure to find approximate solutions of partial differential equations. It developed due to the need of solving complex elasticity and structural analysis problems in civil, mechanical and aerospace engineering. FEA is the practical method and application of finite element methods; as an example, it can be used to analyse the design of a new product using numerical mechanics of materials [1] before its production. FEA helps in detailed visualization of the distribution of stresses and strains inside the body of

V. Kumar (✉) · A. R. Bakhtari · P. Himanshu · W. Akhtar
Sharda University, Knowledge Park III, Greater Noida 201310, India
e-mail: vineet.kumar5@sharda.ac.in

A. R. Bakhtari
e-mail: ahmadreshadbakhtari@yahoo.com

a structure. The first application finite element method in bone biomechanics goes back to the analysis of the mechanical behaviour of skeletal parts in 1972 [2]. Later, this method has steadily become a tool for analysing the fracture, stress generation, etc., in biomechanics.

1.2 Femur Bone

The femur bone or thighbone is the longest and strongest bone in the human body. The long bone's primary function is as the major support system of the body and as a movement facilitator. The two femur bones serve as pillars in our legs that allow us to walk, run, jump and make all kinds of other movements. As the femur bone is the only bone in the thigh, it serves as an attachment point for all the muscles that exert their force over the hip and knee joints. Femur bone encompasses almost 26% of the height of a person [3] (see Fig. 1) as its thickness varies from 4 to 8 mm and length varies from 260 to 293 mm [4].

Fig. 1 Human femur bones [5]

1.3   Finite Element Analysis of Human Femur Bone

When the applied load exceeds the ultimate strength of the bone, the bone tends to fracture. Finite element analysis is a way of analysing and indicating the approximate stress concentration, which compels the structure to failure and fracture. It is the most common used technique to analyse and examine the structural stresses [1]. FEA is the easiest way to investigate the fracture mechanism, fatigue and reaction of the bone towards the loads applied on it. From the first application of FEA in biomechanics [2] onward several studies and analyses using FEA have been carried out on human bones.

R. Chand in 1976 with the help of FEA software NASTRAN analysed the contact stress between the bones of human knee joints (femur and tibia) [6]. B. R. Simon in 1977 studied the internal fixation of bone configuration by using FEA and experimental studies by using titanium alloy as the plate material [7]. Williams Svensson [8] and Valliappan et al. [9] performed experiments to analyse the distribution of stress across the neck of the femur bone, and Elkholy et al. [10] analysed it by developing the finite element models under normal conditions. Assessment and investigation of the stress distribution are a key method to know the fracture mechanism of a structure. In 1986, P. K. Basu has performed the stress analysis of an adult human femur bone using CT scans and P-version FEA [11]. Later on, researchers around the world have conducted several studies; Z. Yosibash in 2007 through experimental observations has shown the reliable simulations of the human proximal femur by high-order finite element analysis [12]. Ural in 2011 by the help of FEA studied the effect of strain rate on cortical bone [13]. R. Sherekar in 2014 performed a study and analysis on the human clavicle's response during collision [14]. U. Mughal in 2015 using FEA software ANSYS analysed the stress distribution and stresses experienced by human femur bone [15]. In the latest research works, Yekutiel Katz in 2018 conducted a study of patient-specific FEA of femurs with the help of cemented hip implants. In his study, he found that the strains observed by FEAs were in excellent correlation with the experimental outputs [16].

2   Methodology

In the current analysis, FEA software ANSYS is used. FEA (ANSYS) has three main stages: pre-processing, processing and post-processing. In the pre-processing stage, one creates the CAD model of the geometry, meshes the geometry and assigns the material properties. In the processing stage, it applies the boundary conditions (loads and constraints) and then the software solves the problem. In the post-processing stage, the software gives the required results (graphs, stress distribution and deformation). Figure 2 gives a view of the general procedure for applying the FEA. Static structural type of analysis is used for the current analysis.
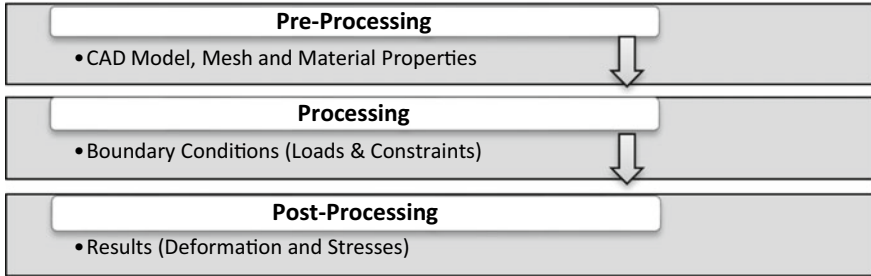
Fig. 2 Stages of bone finite element modelling

2.1 Pre-Processing Stage

Geometry (CAD model). The CAD model of femur bone is too difficult to generate with the exact shape and geometry, but thanks to the advanced technology that gives us, the ability to generate the precise and exact CAD models of human body parts. The first step to generate the CAD model of the femur bone is to collect the cloud points of the bone geometry through a CT scan, which gives in the file format of (.sat). Then by using SolidWorks, the CAD model will be generated. Figure 3 shows the CAD model of the femur bone, which is generated through the SolidWorks and CT scans.

  Material properties. Three types of materials are used for the current analysis (bone material, titanium alloy and structural steel). Table 1 shows the basic properties of the materials required to perform the analysis. The material properties of bone assumed for a 65 kg in weight adult to be as follows [17].

Fig. 3 CAD model of femur
bone
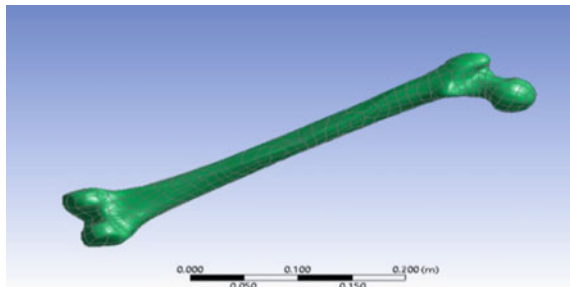
Table 1 Properties for three
materials

Property	Bone	Ti alloy	Stainless steel
Young's modulus	17 GPa	96 GPa	193 GPa
Poisson's ratio	0.3	0.36	0.31
Density	2000 kg/m^3	4620 kg/m^3	7750 kg/m^3
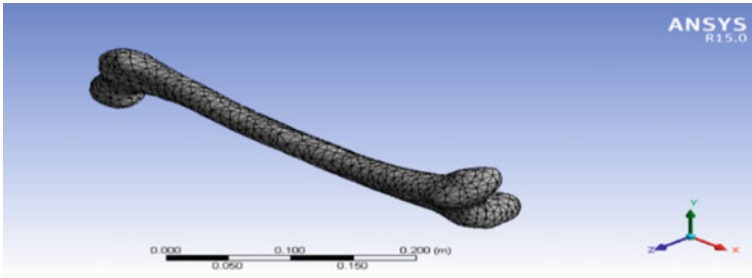
Fig. 4 Finite element meshing of femur bone in ANSYS

FEA meshing of femur bone. To mesh the model first the type of element should be specified. For the current model, the quadrilateral type of element is chosen. The mesh consists of nodes and elements; the current model's mesh has 3861 and 7201 elements and nodes, respectively. Figure 4 shows the model after meshing.

2.2 Processing Stage

Boundary conditions (BC). The problem is analysed under two conditions:

a. Axial loading
b. Bending loading

At first condition, the axial load on the upper body of the femur bone (on hip) is applied and the other end of the bone kept fixed as shown in Fig. 5a. In the second condition, the bending load on the upper body of the femur bone (on hip) is considered and the other end of the bone kept fixed as shown in Fig. 5b. After applying all the boundary conditions, the software is initiated to solve the problem for the desired results.
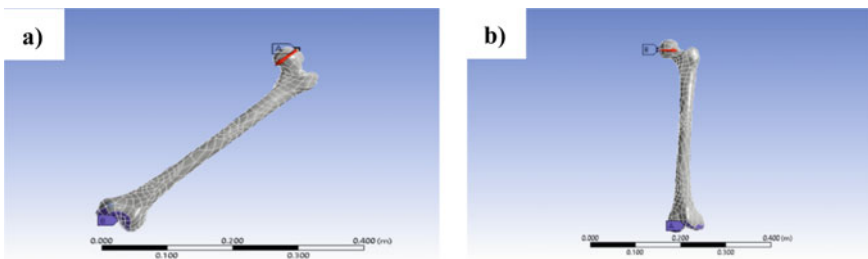
Fig. 5 a BC under axial loading and **b** BC under bending

Table 2 Human femur bone under different loading with bone material properties

Axial load	Max. principle stress (Pa)	Max. deformation (m)
100	2.21E+06	5.82E–04
200	4.41E+06	1.16E–03
300	6.62E+06	1.75E–03
400	8.83E+06	2.33E–03
Bending load	Max. principle stress (Pa)	Max. deformation (m)
100	1.1408e+007	2.675e–003
200	2.2816e+007	5.35e–003
300	3.4223e+007	8.025e–003
400	4.5631e+007	1.07e–002

2.3 Processing Stage

Tables 2, 3 and 4 show the results for each material type under different loading conditions. By using the ANSYS solver with the selected boundary conditions, the desired results were obtained for maximum principal stress and maximum deformation for each material type under different loadings. Figure 6 shows the graphs of maximum deformation against different axial and bending loads for each material type. Table 5 shows the specific strength of the three materials under the load of 300 N.

Table 3 Human femur bone under different loading with titanium alloy material properties

Axial load	Max. principle stress (Pa)	Max. deformation (m)
100	2.21e+06	1.03e–04
200	4.42e+06	2.06e–04
300	6.62e+06	3.09e–04
400	8.83e+06	4.12e–04
Bending load	Max. principle stress (Pa)	Max. deformation (m)
100	1.1421e+007	4.7357e–004
200	2.2842e+007	9.4715e–004
300	3.4262e+007	1.4207e–003
400	4.5683e+007	1.8943e–003

Table 4 Human femur bone under different loading with stainless steel material properties

Axial load	Max. principle stress (Pa)	Max. deformation (m)
100	2.21e+06	5.13e–05
200	4.41e+06	1.03e–04
300	6.62e+06	1.54e–04
400	8.83e+06	2.05e–04
Bending load	Max. principle stress (Pa)	Max. deformation (m)
100	1.141e+007	2.3562e–004
200	2.2819e+007	4.7123e–004
300	3.4229e+007	7.0685e–004
400	4.5638e+007	9.4246e–004
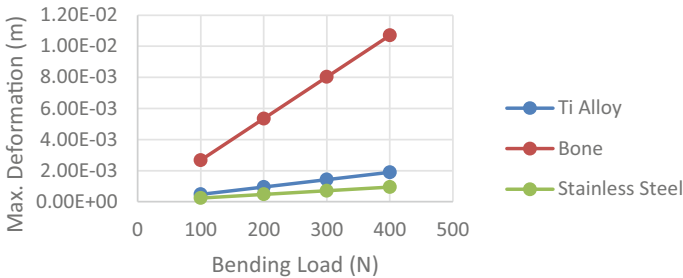
Fig. 6 Graphs of maximum deformation for different material type under bending load

Table 5 Specific strength of the three materials under the load of 300 N

Property	Bone	Ti alloy	Stainless steel
Max. stress	3.35E+07 Pa	3.36E+07 Pa	3.36E+07 Pa
Density	2.00E+03 kg/m^3	4.62E+03 kg/m^3	7.75E+03Kg/m^3
Specific strength	16773.80715 N m/kg	7269.778224 N m/kg	4329.241735 N m/kg

3   Conclusion

The achieved results show the vulnerability of the three different materials towards deformation under axial and bending loads. Figure 7 shows the graphs of deformation against the different axial and bending loads for each material. The bone material appears to be weaker than the other two materials. By comparing them, the stainless steel found to be the strongest material among them as it deforms less than the other two materials. But considering the weight an important aspect while developing synthetic bone substitutes the strength-to-weight ratio or specific strength of each material is considered. Table 5 shows the specific strength of each material. The
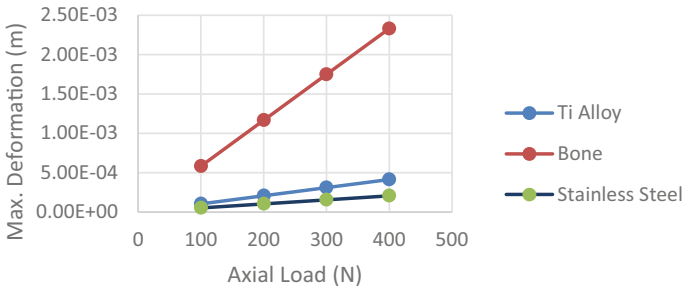
Fig. 7 Graphs of maximum deformation for different material type under axial load
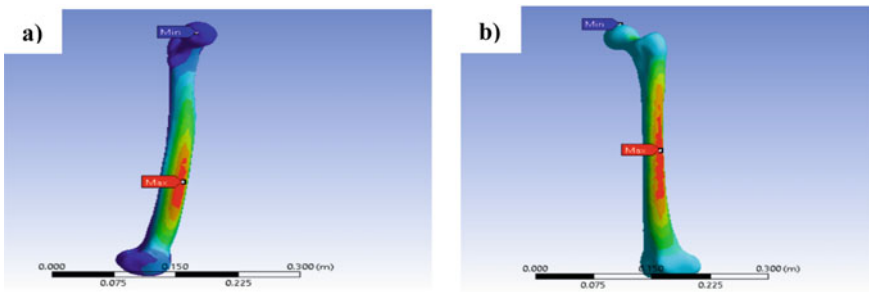
Fig. 8 Principal stress distributions under **a** bending load and **b** axial load

bone material has the highest specific strength followed by Ti alloy and stainless steel. Thus, Ti alloy is suggested as the best option for developing synthetic bone substitutes concerning specific strength. In the twenty-first century, Ti alloy is the most used material as the implant material due to its high biocompatibility [18]. Figure 8a and b shows the position or the area at which the femur bone has the highest risk of fracture under axial and bending load.

Figure 9 shows the distribution and position of the deformation in terms of maximum and minimum that the human femur bone will experience under loading. The results give an overview and idea for the orthopaedists to develop such synthetic bone substitutes that will withstand the applied loads and the graph in Fig. 7 can help them to select the appropriate type of material for developing the synthetic bone substitute.

Fig. 9 Deformation of bone under loading
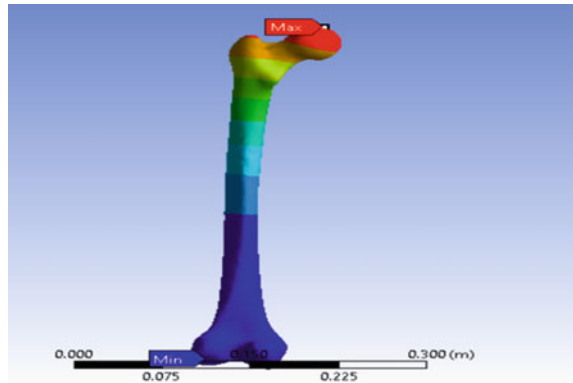
References

1. Stolarski T, Nakasone Y, Yoshimoto S (2018) Engineering analysis with ANSYS software. Butterworth-Heinemann
2. Huiskes R, Chao EY (1983) A survey of finite element analysis in orthopedic biomechanics: the first decade. J Biomech 16(6):385–409
3. Burstein AH, Currey JD, Frankel VH, Reilly DT (1972) The ultimate properties of bone tissue: the effects of yielding. J Biomech 5(1):35–44
4. Francis A, Shrivastava A, Masih C, Dwivedi N, Tiwari P, Nareliya R, Kumar V (2012) Biomechanical analysis of human femur: a review. J Biomed Bioeng 3(1)
5. https://imgur.com/gallery/Sz5Q6eN. Last Accessed 25 Dec 2019
6. Chand R, Haug E, Rim K (1976) Stresses in the human knee joint. J Biomech 9(6):417-IN5.
7. Simon BR, Woo SY, Stanley GM, Olmstead SR, McCarty MP, Jemmott GF, Akeson WH (1977) Evaluation of one-, two-, and three-dimensional finite element and experimental models of internal fixation plates. J Biomech 10(2):79–86
8. Williams JF, Svensson NL (1971) An experimental stress analysis of the neck of the femur. Med Biolog Eng 9(5):479–493
9. Valliappan S, Svensson NL, Wood RD (1977) Three dimensional stress analysis of the human femur. Comput Biol Med 7(4):253–264
10. Elkholy AH, Ghista DN, D'Souza FS, Kutty MS (2005) Stress analysis of normal and osteoarthritic femur using finite element analysis. Int J Comput Appl Technol 22(4):205–211
11. Basu PK, Beall AG, Simmons DJ, Vannier M (1985) 3-D femoral stress analysis using CT scans and p-version FEM. Biomater Med Devices Artif Organs 13(3–4):163–186
12. Yosibash Z, Trabelsi N, Milgrom C (2007) Reliable simulations of the human proximal Femurby high-order finite element analysis validated by experimental observations. J Biomech 40(16):3688–3699
13. Ural A, Zioupos P, Buchanan D, Vashishth D (2011) The effect of strain rate on fracture toughness of human cortical bone: a finite element study. J Mech Behav Biomed Mater 4(7):1021–1032
14. Sherekar R, Ganjare A, Pawar A (2014) Finite element analysis of human clavicle bone: a methodology review. American J Mech Eng Autom 1(5):54–59
15. Mughal U, Khawaja H, Moatamedi M (2016) Finite element analysis of human Femurbone. Int J Multiphy 9(2)
16. Katz Y, Lubovsky O, Yosibash Z (2018) Patient-specific finite element analysis of femurs with cemented hip implants. Clin Biomech 1(58):74–89
17. Lai YS, Chen WC, Huang CH, Cheng CK, Chan KK, Chang TK (2015) The effect of graft strength on knee laxity and graft in-situ forces after posterior cruciate ligament reconstruction. PLoS ONE 10(5):e0127293

18. Saini M, Singh Y, Arora P, Arora V, Jain K (2015) Implant biomaterials: a comprehensive review. World J Clin Cases WJCC 3(1):52

Design and Development of an Unmanned Aerial Cargo Vehicle Using Additive Manufacturing

Ashish Kumar, Shourya Sahdev, Avhishek Jha, Amit Kumar Gupta, and Samsher

Abstract Due to the rising need of the fast delivery among the many e-commerce companies, the possibility of introducing unmanned aerial cargo vehicle as a door-to-door delivery option is very much viable to the significant number of the delivery service industry in coming future. The introduction of unmanned aerial cargo vehicle technology can also help in reducing the CO_2 emission in the delivery service industry. The purpose of the research is to design and develop a model for the UACV and to study the effect of different design parameters on the performance of the aerial cargo vehicle. The mathematical modeling of the UACV with a load-carrying capacity of up to 350 gms helps to select the effect of design parameters. The model of its rotational, linear dynamics has been done using Simulink, and the PID control system was integrated into a model. The study was done on its attitude and altitude control. The aerial vehicle frame parts were designed considering the structural and aerodynamic stability of the aerial cargo vehicle using SolidWorks and analysis performed using Ansys 18.0 and Autodesk fusion. The material study performed for the design using Pugh's method for the additive manufacturing of the UACV. The most significant results mainly discuss the payload effect on the frame design and the effect on the control system of the UACV. The study definitively answers the effects of the environmental disturbances and the payload effect in the design of unmanned aerial cargo vehicle frames and its control systems.

Keywords Unmanned aerial vehicle · Cargo vehicle · PID control system · Delivery service industry · Additive manufacturing

A. Kumar (✉) · S. Sahdev · A. Jha · A. K. Gupta · Samsher
Delhi Technological University, Shahbad Daulatpur, Main Bawana Road, Rohini, Delhi 110042, India
e-mail: ashishkumar_bt2k16@dtu.ac.in

S. Sahdev
e-mail: shourya.sahdev@gmail.com

1   Introduction

Unmanned aerial vehicles (UAVs) or called drones are software-controlled where flight paths controlled by remote or autonomously installed with global positioning system (GPS) and various sensors on-board and used for various operations like flooding inspection [1], border surveillance [2], wildlife surveillance [3], and medical aids in calamity situations [4]. Emission of CO_2 produced by delivery vehicles is increasing day by day, and due to the rising demand for fast delivery by many e-commerce companies demands the new technology can make this process efficient and environmentally friendly. This project aims to build an unmanned aerial cargo vehicle that can deliver these purposes most efficiently.

The main objective of our research is to model and analyze the effect of the environmental conditions and design of UAVs on the load-carrying capacity of the UAVs. The primary design objective was to carry a payload of 350 gms with stable flight conditions, so to design such a load-carrying system, various constraints get scrutinized as lightweight, optimized dimensions, user-friendly interface, control systems, and lack of maintenance. UACV is designed and then fabricated; in the designing phase of UACV, material selection plays a vital role, which determines the overall weight, toughness, and durability of the drone. The material also plays a vital role in the design as if the overall weight of drones can directly affect the consumption of power to lift. The payload carry design considers the maximum amount of load it can carry along with installation constraint and stable operating condition. We are aiming in this research to design UACVs using inexpensive and lightweight materials that are having high mechanical performances.

2   Literature Review

This literature review explores the recent researches that have been performed for managing UAVs. Additionally, the research performed provides several avenues of future exploration in improving human factors for UACV operations as well.

Fahman et al. [5] manufactured four different strips of rectangular shapes of carbon fibers through vacuum bag technique (VBT) and compared them to real samples of UAVs. The chemical composition of real UAV samples that have been taken is of CF-100 and CF-200 range.

Fiaz et al. [6] have introduced dual impulsive techniques to do work on passive aerial grasping and explained the importance of horizontal translational freedom and counter-torque. Fiaz et al. [2] also proposed a new gripper design that outperforms in commercial availability and terms of power consumption and autonomous aerial grasping capabilities.

Mercado et al. [7] countered the issue regarding navigation and control for UAVs and developed a mathematical model as a hybrid system. Newton–Euler formalism has been used to obtain the continuous dynamics mathematical model.

Cuadrado et al. [8] designed a two-fingered gripping mechanism using grasp action and gripping mechanism. This has been formulated by taking into consideration various factors like the grasping index, performance index kinematic, and static characteristics.

Agarwala et al. [9] use additive manufacturing techniques for the fabrication of UAVs, which provides more flexibility to manufacture even more complex shapes.

Amelink et al. [10] made abstraction sophistication analysis (ASA) in use to make a more comprehensible user interface of a UAV swarm, where the task was to fly a UAV with fixed use to perform simple surveillance and navigation missions.

3   Simulink Model and Control System

The mathematical model developed for the unmanned aerial cargo vehicle and the Simulink model helps in simulating the full dynamics of the UACV as well as location and wind disturbances. The integration of the PID control system helps to control the position and altitude of the UACV.

The major forces which come into play during the motion of the UACV are motor thrust, wind disturbances, weight, motors/propellers torque, and the aerodynamic drag. The battery consists of four high discharge capacity Li–Po cells mounted in series. Each cell has a nominal voltage of 3.7 V. Its maximum discharge capacity is 40 °C (149.2 A). The battery gives us a maximum operating voltage of 14.8 V and a maximum discharge current of 149.2 A. These parameters allow us to limit the performance of the motor to realistic values.

Here, the assumption made for motor 0% RPM drop from Kv at 0 V and a 25% drop from Kv at a maximum voltage (14.8 V) due to the development of back emf in the motor at different angular velocity.

The propeller thrust modeled using blade element theory, where each blade of the propeller cut into small sections and the lift and drag of each of these sections analyzed and summed up. Individual propeller blades can be assumed to operate without interference from each other when spacing-to-chord ratio is sufficiently high. Figure 1 shows the forces acting on the propeller blade cross section.

Fig. 1 Forces acting on the cross section of propeller blades
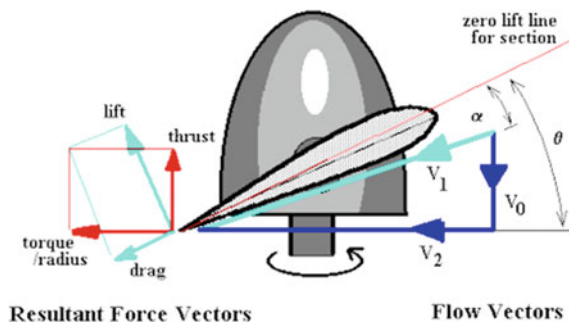
The difference between lift and thrust vector is $\varphi = \theta - \alpha$.

Total thrust and the torque for the propeller blade shown as:

$$\Delta T = \frac{\rho V^2 (C_l \cos \varphi - C_d \sin \varphi) \times B \times c \times dr}{2}$$

$$\Delta Q = \frac{\rho V^2 (C_l \sin \varphi + C_d \cos \varphi) \times B \times c \times r \times dr}{2}$$

In DC motor, torque and current are proportional to each other according to the following formula:

$$T = K_T I$$

The linear dynamics model for the UACV developed assuming the mass uniformly distributed across the aerial cargo vehicle. The motion of the aerial vehicle in space developed using the translational and rotational motion in three axes (X, Y, and Z).

Using Newton's second law of motion:

In the X-direction: $F_x = ma_x$.

In the Y-direction: $F_y = ma_y$.

In the Z-direction: $F_z = ma_z$.

Similarly, for the rotational dynamic model:

About the x-axis (Pitch): $M_x = I_x \ddot{\theta}_x$.

About the y-axis (Roll): $M_y = I_y \ddot{\theta}_y$.

About the z-axis (Y_{aw}): $M_z = I_z \ddot{\theta}_z$.

Where M the external torque or moments in Nm, I the moment of inertia in Kg m^2, and $\ddot{\theta}$ for the rotational acceleration in rad/s^2.

For motor propeller block, roll and pitch thrust vectors can be given as:

$$F_{\text{prop}_x} = \sin(\theta_y) \times \cos(\theta_x) \times (F_1 + F_2 + F_3 + F_4)$$

$$F_{\text{prop}_y} = \sin(\theta_x) \times \cos(\theta_y) \times (F_1 + F_2 + F_3 + F_4)$$

$$F_{\text{prop}_z} = \cos(\theta_y) \times \cos(\theta_x) \times (F_1 + F_2 + F_3 + F_4)$$

The forces $F_1, F_2, F_3,$ and F_4 each represent the thrust of their respective propeller. F_1 and F_2, as well as $F4$ and $F3$, are, respectively, coupled to induce pitch. F_4 and F_1, as well as $F3$ and $F2$, are, respectively, coupled to induce roll motion (Fig. 2).

The implementation of a dynamic system controller is to stabilize the unmanned aerial cargo vehicle desired motion and altitude. Figure 3 shows the Simulink model using a user-defined function block for human control input, motor propeller, gust disturbance, rotational dynamics, and linear dynamics blocks.

The PID control system is integrated into the model to achieve the required altitude and attitude control. User-defined MATLAB functions used to develop the blocks
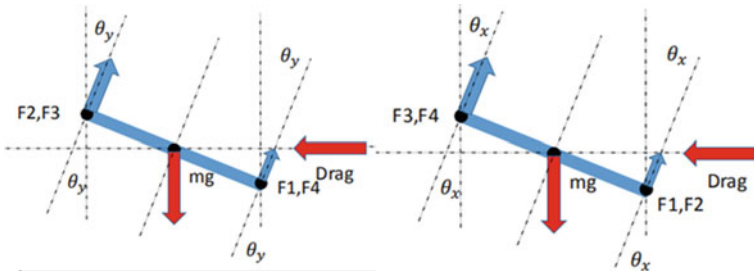
Fig. 2 Vector representation of roll and pitch thrust
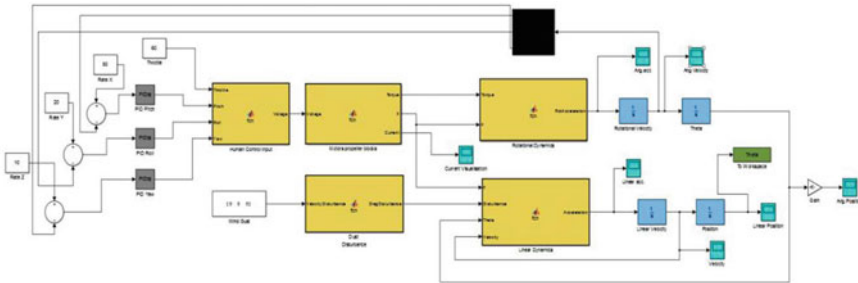
Fig. 3 Closed-loop control Simulink model for UACV

like human control input, which converts the input signal from the ground station like the throttle percentage, rate to roll, pitch, and yaw and convert it into the voltage. In the motor blocks, the torque and force are developed using the input from the voltage.

The linear dynamics model of the UACV delivers the linear acceleration under the environmental disturbances like wind gust and also considers the torque, force, and angular position of UACV.

For the throttle of 50% and the rate angular rotation along X is 50, along Y is 20, along Z is 10, and the wind gust of 5 m/s in the negative z-direction. Considering the payload of 350 gms, the results on UACV angular velocity are shown in Fig. 4. The pitch motion of 0.035 and yaw motion of 0.5 shows the path of UACV in 3D space in Fig. 5. The result is for the maximum payload condition.

The path of the unmanned aerial cargo vehicle is the motion in the x, y, and z axes. The graph shown in Fig. 6 shows the path for the maximum payload condition. It is expected that aerial vehicle should show the gradual movement and stability in the given external conditions of a wind gust of 5 m/s. The motion starts from point A and with half of the thrust vehicle attains altitude of 5 m from where the yaw and pitch motion starts acting which results in 10 m movement in $+ X$-direction, and after half rotation of yaw, the graph shows the movement in the $–X$-direction. The movement of the vehicle is gradual and shows excellent aerodynamic stability.
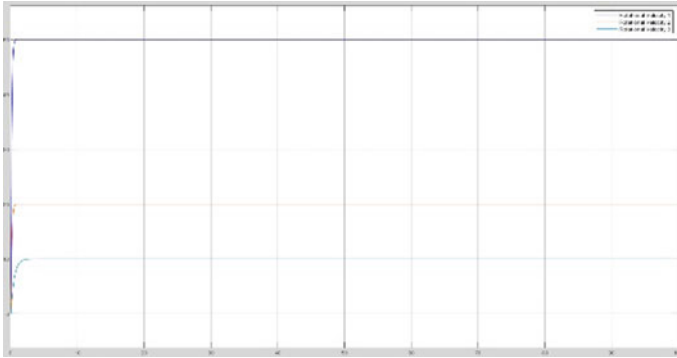
Fig. 4 Angular velocity in X, Y, and Z components
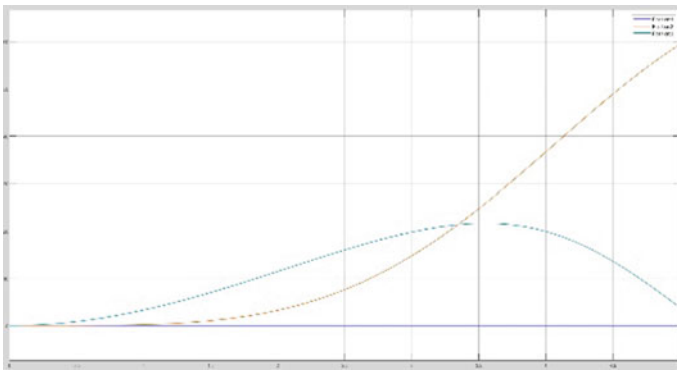
Fig. 5 Linear position of UACV in X, Y, and Z axes
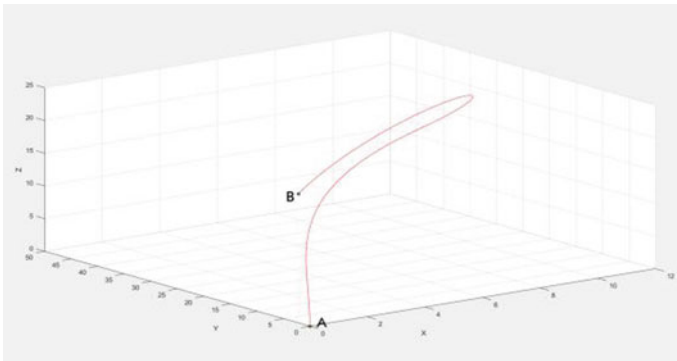
Fig. 6 Path of UACV in 3D space

Fig. 7 Topology optimization results of the frame arm
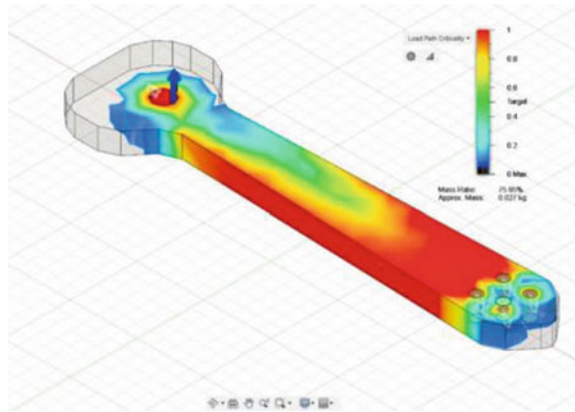
4 Design Considerations and Analysis

The design of each part of the UACV plays a very vital role in the overall mechanical performance under extreme conditions. The detailed design considerations and analysis aim to develop high strength and low weight for the vehicle.

4.1 Frame Arm Topology Optimization

The objective is to decrease the inadequate mass of the frame without affecting the structural integrity of the design. Topology optimization was done on Autodesk Fusion 360 using the load conditions developed by the propeller thrust at a distance of 127 mm from the arm chassis contact region. Figure 7 shows the topology optimization result in the frame. The thrust/motor needed to hover the drone is 4.12 N, which we get from the aerodynamic study of the drone. The results show that the critical section contour where the maximum stress developed, and by extracting mass from the low-stress region significant reduction of the design weight can be observed.

There is a reduction of approximately 25% in mass, keeping the strength of the frame unaffected.

4.2 Frame Arm Structural Analysis

The load of 4.12 N applied at 127 mm from arm chassis mounting point. For this analysis, the four mounting holes considered fixed constraints. The frame modeled in SolidWorks, and then the file imported into Ansys for static structural analysis. Face meshing used to attain an orthogonal quality of 0.92. The different material

Table 1 Results of total deformation and stress for different material

S. No.	Material	Total deformation (mm)	Von Mises stress (MPa)
1	Acrylonitrile butadiene styrene (ABS)	0.008	1.759
2	Nylon PA220	6.68	1.757
3	Polyactide (PLA)	35.9	1.756
4	Polycarbonate(PC)	20.92	1.758
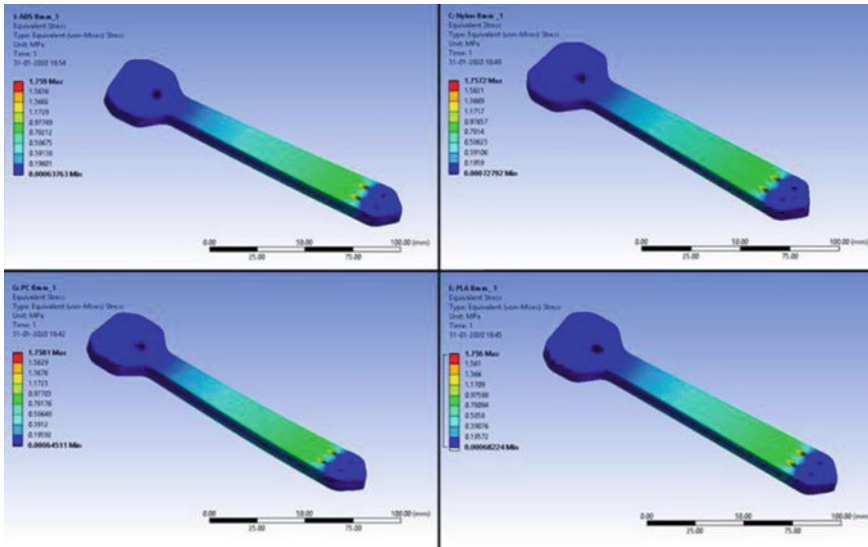
Fig. 8 Equivalent stress of frame arm for different materials

considered for the frame design and the same has been used in the analysis (Table 1). The materials used are polylactide (PLA), acrylonitrile butadiene styrene (ABS), polycarbonates (PC), and Nylon PA2200. The Nylon PA2200 was considered as an optimal option considering its machinability and other mechanical properties. The results of von Mises stress and the total deformation has been shown in Figs. 8 and 9. The machinability is also taken under consideration, which makes Nylon PA2200 is the best-suited material for the UARCV.

4.3 Frame Chassis Structural Analysis

The weight load of 6.76 N applied at the COM of the assembly. The individual thrust of 4.12 N is applied on the arm motor mounting holes. The contact region between the arm and the base plate is considered as a fixed constraint. The model developed in
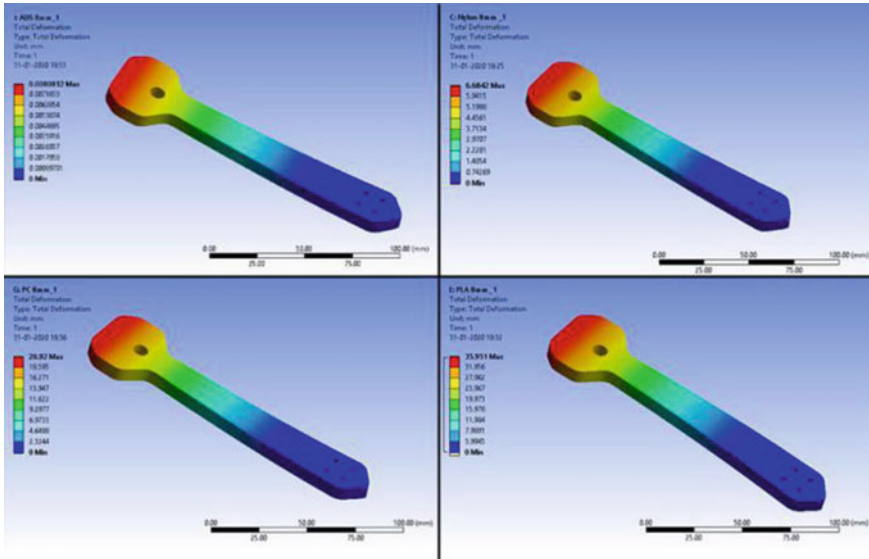
Fig. 9 Total deformation of frame arm for different materials

Fig. 10 Equivalent stress on frame chassis
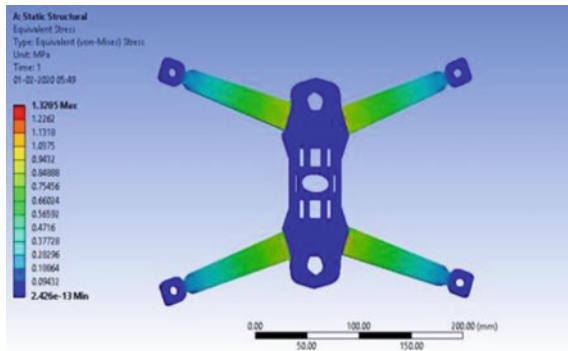
SolidWorks and the IGS file is imported into Ansys for the static structural analysis of the chassis. The material used for the analysis was Nylon PA2200. The result in Figs. 10 and 11 shows that von Mises stress is 1.3205 MPa, and the maximum total deformation as 5.596 mm, which is much under the failure region.

4.4 Landing Support Analysis

The weight load of 1.716 N is applied at the bottom of the landing support. The upper side of the landing support is considered as a fixed constraint. The model developed in

Fig. 11 Total deformation in frame chassis
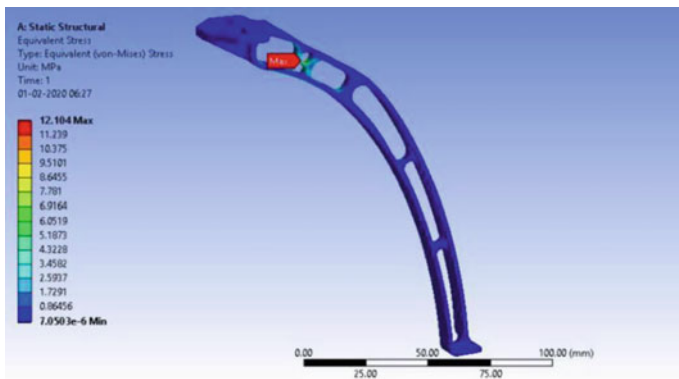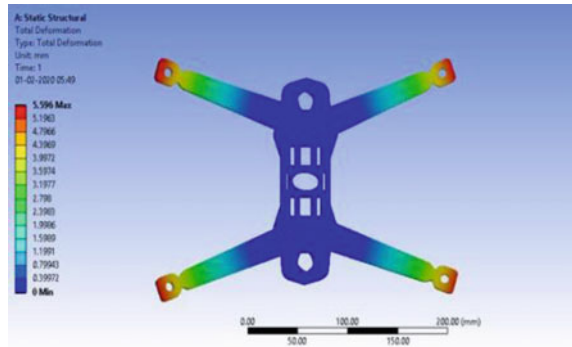
Fig. 12 Equivalent stress on landing support of UACV

SolidWorks and the STEP file is imported into Ansys for the static structural analysis of the landing support as shown in Fig. 12. The material used for the analysis was Nylon PA2200. The result shows that von Mises stress is 12.104 MPa.

The final iterative 2D CAD results after considering and optimizing the design are shown in Fig. 13.

The UACV is designed considering the additive manufacturing materials properties. The reason for the selection of the manufacturing material was the low cost and ease of availability. The final prototype of the UACV is shown in Fig. 14.

4.5 Payload Carry–Drop Mechanism

The integration of the pick-up mechanism of the payload is in the bottom part of the UACV chassis. The mechanism is the conversion of the rotational motion of servo into translational motion. The input signal from the ground station controls the servo

All dimensions are in mm
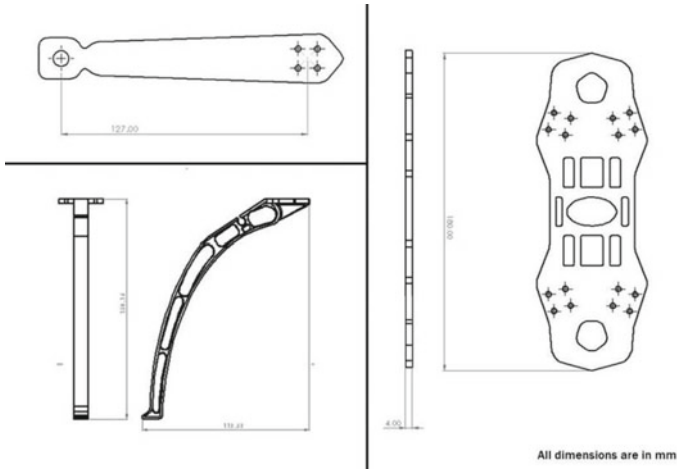
Fig. 13 2D CAD of frame arm, chassis, and landing support

Fig. 14 Assembled UACV prototype

motion using the receiver channel. The payload is carried in between the blocks where the pin enters the payload slot and constraint its motion in every possible direction (shown in Fig. 15).

Fig. 15 Payload carry–drop mechanism
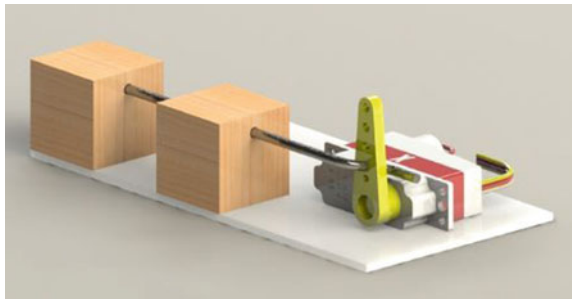
5   Material Selection and Development

The one important factor while designing the UARCV was to consider the strength and weight of the material for additive manufacturing.

Based on the design criteria and QFD, the Pugh's concept selection technique was adopted. The decision matrix with a weighted average is given to each category for critical design consideration. Pugh's method or Pugh Concept Selection, invented by Stuart Pugh, is a qualitative technique used to rank the multi-dimensional options of an option set. The score is provided based on quality function deployment (QFD) to each category according to the following scoring criteria shown in Table 2.

For the frame, variety of materials was considered, like polylactic acid (PLA), acrylonitrile butadiene styrene (ABS), PA Nylon, and PC. The simplify3d [11] gives the material properties of the material ABS, PLA, Nylon PA, PC, which helps to develop a decision matrix as per our requirements.

The decision matrix is prepared, and the conclusion to use the PA Nylon as the material was taken based on various metrics (Table 3).

It is also preferred by many users for the manufacturing of various tools, functional prototypes, and mechanical parts. PA Nylon is a semi-crystalline thermoplastic with low density and very high thermal stability. Polyamides have outstanding wear resistance, good coefficient of friction, and excellent impact properties.

Table 2 Category score criteria for the decision matrix

Score	Quality
5	Excellent
4	**Good**
3	Average
2	**Poor**
1	Very poor

Table 3 Decision matrix

Metric	Weightage (%)	PLA	ABS	PA Nylon	PC
Tensile strength	25	2	2	4	3
Chemical resistance	**10**	**1**	**1**	**4**	**3**
Stiffness	8	2	2.5	2.5	3
Printability	**20**	**4.5**	**4**	**4**	**3**
Impact resistance	10	2	3	4	3
Fatigue resistance	**5**	**2**	**2**	**4**	**4**
Durability	12	2	4	5	5
Availability	**10**	**4**	**3**	**4**	**2**
Total	100	2.6	2.78	4	3.19

Fig. 16 Additive manufactured parts

Fig. 17 Fully assembled UACV

The final development of the UACV is done using the PA Nylon material. Figure 16 shows the parts made using additive manufacturing, and Fig. 17 shows the fully assembled unmanned aerial cargo vehicle. The laser type used in additive manufacturing is CO_2,30 W with precision optics of F-theta lens, high-speed scanner. The scanning speed during the building process is 1 m/s and a building rate is of 1 l/h. EOS Parametric Editor and PSW3.6 are used for data development. The infill of 80% is used with 3D honeycomb infill (Trihexagonal).

6 Conclusion

Hence, the complete procedure of the development of an unmanned aerial cargo vehicle is discussed in the paper. The various disciplines are involved in the development process from the design of parts to the control system. The design delivers excellent results to carry payload up to 350 gms. The diagonal length of the frame can significantly increase the payload capacity of the UACV. The aerodynamic stability

starts decreasing and the response time increases with an increase in weight of the payload. The very fined accuracy in design is achieved by using additive manufacturing technology. The model shows that the increase in the payload weight decreases the overall performance of the aerial vehicle. The limitation of the research is the use of the empirical model for the model of propeller blades; the more real condition can be developed using the different Simulink model which can provide advance ratios, coefficient of thrust and power at different RPMs of the propeller blades. For further research purposes, the autonomous motion planning of the UACV where the path is planned according to environmental conditions can be studied.

References

1. Gallucci M (2017) Insane drone footage shows widespread damage and flooding at California's Oroville dam. https://tinyurl.com/y56abpeq. Accessed 10 Jan 2018
2. Boyd A (2016) Border patrol calls on silicon valley for advice on small drones. https://tinyurl.com/y59b9ndr. Accessed 10 Jan 2018
3. Nuwer R (2017) High above, drones keep watchful eyes on wildlife in Africa, https://tinyurl.com/y436mtan. Accessed 10 Jan 2018
4. Mezzofiore G (2018) New lifesaving drone rescues swimmers by dropping inflatable pods. https://tinyurl.com/yxsgxusr. Accessed 24 Aug 2018
5. ElFaham MM, Mostafa AM, Nasr GM (2020) Unmanned aerial vehicle (UAV) manufacturing materials: synthesis, spectroscopic characterization and dynamic mechanical analysis (DMA). J Mol Struct 1201:127211. https://doi.org/10.1016/j.molstruc.2019.127211
6. Fiaz UA, Abdelkader M, Shamma JS (2018) An intelligent gripper design for autonomous aerial transport with passive magnetic grasping and dual-impulsive release. IEEE/ASME Int Conf Adv Intell Mechatron AIM 1027–1032. https://doi.org/10.1109/AIM.2018.8452383
7. Mercado Ravell DA, Maia MM, Diez FJ (2018) Modeling and control of unmanned aerial/underwater vehicles using hybrid control. Control Eng Pract 76:112–122. https://doi.org/10.1016/j.conengprac.2018.04.006
8. Cuadrado J, Naya MA, Ceccarelli M, Carbone G (2002) An optimum design procedure for two-finger grippers: a case of study. IFToMM Electron J Comput Kinemat 15403(1):2002
9. Goh GD, Agarwala S, Goh GL, Dikshit V, Sing SL, Yeong WY (2017) Additive manufacturing in unmanned aerial vehicles (UAVs): challenges and potential. Aerosp Sci Technol 63(December):140–151. https://doi.org/10.1016/j.ast.2016.12.019
10. Amelink M, Mulder M, van Paassen M (2008) Designing for human-automation interaction: abstraction-sophistication analysis for UAV control. In: Proceedings of the International MultiConference of Engineers and Computer Scientists, pp 1–6
11. https://www.simplify3d.com/support/materials-guide/properties-table/?filas=abs,pla,nylon,polycarbonate

Progressive Die Design and Development Using AutoCAD

Pankaj Shakkarwal, Rajender Kumar, and Rahul Sindhwani

Abstract From the past three decades, the manufacturing context always in the motion to improve the plant efficiency and efficacy. With the objective of improving the production capacity in no's of part produced, most of the sheet metal industries are now using progressive dies. Still there is the consequence among the sheet metal industries regarding the design and development of the progressive die. The present paper reveals the progressive die design with the help of AutoCAD software which is in general the 2-D drafting tool. In addition, the various components of progressive die along with their specification, and the general mathematical calculations give the better understanding to audience about the die design and development process.

Keywords AutoCAD · Progressive die · Tools · Stock strip

1 Introduction

In the manufacturing industries especially dealing with sheet metal products, press tool operation is the important one. In general, it is used for custom fit operations as desired by the end customers. The metal sheets are to be cut/draw/bend/blank/pierce by the press tool operation [1]. The efficiency in terms of no's of product produced/fabricated by the press tool in a single stroke is mainly based on the types of die used. The various types of dies used in press tool are discussed below:

P. Shakkarwal · R. Kumar
MED, FET,, Faridabad, India
e-mail: pankajshakkarwal.fet@mriu.edu.in

R. Kumar
e-mail: Rajender6291@gmail.com

R. Sindhwani (✉)
Department of Mechanical Engineering, Amity School of Engineering and Technology, Amity University, Noida, Uttar Pradesh 201313, India
e-mail: rsindhwani@amity.edu

- **Simple Die**: As the name suggests, the simple die is designed to perform only one operation at a time or in single stroke. The kind of operations performed by the simple dies is blanking, piercing, notching, trimming, etc.
- **Progressive Die**: In the progressive die, two or more operation is combined in one die. In the progressive die, tool steel is used for the die development usually.
- **Compound Die**: The compound tool is to produce two or more cutting operations per stroke in one station such as piercing and blanking [2, 3].

Though, almost in all operations in metal working, only one operation is performed on the workpiece in one stock of tool operation, the progressive die gives an advantage to perform more no. of operation in the single stock of tool operation. In the progressive die, the raw metal sheet/strip will pass the various stages to give the final shape. The sheet metal strip is pushed toward the stations by the mechanical operated feeding system, and at each station, one or more operations are performed. In the progressive die, the final station is known as the cutoff station. At this station, the finished product is separated from the carrying web which is punched away in previous operations (treated as scrap) [4]. The various types of sheet metal operations done by progressive dies are as follows:

- **Piercing**: When openings (e.g., holes) are punched into a blank or a semi-finished product, the operation is known as piercing. The unwanted material is scrap which is called slug.
- **Blanking**: The operation of punching about a complete contour to produce blank. The blank is punched cut of a plain stock strip (coil).
- **Piloting**: The operation is used for guiding previously pierced hole.

The benefit of the progressive die is the (a) cost-effective, (b) reduced production timing, (c) improved productivity, (d) minimum process handling, etc., whereas the progressive dies have the limitation such as not in commonly used for the custom fit products. It is used for the mass production where production rate requisition is high, and the workpiece needs more than one operation for the conversion into the final product.

2 Progressive Die Design: General Concept and Specifications

The design considerations in the progressive die design are the most important one. In the progressive die, the basic elements of progressive die are the top plate and the bottom plate mating together with the guide bushes and pillars shown in Fig. 1. While designing, the proper mating alignment of both the plates is the main consideration [5]. The design of die including parts and their specifications is as discussed below:

Fig. 1 General design for washer progressive die [8]
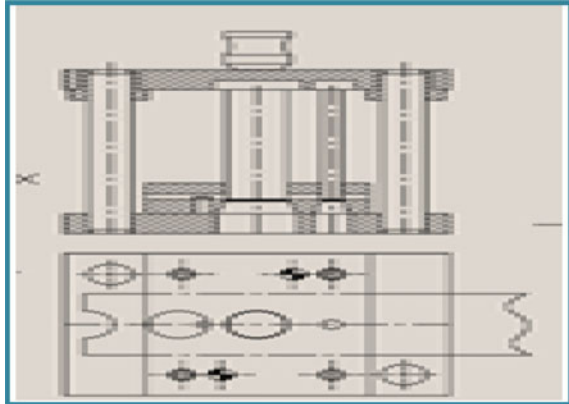
2.1 Step-1: Selecting the Die Set

The following ten points are considered for the selection of die set:

- Make or manufacture,
- Type of material used for die,
- Size of the workpiece,
- Type of material upon which die can perform the operations,
- Die holder thickness,
- Punch holder thickness,
- Bush type and length,
- Lengths of guideposts,
- Shank diameter,
- Grade of precision [4, 6, 7].

2.2 Step-II: Die Set Components and Materials [3, 8] (Fig. 2)

- **Punch** Preferably high carbon high chromium (HcHcr) steel. Hardened and tempered 60–62 HRC.
- **Die** Preferably high carbon high chromium (HcHcr) steel. Hardened and tempered 60–62 HRC.
- **Bottom plate** Graded cast iron or EN8 steel.
- **Top plate: -** Graded cast iron or EN8
- **Guide pillar and guide bush** Carbon steel/case carburizing steel. Hardened and tempered 55–58 HRC.
- **Punch holder plate**: EN8
- **Thrust plate:** EN8
- **Shank** Mild steel
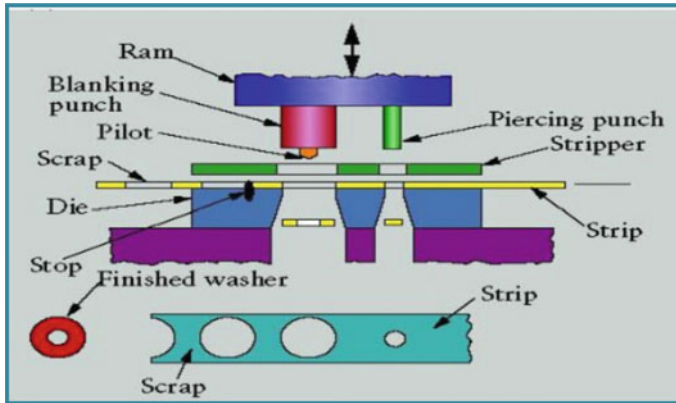
Fig. 2 Machine and die adjustment on machine tool [1]

2.3 Step-III: Calculation of Various Parameters [5, 9]

While designing the progressive die, the following parameters are to be considered:

- The press tool tonnage capacity,
- The workpiece size and shape,
- Shut height of the tool,
- Die thickness and margins as per the material,
- Drawing strip layouts and comparing material utilization,
- Locating device design,
- Drawing die plan,
- The punch length and mounting on the plate,
- Finding center of pressure and check scrape disposal,
- Drawing details [7, 8].

The design calculations are as follows:

- Component, drawing and specification

$$
\begin{aligned}
\text{Outer diameter} &= 24 \text{ mm}, \\
\text{Inner diameter} &= 12 \text{ mm}, \\
\text{Thickness} &= 1.00 \text{ mm}, \\
\text{Shearing strength} &= 28 \text{kg/mm}^2.
\end{aligned}
$$

- **Strip layout design**: The die is fabricated from the die drawing operation on the metal strip. In the strip layout design, the following analytical calculation is done to find out the economy factor of the operation [10, 11].

Economy factor = Area of component x number of rows $\times$ 100/width of the strip x pitch.

Generally, the 60% economy factor is requisite in case of strip. The position of the blank in the strip decides the economy factor. In our component design, I.D is 24 mm and O.D is 12 mm. scrap bride width $= 1.2 \times S$

$$= 1.2 \times 1.0 = 1.2 \text{ mm}$$
$$E = \text{Area of component} \times \text{number of rows} \times 100/\text{width of the strip} \times \text{pitch.}$$
$$\text{Pitch} = 24 + 1.0 = 25 \text{ mm}$$
$$\text{Strip width} = 24 + 1.0 + 1.0 = 27 \text{ mm}$$
$$\text{No. of rows} = 1$$
$$\text{Area of blank} = 3.142 \times 24 \times 24/4$$
$$= 452.16 \text{ mm}^2$$
$$E = 452.16 \times 100 \times 1/26 \times 25 = 69\%$$
$$\text{Strip utilization} = 69\%$$

- **Cutting Clearance**: In the progressive die, the cutting clearance is the major concern for the tool operation. It is the gap between the side of the punch and the corresponding side of the die opening on one side of the edge, when the punch is entered into the die opening. Therefore, the cutting clearance should always be thought and expressed as the amount of clearance per side.

The ideal clearance could be found by the following formula and depends on co-efficient of 'C'.

$$\text{Clearance for } \prime S\prime \text{ up to 3 mm} = C \times S \times \sqrt{T_{\max}/100}$$
$$\text{For } \prime S\prime \text{ above 3 mm clearance} = (1.5 \times S) \times (S - 0.015) \times \sqrt{T_{\max}/100}$$

Where 'S' is the sheet thickness in mm
'C' is constant $= 0.005$
$T_{\max} = $ shear strength $= 80\%$ UTS. It is expressed in N/mm^2. If we take 'c' as 0.005, we get a clearance, which yields a better and cleanest workpiece, but requires higher cutting forces and considerably more energy. If we take 'C' as 0.01, the cutting force energy as its minimum, but finish is bad. The usual practice however is to take 'C' as 0.01 mm.

Now in our component, $S = 1$ mm

Clearance $= C \times S \times \sqrt{T_{\max}/10}$

$= 0.01 \times 1 \text{ mm} \times \sqrt{300/10}$

$= 0.1$ mm/side

Therefore, clearance on one side $= 0.1$ mm

- Cutting force and stripping force: In the press tool operation, the force required to perform the operation has its importance because the efficiency of the operation is directly based on it. [10] The cutting force is further dependent on the cut length area (in case of straight cuts), the workpiece material and the sheet thickness.

Cutting force $= L \times S \times T_{max}$
$L =$ Length of periphery to be cut in mm
$S =$ Sheet thickness in mm
$T_{max} =$ Shear strength in kg/mm^2
$F = 2\pi r \times T \times s$
$= 2 \times 3.14 \times 12 \times 1 \times 40$
$= 3.7$ Tons.

Stripping force $=$ It is usually varying between 5 and 20% of blanking force and can be calculated $3 \times 20\% = 0.6$ ton

Total cutting force $=$ Cutting force $+$ stripping force $= 3.6$ Tons.

2.4 Design of the Die Parts

Die plate: **As literature revealed, there is two types of die top and bottom plate** [12–14]. One another plate named die plate which is mounted on bottom plate. In general, the high carbon high chromium steel material is used for the die plate having 60–62 HRC. Die plate thickness is decided on the basis of stock material being cut. Thickness of die block is given by the formula;

$$T_d = \sqrt[a]{\text{Shear Force}}$$

where

T_d: Thickness of the die plate in (mm)
$T_d = \sqrt[3]{3.70 * 1000}$
$T_d = 15.4 = 16$ mm

- **Bottom Plate**: **This plate gives a cushioning effect to the die as well as provides enough room for the tool to be clamped to the press bed.** There may be an opening in the backplate which allows the blank or slug to fall clear off the tool. Thickness of bottom plate is given as;

$$T = 1.5 \times T_d.$$
$$T = 1.5 \times 16 = 24 \text{ mm}$$

- **Top plate**: The assembly including the punch, punch holder, is mounted on the top plate. The tool shank that locates the whole tool centrally with the press ram is also screwed on the top plate. The top plate is made of mild steel or cast iron. This plate should be thick enough to prevent bending.

$$\text{Top plate} = 1.25 \times 16 = 20 \text{ mm}$$

- **Punch plate**: All the punches are accurately held in this plate. This plate should be thick enough to accommodate punch shoulder and keep the punches perpendicular. It is made out of mild steel. Punch plate is made out of single piece, and a need base is also made out of more than single piece.

$$\text{Punch plate} = 0.5 \times T_d$$
$$= 0.5 \times 16 = 8{-}0 \text{ mm}$$

- **Guide pillar**: In the progressive die design, the guide pillar**s** play an important role basically guides the plate. These are the precision pins mounted on the top plate and press fitted in accurately bored holes at the bottom plate. They are engaging guide bushings to align punch and die components with a high degree of closeness and accuracy. Guide pillar is subjected to bending due to the weight of the top tool. The deflection should be kept below 0.0025 mm. These can be treated as cantilevers. The bending force 'W' on the pillar can be found from the following equation.

$$W_1 \times A = W \times B$$
$$W = W_1 \times A/B$$
$$W_1 = \text{Weight of the top tool (Kg)}$$

$A = $ Distance between pillar center and center of gravity of top tool (mm).
$B = $ Distance between bottom bolster and guide bush bottom face
when tool is in run $-$ up position (mm).

If two rear pillars are used, then pillar dia.$= \frac{\sqrt{Wb^3}}{15.3}$.

- It should be remembered that W_1 is the weight of the top tool and not cutting force V.

2.5 Step-IV: Estimation of Cost

In an organization, designer is estimating the cost of designed sheet metal tooling. The cost includes the following section [15–17]:

1. Material cost: Used for the die design and development purpose,
2. Machining cost: the actual cost of operation including the direct and indirect cost,

Table 1 Thumb rule for estimation

Group No.	Operations involved	Total cost
1.	Only shaping, turning, drilling and fitting	3 times raw material cost (rmc)
2.	Shaping/turning, drilling, fitting plus milling.	4 times (rmc)
3.	Above plus jig boring	5 times (rmc)
4.	Punch and die grinding and hardening	6 times (rmc)
5.	Profile grinding + wire cutting	8 times (rmc)

3. Heat treatment charges,
4. Assembling, tryout and adjustment cost.

- Material cost: It is estimated by finding out the volume of raw material required multiplying the volume by specific gravity gives the weight of raw material.
- Machining cost: It depends upon the type and size of the machine necessary for machining. The hourly rates of heavy machines can be 2–3 times rates of a smaller machine.
- Heat treatment cost: It is the cost which depends upon the weight of the parts at the time of heat treatment. It can cost as much as the cost of the material.
- Assembly and try out: It includes the drilling and fitting costs. These are usually estimated in hours/shifts. This time depends upon the number of parts, precision and sophistication necessary in a press tool (Table 1).

3 Results and Conclusion

In the press tool working, the progressive die is reported as one of the most economical types of die to form/cut/bend the metal components. In addition, the variety of characteristics in progressive dies such as strength, durability and wears resistance offers the competitive advantage over the other types. In the present research work, the three-stage progressive die to manufacture the automotive component (washer) is designed with the help of AutoCAD software, and the parameter calculation is done manually. While going through the operational aspect, it is observed that the progressive tool is better choice for the high production rate and economical way of producing. In this study, the various analytical calculation considered in the die design is explained carefully. The total tonnage required to manufacture washer is 3–5 tones including 30% of factor of safety. In future, the FEM and other advance tools can be implemented to understand the gap between the analytical and FEM result.

References

1. Joshi PH (2003) Press tools design and construction. A.H. Wheeler and Co., Ltd, K.G. Marg, New Delhi
2. Cakir MC, Irfan O, Cavdar K (2005) An expert system approach for die and mold making operations. Roboti Comput Integrat Manuf 21:175–183
3. Mittal VK, Sindhwani R, Singh PL, Kalsariya V, Salroo F (2018) Evaluating significance of green manufacturing enablers using MOORA method for Indian manufacturing sector. In: Proceedings of the international conference on modern research in aerospace engineering. Springer, Singapore, pp 303–314
4. Hambli R, Miller H (2003) BLANKSOFT: a code for sheet metal blanking processes optimization. J Mater Process Technol 141:234–242
5. Pilani R, Narasimhan K, Maiti SK, Singh UP, Date PP (2000) A hybrid intelligent systems approach for die design in sheet metal forming. Int J Adv Manuf Technol 16:370–375
6. Kumar K, Dhillon VS, Singh PL, Sindhwani R (2019) Modeling and analysis for barriers in healthcare services by ISM and MICMAC analysis. In: Advances in interdisciplinary engineering. Springer, Singapore, pp 501–510
7. Mastanamma CH, Rao KP, Rao MV (2012) Design and analysis of progressive tool. Int J Eng Res Technol 1(6):24–37
8. Mittal VK, Sindhwani R, Shekhar H, Singh PL (2019) Fuzzy AHP model for challenges to thermal power plant establishment in India. Int J Operat Res 34(4):562–581
9. Nee AYC (1986) Developing CAD/CAM software for the tool and die industry: a role to be played by tertiary institutions. Int J Mech Eng Educ 14:263–271
10. Rehaman MI, Reddy PS, Matta M, Murthy NG (2011) Design and analysis of progressive die for chain link plate. Int J Sci Eng Adv Technol IJSEAT 2(11):32–43
11. Shirai K, Murakami H (1989) A compact and practical CAD: CAM system for progressive die. Bull Japan Soc Prec Eng 23:25–30
12. Sindhwani R, Singh PL, Prajapati DK, Iqbal A, Phanden RK, Malhotra V (2019a) Agile system in health care: literature review. In: Advances in industrial and production engineering. Springer, Singapore, pp 643–652
13. Sindhwani R, Singh PL, Iqbal A, Prajapati DK, Mittal VK (2019b) Modeling and analysis of factors influencing agility in healthcare organizations: an ISM approach. In: Advances in industrial and production engineering. Springer, Singapore, pp 683–696
14. Sindhwani R, Singh PL, Chopra R, Sharma K, Basu A, Prajapati DK, Malhotra V (2019c) Agility evaluation in the rolling industry: a case study. In: Advances in industrial and production engineering. Springer, Singapore, pp 753–770
15. Singh PL, Sindhwani R, Dua NK, Jamwal A, Aggarwal A, Iqbal A, Gautam N (2019) Evaluation of common barriers to the combined lean-green-agile manufacturing system by two-way assessment method. In: Advances in industrial and production engineering. Springer, Singapore, pp 653–672
16. Soman A, Campbell M (2002) A grammar-based approach to sheet metal design. In: Proceeding of DETC02 ASME design engineering and technology conference. Montreal, Canada, 485–493
17. Tor SB, Britton GA, Zhang WY (2003) Indexing & retrieval in metal stamping die design using case based reasoning. J Comput Inf Sc Eng (ASME) 3:355–362

Design, Analysis and Fabrication of Automatic Braking System

Yash Sharma, Shashank Shekhar Singh, Mohd. Asif Nawaz, Vipin Kaushik, Sumit Sharma, Rahul Sindhwani, and Punj Lata Singh

Abstract In this paper, we have discussed the design, analysis and fabrication of automatic braking system for a vehicle. The design process for a vehicle's braking system has been studied thoroughly. Every step taken for fabrication of this prototype is based on the thorough study conducted. This task was divided into different stages which include analysis, design, fabrication, assembly, trial and finally the approval of the vehicle. This prototype uses batteries and a chain sprocket assembly as a power source to run the vehicle and a braking circuit attached to a pair of IR sensors. The design discussed in this paper increases the braking efficiency of the vehicle effectively. The design and analysis of the disc brake rotor have been conducted to select the suitable material for the disc brake. At the end of the design and analysis, the overall system has been implemented with a constructed work, tested working and perfectly functional prototype.

Keywords Automatic brake · IR sensors · Arduino · Relay

Y. Sharma (✉) · S. S. Singh · Mohd. A. Nawaz · V. Kaushik · S. Sharma · R. Sindhwani
Department of Mechanical Engineering, Amity School of Engineering and Technology, Amity University, Noida, Uttar Pradesh 201313, India
e-mail: ssharma03@amity.edu

S. S. Singh
e-mail: Shashank.bps2802@gmail.com

Mohd. A. Nawaz
e-mail: asif.nawaz0@gmail.com

V. Kaushik
e-mail: vkaushik@amity.edu

R. Sindhwani
e-mail: rsindhwani@amity.edu

P. L. Singh
Civil Engineering Department, Amity School of Engineering and Technology, Amity University, Noida, Uttar Pradesh 201313, India
e-mail: plsingh@amity.edu

1   Introduction

In today's scenario, with the increasing number of road accidents, the safety of the driver and that of the fellow passengers is a major concern for the automobile manufacturers. In Indian markets, the manufacturers are laying more focus towards the safety of the humans both inside and outside of the vehicle. So far, anti-lock braking system, brake assist, etc. are been used to resolve the purpose [1]. In this paper, we have discussed the details of a similar safety system which can be installed in a vehicle. This braking system includes a pair of IR sensors (transmitter and receiver), Arduino, relays, DC motors, brake wires, disc brake rotors, braking callipers and a chain sprocket assembly [1]. All these components are assembled, and a prototype has been developed. The transmitter transmits the IR waves, and when these waves strike an obstacle, the signal is sent back to the receiver [2]. After the receiver interprets the signal, the signal is further sent to the Arduino and then to the relays, which will initiate the braking of the vehicle with the help of DC motor and brake wires [3, 4].

The primary functions of an efficient braking system include:

- Deacceleration of the vehicle,
- Stopping the vehicle within the minimum possible distance,
- Absorption of kinetic energy of the vehicle.

In large-scale industries, there are various methods to transport the material within the industrial facility like conveyer belts, pallet jacks, material lifts, etc. As these material handling devices are costly and cannot be used by other industries [5]. Therefore, this braking system can be equipped with the four-wheel trolleys and can be used in small-scale industries as a material handling device as it is efficient as well as cost-effective. Further, in this paper, we have discussed the basic components of the prototype in Sect. 2, in Sect. 3, circuit diagram and specifications of the prototype have been discussed, Sect. 4 includes the working of prototype, and Sect. 5 includes the conclusion.

2   Basic Components

The following components have been used in the prototype [6–8].

2.1   Infrared Sensors:

Infrared sensor is a module which can be used to sense the presence of any object in its surrounding. In this paper, we are using it to detect an obstacle. Whenever an

Fig. 1 Infrared sensor module [5]

obstacle is detected by the IR sensor, the receiver modular provides an excessive output which is connected to Arduino. The sensors used are shown in Fig. 1.

2.2 Control Unit

Arduino has been utilized as a control unit within this paper. Arduino is a microcontroller board [9, 10]. Coding of ARDUINO is done in C language. The Arduino dumped C programming calculations have taken place in the PIC controller by including the maximum stopping distance and the distance between the obstacle and the automatic system [7, 8]. The Arduino module is shown in Fig. 2.

2.3 Disc Brake

Disc brake is a type of brake in which callipers are used to squeeze the brake pads inwards so as to stop the vehicle by creating friction [11, 12]. In this paper, we have used a silver steel disc brake which will be run by the DC motor via wire as shown in Fig. 3.
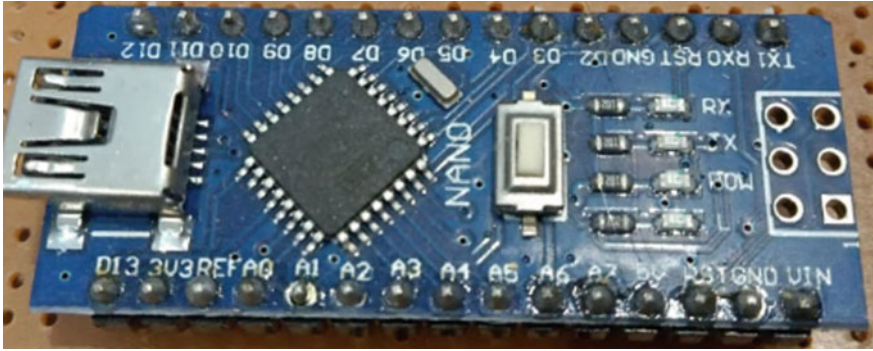
Fig. 2 Arduino [7]

Fig. 3 Disc brake [4]
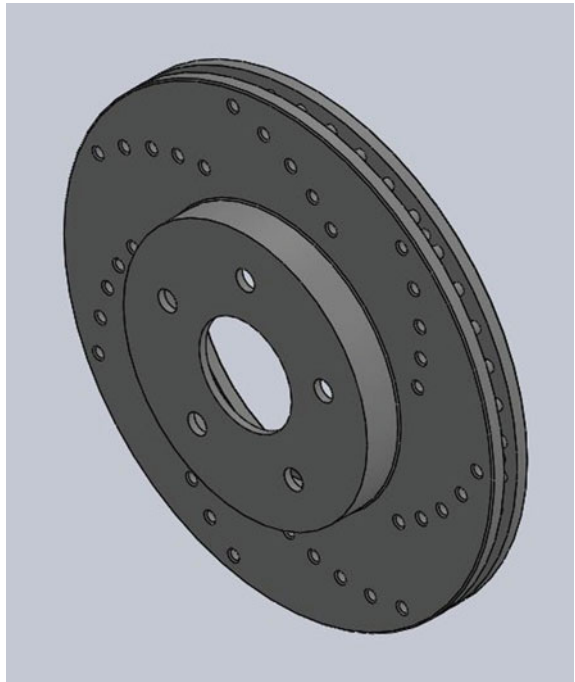
2.4 DC Motor

In this paper, we have used the DC motor to run the brakes. The motor is directed by
the relay as when to apply brakes [13, 14]. The motor used is shown in Fig. 4.

Fig. 4 DC motor [4]

Fig. 5 Relay [4]
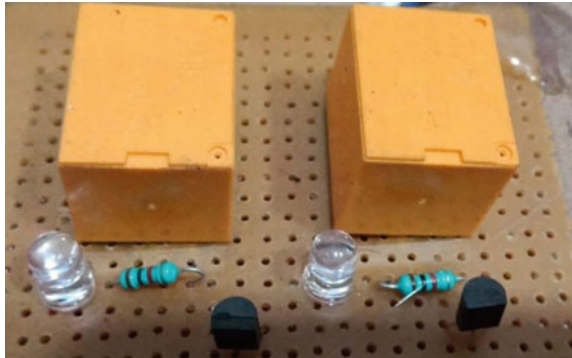
2.5 Relays

A relay is an electrical switch that opens and closes under control of another electrical circuit. The relay is directed by the ARDUINO whenever receiver sensor provides output [15]. Then the relay directs the motor to apply brakes. Relay used is shown in Fig. 5.

3 Circuit Diagram and Specifications

3.1 Circuit Diagram of Automatic Braking System

The circuit which is used to control the braking functions is shown in Fig. 6.
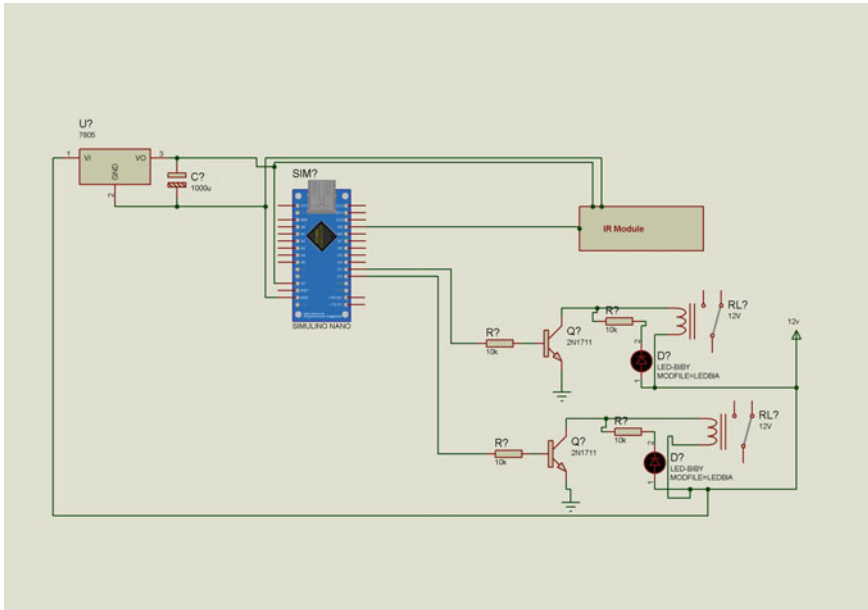
Fig. 6 Circuit diagram

3.2 Specification

Material of disc brake used is silver steel. Material of frame fabricated is mild steel, and dimensions of frame are 762 mm * 457.2 mm.

- Power generated- 3 DC motor 4 V each
- 2 relays 6 V each
- 3 batteries 12 V and 1 A each
- Overall dimension of prototype: 762 mm * 635 mm * 330.2 mm
- 2 N-P-N transistors are used
- Wheel size: 330.2 mm diameter; 50.8 mm thickness.

This prototype uses chain sprocket assembly, and silver steel rod has been used for both front axle and rear axle. The circuit of electronic unit has been placed o printed circuit board.

Fig. 7 Actual prototype

4 Working

4.1 Actual Prototype

This prototype (shown in Fig. 7) is being made as a rear wheel moved prototype which has infrared sensor-based automatic braking system inbuilt.

4.2 Construction

The prototype is constructed of a mild steel frame of dimensions 762 mm * 457.2 mm. There are two wheels in front and two wheels at the rear each of 14 inches diameter. A drivetrain consisting of a chain and a chain sprocket is mounted on the rear axle which is connected by a DC motor of 4 V. The IR sensor is mounted in front of the frame at the centre which is connected to Arduino. Arduino is connected to two relays. Both of the relays and the Arduino are placed over an O printed mustard circuit board which in turn is mounted over the mild steel frame.

Now the relays are connected to the two DC motors of 4 V each which are run by two batteries also placed over the O printed mustard circuit board. The motors are connected to the two silver steel disc brakes on each of the front wheels by a wire. Brake callipers and brake pads are mounted on the disc brakes, respectively. The motor on the rear part of the prototype is also connected to the batteries placed over circuit board.

4.3 Working

This prototype runs on DC motor such that when circuit is kept ON the motor (4 V) at the back of the frame gets power. Due to the motor, the drivetrain rotates due to which both the rear wheels move since it is a rear wheel moved prototype. Now whenever an obstacle comes in front of the prototype, it will work automatically rather than any kind of manual force. In this process, two IR sensors will be used. They are transmitter and receiver. Whenever an obstacle will arrive in the path of the prototype, it will be detected by the transmitter as it will send some signals to it and then those signals will be reverted back to receiver. Now the signals received by the receiver module of IR sensor will be sent to ARDUINO which will get activate one of the two relays. After the relay is ON, it will connect the power of both the front motors (4 V each) which are run by batteries of 12 V, and hence, both the motors will work in the clockwise direction. Thus, the brakes are applied. A flow chart for the working of prototype is shown in Fig. 8.
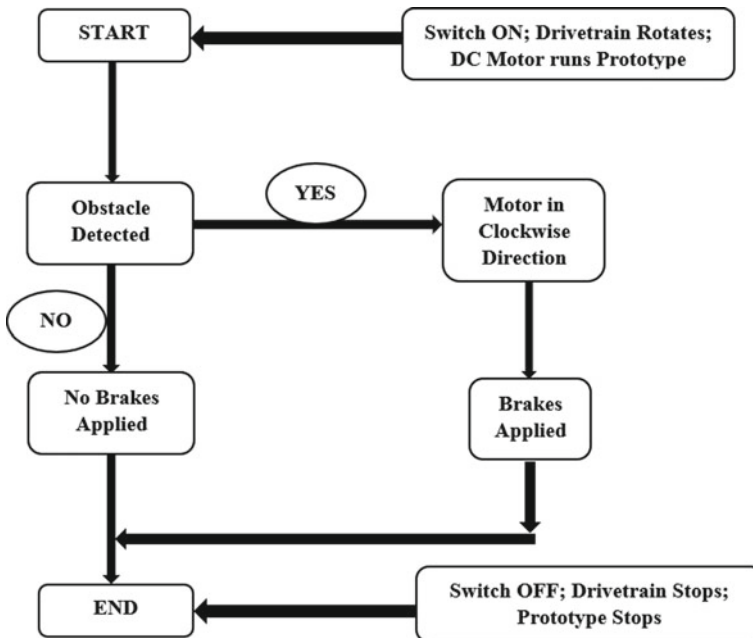
Fig. 8 Flow chart of the system [8]

5   Conclusion

All the components required for the automotive braking system were taken into consideration. Each and every component has been studied thoroughly. Then all the components required are chosen accurately. Then assembly of both mechanical unit and electronic unit was done so as to construct the prototype. After successful fabrication of the prototype, certain conclusions have been drawn:-

- The fabricated automotive system is reliable and configurable.
- The installation of IR sensors is easy and is long-lasting.
- This system of applying brakes provided by the combination of Arduino, relays and DC motor is less complicated than the use of solenoid and wiper motor [7].

This arrangement will be an answer to many environmental-related issues existing in our country like air pollution, shortage of energy and parking issues. It can be used in four-wheeler vehicles so as to reduce occurrence of accidents. It is eco-friendly and hence will be a flag bearer of environment conservation process in automobile industry. It also has a great application in the industries as material handling trolley and machinery. Also, it can be in used in defence industry as in spy robots.

References

1. Gao Y, Ehsani M (2001) Electronic braking system of EV And HEV Integration of regenerative braking, Automatic braking force control and ABS. SAE Trans 576–582
2. Kumbhojkar NV, Kuber CA (2014) Ultrasonic automatic braking system for forward collision avoidance with accelerator pedal disengagement mechanism. Posted By Yuva Eng 1:1–5
3. Badamasi YA (2014) The working principle of an Arduino. In:2014 11th international conference on electronics, computer and computation (ICECCO). IEEE, pp 1–4
4. Xiang W, Richardson PC, Zhao C, Mohammad S (2008) Automobile brake-by-wire control system design and analysis. IEEE Trans Veh Technol 57(1):138–145
5. Thivagar S, Kumar CN (2016) Automatic hand brake system. Int J Eng Res General Sci 4(1)
6. Sindhwani R, Singh PL, Iqbal A, Prajapati DK, Mittal VK (2019) Modeling and analysis of factors influencing agility in healthcare organizations: an ISM approach. In: Advances in industrial and production engineering. Springer, Singapore, pp 683–696
7. Sindhwani R, Singh PL, Chopra R, Sharma K, Basu A, Prajapati DK, Malhotra V (2019) Agility evaluation in the rolling industry: A case study. In: Advances in industrial and production engineering. Springer, Singapore, pp 753–770
8. Koli G, Patil A, Patil P, Sokashe S (2017) Intelligent braking system using the IR sensor. Int J Adv Sci Res Eng. ISSN 2454–8006
9. Sairam GV, Suresh B, Hemanth CS, Sai KK (2013) Intelligent mechatronic braking system. Int J Emerging Technol Adv Eng 3(4):100–105
10. Mittal VK, Sindhwani R, Shekhar H, Singh PL (2019) Fuzzy AHP model for challenges to thermal power plant establishment in India. Int J Operat Res 34(4):562–581
11. Kumar K, Dhillon VS, Singh PL, Sindhwani R (2019) Modeling and analysis for barriers in healthcare services by ISM and MICMAC analysis. In: Advances in interdisciplinary engineering. Springer, Singapore, pp 501–510
12. Sindhwani R, Mittal VK, Singh PL, Kalsariya V, Salroo F (2018) Modelling and analysis of energy efficiency drivers by fuzzy ISM and fuzzy MICMAC approach. Int J Product Q Manage 25(2):225–244

13. Labayrade R, Royere C, Aubert D (2005). A collision mitigation system using laser scanner and stereovision fusion and its assessment. In: IEEE Proceedings. Intelligent vehicles symposium, 2005. IEEE, pp 441–446
14. Singh PL, Sindhwani R, Dua NK, Jamwal A, Aggarwal A, Iqbal A, Gautam N (2019) Evaluation of common barriers to the combined lean-green-agile manufacturing system by two-way assessment method. In: Advances in industrial and production engineering. Springer, Singapore, pp 653–672
15. Mittal VK, Sindhwani R, Singh PL, Kalsariya V, Salroo F (2018) Evaluating significance of green manufacturing enablers using MOORA method for Indian manufacturing sector. In: Proceedings of the international conference on modern research in aerospace engineering. Springer, Singapore, pp 303–314

Design, Analysis and Fabrication of Wheel Assembly for Formula Type Automotive

Honey Bhural, Saurabh Bhatnagar, Sarthak Nautiyal, Vipin Kaushik, Sumit Sharma, Rahul Sindhwani, and Punj Lata Singh

Abstract This paper reviews design, analysis and fabrication of wheel assembly for infinity motorsports, a Formula Society of Automotive Engineers (FSAE) team of Amity University Noida, with accordance to rules and safety regulation of FSAE. Wheel assembly is the system which connects the suspensions from the chassis to the wheels; in doing so, it has multiple purposes to be fulfilled and experiences immense forces while doing so. The tests run on the previous year car provided the merits and demerits of the previously used wheel assembly. It showed the room for improvements which in turn paved the path to work for finding a more efficient material and designs. The further changes in the design were made according to the test results of Formula Bharat 2019 competition, and improvements were made for Formula Bharat 2020. The plan included various step-by-step procedure, i.e. running various tests and iterations on previous year vehicle and other research papers, checking the room for improvement, making changes in the design, doing calculations and analysis to check the result of various forces which wheel assembly faces and on the overall car in different working conditions and finally assembling all the components for performing satisfactory test runs.

Keywords FSAE vehicle · Suspension, materials, vehicle dynamics · Component packaging

1 Introduction

If all the systems of a vehicle are working as they are desired to, then only it is said to work efficiently. There are two types of masses in a vehicle, i.e. sprung and unsprung masses. Sprung masses are the masses which are damped by a damping system. The

H. Bhural · S. Bhatnagar · S. Nautiyal · V. Kaushik · S. Sharma · R. Sindhwani (✉)
Department of Mechanical Engineering, Amity School of Engineering and Technology, Amity University, Noida (U.P), Noida, Uttar Pradesh 201313, India
e-mail: rsindhwani@amity.edu

P. L. Singh
Civil Engineering Department, Amity School of Engineering and Technology, Amity University Noida (U.P), Noida, UttarPradesh 201313, India

wheel assembly and the wheels together comprise of unsprung masses as it is not damped by the spring.

The ability of a formula car to compensate during a turn and providing maximum control to the driver depends on many factors such as suspension, aerodynamics and weight distribution. The weight of unsprung mass also affects this ability, and the less the unsprung mass the more the stability of the car [1].

Furthermore, reducing the weight of the wheel assembly would provide with a greater fuel economy, and also as per FSAE rules, air intake can have a maximum of 20 mm opening, so to provide more power from the engine to the tires will increase power output [2].

A decent wheel assembly can continue such powers over a more extended time-frame. In this manner, it is required to structure the wheel get together thinking about every one of these components. A disappointment of any segment of wheel components implies a damage of car and may likewise be dangerous for the driver. Along these lines, most extreme consideration must be concerned while structuring the wheel components. Target of improvement is consistently to locate most ideal and reasonable measurement. It is on the grounds that improvement does not constantly mean lessening measurements, but it likewise means discovering the measurements which will only enough to support the powers.

1.1 Function

There are multiple functions which a wheel assembly serves firstly suspension pickup points to connect the chassis to the wheel. The current design also facilitates adjustable camber angle according to the vehicle performance on track which is a suspension parameter, and the front and rear track width can also be adjusted by adding shims in between the suspension mounting on the upright [3].

Depending upon the driving wheels, it also connects the transmission system to the wheels, i.e. the axle. As a rear wheel drive approach is suitable for formula type automotive, we have to make two sets of designs, one in front and another in rear compensating additional space for axle's tripod to deliver power to the wheels [4].

It also provides brake rotor mounted on the hub, brake calliper mounted on upright, and to link steering arm to the steering tie rod coming from the rack for actuation according to the Ackerman geometry.

1.2 Components

The wheel assembly comprises two major components that are:

- The hubs which is the rotating part,
- The uprights which is the fixed part.

The minor components are as follows:

- **Thrust bearings**: They are rotary bearings which are used for axial loads.
- **Steering arm**: It is a rod which connects the upright to the rack and pinion.
- **Suspension mounts**: These are mounts separately made and then fitted on uprights for A-arm connection.

Figures 1 and 2 show the exploded view of wheel assembly revealing various components of it.

In contrast to the weight of tie rod, control arms, and ball joints, the weight of the wheel assembly is much greater, so it is essential to reduce the weight of complete wheel assembly for better performance of the vehicle without compromising the structural stiffness and strength of the assembly as it experiences various dynamic and static loads [4].

Wheel Hub

As shown in Fig. 3, the motivation is to transfer force and join wheel to the suspension and keep the wheel turning uninhibitedly. On the off chance that the centre is set in drive hub, engine power travels from centre point to wheels. The centre points additionally hold brake rotor so as to move braking force to the haggle vehicle.

Fig. 1 Exploded view of WA without wheel
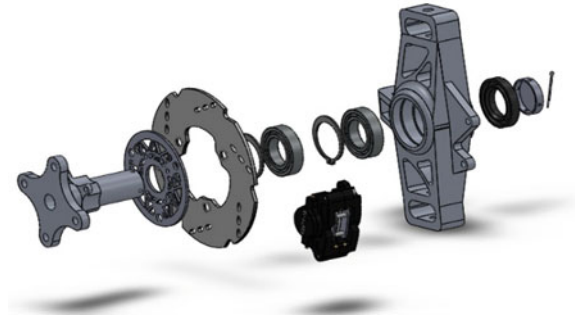
Fig. 2 Exploded view of WA with wheel
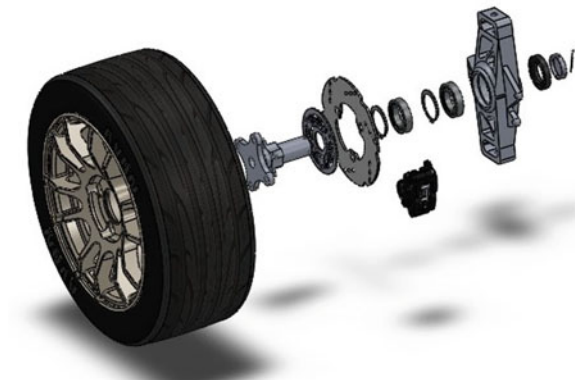
Fig. 3 Wheel hub
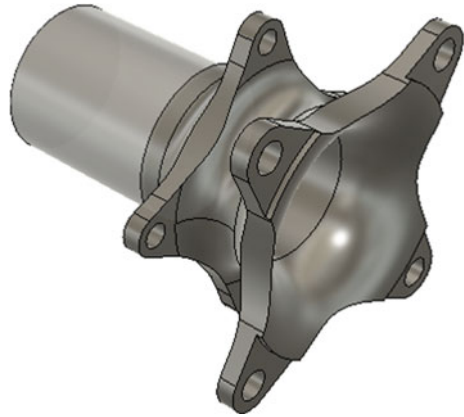
Upright

As shown in Fig. 4, it is a necessary vehicle element which associates suspension segments between the haggle vehicles. It gives a connection between up and low rotating conjunctures. The upstanding interfaces parts, for instance, the A-arms, guiding tie pole, springs, dampers, brakes, tires and at the back it associates the axles. The uprights must be adaptable and unbending enough to withstand deviations, and some may happen at the same time for instance during slowing down and a corner.

Fig. 4 Upright
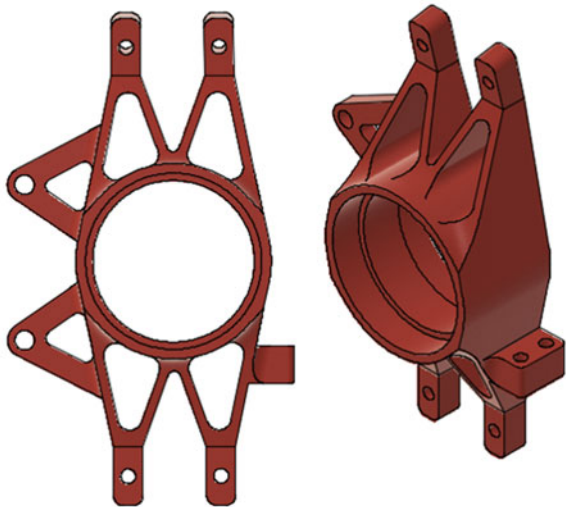
2 Methodology Used

2.1 Review of Current Wheel Assemblies

Various wheel assemblies are reviewed which are available in the market or the wheel assembly previously used assemblies used by other competing teams in their formula student cars.

Constraints: There are always some constraints present that had to be kept in mind for any design before even starting the design. Some of the constraints according to which the designing and manufacturing had to take place are as follows,

Physical constraints: As wheel components are covered by wheel itself, wheel assemblies' dimensions should be kept within the space pocket that is been provided by the wheel rims, and no contact of the assembly and rims should be there other than the bolted connection. As discussed, the wheel assembly serves multiple purposes for the suspension, brake and steering department, and we are required to design so that their geometries and components are not to be changed.

Material constraints:

We have a wide range of materials that can be used for the design, but as we are a student team, we also have a tight budget to work with, and without compromising the properties of the materials needed, we also have to stay on the budget. Hence, a budget constraint on material selection according to the team funds has to be considered.

Manufacturability: The manufacturing technique that is feasible and readily available is three-axis CNC machining. The wheel assembly is a highly critical part which undergoes various forces, to endure these forces we need to have a stiff and durable design, and still the complexity of the design should be kept to minimum so that it does not take much of the time in CNC machining which will increase the machining cost if not been checked [5].

2.2 According to Formula Bharat 2020 Rulebook

Formula Bharat Rulebook is revised every year keeping in mind the development going on in the current world. The design dimensions and parameters are done keeping in mind these rules. These rules are there for designing an optimum and safe component.

According to rule T.1.7.1, the minimum diameter of wheel that can be used is 203.2 mm (8 inches).

According to rule T.1.3.3, the suspension pickup points should not have any play and must be visible for inspection [6].

Further design and analysis are done on software like Fusion 360, SolidWorks, Ansys and HyperWorks keeping in mind the factor of safety.

Table 1 Materials and their properties

S.No.	Material	Properties
1.	Titanium	Density as 4.506 g/cc M.P. of 3038.4 °F (1670.1 °C) B.P. of 5949 °F (3286 °C) Mohr's number as 6
2.	Aluminium 7075	Density as 2.81 g/cc Tensile strength of 572 MPa Yield strength of 503 MPa Melting point of 477–635 °C
3.	Alloy Steel	Density as 7.85 g/cc Tensile strength as 744.9 MPa Yield strength as 471.02 MPa Melting point at 1427 °C

Table 2 Properties - Al 7075 T6

1	ρ	2.794 g cm^{-3}
2	E (Young's mod.)	71.02 GPa
3	V (Poisson ratio)	0.326
4	K (Bulk mod.)	69.63 GPa
5	G (Shear mod.)	26.688 GPa
6	S_{ut}	565.367 A

3 Material Selection

Optimum material selection with cost of material and material properties is done and is shown in Table 1. The material selected should handle the forces faced by wheel assembly during cornering, turning, acceleration and braking. The material should also be cost efficient and lightweight [7].

As shown in Table 1, the material decided to be taken is Aluminium Alloy 7075-T6 as it has a high strength to weight ratio and better fatigue properties than the other lightweight aluminium alloys such as 6061-T6 [8, 9].

The properties use for the analysis was as follows:

Material properties of Al 7075-T6 properties are as shown in Table 2 [10, 11].

4 Calculations and Analysis

4.1 Forces Faced by Knuckle [12, 13]

In this section, longitudinal force for braking and flank forces is explained. Force due to steering on steering arm and on calliper mounting point (braking torque) is also explained below.

Longitudinal force (Braking).

When applying brakes, all the components of vehicle apply force on the front. Its right hand impacts the knuckle.

Consider Max. acc. of 1 g, i.e. 9.809 m/s^2

On front, force = rear mass of vehicle × acc.

Assumption weight distribution 40 front 60% rear

Force = .6 × 300 × 9.809 = 1765.81 N

Lateral weight distribution is 1:1, so force on a single wheel = 1765.81/2

Thus, longitudinal force = 882.9 N

Flank (Lateral) forces.

Sidelong powers occur because diffusive power and horizontal burden travel along out to inside of vehicle. The outspread power is taken as pursues.

Assumption turning radius is 6 m, and speed is 30 km/h

$r = 6$ m

$v = 30$ km/h = 8.3333 m/s

Centrifugal force = mv^2/r = (0.4 × 300x8.3333^2)/6 = **1388.77 N**

The front weight is = 120 kg

If it gets transferred to one side = 120 × 9.81 = **1175.5"**

Force due to steering on steering arm [14, 15].

As indicated by the controlling exertion, the power on guiding arm was discovered to be 1165.52 at a point of 8.5560. Subsequent to settling these powers.

force due to steering on steering arm = 1165.52 N

Force on calliper mounting point (braking torque).

Radius (upper calliper mount) = 89.21 mm

Radius (lower calliper mount) = 60.332 mm

Min. radius will experience max. force. Hence,

force (lower arm) = Torque/Radius = 130000/60.233 = 2158.28 N

Figure 5 contains the FBD of upright in which various forces acting on it are shown.

4.2 Analysis of Upright

Figure 6 shows the stress analysis of upright done in Fusion 360 with factor of safety.

Figure 7 shows the stress concentration in the upright when deformation occurs due to applied forces.

4.3 Bolt

Selecting bolt for up and down bracket (knuckle).

They are standard and contain characterized estimation of yield quality. All bolts utilized are comprised of at least 8.8 class.
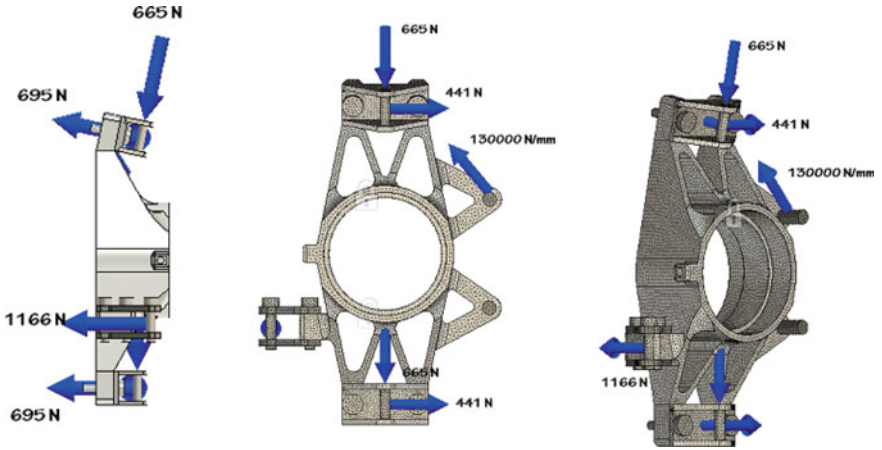
Fig. 5 FBD of upright
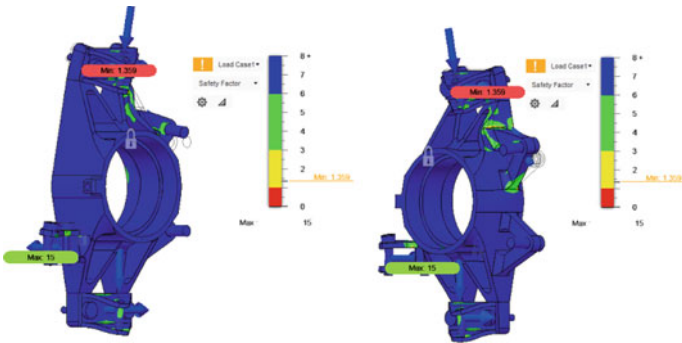
Fig. 6 FOS of upright
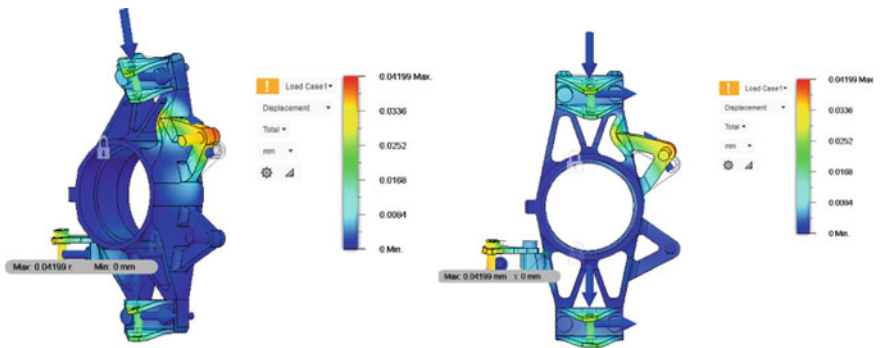
Fig. 7 Upright deformation

$Syt = 580.11 \text{ N/mm}^2$
$FOS = 2.0$

"Shear force $= \sqrt{442^2 + 695^2} = 823.64 \text{ N}$"

"Shear stress $= T = (Syt \times 0.5)/2 = 145 \text{ N/mm}^2$"

Now, $T = F/A$
$145 = 823.64/(2 \times 0.785 \times dc^2)$
$dc^2 = 1.9016 \text{ mm}$
$d = dc/0.8$
$d = 1.9016/0.8$
$d = 2.37 \text{ mm}$
"M8 size of bolt is used for knuckle"

Selecting bolt for Calliper Mounting.
Shear stress on bolts $= T = (Syt \times 0.5)/2 = 145 \text{ N/mm}^2$
The force is given by
Now, $T = F/A$
$145 = 2158.23/(2 \times 0.785 \times dc^2)$
$dc^2 = 4.3533 \text{ mm}$
$d = dc/0.8$
$d = 4.3533/0.8$
$d = 5.44 \text{ mm}$
"M8 size of bolt is selected for calliper mounting."

Selecting bolt for Steering Arm.
Shear Stress on bolts $= T = (Syt \times 0.5)/2 = 145 \text{ N/mm}^2$
The force is given by
Now, $T = F/A$
$145 = 1165.52/(2 \times 0.785 \times dc^2)$
$dc^2 = 2.2621 \text{ mm}$
$d = dc/0.8$
$d = 2.2621/0.8$
$d = 2.821 \text{ mm}$
"M8 size bolt is used for steering arm."

Selecting bolt for wheel.
Shear stress on bolts $= T = (Syt \times 0.5)/2 = 145 \text{ N/mm}^2$
The force on the steering arm is given by
Now, $T = F/A$
$145 = 880/(2 \times 0.785 \times dc^2)$
$dc^2 = 2.99 \text{ mm}$
$d = dc/0.8$
$d = 2.99/0.8$
$d = 3.74 \text{ mm}$
Thus, taking the wheel bolt size as M12.

Selecting bolt for Brake Disc.
Shear stress on bolts $= T = (Syt \times 0.5)/2 = 68.75 \text{ N/mm}^2$
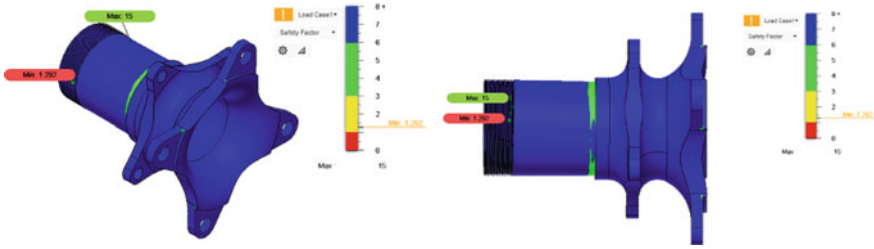
Fig. 8 FOS of wheel hub
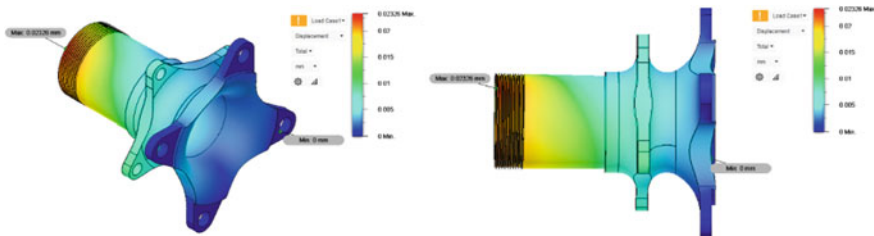
Fig. 9 Displacement of hub

The force is given by

Now, $T = F/A$

$68.75 = 879.89/(2 \times 0.785 \times dc^2)$

$dc^2 = 2.99$ mm

$d = dc/0.8$

$d = 2.99/0.8$

$d = 3.74$ mm

Thus, taking the bolt size as M8 [16].

Analysis of Hub.

Figure 8 shows the stress analysis of wheel hub with its factor of safety.

Figure 9 shows the stress analysis of the displacement of the wheel hub.

4.4 Stress Conc. on Wheel Components

Figure 10 contains the stress conc. of wheel components combined together with its FOS. Figure 11 contains the stress conc. of the displacement on the wheel components.

Fig. 10 FOS of wheel components
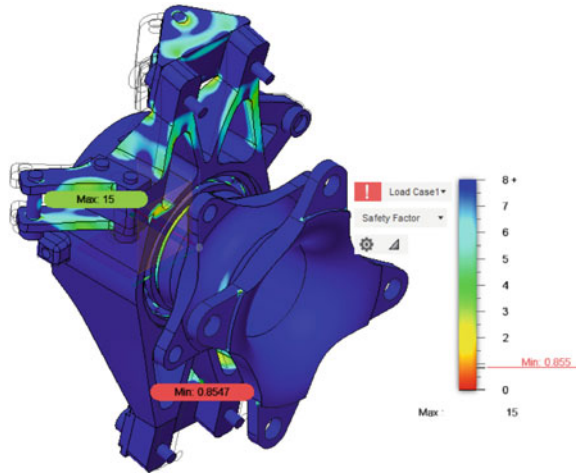
Fig. 11 Displacement of wheel assembly
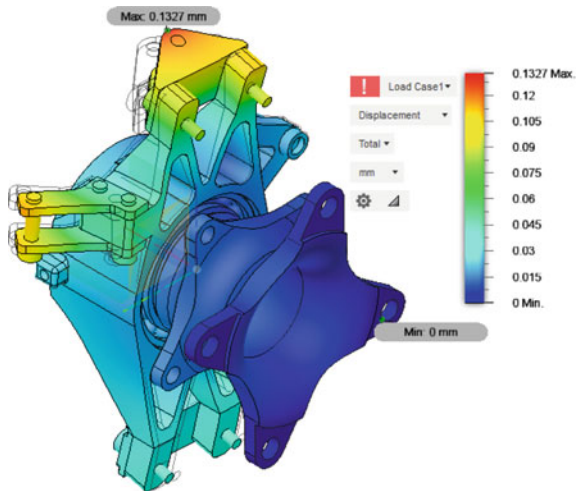
5 Result, Discussion and Conclusion

The in-depth study to ultimately arrive at the final design for the wheel assembly and its analysis was reviewed by this paper. We observed an inter-department cooperation and communication, and the needs and parameters provided by different department meet with great efficiency. We achieved greater stability and ease of manoeuvrability for the driver due to using Al7075 T6 as the unsprung mass of the vehicle was highly reduced. The new design had many valuable changes from the previous ones as it has suspension mounting point separately attached with the uprights, and it gives versatility for it to be used with different chassis just by changing the mounts. Also

the steering arm is being assembled separately, and it gives room for adjustment for toe in and out depending upon the vehicle performance on track. The reduction in overall dimension of the wheel assembly provides a wider range of rims to be attached to the chassis. The compact size of the upright helped in the proper mounting of A-arms, connecting rods and callipers and in turn lowering the centre of gravity, which is considered a key component while designing a fast-moving automobile. Being able to use 10" rims helped us in attaining better stability and lower centre of gravity. The system also granted ease of installation, adjustability and ease of serviceability which is very helpful when the work is to be done at a faster pace. This design helped to fulfil all the areas of improvements observed from the previous design and test runs.

References

1. Hrovat D (1988) Influence of unsprung weight on vehicle ride quality. J Sound Vib 124(3):497–516
2. Fornace LV (2006) Weight reduction techniques applied to formula SAE vehicle design: an investigation in topology optimization. Doctoral dissertation, University of California, San Diego
3. Shinde P, Jirage R, Garde K (2015) Design and Optimization of hub and knuckle for formula SAE car. Research Gate 1–4
4. Axerio-Cilies J, Issakhanian E, Jimenez J, Iaccarino G (2012) An aerodynamic investigation of an isolated stationary formula 1 wheel assembly. J Fluids Eng 134(2)
5. Azmeer M, Basha MH, Hamid MF, Rahman MTA, Hashim MSM (2017) Design and optimizing of rear uprights for UniMAP automotive racing team formula SAE. In: Journal of physics: conference series, vol. 908, no. 1. IOP Publishing, p 012051
6. Das A (2015) Virtual prototype of upright assembly of a race car for SUPRA SAEINDIA competition. Int J Mech Ind Technol 2(2):79–86
7. Sindhwani R, Singh PL, Iqbal A, Prajapati DK, Mittal VK (2019) Modeling and analysis of factors influencing agility in healthcare organizations: an ISM approach. In: Advances in industrial and production engineering. Springer, Singapore, pp 683–696
8. Garg A (2017) Fatigue analysis and optimization of upright of a FSAE vehicle. Int J Sci Res (IJSR), 6(9)
9. Sindhwani R, Mittal VK, Singh PL, Kalsariya V, Salroo F (2018) Modelling and analysis of energy efficiency drivers by fuzzy ISM and fuzzy MICMAC approach. Int J Prod Q Manag 25(2):225–244
10. Clark Jr, RB, Traina I, Hernandez A, Scheck T, Etuk C et al (2005) On correlation of mechanical as well as physical properties of Al alloy 7075-T6. Eng Failure Anal 12(4):520–526
11. Singh PL, Sindhwani R, Dua NK, Jamwal A, Aggarwal A, Iqbal A, Gautam N (2019) Evaluation of common barriers to the combined lean-green-agile manufacturing system by two-way assessment method. In: Advances in industrial and production engineering. Springer, Singapore, pp 653–672
12. Mittal VK, Sindhwani R, Singh PL, Kalsariya V, Salroo F (2018) Evaluating significance of green manufacturing enablers using MOORA method for Indian manufacturing sector. In: Proceedings of the international conference on modern research in aerospace engineering. Springer, Singapore, pp 303–314
13. Sindhwani R, Singh PL, Chopra R, Sharma K, Basu A, Prajapati DK, Malhotra V (2019) Agility evaluation in the rolling industry: a case study. In: Advances in industrial and production engineering. Springer, Singapore, pp 753–770

14. Mittal VK, Sindhwani R, Shekhar H, Singh PL (2019) Fuzzy AHP model for challenges to thermal power plant establishment in India. Int J Operat Res 34(4):562–581
15. Kumar K, Dhillon VS, Singh PL, Sindhwani R (2019) Modeling and analysis for barriers in healthcare services by ISM and MICMAC analysis. In: Advances in interdisciplinary engineering. Springer, Singapore, pp 501–510
16. Dabb A, Mukati A, Rathod Y, Nair A, Radhanpura A, Gadekar S (2019) Design and optimization of wheel hub for formula ATA race car

Optimization of Design Problems Using TLBO and mTLBO Algorithms

A. S. Pendse and Avinash Kamble

Abstract Every design problem requires optimization. There are many traditional and advanced optimization techniques available. Teaching-learning-based optimization algorithm has been proved beneficial in many engineering applications. This algorithm is free from any algorithm-specific parameters and can be adapted to all types of design problems. However, there are some limitations like convergence to local optimal solution, large computational time and slow convergence rate for complex functions. Some modifications were introduced to overcome these drawbacks in mTLBO algorithm. This paper gives better idea of both algorithms by applying them to optimize standard engineering design problems. Their performance was compared with differential evolution algorithm and some hybrid approaches of this algorithm. Best solution was obtained for all the testing problems using mTLBO algorithm. Also the solutions were obtained using less number of evaluations than other algorithms. Therefore, from present work, it can be inferred that mTLBO algorithm gives global optimum solution and requires less computational efforts.

Keywords Optimization · Design problems · TLBO · mTLBO · Differential evolution

1 Introduction

Optimization is the selection of parameters within range to get the best solution possible while satisfying all constraints. It is used in various fields like engineering, medicine, economics, etc. There are many techniques available for optimization. Linear programming, nonlinear programming, quadratic programming, dynamic programming, geometric programming, generalized reduced radiant method, etc. are some of the traditional optimization techniques. These algorithms are commonly

A. S. Pendse (✉) · A. Kamble
School of Mechanical and Civil Engineering, MIT Academy of Engineering, Alandi, Pune 412105, India
e-mail: aspendse@mitaoe.ac.in

used for solving simple optimization problems. But, whenever we fail to solve any problem with traditional techniques, we find new ways to solve such problems. Many researchers have developed algorithms based on natural phenomenon. Genetic algorithm (GA) is inspired by Charles Darwin's theory of natural evolution [1]. This algorithm uses the survival of the fittest criterion. Evolution strategies (ESs) also use principles of natural evolution [2]. Some other popular optimization algorithms are simulated annealing (SA), ant colony optimization (ACO), differential evolution (DE), cultural algorithm (CA), particle swarm optimization (PSO), evolutionary programming (EP), etc. [3].

Teaching-learning-based optimization (TLBO) algorithm is based on a relationship between teacher and students. Sample population considered for optimization can be considered as a group of students. Various design variables considered for evaluation are similar to different subjects taught in a class. Teacher in TLBO is analogous to the best solution so far. It works in two phases: teacher phase and learner phase. In mTLBO algorithm, modification was suggested in the learner phase.

In this paper, TLBO algorithm is discussed along with mTLBO. This paper is organized as follows: Sect. 2 gives summary of material and method used. Section 3 provides basic idea of TLBO algorithm. Section 4 explains the modification made in TLBO algorithm. Section 5 states the standard design problems. In Sect. 6, results are compared and discussed. In Sect. 7, paper is concluded.

2 Materials and Methods

Many evolutionary algorithms have been proved good for solving optimization problems. PSO was used to optimize various types of heat exchangers [4]. Artificial bee colony (ABC) algorithm was used to optimize mechanical draft counter flow wet-cooling tower [5]. The performance of these algorithms greatly depends upon their own algorithm-specific parameters. For example, PSO requires tuning of inertia weight and cognitive and social parameters, and GA requires tuning of mutation probability, selection operator, cross-over probability, etc. Also there are other issues like computation time and cost, convergence rate, population or swarm size, etc. which are of much concern. There were several modifications and variants made to overcome these problems.

TLBO algorithm was proposed to overcome parameter dependency of other algorithms [6]. Main advantage of this algorithm is that it is independent of any algorithm-specific parameters. It was successfully used for optimization of various engineering applications like casting process, flat plate solar air heater Stirling engine, etc. Recently, TLBO algorithm was used for thermo-economic analysis and optimization of a solar micro-CCHP [7]. Also TLBO along with DE was used for optimization of critical parameters of PEM fuel cell [8]. However, there are some drawbacks of TLBO algorithm like convergence to local optimal solution, slow convergence rate and large computational time for complex functions. Therefore, some modifications in the original algorithm were suggested in mTLBO algorithm [9]. Along with basic

teaching-learning process, concept of tutorials was incorporated in the algorithm by adding one term in learner phase.

A hybrid approach based on differential evolution and tissue P systems (DETPS) was used to solve some standard design problems [10]. Modified differential evolution (MDE) algorithm and two-hybrid approaches, local search hybrid (MA-MDE) and harmony search hybrid (MDE-IHS) were also used by a researcher to optimize these problems [11]. TLBO or mTLBO algorithms have not been used to optimize these problems. In this paper, both TLBO and mTLBO algorithms are applied to these problems. The results are compared with DETPS, MDE, MA-MDE and MDE-HIS algorithms.

3 TLBO

Following are the five steps in working of TLBO algorithm.

3.1 Problem Statement or Function Definition

Mathematical modeling of given problem is required for its optimization. Population size (N) is determined according to complexity of problem, number of design variables (D), constraints (G), etc. Population size and number of design variables are analogous to number of students and number of subjects, respectively.

3.2 Initialization

Population of i rows and j columns is generated randomly using following equation:

$$X_{(i, j)} = X_j^{\min} + \left(X_j^{\max} - X_j^{\min} \right) * \text{rand} \tag{1}$$

where rand represents a uniformly distributed random variable within the range (0, 1), and $X^{\min}$ and $X^{\max}$ represent minimum and maximum value for jth parameter, respectively. Initial solution is obtained by using these values in objective function and constraints.

3.3 Teacher Phase

Mean of each subject is calculated. The learner which gives the least objective function value (for minimization problem) is considered as the teacher for respective iteration. In this phase, mean of learners is shifted toward their teacher. Difference mean is calculated using following equation:

$$\text{Diff\_mean\_X}_{(i,\ j)} = r\left(\text{Teacher\_X}_j - \text{mean\_X}_j\right) \tag{2}$$

This difference mean is added to respective $X_{(i,\ j)}$, and new function values are obtained. Initial solution and newly obtained solution are compared, and the best function values are selected. This modified solution is the teacher phase solution.

3.4 Learner Phase

In this phase, the learners interact with each other. The process of mutual random interactions tends to improve their knowledge. For a given learner X_i, another learner X_r is randomly selected ($i \neq r$). The ith parameter of the matrix X_{new} in the learner phase is given as

$$X_{\text{new}\ (i)}^{g} = X_{(i)}^{g} + \text{rand} * \left(X_{(i)}^{g} - X_{(r)}^{g}\right) \text{ if } X_{(i)}^{g} < X_{(r)}^{g}$$
$$\text{or} \tag{3}$$
$$X_{\text{new}\ (i)}^{g} = X_{(i)}^{g} + \text{rand} * \left(X_{(i)}^{g} - X_{(r)}^{g}\right) \text{ if } X_{(i)}^{g} < X_{(r)}^{g}$$

New function values are obtained, and newly obtained solution is compared with teacher phase solution, and the best function values are selected. This modified solution is the learner phase solution.

3.5 Algorithm Termination

After some iteration, final solution is obtained, and algorithm is terminated.

4 mTLBO Algorithm

In this algorithm, teacher phase remains same. Only learner phase is modified. Concept of tutorials given by teacher to students is used to improve the final solution. TLBO may not always give global optimum solution. It sometimes provides local optimum solution. To obtain global solution, an extra term was added to learner phase equation mentioned in Sect. (3.4).

$$X_{\text{new}(i)}^{g} = X_{(i)}^{g} + \text{rand}*\left(X_{(i)}^{g} - X_{(r)}^{g}\right) + 0.5*(1 + \text{rand})$$
$$*\left(X_{\text{Teacher}}^{g} - X_{(i)}^{g}\right) \text{ if } X_{(i)}^{g} < X_{(r)}^{g}$$

or

$$X_{\text{new}(i)}^{g} = X_{(i)}^{g} + \text{rand}*\left(X_{(r)}^{g} - X_{(i)}^{g}\right) + 0.5*(1 + \text{rand})$$
$$*\left(X_{\text{Teacher}}^{g} - X_{(i)}^{g}\right) \text{ if } X_{(r)}^{g} < X_{(i)}^{g}$$

$$(4)$$

where X_{Teacher}^{g} is the minimum objective function value after teacher phase.

5 Optimization Problems

Six design problems are chosen for optimization [12]. They contain continuous and binary type variables. Details of the problems are given in Appendix.

6 Results and Discussions

For both TLBO and mTLBO algorithms, population size of 50 is selected in all problems. Mean solution for each problem was obtained after extensive number of runs. Numbers of evaluations were calculated for each run, and average numbers of evaluations are taken into consideration. Standard deviation (SD) was also calculated among the population in all problems. Mean SD was calculated for all problems. Results are obtained for TLBO and mTLBO algorithms as shown in Table 1.

Table 1 Results of TLBO and mTLBO

Problem		TLBO	mTLBO
1	x	[10.8044, 2.0247]	[12.5, 0]
	y	[0.5409, 0]	[0.625, 0]
	f	85.3531	**84.6875**
2	x	[1.118, 1.3104]	[1.118, 1.3104]
	y	[0, 1, 1]	[0, 1, 1]
	f	7.6672	**7.6672**
3	x	[0.2, 0.8, 1.908]	[0.246, 1.031, 2.016]
	y	[1, 1, 0, 1]	[0.556, 0.758, 0.392, 0.952]
	f	4.5793	**3.1962**
4	x	[0.5]	[0.5]
	y	[1]	[1]
	f	2.0000	**2.0000**
5	x	[1.3749]	[1.37485]
	y	[1]	[1]
	f	2.1246	**2.1245**
6	x	[0.59, −1.471]	[0.586, −1.471]
	y	[0.4281]	[0.428]
	F	0.5408	**0.5374**

From Table 1, it can be observed that mTLBO gives the least value of function in all problems, but the difference in solution of both TLBO and mTLBO is small. Table 2 gives the comparison of results obtained by various algorithms.

From Table 2, various observations can be made. Smallest function value is obtained by using mTLBO algorithm in all problems. For problems 2 and 4, TLBO also gives the least function value. Also mTLBO solves the problems in minimum number of evaluations. Standard deviation (SD) seems to be the least in case of DETPS except in problem 05 where MA-MDE has the minimum SD.

Table 2 Statistical result of mean solutions, standard deviations and numbers of evaluations

Problem		DETPS	MDE	MA-MDE	MDE-IHS	TLBO	m-TLBO
1	Mean	87.500012	89.879034	88.230145	87.497550	85.353100	**84.845900**
	SD	**0.000002**	2.768746	1.899683	0.002118	0.006850	0.003150
	Evaluations	14360	7777	4436	5359	3215	**2000**
2	Mean	7.931112	7.918619	7.883841	7.848896	**7.667200**	**7.667200**
	SD	**0.000000**	0.047891	0.098982	0.121909	0.006460	0.024130
	Evaluations	100000	96718	93524	83442	8653	**5088**
3	Mean	4.579593	4.661414	4.579595	4.579599	4.579300	**3.1962**
	SD	**0.000000**	0.311365	0.000003	0.000005	0.001500	0.000210
	Evaluations	7254	7688	13023	14518	6797	**3586**
4	Mean	2.000000	2.009348	2.000000	2.000001	**2.000000**	**2.000000**
	SD	**0.000000**	0.043579	**0.000000**	**0.000000**	0.000219	0.000001
	Evaluations	1720	1075	1430	3297	1000	**1035**
5	Mean	2.182346	2.167894	2.124574	2.124604	2.124600	**2.124500**
	SD	0.149789	0.132196	**0.000071**	0.000076	0.128315	0.099315
	Evaluations	1726	827	653	1409	584	**320**
6	Mean	1.076700	1.124453	1.099805	1.094994	0.540800	**0.537400**
	SD	**0.000391**	0.075163	0.055618	0.052898	0.015325	0.008472
	Evaluations	5309	30986	25766	22146	2700	**2500**

7 Conclusions

Following conclusions are drawn from the results obtained:

i.   Modified teaching-learning-based optimization algorithm (mTLBO) gives the best solution in all problems satisfying all constraints.
ii. Compared with other algorithms, mTLBO has faster convergence rate.
iii. Teaching-learning-based optimization (TLBO) algorithm gives better results than all algorithms except mTLBO.
iv. Both TLBO and mTLBO give better solution in different types of problems and hence can be used in many engineering applications.

Appendix

Problem 01

$$\min f = 7.5y_1 + 6.4x_1 + 5.5y_2 + 6.0x_2$$

Subject to:

$$0.8x_1 + 0.67x_2 = 10$$

$$x_1 - 20y_1 \leq 0$$

$$x_2 - 20y_1 \leq 0$$

$$x_1, x_2 \in [0, 20]$$

$$y_1, y_2 \in \{0, 1\}$$

Problem 02

$$\min f = 2x_1 + 3x_2 + 1.5y_1 + 2y_2 - 0.5y_3$$

Subject to:

$$x_1^2 + y_1 = 1.25$$

$$x_2^{1.5} + 1.5y_2 = 3$$

$$x_1 + y_1 \leq 1.6$$

$$1.333x_2 + y_2 \leq 3$$

$$-y_1 - y_2 + y_3 \leq 0$$

$$x_1, x_2 \in [0, 2]$$

$$y_1, y_2, y_3 \in \{0, 1\}$$

Problem 03

$$\min f = (x_1 - 1)^2 + (x_2 - 2)^2 + (x_3 - 3)^2 + (y_1 - 1)^2$$
$$+ (y_2 - 2)^2 + (y_3 - 1)^2 - \log_{10}(y_4 + 1)$$

Subject to:

$$x_1 + x_2 + x_3 + y_1 + y_2 + y_3 = 5$$

$$x_1^2 + x_2^2 + x_3^2 + y_3^2 = 5.5$$

$$x_1 + y_1 \leq 1.2$$

$$x_2 + y_2 \leq 1.8$$

$$x_3 + y_3 \leq 2.5$$

$$x_1 + y_4 \leq 1.2$$

$$x_2^2 + y_2^2 \leq 1.64$$

$$x_3^2 + y_3^2 \leq 4.25$$

$$x_3^2 + y_2^2 \leq 4.64$$

$$x_1 \in [0, 1.2]$$

$$x_2 \in [0, 1.281]$$

$$x_3 \in [0, 2.062]$$

$$y_1, y_2, y_3, y_4 \in \{0, 1\}$$

Problem 04

$$\min f = 2x + y$$

Subject to:

$$1.25 - x^2 - y \leq 0$$

$$x + y \leq 1.6$$

$$x \in [0, 1.6]$$

$$y \in \{0, 1\}$$

Problem 05

$$\min f = -y + 2x - \ln(x/2)$$

Subject to:

$$-x - \ln(x/2) + y \leq 0$$

$$x \in [0.5, 1.4]$$

$$y \in \{0, 1\}$$

Problem 06

$$\min f = -0.7y + 5(x_1 - 0.5)^2 + 0.8$$

Subject to:

$$-\exp(x_1 - 0.2) - x_2 = 0$$

$$x_2 + 1.1y \leq -1$$

$$x_1 - 1.2y_1 \leq 0.2$$

$$x_1 \in [0.2, 1]$$

$$x_2 \in [-2.22554, -1]$$

$$y \in \{0, 1\}$$

References

1. Holland JH (1975) An introductory analysis with applications to biology, control, and artificial intelligence. In JH Holland (ed) Adaptation in natural and artificial systems. University of Michigan Press, Ann Arbor, p 183
2. Bäck T (1991) A survey of evolution strategies. In: 4th international conference on genetic algorithms. Morgan Kaufmann, San Diego, pp 2–9
3. Pratihar DK (2012) Computational optimization and applications. Narosa Publishing House Pvt. Ltd, New Delhi
4. Rao RV, Patel VK (2011) Optimization of mechanical draft counter flow wet-cooling tower. Energy Conver Manage 52(7):2611–2622
5. Rao RV, Patel VK (2010) Thermodynamic optimization of cross flow plate-fin heat exchanger using a particle swarm optimization algorithm. Int J Thermal Sci 49(9):1712–1721
6. Rao RV, Savsani VJ, Vakharia DP (2011) Teaching-learning based optimization: a novel method for constrained mechanical design optimization problems. Comput-Aided Design 43:303–315
7. Azizimehr, B, Assareh E, Moltames R (2020) Thermoeconomic analysis and optimization of a solar micro CCHP by using TLBO algorithm for domestic application. In: Energy sources, part a: recovery, utilization, and environmental effects 1747–1761
8. Guo C, Lu J, Tian Z, Guo W, Darvishan A (2019) Optimization of critical parameters of PEM fuel cell using TLBO-DE based on Elman neural network. Energy Conver Managem 149–158
9. Satapathy S, Naik A (2013) A modified teaching-learning-based optimization (mTLBO) for global search. Recent Paten Comput Sci 13(6):60–72
10. Zhang H, Cheng J, Gheorghe M, Meng Q (2013) A hybrid approach based on differential evolution and tissue membrane systems for solving constrained manufacturing parameter optimization problems. Appl Soft Comput 13(3):1528–1542
11. Liao T (2010) Two hybrid differential evolution algorithms for engineering design optimization. Appl Soft Comput 10(4):1188–1199
12. Mathur M, Karale S, Priye S, Jayaraman V, Kulkarni B (2000) Ant colony approach to continuous function optimization. Ind Eng Chem Res 39(10):3814–3822

GSM-Based Operation System for Agricultural Pumps

Ajit Lokhande, Akash Neharkar, Akash Salunke, Rupesh Satpute, and Avinash Kamble

Abstract Agricultural sector in India is one of the most prominent sectors of Indian economy which accounts for 18% of India's gross domestic product. Out of number of irrigation sources, the tube wells and traditional wells account for more than 50% of irrigation sources. In summer, the groundwater sources get depleted, and there may be possibility of dry run of the pump, which creates serious consequences such as excessive heating of motor winding. This paper is aimed to present a way which implements Internet of Things tools to protect the water pump from dry run and to enhance the control on ongoing operations in agriculture. The paper describes a new approach to make sensors and automation affordable and inter-operable by designing a system and using well-established standards for data communication by using Global System for Mobile Communications. A system is presented to prevent the dry run of the pump used in farms and its switching ON and OFF whenever required by using suitable microcontrollers and sensors. The proposed system uses an Arduino Uno microcontroller, GSM module, relay, a rotameter, centrifugal pump and humidity sensor. The design is made in such a way that to keep its operation simple and setup cost less. The limitations of traditional practices in agriculture have overcome by proposed system, which utilizes water resource efficiently, saving labor costs and safe operation of water pump.

Keywords Internet of things · Global system for mobile communications · Agricultural automation

1 Introduction

India, being one of the large exporters of food items to the world, has large amount of population involved in agricultural sector. This emphasizes a need to bring automation and use the modern tools to reduce human efforts and to make a system efficient. Researchers have proposed various ways to automate the agricultural activities. These

A. Lokhande (✉) · A. Neharkar · A. Salunke · R. Satpute · A. Kamble
MIT Academy of Engineering, Alandi, Pune, India
e-mail: anlokhande@mitaoe.ac.in

577

methods were studied, and a new approach to address the above-stated problems has been developed using IoT technology. The day-to-day activities of farmers are monitored, and problems encountered by them are noted. In summer, due to shortage of groundwater resources, the dry run of the pump is commonly occurring problem for the farmers who use tube well and wells for irrigation purpose. Also, farmers used to switch ON the pumps whenever they wish to do so. This does not ensure that the watering to plants is done when it is necessary. There is strong need to implement advanced technology in agriculture like other industry sectors. The aim of this paper is to propose a design which will prevent the occurrence of dry run of the motor pump and to systemize its operation, i.e., to switch ON the pump when humidity level of soil falls below the certain limit prescribed by concerned agency by incorporating sensors and microcontroller.

The rapid emergence of Internet of Things (IoT) based technologies redesigned almost every industry, agriculture being no exception. Ayaz et al. [1] discussed in his paper the various tools and techniques which can be implemented in agriculture industry to make it smarter, better and more efficient. Our paper discusses design of a system which will smoothen the agricultural operations and reduces the human work. The system enables farmer to control the operation of the pump remotely. The microcontroller incorporated sends signal to the mobile device of the farmer, and the farmer can send the commands to the microcontroller by using his cell phone. This enables two-way communication between the user and the microcontroller, which is the heart of whole system. The system can result in great outcomes which are reduction in failure of the water pump, as dry run is avoided, reduces human efforts, watering of the plants only when it is required. Given this context and the importance of the problem, this paper discusses how the issues mentioned above can be addressed using the approach of IoT.

2 Literature Survey

The revolutionary advancements in technology are bringing a lot of change in today's industry, the movement well anticipated as Industry 4.0. A lot of researchers are working in agricultural sector too to automate various processes. Khaled et al. [2] worked on designing a system for remote operation of submersible pump based on Global System for Mobile Communications (GSM) and short messaging services (SMS). He proposed an embedded system which can remotely ON/OFF and monitoring pump status through sending and receiving messages on mobile phones to help the farmer. With this system, remote powering submersible pumps and continuous monitoring faults were realized. Nandi and Mondal [3] worked on GSM-based pump operation. They added an additional feature by which number of people authenticated by owner can also operate the pump. Priyadharsini et al. [4] presented the work on GSM-based motor control for irrigation system in their research paper. The proposed system uses level sensors to detect the level of water in sump, and accordingly, it

sends signal to the microcontroller. The system ensures safety of motor against overloads, dry running and phase imbalances. It also provides automatic restarting of motors. Also, the program ensures watering of plants at regular intervals. Sagar and Prasad [5] worked on designing a system for three-phase water pump control and level sensing using GSM and mobile. The author proposed a system consisting of 89V51 microcontroller, and the system architecture is designed using EAGLE PCB design software. The system enables the user to control the water pump from remote areas.

Swami et al. [6] worked on controlling three-phase motor using GSM. The design incorporates the microcontroller and GSM to control the three-phase motor used in agricultural operation. The system ensures protection against over voltage, over current, single phasing and dry run. Also, it intimates the user when the abnormal condition such as dry run occurs and automatically switches OFF the motor. Ravikiran et al. [7] worked on a system for a solar energy operated pump to prevent the pump from dry run. Their aim is to use solar radiation energy from the sun to pump the water from lower tank to upper tank. The system consists of solar-driven automatic water level controller with dry run protection (SDWLC) to control the water pump. Ulaganatha et al. [8] designed a system for submersible pump to prevent the pump against over loading, dry running and single phasing. The author proposed a system using PIC16F877A microcontroller and GSM module to control the motor. This system offers protection against overloads, overheating and dry run of the pump. It also incorporates to send commands to the microcontroller by missed calls and SMS. Davange et al. [9] presented their work on design of IVRS for three-phase motor control using GSM for agricultural field, and the authors designed a system using Interactive Voice Response System (IVRS), GSM model and Renesas microcontroller to control the water pump. The system uses dry run protection sensor to prevent it from dry run, and additionally, single-phase protection device is also used. The user can send commands using missed calls and SMS. Jadhav et al. [10] presented his work in the field of controlling three-phase motor pump using GSM. The author used AT89C51 microcontroller along with GSM module. The designed system ensures protection of motor against overloads, overheating and phase imbalances. The author added an additional feature which restarts the motor pump once normal conditions are established.

The systems developed in GSM-based pump control emphasize on the system architecture to aware farmer about the fault and prevent the pump from dry run. Different authors addressed different concerns by implementing number of IoT technologies. But a system which is completely dedicated to control operation of the pump, to prevent the pump from dry run, to enable farmer to switch ON the pump from remote location is unavailable. Along with that, the farmer can get alert when the moisture level of soil goes below the pre-set limit. So that farmer can ensure watering of plants only when it is needed. Therefore, authors have proposed a system which will take care dry run of the pump and its efficient switching ON/OFF only when the humidity level of the soil goes below the limit, thus saving electricity and man-hours.

3   Design of Control System

From the current available technologies for wireless communication, the GSM modem is one of the best choices to send the commands to controller via users' mobile device. The controller is programmed in such a way that it will receive the command from user and operates the pump. The system is equipped with dry run protection by incorporating a rotameter in the discharge pipe. The rotameter will rotate when the water flow is available, generating the 5 V DC, which is fed to the microcontroller. The microcontroller is programmed to switch the relay OFF when the 5 V DC is not available, i.e., absence of the bulk liquid motion. The user will get notification on his mobile device when the pump is switched OFF due to dry run condition. The soil moisture sensor is used to detect the moisture level in soil, output of which is sent to the Arduino controller. The Arduino will generate a text message when the moisture content of soil falls below pre-determined level, and the user is informed about the condition by SMS. The design approach presented is generic to any microcontrollers to monitor parameters like humidity of soil, safety of the pump and controlling operation of the pump from remote area.

The proposed low-cost automation designed using proposed approach has components as described below:

- Arduino Uno: Arduino is a microcontroller based on open-source electronic proto-typing board which can be programmed with the help of Arduino IDE. Arduino consists of a physical program. The Uno is most popular board in Arduinos. The major components of the Arduino Uno board are USB connector, power port, microcontroller, analog input pins, digital pins, reset switch, TX RX, etc.
- GSM Module: GSM stands for global system for mobile communication. It is used for voice and data communication. Mobile phone is a handheld device that communicates with GSM network as a voice and data communications. It receives and sends the messages to the user based on program. The major components of the GSM module are SIM900, SMA antenna, power button, RST button, SIM card, TX RX, etc.
- Rotameter: Rotameter is the device which converts flow into voltage. Rotameter consists of a DC motor to which a plastic propeller is connected. As the propeller rotates DC motor generates some amount voltage and sends to the Arduino. Further actions are taken by microcontroller according to the pre-set commands and input received from DC motor which is connected to rotameter.
- Relay: Relay, being one of the simplest electronic components, is also most important because it can be used to operate high voltage devices using low voltages. Relay basically consists of a coil generates magnetic field when current passes through it. This magnetic field pulls switch into the close to allow current flow from the other side. We use 5 pin relays in this circuit.
- Soil Moisture Sensor: It is an analog sensor which is used to measure water/humidity content of the soil. When the soil is having water shortage, the module output is at high level, or else the output is at low level. It uses capacitance

to measure dielectric permittivity of the surrounding medium. The voltage and current requirements for the sensor are 5 V and 20 mA, respectively.

Figure 1 shows the block diagram for the controller system and inter-relation among various components. Figure 2 enlists the components of the designed system. Also, it depicts the arrangement of the components and their inter-relation with each other. Arduino Uno being the heart of the system, all sensors and outputs are connected with it. The 230 V supply is given to relays. The microcontroller can be powered with 9 V battery.

Fig. 1 Block diagram of the system for controlling operation of the pump
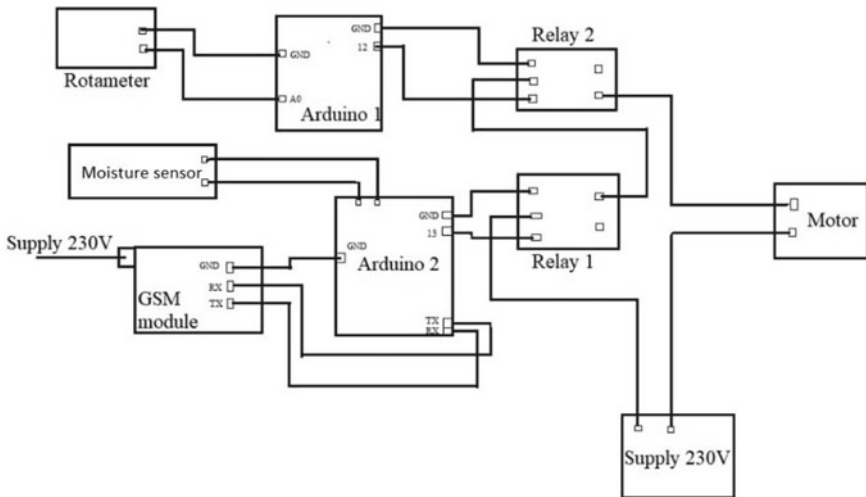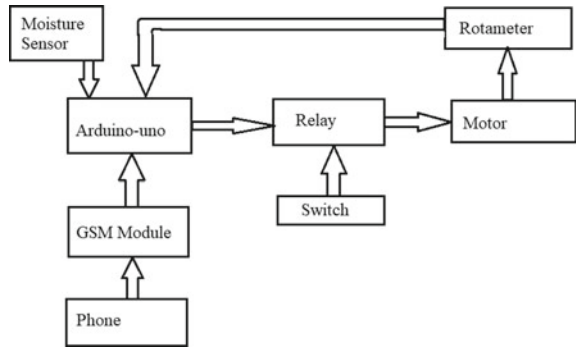
Fig. 2 Circuit diagram of the system for controlling operation of the pump
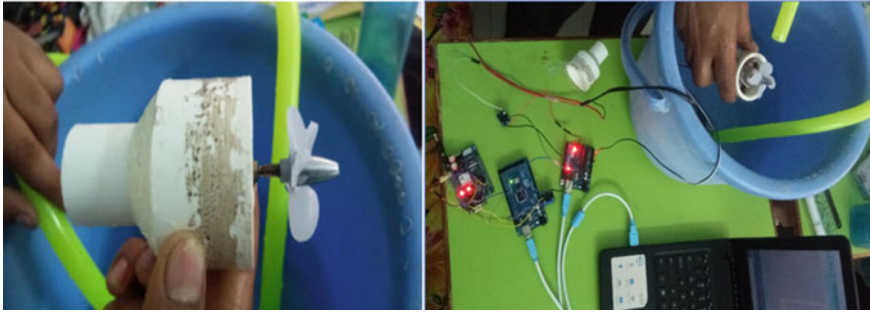
Fig. 3 Experimental setup for the trial of developed system

4   Implementation of Design in Agricultural Application

This section describes the automation system being developed for agricultural application using proposed approach. The rotameter is a simpler device used to detect flow of water. It can be placed in the discharge of the pump. The Arduino Uno controller is equipped with the 9 V DC battery supply. The GSM module with SIM card is connected to the microcontroller. The soil moisture sensor can be placed in the farm wherever required, and its output is fed to the controller. The user of the system can send text message to assigned number to operate the pump, and he gets notifications when the pump is switched OFF due to dry run condition and when the soil moisture falls below pre-set value.

Figure 3 depicts the experimental setup for the said solution. The trials have come out successful, and the microcontroller effectively operates the pump according to the commands came from GSM module. The system can be readily installed in the field operation, and its performance can be monitored. Since this system is part of a pilot study, it will be implemented only after testing its performance on a large scale.

5   Results and Discussion

This section describes the output of implemented system. A random location is chosen to test the designed system. The arrangement is done on 5 HP submersible pump. Mobile number of concerned user is fed to the controller. The system is designed such as it turns off the pump as soon as dry run occurs. Also, the microcontroller is programmed in such a way that it sends the message on users' mobile phone when the dry run occurs. The motor is made to run in a dry run condition using some artificial arrangements. The microcontroller sends the text alert to users' mobile phone, which proves the microcontroller is working as per the pre-set commands. The ON–OFF switching of motor is also made possible through the designed system, and same is checked by sending text commands to the microcontroller. The humidity

sensor is located in the irrigated land, and its output is fed to microcontroller. It is tested and calibrated with another standard. The humidity of soil is altered to check its normal working and whether it works as per the program or not. The designed system is checked by creating artificial conditions, and its working is checked in every possible condition, viz. normal operation, dry run and decrease in moisture content of soil. The system is found to be user-friendly and economical to use.

6 Conclusions

The popularity of IoT technology in day-to-day application has increased significantly in recent times. The newer technologies coming are bringing revolution in every sector, agriculture being no exception. It has changed the traditional approaches of working. The proposed system keeps the pump safe from dry run condition. It also enables user to operate the pump remotely and helps monitoring moisture content of the soil. This paper has described an approach for the design and development of a new system, which uses microcontroller, sensors and standard devices for data communication. The proposed solution addresses the problem of dry run of the pump in most cost-effective way. The system reduces burden on the user. Also, the low costs associated with the system make it more affordable to farmers. The design is made simpler that other features such as weather forecasts, irrigation planner, and calamity warnings can be added. Such a system will help farmers, researchers and students to develop automation system for agricultural application.

References

1. Ayaz M, Sharif Z, Mansour A, Aggoune HM (2019) Internet-of-things (IoT) based smart agriculture: towards making the fields talk. IEEE Access 7:129551–129583
2. Khaled M, Nouby MG, Nabhan A (2016) Design a remote control system for submersible pumps based on GSM-SMS. American J Eng Technol Res 16(2):68–79
3. Nandi B, Mondal S, Ghosh K (2015) GSM based pump automation. Int J Adv Res Comput Sci Softw Eng 5(9):446–452
4. Priyadharsini M, Arunbalaji V, Karthikaa T (2016) GSM based motor control for irrigation system. Int J Adv Res Electri Electron Instrument Eng 5(1):16–18
5. Swami LB, Rajguru V (2018) Three phase motor control using GSM. Int J Inn Eng Res Technol 2(1):68–71
6. Sagar TM, Madhu Prasad N (2015) Real application of three phase water pump control and level sensing using GSM and mobile. Int J Sci Res Develop 3(2):1171–1177
7. Ravikiran V, Damodar Reddy M (2015). Solar driven automatic water level controller with dry run protection. Int J Eng Res Appl 5(11):49–53
8. Ulaganatha G, Periasamy A, Murugan E (2014) Embedded system based submersible motor control for agricultural irrigation using GSM and to prevent it against over loading, Dry running and single phasing automatically. Int J Sci Res Develop 2(7):454–456

9. Davange MV, Gavali AN (2017) IVRS for three phase motor control using Gsm for agricultural field. Int J Adv Res Inn Ideas Educ 3(2):5366–5370
10. Jadhav RR, Pandit PP, Pal SD, Risbud VH (2015) Three phase motor control using GSM. Int J Inn Res Electri Electron Instrument Control Eng 3(5):19–20

Optimization in Brake Pedal of All-Terrain Vehicle

Shashwat Kulshreshtha, Naman Varshney, Shikhar Verma, Shantanu Tiwari, Rahul Khanna, and Mayank Kushwaha

Abstract One of the most necessary systems of a vehicle is its braking system. It de-accelerates a moving vehicle by transforming its kinetic energy into heat energy and sound energy by modes of friction between components. Since it is a system, it consists of a number of parts which are inside as well as outside the cabin of that vehicle. Braking system is an assembly of many parts working together to retard of control vehicle intentionally or in some unwanted emergency condition. These parts are brake pedal, vacuum booster, master cylinder, brake lines (both metallic and non-metallic), brake caliper, brake pads, disk rotors and brake fluid (in hydraulic brakes). Only brake pedal is the part of braking system which is inside driver's cabin and by which brakes can be employed in real time of performance. It works like any of three classes of lever, which consists of load, effort and fulcrum. It transfers the force from driver's lower limbs to the hydraulic fluid inside master cylinder, through a plunger attached to piston. Sometime, the force applied by driver's feet is not enough to slow large vehicles such as trucks and land movers. Therefore, a proportion (leverage) or a vacuum booster or both are taken into account. This magnifies the force applied by driver many times, by which a large pressure is created inside the master cylinder which is conveyed by brake fluid to the caliper. This pressurized brake fluid when comes in contact with the piston of caliper creates an axial force that depends on the surface area of the piston of brake caliper. The pressure of the brake fluid pushes the caliper piston outwards by which is in contact with the brake pads that grasp the disk rotor and slow down or stop the vehicle according to the driver's requirement. Therefore, the movement of the brake pedal should be enough and must be comfortable for driver which will push the piston outside to an optimum length to retard the motion of vehicle.

Keywords Brake pedal · Brake force · Leverage · Pedal ratio · All-terrain vehicle · ATV

S. Kulshreshtha · N. Varshney (✉) · S. Verma · S. Tiwari · R. Khanna · M. Kushwaha
Department of Mechanical, ABES Engineering College, Ghaziabad, India
e-mail: namanvarshney99@gmail.com

1 Introduction

1.1 Basic Introduction and Problem Statement

Brake pedal is an important part of a braking system as it is the primary component which involves with the driver. Therefore, the design of brake pedal must include factors such that driver should not compromise in comfort and even in braking performance of the vehicle within a defined space and area of its movement [1, 2]. A leverage should also be provided to brake pedal which will magnify the force up to a predefined constant according to that leverage ratio. That ratio will be decided according to the requirement of force on the piston of master cylinder. NASA-STD-3000 206 (5th Percentile Male Data) [3] has provided a chart of human performance capabilities from which data is considered for calculations.

1.2 Literature Review

There are many researches on brake pedal which includes the static and dynamic characteristics assessment. The assessment index of brake pedal consists of pedal force-pedal travel curve, the deceleration-pedal force curve and brake distance-pedal travel curve. N and Mangukia (2018) show in his research paper that to design a brake pedal having brake pedal ratio of more than 5:1, as it is suggested that manual braking system (with no power booster) should have a ratio greater than 5 [4]. The length of brake pedal should not be too short or too long that hinders the driving position of the driver's leg. The brake pedal ratio should be such that the driver would not feel fatigue while braking [5].

1.3 Aim and Objective

Optimization in design and fabrication of brake pedal which will amplify the force imposed by driver on it and transfer it to the master cylinder's piston to generate pressure on brake fluid.

1.4 Problem Specification

For a braking system which is not using vacuum booster, the minimum pedal ratio required is 5:1 [5]. It means the force applied by driver will be magnified 5 times, which will create a large pressure in master cylinder which will be conveyed by the brake fluid. As well as the dimensions of brake pedal should be convenient to driver,

i.e., comfortable in use without tangling into other components around it and should be suitable for long saddle.

2 Design and Analysis

2.1 Design

Initially, the pedal ratio was defined according to the forces required for generation of optimum pressure inside master cylinder, and it was decided to be 8:1. The length of pedal was decided by dimensional constrains and pedal ratio. Lever type of class-1 is used in pedal where the pedal is pivoted on a point which lies between effort and output and that point of pivot is decided according to the pedal ratio. Pedal ratio can be understood as the ratio between normal distance between center point of pivot and point where pushrod of master cylinder is attached to the normal distance between point where effort is applied and point where pushrod is attached. The CAD model of brake pedal is made on SolidWorks, and its FEA simulations are also done on same. Here are the side and front views of designed brake pedal shown in Figs. 1 and 2.

Fig. 1 Side view of designed brake pedal
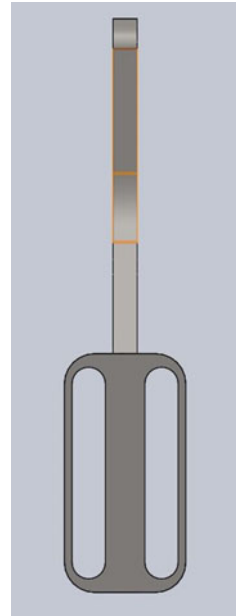
2.2 Material Selection

Three materials were taken and compared for fabrication of brake pedal on the basis of following properties (shown in Table 1).

- Physical and chemical properties,
- Availability,
- Cost,
- Machinability.

We compared all materials which are mentioned above on many parameters such as their properties, price, availability, weld-ability, machinability and the cost of machining. It was concluded that AISI 1020 is standing on many parameters of our

Table 1 Table showing comparison of physical properties of material

Material/properties	AISI 1020	Al-7075 T-6	Al-6061 T-6
Ultimate tensile strength (MPa)	394	572	310
Ultimate yield strength (MPa)	294	503	276
Elongation (%)	36.5	11	17
Density(kg/cm^3)	7870	2810	2700
Price (Rs./kg)	100	486	280

requirement, its strength lies between rest of two materials which were considered, it was available at local vendors of our area, and machining process which was laser cutting is also economical. Brake pedal consisted of two parts which were joined together by gas tungsten arc welding (GTAW). Therefore, AISI 1020 was finalized as the material for our brake pedal.

2.3 Analysis

The FEM analysis of brake pedal was done on SolidWorks, and static-structural simulation was performed on it by taking data of force that a normal male can apply that was 500 N axially. The data is taken from NASA-STD-3000 206 (5th Percentile Male Data) [3] which has provided a chart of human performance capabilities. The simulation was performed on extreme condition considering the pushrod of master cylinder fixed which will indirectly fix the pivot point of the pedal. Therefore, the pivot point is fixed, and an axial force of 500 N is applied on the brake pedal [6].

For meshing, the standard mesh lets us specify a global element size and a tolerance value. It makes use of Voronoi-Delaunay triangulation, which tries to maximize the smallest angle of all triangles, while the geometry is being split into element triangles or tetrahedrons. In our design of brake pedal, the standard mesh tends to avoid skinny triangles and hence helps reduce the number of elements with a high aspect ratio, which can affect the accuracy of our results. The standard mesh does a great job of creating a uniform and reliable mesh.

Standard mesh is applied on the part having an element size of 1.7128 mm, and in fillet region, mesh control was also applied which was having element size of 0.856 mm. Mesh control is applied to 19 faces which increased accuracy of analysis

Fig. 3 Meshed view of pedal
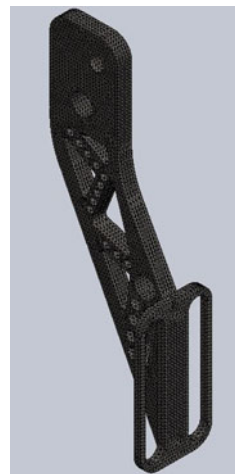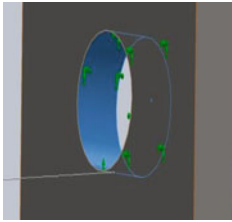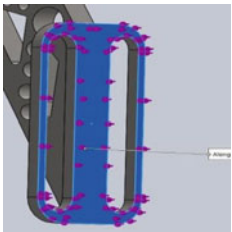
Table 2 Table showing fixed part and part where axial loading is applied of designed brake pedal

Fixture	Image	Entities type
Fixed-1		Single(1) face fixed geometry

Load	Image	Details
Foot load		A load of 500 N perpendicular to face is applied

as shown in Fig. 3. Table 2 shows fixed part and part where axial loading is applied of designed brake pedal.

2.4 Results

The results were favorable, and no failure of component was taking place in that analysis. The maximum stress developed on part was 309.3 MPa according to von Mises theory, and minimum FOS (factor of safety) achieved was 1.13 as shown in Fig. 4 and Table 3.

2.5 Manufacturing

Sheet of different thicknesses were laser cut, the main pedal was made from 6 mm thick sheet of AISI 1020 while the part where the force is applied by driver is made from sheet of same material having thickness 4 mm. Both are welded by gas tungsten arc welding (GTAW) to make the complete brake pedal (shown in Fig. 5).
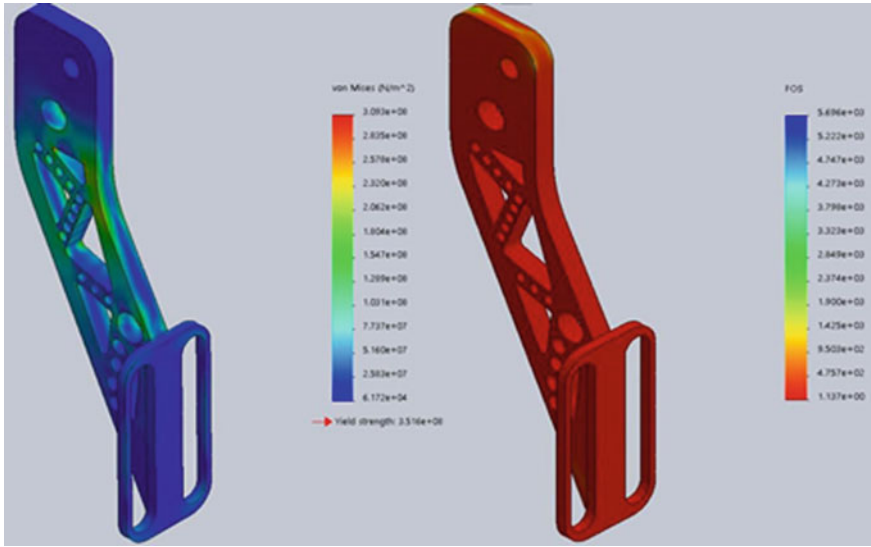
Fig. 4 Static stress analysis and factor of safety results of brake pedal

Table 3 Table showing result analysis data, i.e., static and factor of safety

Study name	Study type	Maximum	Minimum
Stress	von Mises	309.3 MPa	0.672 MPa
Factor of safety	Automatic	569.6	1.137

Fig. 5 Fabricated brake pedal

3   Calculations

Leverage R ratio or P pedal R ratio $= \dfrac{\text{Normal distance between pivot point and push rod connection}}{\text{Normal distance between foot rest and push rod connection}}$

It was a prior decision to keep the pedal ratio 8 to make it convenient for the driver to use it in necessity. Therefore, design was made by keeping these things in mind.
Since

Distance between pivot point and pushrod—197.6 mm
Distance between footrest and pushrod connection—24.7 mm

Therefore,
Pedal ratio $= 197.6/24.7 = 8:1$
Therefore, when a force of 50 N is applied on brake pedal, it will multiply it by 8 times that will be around 800 N. When a maximum of 500 N will be applied, maximum force that will churn out will be 4000 N.
The pressure generated in brake fluid inside master cylinder will be,

Pressure = Force after multiplied by pedal ratio/surface area
Diameter of piston of master cylinder $(d) = 19.05$ mm
Surface area of piston $= \pi(d2)/4 = \pi(19.05)2/4 = 284.87$ mm^2
Pressure $= 800$ N/284.87mm^2 $= 2.8$ N/mm^2 $= 2.8$ MPa
It is enough pressure to clamp the brake pads against the disk rotor.

4   Conclusion

Brake pedals can be made on all three types of classes of levers according to the constrains either geometrical or driver convenience. Finite element analysis (FEA) must be conducted based on the dynamic condition of the vehicle, and by doing this, a clear perception of the working of pedal can be made before fabrication of the part. From the results of simulation done on SolidWorks, it is clear that the design is safe under extreme condition of ATV drive. Pedal ratio of 8:1 will provide a mechanical advantage to amplify the force applied by driver's foot. The weight of the pedal is approx. 340 g which is an optimum weighing pedal for ATV, and it can be further reduced on using aluminum alloys or composite materials.

References

1. Hecht H (1937) Chase the influence of light-adaptation on subsequent dark adaptation. J General Physiol
2. Dhande KK, Janadar NI, Sandeep G (2014) Design and analysis of composite brake pedal: an ergonomic approach. IJMERR 3(3)
3. FMVSS 135—section 7.11

4. Basch R, Sanders P, Hartsock D et al (2002) Correlation of lining properties with brake pedal feel. SAE paper
5. Mangukia N, Mangukia N (2018) Design and fabrication of brake pedal for all terrain vehicle. Int J Eng Res Devel 6(2)
6. Sapune SM (2005) A conceptual design of concurrent engineering design system for the polymeric based composite automotive pedals. Department of Mechanical and Manufacturing Engineering University Putrs Malaysia

Design and Analysis of an Automatic Seed Sowing Machine Using SolidWorks and ANSYS Tools

Gaurav Kumar, Rishabh Singh, Pavan Kumar, Twinkle Rajput, Eram Neha, and Yogesh Shrivastava

Abstract To meet future food demands, it is essential to provide new technologies to the farmers. There are several processes, viz. excavation, planting, irrigation, etc. for which the farmers are still worried. Mechanization reduces the cost of labor and improves overall productivity without any effect on the quality of the soil. Hence, it is necessary to provide them with some useful economic solutions for these problems. In the present work, the problem of seed sowing has been addressed. The conventional method of seed sowing is not efficient and is time-consuming. In the present work, a multifunctional seed sowing machine has been designed, which can sow the seed and can discharge the fertilizer simultaneously. The design of the machine has been done using SolidWorks, and the analysis has been done with the help ANSYS workbench 15.0. From the result, it has been found that the seed sowing machine is safe under self-weight and in other loads.

Keywords Sowing machine · Von mises stress · SolidWorks · ANSYS workbench

1 Introduction

Agriculture makes a massive contribution to the Indian economy for a very long time [1]. In the current situation, a massive area of our cities is being used for construction and other works which are hampering the development of agriculture necessary. Moreover, with the limited land, small farmers face economic crises and have very limited resources to enhance their farming. Sowing of seed is the foremost essential step in farming. However, manual seed sowing usually causes the wastage of seeds and lower productivity [2, 3]. The manual technique incorporates sowing the seeds by throwing them by hand. The main criteria that need to be focused while sowing the seed are; the seeds should be at the proper spacing. The seeds should not get a break during sowing. The amount of seed to be sown in an area should be uniform. However, all these cannot be fulfilled using manual sawing [4]. Considering the

G. Kumar · R. Singh · P. Kumar · T. Rajput · E. Neha (✉) · Y. Shrivastava
Department of Mechanical Engineering, Galgotias College of Engineering & Technology, Greater Noida, UP, India
e-mail: eramneha@gmail.com

present scenario, various sowing machines are available. However, they have several limitations such as:

1. The weight of the machine is more.
2. No arrangement for seedbed preparation.
3. Improper compaction of soil over furrows.
4. The adjustment of row spacing is improper.
5. The cost of the machine is more.

Hence, to overcome all these limitations, it is required to design a new machine. A lot of researchers have contributed to this field for the development of the sowing machine [5–7]. Researchers have developed a multi-seed sowing machine that has proved that the mechanical system is wonderful over the prevailing machines as it can manipulate the seed and fertilizer depth and proper utilization of seeds and fertilizers may be completed with much less loss [8]. It is relative to low cost and quite simple for the layman to function [9]. The layout and fabrication of automated seed sowing machine for the agricultural subject showcased that the yield loss may be substantially reduced with the aid of utilizing operated by hand seed and fertilizer planter. This seed and fertilizer planter can fulfill most of the farmer and subject requirements effectively at some point in the peak season [10]. However, these machined either need electricity or fuel which sometimes limits its uses.

Some of the researchers have developed the layout of a solar-powered seed sowing machine that operates on solar power. While in comparison with specific traditional seed sowing techniques, it has less guided energy intake. Pollutants are managed in conjunction with a regulation on the sowing rate and seed spacing [11]. In this design, the entire weight of the solar panel, battery, and the hardware has been placed on agribot which is supported by the chassis. This makes it suitable to perform operations skillfully and efficiently. Wireless connectivity among the system and the controller has also been designed by the researchers [12, 13]. However, all these designs have certain flaws, as they do not need the basic requirement and facilities available to the farmers in a country like India. Hence, in the present work, efforts have been made to design a sowing machine that may meet the basic requirement of the farmers. The proposed benefits of the developed machine are as follows:

1. In this model, seed sowing method is automatic to reduce the human effort and increase the yield. The plantation of seeds has been accomplished efficaciously using DC motor.
2. The space among the two seeds is managed by the use of a microcontroller.
3. Different kinds of strategies of seed sowing and fertilizer placement inside the soil can be performed.

The steps followed in the present work starts from the 3D modeling of the sowing machine followed by the finite element analysis (FEA). After which the design has been analyzed using ANSYS software.

2 Methodology

The study begins with the requirements of agricultural seed planter. The study includes an overview of the current manual as well as an automatic seed planting process and formulation of the initial design proposal for the proposed new method of seed planting. The methodology steps are shown in Fig. 1. The steps involved are as follows:

STEP 1: Collect all required authentic data for studies such as materials properties, dimensions of structures, and boundary conditions.

STEP 2: Find previous research and studies done by other researchers. Collect information by this study for innovation.

STEP 3: Create a 3D model using SolidWorks 2016. SolidWorks is a 3D modeling software developed by Dassault System. Dassault System is USA-based company. This software developed in 1993. It creates part files, assembly files, and drawing files. Part files have.sldprt extension file name. Assembly file has.sldasm extension name. The drawing file has a.slddwg extension name. Create an IGES file to import in ANSYS workbench.

STEP 4: Import IGES file ANSYS workbench. IGES means initial graphics exchange specification. This file also is known as the un-parametric file. Created a finite element model (FEA).

STEP 5: Apply mass of 10–10 kg seeds on Hopper and seedbox. Also apply motor torque on machine under ANSYS workbench. Apply fix support on all three wheels at the bottom face.

Fig. 1 Flow chart
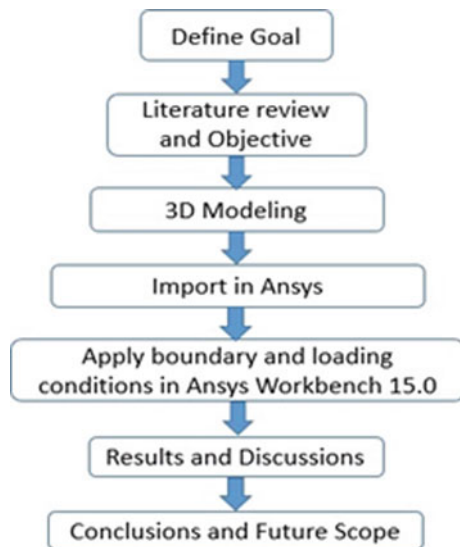
STEP 6: After applying load and boundary conditions on the machine, apply solution process and then obtain results such as total deformation and von Mises stress.

STEP 7: Study the results and behavior of the machine after applying load and create conclusion and future scope.

3 3D Modeling and FEA

A 3D model of the seed sowing machine has been developed in SolidWorks 2016. The model has been first analyzed using FEA as shown in Fig. 2. This machine has mainly 10 components which play a very important role in the working seed sowing machine. That are rear wheel, the front wheel, frame, seed sowing Disk, seed hopper, chain drives, battery, microcontroller unit, seedbox, and funnel. The proposed model is analyzed to obtain net mass, net volume, and equivalent stress acting on the machine. The obtained mass is 66.02 kg as shown in Fig. 3a, and the obtained volume is 9497084.74 mm^3 as shown in Fig. 3b.
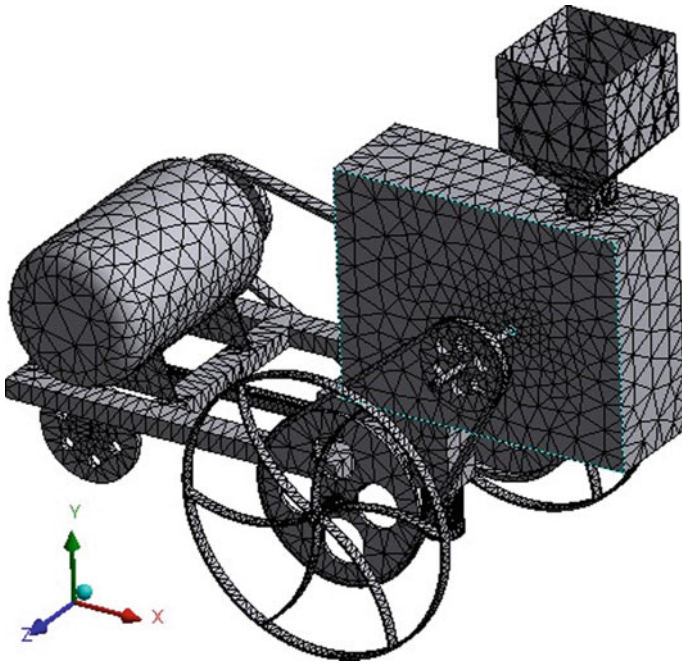
Fig. 2 Finite element model (FEA model) of seed sowing machine

```
Mass properties of Seed Sowing Maching
   Configuration: Default
   Coordinate system: -- default --

Mass = 66.02 kilograms

Volume = 9497084.74 cubic millimeters

Surface area = 7994740.00 square millimeters

Center of mass: ( millimeters )
   X = -2925.94
   Y = -1220.44
   Z = 8.03

Principal axes of inertia and principal moments of inertia: ( kilograms * squa
Taken at the center of mass.
   Ix = ( 0.96,  0.25,  0.10)     Px = 5584533.67
   Iy = ( 0.10, -0.01, -0.99)     Py = 12202683.92
   Iz = (-0.25,  0.97, -0.04)     Pz = 12615419.29

Moments of inertia: ( kilograms * square millimeters )
Taken at the center of mass and aligned with the output coordinate system.
   Lxx = 6084232.86       Lxy = 1693654.94       Lxz = 605808.46
   Lyx = 1693654.94       Lyy = 12175649.61      Lyz = 172562.31
   Lzx = 605808.46        Lzy = 172562.31        Lzz = 12142754.42

Moments of inertia: ( kilograms * square millimeters )
Taken at the output coordinate system.
   Ixx = 104426274.20     Ixy = 237453468.81     Ixz = -944905.00
   Iyx = 237453468.81     Iyy = 577401998.18     Iyz = -474255.85
   Izx = -944905.00       Izy = -474255.85       Izz = 675702635.4
```

Fig. 3 a Seed sowing machine center of mass **b** 3D model calculation data

3.1 Un-parametric CAD Format

To share the 3D model to any other software, un-parametric files are used. Un-parametric format merges all features in a single object, and due to this, it cannot be changed into the previous sketch and feature. This format can be open accessed in 3D model software. But if anyone wishes to relocate the previous steps, it would be let you do that. Some un-parametric formats are IGES, STEP, etc.

3.2 Parametric CAD Format

In such a format, the previous steps of CAD model can be relocated, and changes can be done easily. Some areas extensions for Inventor are.IPT and.IAM and for SolidWorks,.sldprt,.sldasm, etc.

Number of Elements and Nodes
For the meshing of setup, ANSYS created 1968 and 14,722 no. of elements and nodes, respectively, as shown in Fig. 4. For mashing, minimum size used is 0.4500 mm, and the maximum size used is 0.4527 mm.

1D Elements
ANSYS software uses the FEA method for analysis and generates results according to the requirements. For simple geometry, 1D element is being used that can be of the linear, quadratic, or cubic type.

Fig. 4 No. of elements and nodes

	Nodes	14722
	Elements	1968
	Mesh Metric	Element Quality
	Min	0.450036296482645
	Max	0.452716634028344
	Average	0.451278404125773
	Standard Deviation	1.33691606361924E-03

2D Elements

ANSYS software uses the FEA method for analysis and generates results according to the requirements. For area, geometry 2D element is being used that can be of the linear, quadratic, or cubic type.

3D Elements

ANSYS software uses the FEA method for analysis and generates results according to requirements after applied required inputs. For area, geometry 3D element is being used that can be of the linear, quadratic, or cubic type.

4 Results and Discussions

The 3D model created in SolidWorks 2016 is then imported in ANSYS workbench 15.0. After importing the file and applying all required materials properties of machine components, boundary conditions have been applied as fixed support on all three wheels.

For applying the load, it has been considered that 10 kg of seed is in the Hopper and the seedbox. Then torque has been applied to the motor to visualize the analysis using ANSYS workbench 15.0. The obtained total deformation and von Mises stress are shown in Figs. 5 and 6. The seed sowing machine has total deformation (max value) of 0.6396 mm, and max von Mises stress is of 23.137 MPa. From the results, it has been obtained that stress is 23.137 MPa which is very less as compared to the yield strength of mild steel that is 270 MPa. Moreover, the total deformation is 0.693 mm that is very less, as the weight of the machine is nearly about 66 kg. Hence, it may act as a portable machine that can be used easily. Machines have less stress and less deformation that means it is safer and more economic.

5 Conclusions

In the present work, the design and analysis of the seed sowing machine have been done. The design has been analyzed using FEA. From the analysis, it has been found that the design is acceptable because the obtained value of stress is 23.137 MPa which is very less as compared to the yield strength of mild steel that is 270 MPa.
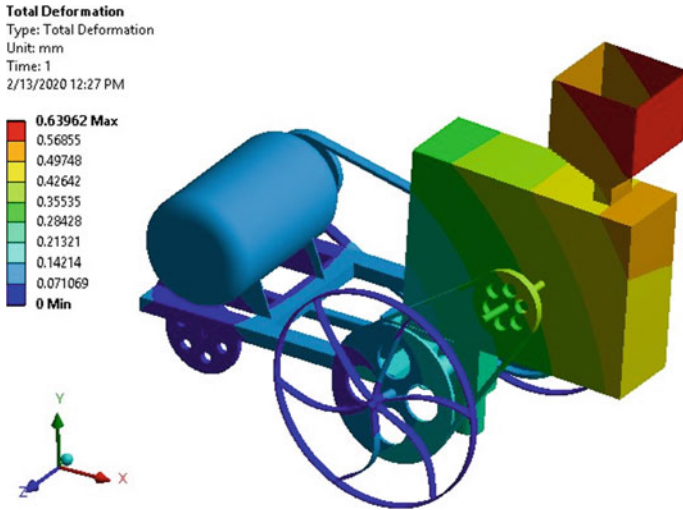
Fig. 5 Total deformation of seed sowing machine
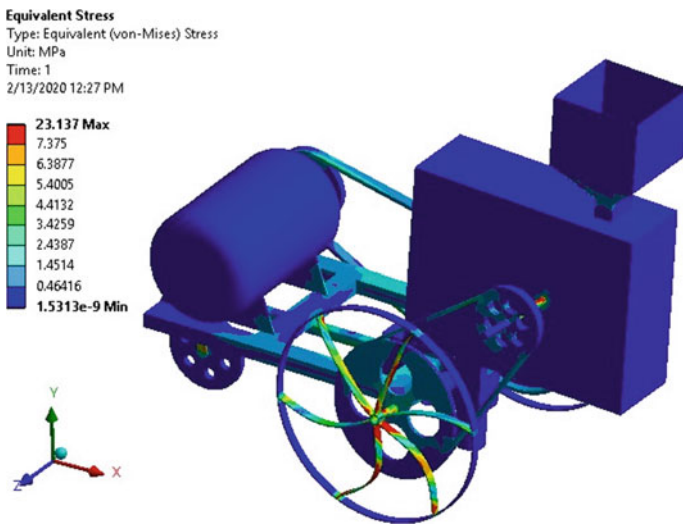
Fig. 6 Von Mises stress of seed sowing machine

Also, the total deformation is 0.693 mm that is very less. The calculated weight of the machine is found to be 66 kg. Moreover, the machine has less stress and less deformation that means it is safer and more economic. In the near future, research may be conducted to add automatic fertilizing setup and automatic digging system to this machine.

References

1. Kumar Y, Singh PK (2019) To study the influence of insurance policy on the agriculture field and Indian economy: concept paper. In: Renewable energy and its innovative technologies. Springer, pp 13–24
2. Mallesh S, Raju JT, Siddiqui MS, Siddiqui MZ (2020) Performance evaluation of hand operated dibbler and for multi seeds. J Pharmacog Phytochem 9(3):1990–1994
3. Kalay K, Moses S, Padam S (2020) Laboratory test of a seed metering device of manually operated multi-crop planter for red gram (C. cajan). Int J Agricul Sci 16(1):52–56
4. Jadhao KK, Narote AS, Shelke PU, Alladwar VN, Dhuldhule AS, Vishwambhare DS (2019) Design and fabrication of manually operated seed sowing machine. Methodology 6(04)
5. Morimoto H (1984) Device for determining a correct sawing position for a portable rotary sawing machine. In Google Patents
6. Suzuki A, Miyamoto K, Takahashi S (1998) Circular sawing machine. In Google Patents
7. Tannewitz CE (1931) Sawing machine. In Google Patents
8. Marode RV, Tayade GP, Agrawal SK (2013) Design and implementation of multi seed sowing machine. Int J Mech Eng Robot Res 2:422–429. ISSN 2278–0149
9. Rohokale AB, Shewale PD, Pokharkar SB, Sanap KK (2014) A review on multi-seed sowing machine. Int J Mech Eng Technol 5(2):180–186p
10. Thapa S (2018) Design, fabrication and testing of pull type multi seed sowing machine. Int Jo Biolog Sci Res 1(1):40–48
11. Swetha S, Shreeharsha G (2015) Solar operated automatic seed sowing machine
12. Senthilnathan N, Gupta S, Pureha K, Verma S (2018) Fabrication and Automation of Seed Sowing Machine Using IOT. Int J Mech Eng Technol (IJMET) 9:903–912
13. Gokul S, Dhiksith R, Sundaresh SA, Gopinath M (2019) Gesture controlled wireless agricultural weeding robot. In: 2019 5th international conference on advanced computing & communication systems (ICACCS) 2019. IEEE, pp 926–929

Design of Low-Power Dynamic Type Latch Comparator Using 18 nm FinFET Technology for SAR ADC

B. Hemalatha and Ajay Kumar Dadoria

Abstract There are multitudinous applications of comparator in diversified areas, notably used in data converters. Since many years, single stage, dynamic type latch as well as double tail comparators have been designed using CMOS technology. But there is a trade-off among the energy consumption and time delay. Concurrently, to alleviate the short channel effects of the design, which is based on traditional CMOS, FinFET has loomed as the most assuring surrogate by its enormous gate control characteristic across the channel region. Here, we examined the performance of a latest dynamic type latch comparator, and a modern design of dynamic type latch comparator is proposed in this paper. Furthermore, 18 nm FinFET technology is considered as a platform for the design of this comparator. The proposed comparator has shown splendid performance with respect to energy consumption, delay, in comparison with the other latest comparator through simulation with Cadence.

Keywords Ultra low power · Dynamic latch comparator · FinFET · Inverter · Delay

1 Introduction

Along with the other applications of comparator like in line decoders, level shifters, data receivers, memory sense amplifiers, one of its important applications is in analog to digital converters [1]. Also, in biomedical imaging applications, an extreme data rate, high resolution and high sensitivity-based ADCs are at present highly demanding [2].

Static comparators are now outdated because of noticeable amount of power consumption and limited speed [3]. Some distinguished features of dynamic type latch comparator which made it more attractive are strong positive feedback, high input impedance, negligible static power consumption and rail to rail output swing

B. Hemalatha (✉) · A. K. Dadoria
Amity University, Gwalior, Madhya Pradesh, India
e-mail: hemalathaece@cvsr.ac.in

603

[4]. In a single stage comparator, because the differential input stage and regeneration latch stage are interconnected, it had a trade-off between the offset voltage and energy requirements and along with the relentless kickback noise [5]. A single tail transistor further has constraints in total flow of current by two output nodes, and this also increases the dependence of offset voltage and performance of various ranges of input common mode voltage [6]. An alternative of single tail comparator has emerged by imparting the required segregation between the preamplifier and latch stages. This new double tail architecture has high accuracy, near supply voltage function, high input common mode voltage range, cascading amplifier stage, so on, [7, 8]. With the advancement in the technology, design of high-speed comparators with low supply voltage is more challenging [9]. To continue scaling, the most assuring alternative approach of CMOS-based technology is FinFET which shall be used for the design of high-speed, low-power dynamic type latch comparator. Few characteristics of this multi-gate structure are improved scalability, higher mobility of carriers, reduction of short channel effects, low value of supply and threshold voltages, reduced dopant fluctuations, higher frequency operations, lower leakage of current near sub-threshold operation and good channel control [10]. Device scaling demands for reduction in power supply voltage, low threshold voltage and high transistor density. Drain gating PMOS and drain gating NMOS technique are employed to low-power applications [11, 12]. Aggressive scaling of single gate CMOS faces many challenges in nanoscale technology. So, double gate FinFET (DGFET) is used to mitigate the leakage current higher ON state current when scaling is beyond 32 nm [13]. In this paper, a modern dynamic latch comparator is designed that shows compelling enhancements in power consumption and power delay. The remaining part of this paper is organized as follows: Sect. 2 explains the operation, advantages and disadvantages of the latest dynamic type latch comparator. In Sect. 3, the proposed modern comparator's operation is discussed. In Sect. 4, results analysis and comparison table are given. Finally, the paper is concluded in Sect. 5.

2 Dynamic Latch Type Comparator

The operation, merits and demerits of already existing dynamic comparator which are designed by Hossain et al. [14] will be discussed in this section shown in Fig. 1. As like the conventional comparators, which works with two clock pulses, here in the starting, at the reset phase of the operation CLK1 = 0 and CLK2 = 1, therefore Ftail1 and Ftail2 will be turned OFF, and the source and drain terminals of F3, F4 will be charged to the supply voltage Vdd through F6, F8 and F5, F7. If Outp and Outn terminals are left with any charge from the previous cycle, it will be discharged to ground through F13 and F14. At the evaluation phase of the operation, the clock cycles will be reversed, and therefore, tail transistors Ftail1 and Ftail2 will be turned ON. The operation path of F1 and F2 depends on the input and reference voltages. Then, node Fa discharges faster than the node Fb, when vin > vref and since F7 as well as F8 are OFF, now they do not have the chance to recharge at this evaluation
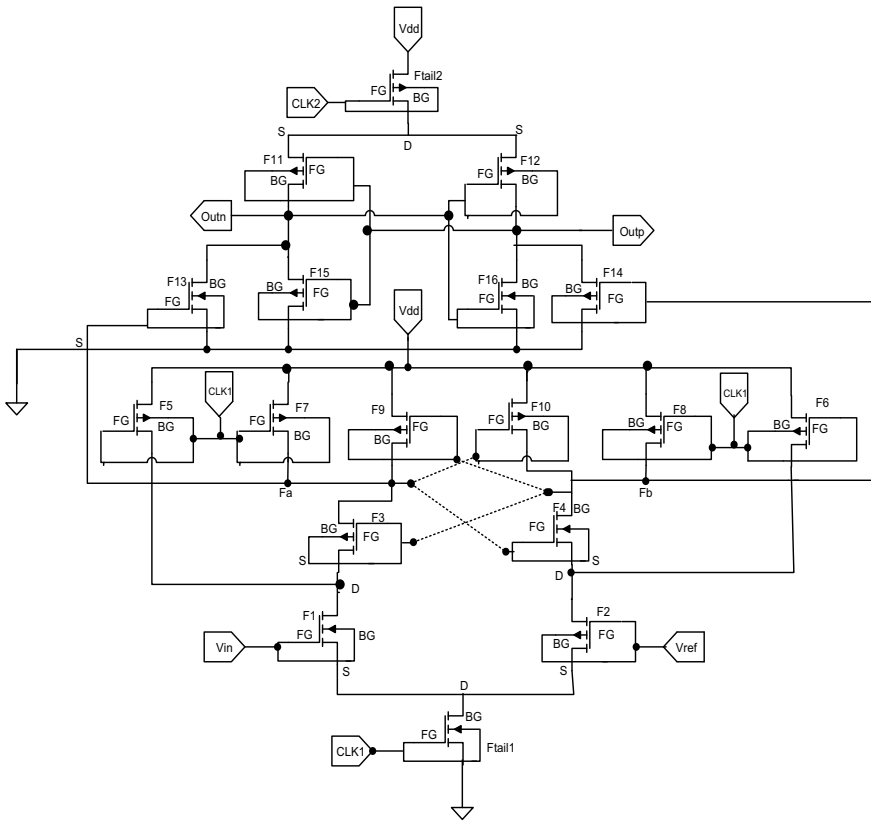
Fig. 1 Circuit diagram of reference dynamic latch comparator [14]

phase. Since Fa is discharged quickly, it will turn OFF F4 and F10. As Fb still holds the charge (Vdd), F9 is turned OFF, and F3 is turned ON in order to expedite node Fa to completely get discharged. Node Fb will be kept ON, as Outp will be discharged to ground through F14. Outp will also turn ON F11 and turn OFF F15, so that Outn will be stayed at Vdd. Outn will cause F12 to turn OFF, so the charging path of OutP is now completely disconnected and turn On F16 to help Outp to be totally discharged.

F3 and F4 in this design are allowing to circumvent the static power consumption by disconnecting the discharge path after reaching decision. The upper tail transistor (Ftail2) inhibits any power consumption during the reset phase of operation. Anyhow, two individual clocks are required, and an appropriate strategy in among them is required to provide the desired accuracy.

3 Proposed Dynamic Latch Comparator

The operation of our proposed dynamic latch type comparator is discussed in detail in this section shown in Fig. 2. Analogous to other conventional comparators, the proposed comparator too works with two individual clock phases. The main idea of this proposed circuit is to prevent the complexity in the coordination of two different clock pulses and to reduce the power consumption. In this circuit instead of using two individual clock pulses, a source CLK is considered. This CLK pulse serves both the phases of the circuit. This CLK is split into two non-overlapping clock pulses, i.e., CLK1 and CLK2. CLK1 is derived from the main source CLK followed by inverter (INV), and CLK2 can be directly taken from the source CLK, but to
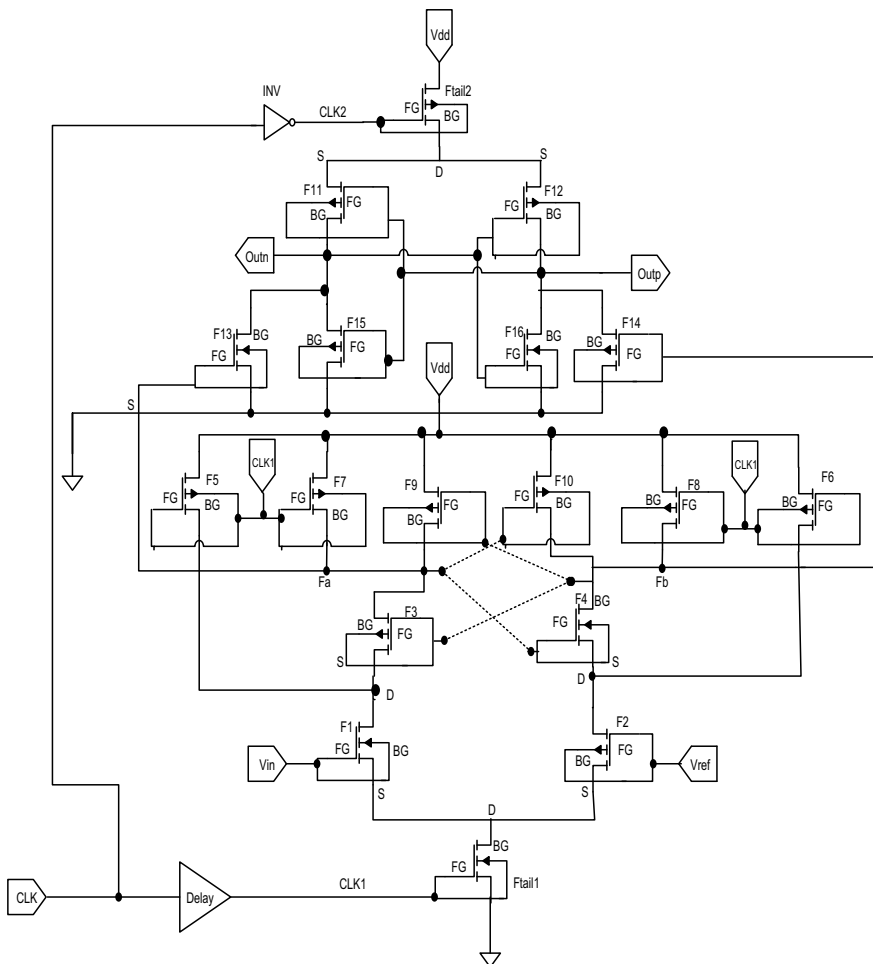
Fig. 2 Circuit diagram of the proposed dynamic latch comparator

match the performance of both the stages, a sufficient delay must be provided. So, CLK2 is derived from the main source CLK followed by a delay circuit. Here, though an additional inverter INV is inserted in the proposed circuit, it will not affect the performance because the power consumed by the inverter compared to the CLK is less.

In the starting, at the reset phase of the operation CLK1 $= 0$ and CLK2 $= 1$, therefore, both the tails, i.e., Ftail1 and Ftail2 go to OFF state, and the source and drain terminals of both F3 and F4 will be charged to the supply voltage Vdd through F5, F7 and F6, F8. Now, Outp and Outn will be discharged completely to ground through F13 and F14.

Next at the evaluation phase, both the clock cycles are reversed, CLK1 $= 1$ and CLK2 $= 0$, and therefore, both the tails, Ftail1 and Ftail2, go to ON state. Now, the conductance of F1 and F2 depends on the input and reference voltages. If Vin is more than Vref, then node Fa will discharge rapidly than node Fb, and now, F7, F8 are OFF, hence, during this evaluation phase, they will not have the chance to get recharged. Since Fa is discharged quickly, it will turn OFF F4 and F10. As Fb still holds the charge (Vdd), F9 is turned OFF, and F3 is turned ON in order to expedite node Fa to completely get discharged. Node Fb will be kept ON, as Outp will discharge to ground through F14. Outn will stay at Vdd, as Outp turns ON F11 and turns OFF F15. Now, the charging path of Outp is disconnected completely, as Outn causes F12 to turn OFF. F16 will be turned ON to help Outp to totally discharge.

4 Results and Discussion

The proposed dynamic latch comparator is designed, simulated, and the results are plotted with Cadence tool, using 18 nm technology. Figures 3 and 4 show the transient response of the proposed circuit.
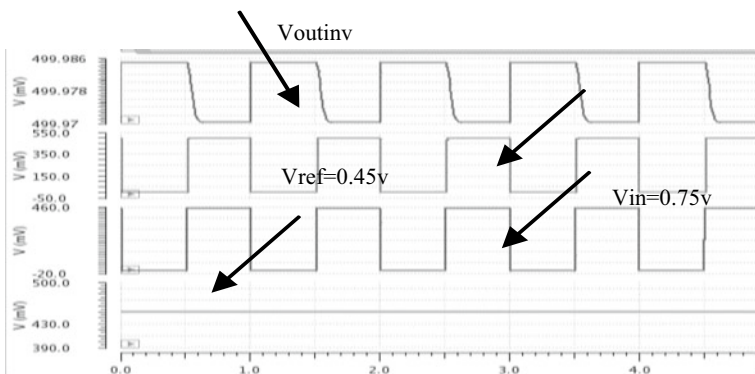
Fig. 3 Input–output waveforms of the proposed dynamic latch comparator
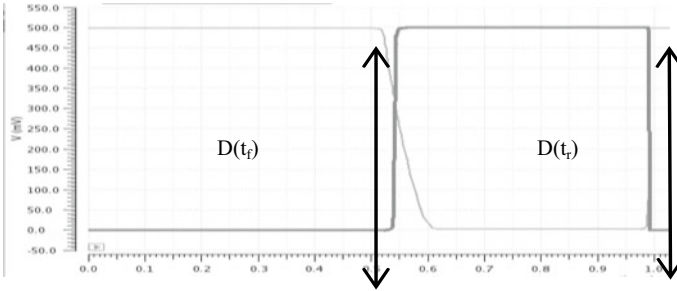
Fig. 4 Transient response of the proposed dynamic latch comparator

Table 1 Summary of comparision of existing and proposed circuits

Parameters	[14]	Proposed
CMOS FinFET technology (nm)	32	18
Supply voltage (V)	0.8	0.75
ΔVin	5	5
Power (μW)	73.36	36
Delay (ps)	12.63	50

Table 1 presents the detailed operational conductance comparison of our proposed dynamic latch type comparator with the existing comparator. The proposed comparator is designed and simulated in 18 nm FinFET technology, operated with a supply voltage of 0.75 V, differential input voltage of 5 V. The average power consumption of our proposed circuit is $36\,\mu$W, which is very low compared to existing comparator. The propagation delay is 50 ps. So, by considering all the measuring criteria, our proposed circuit consumes low power, with faster response.

5 Conclusion

This paper presented the design and analysis of modern dynamic latch comparator. 18 nm FinFET PTM models are used to design the proposed circuit. The proposed circuit is designed in 18 nm FinFET technology, and its competency is verified through simulation results which are performed with Cadence Virtuoso. The time delay and average power consumption are found to be very promising compared to the conventional comparators. The average power consumption is reduced by 49.07% compared to conventional comparator.

References

1. Kobayashi T, Nogami K, Shirotori T, Fujimoto Y (1992) A current-mode latch sense amplifier and a static power saving input buffer for low-power architecture. In: Proceedings of the VLSI circuits symposium digest of technical papers. pp 28–29
2. Radparvar M et al (2015) Superconductor analog-to-digital converter for high-resolution magnetic resonance imaging. IEEE Trans Appl Supercond 25(3):1–5
3. Razavi B, Wooley BA (1992) Design techniques for high-speed, high-resolution comparators. IEEE J Solid-State Circuits 27(12):1916–1926
4. Razavi B (2015) The strong ARM latch [A circuit for all seasons]. IEEE Solid-State Circuits Mag 7(2):12–17
5. Figueiredo PM, Vital JC (2006) Kickback noise reduction techniques for CMOS latched comparators. IEEE Trans Circuits Syst II Express Briefs 53(7):541–545
6. Wicht B, Nirschl T, Schmitt-Landsiedel D (2004) Yield and speed optimization of a latch-type voltage sense amplifier. IEEE J Solid-State Circuits 39:1148–1158
7. van Elzakker M, van Tuijl E, Geraedts P, Schinkel D, Klumperink EAM, Nauta B (2010) A 10-bit charge-redistribution ADC consuming 1.9 μW at 1 MS/s. IEEE J Solid-State Circuits 45(5):1007–1015
8. Schinkel D, Mensink E, Kiumperink E, Tuijl E, Nauta B (2007) A double-tail latch-type voltage sense amplifier with 18ps setup+hold time. IEEE international solid-state circuits conference digest of technical papers. pp 314–315
9. Goll B, Zimmermann H (2009) A comparator with reduced delay time in 65 nm CMOS for supply voltages down to 0.65. IEEE Trans Circuits Syst II Exp Briefs 56(11):810–814
10. Kushwah CB, Vishvakarma SK, Dwivedi D (2016) A 20nm robust single- ended boost-less 7T FinFET sub-threshold SRAM cell under process—voltage–temperature variations. Microelectron J 51:75–88
11. Dadoria AK, Khare K, Gupta TK, Singh RP (2017) Leakage reduction by using FinFET technique for nanoscale technology circuits. J Nanoelectronics Optoelectron 278–285
12. Jeon H, Kim Y (2010) A CMOS low-power low-offset and high-speed fully dynamic latched comparator. In: Proceedings of the IEEE international systems-on-chip conference. pp 285–288
13. Dadoria AK, Khare K, Gupta TK, Singh RP (2017) Ultra low power FinFET based domino circuits. Int J Electron 952–967
14. Hossain MM, Biswas SN (2019) Analysis and design of a 32 nm FinFET dynamic latch comparator. In: IEEE international conference on advances in electrical engineering. 49–54

Damage Analysis of an Inclined Cracked Curved Beam Using ANFIS

Shraddha Lohar and Prases K. Mohanty

Abstract As the damage in the structures grows, failure rate increases rapidly causing weakening of structures which leads to early failure of the structures. Hence, advance identification of damages in structures should be addressed immediately. This paper presents an intelligent technique for damage identification in a curved inclined cracked beam based on vibration signatures. Vibration analysis of the cracked curved beam is carried out using ANSYS$^{©}$ software. The natural frequencies and mode shapes are computed by varying crack severities and crack locations. The results dictate that the vibration parameters are changed for different crack severities and crack locations. These parameters are given as input to adaptive neuro-fuzzy inference system (ANFIS) to predict the damage characteristics for the cracked beam. The results reveal that the proposed intelligent controller could be deployed to locate and quantify the damage in any cracked structure.

Keywords Curved beam · Inclined crack · Finite element analysis (FEA) · Natural frequency · ANFIS

1 Introduction

Structural integrity is the structure capacity to carry loads without undergoing damage. Loss in the structural integrity is the major reason for structural damage. The weak structures, faulty designs, fatigue, etc. cause the structural integrity loss. One of the reasons for the structural damage is crack present in the structures. The crack initiation starts at the points where stress concentration is present, causing the start of the damage in the structures. And when the load varies with respect to time, crack develops. Due to which, early recognition of crack present in the structures is mandatory to eliminate these abrupt breakdowns of the structures. Out of all structures, one of the significant basic structural elements used in variety of day-to-day applications is 'curved beam'. Presence of fault like crack in the curved beam causes

S. Lohar (✉) · P. K. Mohanty
Department of Mechanical Engineering, National Institute of Technology, Yupia, Arunachal Pradesh 791112, India
e-mail: loharshraddha41@gmail.com

611

changes in natural frequency, amplitude response and vibration mode shapes of the beam.

Recent times, many studies are focused on the fault diagnosis of structures, in which crack diagnosis is also an important issue in recent years. Krawczuk et al. [1] investigated circular arches with clamped–clamped end boundary condition and effect of open edge crack on the circular arch. Viola et al. [2] studied thin and thick circular arches with different cross-sections and a single crack. He investigated effect of in-plane vibration on the same. Cerii et al. [3] studied effect of vibration on circular arches and found the dynamic characteristics of circular arches with and without damage. Yang et al. [4] studied free in-plane vibration of general curved beams using finite element method. Chen [5] studied non-prismatic curved beam and found out of plane vibrations for the same. Zare [6] studied simply supported curved beam with crack present in it and analyzed it with analytical and experimental methods. Many heuristics techniques are implemented for diagnosis of damage in cracked structures. Prawin et al. [7] found the damages in the structures with the help of single sensor measurement technique. A damage detection technique was used for the first time to detect location of the crack by Das et al. [8] which was based on zero strain energy node concept accomplished an artificial neural network to predict the position of the crack as well as severity of the crack in a fixed cantilever beam with crack. They used first three relative natural frequency along with mode shape as input to the ANN controller inorder find the damage parameters. Mehrjoo et al. [9] performed a fault detection by inverse set of rules to estimate the damage intensities of joins in truss bridge structure using backpropagation neural network method. From literature survey, it is investigated that identification of open inclined edge crack in curved beam structures using ANFIS has not previously been studied for vibration analysis. ANFIS takes the advantages of the neural network and fuzzy logic.

2   Objective of the Proposed Research

The FEA modeling along with simulations of beam is carried out using software ANSYS$^{©}$ 14.5 [10]. The software SolidWorks 2017 [11] is used to develop the curved beam model. The inclined edge crack depth must be taken as less than otherwise equal to the half of the beam thickness [12]. Starting with the left end support of the simply supported beam, relative angular crack position varies from 0.005 to 0.95. And also relative crack depth varies 0.1–0.5. By using ANSYS$^{©}$ software, the models of curved beam with simple supports by varying relative locations and severities are simulated.

Figure 1 indicates the simply supported curved beam model with an inclined open edge crack, for RCL = 0.21 and $\theta = 35°$, and Fig. 2 indicates the magnified view of inclined open edge crack with crack opening 0.8 mm and crack depth 3 mm. Later, the computed natural frequencies using FEA are given as inputs to the ANFIS model to predict location and quantify the damage in cracked beam.

Fig. 1 Curved beam of $\emptyset = 120°$ with inclined crack at $25.20°$, $\theta = 35°$, RCL $= 0.21$ and $a = 3$ mm
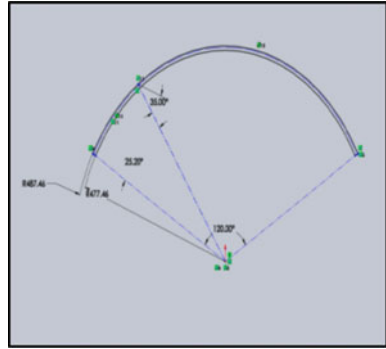
Fig. 2 Magnified view of an inclined edge crack
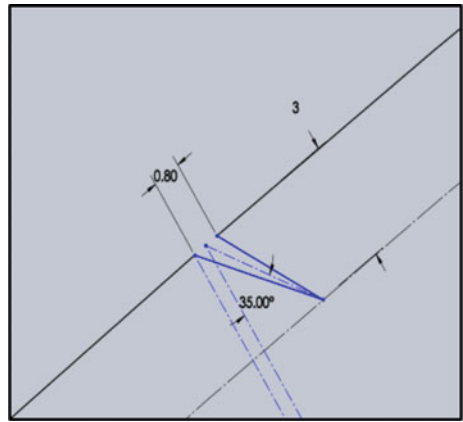
3 Theoretical Analysis

The curved beam with simple supports as well as with loading condition is used to create beam model with open edge crack. The model generation can be achieved with the help of local flexibility approach based on linear fracture mechanics. In beam present crack location, flexibility influence co-efficient (i.e., local compliance, herein S_{ij}) is given by [13];

$$(Sij) = \frac{\partial ui}{\partial Pj} = \frac{\partial^2}{\partial Pi \partial Pj} \int_0^a G(a)\mathrm{d}a \qquad (1)$$

where $G(a) = \frac{\partial u}{\partial a}$ strain energy rate, $u =$ strain energy, $a =$ variable with respect to crack depth.

$$J = \frac{1 - \nu}{E}(K11 + K12)^2 \qquad (2)$$

where K_{11} and K_{12} = stress intensity factors of opening of crack.

The inversion compliance matrix is used to derive the local stiffness matrix which is written as,

$$K = \begin{bmatrix} C_{11} & C_{12} \\ C_{21} & C_{22} \end{bmatrix}^{-1} = \begin{bmatrix} K_{11} & K_{12} \\ K_{21} & K_{22} \end{bmatrix} \qquad (3)$$

4 Finite Element Analysis (FEA) of the Cracked Curved Beam

The FEA simulations of inclined open edge crack as well as un-cracked curved beam with simple supports are carried out using ANSYS© software. From the analysis, natural frequencies along with the consequent mode shapes at various crack locations and severities of crack are computed. The specifications of a cracked curved beam of the current analysis are as shown below,

Opening angle of the curved beam $(\phi) = 120°$.

Curved beam cross-sectional depth $(d) = 10$ mm.

Curved beam cross-sectional width $(w) = 14$ mm.

Relative crack location (RCL) = 0.005–0.95.

Relative crack severity (RCS) = 0.1–0.5.

Figures 3 and 4 indicate the FEA model for the curved beam with simple supports and the magnified details of the crack edge meshing during FEA analysis.

Figures 5, 6 and 7 show the 1st, 2nd and 3rd mode of vibrations of the curved beam with a relative crack severity of 0.3 and relative location at 0.21. These modes of vibrations demonstrate the distortions occurring in the curved beam due to the rotational and translational displacements.

Also it shows the effect of crack on the mode shapes of vibrations.

Fig. 3 Curved beam having simple supports with inclined edge crack at $a = 3$ mm and RCL = 0.2

Crack Zone

Simply Supported Beam
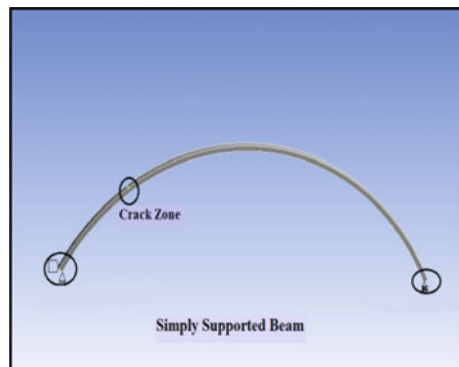
Fig. 4 Magnified details of the meshing at an inclined edge crack zone
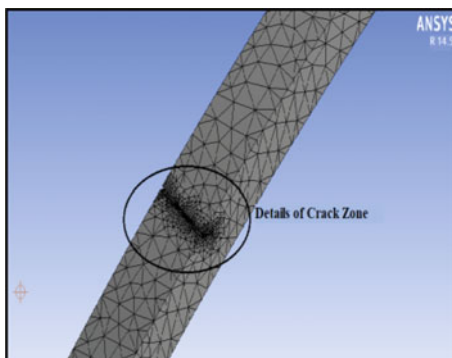
Fig. 5 1st mode shape of curved beam with simple supports for crack at RCS = 0.3, RCL = 0.21 and $\theta = 35°$
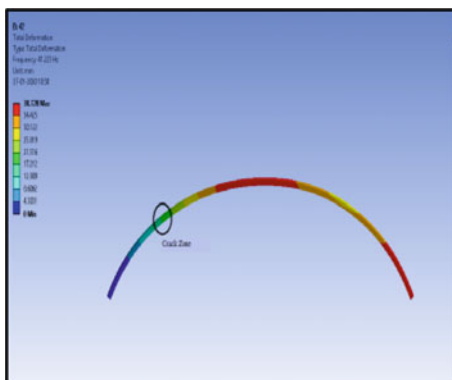
Fig. 6 2nd mode shape of curved beam with simple supports for crack at RCS = 0.3, RCL = 0.21 and $\theta = 35°$
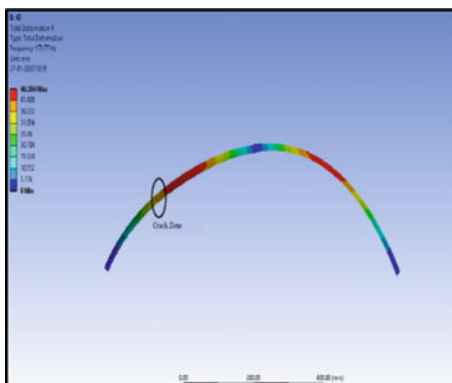
Fig. 7 3rd mode shape of
curved beam with a simple
supports for crack at RCS =
0.3, RCL = 0.21 and $\theta = 35°$
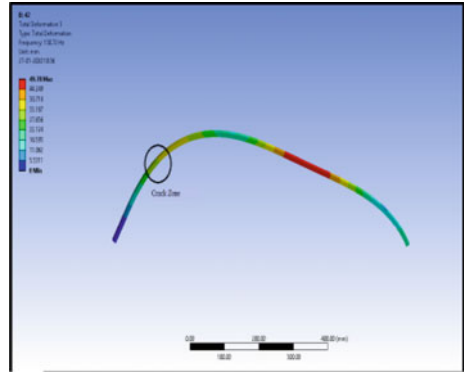
5   Architecture of ANFIS for Damage Detection in Curved Cracked Beam

The ANFIS is a hybrid system which combines the learning ability of neural network and human reasoning ability of fuzzy inference system [14]. The proposed system has the strength to solve complex problems. The function of each layer of ANFIS is explained in [14].

The proposed ANFIS model was framed with three input parameters and two output parameters as shown in Fig. 8.

The main objective of the proposed model is to set a relationship among input and output parameters. The data extracted from FEA was divided into two groups such as training and testing data sets, and 80% of the total data were used as training data and remaining 20% was used for testing data. The ANFIS model was trained with total 1000 data sets. The generalized bell membership function with three membership function for each input and hybrid optimization method was selected in ANFIS model. It has been noticed that after 200 iterations the training data sets became produce steady mean square error (MSE).
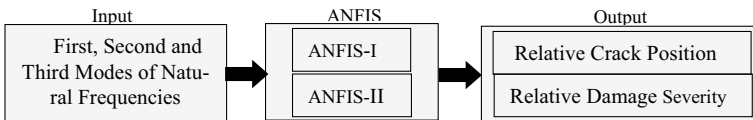
Fig. 8 Proposed ANFIS model for damage identification

6 Result and Discussions

Architecture of ANFIS is used for the dynamic behavior modeling of the curved beam. Figures 9 and 10 show the ANFIS model with absolute error for crack severity and crack locations where 80% of the data set is used for training and remaining 20% for testing and validating.

The results for simply supported curved beam with inclined crack by varying location of crack and severities using FEA and ANFIS model are tabulated in Table 1. Figures 9 and 10 provide the results about mean square error (MSE) between target and outputs on the basis of the topology of the ANFIS. It has been indicated that ANFIS model estimates accurately the damage parameters to actual data. The table shows both FEA and ANFIS outputs are in close proximity with each other which indicates crack identification accuracy in the ANFIS testing process.

As the depth of the crack increases, initially natural frequencies of the beam increases. But as crack location changes from left end of the beam to right end, after
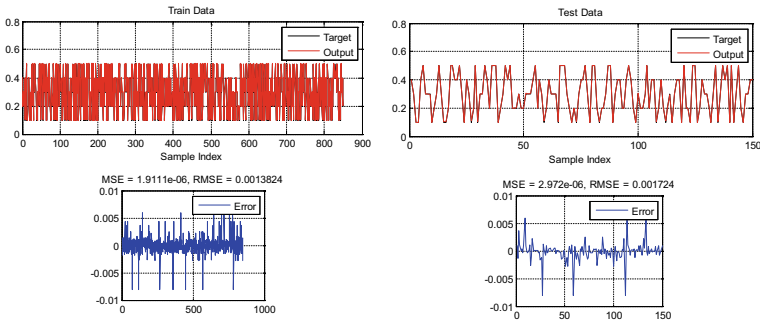
Fig. 9 ANFIS model with absolute error for crack severity
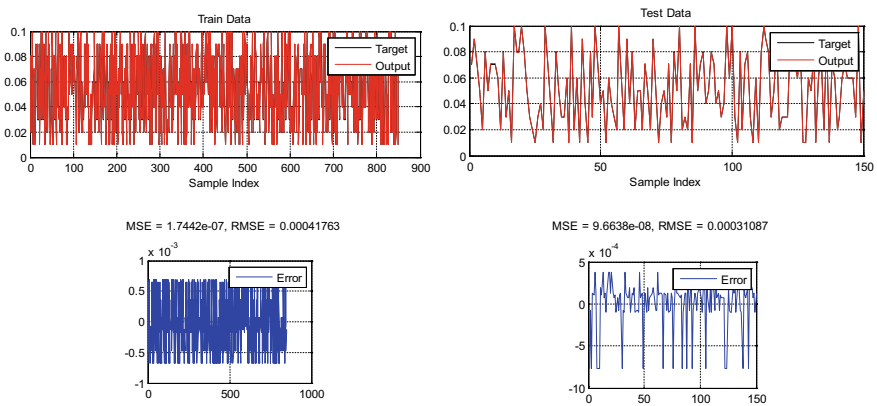
Fig. 10 ANFIS model with absolute error for crack location

Table 1 Sample of FEA and ANFIS analysis comparison results of cracked beam

Sr. No.	Input			Output			
	1st relative natural frequency	2nd relative natural frequency	3rd relative natural frequency	Relative crack location		Relative crack severity	
				FEA	ANFIS	FEA	ANFIS
1	0.997744	0.999484	0.998324	0.005	0.0049	0.025	0.02501
2	0.997986	0.999534	0.998629	0.01	0.099	0.05	0.0499
3	0.998229	0.999584	0.998934	0.015	0.014	0.075	0.07501
4	0.998447	0.999634	0.999162	0.02	0.0199	0.1	0.1009
5	0.998641	0.999684	0.999391	0.025	0.0249	0.125	0.12499
6	0.998836	0.999717	0.999543	0.03	0.029	0.15	0.1501
7	0.999005	0.999767	0.999695	0.035	0.0349	0.175	0.17502
8	0.999151	0.9998	0.999848	0.04	0.0399	0.2	0.1990
9	0.999296	0.999834	0.999924	0.045	0.0451	0.225	0.22499
10	0.999418	0.999867	0.99999	0.05	0.0501	0.25	0.25011
11	0.997744	0.999484	0.998324	0.055	0.0549	0.275	0.27501
12	0.997986	0.999534	0.998629	0.06	0.0609	0.3	0.299
13	0.998229	0.999584	0.998934	0.065	0.06501	0.325	0.32501
14	0.998447	0.999634	0.999162	0.07	0.0699	0.35	0.3499
15	0.998641	0.999684	0.999391	0.075	0.07501	0.375	0.37498
16	0.998836	0.999717	0.999543	0.08	0.08001	0.4	0.3997
17	0.999005	0.999767	0.999695	0.085	0.085003	0.425	0.4249
18	0.999151	0.9998	0.999848	0.09	0.0899	0.45	0.4501
19	0.999296	0.999834	0.999924	0.095	0.095001	0.475	0.47502
20	0.999418	0.999867	0.99999	0.1	0.1003	0.5	0.4991

certain location natural frequency decreases and cycle will go on till the formation of first and second modes of vibration of the curved beam as shown in Figs. 11 and 12.

Compared to the first and second natural frequency, third natural frequency also shows the similar frequency variation. Firstly, frequency increases as variation in the location of crack starting from left end of the beam to right end. After particular location, frequency will be minimum and process repeats forming three modes of vibration. Minimum frequency implies that impact of the crack at that point will be less. This variation is indicated as in Fig. 13.

As the natural frequency and mode shapes are the parameters dependent on each other. Hence, with the change in natural frequency, amplitude of vibration also changes.

Fig. 11 Relative 1st mode of natural frequency versus relative crack locations
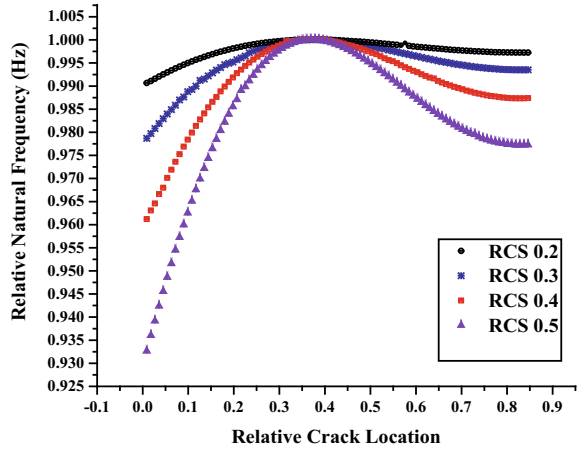
Fig. 12 Relative 2nd mode of natural frequency versus relative crack locations
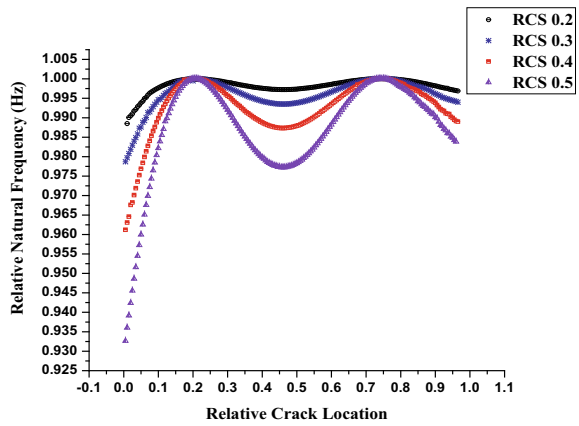
Fig. 13 Relative 3rd mode of natural frequency versus relative crack locations
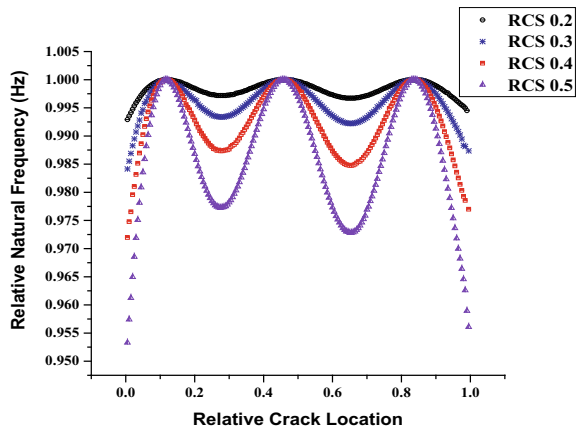
7 Conclusion

The current investigation of simply supported curved beam with inclined crack concludes that:

- Natural frequency of the curved beam varies as the severity of crack as well as the location of crack varies.
- At invariable crack severity, as the location of the crack varies from left end of the beam to the right end, initially natural frequency increases up to certain location of the crack and again decreases, and cycle repeats forming respective mode shapes.
- At invariable crack location, as the depth of crack increases, natural frequency of curved beam decreases and amplitude of curved beam increases.
- By knowing natural frequencies, ANFIS architecture identifies crack location as well as crack depth with close proximity with FEA.
- Fault diagnosis of the complicated dynamic structures with multiple cracks would be considered for future work. Many dynamic structures contain multiple cracks in it.

Acronyms and Nomenclature

ϕ Opening angle of the simply supported curved beam.
d Thickness of the curved beam.
L Inner arc length of the curved beam.
a Crack depth.
w Cross-sectional width of the curved beam.
α Angular position of crack from left end of the beam.
RCS   Relative crack severity $\left(\frac{a}{d}\right)$.
RCL   Relative crack location $\left(\frac{\alpha}{\phi}\right)$.
θ Crack inclination angle of curved beam.

References

1. Krawczuk M, Ostachowicz W (1997) Natural vibrations of clamped-clamped arch with an open transverse crack. J Vib Acoust 119:145
2. Viola E, Tornabene F (2005) Vibration analysis of damaged circular arches with varying cross-section. SID 1(2):155–169
3. Cerri MN, Dilena M, Ruta GC (2008) Vibration and damage detection in undamaged cracked circular arches: experimental and analytical results. J Sound Vib 314:83–94
4. Yang F, Sedaghati R, Esmailzadeh E (2008) Free in-plane vibration of general curved beams using finite element method. J Sound Vib 318:850–867
5. Chen C-N (2008) DQEM analysis of out-of-plane vibration of non-prismatic curved beam structures considering the effect of shear deformation. Adv Eng Softw 39:466–472

6. Zare M (2018) On crack detection in curved beams using change of natural frequency. J Vibroeng 20(2):1–19
7. Prawin J, Lakshmi K, Rao ARM (2019) A novel vibration based breathing crack localization technique using a single sensor measurement. Mech Syst Sig Process 122:117–138
8. Das H, Parhi DR (2009) Applications of neural network for fault diagnosis of cracked cantilever beam. In: World congress of nature and biologically inspired computing. Coimbatore, pp 1303–1308. Article No. 5393733
9. Mehrjoo M, Khaji N, Moharrami H, Bahreininejad A (2008) Damage detection of truss bridge joints using artificial neural networks. Expert Syst Appl 35:1122–1131
10. ANSYS© Release 14.5, Inc. Engineering simulation software
11. SolidWorks (2017) 3D design software—Dassault systems
12. Nandwana BP, Maiti SK (1997) Modelling of vibration of beam in presence of inclined edge or internal crack for its possible detection based on frequency measurements. Eng Fract Mech 58(3):193–205
13. Tada H, Paris PC, Irwin GR, Tada H (2000) The stress analysis of cracks handbook, vol 130. ASME Press, New York
14. Jang J-SR, Sun CT, Mizutani E (1997) Neuro-fuzzy and soft computing: a computational approach to learning and machine intelligence. Prentice-Hall, Upper Saddle River, NJ

Numerical Analysis of Artificial Hip Joints for Standing and Sit-to-Stand Positions

Abhishek and Abhishek Mishra

Abstract This paper deals with the analysis of the artificial hip joint implant (AHI) for the activity like sit-to-stand and the standing position. The simulation was completed in one of the simulation software packages like ABAQUS. For simulation, first step is to create a CAD model, define material properties and then create mesh of the complete model, and apply boundary and load conditions. The artificial hip joint consists of the femoral head which is spherical in shape, backing cup which is of cup shape and acetabular cup which is situated between femoral head and backing cup. The target of the simulation was to perform the analysis and to compute the parameters such as maximum von Mises stress, deflection, sliding distance and contact stress. The contact between acetabular cup and the outer part of femoral head; and the contact between backing cup and the outer part of acetabular cup are very important to study. The contact stress was computed for activities like sit-to-stand and standing in these contacts. The study of different weight patients was done by applying different actual loads corresponding to body weights. After analysis, the comparison of results was done. This can help in evaluating the effect of the increase in body weight on contact stress, total deformation, von Mises stress and sliding distance.

Keywords Numerical analysis · Artificial hip joint · Sit-to-stand position

1 Introduction

The pivot joint in the human body is the hip joint which is attached to the lower limb to trunk. This joint is made in between the femur and acetabular cup which is present in most commonly pelvis area in person [1]. Moreover, hip joint can transfer high forces which are developed by the weight of the person as well as during daily activities. Moreover, motion can be smooth by synovial fluid which is present in contact of geometry [2]. The functionality of this joint may deteriorate over the age

Abhishek · A. Mishra (✉)
Department of Mechanical Engineering, National Institute of Technology Delhi, Sector A7, Narela, Delhi 110040, India
e-mail: abhishekmishra@nitdelhi.ac.in

623

as well as when there is some problem in the patient like osteoarthritis, arthritis and bone tumours. The solution to such a problem is the replacement of the damaged hip joint by an artificial hip joint implant.

1.1 Total Hip Replacement

The total hip replacement needs replacement of the acetabular cup in the hip joint from the femoral head. This replacement gives relief to the patient. This is the era of development of material and improvement of properties of existing material. In the present scenario, the properties of material can be improved and the customized parts can be produced as per need of the customer.

The contact area between two mating parts under load condition is limited. Variation in the area becomes contact is proportional to the applied load. This will reduce the stress generated in cartilage. The surface finish of the material plays a role in the functioning of the joint.

The main components of the artificial hip joint implant are shown in Fig. 1. In the assembly, femoral head acts as ball, and the acetabular acts as socket. The wear of the artificial hip implant may be by chemical reactions or mechanical friction. When the joint has force, then the friction between the contact produces high contact stress that tends to failure of joint. During walking condition, the actual force acting on hip joint is equal to 290% of body weight [3], during sit-to-stand position 160% of body weight [4] and in standing position 190% of body weight [5]. The experimental study of the forces acting on the different joints of the human body under different daily life activities gives some relationships to its body weight to actual weight. The forces developed while the patient is doing different activities are measured for hip joint
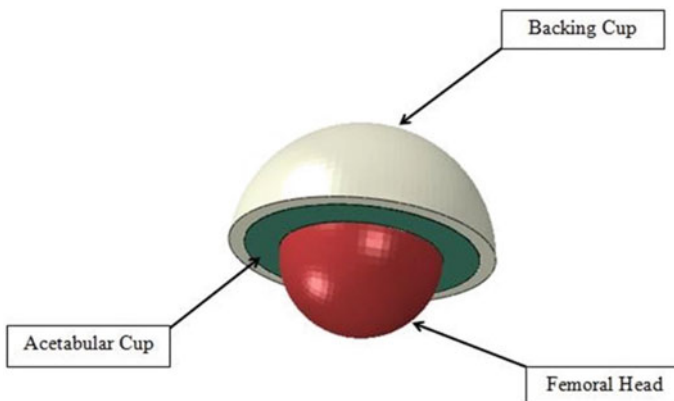
Fig. 1 Model of the artificial hip joint

implants as found in literature. The orientation and forces developed play important roles in the amount of contact stress developed [6].

1.2 *Total Hip Arthroplasty Implant Fixations*

In the case of arthritis patients, generally the joints become painful. The reduction in pain requires the replacement of the failed joint by the artificial hip joint. This replacement is done by the orthopaedics doctor by doing surgery. The types of fixation are "hybrid prosthesis, biologic fixation (cementless fixation) and cemented fixation".

2 Finite Element Analysis

The FEA is mostly used in structural analysis. Generally, when the geometry is complex and the computation of results takes long time, then the simulation software is used. The analytical value can be compared with the simulated value. The procedure of FE analysis is shown in Fig. 2.

Fig. 2 Flow chart of FEA
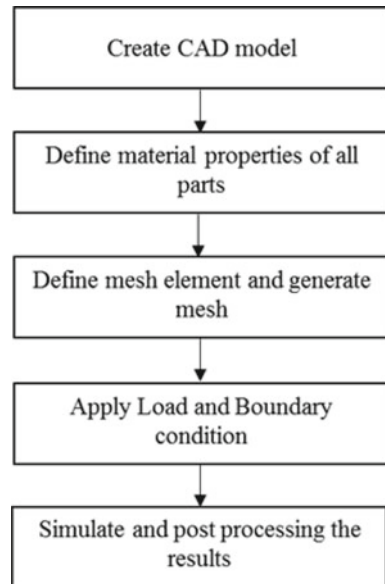
2.1   Geometrical Model

The geometrical model of the AHI was made in ABAQUS geometry part in software. In the assembly part, there was no clearance provided in mating parts. The mating parts were acetabular cup-backing cup and femoral head-acetabular cup. The value of the coefficient of friction was 0.04 in mating parts [7]. The diameter of the femoral head, the thickness of acetabular cup and the thickness of backing cup were taken from literature [8–10].

2.2   Material Selection

The material selection was done based on the property of biocompatibility in the material. The material should be hard enough so that the wear of material must be on the lower side. Corrosion-resistance is one of the properties which is required in the artificial hip implants. The material must be the biocompatible as well as the corrosion-resistant. Another requirement in the artificial hip implant is the strength of the material to be high, which reveals that under high forces the total deflection becomes negligible. The materials selected for the model were Ti6Al4V and ultra-high molecular weight polythene (UHMWPE). UHMWPE was used for the acetabular cup whereas the Ti6Al4V was used for the backing cup and the femoral head. The properties of these two materials, i.e. Ti6Al4V and UHMWPE used for the analysis were modulus of elasticity, Poisson's ratio, tensile strength, etc. [10–12].

2.3   Mesh

Mesh of the AHI was used for discretization of the domain. In this paper, meshing of different parts was done by using the hexahedral shape elements. Refinement of mesh can be helpful in reducing the error, but it will increase the computational time or simulation time. The discretization of the domain gives an insight into the calculation of different parameters at each of the node. When the discretization of whole domain is not proper, then the computational error increases. The regions where discretization of the domain was not done indicates that the region was not included for study; or when few of the elements were unstructured, then it tends to increase in error. The meshing of artificial hip joint implant is shown in Fig. 3.

Fig. 3 Isometric view of
mesh model
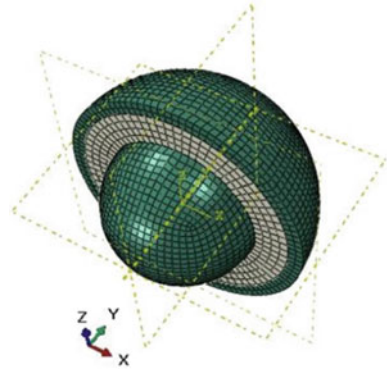
2.4 Load Condition and Boundary Condition

The boundary condition for this analysis was the lower surface or bottom of femoral head was restricted with all degrees of freedom like x-, y- and z-direction. The load condition was the force applied on node present at center of the top surface of the backing cup. The value of force was multiplied by the factor which is given in literature. For example, in the situation of standing position, the multiplication factor is 190%; and in the situation of sit-to-stand, value of multiplication factor is equal to 160% of the body weight. The load values were 1653 N, 1501 N, 1387 N, 1254 N and 1159 N whereas the values of body weight corresponding to these load values were 870 N, 790 N, 730 N, 660 N and 610 N.

3 Results and Discussion

3.1 Sit-to-Stand Position

The sit-to-stand position is one of the activities which is normally practiced several times in daily life. The analysis of results during this activity are shown in Table 1. The value of von Mises stress becomes maximum in the case of highest weight patient and minimum for lowest weight patient. This indicates that as the body weight of patent increases, then the stresses on joint rise; and when the magnitude becomes more than strength of the joint, then failure occurs. These stresses can be compensated by the increase in area. As the body weight increases, then the contact stress as well as total deformation also increase.

The values of von Mises stress vary with the radial distance. The value becomes maximum at the topmost node at the center. The distribution of von Mises stress varies with the change in the body weight. Also, the differences can be observed in the maximum value of von Mises stress. The distribution of von Mises stress in the

Table 1 Results for various person weight for sit-to-stand activity

S. No.	Body weight (in N)	Actual applied load (N)	Maximum von Mises stress (in MPa)	Maximum contact stress (in MPa)	Total deformation (in mm)
1	610	976	130.6	57.09	0.1271
2	660	1056	141.3	65.02	0.1272
3	730	1168	156.3	112.4	0.1272
4	790	1264	169.2	141	0.1273
5	870	1392	186.3	153.4	0.1273

case of maximum body weight patient is shown in Fig. 4a. Moreover, the variation of contact stress was also similar as von Mises stress but it had difference in the maximum value. The distribution contact stress is shown in Fig. 4b. Analysis of total
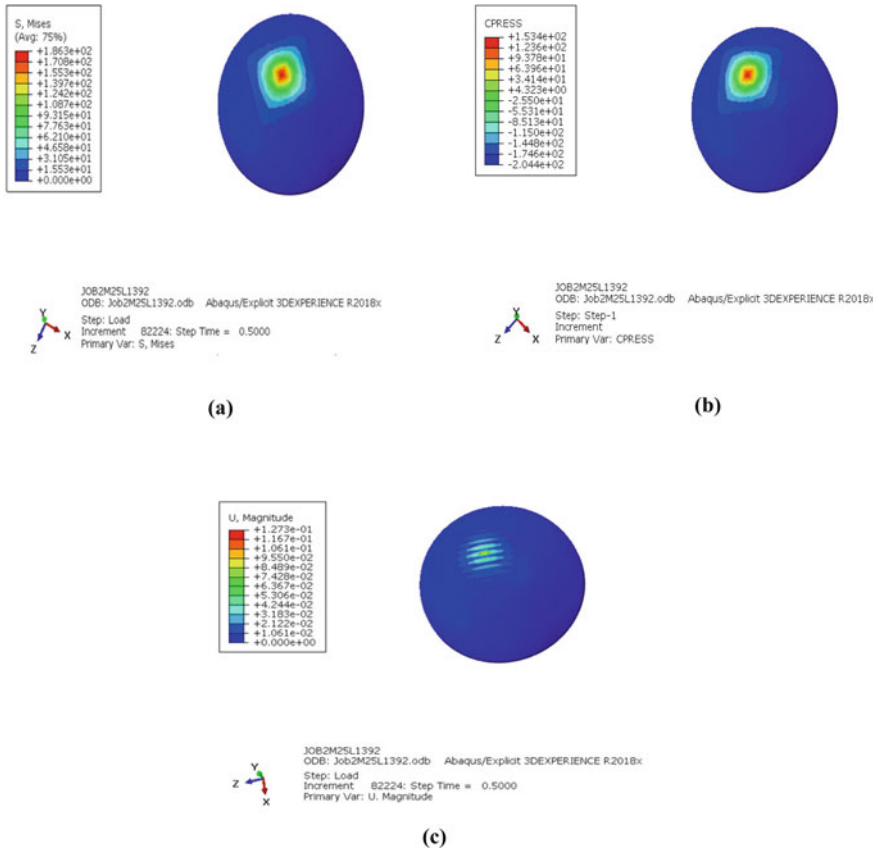
Fig. 4 Variation of **a** von Mises stress, **b** contact stress, **c** total deformation in sit-to-stand position

Table 2 Results for various person weight for standing position

S. No.	Body weight (in N)	Actual applied load (N)	Maximum von Mises stress (in MPa)	Maximum contact stress (in MPa)	Total deformation (in mm)
1	610	1159	155.1	104.1	0.1272
2	660	1254	167.8	122.8	0.1273
3	730	1387	185.6	144.9	0.1273
4	790	1501	200.9	157	0.1274
5	870	1653	221.2	166.6	0.1275

deformation is very important in hip implant because few microns of deformation may give pain to the patient. So, this is very important parameter to analyse. The variation of total deformation is shown in Fig. 4c.

3.2 Standing Position

The standing position is another regular activity in daily life. The analysis is very important because most of the daily works need the standing position. The von Mises stresses produced in standing position are shown and discussed in this part. The distribution of von Mises stress was almost similar as the sit-to-stand position. The differences are in the maximum values. Variation of values with weight change was almost similar as sit-to-stand position. Results of analysed parameters are shown in Table 2.

For the analysis of standing activity, the different parameters i.e. stresses and deformation were evaluated. The variation in the values of these parameters with respect to radial direction is similar to the sit-to-stand case. The difference occurred in the maximum values of computed parameters. The distribution with respect to the change in body weight was similar. The values of computed parameters were increased with increase in body weight. Variation of von Mises stress is shown in Fig. 5a, whereas the variation of contact stress is shown in Fig. 5b. Also, the variation of total deformation is shown in Fig. 5c.

3.3 Comparison of Results of Sit-to-Stand and Standing Position

The comparison of results obtained in sit-to-stand and standing situation can help in the study of the effect of change in the activity with respect to change in von Mises stress, contact pressure and total deformation. Through this analysis, the doctor gives suggestions on limits of such routine activities to the patients of different diseases
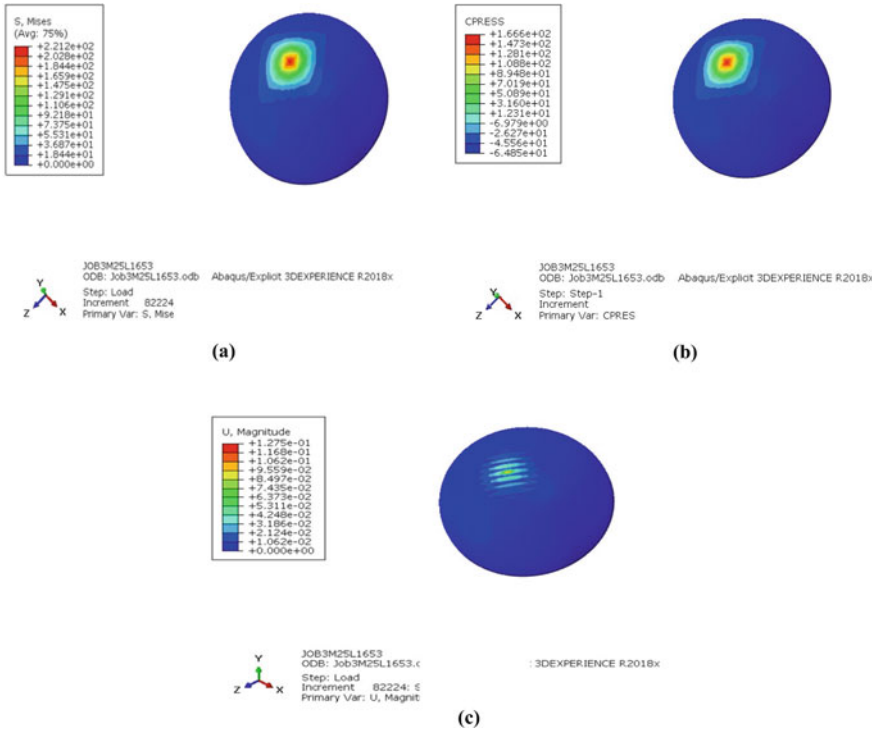
Fig. 5 Variation of **a** von Mises stress, **b** contact stress, **c** total deformation in standing position

arthritis, bone cancer etc. or change of the hip joint of the patients by the artificial hip implant.

The variation of von Mises stress with respect to the different body weights for the activities i.e. standing and sit-to-stand, is shown in Fig. 6a. Variation in the von Mises stress with change in the person (i.e. patient) weight follows a linear relationship. The change in the activity, i.e. from "sit-to-stand" to "standing", was upshifted the profile. Standing activity produces more von Mises stress compared to von Mises stress produced in sit-to-stand position. The value of von Mises stress was increased with an increase in body weight. Variation in the contact stress and the total deformation is also varying linear with respect to the increase in body weight as shown in Fig. 6b and 6c respectively. The values increase with increase of body weight.
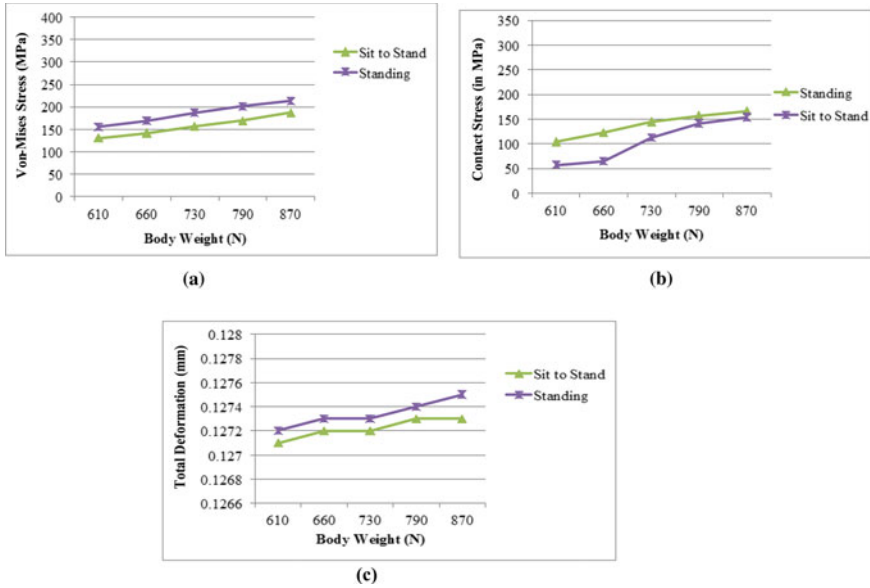
Fig. 6 Comparison of **a** von Mises stress, **b** contact stress, **c** total deformation in sit-to-stand situation

4 Conclusions

The numerical analysis of AHI was done on the standing position as well as for the sit-to-stand position. In this scenario, the artificial implant was developed by using titanium alloys. Titanium and its alloys are biocompatible. Titanium has superior properties like corrosion-resistant, lower young modulus, high strength, etc. UHMWPE is another material which has superior fracture toughness and wear resistance. The analysis was done by using these two materials. From the results obtaining from the analysis, the variation in analysed parameter was linearly varying. The trend was on the positive side like an increase in body weight tends to increase in the value of analysed parameter. The comparison results give an insight to change in values of analysed parameter with respect to change in the activity.

The analysis may be extended to other joints in different activities. Apart from the simulation using FE software, there is need to develop the customized physical model. The approach to solve the problem of different joints may be the similar as used in this paper. Results of analysis can help in better understanding of implants by doctor and designer. The regions under maximum stresses can be strengthened by increasing cross-section or making new composite. The surface may be improved by using coating. Simulation does not include surface condition, so it is one of the options to try to solve such problem in simulation software. The stresses results can also be used in reducing the weight of the implant.

References

1. Margareta N, Frankel VH (eds) (2001) Basic biomechanics of the muscular skeletal system. Lippincott Williams & Wilkins
2. Zhang X, Zheng G, Wang J, Zhang Y, Zhang G, Li Z, Wang Y (2013) Porous Ti6Al4V scaffold directly fabricated by sintering: preparation and in vivo experiment. J Nanomater 2013:1–7
3. Bergmann G, Graichen F, Rohlmann A (2004) Hip joint contact forces during stumbling. Langenbeck's Arch Surg 53–59
4. Brand RA, Pedersen DR, Davy DT, Kotzar GM, Heiple KG, Goldberg VM (1994) Comparison of hip force calculations and measurements in the same patient. J Arthroplasty 9(1):45–51
5. Bergmann G, Deuretzbacher G, Heller M, Graichen F, Rohlmann A, Strauss J, Duda GN (2001) Hip contact forces and gait patterns from routine activities. J Biomech 34(7):859–871
6. Bergmann G, Graichen F, Rohlmann A (1993) Hip joint loading during walking and running, measured in two patients. J Biomech 26(8):969–990
7. Gao Y, Zhang J, Jin Z (2015) Explicit finite element modeling of kinematics and contact mechanics of artificial hip and knee joints. Proceedings of the 14th IFToMM world congress, Taipei, Taiwan, 25–30 October 2015
8. Chauhan R, Paul S, Dhaon BK (2002) Anatomical parameters of north Indian hip joints—cadaveric study. J Anat Soc India 51(1):39–42
9. Mattei L, Di Puccio F, Piccigallo B, Ciulli E (2011) Lubrication and wear modelling of artificial hip joints: a review. Tribol Int 44(5):532–549
10. Jangid V, Singh AK, Mishra A (2019) Wear simulation of artificial hip joints: effect of materials. Mater Today Proc 18(7):3867–3875
11. Katti KS (2004) Biomaterials in total joint replacement. Colloids Surf B 39(3):133–142
12. Steven MK (2009) UHMWPE biomaterials handbook: ultra-high molecular weight polyethylene in total joint replacement and medical devices. Academic Press

A Low-Cost Portable Mechanical Ventilator—A Conceptual Design

Raveendran Meloth Swaroop, Eswar Nithin, and Kizhakkelan Sudhakaran Siddharth

Abstract The current study is an attempt to review the-state-of-art for low-cost portable mechanical ventilators. Over the past few years, many engineers have developed low-cost ventilators, which offer many features of conventional hospital ventilators. Toward the direction of physically realizing an innovative mechanical ventilator, this paper discusses the idea of the design and fabrication of a reusable, low-cost portable mechanical ventilator. The conceptual design is aimed at attaining higher control on the number of operating modes and different parameters like tidal volume, breaths per minute, inspiration-to-expiration ratio, and positive end expiratory pressure. In the current scenario, these ventilators can be used in providing respiratory aid to COVID-19 patients and likewise also be used for similar casualty cases.

Keywords Mechanical ventilator · PEEP · I:E ratio · Tidal volume

1 Introduction

A ventilator, or sometimes known as respirator, is one of the most important life supporting medical equipment in a hospital. A ventilator provides breathing support to a patient by pushing in breathable air into the patient's lungs at the right time, with the right amount of oxygen, volume, and pressure [1, 2]. The different ways of ventilating a patient are by controlling the volume, pressure, flow, rate of flow, amount of oxygen, and allowing the patient to be in charge or the ventilator to oversee the breathing process. Though there are many simpler forms of the ventilator, the most sophisticated ones have many modes including assist mode (AC), pressure control mode (PC), positive end expiratory pressure (PEEP), and pressure support mode (PS) [2, 3].

In assist control (AC) mode (also known as continuous mandatory ventilation), a backup breathing rate is setup to give mandatory breaths to the patient in case he cannot trigger a breath. Usually, this is the most commonly used ventilator mode and

R. M. Swaroop · E. Nithin · K. S. Siddharth (✉)
Amity University Dubai, Dubai, UAE
e-mail: ssudhakaran@amityuniversity.ae

the patient triggers the breaths. The patient tries to take a breath in, which causes negative pressure to be detected by the ventilator and as soon as the negative pressure is detected, it delivers a specific volume of air into the lungs. The volume is set by the medical staff usually in the range of 6–8 ml/kg of ideal body weight (IBW). The back-up rate makes sure that the patient never breaths less than the set value of breaths per minute (BPM) [3–6]. Depending on the compliance of lungs, giving in a specific volume of breath will result in pressure changes inside the lungs. This increase or decrease in pressure will be shown through a pressure read out and an alarm will be set up to notify it [1–3]. There comes the role of pressure control (PC) mode, which allows us to control the pressure and bring it back to acceptable range depending upon the compliance of the lungs and the volume of air given [4–6].

PEEP refers to a mode where a continuous pressure in the range of 5–20 cm of H20 is maintained inside the patients lungs in order to keep the alveolus open in case of invasive intubation and in order to keep the tongue forward (open airway) in case of noninvasive intubation [7]. The pressure support (PS) mode is similar to the PEEP settings but happens only on inhalation and the patient initiates the breathing process in which each breath has a specific amount of pressure [8]. All these features assure perfect breaths for the patient and thereby supports their valuable life in case of a disease affecting the lungs and thereby affecting the patients breathing capacity or during a lung injury.

Though ventilators are very important to the medical world, its acquisition is not so easy due to its high initial and maintenance costs and thereby, its numbers are very limited when compared to the amount of humans who might need it during a mass outbreak of a disease of some kind [9–13]. This has led to a lot of research and development to be done by engineers in the past few years in order to design such ventilators which can be easily manufactured by any manufacturing capacity. Most of such designs are based on Bag Valve Masks (BVM's) which are squeezed by electromechanical means in order to produce airflow at a set rate or volume. But the ability to blow air and being able to manufacture quickly and at high rates are not the only desired qualities that a fully functional ventilator must have. Such simple electromechanically operated ventilator designs bring in further problems such as Barotrauma which is the inflammation or rupture of alveolus due to the excess pressure caused by the forced in air [14–16]. Thus, these ventilators must be able to tightly control many important parameters to allow the patient to breathe well and to avoid further damages. The important functionalities include the ability to control tidal volume, pressure, breaths per minute, oxygen percentage, positive end expiratory pressure (PEEP), and the ability to have patient triggered breaths. Another important functional aspect of a ventilator is the ability to wean off the patient from the ventilator without any complications.

Though most of the existing ventilator designs maybe used as final option during an emergency, they are definitely not fit for long-term use for a patient who might need weeks of manual ventilation. This leads to the need for new innovative ideas to design and manufacture a low cost and easily manufacturable ventilator designs with features nearly equal to the most advanced ones [17–20]. Even though designing a ventilator with such high technological requirements with constraints of cost and raw

materials is highly demanding, its promising to see some new designs in which many of the requirements are met and producing in large numbers require considerably low cost.

The current study is an attempt to review the state of art for low-cost portable mechanical ventilators and proposing an initial conceptual idea of our version of ventilator. Considering the current need, the current study is an attempt to develop a low-cost mechanical ventilator which would prove useful in providing respiratory aid.

2 Portable Low-Cost Ventilators

Toward the direction of developing low-cost ventilators, a portable ventilator was developed by Husseini and his co-workers which had a superior performance [13]. The overall cost of the ventilator was cut short by developing the robust system from low-cost parts. The air is pumped into the patient using the Ambu bag with the help of a pivoting CAM arm. The arm is driven by an electric motor using a 15 V DC battery. The CAM concept utilizes a crescent-shaped cam to compress the Ambu bag, which allows smooth, repeatable deformation to ensure constant air delivery. By controlling the angle of the CAM's shaft, the amount of air volume delivered was accurately controlled. This setup proved to be space efficient and has low power requirements to operate.

A cost effective and portable ventilator was developed by Ghafoor and co-authors in this context [21]. They have taken a very simple approach of compressing the Ambu bag, where an iron arm is placed on top of it to compress the bag. The movement is triggered by a motor with the help of two wooden blocks for support under the Ambu bag. The principal advantage of the prototype was the low power requirement and its lightweight. In this regard, Jürß et al. [22] developed a compact low-cost respirator which had superior advantages over the conventional ventilators. The developed design eliminated the need for respiration tubes and achieved the purpose by using a full-face mask.

Likewise, a cheap ventilator was designed and developed by Islam and co-workers [23] where the Ambu bag was operated by the action of a computer-aided manufacturing (CAM) arm which was controlled via a microcontroller. The main reason for selecting the cam arm was because the servo system provides a high torque. Also, the control signal was visualized by a platform known as the BIOPAC student's laboratory system in the developed design. The model proved to be compact and efficient. The model was shown to be successful in operating at different respiratory rates depending on the age of the patient. Another similar ventilator was developed by Hossain and co-authors [24] where the compressing of Ambu bag was achieved by two arms.

Moving forward in the recent advances, an improved ventilator was proposed by Zhang and co-authors [25] which offers essential pressure and volume control ventilator modes for critical patients. The proposed design of ventilator has volume

and pressure control modes using various pressure sensors and solenoid flow valves which are controlled using microcontrollers and PID controllers. The design consists of a mixing tank which mixes air from a DC blower and oxygen from an oxygen supply and the mixture is then supplied to the patient at suitable levels and pressure which can be decided by the operator. The design also included features like adjustable tidal volumes, breath per minute, PIP, PEEP and humidity control.

Another one in the same league would be the portable ventilator suitable for army-based battlefield applications developed in 2004 by a group of scientists at John Hopkins University [26]. The two systems were named John Hopkins Applied Physics Lab's Mini Ventilation Unit (JAMU) and Far Forward Life Support System (FFLSS). The FFLSS was mainly targeted for military use while the JAMU was aimed at civilian use. The FFLSS system was microprocessor controlled, used standard army battery, had reconfigurable user interface and an LCD display. The system was able to monitor airflow and pressure to deliver optimal level of breaths. It also possessed ventilator modes such as assist control and mandatory breaths.

Similarly, an exhalation valve was developed by Douglas and co-workers [27] which incorporated the functions of both PEEP valve and exhalation valve. Sharp flow corners were reduced thereby in the airflow. The setup reduces the complexity and weight of the entire assembly. Likewise, an intelligent model for the mechanical ventilator was firstly developed in MATLAB/Simulink by Guler and Ata [28], after which a fuzzy-LABVIEW based mechanical ventilator prototype was practically designed by the authors. The fuzzy logic controller was used independently for both the simulation and experimental setup and were successfully applied to many systems. Other notable ventilator is the one developed by Williams and co-authors (2010). The authors demonstrated a cheap gas-efficient ventilator which could be fabricated from industrial components [29]. The ventilator had the advantage of delivering stable nitric oxide concentration by following volumetric principles. Catherine and co-workers [30] performed studies on ventilators with focus on the trigger of inspiration. The authors discussed on the influence of ventilator factors on patient effort or work of breathing, different triggering phases, post-triggering phases, ventilator factors as determinants of patient-ventilator interaction, and different ventilator modes for improving patient–ventilator interaction. Another similar ventilator in the same lines was also developed by Güler and Ata [31] for training purpose for clinicians and students which had superior control over setting the inspiration and expiration time.

In the context of studies related to using a single ventilator for multiple patients, a ventilator was developed by Siderits and team [32], wherein a 3D-printed manifold can be fitted to a ventilator in order to connect it to four masks at the same time. The 3D printing of this small manifold was performed by using fused filament deposition. Likewise, four lung simulators were added in parallel to a single ventilator using available tubings until the ventilator supplied enough air for the four lung simulators [33]. The setup was successful in running for 12 h in two separate modes: pressure control and volume control. A very recent ventilator developed by PulmCrit discusses the possibility of splitting a single ventilator to treat multiple patients without letting each other's ventilation requirements affect each other [34].

Fig. 1 Comparison of the performance and cost of prominent low-cost portable ventilators developed over the past decade
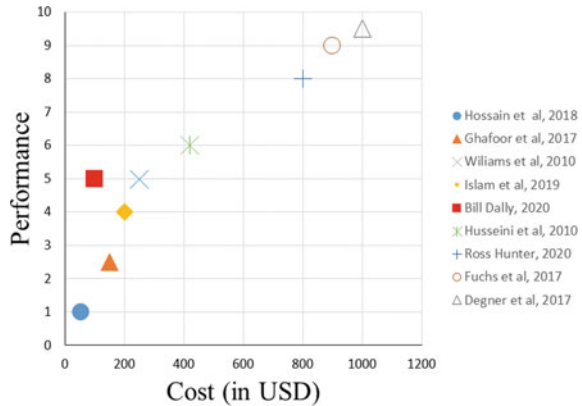
The most recently reported low-cost ventilator was the one developed by Scottish design engineer Ross Hunter in the wake of Covid-19 [35]. The ventilator was applauded globally for being effective in three modes of ventilation as well as being cheap. He has come up with a bellow design as it is an effective means to control air volume and pressure very accurately. This team has achieved PEEP by extending the bellows system so that it can contain even up to 8 L of air. This allowed for a continuous stroke during the expiration phase that maintains a set PEEP. The system could also accurately monitor the volume and pressure due to its positional control and pressure sensors. The group of doctors from Smiths Medical was also successful in developing ventilator of varying features [36].

Figure 1 shows the comparison of performance and cost of different low-cost portable ventilators reported in the last decade, based on the literature review. The performance index has been defined based on the features of each of the ventilators. These features include the number of operating modes, the control over different parameters (volume and breath rate per minute), the design factors (its compactness, strength and stability) as well as the maximum working hours. It is evident from the plot that even though many scientists have tried to incorporate the best features at a cheaper cost, it has remained a challenge till date.

3   Conceptual Design of the Proposed Low-Cost Ventilator

The proposed design is a low-cost, portable, electromechanically operated ventilator which can be used for both invasive and non-invasive type of ventilation. It is designed in such a way that it can be easily carried in an emergency. The air delivery system comprises of an Ambu bag which is pressed by an optimally designed convex pressing surface attached to a rack and pinion mechanism which converts rotary motion of the motor into linear motion required to press the Ambu bag. This design would enable superior control over breathing parameters such as Tidal volume, breaths per

minute, I:E ratio, PEEP and has real-time data monitoring system and an alarm to warn pressure and volume discrepancies. The design also consists of a Hydroscopic condenser humidifier and filter (HCHF) to ensure proper humidification and filtering of the delivered air. An overview flowchart of the conceptual design is shown in Fig. 2 and the proposed pressing mechanism of the Ambu bag is shown in Fig. 3.

A Nema-17 bipolar stepper motor with a stall torque of 60 N-cm is selected for the design so that control over minute values of stroke length can be easily achieved. Figure 6 shows the arrangement of components for achieving the Ambu bag compressing using the rack and pinion arrangement. The stepper motor is controlled by a dual H bridge motor driver which is capable of supplying the motor's stall current and an Arduino MEGA microcontroller which is programmed to give control to the user over parameters such as Tidal volume, breaths per minute and I:E ratio. The control over all these parameters is gained by varying the stroke length, speed of each stroke, and the number of strokes of the rack and pinion mechanism. The relationship data between these and the delivered air volume and flow rate will be experimentally
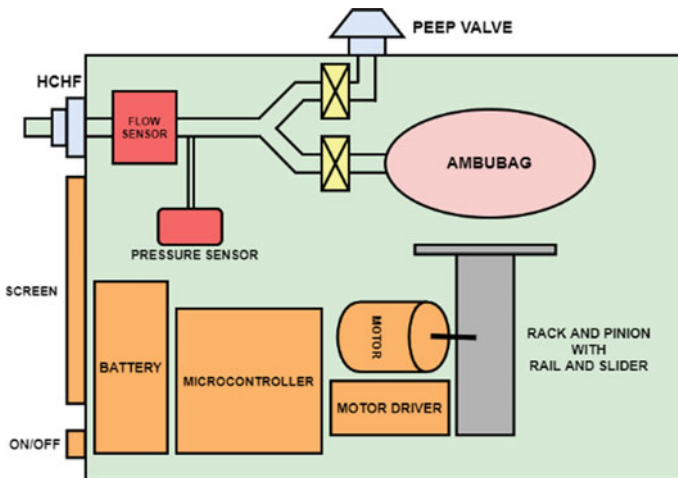
Fig. 2 Flowchart of the conceptual design

Fig. 3 Proposed compressing mechanism design where a convex arm presses the Ambu bag as shown
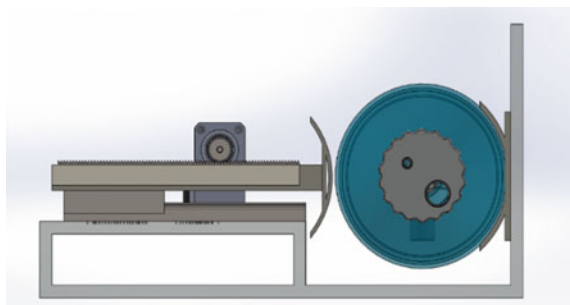
Fig. 4 Conceptual design of the ventilator
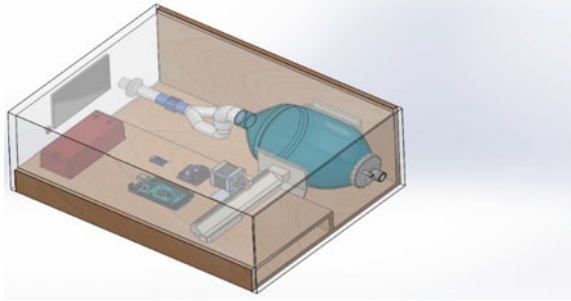
determined using computational fluid dynamics (CFD) simulation and the data is fed into the Arduino program. A solidworks model of the proposed design is shown in Fig. 4.

A WYE connecter is used to divert inspiratory and expiratory flow through two different tubes where one end is connected to the Ambu bag and the other end is connected to a PEEP valve which allows PEEP value to be toggled according to different patient requirements. The single end of the WYE connecter is connected to a pressure sensor and a flow sensor which allows real time monitoring of the patient's breathing parameters through an LCD display. A Sensirion SFM3300-AW mass flow sensor with 250 SLPM bidirectional capacity and an Adafruit MPRLS ported pressure sensor with 0–25 psi sensing range was chosen for the design. The system can be powered by a battery pack or directly from a wall outlet, depending on the situation. A 12-V, Dakota LiFePO4 battery pack with a capacity of 10,000 mA-h was chosen to power the design and it would be enough to power the ventilator for approximately 3 h without any external power. The complete circuit schematic of the proposed ventilator design is shown in Fig. 5.

Figure 6 shows the step by step breakdown of the proposed ventilator design's working. It shows various input points, decision points, and input to output calculation points during the working of the ventilator along with the pressure/volume alarm trigger and patient initiated breath trigger mechanism.

The design incorporates a real-time patient data monitoring system which allows to monitor critical breathing parameters through flow-time graph, volume-time graph, and pressure–time graph of the patients breaths and an alarm to warn pressure and volume discrepancies which is unavailable in almost all of the low-cost ventilator designs. The design also consists of a hydroscopic condenser humidifier and filter (HCHF) to ensure proper humidification of the air before delivering it to the patient and filtering the exhaled air before releasing it into the atmosphere to avoid contamination. The optimally designed 3D-printed convex pressing surface allows maximum air to be squeezed out of the Ambubag (as depicted in Fig. 3) with minimum work done to deliver any amount of tidal volume. The 7-inch LCD display consists of a user-friendly interface which allows real time monitoring and swift way to make necessary changes to the input parameters without interfering with the working of the ventilator.
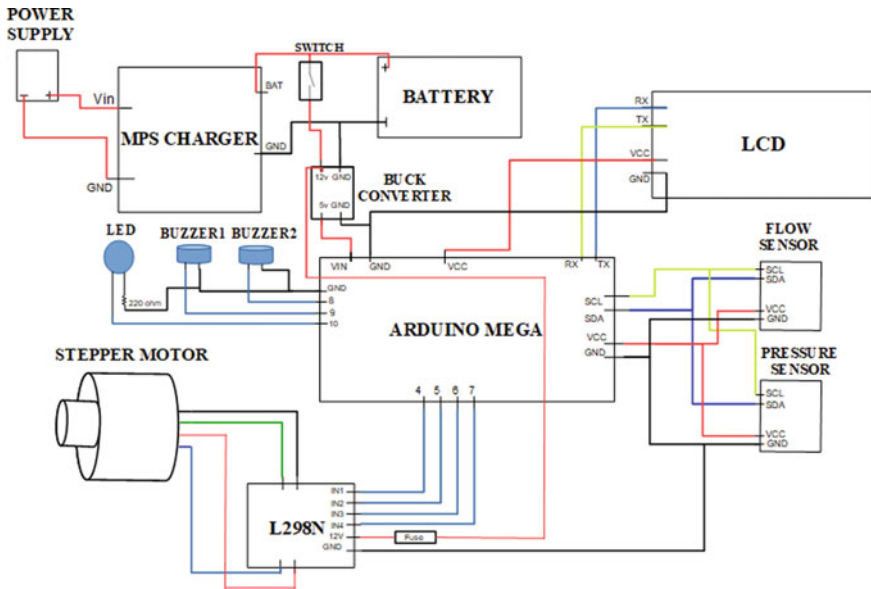
Fig. 5 Circuit schematic of the proposed ventilator

4 Conclusions

The emergence of novel Coronavirus infection in Wuhan, since December 2019 and its rapid spread has led to a global threat. This scenario has led to the inevitable need for the detection, diagnosis, prevention, and protection among the world population. In the wake of such a pandemic, the need for low cost and easily manufactural ventilators abruptly rise to uncontrollable levels. This situation can be overcome by increasing the production capabilities of ventilator manufacturers by increasing the number of ventilators through an easy and fast adaptable way.

Over the past few years, many engineers have developed low-cost ventilators offering many features of conventional hospital ventilators. This utilizes various sources of air such as the conventional bag valve masks, air compressors, etc., coupled with various range of mechanisms to achieve the necessary ventilator features. Our proposed low cost, portable, electromechanical ventilator incorporates some of the major and most critical features of a ventilator such as control over tidal volume, breaths per minute, I:E ratio, PEEP, and patient data monitoring system into a design suitable for emergency situations.
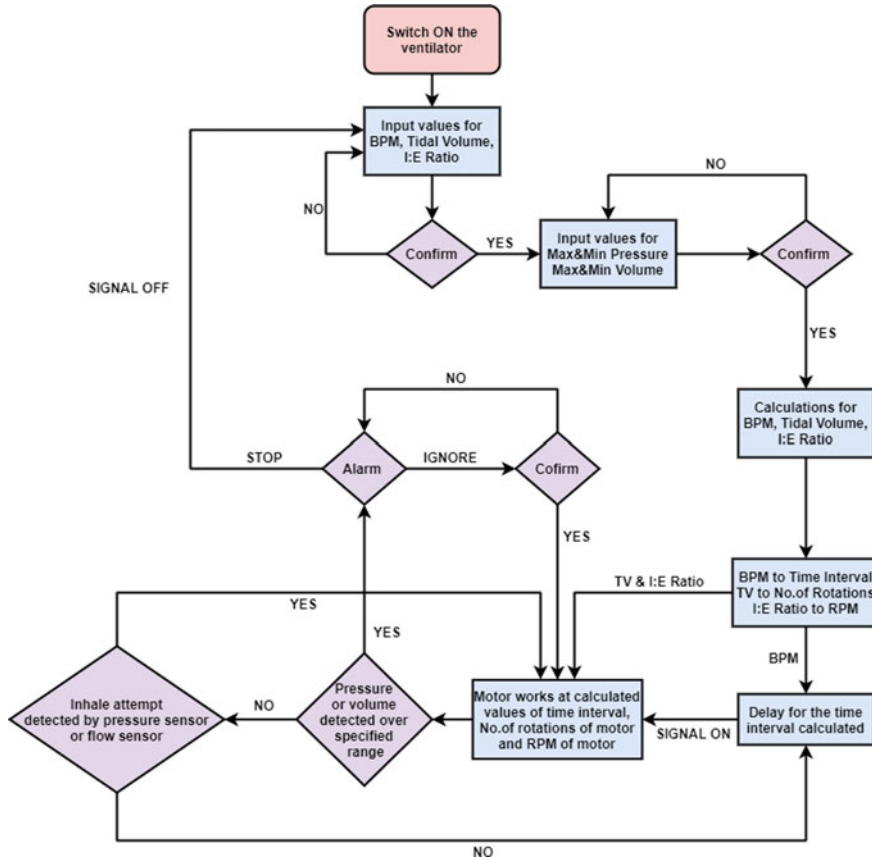
Fig. 6 Process flowchart of the ventilator

References

1. Slutsky AS (1993) Mechanical ventilation. Chest 104(6):1833–1859
2. Tobin MJ (1994) Mechanical ventilation. N Engl J Med 330(15):1056–1061
3. Tobin MJ (2001) Advances in mechanical ventilation. N Engl J Med 344(26):1986–1996
4. Tobin MJ (2006) Principles and practice of mechanical ventilation. Shock 26(4):426
5. Rodriguez P, Dojat M, Brochard L (2005) Mechanical ventilation: changing concepts. Indian J Crit Care Med 9(4)
6. Calfee CS, Matthay MA (2005) Recent advances in mechanical ventilation. Am J Med 118(6):584–591
7. Gottfried SB (1991) The role of PEEP in the mechanically ventilated COPD patient. Ventilatory failure. Springer, Berlin, Heidelberg, pp 392–418
8. Gottfried SB, Reissman HAJO, Ranieri VM (1992) A simple method for the measurement of intrinsic positive end-expiratory pressure during controlled and assisted modes of mechanical ventilation. Crit Care Med 20(5):621–629
9. Neto AS, Filho RR, Rocha LL, Schultz MJ (2014) Recent advances in mechanical ventilation in patients without acute respiratory distress syndrome. F1000 Prime Reports 6

10. Rittayamai N, Brochard L (2015) Recent advances in mechanical ventilation in patients with acute respiratory distress syndrome. Eur Respir Rev 24(135):132–140
11. Khemani RG, Newth CJL (2010) The design of future pediatric mechanical ventilation trials for acute lung injury. Am J Respir Crit Care Med 182(12):1465–1474
12. Marani R, Perri AG Design of advanced electronic biomedical systems. Int J Adv Eng Technol 4(1):15
13. Al Husseini AM, Lee HJ, Negrete J, Powelson S, Servi AP, Slocum AH, Saukkonen J (2010) Design and prototyping of a low-cost portable mechanical ventilator. Trans ASME-W-J Med Devices 4(2):027514
14. Chang, DW (2013) Clinical application of mechanical ventilation. Cengage Learning
15. Kobayashi H, Uchino S, Takinami M, Uezono S (2017) The impact of ventilator-associated events in critically ill subjects with prolonged mechanical ventilation. Respir Care 1379–1386
16. Pearce, JM (2020) A review of open source ventilators for COVID-19 and future pandemics. F1000Research 9(218):218
17. Whitman R (2020) Tesla shows off ventilators made from model 3 parts. Extreme Tech Newslett
18. Pearce J (2020) Distributed manufacturing of open-source medical hardware for pandemics. https://doi.org/10.20944/preprints202004.0054.v1
19. Neighmond P (2020) As the pandemic spreads, will there be enough ventilators? The Coronavirus crisis. Health news from NPR, 14 March 2020
20. Miller J (2020) Germany, Italy rush to buy life-saving ventilators as manufacturers warn of shortages. Reuters, 14 March 2020
21. Ghafoor MJ, Naseem M, Ilyas F, Sarfaraz MS, Ali MI, Ejaz A (2017) Prototyping of a cost effective and portable ventilator. In: 2017 international conference on innovations in electrical engineering and computational technologies (ICIEECT). IEEE, pp 1–6
22. Jürß H, Degner M, Ewald H (2018) A new compact and low-cost respirator concept for one way usage. IFAC-Papers Online 51(27):367–372
23. Islam, MR, Ahmad M, Hossain MS, Islam MM, Ahmed SFU (2019) Designing an electro-mechanical ventilator based on double cam integration mechanism. In: 2019 1st international conference on advances in science, engineering and robotics technology (ICASERT). IEEE, pp 1–6
24. Hossain SMT, Halder MR, Al Aman M, Islam R, Rahman MT (2018) Design construction and performance test of a low-cost portable mechanical ventilator for respiratory disorder. In: International conference on mechanical, industrial and energy engineering. Khulna, Bangladesh, 23–24 December 2018
25. Zhang X, Shah YH, Tumuluru N (2020) Proposal for a low-cost High-fidelity ventilator for COVID-19 pandemic
26. Kerechanin CW, Cytcgusm PN, Vincent JA, Smith DG, Wenstrand DS (2004) Development of field portable ventilator systems for domestic and military emergency medical response. John Hopkins Apl Tech Digest 25(3)
27. DeVries, DF (2000) Exhalation valve for mechanical ventilator. US Patent 6,102,038, issued August 15 2000
28. Guler H, Ata F (2014) Design of a fuzzy-LabVIEW-based mechanical ventilator. Comput Syst Sci Eng 29(3):219–229
29. Williams D, Flory S, King R, Thornton M, Dingley J (2010) A low oxygen consumption pneumatic ventilator for emergency construction during a respiratory failure pandemic. Anaesthesia 65(3):235–242
30. Sassoon CSH (2011) Triggering of the ventilator in patient-ventilator interactions. Respiratory Care 56(1):39–51
31. Güler H, Ata F (2013) Design and implementation of training mechanical ventilator set for clinicians and students. Procedia Soc Behav Sci 83:493–496
32. Siderits R, Neyman G (2014) Experimental 3D printed 4-port ventilator manifold for potential use in disaster surges. Open J Emerg Med
33. Neyman G, Irvin CB (2006) A single ventilator for multiple simulated patients to meet disaster surge. Acad Emerg Med 13(11):1246–1249

34. Farkas J (2020) PulmCrit—splitting ventilators to provide titrated support to a large group of patients, emcrit.org. 15 March 2020
35. Symon K (2020) Scottish designer is finalist in global competition for Covid-19 ventilator, insider.co.uk. 13 May 2020
36. Smiths Medical Homepage. https://www.smiths-medical.com/en-us/covid-19-response. Last accessed 2020/05/10

Steering and Braking Systems Analysis of Go Cart

Shubham Kumar, Apurv Sinha, Shubham Kumar, Harshit Srivastava, and Manoj Kumar Shukla

Abstract With increasing popularity for F1 in India, go carting has started attracting a lot of attention especially among the young engineers and neophyte drivers. This has set many motorsport enthusiasts and other automotive societies to organize go cart competitions and events to fulfill the crave to learn more about automobiles of graduating engineers. Spurred by passion, many engineers have started teaming up to tussle against teams participating from various engineering colleges in India. Steering system is one of crucial areas in designing of go cart as even the slightest of improvement in response of this system could reduce the lap time and help to reach the driver beyond the finish line to win a position. Thus, steering has to be reliable enough such that the driver could have the complete control over the cart even in the toughest tracks.

Keywords Go cart · Steering system · Braking system

1 Introduction

Go cart is a mini racing car. It was first made by Art ingles in late 1950's in USA. It does not have suspension system and does not have differential in it [1]. Differential is not used because of less clearance between go cart base and track surface [2, 3]. The power source of go cart is battery [4]. As the surrounding is getting polluted by petrol and diesel vehicle, the best alternative is electric vehicle. Go cart looks like a formula 1 car but not fast like them as well as it is cheaper than formula 1 cars. Nowadays, go carts are used in racing events where the participants should know what the purpose of the event and their role in event is.

S. Kumar (✉) · A. Sinha (✉) · S. Kumar · H. Srivastava · M. K. Shukla
Galgotias University, Greater Noida, Uttar Pradesh, India
e-mail: shubhamkumarrsingh369@gmail.com

A. Sinha
e-mail: Apurvsinga361@gmail.com

M. K. Shukla
e-mail: manoj.shukla@galgotiasuniversity.edu.in

645

Go carts are also manufactured by Indian companies but the number is less. Large-scale GO cart manufacturers like MRF and Indus have GO cart in range between 1–3 lakh. Go cart, nowadays, is coming up with more modification and sizes. As we have participated in event last year which mainly hosted by Galgotias University itself. The name of event is Imperial society of innovative engineers (ISIE), we won 1st prize in autocross event which is mainly part of competition. We won 1st prize as best lap and best driver; this year, we participated in event which was organized in Coimbatore. The event mainly hosted by Go cart design challenge (GKDC), we won 1st prize in autocross event again and overall, we won 4th prize. In this project, we mainly have done modification in steering and braking systems of our previous existing Go-Cart.

In this Go-CART, we have focus to have the steering radius less than 3 m and 100% Ackermann steering with a stopping distance of 2.5 m with single-disc-type brake having breaking force 8896 N.

2 Problem Definition and Working

2.1 Steering System

The significant purpose of a motorist for a go cart is to enhance the handling capacity of Go cart [5]. This purpose of motorist cannot meet by simply purchasing advanced version of Go cart equipment like wheels or others optional equipment's. For attaining exact rotational capacity of cart that will produce maximum power output ratio for specifically operation. The traditional Steering arrangement kindly delivers the work of rotating the front wheel which is manually operated by motorist [6]. The steering wheel system gets balanced mainly in front of motorist by steering columns by the help of universal joint. Universal joint generally allows the certain amount DOF along the straight line.

The mechanism involved in steering geometry is Ackerman steering geometry according to this geometry that will allow the inside wheel to get turn by larger angle as compared to outside wheel shown in Fig. 1. The larger angle and smaller angle get compared with common turn centre. During the rotation, the speed gets decreased and having the tight turn on that note Ackerman geometry is highly recommended.

2.1.1 Calculations

Maximum Turning Radius (R): 3000 mm.
   Length of the car (L): 1880 mm.
   Width of the car (d): 1093 mm.

Inner Wheel Angle (δ_i): $\text{Tan}(\delta_i) = L/[R - (d/2)] = 1880/[2800 - (1093/2)]$

Fig. 1 Geometry of steering
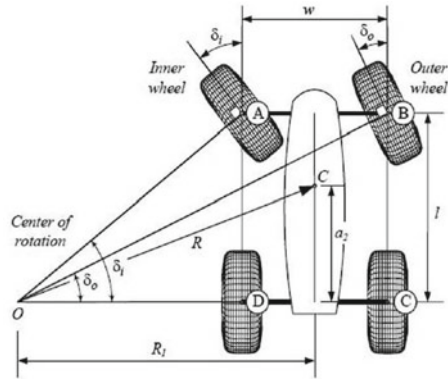
$\delta_i = 38.61°$.

Outer Wheel Angle(δo): $Tan(\delta_o) = L/[R + (d/2)] = 1880/[2800 + (1093/2)]$

$\delta_o = 29.32°$.

In first problem which we are facing in steering part is having a sliding joint in between steering wheel and tie rod that made it tough to rotate the steering wheel properly. We overcome this problem by changing the sliding pair into rolling pair which provide ease to the driver to rotate steering wheel smoothly. The specifications of steering system are given in Table 1.

In new system, we have mainly two bearing part.

1) Outer bearing.
2) Inner bearing.

Table 1 Steering system specification

Type of steering system	Ackermann steering (mechanical linkages)
Components	Steering wheel, steering rod, steering column, pitman arm, ball joint, tie rod
Main highlight	Carbon-fiber steering, wheel, Ackermann geometry
Freeplay	5°
Inner turning angle	38.61°
Outer turning angle	29.32°
Caster	Positive 12°
Camber	Negative 4–5°
King-pin inclination	0°
Tie rod length	330 mm
Steering wheel dimension	Rectangular (254*139.70 mm)

Table 2 Specification of braking system

Brake type	Single disc brake
Components	Disc, calipers, brake fluid, hose pipe, master cylinder, pedal
Disc outer DIA	240 mm
Disc inner DIA	190 mm
Caliper	TVS Apache 200
Brake fluid	DOT 3 or DOT 4
Brake force	8896 N
Pedal ratio	4:1
Master cylinder DIA	10 mm
Caliper piston DIA	25.4 mm

- **Outer bearing.** It is fixed and its act as supportive type.
- **Inner bearing.** It is moveable due to which steering rod move smoothly during steering wheel rotation and whole system is under support of wearing cla.

In earlier existing system, the roll hoop is much larger in size. So, we have removed the larger roll hoop and installed smaller roll hoop till the driver seat. We have removed excess material from the go cart in from of rectangular sheet to make it lighter and achieve the top speed in lesser time. For the events in which we were going to participate the criteria was to keep the weight of Go-Cart under 120 kg and our previous existing system was having 127 kg.

2.2 Braking System

In our existing Go-Cart, the existing braking system which was single control and rear braking but due to guidelines of event in which we were going to take part brake-by-wire system was prohibited. Therefore, we have used Dot3 and Dot-5 braking fluid [connecting link between Pedal and Pump(s)] which has to be doubled. (If we go for use of cable, which has minimum Φ of 1.8 mm and cable clip of flat chip type were able to block it.) Steel, stainless steel, or cast iron as per literature review is found suitable for making Brake Discs. The specifications of braking system are given in Table 2.

2.2.1 Calculations

Normal force applied on the pedal: 350 N.
Top speed: 60 kmph, 16.6667 mps.
Gross weight of vehicle (*W*): 160*9.81 = 1569.6 N.

Pedal ratio: 4:1.
Calculations:

Brake line pressure(p): force on the brakes divided by area of master cylinders:
(pedal ratio $*$ force on the pedal)divided by area of master cylinder
$= 4 * 350/[(\pi/4) * (0.01)2]$
$= 17.8343$ Mpa

Clamping force (cf) $=$ brake line pressure $*$ (area of caliper piston)^2
$= 17.8343 * 10^6 \left((\pi/4) * (25.4 * 10^{-3})^2\right)^2$
$= 18064.6825$ N

Rotating force (rf): cf $*$ no. of brake pads $*$ coefficient friction of brake pads
$= 18064.6825 * 2 * 0.4$
$= 4451.746$ N

Effective disc radius:inner radius $+$ (outer radius $-$ inner radius)/2
$= 95 + (120 - 95)/2$
$= 107.5$ mm
$= 0.1075$ m

Braking torque (tb): rotating force $*$ effective disc radius
$= 14451.746 * (0.1075)$
$= 1553.48$ N m

Braking force:(braking torque/tire radius)
$*$ road friction coefficient between track and dry tyre
$= (1553.48/0.2794) * 2 * 0.8$
$= 8896.092$ N

Deacceleration(a): braking force/mass :55.60 m/s^2

$$V^2 - U^2 = 2 * a * \text{ds} - (16.66672) = 2 * (-55.60) * d_s$$

$d_s = 2.5$ m.
Stopping distance (ds): 2.5 m.
The steering mechanism is meant to resist the stress of safely maneuvering the vehicle through any sort of possible condition at the time of driving. The purpose of the steering mechanism is to supply directional control of the vehicle with minimum input. The main goal for steering is to have steering radius of 3 m or less and to have 100% Ackerman steering.
Stopping Distance (d_s): 2.5 m.
As per our requirements we have selected following brake system for our Go Cart.

3 Conclusion

The analysis performed in this paper for steering and braking system of Go cart results in a safe design for fabrication.

References

1. Padhi A, Joshi A, Hitesh N, Rakesh C (2016) Increase factor of safety of go-kart chassis during front impact analysis. Int J Innov Res Sci Technol 3(04)
2. Nath A (2015) Design and fabrication of a go kart. Int J Innov Res Sci Eng Technol 4(9)
3. Pattanshetti VS (2016) Design and analysis of Go kart chassis. Int J Mech Ind Technol 4(1):150–164
4. Singh S (2016) Design and fabrication of race spec Go-kart. Am J Eng Res 5(6):48–53
5. Thavai R (2015) Static analysis of go-kart chassis by analytical and solid works simulation. Int Open Access J Modern Eng Res 5(4)
6. Raghunandan (2016) Design and analysis of Go-kart chassis. Int J Eng Sci Res Technol

Bending Strength Analysis of Involute Helical Gear Using FEA Software

Shashikant Pradhan, Hardial Singh, and Om Parkarsha

Abstract This paper investigates the simulation of helical gears with varying face width as per the applied transverse load to prevent the bending failure in the power transmission system. The symmetric involute profile of the helical gear has been established in KISSsoft software for more accurate precision in involute profile as it is a Gearbox designing software with a number of implementations of mechanical engineering. The drive side face of the helical gear has been introduced to simulate the meshing properties with fine elements and stress analysis with the use of FEA software, ANSYS 16.0. The numerical computation procedure for maximum bending stress on gear tooth has been estimated with concerning to the assistance of AGMA equations to find out the theoretical results of bending stress analysis which further validate with the simulation results to identify the percentage of error from the analysis. This paper also investigates the bending fatigue failure of alloy steel material with applied increasing load of solid models to find out the yielding point of the material.

Keywords Helical gear · AGMA stress · KISSsoft · SolidWorks · ANSYS

1 Introduction

Gear plays a vital role in transmitting power between the shafts. The design and manufacture of precision gears are made from high strength of materials, so that they will not miss carrying under static and dynamic loading during normal running conditions. It also succeeds as an improvement towards the function of gear speed and efficiency of the gearbox. The material of helical gears should be robust, corrosion resistance, lightweighted and should be durable for long period. The bending stresses and contact stresses have been found to be some of the major matter of concern for the designing of a helical gear pair. The deformation of helical gear can be perceived due to extreme bending stress condition at the root of the gear tooth. The problem can

S. Pradhan (✉) · H. Singh · O. Parkarsha
Amity University Haryana, Gurugram, Haryana, India
e-mail: sibushashikant@gmail.com; shashikant.pradhan232@gmail.com

651

be precisely solved on the minimization of bending stress and contact stress through modified geometry of the gear tooth in highly accurate gear designing software.

Gidado [1] performed the analysis of bending stress of the symmetric helical gear with corresponding to dissimilar face width gears with reference to the AGAM formulation. Deepak [2] investigated the characteristics of a helical gear system mainly focused on bending and contact stress using analytical and FEA. Gambhir et al. [3] found that as the drive side pressure angle increases, the contact stress on teeth reduces as compared to asymmetric involute helical gear. Bozca [4] estimated the gear load carrying capacity would be more if the helix angle of the gear tooth is more, and as a result, the increasing total contact ratio will cause the reduction in bending and contact stress on the helical tooth. Sonali et al. [5] considered five different gear materials to simulate the FEA software to find out the better material for the helical gear, while comparing with the numerical AGMA equation results. Patil [6] presented the work on study of effect of pressure angle and helix angle at root of helical gear tooth under dynamic state to reduce total bulk of the gear box. Miryam [7] obtained the critical value of stress and critical load condition have been obtained, and a complete analysis of the tooth bending strength has been carried out for bending load capacity of helical gear. Sarkar et al. [8] simulated the 3D model of gear in FEA software to find out the bending stress and compare with the AGMA stress. Simon [9] obtained results for the calculation of load and stress distribution in helical gear is developed. The number of tooth and the face width has the strongest effects on the load distribution factors. Jabbour [10] presented a method to calculate the distribution of the stress at the tooth root and of the bending stress is maximum on each line of a pair helical gear. Zeyin et al. [11] approached a mathematical model with practical engineering in which dynamic contact finite element method has been used for radiation noise prediction of gear system. He [12] covered the contact path and the function of transmission errors with misalignment, included the comparison of helical curve face gear and straight curve face gear.

2 Design of Gear

The extremely intricate part of any gear model is the involute profile of its teeth, which has been optimized with the approach of the gear design software KISSsoft modeller which provides all valid calculation of parameters such as profile shift coefficient, tooth thickness allowances, tolerances, backlash, clearances, and factors. In addition to validate the calculation with respect to required standards (ISO, DIN, AGMA, VDI) are available, it also offers various optimization of design and modification functions for better results. The integrated calculation of KISSsoft software provides the precise involute profile of gear tooth, and gear parameters are calculated based on [13] and represent the involute profile in Fig. 1. The ferrous material such type of having ALLOY STEEL (15Ni5Cr4Mo1) material properties of the gear is considered in Table 1.

Fig. 1 Involute profile of helical gear
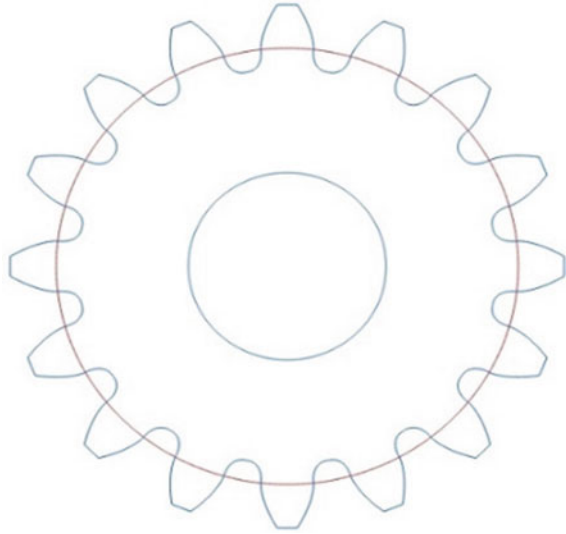
Table 1 Material properties of gear

S. No.	Description	Unit
1	Material type	ALLOY STEEL–15Ni5Cr4Mo1
2	Working temperature	850–1150
3	Tensile strength	1350 Mpa
4	Yield strength	720 Mpa
5	Density	7850 kg/m3
6	Young's modulus	210 GPa
7	Poisson ratio	0.3

To move along with the calculation of the helical gear parameters, the power of 22 KW with input speed of 1465 RPM has been considered to calibrate values of the helical gear which are tabulated in Table 2.

American Gear Manufacturing Association (AGMA) [14] stress theories have been established for calculation methodology for the tooth bending stress. An theoretical approach has been subjected to the parameters like the normal module, helix angle, gear teeth, speed of the gear, and power acting on the pinion shaft to compute the bending stress which depends upon the tangential force acting on the tooth. The theoretical values could be calculated as follows:

Transverse modulus (M_t):

$$M_t = \frac{M_n}{\text{Cos}\beta} \tag{1}$$

Table 2 Characteristics of helical gears

Variable name	Description	Value
Z	No. of teeth	16
M_n	Normal module	3
θ_p	Pressure angle	20
β	Helix angle	16
F	Face width	40
A	Addendum	3
B	Dedendum	3.75
D_t	Tip circle diameter	56
D_r	Root circle diameter	42.5

Pitch circle radius (PCR):

$$PCR = \frac{M_t \times Z}{2} \tag{2}$$

Tangential force (F_t):

$$F_t = \frac{T}{PCR} \tag{3}$$

AGMA bending stress formulae:

$$\sigma_{b1} = \frac{F_t}{F M_n J} \times K_v \times K_o (0.93 \times K_m) \tag{4}$$

To calculate the theoretical value of bending stress, Eqs. (1), (2), and (3) have been combined to evaluate the Eq. (4), and all the necessary factors have calculated from [15] with considering all type of graphs with various limitation such as overload factor (K_o) defined for uniform driven machinery with light shock source of power, velocity factor (K_v) considered after calculating the tangential velocity from the velocity factor graph, load distribution factor (K_m) considered according to loading properties of accurate mounting, small clearance, minimum deflection and precision between gear drives. Figure 2. shows the solid model of the helical gear having 40 mm face width generated in SolidWorks 2016 software.

3   Static Structural Analysis

In order to perform bending stress analysis on the helical gear assembly, a developed model of helical gear has shown in Fig. 2 and proceeded for simulation aside with distinctive face width to Ansys workbench in the static structural module in the

Fig. 2 CAD model of
helical gear

format of STEP. The 3D model has meshed in the static structural module of Ansys software. In this meshing, tetrahedron method has followed with fine quality of division in which the number of nodes and elements are shown in Table 3, and Fig. 3 shows fine-meshed elements of the 40 mm face width alike other four helical gears have meshed as like as the information given in Table 3.

From the above Figures, it is found out that maximum bending stress occurs at helical gear having 40 mm face width in Fig. 4 represents the von Mises stress of 208.92 N/mm², Fig. 5 represents the value of 181.55 N/mm², Fig. 6 represents the

Table 3 Number of nodes and element of varying face width of helical gear

Face width (mm)	40	45	50	55	60
No. of nodes	162,955	194,827	202,580	222,793	328,874
No. of elements	105,292	115,855	125,362	144,687	208,651

Fig. 3 Meshed model of
helical gear
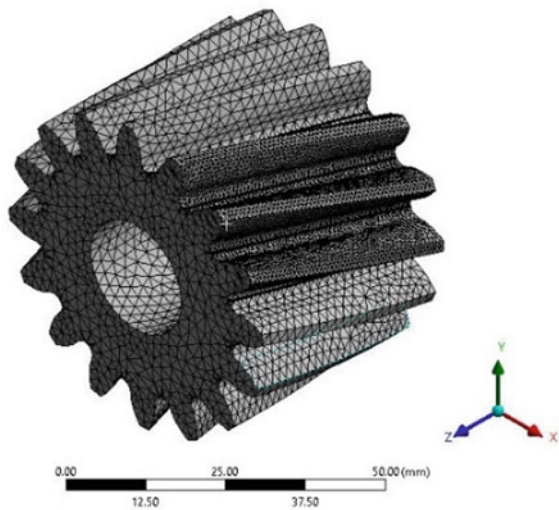
Fig. 4 Gear having face width 40 mm
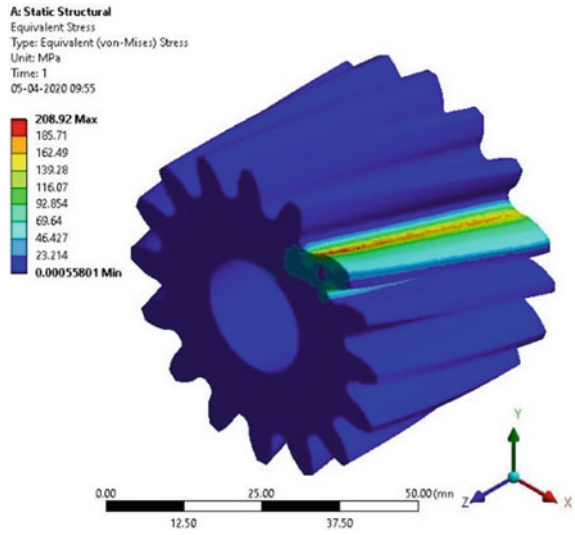
Fig. 5 Gear having face width 45 mm
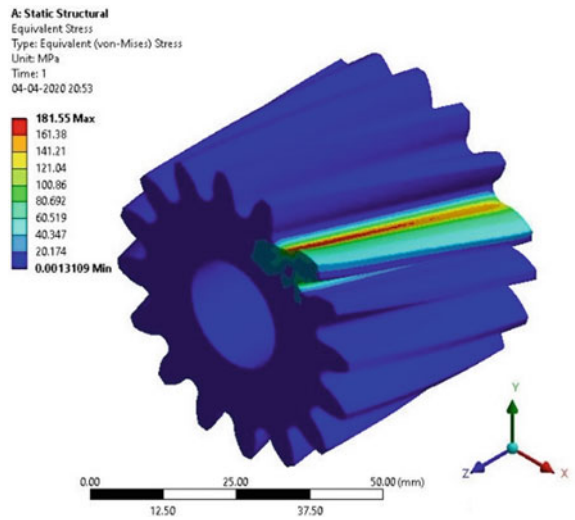
value of 163.45 N/mm², Fig. 7 represents the values of 142.7 N/mm², and Fig. 8 represents the value of 134.75 N/mm², and as a result, it found to be von Mises stress is occurring in decreasing order.

Fig. 6 Gear having face
width 50 mm
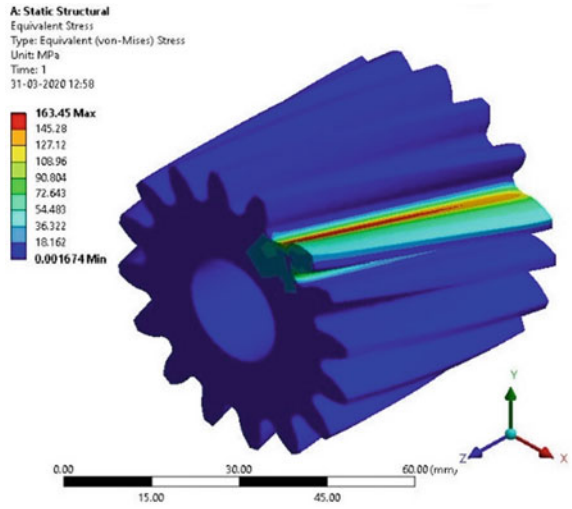
Fig. 7 Gear having face
width 55 mm
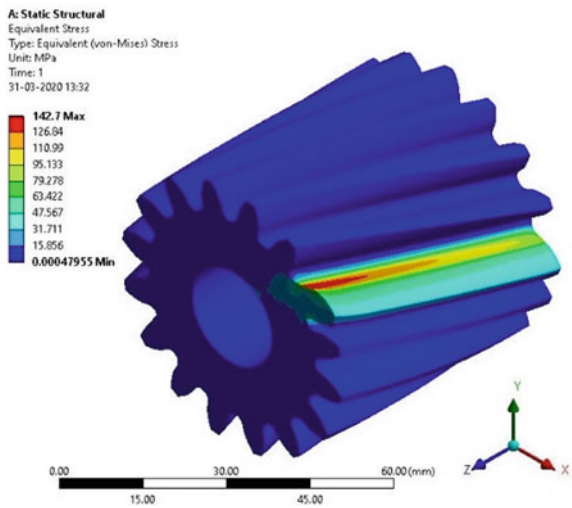
4   Results and Discussion

The use of KISSsoft software provides reports, accurate strength calculation, and
all valid calculation of parameters to modify the involute profile of helical gear.
KISSsoft provides reports and accurate strength calculation of the design, and the
comparison of results and percentage of error could be noticeable in both AGMA
and Ansys values from the simulation of helical gear in Table 4.

The above Table 4 describes that the percentage of error at 55 mm is maximum
which can be observed to be 6.12%. The reduction of von Mises stress can be detected

Fig. 8 Gear having face width 60 mm
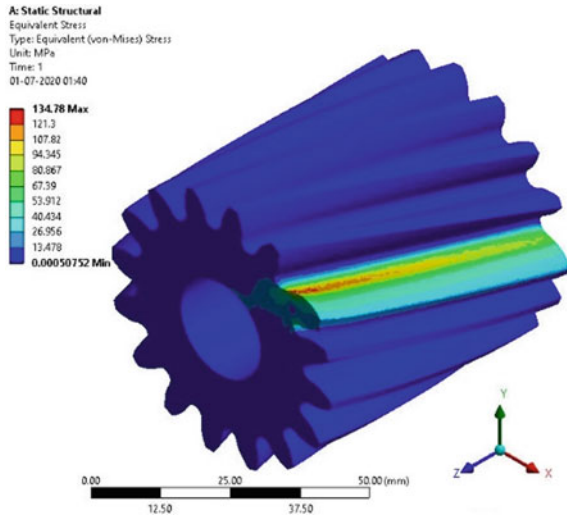
Table 4 Bending stress value for existing design

S/No.	Face width [mm]	AGMA [Mpa]	Ansys [Mpa]	Differences [%]
1	40	209.02	208.92	2.51
2	45	185.79	181.55	2.28
3	50	167.21	163.45	2.24
4	55	152.01	142.7	6.12
5	60	139.34	134.78	3.27

from face width 40–60 mm with a decrease of bending stress of 76.62 N/mm^2, while it has seen that gear with higher face width is convenient for any steady tangential load and speed.

Figure 9 shows the graph between the bending stress (Mpa) and face width (mm). From the graph, it can be seen that bending stress has reduced from 208.92 to 132.30 N/mm^2 due to the increasing amount in face width from 40 to 60 mm, as per the results 33.33% of stress reduction in theoretical approach (AGMA) and 35.48% in analytical values (Ansys). The computational accuracy found 2.31%, and overall reduction in error found to be 3.27%. It also defines a reciprocal relation between the bending stress and the face width.

5   Conclusion

The KISSsoft software was persuaded to procure the more accurate involute profile for the helical gear in Fig. 1 as it is specifically used for designing of the gearbox,
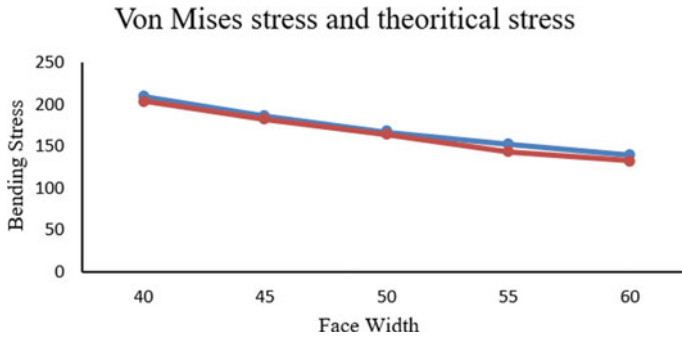
Fig. 9 Comparison of AGMA stress and Ansys stress at 5975 N of tangential load with increase in face width

onwards CAD models have been improvised in Ansys Workbench for simulation, which comprehends several assumptions and simplifications. The conclusion drawn from the simulated results is as summarized below:

- In finite element analysis, very fine-meshed has been the result of high accuracy in simulation values with accurate bending stress of the helical gears.
- The effect of increasing face width in symmetric helical gear reduces the stress concentration at the critical area of the gear.
- The maximum bending load distribution observed to be root fillet area of drive face, and the reduction in bending stress (Ansys) of helical gear creates to be 35.48% at 60 mm face width of the helical gear.
- According the course of action of this study, the design and modification of symmetric involute helical gear could be considered as an economical procedure for future aspects and optimization in reality.

References

1. Gidado AY, Muhammad I, Umar AA (2014) Design, modeling and analysis of helical gear according bending strength using AGMA and ANSYS. Int J Eng Trends Technol (IJETT). ISSN: 2231-5381
2. Deepak D Load sharing based analysis of helical gear using finite element analysis method
3. Gambhir J et al Effect of drive side pressure angle on load carrying capacity of asymmetric involute helical gear
4. Bozca M (2018) Helix angle effect on the helical gear load carrying capacity. World J Eng Technol 6(04):825
5. Sonali A et al Design and FEM analysis of helical gear
6. Patil PJ, Patil M, Joshi K (2018) Investigating the effect of helix angle and pressure angle on bending stress in helical gear under dynamic state. World J Eng
7. Sanchez MB, Pedrero JI, Pleguezuelos M (2013) Critical stress and load conditions for bending calculations of involute spur and helical gears. Int J Fatigue 48:28–38

8. Sarkar GT, Yenarkar YL, Bhope DV (2013) Stress analysis of helical gear by finite element method. Int J Mech Eng Robot Res. ISSN: 2278-0149
9. Simon V (1988) Load and stress distributions in spur and helical gears. pp 197–202
10. Jabbour T, Asmar G (2015) Tooth stress calculation of metal spur and helical gears. Mech Mach Theory 92:375–390
11. Zeyin H et al (2016) Parametric modeling and contact analysis of helical gears with modifications. J Mech Sci Technol 30(11):4859–4867
12. He C, Lin C (2017) Analysis of loaded characteristics of helical curve face gear. Mech Mach Theory 115:267–282
13. Maitra GM Handbook of gear design, 2nd edn
14. ISOigearistandards. https://www.iso.org/
15. Shigley JE (2011) Shigley's mechanical engineering design. Tata McGraw-Hill Education

Material Selection of the Frame of the Hybrid Agricultural Sprayer

Jasveer Kaur, Rythm Jain, Prakriti Saini, Komal, and V. K. Chawla

Abstract Selection of a suitable material is of prime importance in designing and fabrication of the hybrid agricultural sprayer. Material plays an important role as it affects factors such as function, mechanical properties, quality, manufacturability, endurance, performance and cost of the hybrid agricultural sprayer. In this research paper, the solid modelling of hybrid agricultural sprayer has been done on Solid-Works and suitable material is selected by comparing static structural analysis of aluminium, mild steel, stainless steel, epoxy carbon and epoxy E-glass UD-based frames on ANSYS workbench and properties such as density and yield strength. The deformation, equivalent stress and equivalent strain, obtained through analysis on ANSYS workbench, and other properties such as density and yield strength cost are compared for aluminium, mild steel, stainless steel, epoxy carbon and epoxy E-glass UD-based frames to determine the suitable material for the frame of the hybrid agricultural sprayer. Thus, by comparing aluminium, mild steel, stainless steel, epoxy carbon and epoxy E-glass UD-based frames, this research paper determines the appropriate material for the frame of the hybrid agricultural sprayer.

Keywords Agriculture sprayer · ANSYS workbench · Hybrid SolidWorks · Solar energy · Wind energy

J. Kaur (✉) · R. Jain · P. Saini · Komal · V. K. Chawla
Department of Mechanical and Automation Engineering Kashmere Gate, Indira Gandhi Delhi Technical University for Women, New Delhi, Delhi 110006, India
e-mail: jasveerkaur129@gmail.com

R. Jain
e-mail: rythmjain36@gmail.com

P. Saini
e-mail: prakritisaini@gmail.com

Komal
e-mail: komal.mor21@gmail.com

V. K. Chawla
e-mail: vivekchawla@igdtuw.ac.in

1 Introduction

To reap good yields, effective spraying of a number of chemicals is necessary in agricultural field. Adequate spraying of such chemicals can only be accomplished by use of a reliable and efficient sprayer. The performance of the sprayer to a huge extent is influenced by the material of the frame of the agricultural sprayer. Material plays an important role as it affects factors such as function, mechanical properties, quality, manufacturability, endurance, performance and cost of the hybrid agricultural sprayer. Therefore, selection of a suitable material is of prime importance in designing and fabrication of the hybrid agricultural sprayer.

Agricultural sprayer plays an important role in agricultural field, and the performance of the agricultural sprayer depends upon material of frame of agricultural sprayer. Early different types of agricultural sprayer used by the farmer such as backpack type sprayer, fossil fuel type sprayer, mechanical type sprayer and electrical type sprayer in which frame of such agricultural sprayer is made up by mild steel; hence, many analysis is done on different agricultural equipment by using different software such as SolidWorks, CATIA and ANSYS. Simulation is considered to be one of the best procedures to analyse and anticipate the performance of any system or component scrupulously without practically developing it in actual [1–4].

The paper by Karthik et al. [5] deals with the design and development of the solarized agro-based sprayer for rural application. A paper was proposed by Rajashekar et al. [6], and the aim of this paper was to design a three-row agricultural weeder in CATIA, to perform simulation at the frame of agricultural weeder on ANSYS, to calculate functional efficiency on loamy soil, clay soil and sandy soil and to reduce the cost of weeder in order to develop a low-cost weeder for small-scale farmer. The frame of the weeder was made up of mild steel which made its cost economical but increased the weight as well as power required to move the weeder. The paper by Bhanutej et al. [7] deals with the design and modelling of the agricultural sprayer. In this paper, the analysis of the sprayer was carried out to predict the stresses and deformation induced in the components of the sprayer. This paper suggested the use of the polyethylene as the frame material, but it is difficult to bond and flammable characteristics negated its lightweight characteristic Then an agricultural growth nourishing implementor is developed by Sujay et al. [8], and in this paper, solid modelling of model is done on CATIA V5 R20 modelling software, and different components of implementor are done on ANSYS. Also result is obtained by comparing theoretical result with ANSYS result. In the paper by Bhatkar et al. [9], an adjustable manually push operated pesticide spraying machine was proposed. The design and analysis of the machine were carried out to predict the stresses and deformation.

Ghumadwar and Banker [10] proposed a paper in which designing of three-stage low-cost crop cutter machine is done on Creo drawing software. Also in this research paper, in order to analyse force on rolling cutter blade of the crop cutter, a static and dynamic analysis is done on rolling cutter blade by importing crop cutter modelling from Creo in ANSYS workbench 14 software. The mild steel was used as a material for the frame. Meghana et al. [11] performed impact analysis on bumper and car

frame using different materials such as aluminium, stainless steel, structural steel and carbon epoxy. An impact analysis is performed using ANSYS workbench, and result is generated by comparing different materials such as aluminium, stainless steel, structural steel and carbon epoxy on deformation, stress-strain and weight basis. This paper suggested the use of aluminium, stainless steel, structural steel and carbon epoxy as material for the frame of the sprayer.

In order to analyse different components of agricultural sprayer for rose farming, a paper is proposed by Pramodh et al. [4]. In this research paper, an ANSYS workbench is used to analyse deformation, equivalent stress and equipment strain acting on different components of sprayer such as kart wheel, pulley and sprayer head due to application of tension and compression force on these components of the agricultural sprayer. Sagar et al. [12] proposed a paper which deals with design, analysis and fabrication of trolley type agrochemical sprayer. In this paper, UNIGRAPHICS software is used to perform geometric modelling, and then this geometric model is imported in the ANSYS workbench in order to study deformation, equivalent stress, equivalent elastic stain and type of material used for different components of the pesticide sprayer.

Later on, Saheb and Babu [3] developed a low weight agricultural robot. In this paper, carbon fibre is used as a material for frame of robot which analysis on ANSYS workbench and designing of robot done on CATIA V5 software. In the paper, by Subrahmanyam et al. [13], a grass cutting and water spraying rover was proposed. It is a four-wheeled device designed to go around fields, smartly irrigating the lands and trimming the grass. Apart from structural analysis of frame of robot, other components of agricultural robot are also analysed on ANSYS workbench. Pramod and Jithinmon [14] developed an agricultural robot which works on dual prismatic-revolute (PR). This paper also involved kinematic, static and dynamic analysis of the robot in ANSYS workbench which is used to determine the dimensions of dual arm. Also, in this research paper, C17 mild steel material is used for analysis, and to determine thickness of flange, static analysis is performed.

It is clearly evident from the literature review that tremendous amount of work has been done on the agricultural sprayer in the past. Most of the work has been done by considering mild steel as the material for the frame. But mild steel has heavyweight and is susceptible to corrosion. Consequently, greater power is required to impart motion to the agricultural sprayer. All of these disadvantages outweigh its advantage of being economical. In order to overcome the aforementioned research gap, this paper proposes to find a suitable material for the agricultural sprayer.

2 Methodology

This paper provides incite to design and simulate a hybrid agricultural sprayer. In research paper, suitable material for the frame of the hybrid agricultural sprayer is selected by comparing the deformation, equivalent stress and equivalent elastic strain, obtained through analysis on ANSYS workbench, and other properties such as

Fig. 1 Agricultural sprayer model
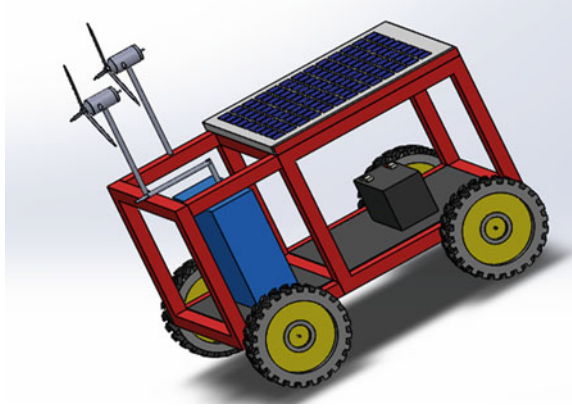
density and yield strength cost for aluminium, mild steel, stainless steel, epoxy carbon and epoxy E-glass UD-based frames. The designing of the model has been carried out on SolidWorks as shown in Fig. 1, and static structural analysis of aluminium, mild steel, stainless steel, epoxy carbon and epoxy E-glass UD-based frames has been carried out on ANSYS workbench. Then the frames based on materials such as structural steel, aluminium alloy, mild steel, epoxy carbon and epoxy E-glass UD are compared to choose the optimum material for the frame of the sprayer, on the basis of their equivalent elastic strain, equivalent stress, deformation, density, Poisson's ratio, tensile yield strength, tensile ultimate strength, weight and cost.

3 Structural Analysis

Structural analysis was done on the hybrid agricultural sprayer to find out the suitable material for frame of the agricultural sprayer. For this purpose, five materials were chosen and were analysed using the ANSYS software.

Static structural analysis was done initially on the following five materials:

1. Stainless steel
2. Mild steel
3. Epoxy carbon
4. Epoxy E-glass UD
5. Aluminium alloy

For the structural analysis of the geometry after the mesh generation process, backside of the frame was fixed, and the force of 400 N was applied in the negative Z-axis direction.

The results were generated for the following:

1. Deformation of the frame,
2. Stress on the frame,

3. Strain in the frame,

The deformation, stress and strain result obtained by static structural analysis of stainless steel is shown in Fig. 2, Fig. 3 and Fig. 4, respectively.
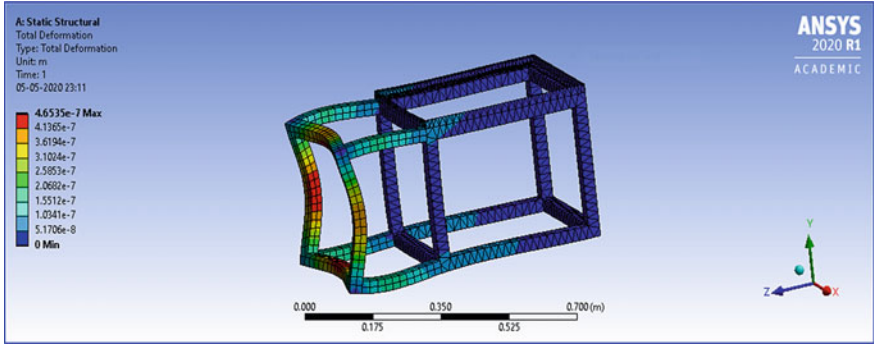
Fig. 2   Deformation of stainless steel
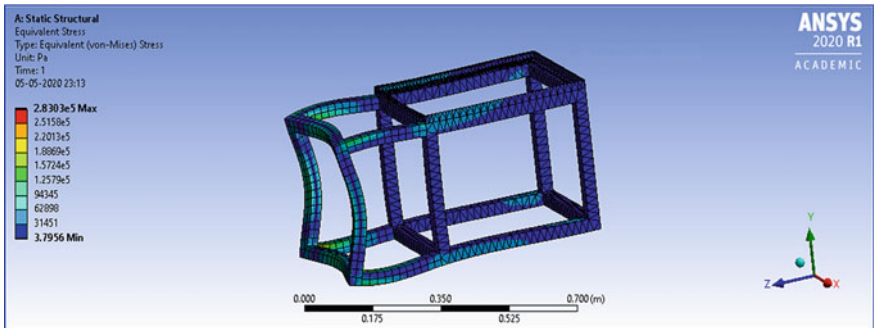
Fig. 3   Stress of stainless steel
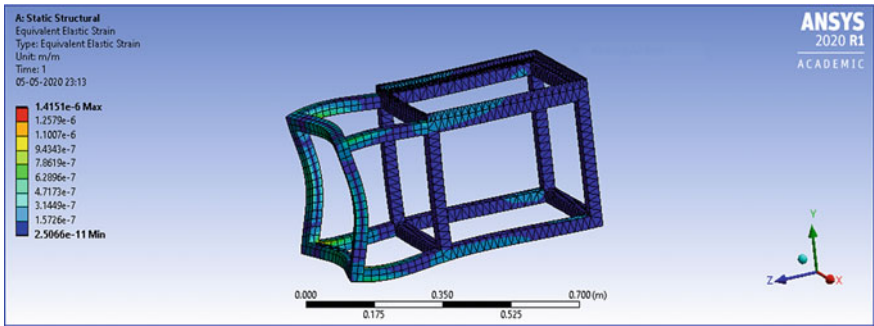
Fig. 4   Strain of stainless steel

The deformation, stress and strain result obtained by static structural analysis of mild steel is shown in Fig. 5, Fig. 6 and Fig. 7, respectively.

The deformation, stress and strain result obtained by static structural analysis of epoxy carbon is shown in Figs. 8, 9 and 10, respectively.
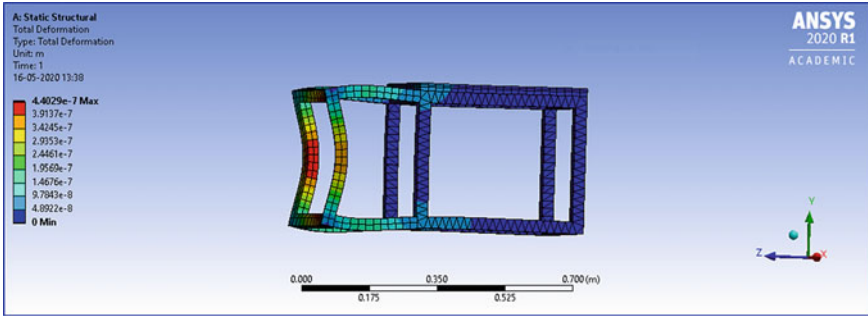
Fig. 5 Deformation of mild steel
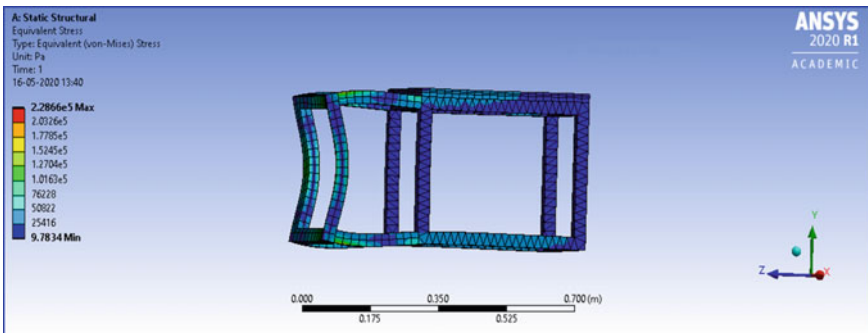
Fig. 6 Stress of mild steel
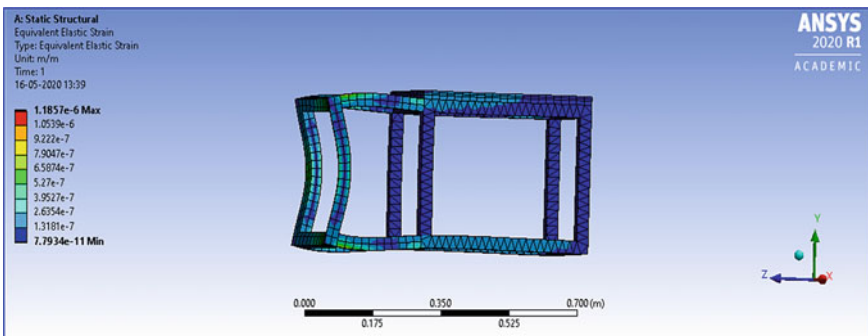
Fig. 7 Strain of mild steel
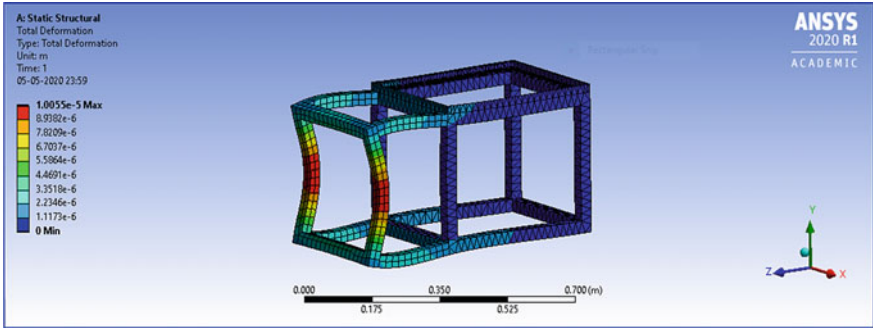
Fig. 8 Deformation of epoxy carbon
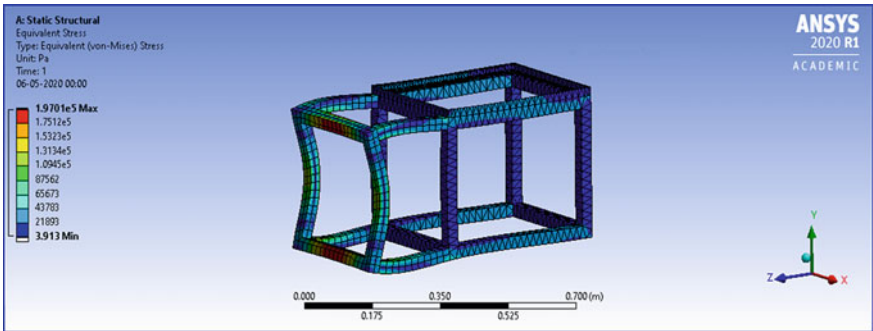
Fig. 9 Stress of epoxy carbon
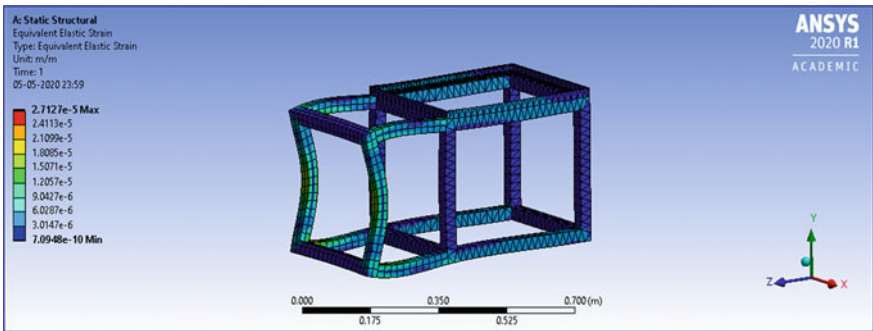
Fig. 10 Strain of epoxy carbon

The deformation, stress and strain result obtained by static structural analysis of epoxy E-glass UD is shown in Figs. 11, 12 and 13, respectively.

The deformation, stress and strain result obtained by static structural analysis of aluminium is shown in Figs. 14, 15 and 16, respectively.
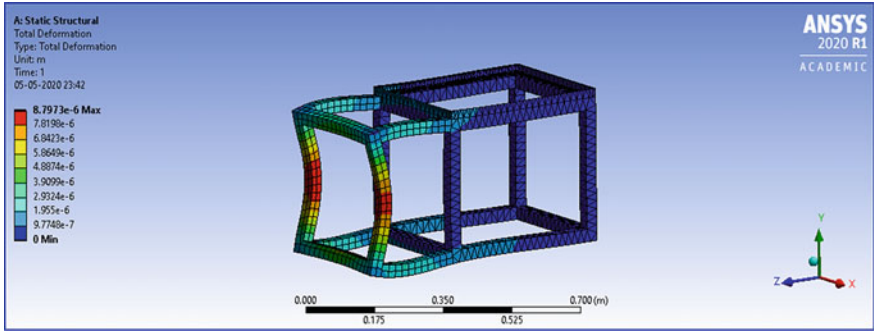
Fig. 11 Deformation of epoxy E-glass UD
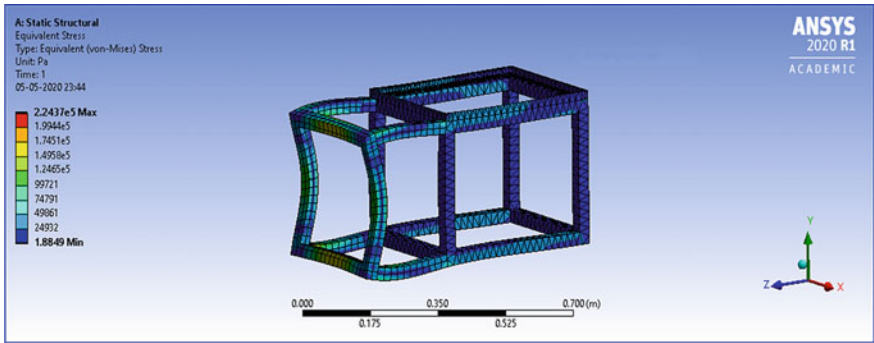
Fig. 12 Stress of epoxy E-glass UD
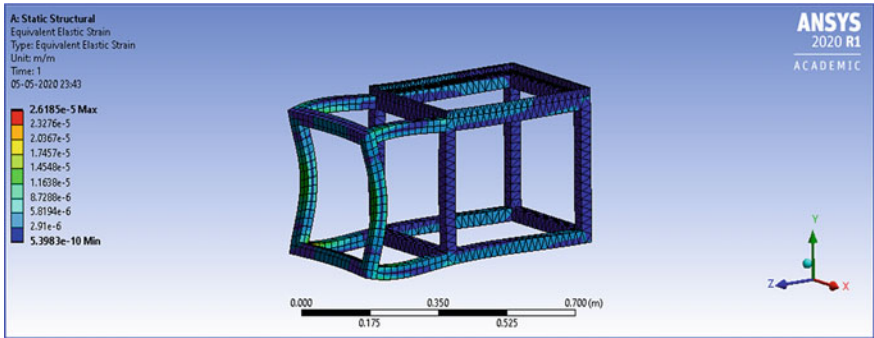
Fig. 13 Strain of epoxy E-glass UD
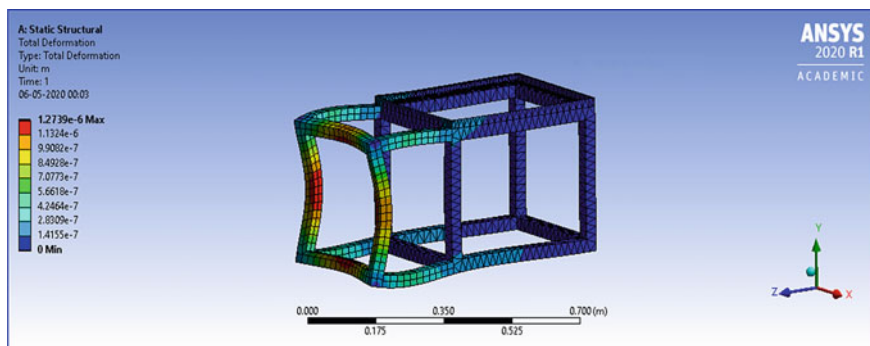
Fig. 14 Deformation of aluminium
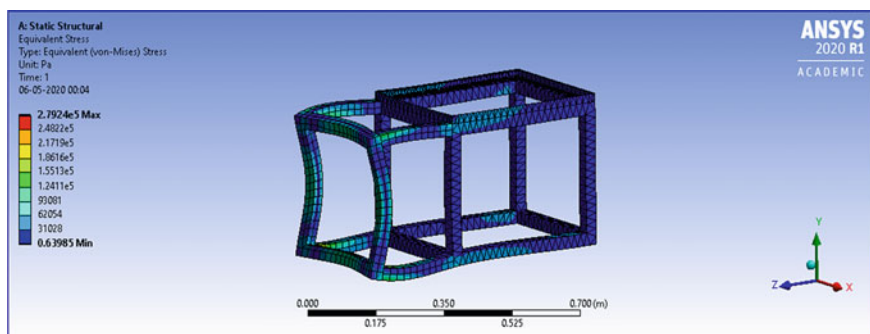
Fig. 15 Stress of aluminium
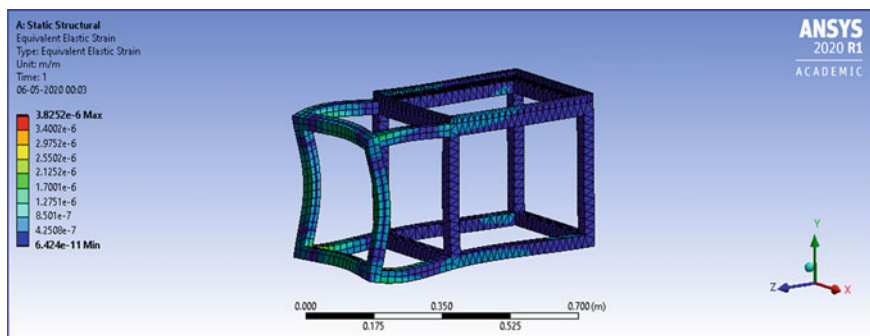
Fig. 16 Strain of aluminium

Fig. 17 Weight versus
strength
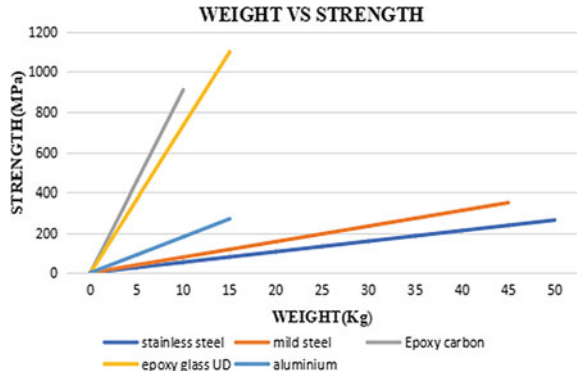
4 Result and Discussion

The graph of weight of sprayer versus the yield strength of material is plotted above as shown in Fig. 17. From the graph, it has been concluded that aluminium alloy is offering strength value very close to mild steel and its weight is very close to that of epoxy carbon. Therefore, aluminium alloy has been chosen as the most suitable material for the frame of the hybrid agricultural sprayer. The below graph in Fig. 18 depicts the relation between the cost and strength of different materials. Here, we can easily conclude that the cost of the material epoxy E-glass UD is the highest making it less economical to use in the fabrication of hybrid agricultural sprayer. This graph also corroborates to the statement made earlier that the best material to use for this hybrid agricultural sprayer is aluminium alloy.

Fig. 18 Cost versus strength
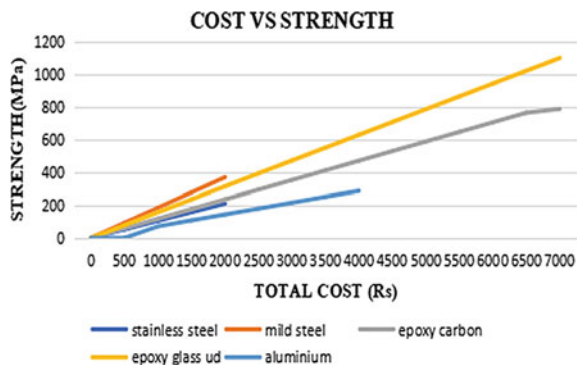
5 Conclusion

The comparison of different materials for frame is shown in Table 1, and from this table, it is observed that mild steel offers minimum deformation of $4.4029e^{-7}$m, stress of $2.2866e^5$ Pa and strain of $1.1857e^{-6}$ for the same load applied. However, it weighs 45 kg. Epoxy carbon offers minimum weight of 8.67 kg. However, it is costly as compared with other materials and might have availability issues in the market. Aluminium alloy gives deformation of $1.2739e^{-6}$ m, stress of $2.7924e^5$ Pa and strain of $3.8252e^{-6}$ that are very close to mild steel. Also, it weighs 15.604 kg and will be easily available in the market. Therefore, it is concluded that for the optimization of the material of the frame of hybrid agricultural sprayer, an aluminium alloy is chosen. Subsequently, this sprayer opens up the scope for improvements and augmentations:

1. Various other alloys and materials can be explored to serve as the frame material of the agricultural sprayer.
2. Dynamic analysis of these sprayers can be carried out to study the motion of the agricultural sprayer and to study the impact of forces.
3. The analysis of the frame can also be carried out by considering forces acting on the sides of the frame in case of impact as well as forces acting due to the weight of the components of the sprayer acting in downward direction.

Table 1 Comparison between different materials

		Stainless steel	Mild steel	Epoxy carbon	Epoxy E-glass UD	Aluminium
Deformation (m)	Minimum value	0	0	0	0	0
	Maximum value	$4.6535e^{-7}$	$4.4029e^{-7}$	$1.0055e^{-5}$	$8.7973e^{-6}$	$1.2739e^{-6}$
Equivalent stress (Pa)	Minimum value	3.7956	9.7834	3.913	1.8849	0.63985
	Maximum value	$2.8303e^5$	$2.2866e^5$	$1.9701e^5$	$2.2437e^5$	$2.7924e^5$
Equivalent elastic strain	Minimum value	$2.5066e^{-11}$	$7.7934e^{-11}$	$7.0948e^{-10}$	$5.3983e^{-10}$	$6.424e^{-11}$
	Maximum value	$1.4151e^{-6}$	$1.1857e^{-6}$	$2.7127e^{-5}$	$2.6185e^{-5}$	$3.8252e^{-6}$
Density (kg/m^2)		7850	7800	1600	2000	2770
Poisson's ratio		0.3	0.3	0.27	0.3	0.33
Tensile yield strength (MPa)		250	370	805	1100	280
Tensile ultimate strength (MPa)		460	400	1717	4800	310
Weight (kg)		47.5	45	8.675	11.645	15.604
Cost per kg		50	42	788	600	250

References

1. Chawla VK, Chanda AK, Angra S (2020) Evaluation of tool selection rules in the flexible manufacturing system. Int J Indus Eng Prod Res 31(1):131–142
2. Chawla VK, Chanda AK, Angra S (2019) Automatic guided vehicle systems in flexible manufacturing system–a review. Int J Indus Eng: Theory Appl Practice 26(5)
3. Himam S, Satish Babu Shaik G (2017) Design and analysis of light weight agriculture robot. Global J Res Eng [S.l.]
4. Pramodh R, Santhosh D, Manjesh KS, Lakshminarasimha N (2017) Concept, design, analysis and fabrication of pesticide sprayer for rose farming. Int J Sci Res (IJSR) ISSN (Online): 2319–7064 Index Copernicus Value (2015):78.96| Impact Factor:6.391
5. Karthik M, Jothibasu M, Pradeep E, Ganeshmurthy R, Kumar NA (2012) Design and development of SolarisedAgro Sprayer for rural applications. In: 2012 International conference on computing, electronics and electrical technologies (ICCEET), IEEE, pp 389–393
6. Rajashekar M, Heblikar VK, Mohan Kumar S (2014). Simulation and Analysis of Low Cost Weeder. International Journal of Research in Engineering and Technology eISSN: 2319–1163| pISSN: 2321-7308. Volume: 03 Special Issue: 03
7. Bhanutej JV, Phani Kumar S, Pradeep Kumar B (2015) Design and modelling of agricultural sprayer. Int J Eng Trends Technol (IJETT) 23(6)
8. Mithu Sujay S, Ullas R, Rajesh Babu BR, Vijay K (2015) Design and development of agricultural growth nourishing implementor (A.G.N.I). Int J Eng Res General Sci 3(4). ISSN 2091–2730
9. Akhilesh KB, Khope PB, Chaudhari PS (2016) Design and working of adjustable manually push operated pesticide spraying machine. Int Res J Eng Technol (IRJET) 03(12). e-ISSN: 2395 –0056, p-ISSN: 2395-0072
10. Ghumadwar RA, Bankar VH (2016) Des Anal Crop Cutter. Int Res J Eng Technol (IRJET) 03(07). e-ISSN: 2395–0056|p-ISSN: 2395-0072
11. M. Meghana, Ch. Shashikkuma, M. Pradeep kumar. (2016). Impact Analysis of Bumper and Car Chassis Frame Due to Frontal Collision for Different Materials. International Journal of Engineering and Management Research ISSN (ONLINE): 2250–0758, ISSN (PRINT): 2394-6962. Volume-6, Issue-1
12. Sagar SB, Punith G, Rakesh CN, Prakash MH, Lakshminarasimha N (2017) Design and development of trolley type agrochemical sprayer. Int Digital Library Technol Res Special Issue
13. Subrahmanyam RV, Vikas N, Prashanth BN (2019) Design and fabrication of grass cutting and water spraying rover. In: IOP conference series: materials science and engineering, IOP Publishing, vol 577, No 1, pp 012170
14. Pramod AS, Jithinmon TV (2019) Development of mobile dual PR arm agricultural robot. J Phys: Conf Ser 1240(1):012034

Experimental Study on the Influence of Material Properties of Dissimilar Aluminium Alloys on Formability Using Tensile Test

Praveen Kumar and Satpal Sharma

Abstract The dissimilar aluminium alloy sheets of 5xxx and 6xxx series are commonly used for the industrial applications in the marine, aerospace, and automobile sector due to its excellent physical and mechanical properties. In the present research, four dissimilar aluminium alloys (AA) such as 6082-T6, AA5083-O, AA6082-O, and AA5052-H32 having 2 mm thick sheets were used. The uniaxial tensile tests were performed to evaluate the plastic strain ratio (r), anisotropy (mean, normal, planar), strength coefficient (K), and strain hardening exponent (n) of materials. During the calculations of anisotropy, n, and K value, the samples were oriented at 90˚,45˚, and 0˚ with respect to the rolling direction of the sheet to determine the influence of material properties on sheet metal forming. It has been observed that the direction of the fracture line was completely dependent on the anisotropy ratio of blank in the tensile test. The comparative study has been made to evaluate the anisotropy, n, and K value of each aluminium alloys. It was found that these material properties were a good correlation with the formability effect of the sheets.

Keywords Tensile test · Anisotropy · Strength coefficient · Strain hardening exponent

1 Introduction

The anisotropy is a property of a substance which exhibits the physical properties of the material. Also, the anisotropy is dependent along several axis with respect to the rolling direction of the sheet metals. The anisotropy also clearly shows the effect on the texture, grain, and tensile strength of the material. The tensile test was performed to investigate the effect of temperature on mechanical properties

P. Kumar (✉) · S. Sharma
Gautam Buddha University, Gautam Buddha Nagar, Uttar Pradesh 201312, India
e-mail: praveen.jbm@gmail.com

P. Kumar
Delhi Institute of Tool Engineering, Okhla, New Delhi 110020, India

such as anisotropy. Aluminium alloy (AA)5754-O is used to investigate the mechanical behaviour during plastic deformation under different temperature. Many experimental tests have been done to check the mechanical behaviour during plastic deformation of the material. The monotonous tensile test were carried out from room temperature up to 200 °C with a tensile testing machine involving the heating of specimen by joule effect. The shear test was performed at the same temperature, which clearly shows the anisotropy coefficient is constant within the same temperature limits, with a variation of less than 8%. It was observed that the anisotropy properties have major effect on the formability of AA5754-O. It has maximum formability at above 150 °C temperature [1]. The elastic behaviour of the aluminium alloys such as AA5052-O and AA6016-T4 was determined by the tensile test, biaxial stretching tensile test, and tension–compression test. The R-value (planar anisotropy) exhibited by both the sheets, basically for the AA6016-T4 sheet, is extremely strong. The sheets of AA5052-O and AA6016-T4 show strong cyclic hardening with weak Bauschinger effect [2]. The effect of the material properties on the formability behaviour was disused in the review study. In this paper, they described the importance of the impact of the anisotropy, n, and K value on sheet metal forming operations. It was concluded that higher anisotropy value means high formability [3]. The material AA6061-T6 is used for structural applications in various aerospace and automotive industries because of its excellent mechanical and physical properties. To evaluate the effect of plastic anisotropy of the T6 (tempered with aged hardened) sheet on formabilty using a stretching test, It was observed that the direction of crack propagation affected by the plastic anisotropy in tension [4]. The material aluminium and lithium (Al–Li) were used to determine the effect of texture and grain size of the sheet on yield strength anisotropy under the tensile test. The experimental results clearly show the yield strength anisotropy reduced by the thermo-mechanical process. The yield strength anisotropy was mainly effected by the grain size and shape [5]. The aluminium alloy sheets are used to determine the effect of texture components on plastic anisotropy. The experimental and analytical results have clearly shown that the grain structure and texture of material have a valuable impact on the drawability of the aluminium sheet [6]. The material Al-12Si samples were used to investigate the effect of anisotropy in microstructure study using tensile test. The tensile test data were obtained from the experimental tests clearly shown that the mechanical properties of the material have not any influence on mechanical properties in the macroscopic level of Al-12Si [7]. The analytical and experimental study was made to compare the influence of temperature on anisotropy behaviour in sheet metal forming operation using AA6061-T4 material. It was observed that the temperature has a major influence on the thickness distribution of the sheet [8, 9]. In this present study, the anisotropy values, strength coefficient, and strain hardening exponent of dissimilar aluminium alloy sheets such as AA6082-O, AA6082-T6, AA5083-O, AA5052-H32 were calculated using tensile test with extensometer set-up. The uniaxial tensile tests were evaluated for correlation of the mechanical properties on the formability effect of the selected materials.

Table 1 Chemical composition of selected aluminium alloys

Alloys percentage	6082-T6	5083-O	5052-H32	6082-O
Manganese (Mn)	0.83	0.83	0.1	0.8
Iron (Fe)	0.60	0.48	0.48	0.60
Magnesium (Mg)	1.33	4.37	2.72	1.50
Silicon (Si)	0.30	0.10	0.25	0.30
Copper (Cu)	0.10	0.10	0.45	0.10
Zinc (Zn)	0.20	0.44	0.1	0.25
Titanium (Ti)	0.10	0.23	0.30	0.10
Chromium (Cr)	0.37	0.05	0.32	0.35

2 Materials and Methods

2.1 Material Characterization

Aluminium alloy (AA)6082 has excellent corrosion resistance, good weldability, highest mechanical strength due to the addition of the percentage of manganese alloys with aluminium. In this study, the different temper of AA6082 was used. AA6082-O implies the annealed condition or soft material that has the highest ductility. AA6082-T6 temper is then heat-treated by solution and ageing material. Another series of 5xxx aluminium alloys such as AA5083-O is a non-heat-treatable alloy, which has also highly corrosion resistive material. AA5083-O gains mechanical strength after the welding process. The 'O' temper implies the soft annealed material. AA5052-H32 is a medium-strength magnesium alloy, which has good formability and weldability property. The H32 temper implies that the strain hardened and stabilized. The main application of these aluminium alloys is used in automobile, irrigation, marine, and aerospace industries. Therefore, in this present study, four dissimilar aluminium alloys such as AA6082-O, AA5083-O, AA6082-T6, and AA5052-H32 having the same thickness of 2 mm were selected. The chemical composition of the dissimilar aluminium alloys was inspected by the energy-dispersive X-ray spectroscopy (EDEX) analysis method. The chemical composition of the aluminium and their percentages of alloys are illustrated in Table 1.

2.2 Anisotropy Calculation

There are a major contribution and influence of anisotropy in raising the material flow depending upon the material's mechanical properties. The formability of the specimen and its tensile strength can highly improve by appropriate selection of blank's orientation angle with respect to its rolling direction. The sheet's forming
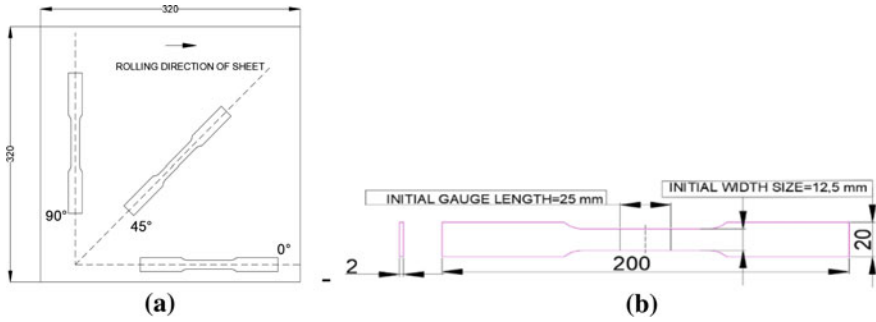
Fig. 1 **a** Specimens for the tensile **b** Full-size tensile

behaviour is indicated by its planar anisotropy, normal anisotropy, and on its plastic strain ratio.

2.2.1 Sample Preparation for Anisotropy Test

For preparing the tensile specimens, 2 mm thick blanks were taken, and the specimens were cut along the orientation, i.e. 0˚, 45˚ and 90˚ with respect to the rolling direction of the sheet as per the ASTM E8M-04 standard [5]. For checking the accuracy and repeatability of the result, three samples were prepared for each orientation. As shown in Fig. 1a, the tensile specimens were cut in a different orientation from the rolled sheet size of $320 \times 320 \times 2$ mm^3 using waterjet machining operation.

2.2.2 Determination of Anisotropy

Before the uniaxial tensile test, the width and initial gauge length of the tensile specimen were taken 12.5 and 25 mm, respectively. The 2D drawing of a marked size in the tensile specimen is shown in Fig. 1b.

During the tensile test process, both the ends of the tensile specimen were properly clamped and fixed on a universal testing machine (UTM) made by Tinius Olsen. Along with the longitudinal strain value, the maximum elongation of all the specimens was observed up to 15%. For the accurate measurement of length, width, and thickness strain values, the sensitive extensometer was used. The UTM with an extensometer setting were used. After performing the tensile test, the width strain and thickness strain values were calculated. These values, which were measured then, were directly used to calculate the plastic strain's value in 0˚, 45˚, and 90˚ orientation angle to the rolling direction of the sheet. The width and thickness of the specimen decreased when the total elongation increases. Until the UTS is reached, the value of anisotropy remained the same. Due to this reason, the elongation up to 15% of the longitudinal strain was observed in specimens.

The plastic strain ratio (r) is the ratio of true width ($\mathcal{E}_w$) to true thickness strain value ($\mathcal{E}_t$) given in Eq. (1). The value of r is calculating as per the ASTM E 517 standard [8].

$$r = \mathcal{E}_w / \mathcal{E}_t \tag{1}$$

where $\mathcal{E}_w = \ln(W_t/W_O)$ and $\mathcal{E}_t = \ln(t_t/t_O)$. Where W_t is the change in width, and W_O is the original width of the tensile specimen. t_t is a change in thickness, and t_o is the original thickness of the tensile specimen. By taking three directions, i.e. $0°$, $45°$, $90°$ to the rolling direction, the average value of r is obtained in the three directions. The normal anisotropy was calculated by using Eq. (2) [4].

$$R = \{r_0 + 2(r_{45}) + r_{90}\}/4 \tag{2}$$

where r_{90}, r_{45}, and r_0 are the anisotropy value for the $90°$, $45°$, $0°$. r_{90} is transverse to the rolling direction. r_{45} is the $45°$ to the rolling direction. r_0 is longitudinal to the rolling direction of the sheet. Planar anisotropy (earing tendency of the sheet) is also a directional property of the sheet metal. The earing was obtained by the planar anisotropy, and the formula for the planar anisotropy was calculated with Eq. (3) [3].

$$\Delta R = \{r0 - 2(r45) + r90\}/2 \tag{3}$$

2.3 Calculation of N and K Value Using Tensile Test

Strain hardening exponent (n) is conventional sign of formability or drawability of sheet metals. As per ASTM E646 standard, determining n and K in Holloman's Law from the tensile test result is given in the Eq. (4) [3].

$$\sigma = K\varepsilon^n \tag{4}$$

where $\varepsilon =$ true strain, $\sigma =$ true stress, $n =$ strain hardening exponent and $K =$ strength coefficient (MPa), which also approximates the relation between true strain and true stress, during deformation of the material. The role of n in sheet metal forming is very crucial. The more the value of n, the more elongation can be observed in the material before necking. The n value is equal to 0, it represents the perfectly plastic solid material, and $n = 1$ means the elastic solid for most of the material having a value of n between 0.1 and 0.5. In the case of the n value, it is found that the greater value of n represents the better stretchability of sheet, and the strain has distributed uniformly during dome height test. The failure of the sheet during stretching condition depends upon the n value. At higher value, better formability exists. The strength coefficient (K) is an experimental constant, which is calculated from the line fit of the data to

the true stress–strain curve. As per standard, ASTM E-646 represents the procedure to determine the values of *n* and *K* using a uniaxial tensile stress test.

3 Result and Discussion

3.1 Result for Plastic Strain Ratio, Anisotropy (Mean, Planar, Normal), Strength Coefficient, and Strain Hardening Exponent Values Using Tensile Test for Used Aluminium Alloys

The tensile tests were performed successfully. The specimens of AA6082-O, AA6082-T6, AA5083-O, AA5052-H32 with the orientation at 90°, 45°, 0° to the rolling direction of the sheet were prepared. The *r*, *R*, ∆*R*, *n*, and *K* values were calculated whose values are given in Tables 2, 3, 4, and 5 for different aluminium alloys such as AA6082-T6, AA5083-O, AA6082-O, and AA5052-H32, respectively. The average value of normal anisotropy for AA6082-T6 is 0.92, AA5083-O is 0.64, AA6082-O is 0.464, and AA5083-O is 0.537. It was also indicated that with higher *R*-value, there might be a reduction in the wrinkling of formed parts. At 45° and 90° orientation angle, the value of anisotropy is more than unity for AA6082-T6, which indicates that the thickness strain is lower than the width strain value. It is shown that the greater strength lies in the thickness direction and, generally, a resist to thinning. In remaining aluminium alloys, the *R*-value varies from 0.3 to 0.7 in all orientation, i.e. 90°, 45°, 0°, to the rolling direction of the sheet. It indicates the AA6082-O, AA5083-O, and AA5052-H32 have low *R*-values, which improves the formability of sheet. It was concluded that the *R*-value is lesser in annealed condition, i.e. AA5083-O and AA6082-O as compared to other tempered or heat-treated alloys, i.e. AA5052-H32 and AA6082-T6. It results that the formability is better in

Table 2 Material properties of AA6082-T6 under tensile test

Sample	Orientation	*r*	Mean of *r*	*n*	*K*	*R*	∆*R*
T1	0°	0.84	0.82	0.17	499.3	0.92	−0.1
T2		0.89					
T3		0.74					
T1	45°	1.07	0.98	0.15	442.3		
T2		0.85					
T3		1.01					
T1	90°	0.75	0.91	0.15	458.75		
T2		1.00					
T3		0.98					

Table 3 Material properties of AA5083-O under tensile test

Sample	Orientation	r	Mean of r	n	K	R	ΔR
T1	0°	0.64	0.60	0.44	595.03	0.64	−.003
T2		0.52					
T3		0.65					
T1	45°	0.73	0.67	0.40	580.56		
T2		0.64					
T3		0.66					
T1	90°	0.72	0.65	0.41	573.25		
T2		0.65					
T3		0.58					

Table 4 Material properties of AA6082-O under tensile test

Sample	Orientation	r	Mean of r	n	K	R	ΔR
T1	0°	0.44	0.43	0.29	235.35	0.43	0.08
T2		0.45					
T3		0.40					
T1	45°	0.43	0.38	0.28	229.24		
T2		0.42					
T3		0.31					
T1	90°	0.57	0.52	0.28	219.2		
T2		0.52					
T3		0.47					

Table 5 Material properties of AA5052-H32 under tensile test

Sample	Orientation	r	Mean of r	n	K	R	ΔR
T1	0°	0.58	0.564	0.25	344.92	0.537	0.01
T2		0.56					
T3		0.56					
T1	45°	0.48	0.527	0.23	333.22		
T2		0.49					
T3		0.60					
T1	90°	0.56	0.527	0.23	359.61		
T2		0.61					
T3		0.34					

the annealed condition. According to the result of planar anisotropy, the value of ΔR of AA6082-O, AA5052-H32, and AA5083-O is nearer to the zero. It indicates the minimum tendency to tear in the stretching test (dome height test) [6, 8]. AA6082-T6 has maximum ΔR value, i.e. 0.1. It means the earing tendency is more as compared to other aluminium alloys.

It is observed that the AA5083-O has maximum n value as compared to other aluminium alloys. The lesser strain hardening exponent value represents the increases in the formability of the sheet during dome height test [9, 10]. Similarly, the strength of materials depends upon the formability of the sheet. The lesser K value indicates more percentage elongation and less tensile strength of the material, which results in better formability of the sheet [3, 11]. AA6082-O has lesser K value means better formability as compared to other aluminium alloys.

4 Conclusions

From the finding of this present study, the following conclusion has been drawn.

1. During the tensile test, AA6082-T6 is higher anisotropy value than the other base materials such as AA 6082-O, AA 5083-O, and AA 5052-H32. The calculations of normal anisotropy have been used as an indicator of the formability. The average anisotropy values of AA6082-T6 were less than one, which leads to a reduction of its formability limit of the sheet.
2. The planar anisotropy value is directly related to the earing of the formed sheet. During the calculation of ΔR value for each aluminium alloy, it is found that the ΔR value is nearer to zero of AA6082-O and AA5083-O, and these alloys have less chance to the tendency of earing during dome height test as compared to remaining alloys
3. It is found that the greater value of n represents the better stretchability of sheet, and the strain has distributed uniformly during dome height test. AA6082-O and AA5083-O have maximum n value than other aluminium alloys. Both the materials have increased formability by 30% as compared to AA6082-T6 and AA5052-H32.
4. AA6082-O has least value of K means maximum formability as compared to other aluminium alloys. The minimum K value of AA6082-O was 235 MPa which has 65.4% of AA5052-H32, 39% of AA5083-O, and 47% of AA6082-T6.
5. It was concluded that these material properties were a good correlation with the formability of the sheet. With the help of the material properties, the effect on formability can be achieved before stretching test.
6. The value of mechanical properties of material helps to the right selection of orientation of sheet for the formability test and further use for friction stir welding tailor welded blanks.

References

1. Laurent JCCBH, Thuillier AAS (2011) The effect of temperature on anisotropy properties of an aluminium alloy. Soc Experim Mech 1185–1195. https://doi.org/10.1007/s11340-010-9415-6
2. Tamura S, Sumikawa S, Uemori T, Hamasaki H, Yoshida F (2011) Experimental observation of elasto-plasticity behavior of type 5000 and 6000 aluminum alloy sheets. Mater Trans 1(52):868–875
3. Sivam SPSS et al (2017) Overview and assessment of formability effect of material properties of sheet metal—a short communication. Jr Ind Pollut Control 33:1732–1738
4. Barnwal VK, Tewari A, Narasimhan K, Mishra SK (2016) Effect of plastic anisotropy on forming behavior of AA-6061 aluminum alloy sheet. J Strain Anal Eng Des 51:507–517
5. Cho KK, Chung YH, Lee CW, Kwun SI, Shin MC (1999) Effects of grain shape and texture on the yield strength anisotropy of Al-Li alloy sheet. Scr Mater 40:651–657
6. Hu J, Ikeda K, Murakami T (1998) Effect of texture components on plastic anisotropy and formability of aluminium alloy sheets. J Mater Process Technol 73:49–56
7. Maity T, Chawake N, Kim JT, Eckert J, Prashanth KG (2018) Anisotropy in local microstructure – Does it affect the tensile properties of the SLM samples. Manuf Lett 15:33–37
8. Laurent JCCBH, Thuillier AAS (2011) The effect of temperature on anisotropy properties of an aluminium alloy. Int J Mat Form 1185–1195. https://doi.org/10.1007/s11340-010-9415-6
9. Laurent H et al (2011) Mechanical behaviour and springback study of an aluminium alloy in warm forming conditions. ISRN Mech Eng
10. Green SJ, Langan JJ, Leas JDA, Yang WH (1971) Verti. Material properties, inslucing strain rate effect as related to sheet metal forming. Metall Trans 0.25(2)
11. Frodal BH, Morin D, Børvik T, Hopperstad OS (2020) On the effect of plastic anisotropy, strength and work hardening on the tensile ductility of aluminium alloys. Int J Solids Struct 188–189:118–132

Experimental Investigation of Parabolic Trough Collector Using Cut Tube Receiver and Chronological Tracking

Karan Motwani and Jatin Patel

Abstract A small-size parabolic trough collector (PTC) can be a suitable option for low- and medium-temperature industrial process heating (IPH) applications. The major hindrance of PTC technology is cost, which is not much competing with the conventional technologies available in the market. There are three major components in PTC, which affect the total cost of the system, such as the receiver tube, reflector, and tracking system. In this paper, a novel cut tube receiver and low-cost chronological tracking system are developed and tested experimentally. A novel receiver tube is designed to reduce the total surface area, which ultimately helps to decrease losses. The performance of the novel tube is studied with and without insulation on the upper part of the tube. Furthermore, to boost the performance of PTC, an electric linear actuator with a microcontroller is used to track the sun movement of 0.5° at an interval of 2 min. The potential of the novel receiver tube and linear actuator was examined by determining the stagnation temperature of the PTC system. Experiments were conducted using working fluid as sigma therm-K. Results declared from the experiments reveal a maximum stagnation temperature of 142.26 °C with no insulation and 169.96 °C with insulation on the upper part of the tube.

Keywords Cut tube receiver · Chronological tracking · Parabolic trough collector · Stagnation temperature

1 Introduction

In India, coal and oil are the primary source of fuel to meet the energy demand of the country. A major drawback connected with the usage of coal and oil is importing

K. Motwani (✉)
School of Technology, Pandit Deendayal Petroleum University, Gandhinagar, India
e-mail: karan_motwani19@yahoo.com

Mechanical Engineering Department, Marwadi University, Rajkot, India

J. Patel
Mechanical Engineering Department, School of Technology, Pandit Deendayal Petroleum University, Gandhinagar, India

this energy from other countries. India's import dependency on coal is 36%, and oil is about 85% of its total energy needs in 2016 [1]. Figure 1 shows the contribution of primary fuel-wise energy statistics. Recently, the government of India has set targets for reducing oil import of 10% by 2022 and then 50% by 2030 [2]. Also, India's CO2 emission has cross 2.5 gigatons, which is around 6.5% of the whole world emissions [3].

India's industrial sector is found to be consuming the highest share of energy from the total energy generation. It can be noted from Fig. 2 that industrial sector alone consumes 57% of the total energy generation [4]. Figure 2 shows the sector-wise energy consumption of India.

Thermal energy (heat) required in the industrial sector is termed as IPH. The industrial sector consumes about 40% of thermal energy for process heating applications. Out of which, 30% is used for applications below 100 °C, 27% is used for temperature range 100–400 °C, and 43% is used for temperature range above 400 °C [5]. The need for thermal energy in industry is fulfilled by using boilers such as gas-fired (65%), oil-fired (28%), and electric (7%) [6]. Furthermore, IPH applications are divided into three categories based on temperature as low, medium, and high. The application below 80 °C is low temperature, 80–250 °C is categorized as medium temperature, and requirement of more than 250 °C is counted for high-temperature application. It is estimated that low- and medium-temperature industries have almost two-thirds of the thermal energy requirement below 250 °C [7].

Emphasizing the use of solar energy under such conditions for IPH applications can be boon for developing countries like India to overcome the challenges of conventional fuel and issues related to its use. Furthermore, solar is a nonconventional, pollution-free, and being a natural source of energy [8]. Therefore, in this research

Fig. 1 Primary fuel-wise energy statistics [4]
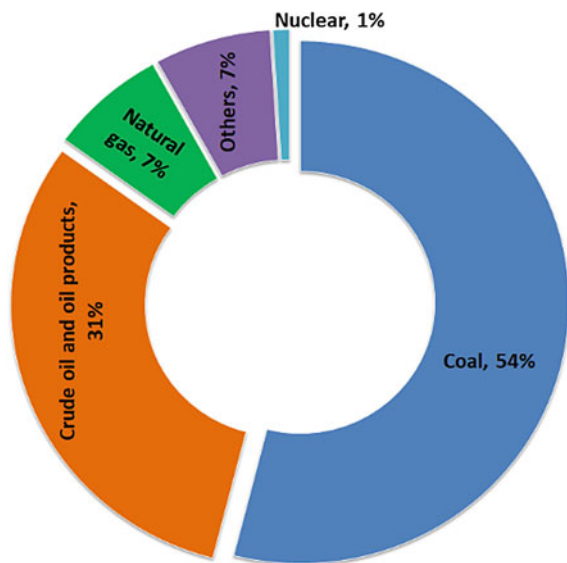
Fig. 2 Sector-wise energy consumption of India [4]
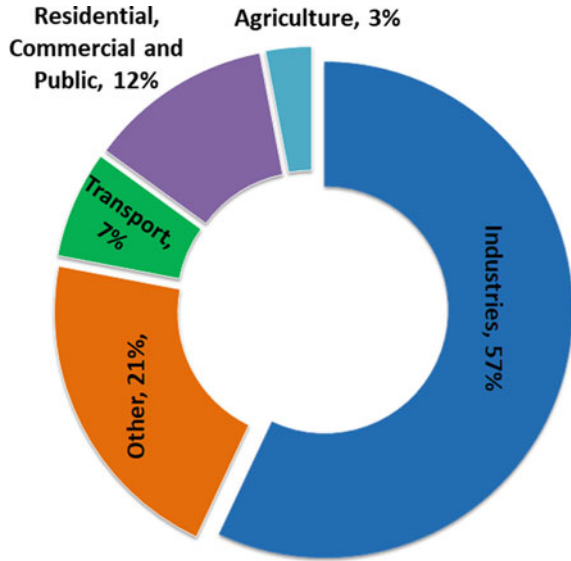
work, the attention pertaining to the use of solar energy for the IPH is carried out. Additionally, the share for maximum thermal energy demand is below 250 °C, so focus on low- and medium-temperature IPH is selected. Furthermore, concentrating collectors such as PTC are more appropriate solar collector for low and medium temperature IPH applications [9]. The parabolic dish and solar tower are capable of generating thermal power above 250 °C, which can be more favorable for high-temperature IPH applications. Therefore, the maximum process heating requirement between 80 and 250 °C of the industrial sector can easily be thermally powered by the use of PTC.

2 Literature Review

In earlier times, the attention on solar concentrating technology was negligible for many years. However, in the 1970s, the oil crisis in many countries and growing environmental impact has made it mandatory to find some alternative options of fossil fuel for sustaining the world and that causes the development of several solar collectors.

Later in the 1980s, this technology has managed to enter the market for small IPH, and some American companies manufactured and marketed a number of PTCs. Further, the commercialization of a PTC was divided into two categories based on temperature requirements. A large-size PTC is counted as one of the big achievements of LUZ international. They developed three PTC designs named as LS1, LS2, and

LS3. These types of collectors were capable of generating a temperature range above 300 °C, which can be used directly or indirectly in a steam power plant.

In the late twentieth and early twenty-first century, R&D was also initiated to develop small-size PTC. Collectors producing temperature below 300 °C were called as small-size PTC. Such collectors were designed for a wide variety of applications like IPH, space heating, swimming pool, etc. There are three major components in PTC, which affect the total cost of the system, such as the receiver tube, reflector, and tracking system. While talking about PTC, a receiver tube is considered to be the heart of the system. Generally, the receiver tube is covered with a vacuum glass tube, i.e., an evacuated tube for reducing the heat losses. The use of such an evacuated tube is highly preferable for high-temperature applications (above 300°C) in which the receiver tube generates higher surface temperature [10]. It is one of the critical components of PTC from the efficiency and cost aspect. The price of the evacuated tube in 2010 was estimated about 850 Euro/unit (nearly Rs. 51,500 in Indian currency). Till 2010, only three manufacturers of the evacuated tube were available in the market [11]. The problem of evacuated tube costs and limited manufacturers may directly affect to high system cost. This can be measured as one of the biggest reasons for less penetration of this technology in the market.

The use of an evacuated tube in PTC can be eliminated for low and medium applications due to lower surface temperature. This provides an opportunity for research to improve the performance of PTC without using an evacuated tube. The main objective of the paper is to employing PTC technology for low- and medium-IPH applications by cost-cutting technologies. The following objective has been an attempt by developing a novel cut tube receiver and a low-cost chronological tracking system.

In the next subsequent sections, discussion on cut tube receiver and chronological tracking system has been discussed.

3 Cut Tube Receiver

The convection and radiation heat losses are proportional to the surface area of the receiver and its temperature. In the working of PTC, the upper part of the receiver tube does not receive the concentrated radiation. The parametric analysis was conducted with three different cuts, such as 50, 45, and 40%, and compared the percentage change in area with the uncut tube. The analytical results show that under practical conditions, the 45% cut receiver tube is more preferable as compared to rests [12]. Therefore, in this study, the upper portion of the cut tube receiver is cut by 45%, and then it is closed by welding with a mild steel plate, as shown in Fig. 3. The cutting of the receiver tube helps to reduce the losses by decreasing the total surface area of the tube. Also, a mild steel plate at the upper portion of the tube causes temperature difference at the up and down portion of the receiver tube. Figure 3 shows the cross-section of the cut tube receiver.

Fig. 3 Cross-section of cut
tube receiver
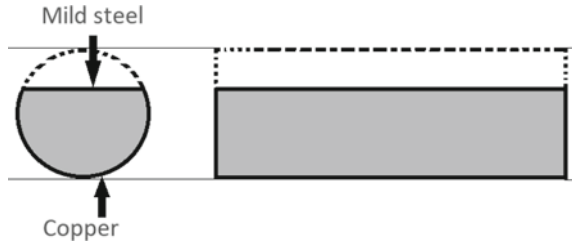
4 Tracking System

The transformation of solar energy into thermal or electric energy is thorough with the help of the solar collector. The maximum output generated by these solar collectors depends on the amount of solar energy collected by the system [13]. A solar tracker is considered as ideal devices for capturing maximum available solar radiation from the sun and improves the performance of these solar collectors. There are mainly three types of energy losses in solar PTC, such as thermal, optical, and cosine. The thermal loss is basically due to the temperature difference between the receiver tube and ambient. Optical loss is caused by the materials of the glass envelope and reflector. The cosine loss can reach up to 50%, which happens due to the non-zero angle of incidence of solar radiation. This issue generally arises due to improper tracking of the solar collectors [14].

Solar trackers are mainly of two types: (i) single axis and (ii) double axis. A single-axis tracking system tracks the path of the sun from one side to another through a single hinge point for rotation. The single-axis tracker is mostly suitable for line focusing collectors.

The single-axis tracker is simple to design, installed, and inexpensive, but efficiency is less as compared to the dual-axis. While to reduce the cosine angle losses, a dual-axis solar tracking system should be used. The dual-axis tracker is mostly suitable for point focusing collectors such as parabolic dish and power tower. This type of system provides a higher degree of accuracy due to rotations in the horizontal and vertical axis, which also makes the system complex and costly [15].

Gaafar and Zobaa [16] compared the performance of solar PTC experimentally with dual-axis tracking and fixed axis. Two types of experiments were conducted with and without the flow of heat transfer fluid (HTF) as water. Under the no-flow condition, an increase in thermal energy was found at about 54.25%, whereas 50.59% was noted in flow condition. The authors concluded that the performance of the dual-axis tracking is found more superior to the fixed axis. Kalogirou [17] designed and constructed a single-axis tracking system using a light-dependent resistor (LDR) and DC motor. LDR was used to identify the status and position of the sun. The received signal is fed to a control system that is used to operate a dc motor. The power of a DC motor via a speed reduction gearbox helps to rotate the collector. The cost of the tracking system was estimated about US$ 250.

Sun et al. [18] investigated an optimized double-axis (O2A) tracking for small-scale PTC under practical and theoretical conditions. The proposed O2A strategy will allow the motor running twice a day instead of the long run, and a rotating frame would be stable against wind load for a long time due to automatic lock. The experiment results show a higher heat gain of about 68.8% and improvement in the collector efficiency of 15~17% as compared to single-axis tracking.

Hafez et al. [19] presented a broad review of solar tracking systems and their prospective for different solar applications. The authors have broadly reviewed different solar tracking drive types and technologies also. The review paper concluded that nearly 42.57% of studies had been done on single-axis tracking, and 41.58% of studies are conducted on a dual-axis tracking system till 2018. The use of active tracker as a solar drive in tracking was found highest around 76.42% then followed by the chronological type.

Solar tracking has excellent potential for improving collector thermal efficiency. Concentrating collectors such as line focus are recommended for single-axis tracking, and point focus collectors should pursue with dual-axis tracking. Many researchers have attempted different types of drives and techniques used in solar tracking. The selection of proper solar tracking is dependent upon the type of solar applications, operating temperature, and cost. The cost of solar tracking is an additional cost to the total system, which can be considered as one of the significant factors. Major literature review for solar tracking has been focused on large-scale plants using solar PTC. For improving the performance of small-size solar PTC which can be implemented for low- and medium-temperature applications, using solar tacking may require lots of research studies.

In this study, the single-axis tracking system has been designed and developed for improving the performance of PTC. Tracking of east-west was done continuously, and north-south (tilt angle) was set for a particular day.

5   Experimental Setup and Procedure

The testing apparatus consists of five main components. Table 1 represents the specification of PTC. First, a parabolic frame made from square pipes bent according to the required parabolic design, second, the circular shaft on which the frame is mounted, allowing certain degrees of freedom to accommodate solar tracking during the day, third, a receiver tube that is mounted at the focal point of the parabola to achieve a line concentration along the path of the tube, fourth, set of mirrors with high reflectivity to increase the solar concentration, moreover, lastly, an electrical linear actuator which is responsible for the precise movement of the parabolic frame along with the receiver tube to achieve accurate tracking. The whole system is mounted on a structure to provide rigidity to the system. Figure 4 shows a PTC experimental setup for single-axis tracking.

The receiver tube was partially filled with HTF as a sigma therm-K. To register the temperature changes along the tube and inside the fluid, a total of eight sensors are

Table 1 Specification of PTC

Parameters	Value
Collector aperture	2.03 m
Aperture area	2.36 m^2
Receiver area	0.09 m^2
Rim angle	90°
Focal distance	0.50 m
Receiver outside diameter	0.05 m
Concentration ratio	12.61

Fig. 4 PTC experimental setup for single-axis tracking
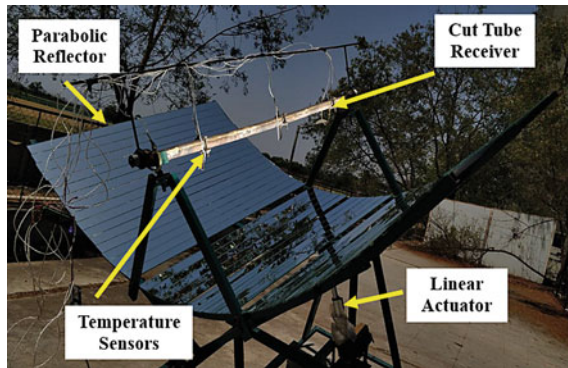
placed, among which two are placed at each end of the receiver tube to measure the temperature of the fluid inside it. Six sensors are placed on the surface of the tube. To accumulated data and increase its reliability, Arduino board, along with PLX–DAQ program, is used which allows data registration at an interval of 1 s from each of the eight sensors mounted on the tube.

In this study, an electric linear actuator is used along with a microcontroller to operate the PTC system, which enables tracking the movement of the sun from east to west. This inclusion of electric linear actuator helps to gain the maximum energy from the sun and to reduce the price of the solar tracking system. Moreover, using an Arduino and relay circuit provided an accuracy of 0.5° moment for the parabolic frame along with its receiver tube. The Arduino program is set to operate the actuator with an interval of 2 min, which results in the precise movement of 0.5° of the PTC.

6   Result and Discussions

Two experiments were conducted using a cut tube receiver with and without insulation. The experiments were conducted in the month of February, March, and April 2019. The reason for not able to conduct in a particular single month was due to weather conditions.

Primarily, the experiments were conducted using the receiver without insulation. The total five experiments were performed for the duration in between 2.5 and 3.5 h. The maximum surface and fluid temperature were noted on 18 February 2019, with the intensity of solar radiation about 1008 W/m^2. Figure 5 shows solar radiation versus fluid/surface temperature for cut tube receiver without insulation. Laterally, the experiments were conducted using a receiver with insulation. A total of five experiments were performed for the duration in between 2.5 and 3.5 h. The maximum surface and fluid temperature were noted on 29 March 2019, with the intensity of solar radiation about 1007 W/m^2. Figure 6 shows solar radiation versus fluid/surface temperature for cut tube receiver with insulation. Tables 2 and 3 represent the stagnation temperature test without and with insulation on the cut tube receiver.

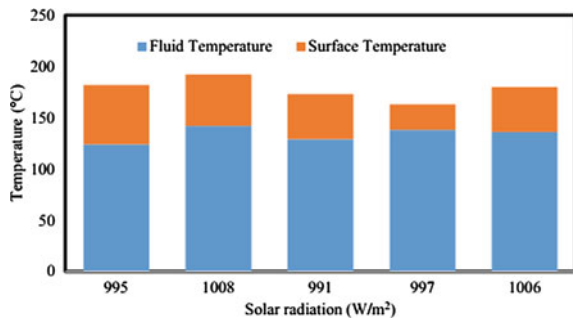**Fig. 5** Solar radiation versus fluid/surface temperature for cut tube receiver without insulation

Fig. 6 Solar radiation versus fluid/surface temperature for cut tube receiver with insulation
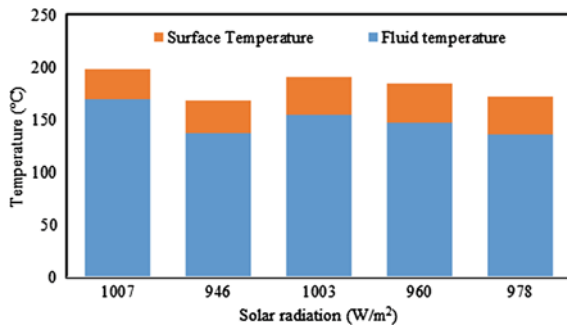
Table 2 Stagnation temperature test without insulation on the cut tube receiver

Date	Start time (am)	End time (pm)	Solar radiation (W/m^2)	Wind speed (m/s)	Tilt angle (θ)	Maximum surface temp. (°C)	Maximum fluid temp. (°C)
16/2/19	11:10:36	14:37:13	995	2.3	36.8	181.79	124.96
18/2/19	11:01:50	14:38:02	1008	1.6	35.2	192.11	142.26
19/3/19	11:27:48	14:36:52	991	1.9	29.6	173.41	129.82
22/3/19	10:51:10	14:39:40	997	2.3	28.4	163.24	138.53
23/3/19	10:56:14	14:31:49	1006	1.6	27.7	180.25	136.8

Table 3 Stagnation temperature test with insulation on the cut tube receiver

Date	Start time (am)	End time (pm)	Solar radiation (W/m^2)	Wind speed (m/s)	Tilt angle (θ)	Maximum surface temp. (°C)	Maximum fluid temp. (°C)
29/3/19	11:01:25	14:26:08	1007	1.4	22.9	197.74	169.96
30/3/19	10:54:25	14:14:30	946	4.6	22.1	167.76	137.26
01/4/19	11:04:42	14:15:18	1003	1.9	21.6	190.73	153.94
05/4/19	10:49:39	14:38:25	960	2.7	20	183.97	146.54
06/4/19	10:58:32	14:30:22	978	3.5	19.4	171.29	135.19

The experiment results also indicate that the intensity of solar radiation and wind speed has a significant effect on achieving maximum temperature. The total cost of the cut tube receiver and chronological was estimated about Rs. 7750.

7   Conclusion

In this study, an experimental approached was conducted to investigate the effect of cut tube receiver and chronological tracking on the performance of the PTC. The aim of designing a cut receiver tube was to reduce the surface area and its temperature. A chronological tracking system was built to track the path of the sun by 0.5° at an interval of 2 min. The stagnation temperature test was conducted for the bare cut tube receiver with and without insulation. Following results of the experiment are mention below:

- The maximum stagnation temperature of the fluid in the cut tube receiver without insulation is noted to be 142.26 °C.
- The maximum stagnation temperature of the fluid in the cut tube receiver with insulation is noted to be 169.96 °C.

The estimated price of the cut tube receiver and tracking system was found to be much competitive. This modification in the technology can help to cut down

the overall price of the PTC system and sustainable enough for low- and medium-temperature IPH applications.

References

1. Energy Statistics (2017) Central Statistics Officers Ministry of Statistics and Programme Implementation Government India. http://www.mospi.nic.in/sites/default/files/publication_reports/Energy_Statistics_2017r.pdf.pdf. Accessed July 2 2019

2. India (2020). https://niti.gov.in/sites/default/files/2020-01/IEA-India2020-In-depth-EnergyPolicy_0.pdf Accessed July 2 2019

3. Liu Z (2016) National carbon emissions from the industry process: Production of glass, soda ash, ammonia, calcium carbide and alumina. Appl Energy 166:239–244. https://doi.org/10.1016/j.apenergy.2015.11.005

4. United Nations Industrial Development organization India's CST Sector-Vision 2022 MNRE-GEF-UNIDO government of india ministry of new and renewable energy. https://open.unido.org/api/documents/12714793/download/IndiaCSTRoadmap2022.pdf. Accessed April 25 2020

5. Naik H, Baredar P, Kumar A (2017) Medium temperature application of concentrated solar thermal technology: Indian perspective. Renew Sustain Energy Rev 76:369–378. https://doi.org/10.1016/j.rser.2017.03.014

6. Weiss W, Rommel M (2019) EA SHC-Task 33 and solarPACES-Task IV: solar heat for industrial processes. https://www.iea-shc.org/Data/Sites/1/publications/task33-Process_Heat_Collectors.pdf. Accessed July 2 2019

7. Motwani K, Patel J (2019) Cost analysis of solar parabolic trough collector for cooking in Indian hostel–a case study. Int J Ambient Energy 1–17. https://doi.org/10.1080/01430750.2019.1653968

8. Gautam A, Chamoli S, Kumar A, Singh S (2017) A review on technical improvements, economic feasibility and world scenario of solar water heating system. Renew Sustain Energy Rev 68:541–562. https://doi.org/10.1016/j.rser.2016.09.104

9. Chafie M, Fadhel M, Aissa B, Bouadila S, Balghouthi M, Farhat A, Guizani A (2016) Experimental investigation of parabolic trough collector system under Tunisian climate: design, manufacturing and performance assessment. Appl Therm Eng 101:273–283. https://doi.org/10.1016/j.applthermaleng.2016.02.073

10. Chandra YP, Singh A, Mohapatra SK, Kesari JP, Rana L (2017) Numerical optimization and convective thermal loss analysis of improved solar parabolic trough collector receiver system with one sided thermal insulation. Sol Energy 148:36–48. https://doi.org/10.1016/j.solener.2017.02.051

11. Moya EZ (2012) Parabolic-trough concentrating solar power (CSP) systems. Conc Sol Power Technol 197–239. https://doi.org/10.1533/9780857096173.2.197

12. Motwani K, Chotai N, Patel J, Hadiya R (2020) Design and experimental investigation on cut tube receiver for solar parabolic trough collector, energy sources. Part A Recover Util Environ Eff 00:1–20. https://doi.org/10.1080/15567036.2020.1773964

13. Khalifa AJN, Al-Mutawalli SS (1998) Effect of two-axis sun tracking on the performance of compound parabolic concentrators. Energy Convers Manag 39:1073–1079. https://doi.org/10.1016/S0196-8904(97)10020-6

14. Xu C, Chen Z, Li M, Zhang P, Ji X, Luo X, Liu J (2014) Research on the compensation of the end loss effect for parabolic trough solar collectors. Appl Energy 115:128–139. https://doi.org/10.1016/j.apenergy.2013.11.003

15. Chang C (2016) Tracking solar collection technologies for solar heating and cooling systems. Elsevier Ltd. https://doi.org/10.1016/B978-0-08-100301-5.00005-9

16. Gaafar AE, Zobaa AF (n.d.) Economical design of a two-axis tracking system for solar collectors pp 1–6

17. Pih P, Kalogirou SA (1997) Design and construction of a one-axis sun-tracking system 57:465–469
18. Sun J, Wang R, Hong H, Liu Q (2017) An optimized tracking strategy for small-scale double-axis parabolic trough collector. Appl Therm Eng 112:1408–1420. https://doi.org/10.1016/j.applthermaleng.2016.10.187
19. Hafez AZ, Yousef AM, Harag NM (2018) Solar tracking systems: technologies and trackers drive types–a review. Renew Sustain Energy Rev 91:754–782. https://doi.org/10.1016/j.rser.2018.03.094

Process Parameter Characterization of Dielectric Elastomer-Based Electro-Mechanical System

Rajeev Kumar and Anuj Kumar Jain

Abstract In recent times, dielectric elastomer-based electro-mechanical system is used widely as actuators and energy harvesters. The material property of elastomer is such that under linear actuations, it can undergo very large deformation. In order to demonstrate large demonstration in actuation, several challenges need to be met. These include the possibility of electro-mechanical instability or electric breakdown and loss of tension in the elastomeric film. In the current work, a material formulation of deformation of soft dielectric material is postulated. Thus, a mathematical model for deformation of dielectric elastomer is created to address processes involved in dielectric elastomer-based energy harvester. Further, the dielectric elastomer material response in tensile testing as well as dielectric permittivity of elastomeric material is evaluated experimentally. The current electro-mechanical model utilizes variation in geometry for change in capacitance which results in storage of more potential at output battery. Efforts are also applied on optimizing the energy harvesting to address various failure situations under electro-mechanical actuations

Keywords Soft dielectric material · Energy harvesting process · Formulation of material response · Electro-mechanical system

1 Introduction

Dielectric elastomers are classified as a class of soft deformable electro-active material, which are also considered as smart materials. This material has got unique mechanical and electrical properties which enable it to stimulate with application of electro-mechanical fields. As a result, dielectric elastomers are considered suitable for various actuations which are observed under electro-mechanical actuators

R. Kumar (✉)
Pranveer Singh Institute of Technology, (Affiliated to AKTU Lucknow), Kanpur, India
e-mail: rajeevnitwkhagoli@gmail.com

A. K. Jain
ABES Engineering College, (Affiliated to AKTU Lucknow), Ghaziabad, India
e-mail: anujjainkanbay@gmail.com

695

and energy harvesters. Especially for applications requiring large actuation at high voltage and low cost, dielectric elastomers provide a lightweight alternative to other technologies. Most dielectric elastomer actuator designs were developed during the early 2000s [1, 2]. Further application of this technology as a buoy generator and a heel strike generator has been reported [3]. Practical self-priming circuits, that boost the low-voltage source so that dielectric elastomer generators (DEGs) can harvest energy effectively, have been developed [4].

The general problem of a soft dielectric material undergoing large deformations due to the application of an electric field is the one that assumes renewed interest in the light of the emergence of technologies based on dielectric elastomers. Factors limiting the application of these emerging technologies are many. During usage, as very high electric field is required for deforming these elastomers, hence possibility of electric breakdown and electro-mechanical instability is the most common concern [5–7]. In order to understand these concerns, the basic working of elastomer-based actuators should include important parameters during electro-mechanical deformations.

Consider the case of the thin elastomer between compliant electrodes as shown in Fig. 1. This is a generic configuration adopted in many applications. When a voltage φ is applied on an unconstrained dielectric film, its thickness decreases. The decrease in thickness induces a higher electric field and hence, a higher compressive Maxwell stress, which, in turn, thins it further. At a critical point, the positive feedback may cause the dielectric to thin down abruptly, leading to, what is known as 'pull-in instability.' Wrinkling of the film is commonly observed during pull-in instabilities. Hence, in order to address these failure situations, various parameters influencing
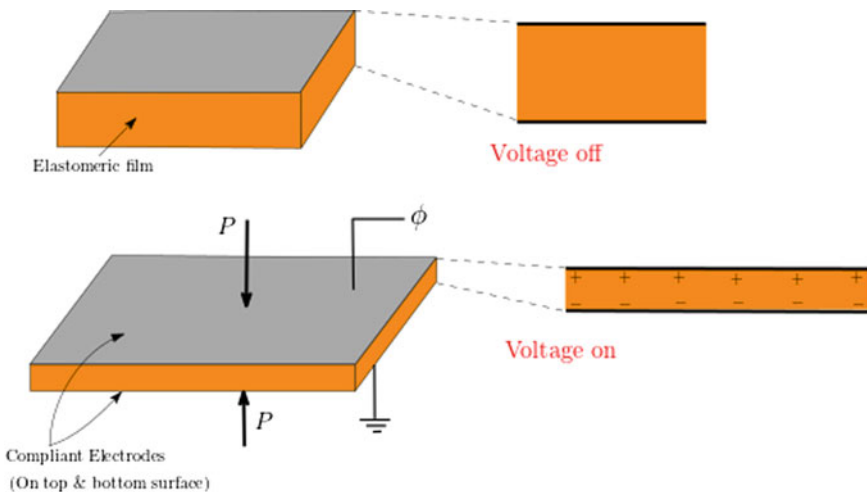

Fig. 1 Schematic diagram showing working principle of dielectric elastomer. When electric charges are placed over an elastomer thin sheet, coated on both sides with compliant electrodes, electrostatic forces, *P* acts to squeeze the film along thickness direction and expands it in plane

the deformation process need to be highlighted for which a mathematical model is required.

2 Theory of Deformable Dielectric Elastomer

In this section, the equations governing the deformation behavior of highly deformable nonlinear elastic dielectric materials under the coupled influence of mechanical and electric fields are derived. The situation is shown in Fig. 2, where a point P with position vector X in the reference configuration of a solid body V_o^+ is mapped to point p with position vector x in the deformed configuration denoted V^+ by a motion $x = \beta(X, t)$. The body is subjected to a body force distribution $B(b)$ in the reference(deformed) configuration over $V_o^+(V^+)$ and mechanical surface tractions $T(t)$ applied on a part of the boundary $\partial V_0^+ (V^+)$ with $N(n)$ being normal to the surface. In addition, the body has a material (spatial) distribution of free charge per unit volume $\dot{Q}(X, t)$ $(q(x, t))$, as well as charge per unit area $\omega_o(\omega)$ per unit surface area $\partial V_0(V)$. The deformable dielectric body is embedded in an electric field $\dot{E}(X, t)$ in the reference or $E(x, t)$ in the deformed configuration. The reference and deformed configuration are both embedded in free space, $(V_0)^-$ and V_t^- respectively. The outer boundary of the free space lies far away, and all field quantities decay to zero there.
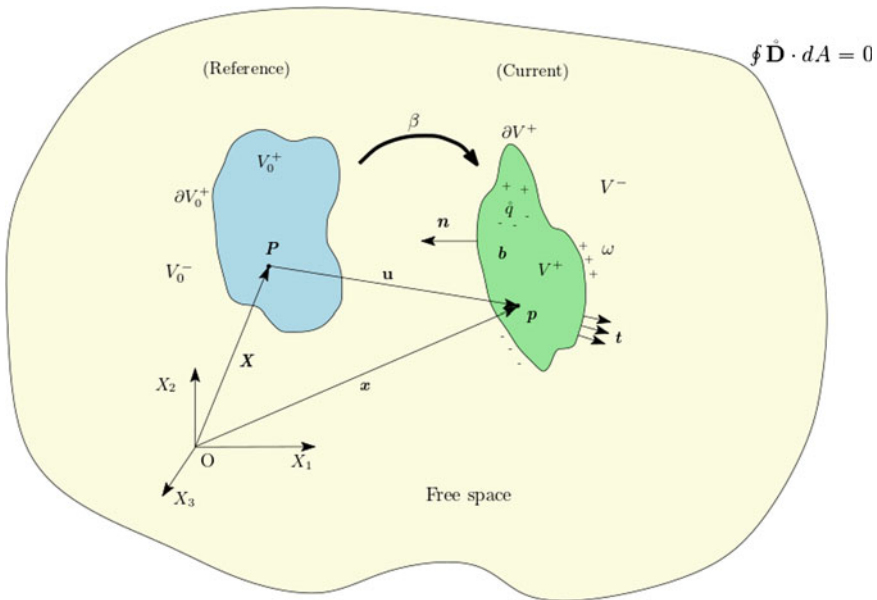

Fig. 2 General electro-mechanical loadings on deformable dielectrics

Here, the development of equations governing electro-mechanical deformations is casted in reference configuration. In the reference configuration, the electric field $\dot{E}(X)$, potential $\dot{\varphi}(X)$, electric displacement $\dot{D}(X)$ and surface charge density ω_o are connected through Maxwell's equations:

$$\dot{E} = -\frac{\partial \dot{\varphi}}{\partial X}, \tag{1}$$

$$\nabla_0 \cdot \dot{D} = \frac{\partial \dot{D}_i}{\partial X_i} = \dot{Q}, \tag{2}$$

in $V_o = V_o^+ \cup V_o^-$ and the jump condition on ∂V_o^+,

$$\left\| \dot{D} \cdot N \right\| = \omega_o. \tag{3}$$

Here, N is the outward normal to the surface ∂V_o^+ in the fixed Cartesian system(X_1, X_2, X_3). Further, $\|\cdot\|$ implies a jump in a quantity across surface, so that $\left\| \dot{D} \right\| = \dot{D}^- - \dot{D}^+$, with N always taken to point from the + side to the - side. The above shown constitutive relation between $\dot{E}$ and $\dot{D}$ in the reference configuration is through a deformation-dependent permittivity tensor. The deformation gradient, Jacobian of the deformation and the right Cauchy–Green deformation tensor are given by the usual relations:

$$F = \frac{\partial x}{\partial X}, \ J = \det F \text{ and } C = F^T F \tag{4}$$

Principle of conservation of linear momentum for quasi-static condition is expressed as:

$$\int\limits_{V_o^+} \left(B + B^E\right) \mathrm{d}V_o^+ + \int\limits_{\partial V_o^+} \left(T + T^E\right) \mathrm{d}S_o = 0, \tag{5}$$

where the left-hand side envisages that the body forces and surface tractions, acting on the deformable body, have mechanical and electrostatic origins. The quantity B and T are usual mechanical body force and traction, while B^E and T^E are corresponding electrostatic load components for body force and traction, respectively. Toupin [8] related the electric body force to Maxwell's stress using

$$B^E = \nabla_o \cdot P^E, \tag{6}$$

leading to traction $T^E = \left\| P^E \right\| N$ on ∂V_o^+. As per [9], relation between surface traction and jump in total nominal stress is given by: $T = \left\| P + P^E \right\| N$.

After performing few manipulations and utilizing expression of electric traction in terms of Maxwell stress P^E, we are expressing here the localized equation describing balance of linear momentum as:

$$(\nabla_o \cdot P) + (B + B^E) = 0, \tag{7}$$

where P is the first Piola-Kirchhoff stress.

For an isotropic and isothermal material undergoing deformation, Helmholtz's free energy density is considered to constitute deformation gradient as well as electric displacement and is shown of form:

$$\widetilde{\Upsilon} = \overline{\Upsilon}(F, \dot{D}) \tag{8}$$

Further constitutive relations are considered into two parts, one with pure mechanical component, while other consisting of electro-mechanical parts as shown below:

$$P + P^E = \frac{\partial \widehat{\Upsilon}}{\partial F}, \tag{9}$$

$$\dot{E} = \frac{\partial \dot{\widehat{\Upsilon}}}{\partial D} \tag{10}$$

3 Mathematical Modeling of Elastomer-Based Energy Harvester

A dielectric elastomer is basically a soft hyperelastic material with a reasonably high dielectric permittivity ε. Dielectric elastomeric generator (DEG) has been shown to exhibit favorable energy densities, when used for energy harvesting, e.g., in heel strike generators and harvesters from ocean. The example worked out in this section closely follows their derivation in previous section. The stages in the operation of a DEG are shown in Fig. 3. A thin sheet of elastomer, a 3 M, VHB 4910, with thickness L_3, is used at computational mechanics laboratory, IIT Kanpur, with flexible electrodes at $X_3 = 0$, and L_3. It is bi-axially stretched to a stretch of λ_m in the process (a)–(b). The stretch is held fixed from (b)–(c), while charges $\dot{Q}_m$ are transferred to the electrodes from ϕ_{in}. In (c)–(d), switches S_1 and S_2 are opened so that the charges cannot escape. The elastomer is relaxed to $\lambda = 1$. Finally, in the process (d)–(a), the switch S_2 is closed so that charges are transferred to ϕ_{out}. If $\phi_{\text{out}} > \phi_{\text{in}}$, the process has been able to transfer charge from a lower to a higher potential and thus converted the mechanical energy of stretching to stored electrical energy in ϕ_{out}.

For hyperelastic material, free energy density is considered as:

$$\overline{\Upsilon} = \underbrace{\breve{\Upsilon}(C)}_{\text{mechanical}} + \underbrace{\widehat{\Upsilon}(C, \dot{D})}_{\text{electro}-\text{mechanical}}, \tag{11}$$
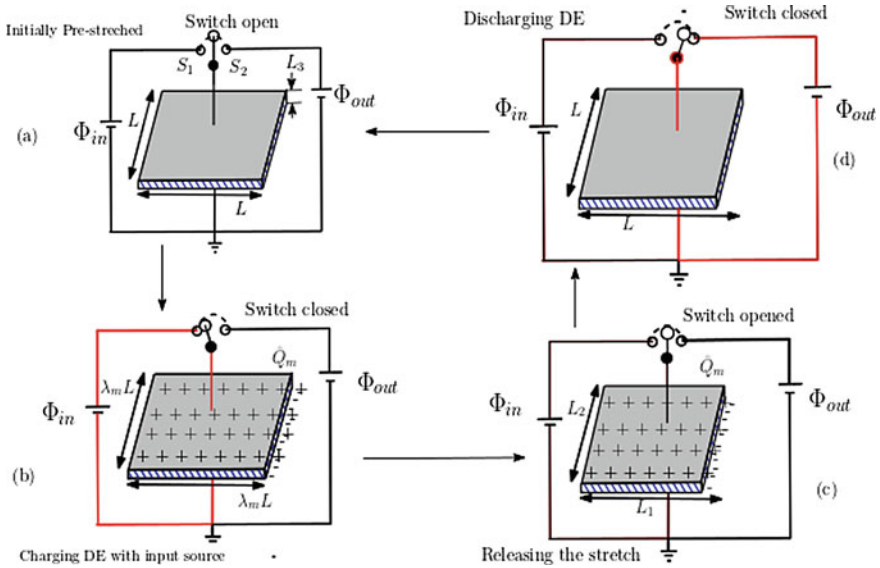
Fig. 3 A parallel plate capacitor, with hyperelastic dielectric elastomer and flexible electrodes, acts as a dielectric elastomeric generator (DEG). Stages of operation: **a** through **d**

where electro-mechanical component is given by $\widehat{\Upsilon}(C, \dot{D}) = \frac{\dot{D} \cdot C \cdot \dot{D}}{2\varepsilon J}$. Apart from this, hyperelastic material elastomer behaves nearly as impressible material; hence, constitutive relation can be shown as:

$$P + P^E = \frac{\partial \overline{\Upsilon}}{\partial F} - p_o F^{-T}, \tag{12}$$

where p_o is called as Langrage multiplier. In case of DEG, we have assumed the energy density functions to be depending upon principle stretches as well as reference electric displacement. Here, the constitutive relation gets modified as:

$$P_\alpha + P_\alpha^E = \left[\frac{\partial \breve{\Upsilon}}{\partial \lambda_\alpha} + \frac{\partial \widehat{\Upsilon}}{\partial \lambda_\alpha} \right] - \frac{p_o}{\lambda_\alpha} \tag{13}$$

where $\breve{\Upsilon}(\lambda) = \frac{\mu_1}{\alpha_1} \left[\lambda_1^{\alpha_1} + \lambda_2^{\alpha_1} + \lambda_3^{\alpha_1} - 3 \right]$ and $\breve{\Upsilon} = \breve{\Upsilon}(\lambda_1, \lambda_2, \lambda_3, \check{D})$. Here, coefficients $\mu_1 = 29.54$ kPa and $\alpha_1 = 1.615$. Dielectric permittivity $\varepsilon = 4.832 \times 10^{-11} \left(\frac{F}{m} \right)$. All these values are calculated for VHB 4910, by undergoing tensile testing at Aerospace Engg. Laboratory, IIT Kanpur. Now, all the four stages in DEG are formulated using the above defined constitutive relations. The initial elastomer sheet is square with $L_1 = L_2 = 40$ mm and $L_3 = 1$ mm. When the free energy is given in terms of principal stretches, eq. (12) gets transformed as:

$$\frac{\partial \tilde{\Upsilon}}{\partial \lambda_\alpha} = \frac{\lambda_\alpha \dot{D}_\alpha^2}{\varepsilon J} - \frac{1}{2\varepsilon J} \frac{\partial J}{\partial \lambda_\alpha} (\lambda_i^2 \dot{D}_i^2) \tag{14}$$

In case of the DEG, using the Ogden model and equi-biaxial stretches so that $\lambda_1 = \lambda_2 = \lambda$; incompressibility further dictates that $\lambda_3 = 1/\lambda^2$. Also $D_3 \neq 0$, $D_1 = D_2 = 0$, we get:

$$P = P_1 + P_1^E = P_2 + P_2^E = \mu_1 \lambda^{\alpha-1} - \frac{\dot{D}_3^2}{2\varepsilon\lambda^5} - \frac{p_o}{\lambda}, \tag{15}$$

$$P_3 + P_3^E = \mu_1 \lambda^{-2\alpha_1 + 2} + \frac{\dot{D}_3^2}{2\varepsilon\lambda^2} - p_o\lambda^2. \tag{16}$$

As per traction boundary condition, total nominal stress acting on top and bottom surfaces is vanished. Hence, $P_3 + P_3^E = 0$ is considered throughout the operating cycle. Therefore, $p_o = \mu_1 \lambda^{-2\alpha_1} + \frac{\dot{D}_3^2}{2\lambda^4}$. Now, inserting value of p_o in expression of P, we get:

$$P = \mu_1 \left[\lambda^{\alpha_1 - 1} - \lambda^{-2\alpha_1 - 1} \right] - \frac{\dot{D}_3^2}{2\varepsilon\lambda^5} \tag{17}$$

Further, the electrostatic constitutive relation is given as:

$$D_3 = \varepsilon\lambda^4 \dot{E}_3 . \tag{18}$$

Equations (17) and (18) can now be used to plot the entire cycle on the $P - \lambda$ and $E_3 - \dot{D}_3$ plane. Note that as $\dot{D}_3 = \frac{\dot{Q}}{L^2}$, and $\dot{E}_3 = \frac{\dot{\phi}}{L_3}$. where $\dot{Q}$ is the charge transferred to the electrodes and $\dot{\phi}$ is the potential applied, then $E_3 - \dot{D}_3$ plot becomes equivalent to $\dot{\phi} - \dot{Q}$ plot.

For process (a)–(b), the deformation gradient is given as:

$$F = \lambda e_1 \otimes e_1 + \lambda e_2 \otimes e_2 + \frac{1}{\lambda^2} \lambda e_3 \otimes e_3, \tag{19}$$

where λ varies from 1 to $\lambda_m = 4$, and $\dot{D}_3 = 0$. The complete process from (a) to (d) is shown in Figs. 4, 5, respectively. Further, ϕ_m is varied here for the VHB 4910 elastomer having thickness of 1 mm. Maximum value of voltage applied is 1 kV for a fixed stretch of $\lambda_m = 4$ during process (b)to (c). Further at point (d), the negative stress is undesirable as it might cause loss of tension. The point (d) lies outside the limits of this plot and so, is indicated by an arrow in Figs. 4, 5, respectively.
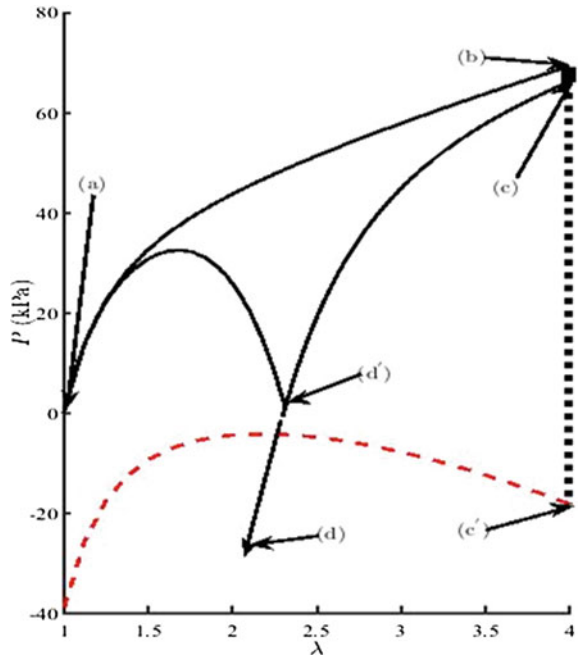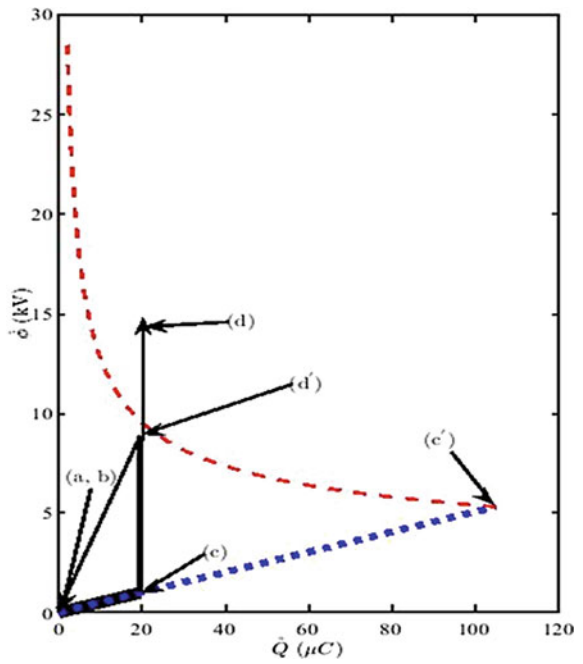
Fig. 4 Nominal stress versus stretch plot

Fig. 5 Voltage–charge plot for no failure

3.1 Limits on $\dot{Q}_m$

The process from (b)–(c) involves loading the elastomer with charge. At $\lambda_m = 4$, $\dot{\phi} = 1\,kV$, the charge that can be loaded onto the DE capacitor is $\dot{Q}_m = 19.8\,\mu C$. However, the maximum charge that can be loaded onto the capacitor at stage (c) is limited by the breakdown characteristics of the DE material. The breakdown field varies with stretch, and for the purpose of the following calculations, we consider a fit to experimental data of the form: $E_B = -0.16667\,\lambda^3 + 2.5257\lambda^2 + 9.7024\lambda + 16.4$.

Further, we have tried to include electric breakdown field expression in $P - \lambda$ plane and $\dot{\phi} - \dot{Q}$ plane respectively as:

$$P = \mu_1\left[\lambda^{\alpha_1-1} - \lambda^{-2\alpha_1-1}\right] - \frac{\varepsilon E_B^2}{\lambda}, \text{ and } \dot{D}_3 = \varepsilon\lambda^2 E_B. \qquad (20)$$

These plots are shown as dotted lines in red, which limits the extent for charge on stretched elastomer. For a practical dielectric elastomer generator device, it is now clear that we follow $\dot{\phi} = 1kV$ and de-stretch up to (d') and then de-stretch and discharge at the same time along the curve (d')–(a) as shown in Figs. 4 and 5. The combined relaxation and discharging process should be done in a manner such that the curve from (d') to (a) does not cross the breakdown curve and does not lead to negative value of P. The point (d') has been chosen such that neither loss of tension nor electrical breakdown occurs anywhere in the domain. The bow-shaped curve from (d') to (a) shown in Fig. 4 is near to realistic, where we have chosen (d') to have stress very close to 0. It is more practical to move (d') to a higher value of λ.

4 Conclusion

In the present work, constitutive relations using material coordinates for deformation of elastomeric material under both electrical and mechanical load are postulated. Based on the derived constitutive relation, a suitable mathematical model is envisaged, and its working is shown. Further, various points on stretch and stress plot are drawn during deformation process. Corresponding situations are also shown at voltage charge graph. These two characteristic plots determine the influencing positions during deformation of elastomer. Limits of failure points are also ascertained, which provide a glimpse of necessary action to be used while designing a prototype dielectric elastomer-based energy harvester.

References

1. Kornbluh RD, Eckerle J, McCoy B (2011) A scalable solution to harvest kinetic energy. In SPIE Newsroom
2. Pelrine R, Kornbluh R, Eckerle J, Jeuck P, Oh S, Pei Q, Stanford S (2001) Dielectric elastomers: generator mode fundamentals and applications. Proc SPIE Smart Struct Mater 4329:148–156
3. Prahlad H, Kornbluh R, Pelrine R, Stanford S, Eckerle J, Oh S (2005) Artificial muscle: the next generation of robotic actuators. In: Proceedings of the ISSS, Bangalore, India, 28–30, July 2005
4. McKay T, O'Brien B, Calius E, Anderson I (2010) Self-priming dielectric elastomer generators. Smart Mater Struct 19:055025
5. Huichan Z, Aftab MH, Mihai D, Daniel MV, Robert JW, David RC (2018) Compact dielectric elastomer linear actuators, Advanced functional materials, vol 1804328, pp 1–12. https://doi.org/10.1002/adfm.201804328
6. Duduta M, Hajiesmaili E, Zhao H, Wood RJ, Clarke DR (2019) Realizing the potential of dielectric elastomer artificial muscles. PNAS. https://doi.org/10.1073/pnas.1815053116
7. Minaminosono A, Shigemune H, Okuno Y, Katsumata T, Hosoya N, Maeda S (2019) Deformable motor driven by dielectric elastomer actuation and flexible mechanisms. Front Robot AI. https://doi.org/10.3389/frobt.2019.00001
8. Toupin RA (1963) A dynamics theory of elastic dielectrics. Int J Eng Sci 1:101–126
9. McMeeking RM, Landis CM (2005) Electrostatic forces and stored energy for deformable dielectric materials. J Appl Mech ASME 72:581–590

Numerical Study on Effect of Coexistent States and Dielectric Breakdown on Soft Elastomeric Material

Rajeev Kumar and Anuj Kumar Jain

Abstract The principle of operation of a dielectric elastomeric actuator is simple and can be explained with the example of a parallel plate capacitor. The highly deformable dielectric material is placed between compliant electrodes, where the lower electrode is grounded and a potential φ is applied to the upper one. Due to electrostatic forces occurring between compliant electrodes, under a pre-stretched configuration, elastomer material undergoes a squeezing action. The thickness of dielectric elastomer under such situations takes place. In the present work, a geometrically nonlinear enhanced strain mixed method is developed and is utilized for numerical study of deformation under electromechanical force fields. The current FEM model results show the phenomena of coexistent states as well as effect of electric breakdown under various conditions. Apart from these, a wrinkled deformation pattern at the end of failure, due to parameters like the electromechanical instability, is also ascertained. It has been deduced that ratio of shear modulus to dielectric permittivity as well geometrical inhomogeneity plays larger role than incomprehensibility factor of soft dielectric elastomer in exhibiting various electromechanical instabilities.

Keywords Electromechanical instability · Dielectric breakdown · FEM model · Nonlinear material behavior

1 Introduction

The principle of operation of a dielectric elastomeric actuator is simple and can be explained with the example of a parallel plate capacitor. This is illustrated in Fig. 1.

The highly deformable dielectric material is placed between compliant electrodes, where the lower electrode is grounded and a potential ϕ is applied to the upper one.

R. Kumar (✉)
Pranveer Singh Institute of Technology (Affiliated to AKTU), Lucknow, India
e-mail: rajeevnitwkhagoli@gmail.com

A. K. Jain
ABES Engineering College (Affiliated to AKTU), Lucknow, India
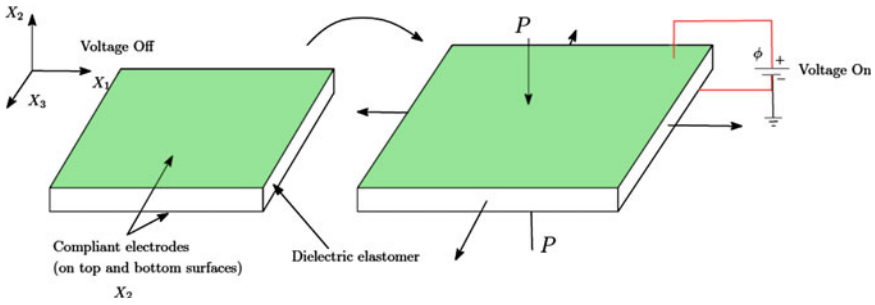e-mail: anujjainkanbay@gmail.com

Fig. 1 Operational principle of dielectric elastomer

The application of a high enough value of ϕ causes the dielectric to thin down and expand in the $X_1 - X_3$ plane. Potentially, this actuator may be used to deliver useful work, say, by pushing a workpiece as it expands in the $X_1 - X_3$ plane. The compliant electrodes used in most cases are basically coatings of carbon grease (a mixture of conducting graphite powder and a pasting liquid), though other more durable electrode designs have been explored [1–5].

The thinning of the dielectric, however, cannot go on indefinitely. One of the three possible scenarios might cause the actuator to break down. Stretching the electrode beyond a point might cause it to tear. Also, if the electric field in the X_3 direction exceeds the breakdown field of the elastomer, the actuator will fail. The third mechanism of failure has been termed as 'electromechanical instability' and is probably the most interesting of the three. A schematic showing the three modes of failure is shown in Fig. 2.

Fig. 2 Modes of failure in dielectric elastomer
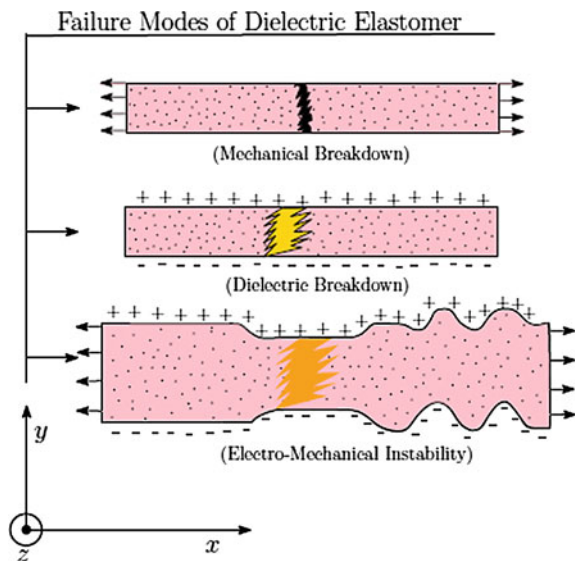
1.1 Coexistent States in a Parallel Plate Dielectric Elastomeric Actuator

The mechanics of electromechanical instability has been explained by Koh et. al [6]. A situation where multiple configurations of the dielectric elastomer are possible for the same applied ϕ is termed as 'electromechanical instability.' In the current work, we investigate the situations where a non-unique solution to the electromechanical problem of a dielectric elastomeric material subjected to a potential φ, first occurs.

A typical $\phi - Q$ response of the dielectric elastomer, where this might manifest is shown in Fig. 3. The charge on the electrodes Q increases with ϕ till the point A. At this point, when we try to increase ϕ further, the solution Q for jumps to A', which involves a sudden change in the thickness of the dielectric. Similarly, a sudden increase in thickness will occur from B to B' while the potential is decreased. States of the dielectric elastomer that lie below A A' and above B B' are called 'coexistent states' (Huang and Suo [7]) and will occur if the $\phi - Q$ response of the elastomer decreases and increases as in the shaded part of Fig. 3.

Electromechanical instability arises due to a complex interplay between various factors like the material and geometry of the elastomer as well as mechanical and electrical boundary conditions Pelrine et. al. [8]. Currently, we have used a simple model of a pre-stretched elastomer to study the interplay between material properties and the extent of pre-stretch on the occurrence of failure due to electromechanical instability. Similar strategies are also initiated by Simone et. al. [9], Zhou et. al. [10], Gacia et. al. [11]; Deepak and Somnath [12], while performing pull-in instability mechanism. In particular, we are interested in understanding the role of material parameters in determining whether the elastomer will fail due to the onset of instability or by simple electrical breakdown.

Fig. 3 A schematic plot of the relation between the voltages applied between the two electrodes and the magnitude of the electric charge on either electrode
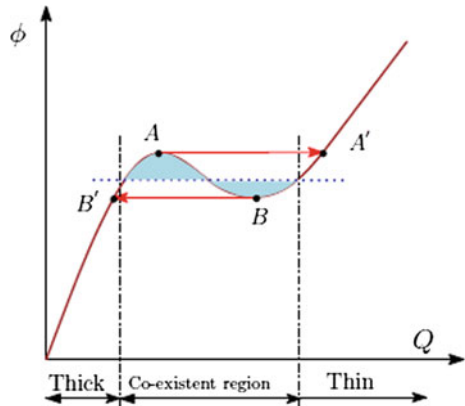
1.2 Introduction to FEM Model

The set of equations which are utilized for generalized weak form for staggered electromechanical and electrostatic part (Fig. 4) of problem are listed as;

$$\int_{V_o^+} \left[\left[b\left(u, \tilde{h}\right) \right] \{\delta u\}^T \right] \left\{ \tilde{\tau}\left(u, \tilde{h}, \dot{D}\right) \right\} dV_o^+ - \delta \Pi_{\text{ext}} = 0 \tag{1}$$

$$\int_{V_o^+} \left[\{\delta h\}^T \right] \left\{ \tilde{\tau}\left(u, \tilde{h}, \dot{D}\right) - \tau \right\} dV_o^+ = 0 \tag{2}$$

$$\int_{V_o^+} \left[\{\delta \tau\}^T \left\{ \tilde{h} \right\} \right] dV_o^+ = 0 \tag{3}$$

Additionally, the electrostatic problem is defined as:

$$\int_{V_o} \varepsilon J \{\nabla_o \phi\}^T \cdot C^{-1} \cdot \{\nabla_o(\delta\phi)\} dV_o = 0 \text{ on } V_o \tag{4}$$

Here, we have different boundaries to consider for the electrostatic part governed by Eq. (4) and electromechanical part governed by Eqs. (1), (2), (3), respectively. We mesh the region V_o^+ of the body as well as region of air/ medium adjacent to it. We have also taken into consideration the traction T^{E-}, applied on the elastomer material due to difference in permittivity between elastomer and the surrounding. For the electrostatic part, nodal potential ϕ_I and electric field vectors at integration point $\dot{E}$ are calculated and transferred to the electromechanical problem. This
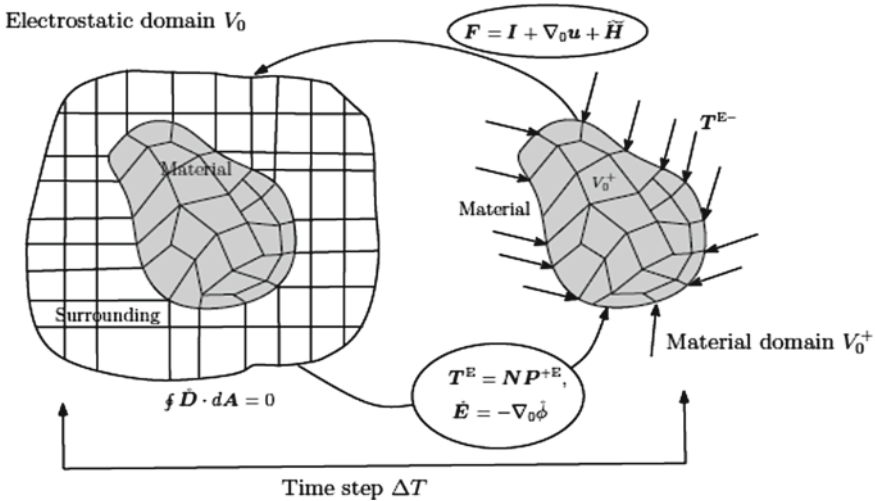

Fig. 4 Staggered solution of electrostatic problem and eletro-mechanical problem

further enables the calculation of nodal tractions T^{E-} on the boundary. In the electro-mechanical part, nodal displacements u of the elastomer are calculated under mechanical force/displacement boundary conditions as well as the forces due to electrostatics, i.e., T^{E-} and internal forces due to P^{E}. The updated deformation gradient F thus generated is fed to the electrostatic part.

2 Theoretical Model

A plane strain model of the dielectric elastomer has been taken as shown in Fig. 5.

The elastomer occupies a volume defined by: $0 \leq X_1 \leq L_o, 0 \leq X_2 \leq b_o - \Delta \sin \frac{\pi X_1}{L_o}$. The quantity Δ is small compared to b_o and is used in order to trigger the instability. The curved profile at the top serves as a surrogate for a real dielectric elastomer that may not have uniform thickness all along X_1. Initially, the boundary conditions are:

$$u_1(0, X_2) = 0, \quad \text{for} \quad 0 \leq X_2 \leq b_o \tag{5}$$

$$u_2(X_1, 0) = 0, \quad \text{for} \quad 0 \leq X_1 \leq L_o \tag{6}$$

Additionally, in order to pre-stretch the elastomer, we apply a displacement

Fig. 5 Schematic model depicting process comprising two stages: a dielectric material undergoes pre-stretch λ along X_1 in stage **a**. In stage **b**, a voltage ϕ_o is applied on elastomer while maintaining the pre-stretch of stage **a** until dielectric breakdown or electromechanical instability occurs
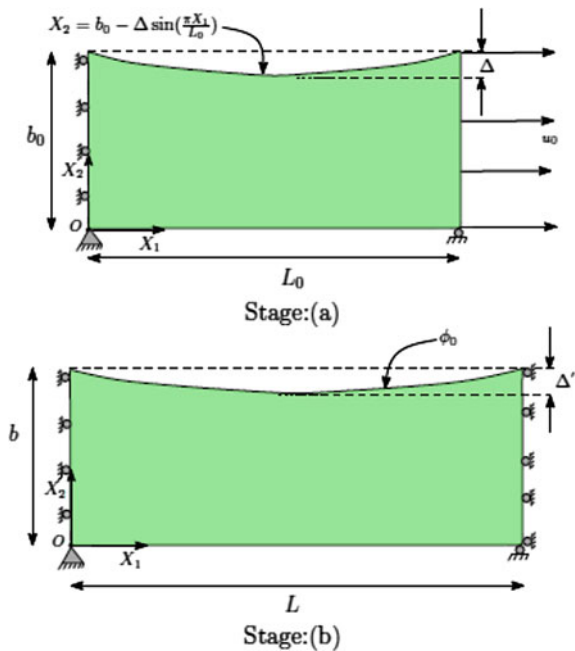
$$u_1(L_o, X_2) = u_o, \quad \text{for } 0 \le X_2 \le b_o \tag{7}$$

so that we attain a stretch of $\lambda_p = \frac{L}{L_o}$, in the configuration shown in Fig. 5b. The pre-stretching process is purely mechanical. Once the pre-stretching is complete, the right edge is fixed, i.e.,

$$u_1(L, X_2) = 0 \quad \text{for } 0 \le X_2 \le b \tag{8}$$

and the electrostatic boundary conditions are applied, i.e.,

$$\phi = \begin{cases} \phi_o, & \text{for } [0 \le X_1 \le L] \text{ and } X_2 = b - \Delta' \\ 0, & \text{for } [0 \le X_1 \le L] \text{ and } X_2 = 0 \end{cases} \tag{9}$$

It is considered here that for negligible Δ' and incompressibility of the material, the configuration shown in Fig. 5b cannot undergo any further homogeneous deformation due to the application of ϕ_o. Also, we should have $b = \frac{b_o}{\lambda}$. However, we are observing the pre-stretched elastomer which will undergo severe non-homogeneous deformations due to application of ϕ_o. Typically, we have used Δ in range of 0.025 b_o to 0.075 b_o.

3   Numerical Results on Deformation Pattern

A typical deformation sequence of a dielectric elastomer in plane strain situation is shown; here, it is pre-stretched to $\lambda_p = 4.8$ as shown in Fig. 6a through d. The un-deformed configuration with the FE mesh is shown in Fig. 6a. Here, the inhomogeneity on top surface of a plane as shown in Fig. 5 is given by $\Delta = 0.025b_o$, where b_o is initial thickness of elastomer. Further, $X_1 = 10$ and $X_2 = 1$ correspond to intital coordinate of ends of elastomer. The elastomer is then pulled to a pre-stretch of $\lambda_p = 4.8$ as shown in Fig. 6b and subject to $\phi_o = 969V$. The distribution of the absolute electric field $|\boldsymbol{E}|/E_b$ over the elastomer has been shown. Here, E_b is the breakdown strength of the elastomer, assumed to be independent of stretch. In Fig. 6c, for $\phi_o = 2907V$, the field is reasonably uniform over the domain (with a bit of thinning at the middle), but at $\phi_o = 3230V$, (Fig. 6d), the stretched elastomer abruptly deforms into a wrinkled pattern. The elastomer undergoes an almost periodic pattern of increase and decrease in thickness.

For a perfectly flat geometry (i.e., $\Delta = 0$), an incompressible elastomer cannot undergo any further homogeneous deformation. So, when ϕ_o is applied, no change in the configuration should take place.

However, inhomogeneous solution to the problem that preserves the overall volume (i.e., do not violate incompressibility constraint) is indeed possible. It is interesting to see if, while ϕ_o is increased, our code can capture the spontaneous and abrupt homogeneous $\rightarrow$ inhomogeneous transition in the geometry.

Fig. 6 Tthe reference configuration is shown in **a**. **b** The elastomer has been pre-stretched to $\lambda_p = 4.8$, with $\phi_o = 969$ V. In **c**, $\phi_o = 2907$ V has been applied leading to thinning at the middle. **d** At $\phi_o = 3230$ V, electromechanical instability sets in the form of wrinkling of the elastomer
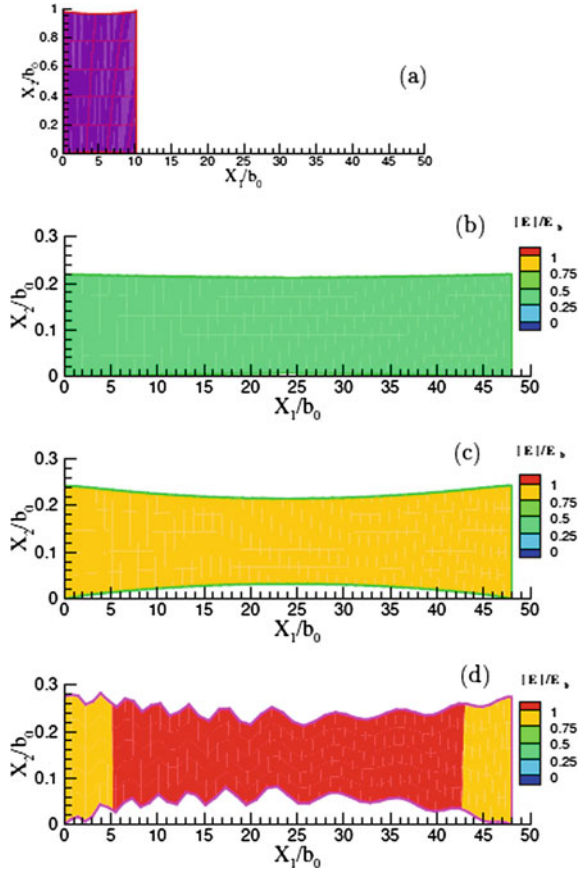
Similar transitions to a wrinkled geometry are also seen in experiments. For example, in Fig. 7, wrinkling in a thin elastomeric sheet held at its boundaries with

Fig. 7 Wrinkling in dielectric elastomer under a potential of about 4 kV applied in the *z*-direction. The elastomer is held all around by the periphery by a rigid frame
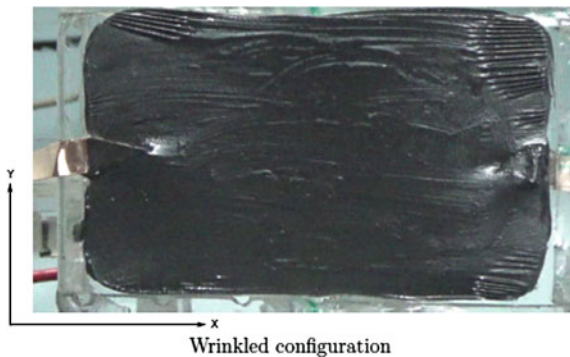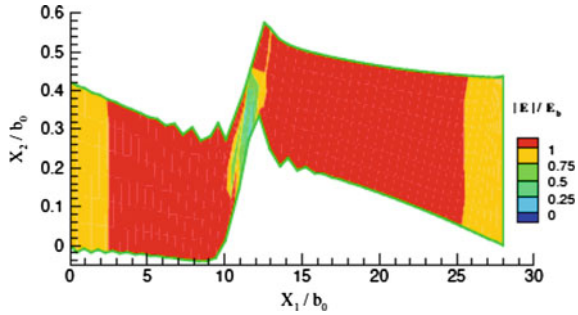

Wrinkled configuration

Fig. 8 Contour plot for pull-in instability in dielectric elastomer for $\Delta = 0.075$ mm

a rigid frame and subjected to a potential difference of about 4 kV perpendicular to its surface has been shown. This ability to approximate the part buckled shapes is probably due to the enhanced displacement gradient formulation adopted in this work. The homogeneous $\rightarrow$ inhomogeneous transition also leads to formation of regions with high local electric fields that cause breakdown.

However, the wrinkled shape is not the only unstable shape that emerges. For example, $\Delta = 0.075 \, b_o$, a kink deformation occurs for $\lambda_p = 2.8$ and $\phi_o = 5500$ V. This is shown in Fig. 8. Note that both the kinked and the wrinkled deformations are possible inhomogeneous deformations under incompressible conditions. In the current work, we have assumed that elastomeric material has a stretch-independent breakdown strength E_B, hence the value of ϕ_o^b at which breakdown occurs is varied according to:

$$\phi_o^b = E_B \frac{b_o}{\lambda_p}, \tag{10}$$

with a pre-stretch λ_p. The variation of $\frac{\phi_o^b}{E_B b_o}$ with λ_p is plotted in Fig. 9.

4 Conclusions

In the current work, we have considered a number of parameters like incompressibility, ratio of shear strength to dielectric value $\sqrt{\left(\frac{\mu}{\varepsilon}\right)}$ which represents the electromechanical coupling in the material. Along with these parameters, inhomogeneous top surface of elastomer is also assumed for instigating the instability process. All these three parameters have shown positive influence in simulating electromechanical instability in elastomeric film which is pre-stretched. We have performed a large number of simulations by varying these parameters. In each case, we carried the simulations out till abrupt instabilities of the types described in the previous section occurred. The value of ϕ_o at which the instability occurred is denoted as ϕ_o^{inst}. If, for a given value of pre-stretch and $\sqrt{\frac{\mu}{\varepsilon}}$, $\phi_o^{\text{inst}} < \phi_o^b$, the failure is said to occur

Fig. 9 Variation of $\frac{\phi_o^b}{E_B b_o}$ with pre-stretch λ_p with electromechanical coupling parameter $\sqrt{\left(\frac{\mu}{\varepsilon}\right)}$
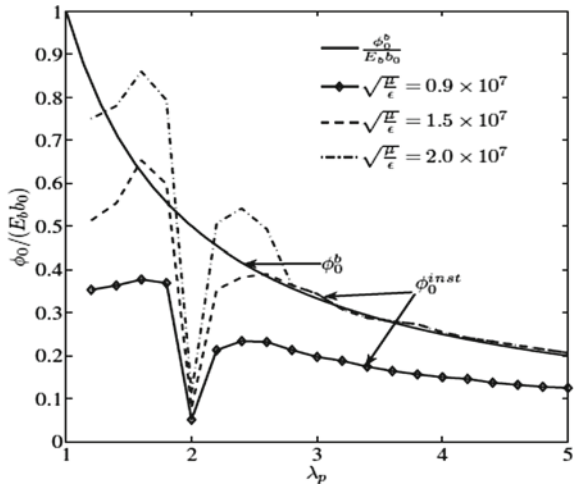
by electromechanical instability, otherwise, the failure is said to occur by electrical breakdown. Onset of instability lowers the potential that can be applied across the elastomer and therefore, limits the utility of the devise. Based upon the simulated results, we come across the importance of electromechanical parameter $\sqrt{\left(\frac{\mu}{\varepsilon}\right)}$, which is showing promising result in instigating pull-in instability in stretched elastomer subjected to high initial voltage.

References

1. Yoseph B-C (2000) Handbook on biomimetics: 'electroactive polymers as artificial muscles-capabilities. Potentials and Challenges'. NTS Inc, Lubbock, Texas, United States
2. Bozlar M, Punckt C, Korkut S, Zhu J, Foo CC, Suo Z, Aksay IA (2012) Dielectric elastomer actuators with elastomeric electrodes. Appl Phys Lett 101:091907
3. Shankar R, Spontak RJ (2007) Dielectric elastomers as next-generation polymer actuators. Soft Matter 3:1116–1129
4. Zhang QM, Li H, Poh M, Xia F, Cheng Z-Y, Xu H, Huang C (2002) An all-organic composite actuator material with a high dielectric constant. Nature 419:284–287
5. Zhou X, Zhao X, Suo Z, Zou C, Runt J, Liu S, Zhang S., Jang QM (2009) Electrical break-down and ultrahigh electrical energy density in poly-vinylidene fluoride-hexafluoropropylene copolymer. Appl Phys Lett 94:162901
6. Koh SJ, Keplinger C, Kaltseis R, Foo C-C, Baumgartner R, Bauer S, Suo Z (2017) High-performance electrome chanical transduction using laterally-constrained dielectric elastomers part i: actuation processes. J Mech Phys Solids 105:81–94
7. Huang R, Suo Zhigang (2012) Electromechanical phase transition in dielectric elastomers. Proceed Royal Soc A 468:1014–1040
8. Pelrine Ron, Kornbluh Roy, Kofod Guggi (2000) High-strain actuator materials based on dielectric elastomers. Adv Mater 12(16):1223–1225
9. Simone F, Linnebach P, Rizzello G, Seelecke S (2017) FE simulation of a dielectric elastomer actuator (DEA) driven contactor in COMSOL. In: Conference: VDI Fachtagung Mechatronik

10. Zhou F, Yang X, X Y, Zhu Z, Li T, Zhongbin X (2020) Electromechanical analysis and simplified modeling of dielectric elastomer multilayer bending actuator. AIP Adv 10:055003. https://doi.org/10.1063/5.0007073
11. Garcia LA, Trindade MA (2019) Finite element modeling and parametric analysis of a dielectric elastomer thin-walled cylindrical actuator. J Brazil Soc Mech Scie Eng 1(18)
12. Kumar D, Sarangi S (2019) Dynamic modeling of a dielectric elastomeric spherical actuator: an energy-based approach. J Soft Mater. https://doi.org/10.1080/1539445X.2019.161655

Modeling and Simulation of Human Temporomandibular Joint Using Bond Graphs—A One-Dimensional Model

Mehak Sharma, Vikas Rastogi, and Manoj Soni

Abstract This study is proposed to devise the behavior of temporomandibular joint (TMJ) while jaw opening and closing movements in human beings using bond graph. TMJ is the most active and extensively used biomechanical joint. To diagnose TMJ disorders and provide correct medical care by exploring jaw behavior, accurate dynamic modeling of TMJ is a necessity. This study is limited to in vitro analysis and modeling techniques because it is challenging to study the actual dynamic functioning of TMJ, being an inner body joint. The primary focus of this work is to model TMJ through bond graph considering its physical resonance with a mechanical system. For this study, the human masticatory system is devised into mathematical one-dimensional model. It included morphology, the behavior of the muscle as well as its dynamic properties. The simulation has been carried out for different force patterns replicating proportional jaw activities like mouth opening and closing. The functional role of TMJ muscles has been represented by assigning nonlinear stiffness values through available literature. The muscle strength has been attributed as a damping characteristic of the jaw. The various elements of jaw, i.e., bite force, jaw mass, reaction force and velocity, have been attributed into the model, which accounts for symmetrical jaw motions.

Keywords Stiffness · Damping · Dynamics · TMJ · Bond graph · Modeling · Simulation

1 Introduction

The dynamic modeling of joints of human limbs is very complex, and the temporomandibular joint is extremely intricate in the human body. It controls mastication and

---

M. Sharma (✉) · M. Soni
Department of Mechanical and Automation Engineering, Indira Gandhi Delhi Technical
University for Women, New Delhi, India
e-mail: er.mehaksharma@gmail.com

V. Rastogi
Department of Mechanical Engineering, Delhi Technological University, New Delhi, India

speech. The nerves and muscles in the human jaw and face are intricately connected to the brain. It is a reciprocal synovial hinge between the mandible and temporal bone with articular disk and various muscles intertwined to perform basic jaw functions like speaking, eating, yawning, drinking, opening and closing of the mouth. Mechanically speaking, since TMJ is both ginglymus (hinging joint) and arthrodial (sliding joint), it is often labeled as a ginglymoarthrodial joint.

The unique prospect of this research work is that though there is expansive literature available on the dynamic or kinematic study of the human jaw, masticatory system and jaw muscles but this is the first attempt at studying the dynamic behavior of human jaw using bond graph technique. The dynamic behavior and movements of the jaw have been studied for decades [1–4]. The muscle activation during various jaw movements has been studied with the help of EMG data or mathematical modeling [5–9]. Three-dimensional static mathematical calculations have been also performed for jaw opening movements [10]. Muscle models, stiffness and damping characteristics have been studied and modeled in the later years [10, 11], and most recently, nonlinearity and 3D finite models for muscles are also being focused for dynamic behavior [12–14]. The present work has taken inspiration from the works of Vaz [9] who has presented bond graph modeling for a human joint with soft articular cartilage and also from Tyagi [15] who has worked on bond graph modeling of lumbar vertebrae of the spine. This paper intends to model the temporomandibular joint by using bond graphs [15] and validate the model with the available literature on TMJ biomechanics.

1.1 Biological Model–TMJ

The human skull has three main structural elements which primarily help in mastication: the mandible, the maxilla and temporal shown in Fig. 1. The maxilla remains fixed at the upper side and the mandible pivots to TMJ. The TMJ is controlled actively by the following mastication muscles: the masseter, medial Pterygoid, lateral Pterygoid and the temporalis. This allows mastication, swallowing, chewing, social interaction and speech in humans.

Due to such complex structure and intertwined connections between muscles and bone elements, it is often difficult to model TMJ accurately. We aim to model TMJ with the perspective of studying system dynamics as being an inner body joint, it is difficult to precisely understand its dynamic characteristics and functioning with experimental techniques. Hence, researchers are keen to apply in vitro techniques for studying human TMJ. The application of bond graph modeling technique to TMJ is expected to be useful for simulation and control of biomechanical prostheses, robotic equipment, and virtual reality devices. The vital focus of this research work is to study the dynamic performance of TMJ for various jaw motions like biting, chewing, eating, speaking, opening and closing of the mouth, etc.
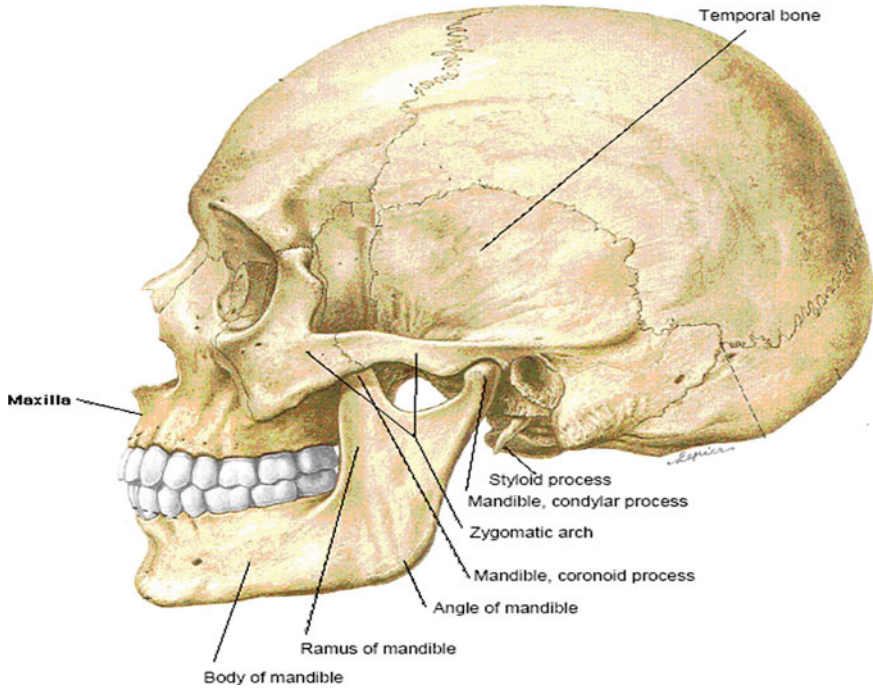
Fig. 1 Human skull (side view, [10] showing TMJ anatomy

2 Materials and Methods

2.1 Physical System

To model a bond graph for TMJ, its anatomy is studied which helps in determining the cross-sectional area of muscles, activation points and point of application of various forces. The anatomical data is evaluated and converted into a free body diagram. The schematic free body diagram of human TMJ is presented in Fig. 2.

The present work has used the schematic model of TMJ based on various forces involved from the literature [10]. The forces calculated in this model by static analysis are used for modeling of human TMJ. The muscle forces involved in this system are the temporal muscle (F_T), masseter muscle (F_M) and Pterygoid muscle (F_P). F_N is the normal force. By using three muscles and constraining the maxilla's articulating portion, the system is deemed to be statically indeterminate due to the presence of four variables: F_T, F_M, F_P, and F_N. To completely define the force system, four non-redundant equations are established. The model is calculated for all equation variables. Considering,

$$\sum F_x = 0$$

Fig. 2 Schematic of TMJ free body diagram [10]
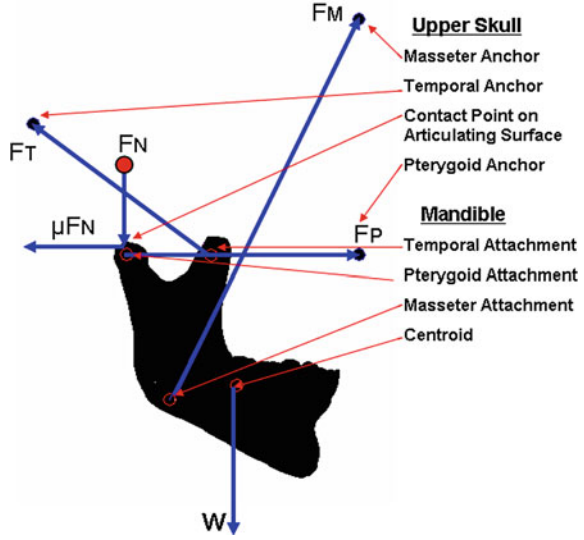
$$\sum F_y = 0$$
$$\sum M_o = 0$$
$$F_N = \text{Constant}$$

Hence, the equations of motion of the temporomandibular joint of a human skull in a static equilibrium are written as:

$$\sum F_x = F_{Tx} - F_{Mx} - F_{Px} + F_{Nx} + \mu F_{Nx} = 0 \tag{1}$$

$$\sum F_y = F_{Ty} + F_{Py} + F_{My} - F_{Ny} + \mu F_{Ny} \cdot W = 0 \tag{2}$$

$$\sum M_o = F_{Tx}^*(T_{yp}) - F_{Ty}^*(T_{xp}) - F_{My}^*(M_{yp}) - F_{Nx}^*(N_{yp}) + F_{Ny}^*(N_{xp})$$
$$- \mu F_{Nx}^*(N_{yp}) - \mu F_{Ny}^*(N_{xp}) + W^*(C_{xp}) = 0 \tag{3}$$

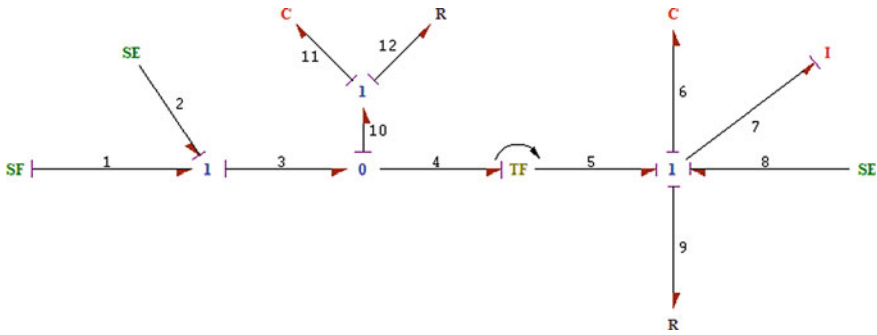$$\Delta PE_C = F_T * D_T + F_M * D_M + F_P * D_P + \mu F_N * D_N \tag{4}$$

Fig. 3 Bond graph model TMJ in one-dimensional system

2.2 TMJ: One-Dimensional Computational Bond Graph Model

To obtain a simplified model, consider the free body diagram shown in Fig. 2. All forces are considered to be in static equilibrium. The dynamic behavior of TMJ is simulated by appropriating a one-dimensional rigid element of TMJ with material damping and synovial viscous damping as a case study. In this model at Fig. 3, SE at link 2 represents reaction force and SF at 1 depicts the initial velocity of the model. SE at 8 is the bite force that can be assigned values to simulate the model. Linear muscle stiffness of the model is represented by C, capacitance at 6 and damping of the muscle is depicted by R, resistance at 9. Nonlinear stiffness and damping are modeled at C (link 11) and R (link 12) respectively. Inertia I at link 7 represents the mass of jaw. TF is the transfer function with modulus as *x/y* representing a fraction of distances between bite point to reaction point and muscle action point.

2.3 Simulation for a One-Dimensional System

The bond graph of the temporomandibular joint is simulated on SYMBOLS—Shakti software using Runge–Kutta fourth-order method. While simulating, the relative motion of the muscles and bones is modeled using a minimal and frictionless coefficient of friction. The average mass of the human jaw (internal body) is taken as 0.30 kg [9]. The table below represents the parameters for simulation: (Table 1).

3 Results and Interpretations for One Dimensional Model

In this simulation, results are produced for average values of bite force. The simulation results are validated from the other mathematical studies, and 40–50 mm of

Table 1 Parameters used for one-dimensional model simulation

Type of properties (Jaw)	Range
Joint reaction force (jaw opening)	2.71-48.61 N
Joint reaction force (jaw closing)	7.7–64.9 N
Velocity during mastication	28–98 mm/s
Distance b/w premolar and joint	105.6 ± 0.05 mm
Distance b/w molar and joint	111.2 ± 0.3 mm
Distance between incisor and joint	100.6 ± 0.1 mm
Mass of mandible	3.1 ± 0.3 N
Bite force	200–1000 N
Muscle stiffness	10–15 N/mm
Damping muscle	1.2 Ns/mm
Muscle stiffness nonlinear	10.9 N/mm
Damping muscle nonlinear	2 Ns/mm

the jaw opening (displacement) for a bite force of 600 N has been obtained from the simulation results. The results analyzed for 600 N bite force through FFT analyzer tool of SYMBOLS—Shakti are shown in Figs. 4, 5 and 6.

- Figure 4 represents the force value of 600 N (average) which has been simulated using bond graph while biting action in continuous movements (jaw opening).
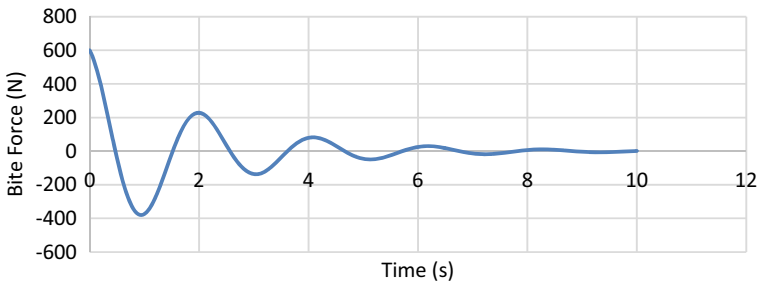

Fig. 4 Average bite force (600 N)

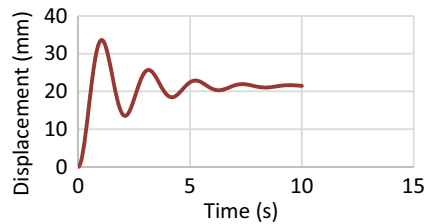**Fig. 5** Displacement at 600 N jaw opening

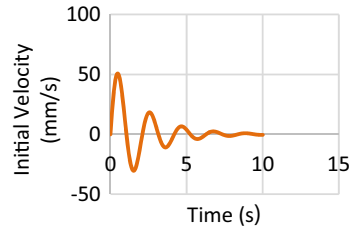**Fig. 6** Initial velocity for biting at 600 N

Table 2 Comparison of obtained results from present study with available literature

Type of parameter	Present study	Past studies (cited values)
Average biting force (N)	600 N	400–600 N [10]
Average jaw opening (mm)	35 mm	30–40 m [16]

- In Figs. 4 and 5, the graph shows the force and displacement values at its peak and trough, which represents jaw in action from bringing it in a state of motion from a state of rest.
- In Fig. 6, the maximum initial velocity due to biting action has been plotted.
- The average bite force in humans in masticatory action has been precisely modeled and simulated using bond graphs. This has been studied and reviewed previously by using experimental as well as simulation techniques (Table 2).

4 Conclusion

This paper has proposed a novel method to study the dynamic simulation of the human jaw using bond graph modeling technique. This paper represents bond graph model for TMJ dynamic simulation for the first time in the field of TMJ biomechanics. It can be further elaborated and used for biomechanical purposes like prostheses simulation, robotics and virtual reality systems. From the results of the present study, the following conclusions can be interpreted:

1. Bond graph model is a unique tool to study the biomechanics of TMJ which involves complex muscle motion and activation.
2. A biting force of 600 N produces a jaw (opening) displacement of a maximum of 35 mm which is similar to the values found in the available literature.
3. The effectiveness of the simulated bond graph model for one-dimensional model of TMJ in the present study is validated from the relevant biomechanical studies.

References

1. Barbenel JC (1974) The mechanics of the temporomandibular joint: a theoretical and electromyographical study. J Oral Rehabil 1:19–27
2. Van Eijden TMGJ, Klok EM, Weijs WA, Koolstra JH (1988) Mechanical capabilities of the human jaw muscles studied with a mathematical model. Arch Oral Biol 33(11):819–826
3. Van Eijden TMGJ (1990) Jaw muscle activity in relation to the direction and point of application of bite force. J Dent Res 69(3):901–905
4. Koolstra JH, van Eijden TMGJ (1995) Biomechanical analysis of jaw-closing movements. J Dent Res 74(9):1564–1570
5. Osborn JW (1995) Biomechanical implications of lateral pterygoid contribution to biting and jaw opening in humans. Arch Oral Biol 40(12):1099–1108
6. Slager GEC, Otten E, Van Eijden TMGJ, Van Willigen JD (1997) Mathematical model of the human jaw system simulating static biting and movements after unloading. J Neurophysiol 78(6):3222–3233
7. Kuboki T, Takenami Y, Maekawa K, Shinoda M, Yamashita A, Clark GT (2000) Biomechanical calculation of human TM joint loading with jaw opening. J Oral Rehabil 27:940–951
8. Zhang F, Peck CC, Hannam AG (2002) Mass properties of the human mandible. J Biomech 35(7):975–978
9. Vaz A, Hirai S (2004) A simplified model for a biomechanical joint with soft cartilage. In: IEEE International conference on systems, man and cybernetics (IEEE Cat. No.04CH37583).1, pp 756–761
10. Galer B, Hockenberry N, Maloof J, Monte-Lowry M, O'Donnell K (2007) Human jaw motion simulator. Mechanical engineering undergraduate capstone projects, Paper, p 65
11. Cid M, Coutant JC, Mesnard M, M., J. Morlier, J., Ballu, A. (2011) Mechanical modeling of the temporomandibular joint, a kinematic discrimination approach. Comput. Methods Biomech Biomed Eng 10(1):189–190
12. Ovesy M, Nazari MA, Mahdavian (2016) Equivalent linear damping characterization in linear and nonlinear force–stiffness muscle models biological Cybernetics 110:73–80
13. Tyagi P, Rastogi V, Arora AS (2016) Modeling and simulation of the cervical region of the spine using bond graphs. In: Proceedings of the international conference on bond graph modeling and simulation (ICBGM '16). Society for computer simulation international, San Diego, CA, USA, pp 115–121
14. Gallo LM, Colombo V (2019) Functional anatomy and biomechanics of the temporo-mandibular joint. In: Connelly ST, Tartaglia GM, Silva RG (eds) Contemporary management of temporomandibular disorders. Springer, Cham
15. Tyagi P, Rastogi V, Arora AS (2009) Indian Journal of Biomechanics; In: National conference on biomechanics (Special issue), pp 133–137
16. Mukherjee A (2005) In: SYMBOLS Shakti User's Manual, High-Tech Consultants, STEP, Indian Institute of Technology, Kharagpur, India

Finite Element Analysis of Laser Drilling on Ti-6Al-4V Alloy

Satish Namdev, Anand Pandey, Arun Kumar Pandey, Rakesh Kumar, and Ashish Goyal

Abstract Titanium alloy (Ti-6Al-4V) is high strength and high thermal resistance alloy. Hole formation is very difficult on this material by traditional drilling process. Laser drilling is an untraditional method that is used for creating hole on titanium alloy. Laser drilling is a thermal energy-based machining process. Selected input parameters and their value affect material quality characteristics. In present study, temperature and thermal stress distribution have been predicted on selected parameters (power and cutting speed) for through-hole formation of 2 mm diameter on titanium alloy during Nd:YAG laser drilling. Finite element software (ANSYS) has been used to simulate the problem and found predicted selected responses are suitable for laser drilling of titanium alloy.

Keywords ANSYS · Heat flux · Laser drilling · Ti-6Al-4V

1 Introduction

Laser drilling is thermal-based machining process. Thermal energy of laser beam is used to remove material during laser drilling. High precise laser beam is concentrated on material. Thermal energy is absorbed by workpiece, and there is an increase in temperature of contact surface area. Once temperature reaches above melting temperature of workpiece, molten process starts. Molten material is removed by using high pressure assist gas, but it develops hole taper [1–6].

Laser drilling parameters and material properties affect material removal process. Pulse frequency, laser power, assist gas pressure, and cutting speed are some laser

S. Namdev (✉) · R. Kumar
Automobile Engineering Department, Manipal University Jaipur, Jaipur, India
e-mail: satish.namdev@jaipur.manipal.edu

A. Pandey · A. Goyal
Mechanical Engineering Department, Manipal University Jaipur, Jaipur, India

A. K. Pandey
Mechanical Engineering Department, Bundelkhand Institute of Engineering and Technology, Jhansi, India

parameters. Thermophysical properties, material reflectivity, and thickness are material properties. Hole quality may be controlled by controlling of these parameters [4–16].

Titanium grade V (Ti-6Al-4V) is a high strength with high thermal resistance material. Conventional drilling process is not suitable for this kind of (difficult to cut) material. Laser drilling may be used to perform drilling operation on this material [1, 2, 17].

Laser machining process is known for precision machining process. It is very costly process, and high skilled operators are required for performing operation [3, 4].

Some researchers have introduced finite element simulation technique for material removal in laser machining process. In this technique, constant temperature has been used as melting temperature heat source [1–3, 7–9, 15, 16, 18]. Researchers have adopted Gaussian distributed heat source as laser heat source in their study for modeling of drilling process. Finite element method (FEM) is used to create model to analyze thermal stress and temperature distribution on workpiece surface during laser drilling. Various FEM-based software, i.e., ANSYS and COMSOL are used to analyze any type of thermal or structural problem. Following assumptions are used in ANSYS to derive a model [7, 8, 19]:

a. Material is opaque and isotropic.
b. Gaussian distributed heat source is used for spatial distribution at TEM00 mode.
c. Density of laser energy is equal along workpiece thickness with an appropriate focus depth.
d. No vaporization occurs during immediately removal of molten material by pressure of assist gas.
e. Material is re-solidified in small fraction. Thus, phase change is neglected.
f. Inert gas cooling effect is negligible.

2 Material and Methodology

Laser beam machining is a thermal-based machining process and it is very costly machining process [5, 6, 12–14]. So, theoretical analysis has been performed by using FEM-based ANSYS software before experimental study. Once selected input parameters are validated theoretically, then these parameters may be adopted for experimental study.

In this paper, ANSYS software has been used as simulation technique to analyze temperature and thermal stress distribution during Nd:YAG laser drilling to see the effect of decided laser input parameters to create through-hole. Ti-6Al-4V material sheet of 1.2 mm thickness has been used as workpiece to create through-hole of 2 mm diameter.

2.1 Heat Transfer Analysis

Heat source modeling is used to analyze thermal behavior of laser beam during laser drilling. Gaussian beam shape is used as laser beam for thermal modeling. Because of high power, Gaussian beam may be focused on a smallest diameter [9]. Beer–Lambert law is used derive governing equation for transmitted laser energy to workpiece of z thickness. Laser energy is given by [8]:

$$S(z) = I\mathrm{e}^{-\delta z} \tag{1}$$

where

$P =$ Laser output power in watts
$I =$ Intensity of laser, i.e., $P/\pi r^2$ (W/m^2)
$\delta =$ Coefficient of absorption (m^{-1})

Where absorption coefficient of metal has taken around 5e7 m^{-1}. So, absorption of laser energy takes place in a very shallow region with a depth of only a fraction of wavelength of incident radiation. Adequate surface heat flux (W m^{-2}) can be calculated by follows expression [7, 8, 19]:

$$S = I\mathrm{e}^{-\delta}(1 - s)\mathrm{e}^{\left(-(x - r\sin\omega t)^2 + (y - r\cos\omega t)^2/a^2\right)} \tag{2}$$

where

$a =$ Gaussian parameter
$s =$ Surface reflectivity
$\delta =$ absorption coefficient
$\rho =$ Material density (Kg/m^3)
$r = \sqrt{x^2 + y^2}$ where x and y are coordinate axes (laser drilling radius)
$\omega =$ Cutting speed in rpm

Transverse electromagnetic mode (TEM) is used to characterize profile of laser beam. These modes are denoted in form of TEM$_{op}$, where 'o' and 'p' are in subscript, indicate number of nodes in orthogonal direction to propagation of beam. Normally TEM$_{00}$ or TEM$_{01}$ modes are used to characterize laser beam profile. TEM$_{00}$ has Gaussian spatial distribution. It also has uniform phase front. There is smooth drop off radiance from center of beam. So, TEM$_{00}$ is best mode for LBM. It also reduces effect of diffraction and creates small spot size [4].

Heat transfer model must be three-dimensional and transient in laser machining. Transient thermal model can be written as [4,510]:

$$\rho c(T)\frac{\partial T}{\partial t} = \frac{\partial}{\partial x}\left(k(T)\frac{\partial T}{\partial x}\right) + \frac{\partial}{\partial y}\left(k(T)\frac{\partial T}{\partial y}\right) + \frac{\partial}{\partial z}\left(k(T)\frac{\partial T}{\partial z}\right) + Q \tag{3}$$

where $c(T)$ and $k(T)$ are function of temperature of specific heat and thermal conductivity, respectively. Q is internal heat generation rate.

2.2 Thermal Stress Analysis

As laser beam moves, molten material re-solidified rapidly in heated zone, because cooling rate increases in heated zone. High cooling rate develop thermal stress in workpiece [8, 19].

Thermal stress is calculated by given Formula as [8]:

$$\sigma_{\text{therm}} = \frac{E\alpha\Delta T}{1 - \mu} \tag{4}$$

where

E = Modulus of elasticity
α = Coefficient of thermal expansion
μ = Poisson's ratio
ΔT = Temperature difference
Equivalent von Mises stress is found out by given Formula as [8]:

$$\sigma_m = \sqrt{\frac{\left(\sigma_x - \sigma_y\right)^2 + \left(\sigma_y - \sigma_z\right)^2 + (\sigma_z - \sigma_x)^2}{2}} \tag{5}$$

where

σ_x = Principal stress from any point in x-direction of principal axis
σ_y = Principal stress from any point in y-direction of principal axis
σ_z = Principal stress from any point in z-direction of principal axis
These principal stresses are calculated and putting in Eq. 5 to find out σ_m. If von Mises stress reaches at yield strength of material then plastic deformation occurs. Thermal-related material properties are taken from Table 1 to calculate thermal stress.

Table 1 Thermophysical properties of titanium alloy (Ti-6Al-4V) [7]

Melting range 1873 K-1933 K; Modulus of Elasticity–113.6 GPa; Poisson's ratio–0.34; Density–4430 kg/m^3

Temperature (K)	Thermal conductivity (W/m K)	Specific heat (J/Kg K)
373	30.5	300
473	24.5	465
673	20.4	551
873	19.4	591
1073	19.7	633
1273	20.7	675
1473	22	620
1773	24.5	686

The temperature-dependent properties of Ti-GradeV used in calculation are shown in Table 1. The workpiece is clamped from surrounding. No external loading is assumed on workpiece.

2.3 Finite Element Simulation (FES)

FES has used same process parameters adopted in experiments. Therefore, FEM-based software ANSYS is used to find out distribution of temperature and thermal stress in workpiece [7, 8, 19].

There are total three stages in ANSYS to solve any kind of problems. These are preprocessing, solution, and post-processing. Each stage has number of steps. These three stages have following steps for solving the problem in ANSYS [8, 18, 19]:

Stage 1 Preprocessing

1. Specify Jobname.
2. Define element type. (SOLID187 is 3D element for transient thermal and structural analysis).
3. Define material properties. (thermal conductivity, coefficient of expansion, specific heat, modulus of elasticity, etc.)
4. Create 3D model.
5. Specify meshing size to control density.
6. Meshing (tetrahedral) to build elements and nodes.

Stage 2 Solution

7. Specify process parameters as heat flux and define position on material sheet.
8. Solve.

Stage 3 Post-processing

9. Plot temperature distribution and thermal stress distribution.
10. Nodes selection along center of plate.
11. Listed centered nodes location.
12. Listed temperatures and stresses at each node.
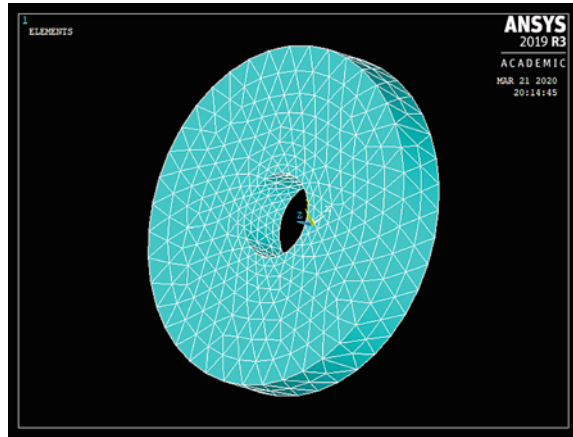
Re-analysis

13. Modify mesh/re-analyze.

Exit

14. Exit and saved all data.

2.4 Model for Transient Analysis Using ANSYS

Firstly, transient thermal model is prepared to find out temperature distribution in material. These results are used as input data for transient structural analysis. ANSYS

Fig. 1 Meshing of object in
ANSYS

Parameter Design Language (APDL) is used as programming language to prepared model for transient analysis. SOLID187 has been used as thermal element type for transient thermal analysis. But, SOLID187 has been implemented as structural element type for transient structural analysis and temperature from thermal stress analysis is used as input data. Size of element meshing plays an important role in finite element analysis, because coarse meshing can give large errors in result. Same mesh size has been used for both type of analysis with different element types. Fine meshing gives best result, but this type of meshing increases computational time. Appropriate element size is chosen based on mesh convergence parametric studies [12–15, 18]. For current study, 0.01 mm element size and tetrahedral meshing have been chosen for 1.2 mm thick Ti-6Al-4V alloy sheet. Selected element size and type of meshing are appropriate for computational efficiency and simulation accuracy to create a hole of 2 mm diameter. Therefore, a circular disk of radius 1 mm with 1.2 mm thickness has been taken, and mesh comprises about 40,000 for same thickness. The details about the mesh are presented in Fig. 1.

3 Results and Discussion

3.1 Transient Temperature Distribution Analysis

Thermal distribution can be studied with real time by this analysis. Thermal properties like thermal conductivity, expansion coefficient, and specific heat have been taken from Table 1.

Heat flux has been used for thermal input parameter in ANSYS mechanical APDL 2019R3. That has been calculated from Eq. 2, where laser power and cutting speed have been taken 150 W and 60 mm/min that has been taken from decided experimental
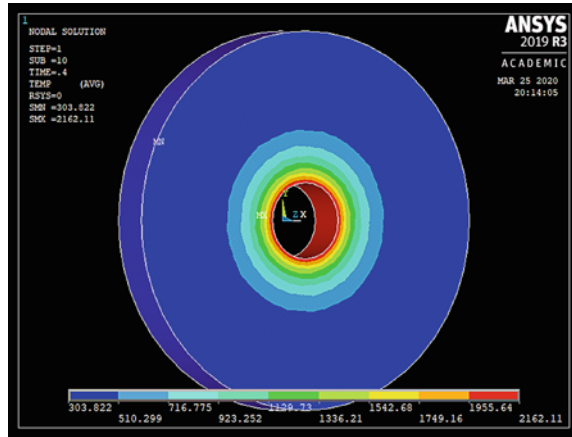
input parameters. Initial (ambient) temperature has been taken 303 K. Heat flux is calculated $22e^6$ W/m^2 and time taken to complete the process in 0.4 s. Temperature distribution for hole diameter 2 mm has been shown in Fig. 2 for Ti-alloy of 1.2 mm thick sheet during thermal analysis. Maximum temperature is 2162.11 K that has been found around hole surface as shown in Fig. 2. Melting temperature for this material is 1933 K from Table 1, maximum temperature is approximately 229 K more than melting temperature. This temperature is enough to evaporate molten metal from workpiece. So, transient thermal analysis model is valid for proven that calculated temperature is enough to perform hole formation for 1.2 mm thick sheet.

3.2 Transient Thermal Structural Analysis

This type of analysis is generally used for study of stress on any type of surface. In laser machining process, thermal energy is used to perform any type of machining operation. By this analysis, thermal stress may be calculated. Temperature has been taken as input parameter here only, i.e., around hole surface. Input temperature 2162.11 K is taken to find out resultant thermal stress (von Mises stress). Mechanical properties like elastic constant and thermal coefficient have been taken from Table 1 to find out thermal stress.

Actual hole diameter at entrance is quite more than desired hole diameter during laser drilling operation due to convergent–divergent characteristics of laser beam [13–16, 18]. It can be seen clearly from Fig. 3, where maximum displacement is 0.013 mm in hole diameter 2 mm. Thermal stress (von Mises stress) distribution is showing in Fig. 4. Maximum von Mises stress has been found out 3130 MPa around hole circumference that is much greater than ultimate stress of titanium grade V (950 MPa) from Table 1.

Fig. 3 Displacement diagram
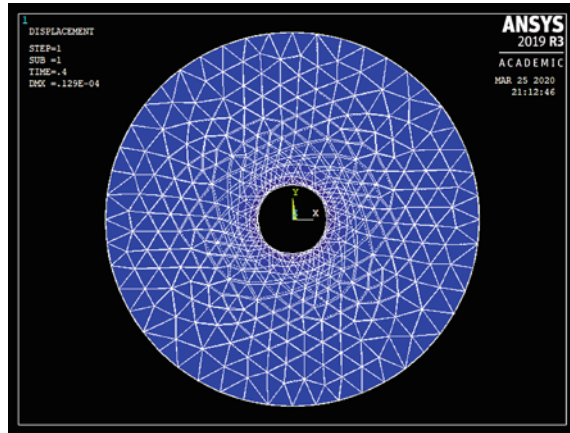
Fig. 4 von Mises stress (thermal stress) analysis
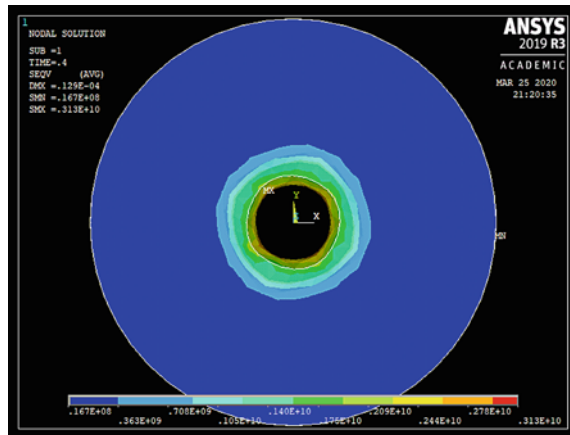
It has been proven that all decided input parameters for thermal distributions are correct and validated by this FEM analysis. Now these selected parameters (power and cutting speed) may be used for further experimental work.

4 Conclusions

It has been proven that selected power and cutting speed is suitable for performing a hole for Nd:YAG laser drilling for 2 mm hole diameter. After applying FEM-based simulation technique (ANSYS), following points have been observed:

Maximum temperature found 2162.11 K around hole circumference that temperature is sufficient to melt the material because this value is much higher from melting

temperature (1933 K) of Ti-6Al-4V alloy. Maximum thermal stress found 3130 MPa around hole circumference is much more than ultimate stress (950 MPa) of Ti-6Al-4V alloy. Maximum displacement has been found during hole formation 0.013 mm for 2 mm hole diameter.

References

1. Steen WM(1991) In: Laser material processing, Springer, London, pp 72–80
2. Yilbas BS, Arif AFM, Abdul Aleem BJ (2010) Laser cutting of rectangular blanks in thick sheet metal: effect of cutting speed on thermal stresses. J Mater Eng Performance 19:177–184
3. Kim MJ (2005) 3D finite element analysis of evaporative laser cutting. Appl Math Model 29:938–954
4. Chryssolouris G (1991) In: Laser machining-theory and practice, Mechanical Engineering Series Springer
5. Reda R, Magdy M, Rady M (2019) Ti–6Al–4V TIG weld analysis using FEM simulation and experimental characterization. Iran J Sci Technol Trans Mech Eng 44:765–782
6. Sifullah AM, Nukman Y, Hassan MA, Hossain A (2016) finite element analysis of fusion laser cutting on stainless steel-304. ARPN J Eng Appl Sci 11(1):181–189
7. Arif AFM, Yilbas BS (2008) Thermal stress developed during laser cutting process: consideration of different materials. Int J Adv Manuf Technol 37:698–704
8. Nyon KY, Nyeoh CY, Mokhtar M, Abdul-Rahman R (2012) Finite element analysis of laser inert gas cutting on inconel 718. Int J Adv Manuf Technol 60:995–1007
9. Bahotre NB, Harimkar SP (2008) In: Laser fabrication and machining of materials, 186–187. Springer, New York, pp 51–52
10. Ion JC (2005) In: Laser processing of engineering materials, Elsevier, Oxford, pp 168–169
11. Radovanovic M (2006) Some possibilities for determining cutting data when using laser cutting. J Mech Eng 52:645–652
12. Namdev S, Pandey A, Pandey AK (2019) Optimization of hole taper in machining of SS316L alloy sheet using laser beam drilling. Int J Adv Sci Technol 28(18):771–778
13. Namdev S, Pandey A, Pandey AK, Kumar R (2019) Experimental analysis on titanium grade-V sheet using laser beam machining process. Int J Adv Sci Technol 28(20):678–690
14. Liverani E, Toschi S, Ceschini L, Fortunato A (2017) Effect of selective laser melting (SLM) process parameters on microstructure and mechanical properties of 316L austenitic stainless steel. J Mater Process Technol 249:255–263
15. Liu Y, Zhang J, Pang Z (2018) Numerical and experimental investigation into the subsequent thermal cycling during selective laser melting of multi-layer 316L stainless steel. Opt Laser Technol 98:23–32
16. Suryawanshi J, Prashanth KG, Ramamurty U (2017) Mechanical behavior of selective laser melted 316L stainless steel. Mater Sci Eng 696:113–121
17. Arif AFM, Yilbas BS (2008) Thermal stress developed during the laser cutting process: consideration of different materials. Int J Adv Manuf Technol 37:698–704
18. https://www.ansys.com/products/structures/thermal-analysis
19. Yilbas BS, Akhtar SS, Keles O (2013) Laser hole cutting in aluminum foam: Influence of hole diameter on thermal stress. Opt Laser Eng 51:23–29

Design and Optimization of 4-Degree-of-Freedom Anthropomorphic Robotic Manipulator

Abhinav Sharma, S. C. Rishabh Bavithran, and Pritish Shubham

Abstract Robotic manipulator is an automated arm widely used for manipulating objects without or minimal human intervention. Maximizing the power efficiency and the dexterous workspace is invariably a primary factor in designing an industrial robot arm. The manipulator structure is an arrangement of joints and links to form a kinematic chain which plays a vital role in deciding the arm's characteristics and overall performance. In this paper, the designing and optimizing of the manipulator structure, workflow of an articulated industrial robot, and its kinematics using D-H convention are presented. The 3D printing technique was considered for structural development, thus DfAM principles were considered for design. The outcome of the work shows the torque requirement, and overall structural weight was reduced by 15 and 20%, respectively, whereas the dexterous space improved by 18% with the proposed design of the robotic arm.

Keywords Anthropomorphic robotic manipulator · Topological optimization · Multi-body simulation · Design for additive manufacturing (DfAM)

1 Introduction

The manipulation refers to handle or control of the physical objects, thus robotic manipulators are automated machines which are used for handling and managing the desired objects autonomously without much human intervention. The robotic manipulator is based on the concept of hard robotics that deals with the use of rigid bodies whose degree of freedom is an exact measurable value.

An industrial robotic manipulator comprises of a number of rigid links and joints arranged in a certain fashion allowing them to move to interact with the surroundings. The interaction mainly depends on the constraints placed by the degree of freedom of the structure, link length and material, and power of actuation. The actuation is mostly provided by servo motors or stepper motors.

A. Sharma · S. C. Rishabh Bavithran (✉) · P. Shubham
Amity University, Noida 201313, Uttar Pradesh, India
e-mail: rishabh0973@gmail.com

A manipulator is required to work for many hours continuously and it has high power consumptions. An efficient robot with minimized power consumption and the improved dexterous workspace is always desired. These characteristics could be achieved with an optimal design of manipulator structure and joint design. Regardless of the link arrangement, the design itself will reduce the overall torque requirement and increase power efficiency significantly which is beneficial regardless of any type of motor used for actuation.

Several types of researches had been carried out to increase the efficiency of the robot and reduce the torque requirement. A study by Mustafa et al. [1] found out the ways to reduce the redundant weight of the robot by optimizing some existing popular robot. Another study by Sahu and Chaudhary et al. [2] shows that the load-carrying capacity, the relation between geometric variations and various materials used to make the link play a major role in determining the overall efficiency. Zhou et al. [3] studied the effect of design changes to improve the robot's payload. Similar outcomes were reported by other researchers too which shows relation between the structural arrangement of links and torque requirement [4–9].

Majority of research in this field focuses on the link arrangement and its connection. Very few papers were found which worked on the optimizing the design of the link. And negligible research focused on topological optimization of link structure and the DFMA for the joint connection configuration using 3D printing technique. Therefore, a novel approach for the designing the optimized structure and the innovative joint configuration design for improving the performance of the manipulator was undertaken in this research work. This paper discusses the complete workflow that goes into the design of a robotic manipulator including the motion simulation and stress analysis.

2 Design Methodology

2.1 Design Considerations

Joint Consideration The type of joints provided in the robot certainly determines the type of workspace that will be enveloped. All prismatic joints in a robot will provide a cuboidal workspace with a limited degree of freedom which means that there is not much freedom in selecting the end-effector orientation approach. The articulated robot that is the most popular in the industrial sector has rotary joints. The degree of freedom for this robot is high with a spherical workspace. Different combinations of prismatic and rotary joints even their sequence can alter the workspace drastically. The anthropomorphic configuration of robotic manipulator was considered for design and optimization.

Degree of Freedom The degree of freedom in a robot is the number of individual parameters or variables that are required to determine the position of the end effector. The DOF of a robot can be found using the Formula as presented in Eq. 1 [10].

$$\text{Degree of freedom} = m(N - 1 - J) + \sum_{i=1}^{J} f_i \tag{1}$$

N = number of links, including ground; J = number of joints
m = degrees of freedom of a single body ($m = 6$ for spatial and 3 for planar body)
f_i = the degree of freedom of joint number 'i'.

Design for Additive Manufacturing (DfAM) The DfAM is a technique which is used in correlation with 3D printing process. DfAM helps to increase the efficiency and flexibility of design and the parts designed through DfAM save a considerable amount of material, cost, and time. For the present work, DfAM technique was used for optimized design of link structure and the gear train for the joint configuration.

Link Design. The dimensions of each link and their order determine the reach of the workspace and the torque required to move the links. Improper link length and arrangement can cause high unnecessary power loss, increased weight of the overall design, and imbalanced center of gravity. The link dimensions and arrangement should be as such that maximum dexterous workspace is obtained along with maximum power efficiency. The generic cylindrical shape was considered as the base for link design and further topological optimization was performed using the Altair Inspire software for improving the performance of the manipulator.

Gear Design. Motion from one link to another is transmitted through actuator system that is positioned at the joint. The electrical actuation system using stepper motors was considered for the present. Stepper motors with high torque transmission capability are bulky and difficult to include in the considered robot design. Therefore, the torque provided by the average stepper motors, if used, needs to be enhanced by some mechanism—thus gear train was considered in the joint configuration. The torque requirement for each joint was obtained by using the multi-body simulation analysis. For configuring the joints and connection between the links—epicyclic gear arrangement was found to be the best solution. This is attributed to its compactness and large speed variation capability. The DfAM technique was used for creating the epicyclic gear train embedded within the link structure for creating the joint configuration. This resulted in improving the torque transmission capability of the motor to the connecting link.

2.2   CAD

The computer-aided design (CAD) is used for creating virtual model of the conceptualized part. CREO parametric software was extensively used for designing and assembly of the components of the manipulator. CREO allows 3D direct modeling, 2D orthographic views, and simulation using various mechanisms for testing the assembly.

For multi-body simulation and topographical optimization, Altair Inspire software was considered due to the ease of workflow and high accuracy achievability. The

motion analysis helps in observing the variation in motion a through intricate contacts between the joints and link and troubleshoot them if needed. Added to this, Inspire simulation predicts the power required to obtain the motion which greatly varies with a lot of variables that can be set within the software itself to mimic the real-life working conditions and obtain the most accurate theoretical results.

2.3 *3D Printing*

The 3D printing (3D-P) is a layered fabrication process which is a subdomain of additive manufacturing. It is majorly used for rapid prototyping processes. The main advantage of 3D-P process is its ability to directly convert the digital CAD design to a real product without much need of human intervention. For the present work, FDM 3D-P was used for developing the prototype of the robotic manipulator for design validation. Ultimate Cura software was used for simulating the 3D-P process and optimizing the print time and material requirement without compromising the strength.

3   Results and Discussion

3.1 *Link Design*

The manipulator design was created with joint configurations and assembled by using 'CREO Parametric' software. Multi-body motion simulation was performed on the designed assembly using Altair Inspire. Based on these simulation results, improvements were made which cumulatively add up to the final design. With different iterations made to the design, reduction in the torque requirement of motors and weight of the links were considered for enhancing the manipulator performance. Figure 1 shows the different design iteration layout along with their workspace envelop. The links were arranged in such a manner that every link can move without any hindrance with the system and surrounding links.

The DeIt-01, the 1st Design Iteration, shown in Fig. 1 was initially developed for high reach capability. But it has issues of non-reachability to the tablespace for picking the object, as well as the dexterous workspace obtained was also minimal with very high torque requirements. Taking cues from the flaws of the first design, alterations were made to the link lengths and the arrangement and developed DeIt-02. The design iteration DeIt-02 requires lower torque, as well as the reachability of the robot had increased by 20%. Both DeIt-01 and 02 have 3 degrees of freedom as the end-effector link was rigid and fixed with link 3 (Figs. 2, 3).

To increase the dexterous workspace, another degree of freedom was added to the manipulator in design iteration DeIt-03 which has 1 DOF for orientation of
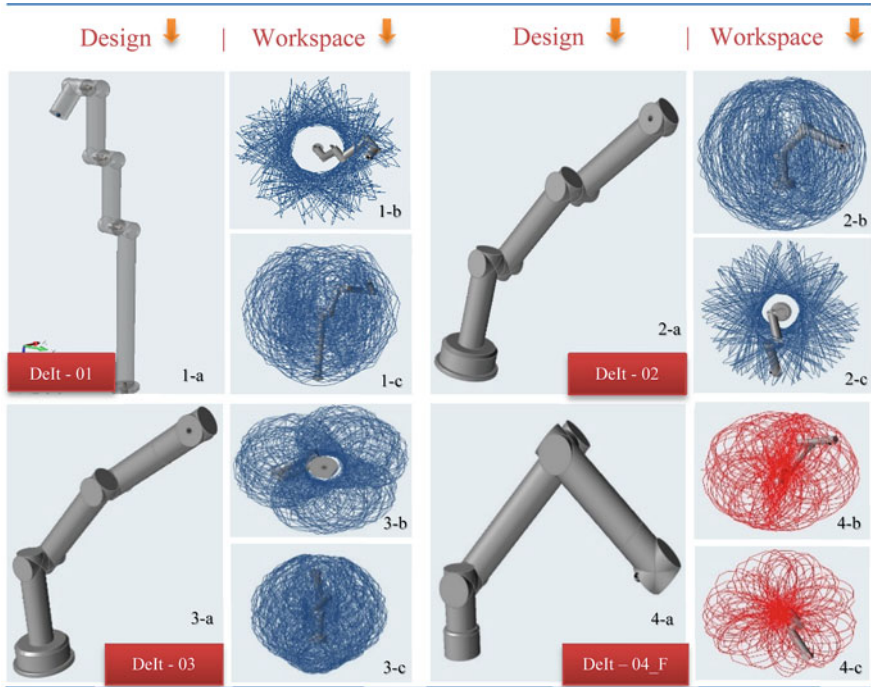
Fig. 1 Design iterations [DeIt 1–4]: **a** link configuration, **b** and **c** workspace envelop
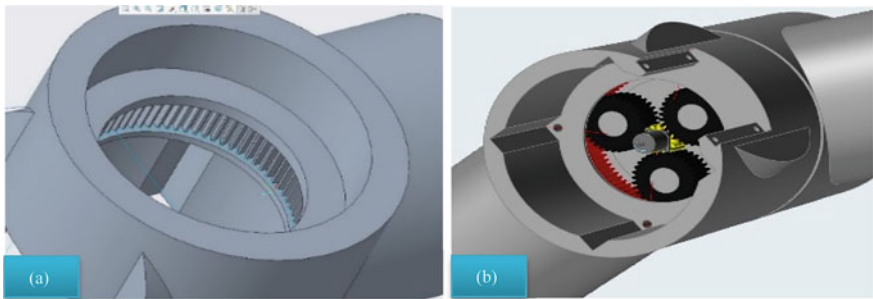
Fig. 2 Joint configuration: **a** ring gear design using DfAM technique and **b** assembly of inbuilt epicyclic gear train inside link

the end effector and 3 for the position. This enhances the Dexterous workspace by 10% as shown in Figs. 1, 3b and c. This final design iteration, DeIt-04_F, minor alterations with lengths, resulted in required torque minimized drastically and the Dexterous workspace further increased by 10%. The DOF for DeIt-03 and 04 was considered to be 4. Table 1 shows the improvement in power efficiency by considering

Fig. 3 D-H convention frame layout

Table 1 Increased power efficiency with each iteration

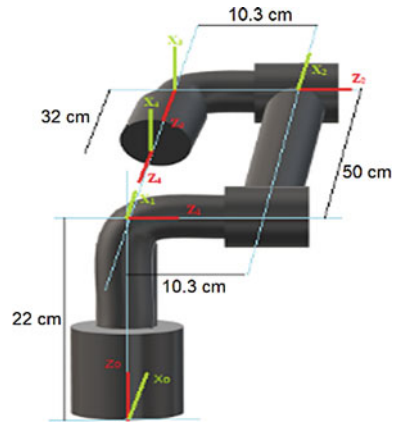| Motor	Percentage reduction with each design iteration			
	DeIt-01 (%)	DeIt-02 (%)	DeIt-03 (%)	DeIt-04 (%)
Base motor	–	−46	23	42
First link motor	–	0	0	34
Second link motor	–	−37	43	−22
E-E orientation motor	–	–	–	50

the previous iteration as the reference for computation in change percentage of the power requirement.

3.2 Joint Configuration Design

Designing planetary gear set for the joints and incorporating them in the link design itself contributed to the aesthetics and significant reduction in the overall weight. Yang Cao's et al. [11] methods were used to design all gears in CAD software. The planetary gear set was designed in such a way that the motor drives the sun gear and the power output is drawn from the planet gears and transmitted to the adjacent link to create movement. Equation 2 represents the speed ratio, from which it can be observed that by increasing the number of teeth on the ring gear and keeping the number of teeth on sun gear as low as possible, a high gear ratio can be attained which in turn results in less torque requirements.

$$\frac{\omega_s}{\omega_c} = 1 + \frac{z_r}{z_s} \tag{2}$$

By including self-designed planetary gear set in the joints, the power of the motor is best utilized. The use of gears reduces the torque requirement of the motor and further reduces the weight of the motor to be used. This makes the manipulator much efficient. For designing the ring gear, it is considered that the diameter of the link is not to be exceeding 100 mm. The joint must be configured within this limit including and for that, the pitch circle diameter of the ring gear was fixed at 80 mm. Thus, the number of teeth on the ring gear will also be 80 for keeping the modulus same. For the sun gear design, to avoiding any size and strength constraints, the pitch circle diameter of the sun gear was computed as 16 mm. As the diametral pitch is kept 1, the number of teeth on the sun gear will be 16. The planet gear teeth calculation (Eq. 3) was done by subtracting the radius of ring gear with the radius of the sun gear.

$$2r_p = (\mathrm{d}_r/2) - (\mathrm{d}_s/2) \tag{3}$$

$$2r_p = 40 - 8; \quad 2r_p = 32$$

To incorporate the epicyclic gear train in the joints, the design of ring gear was included within the link structure itself as shown in Fig. 2a. The planetary gears transmit the motion directly to the adjacent link and to mount them three cylindrical extrusions were made at the end of the connection. The planet gears will have the freedom to rotate around these rods with the help of bearings. Figure 2b shows the gear assembly enclosed within the manipulator link

3.3 Kinematics of Robotic Manipulator

The inverse kinematics with Denavit Hartenberg convention was considered to find the transformation matrices for determining the location of the end-effector. The frame layout along with the dimensions is shown in Fig. 3. The base as a reference is numbered as 0 and links are from 1 to 4. To determine transformation matrix $^0T_4$, which represents the positioning of link 4 with respect to base 0, Eqs. 4 and 5 were considered.

$$^0T_4 \times \, ^4P \, = \, ^0P \tag{4}$$

$$^0T_4 = \, ^0T_1 \times \, ^1T_2 \times \, ^2T_3 \times \, ^3T_4 \tag{5}$$

The homogeneous transformation matrix for determining the position of links can be found through the D–H convention Table 2.

The table shows the four different parameters—joint angle (θ), link twist (α), link length (r), and link distance (d) for relating the link and joint variables. Multiplying all the 4 matrices we get the transformation matrix from 0th frame to 4th frame, we

Table 2 D-H convention table for manipulator kinematics

Frame no.	θ	α	r	d
1	$\theta_1\,(q)$	90°	0	22
2	$\theta_2\,(r)$	0°	−50	10.3
3	$\theta_3(s)$	−90°	0	−10.3
4	$\theta_4(t)$	0°	0	32

get the matrix as shown in Eq. 7. The transformation matrix $^0T_4$ can be found using the values shown in Table 2, represented in Eq. 6:

$$
\begin{bmatrix}
\mathrm{Cos}\theta_n & -\mathrm{Sin}\theta_n\mathrm{Cos}\alpha_n & \mathrm{Sin}\theta_n\mathrm{Sin}\alpha_n & r_n\mathrm{Cos}\theta_n \\
\mathrm{Sin}\theta_n & \mathrm{Cos}\theta_n\mathrm{Cos}\alpha_n & -\mathrm{Cos}\theta_n\mathrm{Sin}\alpha_n & r_n\mathrm{Sin}\theta_n \\
0 & \mathrm{Sin}\alpha_n & \mathrm{Cos}\alpha_n & d_n \\
0 & 0 & 0 & 1
\end{bmatrix}
\tag{6}
$$

$$
\begin{bmatrix}
-S(q)S(t)-S(r+s)C(q)C(t) & -S(q)C(t)+S(t)S(r+s)C(q) & -C(q)C(r+s) & -50C(q)C(r)-32C(q)C(r+s) \\
-S(q)S(r+s)C(t)+S(t)C(q) & S(q)S(t)S(r+s)+C(q)C(t) & -S(q)C(r+s) & -50S(q)C(r)-32S(q)C(r+s) \\
C(t)C(r+s) & -S(t)C(r+s) & -S(r+s) & -50S(r)-32(r+s)+22 \\
0 & 0 & 0 & 1
\end{bmatrix}
\tag{7}
$$

Here, Sin and Cos are represented as 'S' and 'C', respectively. Using Eq. 5, any point in the end effector frame (4th frame) with any angular orientation of the joints, the same point can be found with respect to the 0th frame and vice versa. The point in the 0th frame where the end-effector is supposed to reach is denoted as x, y, and z variables. The point in the end-effector frame is taken as (0, 0, 0). On solving Eq. 5, taking only the translation part of the overall matrix, we get

$$
^0P = \begin{bmatrix} x \\ y \\ z \\ 1 \end{bmatrix} \quad ^4P = \begin{bmatrix} 0 \\ 0 \\ 0 \\ 1 \end{bmatrix}
$$

$$
x = -50\,\mathrm{Cos}(q)\mathrm{Cos}(r) - 32\,\mathrm{Cos}(q)\,\mathrm{Cos}(r+s)
$$
$$
y = -50\,\mathrm{Sin}(q)\mathrm{Cos}(r) - 32\,\mathrm{Sin}(q)\,\mathrm{Cos}(r+s)
$$
$$
z = -50\,\mathrm{Sin}\,(r) - 32\,\mathrm{Sin}(r+s) + 22
$$

The angular variables q, r, and s decide the position of the end effector. The angular variable t is absent from all the three equations. This implies that 't' does not have any impact on the position of the end-effector but the angular orientation of the end-effector.
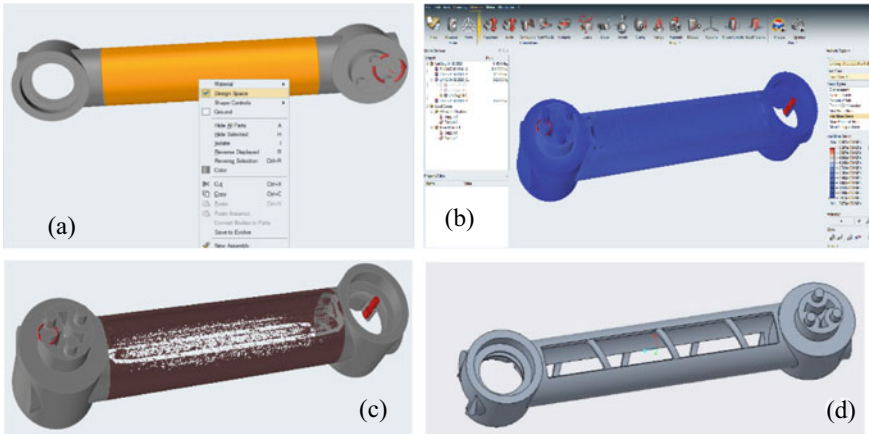
Fig. 4 Topological optimization: **a** design space of link, **b** stress analysis, **c** optimization result, and **d** final link design

3.4 Topological Optimization

Stress analysis and topological optimization of the links were done to reduce the weight of the manipulator. Various constraints were placed on the design such that it mimics the real-time working constraints. Link 3 was the largest and heaviest and hence the optimization was performed on the same. Figure 4a shows the design space consideration in link. Figure 4b and c is the outcome of the optimization, and Fig. 4d is the final design of the link after optimization with overall 20% reduced weight.

4 Conclusion

The anthropomorphic robotic manipulator was designed successfully by considering the DfAM technique for minimizing the weight and assembly of parts without compromising the strength and functionality. The topologically optimized structure reduces the overall weight by 20%. The modified epicyclic gear train arrangement and reduced weight resulted in minimizing the torque by 15%. Additionally, the modified link arrangement and its precise positioning helped to improve the dexterous workspace by 18%.

References

1. Bugday M, Karali M (2019) Design optimization of industrial robot arm to minimize redundant weight. Eng Sci Technol An Int J 22:346–352. Publisher, Location

2. Sahu S, Choudhury BB (2019) Stress and modal analysis of six-axis articulated robot using ANSYS. In: Lecture notes in networks and systems, Springer, Singapore, pp 303–311
3. Zhou J, Yang Z, Chen S (2014) Analysis of the harvesting robot arm modal based on CAE. J Chem Pharm Res 6:669–673. Publisher, Location
4. Daniele M, Ficuciello F, Siciliano B, Stramigioli S (2020) The influence of coordinates in robotic manipulability analysis. R Mech Mach Theory J 146:1–13
5. Baron N, Philippides A, Rojas N (2020) A robust geometric method of singularity avoidance for kinematically redundant planar parallel robot manipulators. Mech Mach Theory J 1–14
6. Madsen E, Skov O, Brandt D, Zhang X (2020) Control engineering practice comprehensive modeling and identification of nonlinear joint dynamics for collaborative industrial robot manipulators. Control Eng Practice
7. Xu R, Luo J, Wang M (2020) Kinematic and dynamic manipulability analysis for free-floating space robots with closed chain constraints. Robot Auto Syst
8. Teng M, Tsai Y, Hsiao C (2013) Mechanical design and kinematic analysis of a 10 DOF robot manipulator, IFAC, pp 301–309
9. Baghli FZ, El Bakkali L, Hamdoun O (2015) Parametric design optimization of two link robotic manipulator. Mech Mach Sci 25–32
10. Modern Robotics homepage (2019). http://hades.mech.northwestern.edu/index.php/Modern_Robotics#Online_Courses. Last Accessed 21 Dec 2019
11. Eng Tut (2019) https://drive.google.com/file/d/0B5meorzDrBfRUVAwQk1VeG1mVkk/view. Last Accessed 20 Nov 2019

Wear Behavior of Polytetrafluoroethylene and Its Composites in Dry Conditions

Priya Gajjal and S. Y. Gajjal

Abstract In this paper, we investigated the friction and wear behavior of PTFE, bronze, and carbon filled PTFE polymers. Friction and wear tests were done on the Pin on Disc machine. The tests were carried out at load 10, 20, 30 N at a speed of 0.35, 0.66, 0.98 m/s at time intervals. The results show that the friction coefficient in PTFE and its composites decreases with an increase in load. The maximum wear and friction were seen at PTFE and 20% glass fiber. Adding bronze and fillers of carbon to PTFE found reduced wear. It has been found that speed has less influence on wear compare to load at high values.

Keywords PTFE · Friction · Wear · Polymer

1 Introduction

Polymers and their composite based are used widely to slide against metals, polymers, and other materials. The friction in polymer generates deformation and adhesion [1–3]. Mechanism of deformation involves complete dissipation of the contact area while adhesion generates friction in polymer and breaks the weak bonding between materials. There are different types of materials in polymers such as PP, PVC, PMMA etc among these, the performance shows better in smooth molecular polymer profiles [4, 5].

In today's era, PTFE is widely used in industry due to its self-lubrication property, high-temperature stability, less friction coefficient, and high chemical resistance. Actually, if we take PTFE only its exhibits high wear and friction but if it is added with additives and fillers such as reinforcement with glass fibers, carbon fibers, and solid lubricants, this will minimize problems [6–9]. Friction is reduced and wear resistance is highly improved when additives are added in polymer with carbon fibre

P. Gajjal (✉)
AISSMS College of Engineering, Pune, India
e-mail: psgajjal.scoe@gmail.com

S. Y. Gajjal
Automobile Engineering, Government Polytechnic Nashik, Nashik, India

and aramid fibre [10]. Few researchers investigated that wear and friction can be reduced by selecting proper material combinations [8, 11–13]. Researchers observed that friction decreases with an increase in load [14–18] while some investigated its value increases with the increase in load [19, 20]. Wang et all [5] investigated that the sliding speed shows a high influence on the wear than the pressure.

In this pap at dry condition, investigations have been done, parameters such as speed, load, and time on friction and wear behavior of PTFE and its additives. AISI 400C stainless steel disc is used against the material in dry condition. The tests were carried out at load 10, 20, 30 N at a speed of 0.35, 0.66, 0.98 m/s at time intervals.

2 Experimental Details

2.1 Friction and Wear Tests

Friction and wear tests are carried out on Pin on Disc Test rig under dry condition at room temperature. The specimens of pin size are 8 mm diameter and 40 mm length were tested against AISI 400C stainless steel disc. Table 1 shows the chemical composition of the stainless steel disc AISI 400C used in this investigation. Surface roughness of disc was found to be 26.3 μm Ra. Figure 1 represents Pin on Disc wear test rig, which is used in this investigation. The description of the machine is that the

Table 1 AISI 400C chemical composition

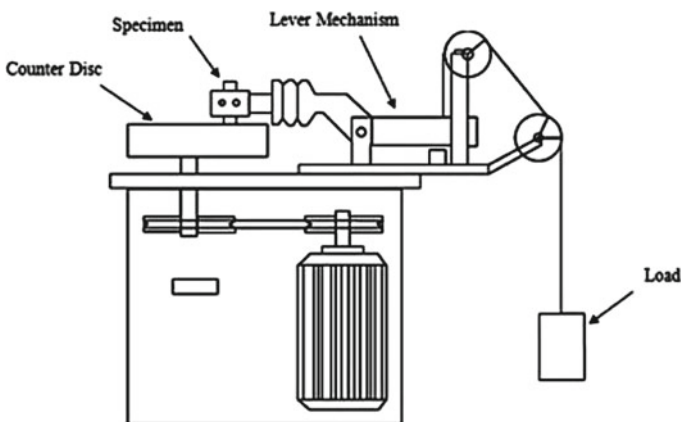| % C	% Si	% Mn	% P	% S	% Cr	% Mo	% Ni
0.96	1.4	0.6	0.036	0.029	18	0.69	0.85

Fig. 1 Schematic diagram of pin on disc test rig

round-shaped specimen can be fitted and pressed into contact of the disc by means of a lever, which is loaded, by lever arm and dead weights. The pin holder carrying the pin is mounted flat, which is free to slide in a direction at right angle to the axis about which the disc rotates. The beam type load cell connected to the indicator measures the tangential force exerted by the disc on the pin. This arrangement avoids any interaction between normal force pressing the pin into contact with the disc and the tangential force arising from friction, thus ensuring accuracy in measurement of friction force. Electric motor through the system of V-belt pulley combination provides necessary rotational speed to the disc. Speed of electric motor can be varied by the use of $1\theta i/p$, 3θ o/p frequencies.

Referring to Fig. 1, in which the pin is fixed onto a rotating disc. The load had applied by means of dead weights through the stationary rod against the rotating specimen. The frictional torque is measured with a load cell fastened on the stationary rod. A DC servomotor to provide sliding speeds at different ranges can control the rotating shaft. The load has been varied at different ranges and the temperature of the pin, has been measured with a thermocouple inserted in the specimen holder. The thermocouple has been connected to a meter to record the reading of temperature. The amount of wear has been measured by weight (pan) balance machine/ electronic balance noting the difference of initial and final weight of the specimen. The experiments are carried out at nominal sliding speed at different ranges from 200 to 2000 rpm. The load and pressure have also at different ranges from 1 to 20 kg and 0.2 to 2 N/mm^2. Duration of each test depends upon the rubbing materials as ranges from 15 min to 2 h. Each test has been conducted as long as the thermal condition or the wear rate is reached at steady-state condition. The test has been terminated due to the high rate of wear and rubbing track on the disc is too deep. The material properties and test conditions of the samples are shown in Table 2.

Table 2 The material properties and test conditions of the samples

Materials	Density g/cm^3	Temperature °C	Load N	Speed m/s
PTFE	2.10	Room temperature	10	0.35
			20	0.66
			30	0.98
PTFE + 20% GFR	2.42		10	0.35
			20	0.66
			30	0.98
PTFE + 25% Bronze	2.98		10	0.35
			20	0.66
			30	0.98
PTFE + 30% C	2.12		10	0.35
			20	0.66
			30	0.98

GFR–Glass fiber reinforced, C-Carbon

3   Results and Discussions

After the readings and investigation, Table 3 depicts coefficient of friction values for PTFE and its composites at dry conditions. Load applied at 10, 20, 30 N and speed at 0.35, 0.66 and 0.98 m/s respectively. Figure 2 depicts the variation of coefficient of friction of PTFE and composites at 0.35 m/s and at different loads. In Fig. 2, the coefficient of friction decreases with increase in load as the property of polymer is viscoelastic. The variation of coefficient of friction follows the equation $\mu = kN^{(n-1)}$ [20], where μ is the coefficient of friction, N is the load, k and n is constant, its value

Table 3   Coefficient of friction for PTFE and its composites at different speed and load

Materials	Load, N	Speed m/s		
		0.35	0.66	0.98
		Coefficient of friction, μ		
PTFE	10	0.34	0.35	0.39
	20	0.2	0.2	0.22
	30	0.15	0.15	0.13
PTFE + 20% GFR	10	0.30	0.29	0.30
	20	0.16	0.16	0.17
	30	0.10	0.10	0.11
PTFE + 25% Bronze	10	0.32	0.32	0.32
	20	0.16	0.175	0.17
	30	0.10	0.11	0.12
PTFE + 30% C	10	0.32	0.34	0.32
	20	0.17	0.18	0.175
	30	0.12	0.11	0.11

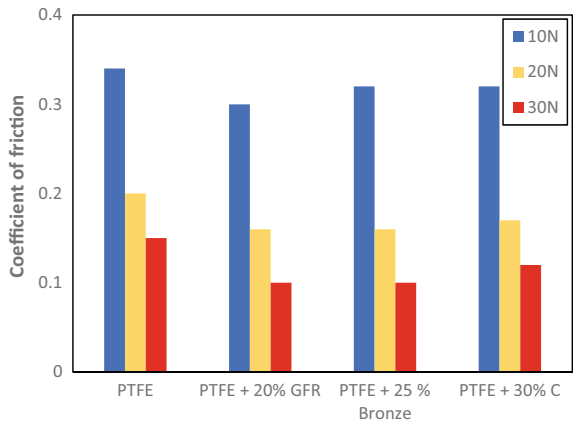**Fig. 2**   At 0.35 m/s, coefficient of friction versus PTFE and its composites

Fig. 3 At load = 20 N, variation of coefficient of friction of PTFE and its composites
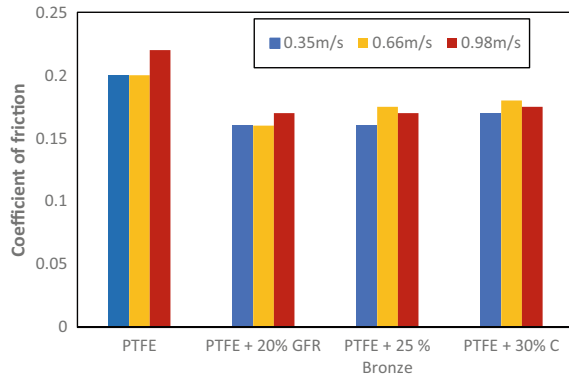

Table 4 Wear loss for PTFE and its composites at a different speed and load

Materials	Load, N	Speed m/s		
		0.35	0.66	0.98
		Wear (mg)		
PTFE	10	16	16	20
	20	20	25	28
	30	24	28	32
PTFE + 20% GFR	10	6	8	9
	20	8.2	9	12
	30	10	13	15
PTFE + 25% Bronze	10	6	10	10
	20	15.6	18.8	15
	30	16	18	18
PTFE + 30% C	10	8	10	12
	20	13	14.8	16
	30	15.4	19	19.3

is 2/3 <n< 1. The above equations show that the friction coefficient decreases with an increase in load. Later after a certain time, as the load increases, the wear and friction will increase due to the critical surface energy of the material polymer. The frictional heat rises the friction temperature at surfaces which comprises leading of molecule chains of polymer. Figure 3 shows the variation at 20 N load at different sliding speeds. In Fig. 3, if we compare Fig. 2, decrease in coefficient of friction seen at all speeds. At 20 N, decrease in coefficient of friction seen, as that this particular load the chemical and tribological changes are stable and can sustain the pressure but later as we increase load, the plastic flow of material will increase and it will try to stick the surface causing resistance in movement and again heat may rise.
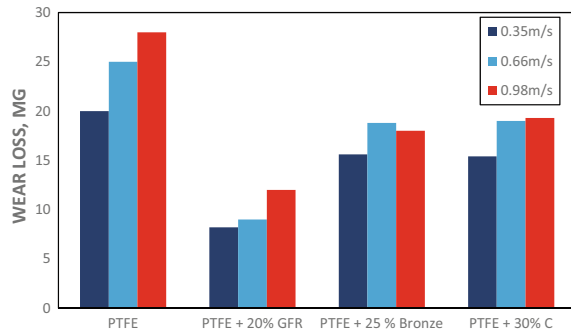
Table 4 shows the wear loss in PTFE and its composites under loads and at different speeds. Figures 4, 5, 6 shows the variation of mass loss at speed and load. From Fig. 4, it understood that speed is not having much influence on mass loss of PTFE and its composites, but Fig. 5 depict that in composite PTFE, wear decreases with an increase in load. In Fig. 5, the material with composites shows resistance to wear and shows its elastic properties, as PTFE.

From Fig. 4, the graph depicts that the highest wear is seen in plain PTFE compare to other PTFE composites. The lowest mass loss was seen at PTFE and 20% GFR, then in bronze and carbon composites, respectively. It is known that the wear loss process involves plastic flow, tribological effects, tribochemical effects, and shearing of material. Due to these effects the changes in wear with load and speed gives rise to wear. With respect to speed there is no maximum significant influence on the wear, if we compare with load on PTFE composite materials. At PTFE and 20% GFR, glass fiber reinforcement is rich in wear resistance material property due to its viscoelastic in nature.

4 Conclusions

From the above study, the following conclusions are drawn.

The coefficient of friction of plain PTFE and its composites decreases when load is applied increases.

Wear also shows a variation with composites of PTFE. Highest wear loss is seen in plain PTFE but PTFE + 20% GFR depicts lowest wear in all. PTFE +30% C gives wear less than bronze. Hence, PTFE with 20% GFR can be considered as very good wear resistance and gives good tribo characteristics between the materials considered in this paper.

Plain PTFE shows maximum wear because of its chemical and mechanical properties, thus PTFE reinforced with glass fiber improves the wear resistance which in turn carries high load capacity in all.

The influence of speed not showing much significant influence on wear, but load depicts a significant effect on wear and shown greater influence on PTFE material and its composites.

References

1. Hutchings et al (1992) Tribology friction and wear of engineering materials. London, Edward Arnold, pp 51
2. Lancaster JK (1973) Dry bearings: a survey of materials and factors affecting their performance. Tribology 219–251
3. Prasad BK (2004) Sliding wear behaviour of bronzes under varying material composition, microstructure and test conditions. Wear 257:110–123
4. Lancaster JK (1971) Estimation of the limiting PV relationships for thermoplastic bearing materials. Tribology 4:82
5. Wang et al (1999) Sliding wear behaviour and mechanism of ultra-high molecular weight polyethylene. Mater Sci Eng A 266:155–60
6. Metals Handbook (1992) vol 18, 10th ed. ASM, Materials Park, OH, pp 741–757
7. Metals Handbook (1979) vol 2, 9th ed. ASM, Materials Park, OH, pp 383–394
8. Archard JF (1958) The temperature of rubbing surfaces. Wear 59:438–455
9. So H (1996) Characteristics of wear results tested by pin-on-disc at moderate to high speeds. Tribol Int 1.29(5):415–423
10. Molesh M, Saka N, Suh NP (2002) A mechanism of high friction in dry sliding bearings. Wear 252:1–8
11. Glaser WA (1967) High temperature bearing materials. Metals Eng Quarterly 7(2):53
12. Midgley JW, Teer GD (1962) An investigation of the mechanism of the friction and wear of carbon,' ASME paper 62-Lub-15
13. Mecklenburg KR (1970) Selection of bearings for lubrication research. In: Proceedings AFML-MRI Conferences on solid lubricants, AFML-TR-70–127, vol 451
14. Clerico M Wear (1969) vol 13, pp 183–97
15. Unal et al (2003) Friction and wear behaviour of unfilled engineering thermoplastics. Mater Design 24:183–187
16. Bharat B (1999) In: Principles and applications of tribology. ISBN: 978-0-471-59407-9
17. Bekir SU (2009) Investigation of tribological and mechanical properties of metal bearings. Bullet Mater Sci 32:451–457

18. Maria M (2013) Analysis of friction and stabilized wear in the area of mechanical energy dissipation. J Tribol 135/041601-7
19. Unal H et al (2003) Influence of test conditions on the tribological properties of polymers. J Ind Lubric Tribol 55(4):178–183
20. Stuart BH (1997) Surface plasticisation of poly(ether ether ketone)by chloroform. Polymer Test 16:49–57

Parametric Investigation of Basic and Evaporative Inlet Air-Cooled Gas Turbine Cycle

Amar Nath Saxena, Aakash Panwar, Shivam Mishra, Anoop Kumar Shukla, and Mukesh Kumar Sahu

Abstract The present paper is an investigation of the effects of different operating parameters on the performance of the basic and inlet-air cooled gas turbine gas cycle. The cooling technique adopted for inlet air is evaporative cooling. Thermal efficiency, work output, compressor work has been chosen as some output parameters while turbine-inlet-temperature, pressure ratio, and ambient temperature are the input variables. The results have been plotted in terms of meaningful graphs. The study reveals that as TIT and pressure ratio is increased, thermal efficiency and net-work output increases and the evaporative cycle has a higher efficiency (variance ~1–2.5%) in comparison to the basic cycle. Also, thermal efficiency was observed to be higher at lower ambient temperature values i.e. nearly 288.15 K, and lowers as the ambient temperature is increased. The highest gas turbine net-work output for inlet air evaporative cooling technique has been observed to be 224.80 kJ/kg of air ($r_{pc} =$ 8, TIT = 1100 K) as well as the highest gas turbine efficiency is found to be ~46% ($r_{pc} = 16$ and TIT = 1100 K).

Keywords Gas turbine cycle · Evaporative cooling · Inlet air cooling · Thermal efficiency

Nomenclature

$t_{\text{comp(e)}}$ Ideal temperature at the exit of compressor in Kelvin (K)

A. N. Saxena · A. Panwar · S. Mishra (✉)
G. L. Bajaj Institute of Technology and Management, Greater Noida, Uttar Pradesh, India
e-mail: shivamnml07@gmail.com

A. K. Shukla
Amity University Uttar Pradesh, Noida, Uttar Pradesh, India
e-mail: shukla.anoophbti@gmail.com

M. K. Sahu
Cambridge Institute of Technology, Ranchi, Jharkhand, India

|	
t_i, t_{amb}	Temperature at the inlet of compressor Or Ambient temperature in Kelvin (K)
r	Pressure ratio
Υ	Adiabatic index ($= 1.4$)
$t'_{comp(e)}$	Actual temperature at the exit of compressor in Kelvin (K)
η_{comp}	Isentropic efficiency of compressor
W_c	Work input on compressor in kJ/kg of air
$\dot{m}_{a,in}$	Mass of air at inlet of compressor in kg/sec
$\dot{m}_{a,e}$	Mass of air at exit of compressor in kg/sec
$\dot{m}_{comb(e)}$	Mass of air at exit of combustion chamber in kg/sec
$\dot{m}_f$	Mass of fuel entering in combustion chamber in kg/sec
LHV	Latent heat of vaporization of fuel in kJ/kg of air ($= 42000$)
η_{comb}	Isentropic efficiency of combustion chamber
P_{loss}	Pressure loss in combustion chamber in bar
$p_{(comb)e}$	Pressure at the exit of combustion chamber in bar
$t_{t(e)}$	Ideal temperature at the exit of turbine in Kelvin (K)
$t_{(comb)e,}$	TIT Temperature at the exit of combustion chamber in Kelvin (K)
$t'_{t(e)}$	Actual temperature at the exit of turbine in Kelvin (K)
η_{gt}	Isentropic efficiency of gas turbine cycle
$W_{gt, net}$	Net work output of the gas turbine cycle in kJ/kg of air
W_{gt}	Work output of gas turbine in kJ/kg of air
$\eta_{gt\,(mech)}$	Mechanical efficiency of gas turbine cycle
ηth	Thermal efficiency of gas turbine cycle
Q	Net heat supplied in kJ/kg of air
$\omega_{eva(e)}$	Specific humidity at exit of evaporator
$\omega_{eva(in)}$	Specific humidity at inlet of evaporator
m_w	Mass of water flow in evaporator in kg
p_{vap}	Partial pressure of vapor
φ	Relative humidity
p_{sat}	Saturation pressure of air
$h_{eva(e)}$	Enthalpy of moist air at exit of air humidifier in kJ/kg
$h_{eva(in)}$	Enthalpy of moist air at inlet of air humidifier kJ/kg
h_w	Enthalpy of water in kJ/kg
$C_{p,eva(e)}$	Specific heat at constant pressure at exit of evaporator in kJ/kg
$C_{p,eva(in)}$	Specific heat at constant pressure at inlet of evaporator in kJ/kg
$t_{eva(e)}$	Temperature at the exit of evaporator in kelvin (K)
$t_{eva(in)}$	Temperature at the inlet of evaporator in kelvin (K)
$T_{DBT(e)}$	Dry bulb temperature at exit of evaporator in kelvin (K)
$T_{DBT(in)}$	Dry bulb temperature at inlet of evaporator in kelvin (K)
$T_{WBT(in)}$	Wet bulb temperature at inlet of evaporator in kelvin (K)
N	Efficiency of evaporator
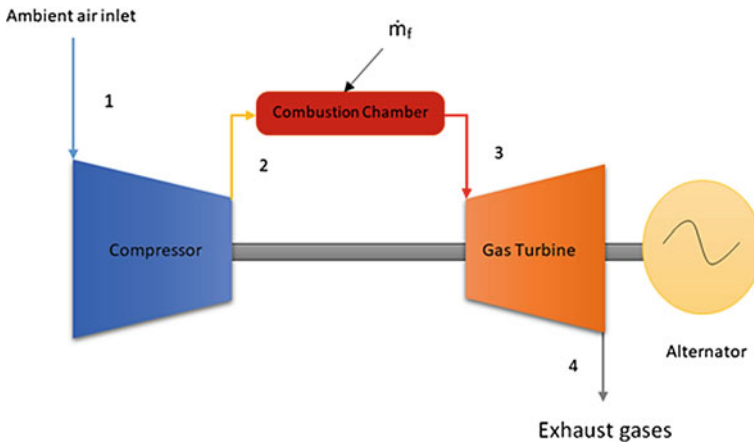
Fig. 1 Schematic diagram of a simple gas turbine cycle without inlet air cooling

1 Introduction

1.1 Simple Gas Turbine Cycle

Gas turbine power plants work on the Brayton cycle and Fig. 1 shows the schematic diagram of simple gas turbine cycle. Here, process 1–2 is an isentropic compression process in which ambient air is compressed and pressure and temperature increases. Process 2–3 is an isobaric heat addition process of the CC in which combustion takes place. Process 3–4 is an isentropic expansion process in turbine, where expansion work is produced and thereafter exhaust gases exits the expansion turbine.

1.2 Inlet Air-Cooled Gas Turbine Cycle

Figure 2 represents schematic diagram of gas turbine cycle with an inlet-air-evaporative cooling technique. In this inlet air evaporative cooling-system is used before the air enters the compressor. In this method, the ambient air first enters the evaporative cooling system and then air compressor. The evaporative cooling system consists of an air humidifier which is a wetted-rigid-pad where water is dispersed throughout the top of the pad and where air passes through the wet porous surface.

Water in the humidifier evaporates by soaking sensible heat from the ambient air entering the cooling system due to which relative humidity increases. There is a decrease in DBT of air but the WBT is constant. The theoretical limit is the WBT, but the performance of the evaporative cooler is usually ~80–90%.
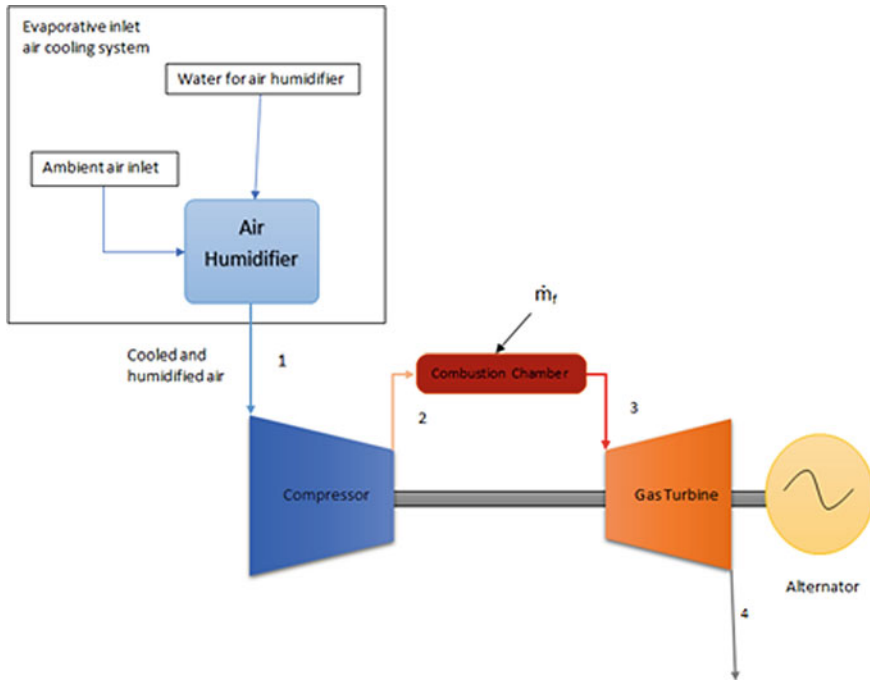
Fig. 2 Schematic diagram of a simple gas turbine cycle with inlet air evaporative cooling system

2 Literature Review

Ceylan et al. [1] carried out a thermodynamic performance investigation as well as psychrometric analysis of an evaporative system with an objective to achieve the desired level of relative humidity using evaporative cooling system. The system was found to be eco-friendly and its average refreshment efficiency and humidity were observed to be 38–54% respectively. Although its efficiency was observed to be lesser compared to the vapor compression system. Shukla and Singh [2] investigated a steam-injected-gas turbine power plant adopting the evaporative inlet air cooling technique. The authors revealed that an increase of ~3.2% in the thermal-efficiency was observed as the inlet air temperature was observed due to the adopted inlet-air-cooling technique. A study regarding performance improvement gas turbine cycle of Lagos-Nigeria was carried by Carmona [3] and the author concluded that adopting the evaporative cooling technique for gas turbine power plants even situated in tropical regions, seems effective while increasing power output and decrease in heat rate. An overview of combined-absorption-power and cooling cycle was studied by Ayou et al. [4], the adopted cycles were evaporative cooling and the mechanical chilling process. The authors further carried out the economic analysis as well and explained that it would be profitable to adopt a hybrid method with wet cooling. A study regarding the analysis of water droplet evaporation in a gas turbine inlet fogging

process was carried out by Kim et al. [5]. The study mainly studied the effect of variation in water injection ratios focusing on the modeling of evaporation in water injection droplets. The authors suggested that in order to increase the power output and thermal efficiency, it is better to adopt inlet air cooling during hot periods. A desiccant based evaporative cooling system subjected to performance augmentation of gas turbine cycle was studied by Zadpoor and Golshan [6]. The technique basically uses a desiccant-based dehumidification which is used for directing the air through a media or spray type evaporative cooler. The authors drew a conclusion that its performance is dependent on the design parameters adopted for the desiccant wheel made up of the same adsorptive material. Several studies [7, 8, 15] carried out an investigation of the performance of gas turbine based CCPP using different inlet air cooling techniques. The study modeled the evaporative cooling system of gas turbine based CCPP using different design parameters such as inlet air velocity, geometry, and size and depth of media, and a thermodynamic investigation was carried out. The study reveals that cycle output at 38 °C and 8% relative humidity, is 11 MW more as compared to without adopting the evaporative cooling. Pascale and Malino [14] wrote a technological review of inlet air-cooled gas turbine cycle and adopted two different cooling systems i.e. inlet air cooling by absorption and mechanical/electrical chillers. They developed commercial codes and thermodynamic modeling was done for both the systems and capabilities of both the systems were studied by taking yearly real temperature profiles of the different sites into consideration.

3 Thermodynamic Modeling

3.1 Compressor

In the present paper, axial flow compressor has been taken into consideration. The polytropic efficiency is taken for considering several thermodynamic losses occurring within it and all input parameters have been mentioned in Table 1.

The exit temperature of the compressor is calculated as,

$$t_{\text{comp(e)}} = t_i \cdot r^{\frac{\Upsilon-1}{\Upsilon}} \tag{1}$$

For the actual temperature leaving of the compressor, the equation would be

$$t'_{\text{comp(e)}} = \frac{t_{\text{comp(e)}} - t_i}{\eta_{\text{comp}}} + t_i \tag{2}$$

Mass balance for the compressor has been given as below:

$$\dot{m}_{a,\text{in}} = \dot{m}_{a,e} \tag{3}$$

Table 1 Input parameters [9–13, 16]

Parameter	Symbol	Unit
Gas properties	Enthalpy $h = C_p(\mathrm{T})\mathrm{d}T$	kJ/kg-K
Compressor	(1) Polytropic efficiency (η_{pc}) = 92.0	%
	(2) Mechanical efficiency (η_m) = 98.5	%
Combustor	(1) Combustor efficiency (η_{comb}) = 99.5	%
	(2) Pressure loss (p_{loss}) = 2.0% of entry pressure	%
	(3) Lower heating value (LHV) = 42.0	MJ/kg
	(4) Natural gas composition:	%
	$CH_4 = 86.21$, $C_2H_6 = 7.20$,	
	$CO_2 = 5.56$, $N_2 = 1.03$	
Gas turbine	(1) Polytropic efficiency (η_{pt}) = 92.0	%
	(2) Exhaust pressure = 1.08	bar
	(3) Exhaust hood temperature loss = 4	K
	(4) Turbine blade temperature = 1123	K

Actual work input (W_c) of the compressor has been calculated using equation given under:

$$W_c = c_{pa} \cdot \left(t'_{\mathrm{comp(e)}} - t_i \right) \tag{4}$$

3.2 Combustion Chamber (CC)

Combustion chamber (CC) of the gas turbine is the component where combustion takes place. When the compressed air from the compressor is fed to the CC, the fuel is injected takes place into the CC. Combustor exit temperature is taken as TIT. A pressure loss of 2% with respect to the compressor exit pressure is assumed within combustion chamber.

By mass and energy balance equation, the rate of mass flow of flue gases in the combustion chamber can be calculated :

$$\dot{m}_{\mathrm{comb(e)}} = \left(\dot{m}_{a,i} + \dot{m}_f \right)_{\mathrm{comb}} \tag{5}$$

$$(\dot{m}_f)_{\mathrm{comb}} \cdot \mathrm{LHV} \cdot \eta_{\mathrm{comb}} = \left(\dot{m}_e \cdot h_e - \dot{m}_{a,i} \cdot h_i \right)_{\mathrm{comb}} \tag{6}$$

Mass of fuel required to achieve required TIT is given as under:

$$\dot{m}_f = \left[\frac{\dot{m}_{a,i} \cdot h_g - \dot{m}_{a,i} \cdot h_{a,i}}{\mathrm{LHV} \cdot \eta_{\mathrm{comb}} - h_{g,e}} \right] \tag{7}$$

3.3 Gas Turbine

We are assuming isentropic expansion in expansion turbine. Flue gas from CC goes to gas turbine and expands on blades and in turn, produces expasnion work.

The inlet pressure of gas turbine is given by Eq. 8:

$$P_{\text{loss}} = p_{(\text{comb})e} - \left(P_{(\text{comb})e} - 0.02\right) \tag{8}$$

The theoretical $(t_{t(e)})$ and actual temperature $(t'_{t(e)})$ at the exit of the gas turbine is given as:

$$t_{t(e)} = t_{(\text{comb})e}/r^{(\Upsilon-1)/\Upsilon} \tag{9}$$

$$t'_{t(e)} = [t_{(\text{comb})e} - (\eta_{\text{gt}}.\left(t_{(\text{comb})e} - t_{t(e)}\right))] \tag{10}$$

The net gas turbine plant work output $(W_{gt,\text{net}})$ has been calculated by the given equation:

$$W_{gt,\text{net}} = W_{gt} - (W_c/\eta_{(\text{mech})}) \tag{11}$$

The efficiency of the gas turbine cycle is calculated by,

$$\eta\text{th} = \frac{W_{gt,\,\text{net}}}{Q} \tag{12}$$

3.4 Mathematic Modeling of Evaporative Cooling System

By applying mass-balance across the evaporator control-volume, we have

$$\omega_{\text{eva}(e)} = \omega_{\text{eva}(in)} + m_w \tag{13}$$

where ω represents specific humidity.

$$\omega = \frac{0.622\, p_{\text{vap}}}{p - p_{\text{vap}}} \tag{14}$$

where $p_{\text{vap}} = \varphi p_{\text{sat}}$ is the partial-pressure of vapor, φ = relative humidity and p_{sat} = pressure of saturated air corresponding to a given temperature value.

To carry out the energy balance across the humidifier we can write:

$$h_{\text{eva}(e)} = h_{\text{eva}(in)} + (\omega_{\text{eva}(in)} - \omega_{\text{eva}(e)})h_w \tag{15}$$

where $h_{\text{eva(e)}}$ and $h_{\text{eva(in)}}$ are the enthalpies of moist-air at exit and entry of the air humidifier system respectively. To find enthalpy at any point we use:

$$h_{\text{eva(e)}} = C_{p,\text{eva(e)}} \cdot t_{\text{eva(e)}} + (2500 - 1.88\, t_{\text{eva(e)}})\omega_{\text{eva(e)}} \tag{16}$$

$$h_{\text{eva(in)}} = C_{p,\text{eva(in)}} \cdot t_{\text{eva(in)}} + (2500 - 1.88\, t_{\text{eva(in)}})\omega_{\text{eva(in)}} \tag{17}$$

To find the exit temperature of evaporator we use [14]:

$$T_{DBT(e)} = T_{DBT(\text{in})} + \frac{N}{100}\left(T_{DBT(\text{in})} - T_{WBT(\text{in})}\right) \tag{18}$$

4 Results and Discussion

The study is the comparison of two different gas turbine cycles, one without inlet-air cooling and the other with adopting evaporative type of air cooling technique. Thermodynamic modeling was discussed earlier and based on that a computer program was written in C++ language for carrying out parametric analysis. The worthy results have been plotted for reflecting the influence of inlet air conditions and other performance parameters on gas turbine cycle performance.

The input parameters considered for the thermodynamic analysis are AT (T_{amb}), pressure ratio (r_{pc}), TIT (TIT), and the output parameters are thermal efficiency (η), compressor work output (W_{comp}), and network output (W_{net}).

4.1 Effect of Different Operating Parameters on the Performance of Simple Gas Turbine Cycle

Figures 3, 4, 5, 6 and 7 represents the effect of different cycle operating parameters on the performance of simple gas turbine cycle. All the results have been plotted using the input parameters given in Table 1.

4.1.1 Effect of Change in Pressure Ratio on Efficiency of Simple Gas Turbine Cycle

Figure 3 shows the effect of pressure ratio on thermal efficiency. The graph has been drawn keeping the AT as 288.15 K and relative humidity as 60%. It can be depicted from the graph that on increasing the pressure ratio the thermal efficiency keeps on increasing to some extent and then decreases, this trend can be observed for any TIT.

Fig. 3 Change in thermal
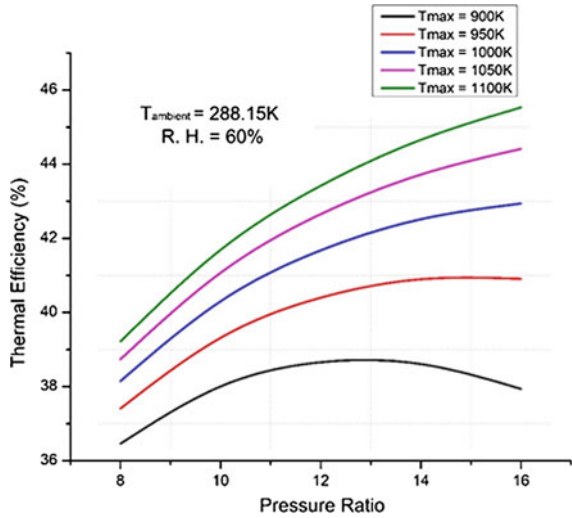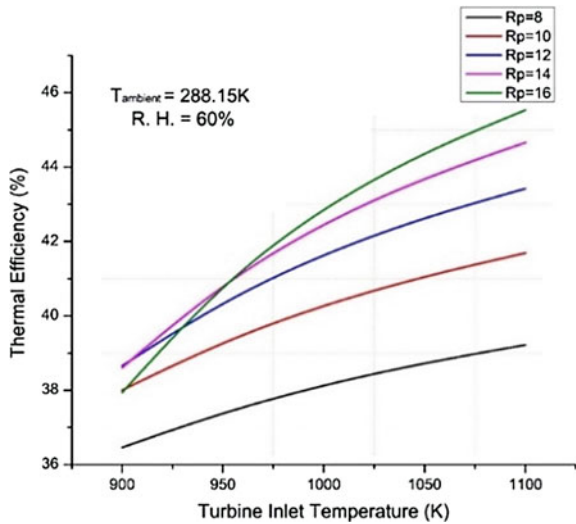efficiency with pressure ratio

Fig. 4 Change in thermal
efficiency with turbine inlet
temperature

The highest efficiency value (45.53%) for the cycle has been observed for highest
temperature i.e. is at pressure ratio 16 and TIT 1100 K.

4.1.2 Effect of Change in TIT on Efficiency of Gas Turbine Cycle

Figure 4 represents the effect of TIT on thermal efficiency and it can be seen from the
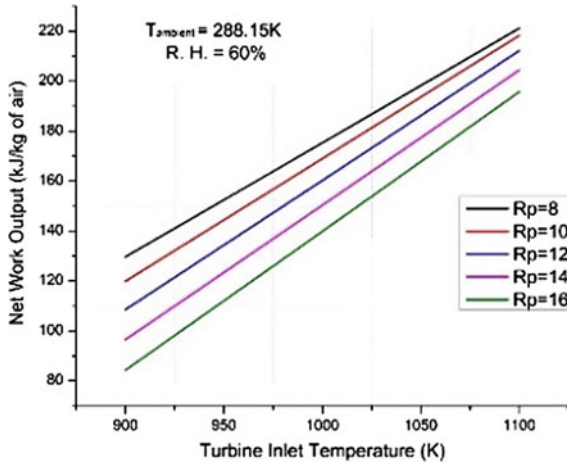curve that as TIT increases, thermal efficiency has also been found to be increasing

Fig. 5 Variation in net-work output with turbine inlet temperature
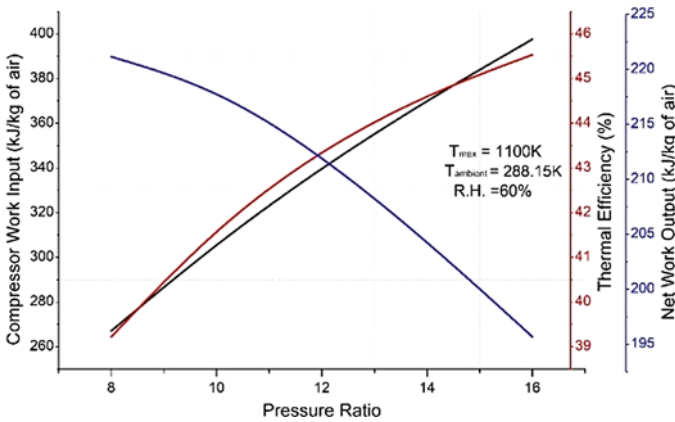
Fig. 6 Combined graph of change in compressor work input, thermal efficiency, network output with pressure ratio

and it has the highest value (45.53%) for TIT $= 1100$ K and $r_{pc} = 16$. This is due to the fact as TIT is increased, the enthalpy at entry to expansion turbine increases and hence work output also increases which further leaves a positive impact on thermal efficiency. The efficiency values are observed to be higher compared to the conventional papers, due to the assumptions taken in the paper.
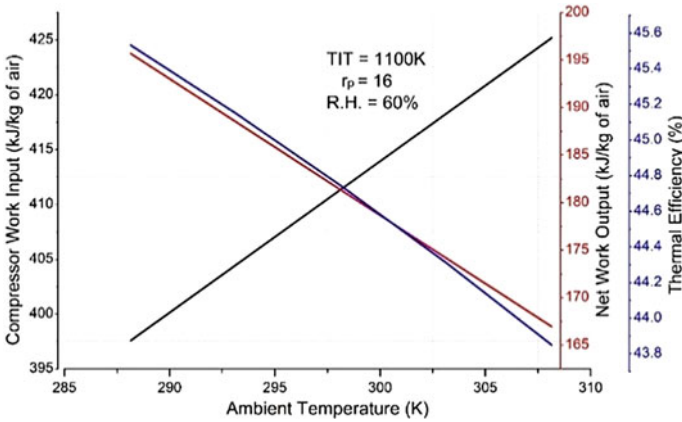
Fig. 7 Combined graph of change in compressor work input, thermal efficiency, network output with ambient temperature

4.1.3 Effect of Change in TIT on Network Output of Simple Gas Turbine Cycle

Figure 5 shows the effect of TIT on net-work output for a constant pressure ratio. The graph has been drawn keeping the AT as 288.15 K and relative humidity as 60%. It can be depicted from the graph that if we increase TIT, the net-work output increases linearly, and a similar trend can be observed for all the pressure ratios. The maximum net-work output (221.143 kJ/kg of air) can be found at $r_{pc} = 8$ and at the point where the TIT is maximum (1100 K).

4.1.4 Performance Curve Representing the Change in Pressure Ratio and Ambient Temperature for Simple Gas Turbine Cycle

Figures 6 and 7 are pictorial representations of effect of pressure ratio and AT respectively on various performance parameters. It can be depicted from Fig. 6 that as pressure ratio increases, an increase in compressor work is observed, the net-work output decreases (as compressor work input has increased and gas turbine output remains same), and thermal efficiency also increases. It can also be concluded that the compressor work input is found to be minimum at low-pressure ratio.

Figure 7 shows the effect of ambient air temperature on various performance parameters. The graph has been drawn keeping the TIT as 1100 K, relative humidity as 60%, and pressure ratio as 16. It can be depicted from the graph that on increasing the ambinet temeparture (AT), the compressor work input increases as compressor inlet temperature increases for a given pressure ratio and hence compressor discharge temperature also increases, and this results in decrease in net-work output and thermal efficiency has also been found to be decreasing. It can be clearly observed from the

curve that maximum efficiency and work output can be found at lower ambient temperature.

4.2   Effect of Different Operating Parameters on Gas Turbine Cycle Performance Using Evaporative Cooling

With the help of evaporator humidifier, we can lower down the temperature of ambient air entering the compressor. By this, the compressor work input will be decreased and in turn net-work output as well as the efficiency will be increased.

The ambient air passes through a spray of water or soaked pad containing water in it. The high temperature and low humid air enters, due to which some water evaporates. The energy that needs to evaporate the water, is taken by the air stream, which results in lowering of temperature of air, which enters the compressor inlet.

4.2.1   Effect on Compressor Work Input with a Change in Ambient Temperature of GT Cycle with and Without Inlet Air Cooling

With the help of inlet-air evaporative cooling, as the temperature of air entering the compressor lowers down, the work input to the compressor also decreases for the same ambient-temperature. Figure 8 shows the effect of inlet air cooling on compressor work with respect to AT, with and without inlet air cooling when all other properties are constant. By using evaporative inlet air cooling technique, the decrease in compressor work is observed to be 1.5–2% of the one when no inlet air cooling technique was used and minimum compressor work was observed at nearly~288 K.

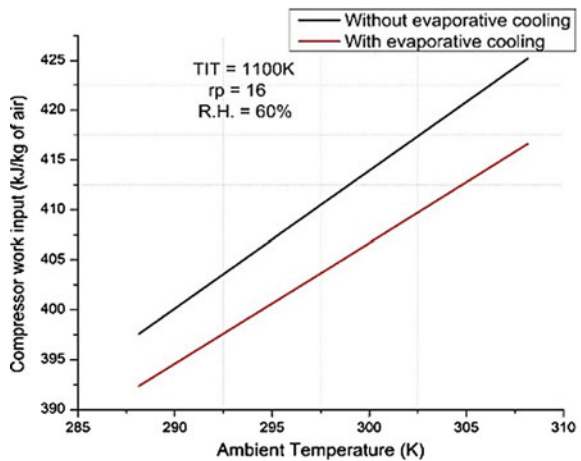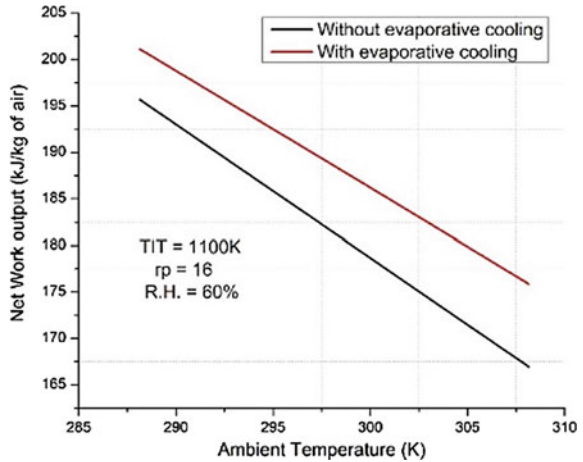**Fig. 8** Graph between compressor work input and ambient temperature (With without inlet and air cooling)

Fig. 9 Graph between
network output and ambient
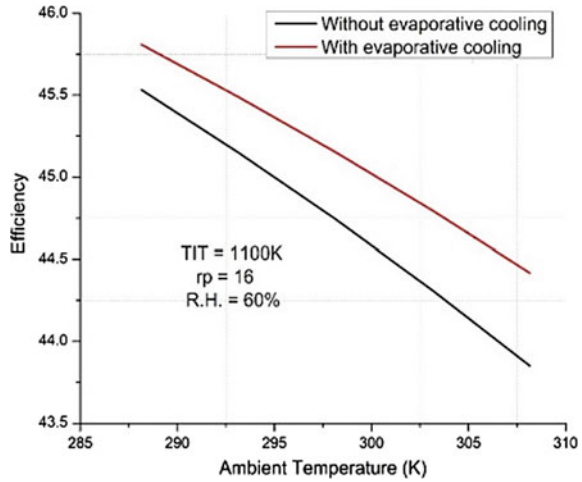temperature (With and
without inlet air cooling)

4.2.2 Effect on Net-Work Output with Change in Ambient Temperature of Gas Turbine Cycle with and Without Inlet Air Cooling

Figure 9 represents the variation of net-work output with change in ambient air temperature. As we decrease the AT, the compressor inlet temperature decreases for a given pressure ratio, and TIT, further net-work output has also been found to be increasing. It can be observed from the curve that there is a variation in net-work output of ~3–6% while adopting with and without inlet air cooling techniques.

4.2.3 Effect on Cycle Efficiency with Change in Ambient Temperature of Cycle with and Without Inlet Air Cooling

As compressor inlet temperature lowers down, the compressor input work decreases for the same turbine work output as pressure ratio and the TIT are constant. Due to which the net-work output increases and as the net-work output increases for the same fuel input, the thermal efficiency of the cycle increases for the same ambient temperature. Figure 10 shows the graph between energy efficiency with respect to AT with and without inlet air cooling when all other properties are taken as constant. By using evaporative cooling, thermal efficiency has been found to be.8–2.0% higher in comparison to the basic cycle when there was no inlet air cooling.

Fig. 10 Graph between thermal efficiency and ambient temperature (With and without inlet air cooling)

4.2.4 Effect on Compressor Work Input with Variation in Compressor Pressure Ratio with and Without Inlet Air Cooling

On decreasing the temperature of air entering the compressor with the help of the evaporator, the compressor work input decreases for the same pressure ratio. Figure 11 represents a comparison of results of compressor work input with a change in pressure ratio with and without inlet air cooling. It can be clearly seen from the curve that as pressure ratio is increased, work input increases but work input in case of evaporative-inlet-air cooled gas turbine is found to be 1–1.5% lesser in comparison to basic cycle.

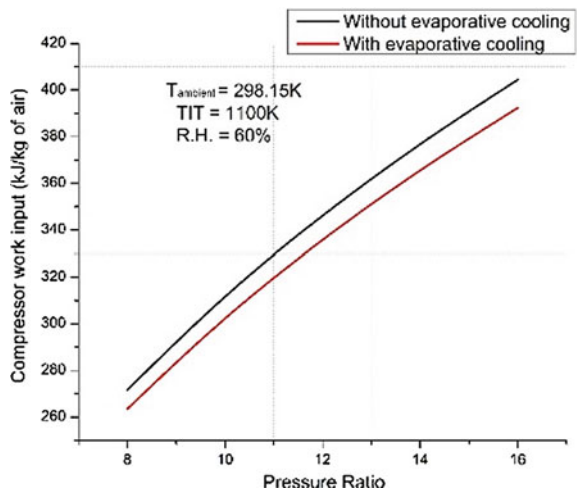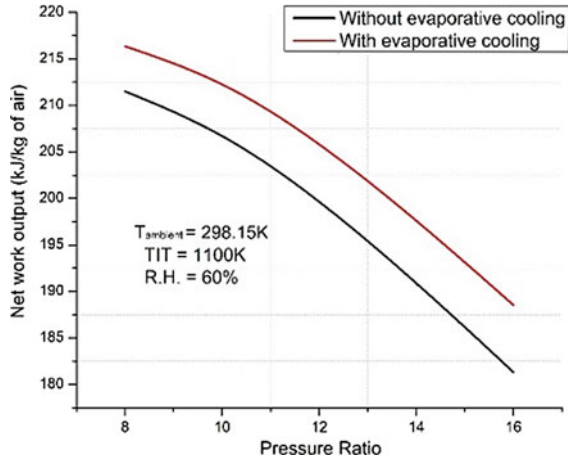**Fig. 11** Graph between compressor work input and pressure ratio (With and without inlet air cooling)

Fig. 12 Graph between net-work output and pressure ratio (With and without inlet air cooling)

4.2.5 Effect on Cycle Output and Cycle Efficiency with Variation in Pressure-Ratio of Gas Turbine Cycle with and Without Inlet Air Cooling

On decreasing the temperature of air entering the compressor (by adopting inlet air cooling), the compressor work input decreases which results in increase in net-work output for a adopted pressure ratio. Figure 12 shows the graph between net-work output with respect to pressure ratio with and without inlet air cooling when all other properties are taken as constant. By using evaporative inlet air cooling technique, the net-work output increases by ~1–2% for inlet air-cooled cycle w.r.t. the simple gas turbine cycle.

Figure 13 shows the graph between thermal efficiency with respect to pressure ratio with and without inlet air cooling when all other properties are taken as constant. As we lower down the compressor inlet temperature (using evaporative inlet air cooling technique), the compressor input work decreases due to which the net-work output increases. Further, the thermal efficiency of the cycle increases for the same ambinet temperature. By adopting evaporative cooling, change in thermal efficiency with respect to pressure ratio was found to be increased by 0.3–0.7% w.r.t. the simple gas turbine cycle.

4.2.6 Effect of Change in TIT on Thermal Efficiency of Gas Turbine Cycle with and Without Inlet Air Cooling

Figure 14 is the representation of variation in thermal efficiency of gas turbine cycle with and without adopting inlet air cooling when TIT is varied. It can be seen from the curve that efficiency for inlet air-cooled cycle has been found to be higher in comparison to without inlet air-cooled cycle. The variation is within the range of

Fig. 13 Graph between thermal efficiency and pressure ratio (With and without inlet air-cooling)
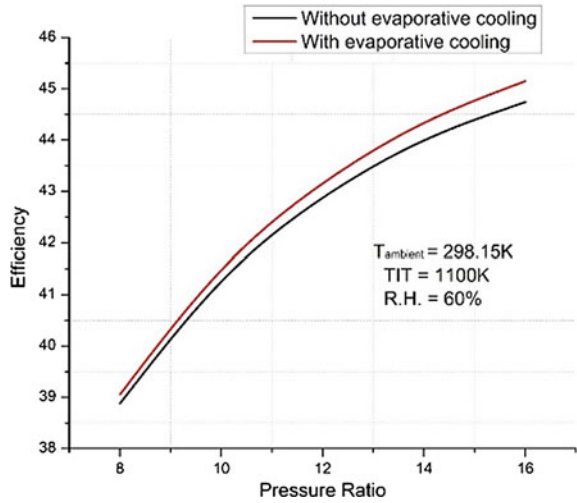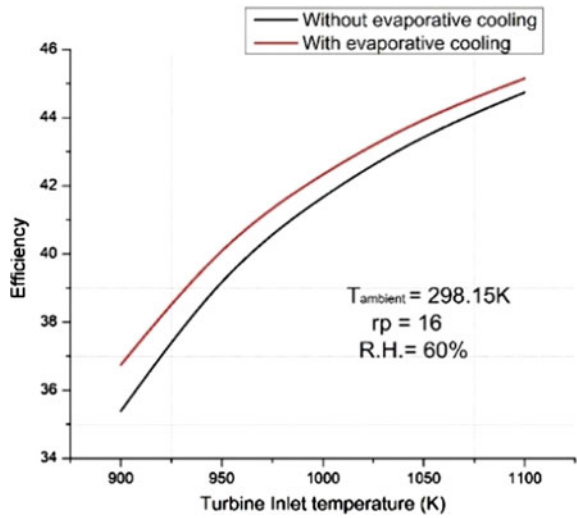

Fig. 14 Graph between thermal efficiency and turbine inlet temperature (With and without inlet air cooling)

~1–2.5%. It is due to the fact that as temperature of inlet air decreases, the compressor work input decreases. Also, since we increase the TIT, gas turbine work output also increases, which results in increase in thermal efficiency.

5   Conclusions

Based on the results obtained from gas turbine cycle with and without evaporative cooling, the following conclusion can be drawn:

- Thermal efficiency of both the gas turbine cycle (with and without evaporative cooling) has been found to be generally increasing with both TIT and r_{pc}.
- The maximum thermal efficiency for evaporative cycle has been found to be ~1–2.5% higher w.r.t. basic cycle, when TIT was being varied.
- Thermal efficiency of the gas turbine cycle decreases with a change in ambient temperature and was found to be maximum at 288.15 K.
- Similar is the case with work output as well i.e. as AT decreases, net-work output decreases.
- Gas turbine net-work output has been found to be increasing with an increase in TIT and r_{pc}.
- The compressor work input increases with an increase in pressure ratio.
- The performance of evaporative cooled gas turbine cycle has been found superior, compared to basic gas turbine cycle (higher work output (range ~1–2%), lower compressor work input (~1–1.5%), and higher thermal efficiency (~1–2.5%).

References

1. Ceylan İ, Ergün A, Acar B, Aydin M (2016) Psychometric and thermodynamic analysis of new ground source evaporative cooling system. Energy Build 119:20–27
2. Shukla AK, Singh O (2016) Performance evaluation of steam injected gas turbine-based power plant with inlet evaporative cooling. Appl Therm Eng 102:454–464
3. Carmona J (2015) Gas turbine evaporative cooling evaluation for Lagos-Nigeria. Appl Therm Eng 89:262–269
4. Ayou DS, Bruno JC, Saravanan R, Coronas A (2013) An overview of combined absorption power and cooling cycles. Renew Sustain Energy Rev 21:728–748
5. Kim KH, Ko HJ, Kim K, Perez-Blanco H (2012) Analysis of water droplet evaporation in a gas turbine inlet fogging process. Appl Therm Eng 33:62–69
6. Zadpoor AA, Golshan AH (2006) Performance improvement of a gas turbine cycle by using a desiccant-based evaporative cooling system. Energy 31(14):2652–2664
7. Hosseini R, Beshkani A, Soltani M (2007) Performance improvement of gas turbines of Fars (Iran) combined cycle power plant by intake air cooling using a media evaporative cooler. Energy Convers Manage 48(4):1055–1064
8. Shukla AK, Singh O (2017) Impact of inlet fogging on the performance of steam injected cooled gas turbine based combined cycle power plant. In: Gas turbine India conference December, American Society of Mechanical Engineers, vol 58509, p V001T03A004
9. Shivam M, Sanjay (2018) Energy and exergy analysis of air-film cooled gas turbine cycle: effect of radiative heat transfer on blade coolant requirements. Appl Therm Eng 129:1403–1413
10. Shivam M, Sanjay et al (2018) Advanced exergy analysis of air-film blade cooled marine gas turbine (LM2500 +), SAE Technical Paper 2018–01–1372. https://doi.org/10.4271/2018-01-1372

11. Shivam M, Sanjay et al (2019) Conventional and advanced exergy analysis of air-film blade cooled gas turbine cycle. In: Advances in fluid and thermal engineering, Springer Nature Singapore Pte Ltd. Book. ISBN: 978–981-13-6415-0
12. Anupam, Mishra S, Mohapatra AK, Sanjay (2019) Energy, exergy and emission performance analysis of air-film blade cooled gas turbine cycle for aircraft applications. SAE Technical Paper 2019-01-1389
13. Mishra S, Sharma A, Kumari A, Sanjay (2020) Response surface methodology based optimization of air-film blade cooled gas turbine for thermodynamic performance prediction. Appl Therm Eng 164:114425
14. De Pascale A, Melino F, Morini M (2014) Analysis of inlet air cooling for IGCC power augmentation. Energy Proc 45:1265–1274
15. Shukla AK, Singh O (2017) Thermodynamic investigation of parameters affecting the execution of steam injected cooled gas turbine based combined cycle power plant with vapor absorption inlet air cooling. Appl Therm Eng 122:380–388
16. Shukla AK, Sharma A, Sharma M, Mishra S (2018) Performance improvement of simple gas turbine cycle with vapor compression inlet air cooling. Mater Today: Proc 5(9):19172–19180